Report

Displacement based seismic assessment of existing bridges in regions of moderate seismicity

Author(s):
Bimschas, Martin

Publication Date:
2010

Permanent Link:
https://doi.org/10.3929/ethz-a-006237119 →

Rights / License:

ETH Library

Displacement Based Seismic Assessment
of Existing Bridges
in Regions of Moderate Seismicity

Martin Bimschas

Institute of Structural Engineering
Swiss Federal Institute of Technology Zurich

Zurich
August 2010

II

Preface

The seismic assessment of existing structures built before the introduction of seismic design codes is a challenge common to the majority of the countries worldwide. It is characterised by a large number of structures featuring qualities peculiar to the local building tradition and needing to be assessed with reasonable rapidity and sufficient accuracy, as dictated by the high costs typically entrained by actual retrofit measures. To face this challenge, the Swiss Federal Roads Office (FEDRO) recently developed a three-phase strategy for the assessment of the more than 3300 bridges of the national road network. While in the first phase a quick screening based on qualitative indicators is carried out, phases two and three both call for a quantitative assessment of the bridge, albeit to a different degree of accuracy.

Mr. Bimschas' doctoral dissertation has been funded by FEDRO with the explicit goal to provide the assessment tools needed by design engineers within phases two and three of the strategy. Quickly recognising the superiority of upcoming displacement-based approaches compared to force-based approaches currently used in Switzerland and in many other countries, the work focuses on both deformation demand and deformation capacity of existing multispan reinforced concrete (RC) bridges with continuous superstructure. Within this bridge typology Mr. Bimschas carried out a very comprehensive investigation by means of numerical, analytical or experimental investigations of a large number of key factors affecting seismic deformations. In the laboratory he conducted original large scale quasi-static cyclic tests on short wall-type RC bridge piers featuring design deficiencies, which shed important new light on the force-deformation behaviour of this kind of structural elements. While the core of the theoretical work is the systematic dissection, analysis and discussion of the nowadays more reputed simplified method for the estimation of the deformation demand of single- and multi-degree-of-freedom-systems with the aim of suggesting modifications improving their performance. Mr. Bimschas succeeded in his quest and was able to assemble an original set of recommendations for the improvement of the four methods that he identified as the most suitable for practical application. In doing so he took the local moderate seismicity and building tradition particularly into account, considering e.g. the effect of the strength degradation of the piers due to progressive failure of the lap-splice featured at the base of nearly all existing Swiss piers.

The significance of Mr. Bimschas' meticulous and inclusive work is twofold: It provides the tools to fulfil an urgent need to meet an important societal challenge in Switzerland and it significantly improves the knowledge about the seismic behaviour of multispan RC bridges. I am firmly convinced that his developments will find immediate application within design practice and that his findings will inspire further research in the field.

Zurich, August 2010   Alessandro Dazio

Abstract

Modern seismological research suggests that the seismic risk has often been underestimated in the past. As a consequence, even in regions of moderate seismicity – as e.g. in Switzerland – the seismic safety of existing structures may not always be sufficient from today's perspective. To cope with this situation, the Swiss Federal Roads Authority (ASTRA) has established a program for the seismic assessment of all bridges on the national highway system. It is considered that modern displacement based analysis techniques are best suited for a possibly realistic estimation of the expected seismic behavior of the bridges. It is the goal of this study to contribute to the establishment of appropriate analysis methods which are, on one hand, sufficiently accurate, while, on the other hand, also being possibly efficient thus allowing their application on a large number of bridges.

International experience from past earthquakes has shown that a variety of damage types can occur to bridges during an earthquake. However, when it comes to a real structural collapse, the cause is typically related either to superstructure unseating or to a failure of the piers. Therefore, these two types of damage need to be prevented by any means. Superstructure unseating can be avoided by providing sufficient seat lengths at all joints where superstructure movements can occur. Simplified criteria for checking the safety against unseating are given in the current Swiss and European codes. These criteria are only based on the geometric conditions of the superstructure seats and their application does not require a seismic analysis of the bridge.

In contrast, the seismic safety of the individual bridge members can only be assessed realistically based on an analysis estimating the seismic response of the structure. The primary purpose of such an analysis should be the prediction of the peak displacement demand of the relevant members – typically being the piers or the supporting frames. The expected peak displacements can then be compared to the deformation capacity of the members in order to evaluate their safety against failure. This text discusses the appropriate modeling of the various parts of the bridge as well as the choice of adequate analysis procedures.

Concerning the modeling of the structure, it is shown that the soil structure interaction at the pier foundations and at the abutments can have a substantial influence on the seismic behavior of a bridge. Recommendations are given for the development of engineering models describing the interaction at spread pier foundations and at the abutments. The proposed models are, on one hand, sufficiently simple for an application in normal bridge assessment cases. On the other hand, it is expected that they can capture important effects of soil structure interaction whose neglect might lead to a rather erroneous representation of the bridge behavior. It is shown that the uplifting or soil yielding at spread foundations can change the plastic mechanism in the pier. It is further shown that the flexibility and the mass of the embankment can control the response of short bridges almost completely. Recommendations are given in the text to cope with the inevitable uncertainties related to the corresponding modeling and the soil properties. It is additionally investigated which influences are to be expected from the torsional and rotational response of the superstructure. A good understanding of these aspects is important for the development of efficient but nevertheless reliable structural models of entire bridge systems.

For the establishment of appropriate analysis approaches, several existing methods are reviewed and their results are compared to response predictions coming from inelastic time history analyses. The primary focus of this review is on the practical applicability in engineering companies, on the provided accuracy and on the efficiency in the application. The various approaches are evaluated with respect to their ability to capture the relevant aspects of seismic bridge response, such as inelastic behavior and higher mode effects. In this evaluation due distinction is drawn between demand levels corresponding to rather moderate seismicity and those being more representative for higher seismic regions. The review identifies typical strengths and weaknesses of each of the considered approaches. These findings are used to develop very specific modifications to the existing procedures in order to improve the quality and reliability of their results while maintaining their simplicity and their efficiency. For each of the modified methods recommendations are given concerning the appropriate field of application and their limitations. A hierarchical concept is proposed in which several procedures can be applied with increasing sophistication, depending on the complexity of the problem and the

required accuracy. Mutual checking based on the various analysis results improves the reliability of the assessment.

Existing bridge piers often feature lap-splices in the potential plastic hinge regions. These can fail successively under severe seismic loading, causing a cyclic degradation of the flexural strength. An approach has been developed to allow for the influence of cyclic strength degradation on the displacement demand of the structure. For this purpose, the seismic response of degrading and non-degrading structures has been compared and an empirical relationship has been developed which approximately describes the increase of the deformation demand due to cyclic strength degradation. Based on this proposal, it is possible to perform the seismic analysis using a simplified procedure which assumes stable non-degrading cyclic behavior of the structure. The thus determined displacement demand can then be modified using the proposed empirical relationship in order to account for the influence of cyclic strength degradation.

Aside from the theoretical investigations concerning the determination of the seismic deformation demand, the results of a test series on three large-scale models of wall-type bridge piers are presented. The design and detailing of the test units was chosen in accordance with that of existing Swiss bridge piers. As a consequence, the test units featured several seismic deficiencies which are commonly encountered in older bridges. This refers especially to insufficient transverse reinforcement and to lap-splices at the pier bases. Existing models for the prediction of the expected shear critical behavior and the cyclic strength degradation have been presented and were applied to the test units. These predictions are compared to the observed behavior of the piers during the static-cyclic tests. The identified differences and the background of the observed failure mechanisms are discussed.

Kurzfassung

Die Ergebnisse moderner seismologischer Forschung legen nahe, dass das Erdbebenrisiko in der Vergangenheit oft unterschätzt wurde. In der Folge kann die Erdbebensicherheit bestehender Bauwerke aus heutiger Sicht selbst in mässig seismischen Gebieten – wie z.B. der Schweiz – unzureichend sein. Um dieser Situation gerecht zu werden, hat das Schweizer Bundesamt für Strassen (ASTRA) ein Programm zur Erdbebenüberprüfung aller Brücken des Nationalstrassennetzes ins Leben gerufen. Es wird davon ausgegangen, dass moderne verformungsbasierte Analyseverfahren sich für eine möglichst realistische Abschätzung des erwarteten Erdbebenverhaltens am besten eignen.

Ziel der vorliegenden Arbeit ist es, einen Beitrag zur Einführung geeigneter Analyseverfahren zu leisten. Diese Verfahren sollen einerseits hinreichend genaue Ergebnisse liefern, andererseits jedoch auch möglichst effizient sein, um eine Anwendung auf eine grössere Zahl von Brücken zu erlauben. Die internationalen Erfahrungen aus früheren Erdbeben haben gezeigt, dass verschiedene Arten von Schadensbildern an Brücken auftreten können. Für einen tatsächlichen Einsturz sind jedoch typischerweise entweder ein Absturz des Überbaus oder das Versagen von Brückenpfeilern verantwortlich. Aus diesem Grund müssen diese beiden Schadensformen unbedingt verhindert werden. Der Überbauabsturz kann durch die Sicherstellung ausreichender Auflagerlängen an allen Fugen vermieden werden. Einfache geometrische Kriterien für die erforderlichen Auflagerlängen des Überbaus sind in den Schweizer und europäischen Normen enthalten. Für deren Anwendung ist eine seismische Analyse der Brücke nicht erforderlich.

Im Gegensatz dazu kann die Erdbebensicherheit einzelner Brückenbauteile nur durch eine seismische Analyse der Brücke realistisch beurteilt werden. Der primäre Gegenstand einer solchen Analyse besteht in der Abschätzung des maximalen Verschiebungsbedarfs der relevanten Bauteile – welche typischerweise die Pfeiler oder die unterstützenden Rahmen darstellen. Die erwarteten maximalen Verschiebungen können dann mit den Verformungskapazitäten der Bauteile verglichen werden, um die Sicherheit gegen Versagen zu beurteilen. Im Rahmen dieses Textes wird sowohl die geeignete Modellierung der verschiedenen Teile einer Brücke behandelt, als auch auf die Auswahl eines angemessenen Analyseverfahrens eingegangen.

Hinsichtlich der geeigneten Modellierung wird gezeigt, dass die Bodenbauwerksinteraktion an den Pfeilerfundamenten und den Widerlagern einen erheblichen Einfluss auf das Erdbebenverhalten einer Brücke haben kann. Es werden Empfehlungen gegeben bezüglich der Entwicklung geeigneter Ingenieurmodelle, welche die Interaktion an Flachgründungen und Widerlagern angemessen beschreiben sollen. Die vorgeschlagenen Modelle sind einerseits hinreichend einfach für die praktische Anwendung in regulären Fällen. Andererseits kann man davon ausgehen, dass sie die massgebenden Effekte der Bodenbauwerksinteraktion erfassen, deren Nichtberücksichtigung zu einer unrealistischen Abbildung des Brückenverhaltens führen könnte. Es wird gezeigt, dass klaffende Sohlfugen und inelastische Bodenverformungen unter Flachgründungen den plastischen Mechanismus von Pfeilern ändern können. Es wird weiterhin gezeigt, dass die Nachgiebigkeit und die Masse des Erddamms hinter Widerlagern das Verhalten von kurzen Brücken nahezu vollständig dominieren können. Im Text werden Empfehlungen zum Umgang mit unausweichlichen Unsicherheiten gegeben, welche im Zusammenhang mit der Modellierung und den Bodeneigenschaften stehen. Es wird weiterhin betrachtet, welche Einflüsse aus dem Torsions- und Rotationsverhalten des Überbaus auf das seismische Brückenverhalten bestehen. Ein solides Verständnis dieser Aspekte ist wichtig für die Entwicklung effizienter und zugleich zuverlässiger Modelle für das Gesamtsystem einer Brücke.

Im Zusammenhang mir der Einführung geeigneter Analyseverfahren werden verschiedene bestehende Methoden betrachtet, und deren Ergebnisse werden mit den Resultaten aus nichtlinearen Zeitverlaufsberechnungen verglichen. Der primäre Fokus dieser Betrachtungen richtet sich auf die praktische Anwendbarkeit in Ingenieurbüros, auf die erzielbare Genauigkeit und auf die Effizienz bei der Anwendung. Die verschiedenen Verfahren werden hinsichtlich ihres Vermögens evaluiert, die relevanten Aspekte der seismischen Brückenbeanspruchung zu erfassen, wie z.B. das inelastische Verhalten oder den Einfluss höherer Eigenschwingungen. In dieser Evaluation wird zwischen Beanspruchungsniveaus unterschieden, die eher mässiger Seismizität entsprechen, und solchen, welche in höheren Seismizitätszonen zu erwarten sind. Die Untersuchung identifiziert typische

Stärken und Schwächen der einzelnen Verfahren. Die daraus resultierenden Erkenntnisse werden genutzt, um gezielte Modifikationen der bestehenden Methoden zu entwickeln. Ziel dabei ist, die Qualität und die Zuverlässigkeit der Resultate zu verbessern, während zugleich ihre Einfachheit und Effizienz bewahrt bleiben soll. Zu jedem der modifizierten Verfahren werden Empfehlungen gegeben hinsichtlich des geeigneten Einsatzbereichs und hinsichtlich seiner Grenzen. Ein hierarchisches Konzept wird vorgeschlagen, im Rahmen dessen in Abhängigkeit der Komplexität des Problems und der angestrebten Genauigkeit mehrere Analyseverfahren mit zunehmender Verfeinerung zur Anwendung kommen. Gegenseitige Kontrollen zwischen den verschiedenen Verfahren steigern die Zuverlässigkeit der Analyseergebnisse.

Bestehende Brückenstützen weisen häufig Übergreifungsstösse in den Bereichen potentieller plastischer Gelenke auf. Diese können unter starker seismischer Beanspruchung sukzessive versagen und dabei einen zyklischen Verlust der Biegetragfähigkeit verursachen. Es wurde ein Ansatz entwickelt, mit dem der Einfluss dieser zyklischen Entfestigung auf den Verformungsbedarf eines Bauwerks berücksichtigt werden kann. Zu diesem Zweck wurde das seismische Verhalten entfestigender und nicht-entfestigender Systeme verglichen und es wurde eine empirische Beziehung entwickelt, welche die Zunahme des Verformungsbedarfs infolge zyklischer Entfestigung beschreibt. Aufbauend auf diesem Vorschlag ist es möglich, die eigentliche Erdbebenanalyse mittels eines vereinfachten Verfahrens durchzuführen, welches von einem stabilen, nicht-entfestigenden zyklischen Verhalten ausgeht. Der derartig bestimmte Verformungsbedarf lässt sich dann unter Verwendung der vorgeschlagenen empirischen Beziehung modifizieren, um den Einfluss der zyklischen Entfestigung zu berücksichtigen.

Zusätzlich zu den theoretischen Betrachtungen hinsichtlich der Ermittlung des seismischen Verformungsbedarfs werden die Ergebnisse einer Versuchsserie an drei gross-massstäblichen Modellen wandartiger Brückenstützen präsentiert. Die konstruktive Durchbildung der Versuchskörper orientierte sich an jener bestehender Schweizer Brückenstützen und enthielt verschiedene seismische Schwachpunkte, wie sie häufig in älteren Brücken anzutreffen sind. Dabei handelt es sich vor allem um unzureichende Querbewehrung und um Übergreifungsstösse der Biegebewehrung am Stützenfuss. Bestehende Modelle zur Vorhersage des erwarteten potentiell schubkritischen Verhaltens und der zyklischen Entfestigung der Übergreifungsstösse werden vorgestellt und auf die Versuchskörper angewendet. Diese Vorhersagen werden mit dem beobachteten Verhaltenen der Brückenstützen während der statisch-zyklischen Versuche verglichen. Die festgestellten Abweichungen und die Hintergründe der beobachteten Versagensmechanismen werden diskutiert.

Table of Contents

x

1 Introduction

1.1 General Background

Earthquakes are phenomena with a pronounced stochastic character. This means that their occurrence by now cannot be predicted in advance, neither with respect to time nor location or magnitude. Typically only their average return period or annual probability of occurrence can be estimated. This leads to the effect that in regions of low or moderate seismicity over a longer period of time no major seismic events might occur. This does not mean that in such regions larger earthquakes are generally impossible. A good example for such a case is the city of Basel in Switzerland, which was struck by a severe earthquake in the year 1356 that destroyed or damaged large part the city's building stock. Based on historical reports the intensity of this earthquake is estimated as about IX on the MSK scale [Bac02]. Although a comparable earthquake has not occurred in the region of Basel since then, this single event shows that it is generally possible and could happen every day again – maybe not only in Basel.

Unfortunately longer periods without significant seismic events in a certain region can make us believe that the earthquake risk in this region is of little relevance and requires no or only secondary consideration. This is even more so as other actions for which structural engineers design buildings and bridges typically are more frequent. As a consequence, they are more present in our consciousness and it is also easier to quantify their required magnitude for design. Especially in regions of moderate or low seismicity, it is therefore not always straightforward to decide on the required design level for earthquake induced loads on structures. The fact that return periods of earthquakes may reach over many generations of human lives may lead to the (possibly unjustified) assumption that large earthquakes can be ruled out for a certain region. Modern seismological research, however, suggests that the difference between higher and lower seismicity refers not so much to the magnitude of the maximum possible earthquake, but rather primarily influences the average return periods of seismic events. As a consequence, even in regions which are considered less seismically active severe earthquakes may be possible. Their probability within a certain period of time is only lower.

As mentioned above, these low probabilities of occurrence for seismic events might lead to the conclusion that they are not of significant importance for the safety of structures, while the more frequent loads, like for example from gravity, wind, or snow, govern the design. However, taking into account that modern design codes typically strive for failure probabilities in the range of 10^{-5} to 10^{-6} per year (see e.g. [EC0], [JCSS01]), even an earthquake having a return period of, say, 1000 years, and thus an annual probability of occurrence in the order of 10^{-3}, can significantly contribute to – or even dominate – the overall failure probability of a structure if this level of seismicity was not taken into account during the design of the structure.

The aforementioned problems with awareness to and definition of seismic loading to structures have led to a significant underestimation of their importance in the past. In particular, up to 1970 in Switzerland there were no provisions for seismic loading included in design codes at all. Starting with 1970, first simplified regulations were included into the codes, which from today's perspective were clearly insufficient. From then on, in every new generation of codes the seismic design provisions became more demanding, reflecting the progressing research on this topic and the resulting better understanding of its importance for structural safety. The currently latest state of development is represented by the so called *Swisscodes* (e.g. [SIA261], [SIA262]) which are based on the Eurocodes (e.g. [EC1-1-1], [EC2-1-1]). The seismic provisions implemented in the *Swisscodes* introduce modern seismic design methodologies including capacity design principles and they are conceptually compatible with Eurocode 8 [EC8-1], [EC8-2]. New structures designed according to them can therefore be expected to have a significantly better seismic performance than older structures for which these concepts had not been followed. Furthermore, the *Swisscodes* represent current knowledge about the Swiss seismic situation based on latest research. As a consequence, and from today's perspective, new and recently built structures can be considered to have a sufficient seismic safety if the design provisions of the *Swisscodes* have been followed.

However, as Switzerland already has a well developed infrastructure network, large part of its existing bridge stock was built before the establishment of these modern seismic design codes, and, as a

consequence, the seismic safety of many of these existing bridges is less clear. Despite the fact that they were not explicitly designed for the seismic level which is considered adequate nowadays, they might happen to have an inherent "natural" capacity which can be considered sufficient (especially taking into account cost-benefit aspects in potential retrofit considerations). However, such an inherent capacity of individual existing bridges is uncertain.

For this reason, the Swiss Federal Roads Authority (*Bundesamt für Strassen – ASTRA*) has established a program to assess all Swiss highway bridges with respect to their seismic safety [ASTRA05a]. The assessment procedure for every bridge consists of two stages. In the first step, a brief screening of some selected bridge characteristics is conducted without any numerical analyses. Based on these characteristics it is decided whether the bridge can already be considered as sufficiently safe right from the beginning. If this is the case, no further analysis of the bridge will be conducted and the assessment finishes at this point. If, however, the bridge features one or more characteristics which might question a sufficient seismic safety, then the assessment procedure advances to a second stage which additionally requires a numerical analysis of the seismic behavior.

Although it is theoretically possible to conduct this numerical analysis using the force based procedures given in [SIA261] and [SIA262] for the design of new structures, a displacement based approach will be more adequate in many cases as it takes the individual displacement capacity of the bridge directly into account. Although it gives more realistic results and does not have to rely on unnecessary over-conservatism, such a displacement based design or assessment approach has not been established in Swiss codes so far. While for the assessment of existing building structures a documentation [SIA2018] has been published which is based on displacement based analysis principles, a comparable guideline for bridges does not exist yet. Despite the fact that the general underlying concepts are similar in the cases of bridges and buildings, a direct application of [SIA2018] on bridges would not be adequate because bridges feature certain characteristics which need special consideration.

To overcome these problems, ASTRA has initiated a research project at ETH Zürich with the goal to develop the basis of a displacement based assessment procedure for existing bridges. The methodology should take into account the particular Swiss situation, which means that (a) consideration is given to the moderate Swiss seismicity and (b) the particular structural types and typical detailing of existing Swiss bridges should be taken into account. The aim is to develop a methodology which, on one hand, is efficient so that it can be applied to a larger number of bridges, while, on the other hand, leading to sufficiently realistic estimations of the seismic bridge behavior. This document contains the results of the first part of this research project having been funded by ASTRA under award number AGB 2003/014. It provides recommendations on the modeling of existing Swiss bridges and the application of appropriate analysis procedures.

1.2   Outline

At the beginning, in Section 2 an introduction is given into the fundamental issues influencing the seismic safety of existing bridges. For this purpose, in Section 2.1 an overview of the various damage types is presented which have been observed after previous international earthquakes. The background of these damage patterns as well as their relevance for the seismic safety of bridges in regions of moderate seismicity are discussed. The subsequent Section 2.2 focuses on the particular situation of Switzerland and the current state concerning seismic safety and assessment of existing bridges. In this context, a summary of the seismic code provisions and their development during the past 60 years is given demonstrating the significant increase of the prescribed seismic demand over the various code generations. General information about the present Swiss bridge stock and the detailed properties of three existing sample bridges are presented as a reference for typical characteristics of older Swiss girder bridges. The current state of seismic assessment provisions in Switzerland is discussed by applying the guideline [SIA2018] on a fictitious bridge structure featuring similar properties as the previously presented real sample bridges. Although [SIA2018] was originally developed for building structures only, it is also referenced in the documentation [ASTRA05a] for the numerical analysis during the second stage of the assessment procedure for bridges. Finally, the general relevance of

seismic risks to the national infrastructure is discussed and the existing formal framework for the seismic assessment of bridges in Switzerland is outlined.

Section 3 is dedicated to selected topics concerning the structural modeling of bridges for seismic analysis. The primary focus of the presented discussions and recommendations is on the behavior of girder bridges with reinforced concrete piers as this type of structures may be considered to have the largest relevance for the Swiss situation. At the beginning, some general remarks are given on the appropriate complexity of structural models for seismic analysis (Section 3.1), on the modeling of the masses (Section 3.2) and on the conceptual approaches for the modeling of the inelasticity in the structural members (Section 3.3). In Section 3.4 the appropriate modeling of the bridge superstructure with respect to its rotational and torsional behavior is discussed. The influence of the rotational inertia is investigated in Section 3.4.1 based on a parametric study on the response of single cantilever piers with translational and rotational mass at their top. The conclusions concerning the multi-degree-of-freedom response of such systems are used to give recommendations on the approximate consideration of the related effects in simplified analyses where the rotational inertia of the superstructure is not taken into account explicitly. In a similar context, Section 3.4.2 contains a brief discussion on the appropriate position of the superstructure axis in simplified 2-dimensional analyses, taking into account that the center of stiffness and the center of mass in the superstructure cross-section do not necessarily coincide. In Section 3.4.3 the influence of the torsional superstructure stiffness on the global and local bridge behavior are investigated. Several modeling alternatives of a sample bridge featuring a bearing supported superstructure with noticeable torsional stiffness are compared. The consequences of the resulting rotational restraint at the pier tops on the development of the plastic mechanisms is studied taking into account the eccentricity between the superstructure axis and the bearing level as well as the limited moment that can be transferred by the bearings.

In Section 3.5 the importance of soil-structure interaction for the seismic behavior of bridges is shown and appropriate ways for its consideration in a dynamic model are presented. In this context, at first in Section 3.5.1 the influence of the soil flexibility and the potential uplifting at spread pier foundations is discussed. It is shown that an engineering model based on inelastic Winkler springs can generally capture the most relevant effects of the nonlinear soil-foundation behavior – including the potential for a plastic hinge in the soil. A practically applicable concept for the determination of the required parameters of the inelastic Winkler springs is proposed which is based on established engineering principles. It is shown that the resulting moment-rotation relationship for the soil-foundation behavior can be introduced efficiently into a structural model by means of a nonlinear spring. The consequences on the seismic response of MDOF bridge structures under transverse excitation are shown for two different foundation sizes. In Section 3.5.2 the importance of the soil-structure interaction at the abutments is demonstrated based on the measured response of two instrumented California highway overpasses. A practically applicable concept is proposed which combines a simple shear wedge model of the embankment with established modulus reduction curves to account for the soil inelasticity. It is shown that using this simple engineering model it is possible to develop a hysteretic spring representing the transverse stiffness of the abutment-embankment system. Furthermore, a simple relationship is proposed to estimate the tributary embankment mass participating in the transverse vibrations. By comparison with the measured response of one of the instrumented overpasses, it is shown that the proposed engineering concept can provide a reasonable estimate of the seismic abutment-embankment behavior.

In Section 4 the general principles of displacement based assessment and appropriate analysis methods for bridges are described in detail. At first, in Section 4.1 the general background and the advantages over traditional force based analysis are outlined. Some general remarks on the representation of the seismic input loading by means of response spectra are given in Section 4.2. The seismic input loading is further specified for the case of multi-support excitation in Section 4.3. The current state of research on its representation and the appropriate implementation into practical analyses are reviewed together with its influence on the potential for superstructure unseating at movement joints. In Section 4.4 the possible ways to model elastic viscous damping in addition to the energy dissipation by the hysteretic member response are reviewed. This also includes a comparison of various empirical equations which have been proposed in the literature for the simplified allowance of the influence of viscous damping on the seismic response.

A certain analogy exists between the influence of inelasticity on the deformation demand of single-degree-of-freedom (SDOF) systems and on the global deformation demand of multi-degree-of-freedom (MDOF) systems. This analogy can be used in displacement based analyses of MDOF systems to take into account the related effects in an efficient and simplified manner. Therefore, in Section 4.5 the seismic response estimation of inelastic SDOF systems is discussed in detail. In this context it is assumed that the seismic loading is given in the form of an elastic response spectrum so that the displacement demand of a linear elastic SDOF system having the same initial period can be determined directly. The background of two conceptual approaches for the approximate demand estimation of inelastic SDOF systems with the help of elastic displacement spectra is discussed. These approaches consist of either (i) the use of displacement modification factors or (ii) the equivalent visco-elastic linearization of the inelastic system. Two empirical relationships for ductility-dependent displacement modification factors proposed in the literature are reviewed. These are complemented by a corresponding proposal for ductility dependent force reduction factors from which a third relationship for a displacement modification factor has been deduced. Concerning the equivalent linearization approach, two sets of empirical equations for the properties of linearized systems proposed in the literature are considered. The resulting inelastic demand predictions from the various approaches, when practically applying them in combination with the response spectra of [SIA261] and [SIA2018], are compared and discussed. In particular, the consequences of different application alternatives of the individual methods are investigated.

The displacement based analysis of multi-degree-of-freedom (MDOF) systems by means of appropriate methods is the subject of Section 4.6. At the beginning, the relevant effects that need to be captured by a simplified analysis method are briefly discussed. Subsequently, the results of a study are summarized which was performed in the framework of a master thesis co-tutored by the author. This study compared the results of various displacement based analysis methods to the mean demand predictions from inelastic time history analyses (ITHA) which were taken as a reference for the evaluation of the simplified procedures. Several displacement based analysis procedures included in current Swiss and European codes and guidelines were also considered in the study. At this stage they were applied exactly in the form defined in the corresponding documents. The analyses were performed on a total of 9 different bridge models featuring different degrees of irregularity. The strengths and weaknesses of each of the simplified analysis methods are discussed in detail for three different seismicity levels, distinguishing between the quality of the global overall demand estimation and the accuracy of the predicted relative displacement shape. Based on further analyses and detailed evaluations of the resulting data, the reasons for potential deficiencies are investigated. These findings, on one hand, serve for the identification of appropriate application ranges for the individual methods and, on the other hand, represent the basis for specific modifications aiming at mitigating the identified deficiencies. The estimation of the overall global demand in the displacement based analysis methods according to the current Swiss and European codes and guidelines is implicitly based on the equal displacement approximation which in some cases yields unacceptably unconservative results. It is shown that by including the previously discussed concepts for the demand estimation of inelastic SDOF systems into the procedures a significantly better prediction of the global displacement demand can be achieved. By comparison with the reference ITHA results appropriate combinations of SDOF and MDOF analysis approaches are identified for different application ranges. Based on these findings a hierarchical concept consisting of several analysis methods with increasing sophistication is suggested.

The presented analysis approaches rely on a stable hysteretic response of the inelastic system throughout the earthquake response. In the case of existing bridges where lap-splices of the longitudinal reinforcement can typically be found at the bases of the piers, such stable hysteretic behavior may not be warranted. The large cyclic-inelastic deformations in the potential plastic hinge regions at the pier bases can cause a failure of the splices resulting in a degradation of the flexural strength. In Section 4.7 the influence of this degradation behavior on the displacement demand of SDOF and MDOF structures is investigated. For this purpose, the results from inelastic time history analyses performed on degrading and non-degrading systems in the framework of a master thesis co-tutored by the author are summarized and evaluated. The hysteretic rules for both types of systems had been calibrated on the observed cyclic response of corresponding bridge piers during large-scale static-cyclic tests performed by the author. The comparison between the response of degrading and

non-degrading systems gives insight into the conditions under which the degradation influences the displacement demand and into the tendencies of such an influence. Based on these findings, a tentative empirical equation is proposed which describes the relationship between the demand of degrading and non-degrading systems related to lap-splice failure. As a consequence, it is possible to perform a seismic analyses first using a simplified displacement based method without consideration of cyclic strength degradation, and subsequently modify the computed response by the proposed equation in order to allow for the influence of the splice related degradation. It is also shown that for Swiss conditions, consisting of moderate seismicity and rather large minimum splice lengths in existing piers, the proposed relationship will often suggest that no modification of the simplified analysis results is necessary.

A test series on 3 large-scale (1:2) models of existing wall-type reinforced concrete bridge piers has been performed by the author at ETH Zürich. The details of this quasi static-cyclic experimental campaign and the observed behavior of the test units are presented in Section 5. After an introduction into the background of and the motivation for the tests is given in Section 5.1, the layout of the test campaign is outlined in Section 5.2. This consists of a detailed description of the design of the test units (Section 5.2.1), an overview of the test setup and the instrumentation (Section 5.2.2), a prediction of the expected behavior during the tests based on theoretical models (Section 5.2.3), and a summary of the applied loading (Section 5.2.4). The piers had been designed featuring typical seismic deficiencies commonly found in older existing structures. In particular, this refers to insufficient transverse reinforcement and lap-splices of the longitudinal reinforcement in the potential plastic hinge region at the pier base. These two details can result in a shear critical behavior and in the above mentioned cyclic strength degradation, respectively. The applied prediction models refer to these types of damage mechanisms. The results from the test series are discussed in Section 5.3, including a detailed description of the observed behavior in Section 5.3.1 and a comparison between the measured and predicted response in Section 5.3.2. The observations are presented in the form of a comparison between the three test units at the various deformation states, discussing the corresponding development of damage, load-deformation response and crack pattern. Based on the comparisons between prediction and measured behavior, the capabilities of the theoretical models are evaluated with respect to the estimation of the inelastic load-deformation behavior, the identification of shear critical behavior, and the prediction of the flexural strength degradation due to lap-splice failure in the plastic hinge zone. In Section 5.4 the findings from the experimental campaign are summarized and the background of the observed failure mechanisms are discussed.

The overall conclusions from this document are presented in Section 6, consisting of a summary of the previous findings in Section 6.1 and an outlook containing recommended future research in Section 6.2.

Three annexes complement the main text by additional background information on selected topics: Annex A1 provides the derivation of the analytical equations describing the moment-rotation behavior of a spread foundation on inelastic Winkler springs discussed in Section 3.5.1. In Annex A2 the theoretical background of the simplified linear and nonlinear displacement based analyses approaches for MDOF systems discussed in Section 4.6 is described. The presented theoretical derivations explain how these methods are related to the principles of classical response spectrum analysis and which assumptions and approximations are implicitly introduced in each of the simplified approaches. Annex A3 contains the detailed results from the various MDOF analyses presented in Section 4.6 using the different simplified displacement based analysis methods and inelastic time history analyses as a reference. For these comparisons, the simplified displacement based procedures were applied in the form including the modifications proposed in Section 4.6. They can thus serve for the verification of the suggested analysis approaches.

2 Fundamentals of Seismic Safety of Existing Bridges

2.1 Typical Types of Seismic Damage to Bridges

Aside from theoretical considerations and numerical analyses, a valuable source of information for the seismic assessment of existing bridges comes from experience gained after previous earthquakes worldwide. Although such experience cannot always be generalized and the findings in many cases may not be directly accessible to quantification, they give an interesting insight into the "real" behavior of bridge structures under severe earthquake excitation. At the same time, when interpreting the damage that occurred during a past earthquake in another country, potential differences between the intensity of the seismic loading as well as differences in structural types and detailing in other countries should be kept in mind. Despite these limitations, it is important to be aware of the variety of damage types that can generally be caused by an earthquake. For this reason the experience gained internationally on different structural solutions and at various seismic levels is very helpful.

Large part of the experience related to seismic structural damage stems inevitably from regions with a higher seismicity than that of Switzerland. This is simply related to the fact that stronger earthquakes are more frequent in those regions. As outlined in Section 1.1, this does not necessarily mean that the level of seismic loading responsible for the observed damage in such cases is always significantly higher than what would be considered appropriate for Switzerland. At least in the higher seismic zones of Switzerland, the design earthquake is comparable to some earthquakes occurring in more seismic regions. Only the return period in Switzerland may be larger than in such regions of higher seismicity. As a consequence, some of the more frequent earthquakes in regions of higher seismicity may be in a similar order of magnitude than the less probable Swiss design earthquake. As the current way of building bridges only dates back to a comparatively short period of time, of say 60 years, it is not possible to rely on experience which is directly coming from Switzerland.

The types of seismic damage that can occur to bridges are multifold and depend on the structural system and the seismic intensity level. Nevertheless, there are some types which are more frequent or more important than others and therefore deserve special attention. The importance of a damage pattern also depends on its potential consequences and might possibly differ between a new design and an assessment situation. While some types of damage may cause significant economic losses, e.g. if required repair measures are not reasonably feasible after an earthquake, not all of them will necessarily represent the danger of a full collapse of the bridge. In a new design situation, it may be reasonable to also focus on such damage patterns which only represent high economical losses if these mechanisms can be prevented with comparatively low effort in the design phase. However, when assessing existing bridges, the primary focus will typically be on collapse prevention. As a consequence, the potential types of damage should also be evaluated with respect to their likelihood of causing a real structural failure.

Aside from a large number of reconnaissance reports which describe the observed damage to structures after individual major earthquakes, comprehensive overviews of typical types of damage to bridges can be found e.g. in [ASTRA05a], [PSC96] and [YK03]. A summary and discussion on some of the damage patterns that may occur is given in the following subsections.

a) Unseating of the Superstructure

One of the most devastating types of failure is related to unseating of the superstructure. Examples are shown in Fig. 2.1 and Fig. 2.2. This failure mode results from insufficient superstructure seat lengths at abutments and expansion joints as they are commonly found in older bridges. Due to non-synchronous ground motions at the different pier foundations and abutments, and in combination with the dynamic relative displacements of the superstructure, the gaps at the expansion joints can open up significantly. If this opening gets too large, the superstructure may loose its support and can drop. Generally, such relative motions can occur at any non-monolithic joint of the superstructure, either at the abutments, at intermediate expansion joints within the spans, or at joints on top of the piers.

Fig. 2.1: Unseating of superstructure at Interstate 5 during Northridge earthquake 1994
left: Gavin Canyon (Source: NISEE), right: Highway 14 (Source: NISEE)
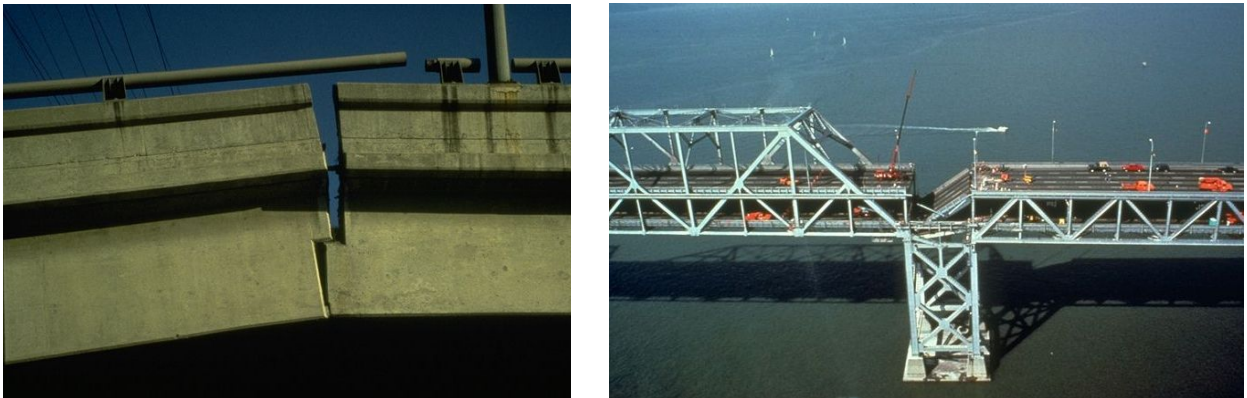
Fig. 2.2: Damage due to unseating during Northridge earthquake 1994 and Loma Prieta earthquake 1989
left: Almost unseating at Interstate10 / Fairfax, Northridge 1994 (Source: NISEE),
right: Complete unseating at San Francisco Oakland Bay Bridge, Loma Prieta 1989 (Source: NISEE)

Care should be taken with relying on the horizontal restraint provided by fixed bearings at the abutments, as these might fail, allowing the superstructure to move (almost) freely. In past earthquakes superstructure unseating has been observed even in cases where special restraining devices were provided, which had been especially designed to prevent seismic unseating. An example is the Nishinomiya bridge in Japan (Fig. 2.3), where one span fell down after an interaction between failure of the fixed bearings and subsequent failure of the restrainers. This shows that sufficient seat length cannot be replaced reliably by fixed bearings, or possibly not even by restrainers as the estimation of their required strength under seismic loading is very difficult. To a similar conclusion come Somaini and Bachmann in [SB89] showing that the horizontal forces in fixed bearings can reach very high levels even during comparatively low seismic excitation, resulting in a high probability of bearing failure.
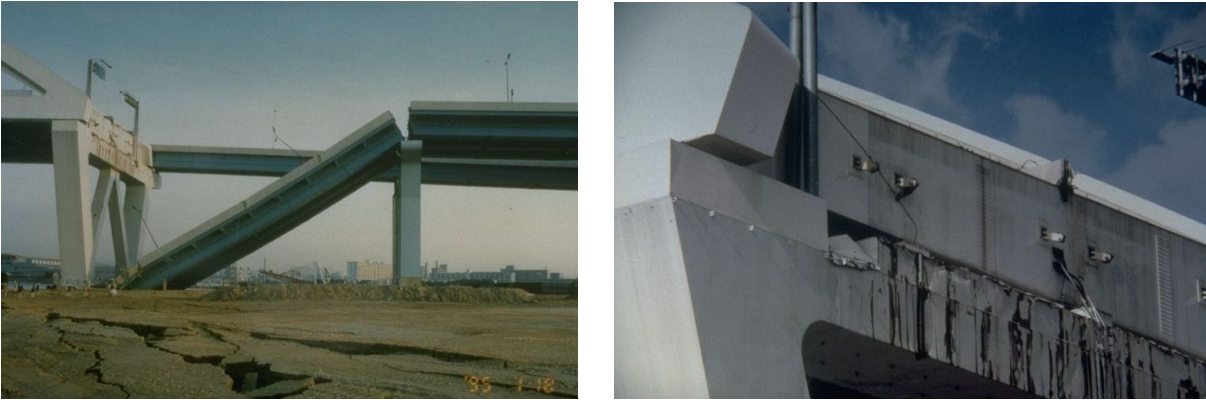
Fig. 2.3: Unseating at Nishinomiya bridge during Kobe earthquake 1995
left: Overview of fallen span (Source: Christopher R. Thewalt, NISEE),
right: Detail of failed restrainers (Source: Christopher R. Thewalt, NISEE)

In a similar way, care should be taken with simply supported steel or precast concrete girders which are directly supported on top of the piers. Although they may be interconnected by in-situ concrete and some reinforcement crossing the joint, this detail may not be sufficient to consider the superstructure as continuous for the issue of unseating. If the girder of one span looses its direct support on top of a pier, the in situ concrete connection would have to transfer the full vertical support force to the pier or to the neighboring span with which it is connected. If this shear force cannot be transferred, unseating with subsequent falling down of the girder will still occur. Especially, a continuous in-situ bridge deck on top of precast girders should normally not be considered as a sufficient measure against unseating. Examples of corresponding failures are shown in Fig. 2.4 and Fig. 2.5.

Fig. 2.4: Unseating of I-5 Highway 14 during Northridge earthquake 1994 (Source: Mark A. Aschheim, NISEE)

Fig. 2.5: Unseating of Ming-Chu bridge during Chi-Chi earthquake 1999 (Source: EERI)

2.1 Typical Types of Seismic Damage to Bridges

Although unseating is normally related to motions in the longitudinal direction, significant shifting of the superstructure can also occur in the transverse direction. If such transverse shifts occur, they are typically accompanied by bearing failure. Examples of transverse superstructure shifting can be found in Fig. 2.6 and Fig. 2.7. The detail in the latter figure shows the destroyed bearing with its shifted upper plate having lost any support by the lower bearing parts.

Fig. 2.6: Large transverse shift of superstructure after Kobe earthquake 1995 (Source: NISEE)

The potential consequences of transverse superstructure shifting depend on the type of girder cross-section and the substructure. For example, a box-girder supported by a wide pier top or a multi-column bent with a cap-beam will not be susceptible to transverse unseating. However, potential consequences related to transverse relative displacements of the superstructure should be checked on an individual basis, taking the particular geometric boundary conditions into account.

Fig. 2.7: Bearing failure and subsequent transverse shift at pier of Hanshin Expressway during Kobe earthquake 1995 (Source: Christopher R. Thewalt, NISEE)

b) Failure of the Substructure (Piers)

Another potential collapse mechanism that has been observed in many bridge structures after previous earthquakes is the damage or failure of the substructure, i.e. typically the bridge piers. In Fig. 2.8 one of the most famous cases, the Hanshin Expressway, is shown which collapsed during the 1995 Kobe earthquake over a length of several spans due to pier failure. It is obvious that pier failure, just as

unseating, can lead to falling down of the superstructure and thus a complete collapse of the bridge. As such, it can be considered a severe failure type which requires special attention in the assessment of existing bridges.
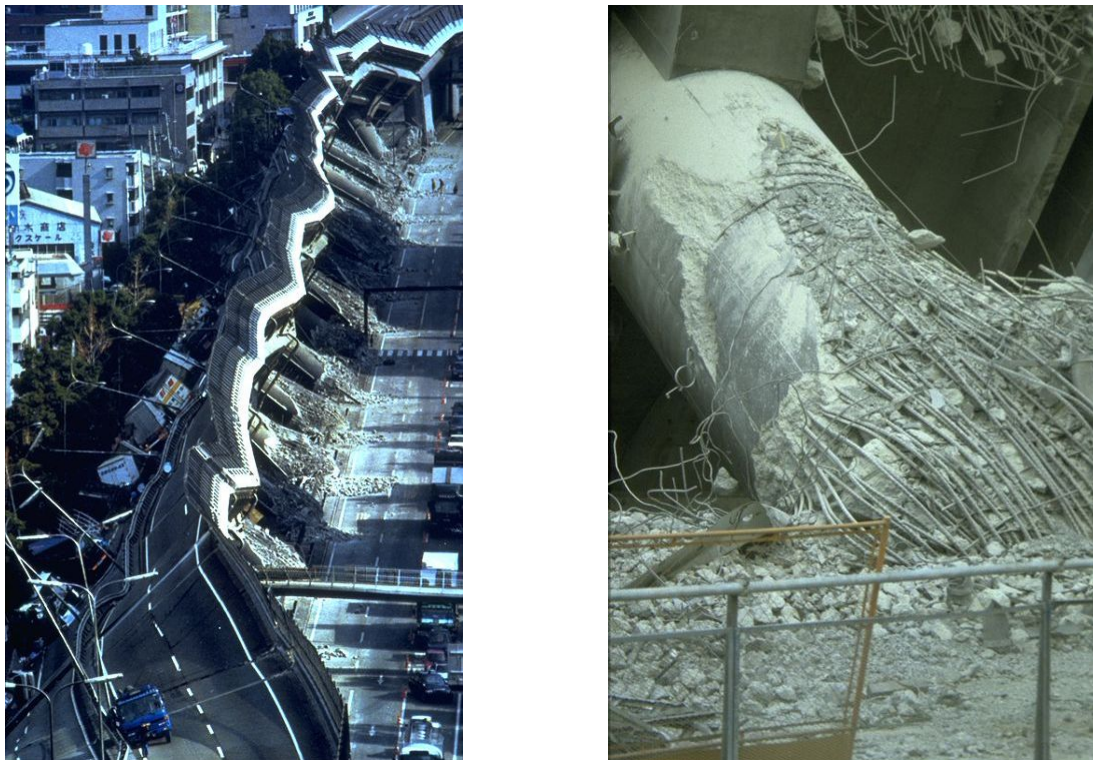

Fig. 2.8: Collapse of Hanshin Expressway during Kobe earthquake 1995 (Source: unknown)

Different kinds of failure modes have been observed in bridge piers which can be subdivided roughly by the actions a pier has to carry into flexural, shear and axial load failure. Pure flexural or shear damage only leads to a loss of horizontal capacity while axial failure will undoubtedly result in a collapse as the weight of the superstructure cannot be carried anymore. In contrast, (partial) loss of horizontal capacity from flexural or shear damage does not necessarily have to result in a total collapse.

As the primary purpose of a pier is to bear the vertical loads, horizontal capacity and stiffness during and immediately after an earthquake are rather required to prevent stability problems e.g. from P-Δ-effects. In a redundant structure with multiple load paths other members may exist that still can provide horizontal stiffness to the total structure, even after single piers have lost part of their horizontal capacity. For example, in a bridge with a continuous superstructure, abutments and some less damaged piers might be able to contribute sufficient horizontal capacity to the system after flexural degradation of individual more heavily damaged piers. This, of course, requires that these horizontally degrading piers can still carry their full axial load, as for the vertical loads normally no alternative load paths exist that could be provided by other members. Furthermore, it needs to be emphasized that the availability of the mentioned horizontal redundancy in many cases may not be certain and can depend on a variety of conditions. The collapse of the Hanshin Expressway, as shown on the left side of Fig. 2.8, is a good example of a structure where a redistribution of horizontal action was not possible. Therefore, great care should be taken in simply relying on horizontal redundancy in the case of flexural or shear degradation.

Furthermore, even if loss of axial load capacity can generally be considered more critical than pure degradation of horizontal capacity, the two issues are often interrelated as flexural and shear damage can, as a consequence, also lead to loss of axial load capacity. Therefore, it may not always be possible to clearly separate horizontal degradation from axial failure in the analysis of a structure.

Generally, flexure requires a tension chord and a compression chord within the member, which are represented by tension reinforcement and a concrete compression zone (together with the compression reinforcement), respectively. Consequently, flexural failure can result from damage to either one of the two chords. Examples of flexural damage to piers during earthquakes are shown in Fig. 2.9.

Fig. 2.9: Flexural damage to bridge piers
left: Hanshin Expressway Pier 54 after Kobe earthquake 1995 (Source: Christopher R. Thewalt, NISEE),
right: Uono-Gawa bridge after Niigata-Ken Chuetsu earthquake 2004 (Source: Mitsutoshi Yoshimine, NISEE)

In the case of continuous reinforcement, the only possible mechanism for a failure of the tension chord is the fracture of the longitudinal reinforcement. This can be a result of previous buckling in compression (during the preceding half-cycle of the seismic loading) which may occur if the longitudinal bars are not closely restrained by transverse reinforcement. In the case of rectangular cross-sections, only the corners of hoops can be considered to provide significant transverse restraint to the longitudinal reinforcement, which is important as in existing structures typically not every longitudinal bar is located close to a hoop corner. For both rectangular and circular cross-sections, a reliable restraint furthermore always depends on the detailing of the hoops. Unless they are closed by hooks fully anchored into the concrete core, or unless they are continuous in the case of spirals, the hoops will open after concrete spalling and loose their effectiveness.

Alternatively, fracture of the tension reinforcement can also result from excessive strains in the cracks. These strains are influenced by the bond behavior and the post-yield stiffness of the bar. Especially non-ductile types of reinforcement with low ultimate strains and low post-yield stiffness are prone to this kind of failure. While the tension strain capacity can be further reduced under reversed cyclic loading, the low post-yield stiffness leads to a significant strain concentration within the cracks.

In many cases, the longitudinal reinforcement is not continuous over the full height of a pier. Lap-splices are a typical weak spot which can fail under cyclic loading. Especially if they are located in regions of the RC member where significant cyclic-inelastic strains develop, as for example typically at the pier bases, lap-splices are likely to fail once the cover concrete has spalled. Actually, concrete spalling can even be expedited by the tension stresses caused by the lap-splice. This is why lap-splices in modern seismic design concepts for ductile structures are normally not allowed anymore within the inelastic regions of reinforced concrete members. It should be noted that other types of splices can also fail, if they are not able to sustain several large cycles of inelastic loading. The primarily flexural failure of the piers shown in Fig. 2.8, e.g., was caused to a large extent by failure of butt-welded splices of the longitudinal reinforcement. Care should therefore also be taken in the case of welded splices or splices by other mechanical devices if those have not been proven to sustain the required level of seismic demand.

A third type of problem in the flexural tension chord can result from premature termination of longitudinal reinforcement. Under earthquake excitation the pier can develop an overstrength moment in the plastic regions, which is related to the tension strength of the reinforcement. In combination with tension shift effects from inclined shear cracking, this can lead to an increase in moment demand outside or between the plastic regions of the pier. If the anticipated moment demand distribution along the pier height, that was used for the design of the reinforcement termination, was only based on the yield moment in the plastic region, it is likely that the longitudinal bars are terminated too early. This deficit of moment capacity at the point of termination can lead to a shift of the plastic hinge to the termination zone. The consequence is a reduced displacement capacity of the pier as the shifted plastic hinge relates to a shorter shear span. An example of a shifted plastic zone due to premature reinforcement termination is shown in Fig. 2.9 on the right side. Here, the damage to the pier occurs at the same height where the inner reinforcement layer is terminated.

Flexural damage to the concrete compression chord typically results from excessive (cyclic) compression strains. Confinement of the concrete by either closely spaced transverse reinforcement or adjacent members can increase the compressive deformation capacity (as well as strength) of the concrete considerably. However, normally in existing bridges that had not been explicitly designed for ductile behavior, the amount and detailing of the transverse reinforcement do not provide significant confinement. As for the case of transverse anti-buckling restraint for the longitudinal reinforcement, the hoops would have to be closed by hooks fully anchored into the concrete core in order to remain effective after concrete spalling. This is typically not the case in existing bridges. While confinement by adjacent members can also be found in existing structures, its effect decreases quickly with distance from the adjacent member and is therefore of little use. As a result, in the majority of cases, the compressive strain capacity of concrete in existing bridge piers will be limited to the value under unconfined conditions. Opening of hoops (after spalling of the concrete cover) and buckling of the longitudinal reinforcement can further promote the disintegration of the compression zone. An example of severely crushed concrete as a result of inelastic flexural loading is shown on the left side of Fig. 2.9.

While fracture of the tension reinforcement or lap-splice failure alone are unlikely to result in a loss of axial load capacity, crushing of concrete, which under cyclic loading progresses towards the center of the cross-section, can lead to an axial load failure. This shows, as mentioned above, that flexural damage in an advanced stage can result not only in degradation of horizontal capacity, but also lead to a loss of vertical load bearing capacity. However, this will normally only occur in very advanced stages of degradation and after severe flexural damage, as the axial load ratio in bridge piers is typically not very high. The concrete therefore needs to be heavily damaged before the remaining core is not capable of bearing the gravity loads anymore. It is more likely that the severely damaged plastic hinge zone first results in shear problems which can subsequently cause an axial load failure. This issue will be discussed below in connection with the shear capacity.

Shear failure is the second potential cause for degradation of horizontal force capacity of bridge piers. It is a failure mode that has been observed many times in bridge piers after earthquakes worldwide. Especially short and rather squat piers are prone to shear failure because, for a given cross-section and thus flexural strength, the shear demand of a member increases with decreasing shear span. Examples for squat piers failing in shear are shown in Fig. 2.10.

In both cases the piers were rather short with massive cross-sections. Coming from traditional force based analysis, at first sight one might think that such high (flexural) strength, coupled with a very short lever arm, should result in high seismic safety of the piers. Unfortunately, often the opposite is true. The very high stiffness of the piers attracts high inertia forces, possibly also related to high spectral accelerations. If the structure cannot bear these forces in its elastic range, it attempts to activate additional displacement capacity by entering into the inelastic range. The very high flexural moment capacity, combined with the short height, can result in extreme shear forces when the pier tries to develop a plastic hinge at the base. If the transverse reinforcement had not been designed for this level of shear demand, a shear failure can be the consequence.

Shear failure is considered particularly critical for two reasons: (a) It is typically rather brittle and can occur already at rather small displacements, limiting the deformation capacity of the pier significantly, and (b) it is often accompanied or followed by a loss of axial load capacity. The axial failure is related

to the wide open diagonal shear cracks which cannot transfer significant stresses anymore and result in the upper part of the pier sliding down along these cracks.

Fig. 2.10: Shear failure of squat bridge piers
left: Hanshin Expressway Pier 57 after Kobe earthquake 1995 (Source: Christopher R. Thewalt, NISEE),
right: Wu-Hsi bridge after Chi-Chi earthquake 1999 (Source: Jack P. Moehle, NISEE)

Particularly brittle behavior occurs if the shear capacity is insufficient to let the pier develop a plastic mechanism, i.e. if the shear capacity is lower than the demand that corresponds to the nominal yield moment in the plastic hinges. In this case, the pier will already fail in the elastic range loosing the entire plastic deformation capacity. This can mean, for example, that a deficit of shear capacity in the order of, say, 20% can result in a loss of deformation capacity of some 80% if the flexural displacement ductility capacity would have been $\mu_\Delta = 5$ without the shear failure.

But even if sufficient shear capacity is provided for a plastic mechanism to develop, a shear failure can still occur in the inelastic range, although the shear demand does not further increase anymore (significantly). This is because the large cyclic deformations cause damage to the internal shear bearing mechanisms leading to a degradation of shear capacity under cyclic inelastic loading. When the degrading shear capacity drops below the demand resulting from the plastic mechanism, a failure occurs.

Fig. 2.11: Loss of shear capacity in heavily damaged plastic hinge region
Mission Gothic bridge after Northridge earthquake 1994 (Source: Graham C. Archer, NISEE)

One particular case of this phenomenon is a localized shear failure in plastic hinge regions that has already been observed many times. These regions can first get heavily damaged by flexural deformations leading to wide open cracks and possibly crushing of the concrete. As a consequence, the shear capacity in the plastic hinge is reduced significantly allowing a transverse movement inside the plastic hinge. Axial load failure can result subsequently. Piers which are rotationally fixed at the top and the base, resulting in double bending, are more prone to shear failure inside a plastic hinge than cantilever type piers. As the moment capacity in a plastic hinge is likely to degrade with

increasing flexural damage, the shear demand in a cantilever pier will be reduced in proportion to this flexural degradation. In members with double bending, the shear force results from the moment capacities of both ends. As a consequence, flexural degradation in only one plastic hinge will lead to a lower reduction of shear demand compared to a cantilever pier. An example of a pier with a heavily damaged plastic hinge region and subsequent loss of shear capacity is shown in Fig. 2.11.

A third type of shear problem, called *sliding-shear failure*, is shown in Fig. 2.12. It can occur in large open flexural cracks which cross the entire cross-section as a result of bidirectional loading. Sliding-shear problems are mostly found at the member ends where they join into other members or into foundations, or, as in Fig. 2.12, at discontinuities along the member length. Construction joints with insufficient roughness of the contact surfaces are more prone to sliding-shear failure. Normally, this phenomenon only occurs in members with low to zero axial force, as this promotes wide open flexural cracks after yielding which may not fully close again in the phase of zero curvature during reversed cyclic loading. In the majority of cases, sliding-shear is not a big problem in bridge piers due to their axial load. Furthermore, the potential consequences normally are not as severe as for other types of shear failure, as sliding-shear is unlikely to result in a loss of axial load capacity. At significant sliding movements, however, the longitudinal reinforcement could be damaged due to large local deformations as a result of kinking in the sliding plane.

Fig. 2.12: Onset of sliding shear in pier of Wu-Hsi bridge during the Chi-Chi earthquake 1999
(Source: Jack P. Moehle, NISEE)

The substructure does not always consist of single piers. An alternative can be multi-column bents which act as frames in the transverse bridge direction. If the superstructure is bearing supported, a cap beam connects the column tops below the bridge girder. In case of a monolithic connection, the cap beam can be integrated into the superstructure, serving also as a cross girder for its cross-section. The load carrying mechanism of such a frame structure in the transverse direction is somewhat more complex than that of individual piers in single or double bending. On one hand, the system provides some extent of redundancy. On the other hand, it also introduces additional points of potential failure.

The columns can generally have similar weak spots as in the case of individual piers. Further potential weak spots can exist in the beam-column joints of the bent as well as in the cap beam. One typical problem is that the frame was designed primarily for gravity loads which result only in negative (closing) moments in the frame corners. However, under transverse seismic loading it is likely that in the joints moment reversals will occur, creating also positive (opening) moments, as these are required for a plastic mechanism. If the dimensioning and the detailing of the columns, cap beam, and joints did not take this opposite sign of the moment into account, a failure is probable which can even lead to the superstructure falling down.

At the same time, the superposition of seismic moments and gravity moments can result in a longer region of negative moments in the cap-beam than from gravity loads only. If (part of) the upper reinforcement was terminated towards the center of the beam, based on an anticipated moment distribution from (primarily) gravity loads, a deficit of moment capacity at the point of termination occurs. Significant damage and failure of the cap-beam are potential consequences.

Aside from that, the beam-column joints are points of complex and severe stress concentrations under cyclic-inelastic loading. Therefore, any general detailing deficiencies in the joints are likely to cause problems for the seismic behavior of the frame. The plastic hinge in the corner region can either develop at the beam end, the column top or within the joint, depending on which part has the lowest flexural capacity. The corresponding weakest component will have to provide the required inelastic deformation capacity. All the damage and failure mechanisms related to shear and flexure discussed above for individual piers can of course also occur in cap-beams, especially if the plastic hinges develop inside of them.

Fig. 2.13: Collapse of the Cypress Viaduct during the Loma Prieta earthquake 1989 (Source: NISEE)

In Fig. 2.13 the Cypress Viaduct in Oakland, California, is shown as a special case. The bridge consisted of two levels of superstructure, resting on a two-story two-column bent as a substructure. Large part of the Cypress Viaduct collapsed during the 1989 Loma Prieta earthquake, with particularly the upper deck falling down. Here, joint failure in the frame corners is considered to have mainly contributed to the collapse of the structure [PSC96].

c) Damage to Abutments

Abutments have considerable contact to the embankment behind the backwall and the wingwalls and to the soil at their bases in the form of spread or pile foundations. The seismic behavior of abutments is therefore strongly influenced by soil-structure interaction. On the other hand, abutments support the superstructure which represents the second boundary condition for their seismic behavior. The influence of the superstructure obviously depends on the degrees of freedom which are connected to the abutment. However, the behavior with respect to these degrees of freedom can change during severe seismic events, compared to the anticipated behavior under design quasi-static loads.

An example for a change of behavior is the destruction of a fixed bearing, particularly in longitudinal direction, which according to [SB89] is rather likely to occur. Once the bearing is destroyed, it will not provide the same level of restraint anymore. Another example for a change in behavior is a sliding bearing in the longitudinal direction, which at first sight would not be expected to transfer significant horizontal forces between superstructure and abutments. However, if the gap between superstructure and abutment is small (possibly under the influence of temperature deformations), it may not be sufficient to accommodate the full relative displacement between the two members. In this case pounding between superstructure and abutment may occur which is likely to transfer significant forces.

Generally, two types of damage can be distinguished: (a) Movements and rotations of the abutment which are likely to remain to a large extent after the earthquake, and (b) structural damage to the abutment itself. An example of an abutment movement is shown in Fig. 2.14. It can be seen that in the case of pile foundations, the piles can be subjected to significant forced deformations which can, as a result, lead to a damage of the piles. A typical movement, especially for high abutments, is a rotation of the abutment about the horizontal transverse axis. It can be caused by high (dynamic) passive soil

pressure from the embankment against the backwall which drives the abutment in direction of the superstructure. The rotation will be further increased if the superstructure pounds against the abutment. The corresponding resultant forces are shown in Fig. 2.15.

Fig. 2.14: Abutment movement at Highway 118 during Northridge earthquake 1994
(Source: Graham C. Archer, NISEE)
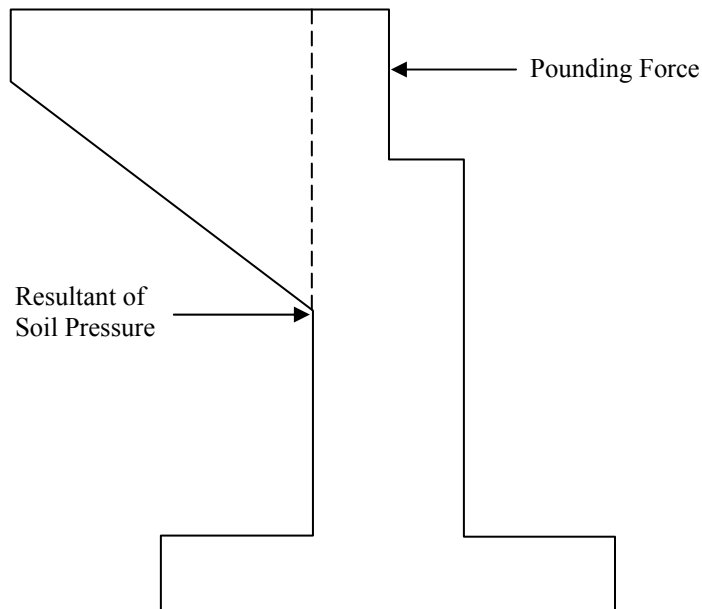
Fig. 2.15: Dynamic forces acting on the abutment in the longitudinal direction
from soil pressure and superstructure pounding

Various types of structural damage to the abutment can occur as a result of the forces coming from the soil and the superstructure. The abutment itself will normally not have significant inelastic deformation capacities, so that damage will be related to excessive forces acting on it. In the longitudinal direction dynamic soil pressure and superstructure pounding are possible causes of damage. As a consequence, particularly damage to the backwalls has been observed in some cases. In

the transverse direction, damage to the wingwalls is possible if the connection to the superstructure is capable of inducing significant forces in the transverse direction. Furthermore, concrete break-out due to anchorage failure of the bearings may occur. This will be further discussed in Subsection *d* in connection with seismic bearing behavior. Examples of structural damage to abutments after earthquakes are shown in Fig. 2.16.

Fig. 2.16: Structural damage to abutments
left: I-5/I-210 Interchange after San Fernando earthquake 1971 (Source: Karl V. Steinbrugge, NISEE),
right: I-5/I-210 Interchange after Northridge earthquake 1994 (Source: NISEE)

Experience of past earthquakes has shown that in some cases more severe damage to the abutments can result as a consequence of other failure mechanisms such as, e.g., failure of the piers which leads to excessive movements of the superstructure [PSC96]. Another type of damage that can occur at the abutments is related to soil deformations or failure such as settlements, soil-liquefaction or slope failure, which may be either independent of the bridge behavior or a result of interaction between abutment and soil. These issues will be discussed in Subsection *g*. Furthermore, damage to expansion joints can occur which will be discussed in Subsection *e*.

It can be seen that damage to the abutments is not an uncommon phenomenon under strong seismic excitation. However, normally the consequences are not as severe as the previously discussed superstructure unseating or pier failure. Abutment failure can cause significant economic damage in a sense that post earthquake repair measures can be very costly. On the other hand, a real collapse of the bridge structure due to abutment failure is rather unlikely. In an assessment situation, damage to the abutments may therefore be considered as*/ less critical than other failure mechanisms which can lead to a total collapse of the structure.

d) Damage to Bearings

Unless superstructure and substructure are not connected monolithically, commonly the superstructure is supported on the piers and abutments by means of some kind of bearings. Aside from their purpose to transfer vertical gravity loads, conventional bearings can be distinguished by their horizontal behavior as either fixed or deformable, which can be different for the longitudinal and transverse direction. The deformability is either accomplished in the form of (laminated) rubber bearings or stainless steel-PTFE sliding interfaces. While rubber bearings cause (linear elastic) reaction forces

when deformed, sliding bearings typically have very low coefficients of friction (under slow motions), resulting in an almost fully released behavior. Seismically induced relative motions at the sliding interfaces have significantly higher speeds than e.g. motions that result from temperature deformations of the superstructure. At these higher rates the coefficient of friction between PTFE and stainless steel can increase considerably, changing the behavior compared to that of quasi-static actions.
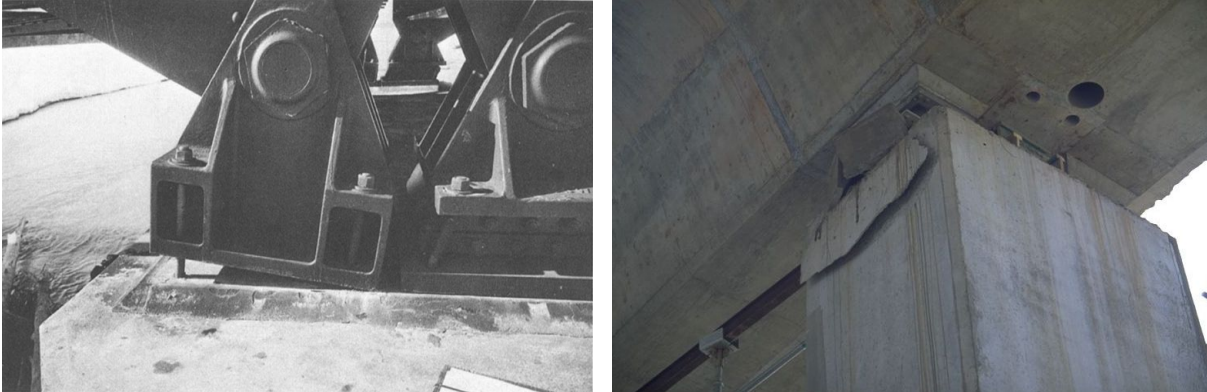

Fig. 2.17: Damage to bridge bearings
left: Bearing anchorage at Snow River Bridge during Alaska earthquake 1964 (Source: McCullogh, NISEE),
right: Concrete break-out at bearing anchorage after Chi-Chi earthquake 1999 (Source: J.P. Moehle, NISEE)

For the transfer of vertical loads and for the horizontally fixed support several solutions have been developed which can also be combined with either of the deformable bearing types to allow relative displacements in one direction. An overview of commonly used fixed bearings in Switzerland is given by Somaini and Bachmann in [SB89] and [Bac90b]. In their study on bearing behavior under longitudinal seismic response they conclude that horizontally fixed bearings are prone to failure as a result of excessive force levels. Their analyses show that even small (inevitable) gaps inside the otherwise fixed bearings can result in a significant increase of bearing forces, compared to the case without internal slack. They distinguish between three general types of bearing damage: (a) failure of the bearing construction itself, (b) failure of the anchorage bolts, and (c) failure of the concrete as a result of local anchorage forces.

In Fig. 2.17 two cases of damage to the bearing anchorages are shown. On the left side, the anchorage bolts of a fixed bearing were pulled out during the 1964 Alaska earthquake. This type of damage was related to the significant height and slenderness of the bearing. In case of a lower and squatter bearing, the bolts would have probably rather been sheared off, or a failure of the concrete below would have occurred, as in the case of Fig. 2.17 right. Here, the damage to the pier top of a bridge is shown which was under construction during the 1999 Chi-Chi earthquake in Taiwan. It can be seen that the anchorage plate is shifted to the left and the concrete failed locally. A structural failure of a bearing itself is shown in Fig. 2.7 in the context of the large transverse superstructure shift at a pier of the Hanshin Expressway. Due to the complete separation between the upper and the lower parts of the bearing, obviously neither vertical nor horizontal support forces could be transferred anymore.

e) Expansion Joints

Expansion joints are provided in longer bridges to allow for unrestrained relative movements due to thermal, creep and shrinkage deformations of the superstructure. Under longitudinal seismic excitations, expansion joints result in an uncoupling of the separated parts, as long as the deformation capacity of the joint is not exceeded. Depending on the details of the construction, when the longitudinal tension deformation capacity is exceeded, damage to the expansion joint may occur. However, compared to the other seismic forces involved in the structure, a significant restraint from the expansion joint will not be expected, unless special seismic restrainers are provided. In contrast, very high pounding forces can occur upon full closure of the gap at the joint. These forces can destroy the joint construction by crushing and possibly lead to a buckling type failure mode, driving the steel

construction upwards. In addition, the pounding can also result in local concrete damage at the pounding surfaces.

Conventional expansion joints without particular seismic provisions typically cannot sustain large relative transverse displacements. Therefore, the bearings at the joints are normally fixed in transverse direction, thus not allowing relative motions in this direction. However, if the restraint by the bearings gets destroyed under severe seismic excitation, some degree of relative transverse motion may become possible which can also lead to damage of the expansion joints.

Fig. 2.18: Damage to expansion joints
left: after Kobe earthquake 1995 (Source: Christopher R. Thewalt, NISEE),
right: after Chi-Chi earthquake 1999 (Source: unknown)

From the point of view of structural safety, damage to expansion joints is not of great importance as it will not provoke a collapse of the bridge, nor is it likely to influence the seismic behavior of the bridge significantly (aside from pounding which is essentially independent from the steel construction of the expansion joint). For very important bridges that are part of so-called lifelines, damage to expansion joints may be of greater concern, as they are required for immediate emergency access after an earthquake. In Fig. 2.18 two types of possible post-earthquake damage conditions are shown. On the left, the joint has a wide open residual gap, while on the right side a steel construction with overlapping steel teeth due to pounding is shown. As can be seen, at least in these two cases the joints are either still accessible at low speed, or can be made accessible again within a short period of time, e.g. by placing steel plates to cover the discontinuities.

f) Damage to the Foundations

Piers and abutments are either founded on spread footings or deep foundations, as e.g. piles. In a new design, based on modern seismic design principles, the foundations would normally be required to remain essentially elastic under seismic loading by providing them with sufficient strength. This type of behavior is typically not guaranteed for existing structures. As a result, inelastic deformations in and damage to the foundation system cannot be ruled out. As the design of existing structures did not only lack modern capacity design principles, but was also based on significantly lower horizontal (seismic) loads, the design of the foundation system in many cases was predominantly for vertical gravity loads. This does not only refer e.g. to the amount of reinforcement but even more so to its general layout and detailing.

A foundation consisting of a group of piles connected by a cap-beam will require moment transfer between the pile tops and the cap-beam under transverse loading due to frame action. However, in existing structures the detailing of the pile-cap joint will rarely be detailed like a frame corner which could provide significant levels of moment transfer. Furthermore, the piles themselves may not have the required moment and shear capacity, and even less probably the detailing to sustain large inelastic deformations. In Fig. 2.19 two cases of pile failure are shown after uncovering the foundation system.

Fig. 2.19: Damage to piles
left: Pile at Struve Slough Bridge after Loma Prieta earthquake 1989 (Source: NISEE),
right: Sheared off piles after Kobe earthquake 1995 (Source: NISEE)

A similar situation can be expected for spread footings. Under seismic actions, they can be subjected to significant moment demand, possibly coupled with uplifting which results in a rocking type of behavior. As a consequence, the soil pressure bearing the vertical gravity loads may concentrate under a rather small part of the foundation close to its edge. This will result in significantly higher moment and shear demand in the concrete cross-section of the footing than compared to a situation with predominantly vertical loads.

The consequence of a deficit in foundation strength (pile or spread footing) is that the force level required to cause inelastic deformations in the piers might not be reached. In this case, the seismic deformation demand will concentrate in the weaker member – here the foundation – which is unlikely to have sufficient deformation capacity. A failure of the foundation cannot be ruled out as a consequence.

g) Soil-Related Damage

Several types of soil-related damage can occur during earthquakes. Aside from the rupture at the immediate site of the fault, these are mainly excessive settlements, soil-liquefaction, loss of bearing capacity at foundations and slope failures. To some extent, these phenomena can also be interrelated among each other or with the bridge structure (i.e. soil-structure interaction).

Fig. 2.20: Soil liquefaction around pier foundation at Nishinomiya bridge after Kobe earthquake 1995
(Source: Christopher R. Thewalt, NISEE)

Settlements can e.g. be caused by soil-liquefaction, which can occur in saturated silts and sands. In the presence of a foundation, as shown in Fig. 2.20, a further interaction with the bridge structure will result. In the case of Fig. 2.20, the deep foundation led to a stabilizing effect on the surrounding soil. Spread foundations, however, would loose their bearing capacity on liquefied soil which can result in significant settlements or even failure of the footing.

Another type of potential interaction between soil and bridge behavior is shown in Fig. 2.21. On one hand, the soil behavior of the embankment influences the seismic response of the abutment, e.g. by means of soil pressure on the backwall. On the other hand, movements of the abutment can cause or increase settlements of the embankment soil behind the backwall.

Fig. 2.21: Settlements of the embankments
left: Abutment backfill after Northridge earthquake 1994 (Source: NISEE),
right: Embankment after Niigata-Ken earthquake 2004 (Source: Mitsutoshi Yoshimine, NISEE)

Damage to the soil may also occur at foundations due to excessive loading. Spread foundations that perform a rocking motion during the earthquake create a large concentration of soil stresses as discussed in Subsection *f*. These can lead to inelastic deformations in the soil or even exceed its bearing capacities. A potential consequence can be the development of a plastic hinge in the soil instead of the concrete structure that is founded on it. In this case, significant residual plastic deformations can be expected after the earthquake.
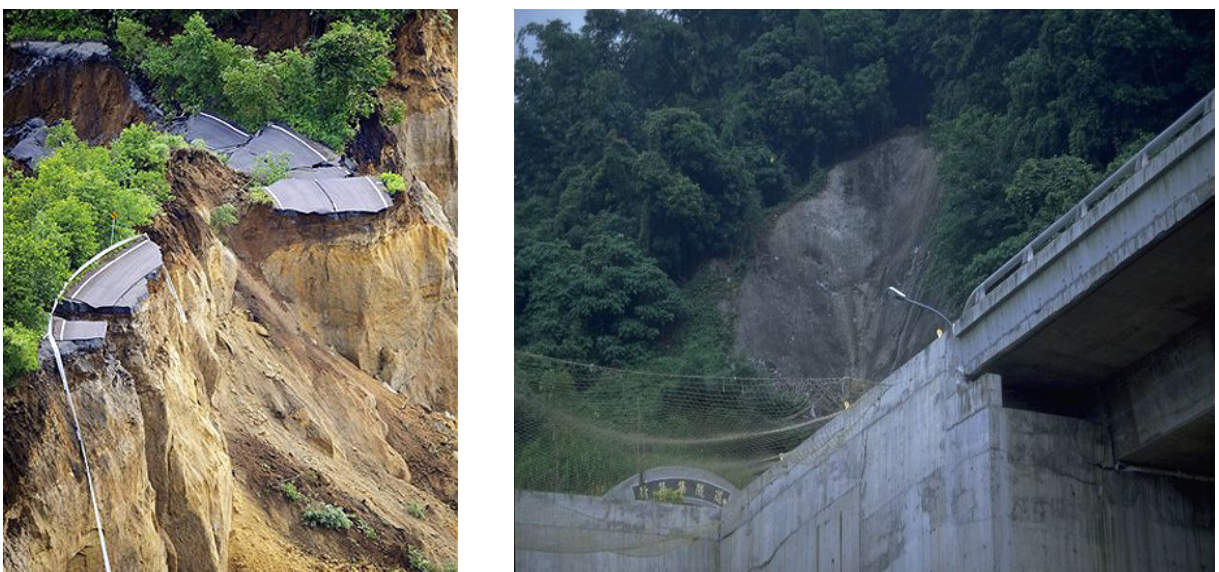

Fig. 2.22: Seismically induced slope failures
left: Road after Iwate-Miyagi Nairiku earthquake 2008 (Source: Kyodo News, AP),
right: Next to Jyi-Lu bridge after Chi-Chi earthquake 1999 (Source: Jack P. Moehle, NISEE)

As bridges are often used to cross valleys, they may be founded on or next to slopes with limited stability. Such slopes can become unstable under seismic excitation. While this can generally also happen without the influence of a bridge structure, the presence of foundation loads may further increase the likelihood of instability. Fig. 2.22 shows two cases of seismically induced slope failures. On the left side it can be seen that the problem is not only related to bridges, but can also impact roads that run along a slope. The right side of Fig. 2.22 visualizes the risk of soil and talus falling onto the bridge if the slope failure occurs above the structure. However, the worst case would be if piers or abutments founded on a failing slope were sliding down, resulting in a collapse of the bridge. As a significant number of bridges in Switzerland is located on or close to slopes, particular attention should be given to this problem.

h) Damage to the Superstructure:

In a new design, based on modern seismic codes, it is typically required that the superstructure remains essentially elastic during the design earthquake. As a consequence, no significant damage would be allowed or expected for a new bridge. Although not explicitly designed in this way, for existing girder bridges with continuous superstructure, it may be expected that in the majority of cases significant damage to the superstructure will not occur either.

A continuous superstructure interconnects the different piers and the abutments, transferring horizontal forces between them especially under transverse excitation. As a result, it will be subjected to horizontal shear forces and bending moments about the vertical axis. For monolithic superstructures these actions are unlikely to result in significant damage as the typically wide cross-sections have a rather high natural flexural and shear strength. In superstructures built of precast girders or segments which are connected by in-situ concrete, the flexural strength may not always be sufficient, resulting in inelastic deformations at these joints. While this might change the global seismic behavior of the structure compared to an essentially elastic continuous superstructure, it may not represent a major risk to the overall safety of the bridge, unless unseating occurs (see Subsection *a*).

In the same way, the superstructure is subjected to vertical seismic excitations which cause bending moments about the horizontal transverse axis. As girders have been designed for high traffic loads, incorporating safety factors, the vertical seismic excitation will normally not cause problems. Special cases are prestressed superstructures where the layout of the tendons is typically designed to compensate part of the gravity loads from the girder weight. Under severe vertical excitation the spectral accelerations in upward direction (including resonance effects) could exceed the net gravity load of the girder (after subtraction of the upward prestressing action). However, no case is known to the author where this phenomenon has caused any significant problem so far.

Fig. 2.23: Damage to the webs of superstructure girders
left: Concrete web at Wu-Hsi Bridge after Chi-Chi earthquake 1999 (Source: Stephen A. Mahin, NISEE),
right: Steel web at Hanshin Expressway after Kobe earthquake 1995 (Source: Christopher R. Thewalt, NISEE)

In past earthquakes, real damage to the superstructure, if any at all, has mostly been limited to local destructions. Potentially critical points are e.g. high webs of steel or precast concrete girders which receive high transverse loads at their supports. Examples of corresponding damage are shown in Fig. 2.23. These webs need to transfer the transverse inertia forces between the deck and the bearings, but typically have not been designed for this type of action. Although local damage may be severe, it is unlikely that a global collapse will result from this problem only.

Another source of damage to the superstructure can be represented by pounding between adjoining spans or against the abutments, as already mentioned in connection with the expansion joints in Subsection *e*. The impact causes very high stresses at the contact surfaces which will typically be significantly higher than the material strengths. Pounding may also be accompanied or triggered by bearing failure. Although pounding can have an important influence on the global seismic behavior of the bridge structure, the damage to the superstructure will normally be limited to local destructions in the impact zones. An example of such a local damage is shown in Fig. 2.24.

Fig. 2.24: Local damage due to pounding at an expansion joint of I-5/Santa Clara River
after Northridge earthquake 1994 (Source: Mark A. Aschheim, NISEE)

It may be mentioned that, especially in multi-story bridge structures, pounding can also occur in the transverse direction. In the case of the Southern Freeway Viaduct, shown in Fig. 2.25, the superstructure of the lower story pounded against the columns of the neighboring upper story. However, as can be seen in the photos, the damage is more relevant to the piers than to the superstructure, which again suffered only minor local concrete spalling at the impact surfaces.

Fig. 2.25: Damage due to pounding in the transverse direction at Southern Freeway Viaduct
after Loma Prieta earthquake 1989 (Source: NISEE)

i) Non-Structural Elements

Non-structural elements are not (directly) relevant for the structural safety of a bridge, and in many cases damage to them might be considered acceptable. For the damaged handrail, shown on the left side of Fig. 2.26, this will certainly be true as the damage is of negligible relevance and can be repaired easily. Damage to a heavy soundwall, as that shown on the right side of Fig. 2.26, can become somewhat more critical and its acceptability might depend on the circumstances. If the soundwall could, for example, fall down from the bridge onto a crowded street, it might represent a risk to the life safety of people there. In that case, a failure of the soundwall – although being a non-structural element – cannot be considered irrelevant anymore.

Fig. 2.26: Seismic damage to non-structural elements of bridges
left: Handrail at I-10/Cloverfield Overpass after Northridge earthquake 1994 (Source: B. Stojadinovic, NISEE),
right: Collapsed soundwall at Interstate 405 after Northridge earthquake 1994 (Source: M.A. Aschheim, NISEE)

Another type of non-structural elements that deserves special attention can be gas pipes running along the bridge. On one hand, the fixation of the pipe will have to bear the inertia forces from dynamic excitation of the pipe. On the other hand, large relative displacements may occur at the points where these fixations are anchored into the bridge structure (e.g. as a consequence of a bearing failure). These will represent forced deformations to the pipe that need to be accommodated by the fixations and the pipe itself. The breaking of a gas pipe, with subsequent potential for fire or explosion, can represent a severe threat to people, and possibly also to the structural integrity of the bridge. Therefore, this can be considered a non-structural element whose damage will hardly be acceptable.

j) Special Bridge Types

The primary focus of this study is on the seismic behavior of conventional girder bridges without significant curvature or skew. Other, more particular, types of bridges, such as skew bridges, arch bridges, strongly curved bridges, cable-stayed bridges, or suspension bridges, may have additional failure mechanisms which have not been covered by the overview given above. Bearing supported skew bridges, e.g., have a tendency for pounding against the abutments with subsequent rotation of the superstructure about the vertical axis. Arch bridges are sensitive to relative horizontal displacements of their abutments which may be the result of non-synchronous excitations. This is likely to occur as the abutments are typically founded on opposite sides of a valley.

The seismic behavior of these types of bridges requires special considerations not being covered by this study. For such cases the reader is referred to specific literature on these bridge forms.

k) Discussion on Importance of Damage Types for the Assessment Process

In the Subsections *a* through *i* above, a variety of potential damage modes for girder bridges have been presented. For the assessment of existing bridges in regions of moderate seismicity, they do not all have the same relevance. This is, on one hand, related to the fact that not all of them are likely to be caused by a seismic event which is considered representative for moderate seismicity, and, on the other hand, they do not all bear the same threat to the structural safety of the bridge.

Obviously, those damage modes which can result in a collapse of the bridge structure are of high importance. These are in first place *unseating of the superstructure*, and *failure of the piers*, or of the sub-structure in general. Both failure modes cannot be ruled out even for moderate seismicity. If the bridge is located at a potentially unstable slope, a *slope failure* may also represent a significant threat of collapse to the structure.

Especially unseating has always devastating consequences. At the same time, its potential occurrence can be discovered rather easily by checking the seat length of the superstructure. Careful consideration should therefore always be given to this detail (see Section 4.3.2). Concerning the risk of a pier failure, more sophisticated analyses of the deformation demand and capacity are required, taking the dynamic behavior of the entire structure and the various possible failure modes of the piers into account. Soil-related threats, as e.g. slope-failure, are not covered by this study. This does not mean that they are of lower relevance. They are only beyond the scope of this text as it concentrates on the structural behavior of existing bridges.

Other damage patterns that can be expected to occur during moderate seismic events are damage to the abutments and bearing failure. As discussed in Subsection *c*, damage to the abutments – e.g. in the form of large residual displacements – can be rather costly to repair after an earthquake. However, it is unlikely that an abutment failure would cause a more severe bridge collapse. Therefore, it can be seen less critical than, for example, unseating or pier failure. Large deformations at an abutment may, however, change the global seismic behavior of the bridge structure and as such influence the deformation demand on the piers. The possibly inelastic behavior of the abutment-embankment system should therefore be modeled adequately in the analysis.

A similar situation exists for the potential failure of bearings. Although it is not unlikely to occur, even under moderate seismic events and especially for fixed bearings on the abutments, its direct consequences do not necessarily represent a major threat to the safety of the entire structure (as long as unseating is prevented). As for the abutment behavior, a bearing failure can, however, lead to a change in the dynamic behavior of the bridge and should therefore be taken into account in its modeling.

Damage and inelastic deformations in the soil-foundation system can also influence the seismic behavior of the structure. This can be of particular importance if it leads to a change of the plastic mechanism that develops under seismic excitation. In this case, plastic hinges may not develop at the base of the concrete (or steel) piers anymore, but will rather occur in the soil-foundation system. Consequently, local deformation demands and corresponding damage distribution can change completely. If soil-liquefaction occurs at a spread footing, it may loose its bearing capacity for the vertical loads.

Local damage to the superstructure, damage to expansion joints, and (minor) settlements of the embankment are normally less critical. They do not endanger the overall safety of the structure and can be repaired at comparatively low cost after an earthquake. These types of damage may, however, have some relevance for the immediate usability after an earthquake which may be required in the case of life-lines for emergency traffic. Damage to non-structural elements is not expected to endanger the safety of a bridge structure either, unless it represents the potential risk for secondary consequences. Gas pipes running through bridges should therefore always be examined as special cases.

2.2 Situation of Switzerland

2.2.1 Historical Development of Seismic Codes

As the majority of existing bridges has been built based on older versions of design codes which do not comply with modern standards, the original requirements on which the design at the time was based can represent a valuable information for the assessment of such structures. In this chapter, at first, a description of the current seismic design provisions is given as a reference. In the following subsections the various evolution steps leading to the current state are summarized in chronological order. The comparison gives an idea of the discrepancies between the originally underlying design requirements of existing bridges, built throughout the past decades, and the level of seismic requirements which is currently considered appropriate. An additional overview of the development of seismic code provisions in Switzerland can also be found in [ASTRA05a].

a) Current Code Generation of 2003

Switzerland can be considered a country of moderate seismicity. The current Swiss code [SIA261] for actions on structures defines four different seismic zones (see Fig. 2.27) with design peak ground accelerations a_{gd} ranging from 0.06 g (Zone 1) to 0.16 g (Zone 3b). These values are modified by factors for importance of structure (γ_f) and soil conditions (S) which can further increase the actual peak ground acceleration.
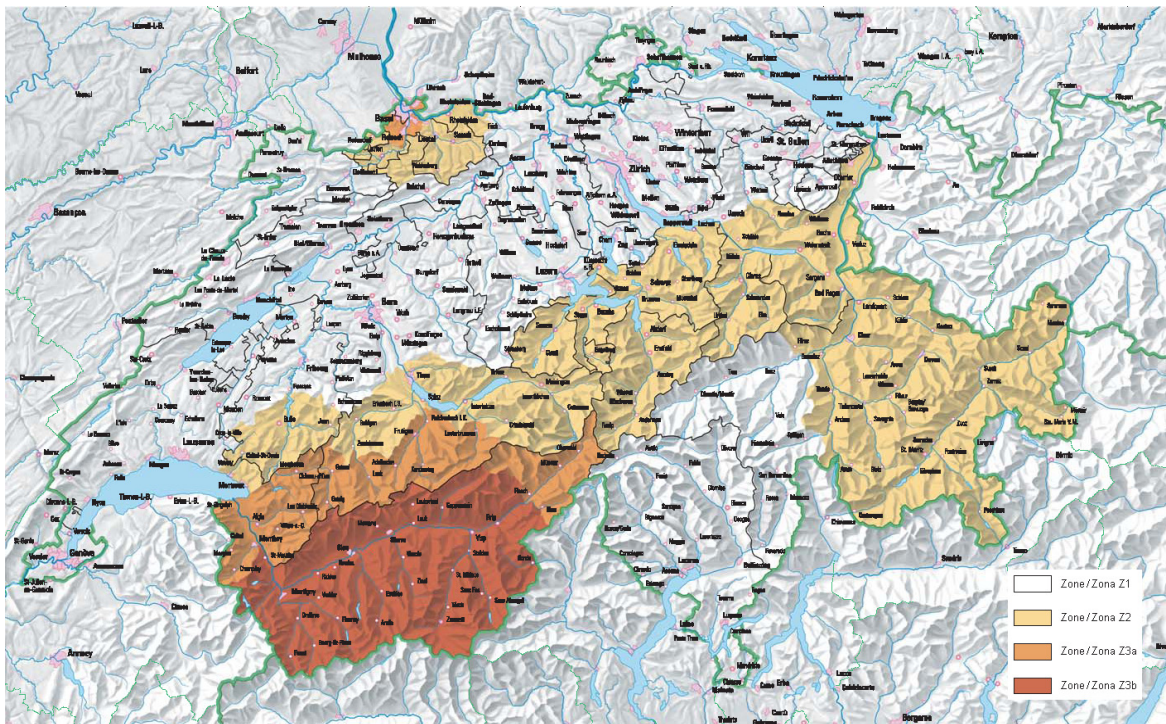
Fig. 2.27: Seismic zones of Switzerland according to the current code [SIA261]

In the upper region of possible seismic demands according to the code, this can e.g. result in a total peak ground acceleration in zone 3b of $a_g = 0.27$ g for the case of soil class B ($v_s = 400...800$ m/s, $S = 1.2$) and importance class III ($\gamma_f = 1.4$). Taking a peak spectral amplification factor of 2.5 into account, the maximum elastic spectral acceleration for this configuration of seismic zone, soil class and importance of structure results as $S_{a,el} = 0.67$ g (for elastic natural periods T between $T_B = 0.15$ s and $T_C = 0.5$ s). The corresponding maximum spectral displacement has a value of $S_{d,el} = 0.17$ m (for elastic natural periods T above $T_D = 2.0$ s). For a design without special detailing measures in order to guarantee a ductile behavior, [SIA261] allows the reduction of the elastic spectral accelerations by a

behavior factor of $q = 2.0$, unless a very brittle reinforcement steel of class A is used[1]. For $q = 2.0$ the maximum design spectral acceleration results as $S_{a,d} = 0.34$ g.

At the lower end of possible seismic demands according to [SIA261], for a bridge being situated in seismic zone 1 ($a_{gd} = 0.06$ g), having only an importance class of II ($\gamma_f = 1.2$), and being founded on soil of class A ($v_s > 800$ m/s, $S = 1.0$) the total peak ground acceleration is only $a_g = 0.072$ g resulting in maximum elastic spectral values of $S_{a,el} = 0.18$ g and $S_{d,el} = 0.036$ m. Using the behavior factor for non-ductile detailing of $q = 2.0$, the maximum design spectral acceleration follows as $S_{a,d} = 0.09$ g. All given spectral values refer to a viscous damping ratio of $\xi = 0.05$. The elastic and design pseudo-acceleration spectra for the two mentioned configurations are shown in Fig. 2.28.
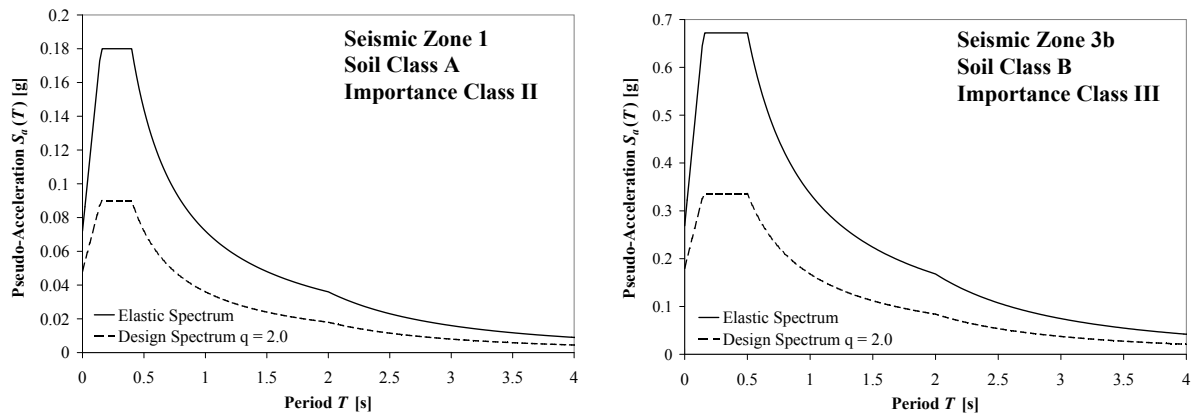

Fig. 2.28: Pseudo-acceleration spectra according to [SIA261]

Based on these values, the seismic demand in zone 1 can be considered as rather limited (especially in the case of good soil conditions and low importance of the structure). At least for a new design of reinforced concrete or steel structures, the corresponding seismic demand is unlikely to cause major problems, even if only a non-ductile behavior is chosen. However, in zone 3b the values given above represent a significant demand which will clearly be the governing horizontal action in the majority of cases. It is likely that here at least some inelastic deformation capacity will be required to withstand earthquakes corresponding to the design level.

In the current Swiss code generation [SIA261], [SIA262], [SIA263] it is possible to design structures either for a ductile or a non-ductile behavior. The corresponding choice affects the behavior factor q, mentioned above, by which the spectral accelerations of the design spectrum are reduced compared to the elastic spectrum. This design concept can therefore be considered as force based, because the displacement capacity of the structure is not taken into account in a direct and explicit manner. Instead, certain fixed requirements concerning the detailing of the members and capacity design principles need to be fulfilled in order to consider the behavior as ductile. Once these requirements are met, the behavior factor q only depends on the ductility class of the reinforcement. This means that the code does not allow for an individual choice of the level of ductility, i.e. deformation capacity, and corresponding layout of the detailing.

Aside from the design for (reduced) inertia forces, [SIA261] also contains regulations for minimum seat lengths of the superstructure in order to prevent its unseating. The chosen design equation is meant to include the influence of non-synchronous ground motions in a simplified manner.

b) Code Generation of 1956 and earlier

SIA codes [SIA160-56] (actions), [SIA161-56] (steel design) and [SIA162-56] (concrete design) of the year 1956 did not contain any regulations concerning seismic actions or design. It can therefore be assumed that earthquake loading at this time was not explicitly considered in the design of bridges.

---

[1]   For steel of ductility class A the behavior factor may only be chosen as $q = 1.5$.

c) Code Generation of 1970

The 1970 version of SIA 160 [SIA160-70] was the first Swiss code to include any seismic provisions. In its article 22 it is determined that structures should be designed either for an earthquake intensity of VII or VIII, based on the *Rossi-Forel* scale used at the time. In the code's annex it is stated that for the whole of Switzerland the intensity level VII should be used. However, the local authorities were given the possibility to raise the design level within their area to an intensity of VIII. According to [ASTRA05a], only the canton of *Basel Stadt* made use of this possibility. It should be noted that in the code's annex it is also recognized that higher earthquake intensities – up to IX or even X (*Rossi-Forel* scale) – have occurred in the Swiss history and that these, therefore, cannot be ruled out in general. However, it was assumed that structures designed for an intensity of VII could also survive earthquakes of intensity VIII. As a consequence, the chosen design loads were considered sufficient for Switzerland. It is noteworthy that the annex contains a certain amount of uncertainty concerning this assumption, as it claims that experience needs to be gathered in the future with respect to this postulation.

The design requirements in article 22 were essentially limited to horizontal loads from mass inertia. For buildings, constant (spectral) accelerations of 0.02 g and 0.05 g were given for design intensities of VII and VIII, respectively. These values were to be applied independent of the building's fundamental period, and the resulting total base shear force should be distributed in the same way as in the *Lateral Force Method* ("*Ersatzkraftverfahren*") of the current code [SIA261].

For the design of bridge piers, period dependent spectral accelerations were determined as follows:

$$\text{for design intensity VII:} \qquad a_{spectral} = \frac{0.02g}{\sqrt[3]{T}} \qquad\qquad (2.1)$$

$$\text{for design intensity VIII:} \qquad a_{spectral} = \frac{0.05g}{\sqrt[3]{T}} \qquad\qquad (2.2)$$

with $T \geq 0.5$ s: Fundamental period
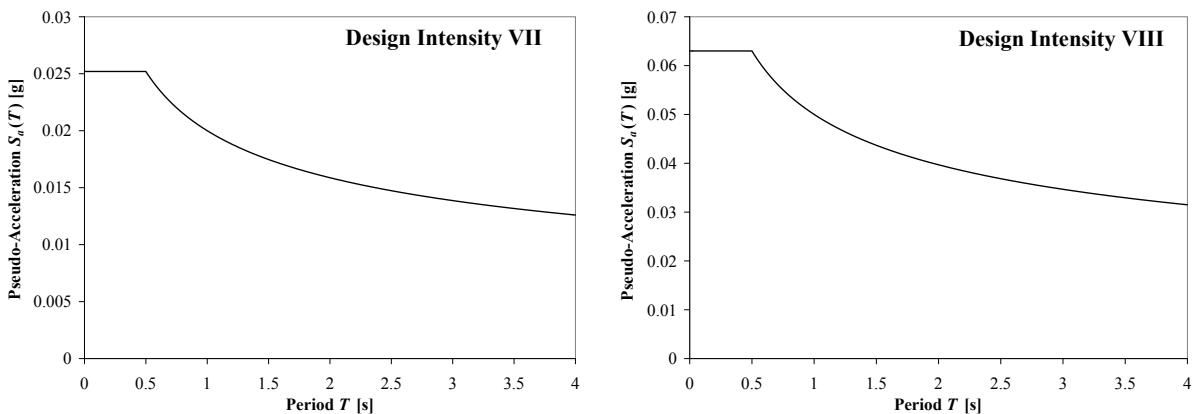
Fig. 2.29: Pseudo-acceleration spectra for the design of bridge piers according to [SIA160-70]

Equations (2.1) and (2.2) can be interpreted as simplified pseudo-acceleration spectra which are shown in Fig. 2.29. It should be noted that article 22.6 of [SIA160-70] also contains a paragraph demanding that the spectral acceleration for bridges should be determined in agreement with the responsible authorities. Aside from the aforementioned regulations concerning design inertia forces, [SIA160-70] did not contain any further seismic provisions for bridges. In particular, there were no requirements for minimum seat lengths of the superstructure at abutments and expansion joints. This is noteworthy as unseating needs to be prevented by any means due to its severe consequences.

d) Code Generation of 1989

In 1989 a new generation of codes was established which for the first time introduced a more complete set of regulations for the seismic design of structures. The general concept in [SIA160-89] was similar to the one of the current *Swisscodes*, containing a map of different seismic zones (see Fig. 2.30) with corresponding peak ground accelerations and pseudo-acceleration response spectra. This seismic map is similar to the one of [SIA261] (Fig. 2.27), also containing 4 zones being named 1, 2, 3a, and 3b. However, the assignment of some regions to the seismic zones still differed from those of the current map in [SIA261]. The code of 1989 [SIA160-89] also allowed for the influence of soil type and introduced three different classes of structure importance.

For the case of importance class I, [SIA160-89] did not require any analysis under seismic loads at all. Only the criteria against unseating of the superstructure (i.e. minimum seat lengths) needed to be fulfilled. In importance class II, a structural analysis under seismic loads was required, while the bearings were accepted to fail under the design earthquake. Only in importance class III the bearings needed to be designed for the full seismic loads. The seismic loads for the dimensioning of the bearings were even increased, compared to those for the rest of the structure, requiring essentially elastic behavior.

The design values of the peak ground accelerations for each seismic zone were formally the same as the values of a_{gd} in [SIA261]. However, due to a different way of application, they cannot be compared directly to the values of [SIA261]. The same is true for the influence of soil conditions and importance class of the structure. While the former according to [SIA160-89] only affects the shape of the response spectrum without changing its peak spectral value, the importance class influences a construction factor C_k which is roughly comparable to the product of the behavior factor q times the importance factor γ_f as used in [SIA261]. Using this approximate analogy, it can be back-calculated that the force demand in [SIA160-89] is based on a general constant behavior factor in the order of 3 to 4 (depending on the type of structural system, e.g. frame, structural wall, girder bridge, arch bridge etc.). This implicit behavior factor in [SIA160-89] is therefore of similar magnitude as the one in [SIA262] for a ductile design. However, in the new code this large behavior factor requires special detailing and the application of capacity design principles which are not included in [SIA160-89]. Without these special measures the new code [SIA262] would only allow behavior factors in the range of 1.5 to 2.

Fig. 2.30: Seismic zones of Switzerland according to [SIA160-89]

In a similar way, the influence of the importance class on the seismic demand of [SIA160-89] can be back-calculated. It follows that the relationship between the highest class III and the lowest class I is in the order of 1.6 (range of 1.54 to 1.79 depending on the type of structural system). The corresponding relation in [SIA261] is $\gamma_f = 1.4$.
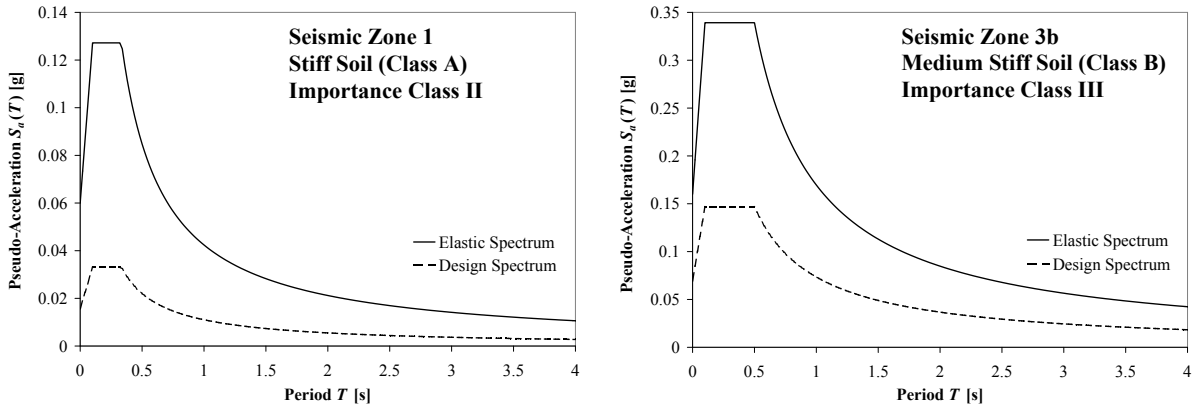

Fig. 2.31: Pseudo-acceleration spectra for the design of girder bridges according to [SIA160-89]

The resulting pseudo-acceleration response spectra from [SIA160-89] are shown in Fig. 2.31 for two sets of conditions (seismic zone, soil type, importance of structure) which are consistent with the ones used in Fig. 2.28 for the case of [SIA261]. In both figures the design spectra refer to structures without special detailing for ductile behavior[2] making them comparable to each other. It can be seen that for both configurations the design forces according to the new code are significantly higher. Large part of this difference is a result of the different (implicit) behavior factors in the case of non-ductile design. Further contributions come from a somewhat higher spectral amplification factor in [SIA261] as well as the new factor S to allow for softer soil types. The higher (implicit) importance factor in [SIA160-89] helps to limit the differences between the two codes for structures of higher importance classes to some degree. Nevertheless, the remaining discrepancies are significant.

From the perspective of displacement based analysis it might also be noteworthy that the spectral shapes of [SIA160-89] do not limit the spectral displacements for increasing period. This is not realistic as the maximum relative displacements should reach a peak level at a certain period, from which on the displacement spectrum does not rise anymore. For large (effective) periods this inconsistency will result in unrealistic displacement demands.

Aside from the design loads, [SIA160-89] also included regulations for minimum seat lengths of the superstructure at abutments and expansion joints to prevent unseating during an earthquake. A detailed discussion on this issue is presented in Section 4.3.2.

e) Comparison of Seismic Demand for the Different Code Generations

The previously shown design spectra for the three code generations [SIA160-70], [SIA160-89], and [SIA261] are compared in Fig. 2.32. On the left side, the spectra representing the lower end demand situation of zone 1, soil class A and importance class II are shown, while the right side contains the high demand situation, consisting of zone 3b, soil class B and importance class III. In the case of [SIA160-70], on both sides the demand defined for earthquake intensity VII (*Rossi-Forel* scale) is shown, as even in the regions which belong to today's zone 3b no use had been made of the possible increase to intensity VIII.

---

[2] For the comparison between elastic and design spectrum it should be noted that the importance class influences in [SIA261] (Fig. 2.28) both the elastic and design spectrum, while in [SIA160-89] it affects only the design spectrum (Fig. 2.31).

For the comparison in Fig. 2.32, the design spectra are used. This way, for all three code generations the seismic force level is compared that was actually applied to the bridge in the design process. Furthermore, all three spectra representing the various codes are valid for structures without any particular detailing or application of capacity design principles which would ensure a ductile behavior. Therefore, the given spectra for the different code generations are consistent with each other and can serve as a basis for comparison. It can be seen that the seismic demand defined in the codes has been subject to major modifications over the decades. This is the case for both configurations of seismic zone, soil type and importance class as they are shown in Fig. 2.32.
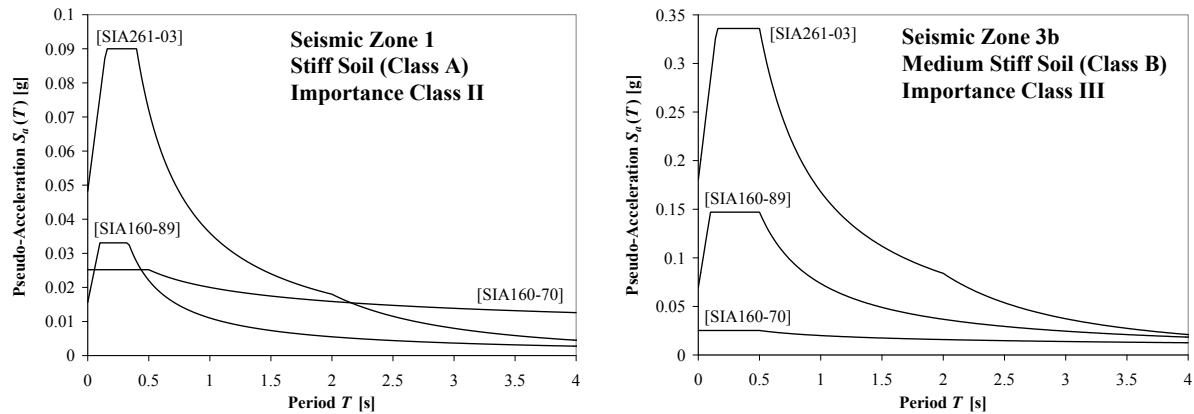

Fig. 2.32: Comparison of design pseudo-acceleration spectra for the different code generations

While in seismic zone 1 the difference between [SIA160-70] and [SIA160-89] is rather limited, for all other cases a significant increase of seismic design forces has always occurred from one code generation to the next. These differences are particularly pronounced in the low to medium period range. At higher periods the relationships become a little hazier as previous code generations in this period range used spectral shapes which do not comply with today's understanding and do not describe adequately the general trends of seismic structural behavior as a function of period. These effects reduce the differences between the different codes at higher periods to some extent. In the case of seismic zone 1 (left side of Fig. 2.32), the old [SIA160-70] defined even higher seismic design forces than the following generations [SIA160-89] and [SIA261]. However, the period range where [SIA160-70] results in higher spectral accelerations than the current code [SIA261] (T > 2.2 s) is of little relevance for normal girder bridges [3]. The fact that the code generations before 1970 ([SIA160-56] and earlier) did not define any seismic loads should be kept in mind, although this is not explicitly shown in Fig. 2.32.

From these comparisons it can be concluded that, if existing bridges only had the seismic capacities as required by the corresponding codes at the time of their design, massive deficits could be expected for many structures. Fortunately, many bridges might possess a somewhat better seismic behavior due to design for other actions (e.g. wind, breaking) or simply naturally immanent capacities. To take these beneficial effects into account, a displacement based assessment approach is best suited, as it attempts to capture the individual characteristics of the structure and their influence on the deformation capacity. This deformation capacity is what directly characterizes the seismic safety. Force based analysis can only try to allow for the deformation capacity in an indirect manner by the use of behavior factors (that would have to depend on the displacement capacity).

---

[3] The period to be used in connection with the design spectra should be based on the elastic stiffness of the structure, i.e. the secant stiffnesses to first yield.

2.2.2 Typical Characteristics of Existing Swiss Bridges

Internationally, a large variety of bridge types and structural solutions for the various parts of a bridge can be found. However, not all of them are used in Switzerland. Furthermore, even for conceptually similar bridges, the typical detailing of the members may differ significantly from one country to another. These structural characteristics can influence the seismic behavior of a bridge considerably and should therefore be taken into account. As this study focuses on the situation in Switzerland, it aims at representing particularly existing Swiss bridges, including typical detailing and potential deficiencies which can influence the seismic behavior.

a) Overview of Swiss Bridge Stock

Currently, about 3340 bridges exist on national highways in Switzerland [ASTRA08]. They are federal property and as such they belong under the responsibility of the Swiss Federal Roads Authority (*ASTRA*). To get an overview of this bridge stock, the database [KUBA05] was used which contains all structures on Swiss national highways. The data were combined with preliminary results of the first assessment stage based on [ASTRA05a]. At the time of the evaluation these results were available for the cantons of St. Gallen (SG), Schwyz (SZ), and Valais (VS). This resulted in a set of around 450 bridges which was analyzed to study the typical characteristics of Swiss bridges.

In Section 2.2.1 it was shown that previous code generations significantly underestimated the seismic demand as it is currently considered appropriate for the Swiss situation. While the code of 1989 [SIA160-89] should normally provide a level of seismic safety that, at least under consideration of cost-benefit aspects, can be deemed acceptable, the previous code generations from 1970 [SIA160-70] and [SIA160-56] do not warrant a sufficient safety. In Fig. 2.33 the relative distribution of age of bridges corresponding to the various code generations is shown. It can be seen that only about 10% of the bridges were opened in 1990 or later, and have thus been designed based on the more recent codes [SIA160-89] or [SIA261]. The vast majority of 90% of the bridges were designed and built either according to [SIA160-70] (52%) or [SIA160-56] (38%), and thus had to comply only with minimum or no seismic requirements, respectively.
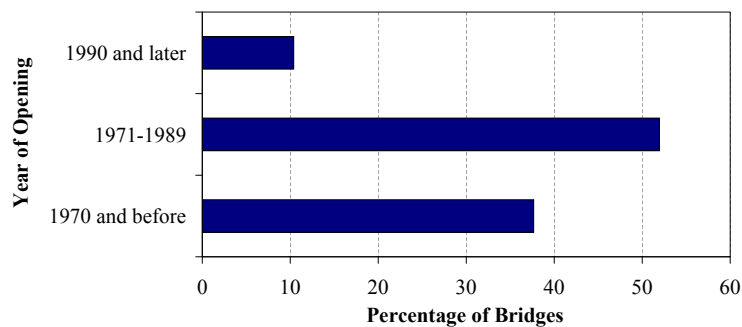
*Fig. 2.33: Relative distribution of bridge ages corresponding to code generations
for bridges on national highways in SG, SZ and VS*

Furthermore, it is necessary to obtain an overview of common bridge types in Switzerland. At first, it was attempted to sort the bridges into certain structural categories. The percentage of bridges in every category is shown in Fig. 2.34. It can be seen that multiple-span girder bridges constitute the largest category representing almost 40% of the bridge stock on Swiss national highways. They are closely followed by monolithic frame type bridges which amount to about 33% of the total stock. Significantly fewer structures belong to the categories "V-Stiel"[4], "single span girder bridge", and "plate type bridge", with each group representing some 8% of all bridges.

Based on this distribution, it appears reasonable to focus in this research project particularly on the seismic behavior of multi-span girder bridges as they represent the largest group. The also large

---

[4]   "V-Stiel" is a special type of two-span frame bridges which is rather wide-spread in Switzerland as highway overpasses.

category of frame bridges, as well as the *V-Stiel* bridges, is considered less susceptible to seismic damage in [ASTRA05a]. Due to their monolithic character and the consequential absence of certain weak spots, such as bearings and expansion joints, they are considered as seismically safe in the first stage of [ASTRA05a], unless they have very high abutments. The conceptual advantage of such monolithic structures over conventional (bearing supported) girder bridges is related to the fact that monolithically supported superstructures are almost impossible to unseat[5].
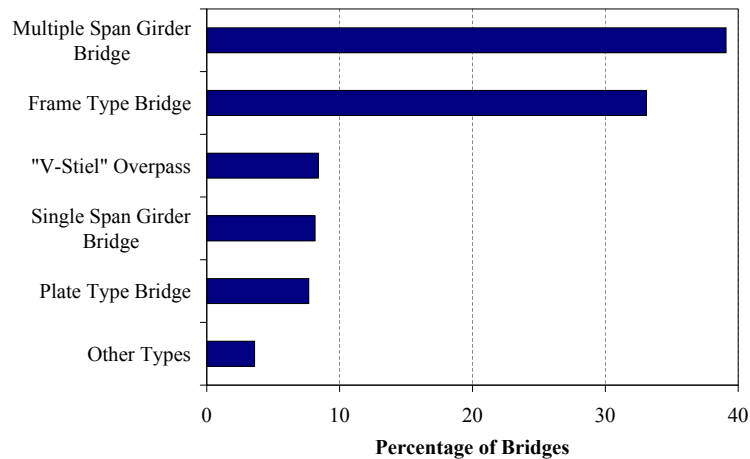

Fig. 2.34: Relative distribution of various bridge types on national highways in SG, SZ and VS

The substructure of a monolithic structure does not necessarily have a better seismic behavior than that of a bearing supported bridge (see Section 2.1b). However, the general principles and methodologies used for the assessment of conventional girder bridges can equally be used for frame type bridges, *V-Stiel* bridges, and plate type bridges. As a consequence, focusing in this study on multiple-span girder bridges provides the general basis for the assessment of a large part of the existing Swiss bridge stock, including the other types mentioned above.

An evaluation of the results for the first assessment step according to [ASTRA05a] is shown in Fig. 2.35, giving the relative occurrence of each criterion in the cantons of St. Gallen, Schwyz and Valais. Five categories, which in total represent a comparatively high percentage of occurrence, are related in some way to potential superstructure unseating. These categories are *Intermediate Expansion Joints*, *Gerber Hinges*, *Unseating (Longitudinal)*, *Coupled Ramp*, and *Unseating (Transverse)*. This corresponds to the high importance of this issue for the seismic safety of bridges (see Section 2.1a).

Further criteria with significant occurrence are *Skewness > 45°*, *Bridge Surface Area > 6000 m²* and *Superstructure Curvature > 30°*. These characteristics do not necessarily refer to a seismic weakness. They rather justify a more detailed analysis as these structures either have a somewhat more complex seismic behavior (skewness, curvature) or are considered more important due to their size[6]. The categories *High Abutment Walls*, *Tension Bearings*, *Slope Failure* and *Gas Pipe* refer to potential failure mechanisms as discussed in 2.1 *c*, *d*, *g* and *i*, respectively.

Criteria for the explicit consideration of seismic weak spots in the piers – or in the substructure in general – as discussed in 2.1b, are not included in the first assessment stage of [ASTRA05a]. The guideline does contain a category *Extreme Differences in Transverse Pier Stiffness* (see Fig. 2.35) which is related to potential damage to the columns. As a direct consequence of such differences in stiffness, higher modes are excited more strongly by the consequential irregularity of the structure. This does not necessarily cause a more critical seismic behavior. But it may require a somewhat more sophisticated analysis procedure to capture the influence of the higher modes. A second, more

---

5   Some care should be taken in case of precast structures if the construction joints do not have sufficient strength or are poorly detailed.

6   Risk is considered a two-dimensional quantity consisting of probability of occurrence and extent of potential detriment. For a constant probability the risk can also increase due to higher potential damage, as e.g. represented by a very large bridge.

implicit, consequence of the differing pier stiffnesses is related to the fact that they are typically a consequence of different pier heights. A short bridge pier being located between two longer piers may have an increased deformation demand which can cause problems as short piers normally have lower deformation capacities. In either case, the criterion *Extreme Differences in Transverse Pier Stiffness* does not take any particular seismic deficiencies of the piers into account, as discussed in Section 2.1b. Furthermore, excessive deformation demands on the piers could also develop under different conditions, i.e. not only in the case of strongly differing stiffnesses.
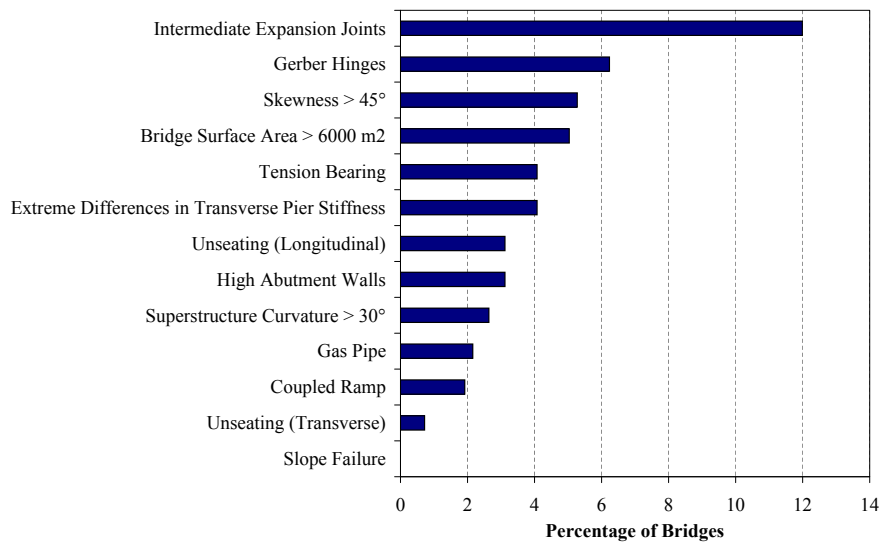
*Fig. 2.35: Relative occurrence of criteria as defined in the first assessment stage of [ASTRA05a]
for bridges on national highways in SG, SZ and VS*

Generally, it is difficult to detect seismic deficiencies of piers in a brief screening procedure comparable to the one defined by the first assessment step of [ASTRA05a]. Both, the deformation capacity and the demand, depend on the reinforcement layout and detailing of the piers (as well as other properties of the structure). These characteristics are not accessible in a brief screening, but rather require a more detailed study of the reinforcement drawings. At the same time, the quantification of seismic deformation demand and capacity requires at least a simplified numerical analysis. Therefore, the seismic assessment of the bridge piers with respect to potential failure modes, as those discussed in Section 2.1b, is difficult to achieve within a screening procedure.

Numerical analyses as part of the current research project have shown that, for the Swiss level of seismicity, primarily short and squat bridge piers are at risk of damage ([Bim06], [BD06]). This is on one hand because of a generally lower (flexural) deformation capacity of short piers and, on the other hand, because of their higher susceptibility to shear failure. For a given cross-section, a short pier has a higher shear demand than a longer pier. As discussed in Section 2.1b, such a shear failure is particularly critical as it represents a brittle failure mode and is often accompanied by a loss of axial load capacity – which can subsequently result in a total collapse of entire bridge spans.

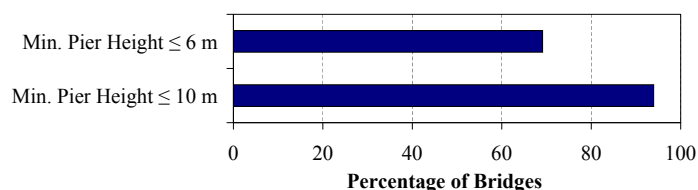*Fig. 2.36: Relative occurrence of short piers in bridges of national highways in SG, SZ and VS*

Based on these numerical analyses and on experiences from previous earthquakes, it can be concluded that special attention should be given within this research project to bridges with comparatively short

and squat piers. The above mentioned set of bridges was used to analyze the occurrence of short piers in Swiss bridges. The available documents on the screening results from St. Gallen, Schwyz and Valais allowed the estimation of the pier heights for 149 of the 450 bridges. Based on these data, it could be evaluated that in almost 95% of the considered bridges the minimum provided pier height was not more than 10 m. In almost 70% of the bridges the minimum pier height was even equal to or less than 6 m (see Fig. 2.36).

Especially the latter percentage is of significance as the analyses of real Swiss bridge piers in [Bim06] and [BD06] have shown that currently established assessment procedures in Switzerland ([SIA2018], [SIA262]) predicted a lack of deformation capacity for a clear pier height of 6 m. For the analyzed pier layout, the assessment methodology predicted a premature brittle shear failure which limited the deformation capacity significantly, resulting in a deficit of displacement capacity (see Section 2.2.3). The study showed that for Switzerland especially short and squat bridge piers might have potentially critical seismic behavior. These geometric characteristics are often found in wall-type bridge piers which due to their large section depth typically feature low aspect ratios L_v/d. Therefore, a set of three sample bridges has been assembled in order to study the typical properties of such bridges with respect to layout and detailing.

b) Sample Bridge Viadukt Untere Weid

The first bridge is the *Viadukt Untere Weid* shown in Fig. 2.37 which was built in 1971. It is a five span highway bridge with a superstructure consisting of precast concrete girders and a total length of 100 m. The two directions consist of two individual bridge structures. In one direction frame-type two-column bents were used as substructure, while the other direction features the wall-type piers shown on the left side of Fig. 2.37. An elevation and the cross-section of these piers are shown in Fig. 2.38. The clear pier heights between foundation and pier head according to the original drawings are 10.69 m, 12.83 m, 12.27 m, 15.30 m, and 12.27 m. The center of mass of the superstructure is located 3.26 m above these levels, resulting in effective heights for the dynamic model of 13.95 m, 16.09 m, 15.53 m, 18.56 m, and 15.53 m. The corresponding effective aspect ratios of the piers (in single bending) are 4.65, 5.36, 5.18, 6.18, and 5.18, respectively.
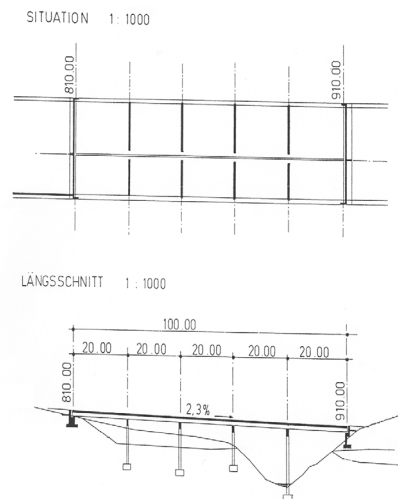
Fig. 2.37: Viadukt Untere Weid on Highway A1 in SG
left: View of piers and soffit of precast concrete girders, right: Plan view and elevation

The following details of the bridge design have a particular relevance for the seismic behavior of the bridge:

- The transverse reinforcement in the piers consists of two interlocking hoops of diameter 12 mm at a spacing of 400 mm. The corresponding transverse reinforcement ratio has a very low value of $\rho_{sw} = 0.08\%$ which provides only a very limited shear strength. The provided

amount and detailing of the hoops results in basically unconfined conditions for the concrete. Furthermore, the large spacing between the hoops does not provide any significant restraint against buckling for the longitudinal reinforcement bars, once the cover concrete has spalled.

- The longitudinal pier reinforcement ratio has a value of $\rho_{sl}= 0.56\%$, which influences its flexural capacity and subsequently also determines its shear demand in the inelastic range. Furthermore, the longitudinal reinforcement ratio has an influence on the member stiffness and thus on the fundamental period of the bridge structure.

- The pier was constructed in individual segments of 3 m height each, with lap-splices of the longitudinal reinforcement being placed at every construction joint. The lap-splice at the joint between the footing and the pier base is particularly unfavorable, as this is the location where large inelastic deformations are expected if the pier develops a plastic hinge at the base. It is noteworthy that the provided splice length of 100 cm (corresponding to 62 bar diameters) is rather high which is likely to have a positive influence on the potential degradation of the lap-splice. However, before the onset of degradation the effective doubling of the reinforcement over part of the splice length can reduce the plastic hinge length, which is further aggravated by the rather long splice.

- Part of the longitudinal pier reinforcement was terminated at about mid-height of the pier. In the upper part the longitudinal reinforcement ratio was consequently reduced to $\rho_{sl} = 0.37\%$, which represents about 2/3 of the value at the pier base.

- The superstructure consists of simply supported precast concrete girders which are connected by cross-beams on top of the piers and by a cast-in-situ concrete deck slab. The open cross-section of the superstructure does not provide a significant torsional stiffness leaving any rotational deformation at the pier tops essentially unrestrained. The seismic behavior of the piers can therefore be represented adequately by cantilever columns. Furthermore, the concrete deck may not provide the same level of coupling between the different spans as a real continuous superstructure.

- The in-plan dimensions of the spread foundations – 5.50 m by 4.00 m – are rather small compared to the cross-section of the wall-type piers. Although the size may be sufficient for the (mainly vertical) loads that were considered during the design, their moment capacity (for the given vertical load) might be limited, e.g. by uplifting, to a level which is not sufficient to cause the development of a plastic hinge at the pier base.
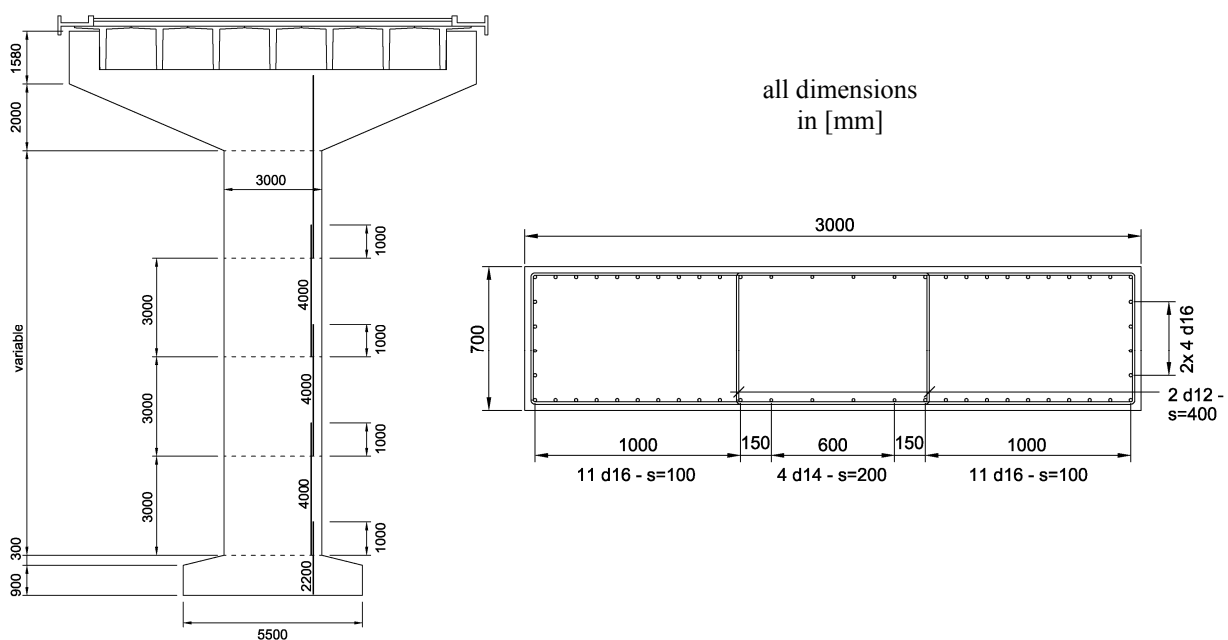

Fig. 2.38: Pier of Viadukt Untere Weid (SG), left: Elevation, right: Cross-section

c) Sample Bridge West-Bypass in Gossau

As a second sample structure featuring wall-type piers, the bridge over the railway as part of the west-bypass in Gossau (SG) is shown in Fig. 2.39. The bridge was built in 1966 and its superstructure consists of a monolithic three-span box-girder with a total length of 155 m. The hollow closed shape of the box-girder provides a considerable torsional stiffness which causes a coupling of the rotational degrees of freedom of the pier tops with the abutments. The clear pier heights between the foundations and the pier tops according to the original drawings amount to 7.03 m and 7.94 m. Taking the center of mass of the superstructure into account, the effective pier heights result as 8.7 m and 9.8 m, respectively. For single bending, these values relate to effective aspect ratios of 2.18 and 2.45, while only half the values result if double bending is considered (due to torsional stiffness of the superstructure), resulting in effective aspect ratios of 1.09 and 1.23 for this latter case.

Fig. 2.39: View of bridge over railway on west-bypass Gossau (SG)
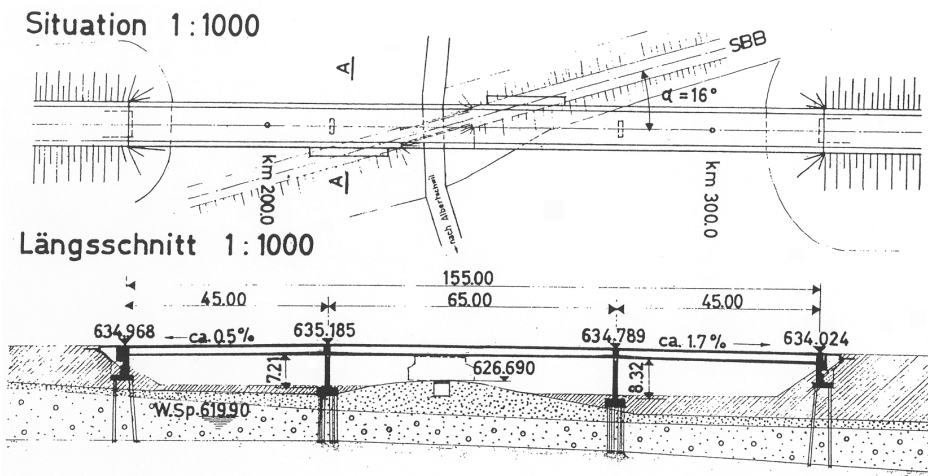
Fig. 2.40: Plan view and elevation of bridge over railway on west-bypass Gossau (SG)

The cross-section of the piers is shown in Fig. 2.41. It has a longitudinal reinforcement ratio of $\rho_{sl} = 0.62\%$. At the base of the piers, the longitudinal reinforcement features lap-splices with hooks at the bar ends. The splice lengths amount to 100 cm corresponding to 36 times the bar diameter. The lap-splices therefore exactly comply with the requirements of [SIA162-56] for the then used reinforcement steel of type II. The amount of longitudinal reinforcement is constant over the entire height of the piers without termination of bars. The transverse reinforcement consists of hoops with a diameter of 14 mm at a spacing of 250 mm, resulting in a transverse reinforcement ratio of $\rho_{sw} = 0.12\%$. Amount and detailing of the hoops do not provide a significant confinement to the concrete and limit the shear capacity of the pier considerably.

The abutments and the piers are all founded on pile groups consisting of 6 and 8 piles for each abutment and pier, respectively. The support of the pier bases can therefore be assumed to be significantly stiffer than in the case of the *Viadukt Untere Weid* described above, although the reinforcement of the piles and caps was not designed and detailed for high seismic loading.
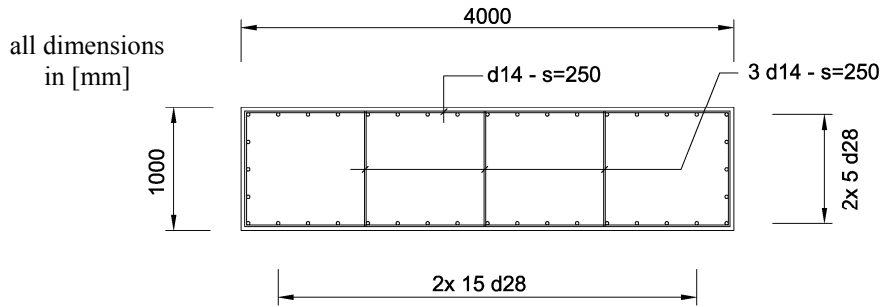
Fig. 2.41: Cross-section of pier at bridge over railway on west-bypass Gossau (SG)

d) Sample Bridge Viadukt Mühle Rickenbach

The *Viadukt Mühle Rickenbach*, shown in Fig. 2.42, was chosen as a third sample bridge having wall-type bridge piers. It is a six span bridge with a total length of 257 m that was built in 1965. The superstructure has an open cross-section in the mid-range of the spans which is closed over the piers by a bottom flange resulting in a full box-girder. Due to the open shape of the cross-section over a longer distance, the superstructure has only a low torsional stiffness, leaving the rotational degree of freedom at the pier tops essentially free. The longest span of 57 m features two expansion joints, resulting in a simply supported girder of length 45 m within the span (see Fig. 2.43).

Fig. 2.42: View of Viadukt Mühle Rickenbach in SG
left: Short pier P1 close to the north end of the bridge, right: Long pier P3 in the center of the bridge
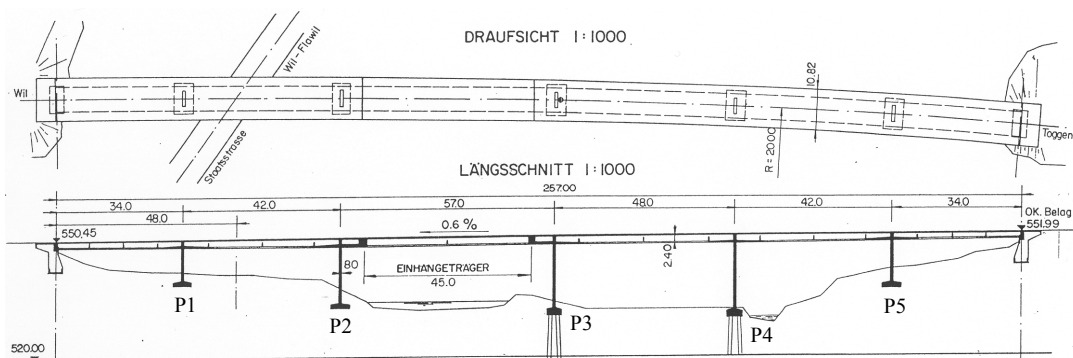
Fig. 2.43: Plan view and elevation of Viadukt Mühle Rickenbach in SG

The outer two piers (P1, P5) have the cross-section shown in Fig. 2.44 with a longitudinal reinforcement ratio of $\rho_{sl} = 0.32\%$ and a transverse reinforcement ratio of $\rho_{sw} = 0.2\%$. The inner three piers (P2, P3, P4) have the cross-section shown in Fig. 2.45. The corresponding longitudinal reinforcement ratio of these longer piers is $\rho_{sl} = 0.45\%$ and their transverse reinforcement ratio amounts to $\rho_{sw} = 0.15\%$. The longitudinal reinforcement is spliced by means of overlapping at the construction joint between the foundation and the pier base. The splice length is not given in the reinforcement drawings. The amount of longitudinal reinforcement is constant over the full height of all piers without termination of bars.

The clear pier heights between foundation and column tops amount to 7.44 m, 12.54 m, 16.33 m, 17.17 m, and 9.75 m for piers P1 through P5. Taking the location of the superstructure's center of mass into account, the effective heights result as 9.04 m, 14.14 m, 17.93 m, 18.77 m, and 11.35 m. Assuming essentially single bending in the piers, the corresponding effective aspect ratios are 2.26, 3.54, 4.48, 4.69, and 2.84.
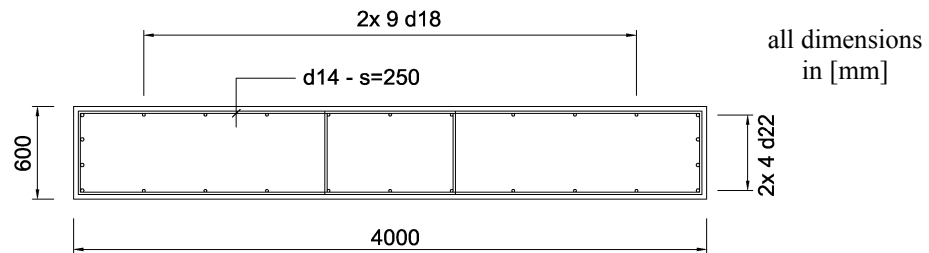
Fig. 2.44: Cross-section of piers P1 and P5 of Viadukt Mühle Rickenbach in SG
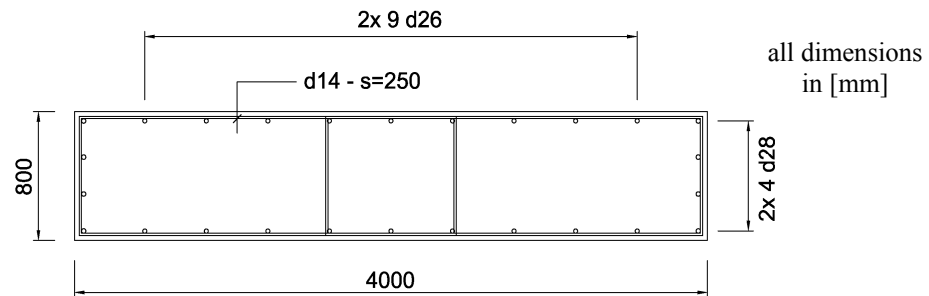
Fig. 2.45: Cross-section of piers P1, P2, and P5 of Viadukt Mühle Rickenbach in SG

The two longer piers P3 and P4 in the center region of the bridge are founded on 4 piles each, while the abutments and the shorter three piers P1, P2, and P5 have spread footings. The in-plan dimensions of these spread foundations are 7.40 m by 3.80 m for the two outer piers P1 and P5, and 8.00 m by 5.60 m for the second pier P2. Especially for the smaller footing, it may not be warranted that its moment capacity is sufficient to reach the yield strength of the piers, which would be required to let them develop plastic hinges at their bases.

e) Summary of Sample Bridges

The most important data characterizing the piers of the three sample bridges described above are summarized in Tab. 2.1. The material strengths are taken from [SIA2018] for the concrete and steel types given in the static calculations.

For the selection of potentially critical – and still representative – Swiss bridge piers, the low effective aspect ratio of 2.2 is of interest, which can be found in two of the bridges. In combination with transverse reinforcement ratios reaching as low as 0.08%, as in the case of *Viadukt Untere Weid*, potentially shear critical piers can result. Further parameters which influence the seismic flexural and shear behavior are the longitudinal reinforcement ratios, ranging in these cases between about 0.3% and 0.6%, as well as the axial load ratio ranging from about 0.06 to 0.09.

		Untere Weid	Gossau	Rickenbach P1, P5	Rickenbach P2, P3, P4
Year of construction		1971	1966	1965	
Generation of Code		1970	1956	1956	
Average Concrete Compression Strength at $t = \infty$ [a]	$f_{cm,t=\infty}$ [MPa]	34.0	35.9	30.4	
Characteristic Concrete Compression Strength at $t = \infty$ [a]	$f_{ck,t=\infty}$ **[MPa]**	**24.0**	**25.9**	**20.4**	
Average yield stress of longitudinal reinforcement [b]	f_{sm} [MPa]	550	530	440	
Characteristic yield stress of longitudinal reinforcement [b]	f_{sk} **[MPa]**	**450**	**480** [e]	**345**	
Average ultimate strength of longitudinal reinforcement [b]	f_{tm} [MPa]	580	680	610	
Characteristic ultimate strength of longitudinal reinforcement [b]	f_{tk} **[MPa]**	**550**	**620** [e]	**510**	
Section width of piers	b_w [m]	0.7	1	0.6	0.8
Section depth of piers	l_w [m]	3	4	4	4
Ratio section width/depth	b_w/l_w [-]	0.233	0.25	0.150	0.200
Minimum effective shear span of piers	min L_v [m]	13.95	8.70 [c] 4.35 [d]	9.04	14.14
Minimum aspect ratio of piers	**min L_v/l_w [-]**	**4.65**	**2.18** [c] **1.09** [d]	**2.26**	**3.54**
Longitudinal reinforcement ratio	ρ_{sl} **[%]**	**0.56**	**0.62**	**0.32**	**0.45**
Transverse reinforcement ratio	ρ_{st} **[%]**	**0.08**	**0.12**	**0.21**	**0.15**
Minimum axial load ratio (based on $f_{cm,t=\infty}$)	min $\nu_{cm,t=\infty}$ [-]	0.053	0.082	0.084	0.079
Average axial load ratio (based on $f_{cm,t=\infty}$)	**avg $\nu_{cm,t=\infty}$ [-]**	**0.057**	**0.082**	**0.088**	**0.087**
Maximum axial load ratio (based on $f_{cm,t=\infty}$)	max $\nu_{cm,t=\infty}$ [-]	0.062	0.82	0.092	0.096

[a] Characteristic values at an age of 28 days according to [SIA2018] for concrete class as given in static calculations. Estimation of average values and influence of concrete age at $t = \infty$ according to [SIA262].

[b] Values according to [SIA2018] for steel type given in static calculations.

[c] Based on assumed single bending (cantilever) behavior of the pier corresponding to zero rotational restraint at the pier top resulting from superstructure torsion.

[d] Based on assumed double bending behavior of the pier corresponding to fixed rotation at the pier top resulting from superstructure torsion.

[e] No data given in [SIA2018]. Characteristic values estimated from average values based on [SIA262] Section 4.3.9.3.3.

Tab. 2.1: Overview of data on piers of sample bridges

2.2.3   Current State of Seismic Assessment Procedures in Switzerland

Currently, in Switzerland no codes or guidelines exist which would regulate the displacement based assessment of existing bridges. In chapter 7 of [ASTRA05a] some recommendations for the conceptual approach are given and reference is made to [SIA2018] for the estimation of the piers' deformation capacity. The latter document, [SIA2018], is a guideline for the seismic assessment of exiting buildings using established displacement based concepts.

A direct application of [SIA2018] on bridges bears two problems: (a) The procedure for the estimation of the deformation demand according to [SIA2018] is specialized on multi-story building structures and therefore not directly applicable on bridges. (b) Bridges typically feature several characteristics and details which influence their seismic behavior but do not occur in buildings (see e.g. Section 2.1). These issues are not dealt with in [SIA2018] as they do not have any relevance for buildings. Concerning the demand estimation, it is noteworthy that the procedure outlined in [SIA2018] is based on the *Equal Displacement Hypothesis* which assumes that a nonlinear single-degree-of-freedom (SDOF) system has a similar seismic displacement demand as a linear system having the same elastic stiffness. [SIA2018] limits the application of this hypothesis to systems having fundamental periods of more than 0.7 s, while not providing any guidance for the treatment of structures with shorter periods.

The estimation of the deformation capacity of reinforced concrete members is not conceptually different for buildings and bridges. Therefore, the recommendations given in [SIA2018] for the determination of the displacement capacity can likewise be applied in the case of bridges. Here, this would mainly refer to the deformation behavior of the piers, as the superstructure will typically not be expected to develop large inelastic deformations.

According to [SIA2018], the deformation behavior of reinforced concrete members is supposed to be estimated on the basis of a plastic hinge model. The given equation (2.3) for the plastic hinge length is in general accordance with [PP92] and [PSC96], only being modified by a factor a_{st} to allow for the influence of the post-yield strain hardening behavior of the longitudinal reinforcement steel. This is related to the fact that the original equations in [PP92] and [PSC96] were calibrated on reinforcement steels with comparatively high strain hardening ratios as, e.g., used in the USA. European steels, however, typically have less post-yield strain hardening which is considered to reduce the plastic hinge length. In this context it should be mentioned that recently in [PCK07] an alternative modification has been proposed to take into account the strain hardening ratio. Furthermore, in [PCK07] also a separate equation for the estimation of the plastic hinge length in structural walls has been presented.

$$L_{pl} = a_{st} \left(0.08 \cdot L_v + 0.022 \cdot f_s \cdot d_{bl} \right) \quad ; \quad f_s \text{ in [MPa]} \tag{2.3}$$

with a_{st}:   Correction factor for post-yield behavior of longitudinal reinforcement
$\qquad\qquad a_{st} = 1.0$ for $(f_t/f_s) \geq 1.15$ and $a_{st} = 0.8$ for $(f_t/f_s) < 1.15$
$\qquad L_v$:   Length of shear span
$\qquad d_{bl}$:   Diameter of longitudinal reinforcement bars
$\qquad f_s$:   Yield strength of longitudinal reinforcement
$\qquad f_t$:   Ultimate tension strength of longitudinal reinforcement

To ensure that the plastic mechanism can develop in a pier, the shear capacity needs to exceed the shear demand resulting from the bending strength of the plastic hinge(s). Due to the importance of this requirement, in the ductile design of new structures it is common practice to use an overstrength flexural strength for the estimation of an upper bound shear demand, which corresponds to at least realistic material parameters. This procedure intends to ensure a sufficient safety against brittle premature shear failure. It should be noted that a significant margin between shear demand and capacity is justified because a comparatively small deficit of shear capacity can already result in a large reduction of the member's displacement capacity. Furthermore, as described in Section 2.1b, shear failure has a high risk of being accompanied by an axial load failure which can lead to a full structural collapse. In line with this general concept, the provisions in [SIA262] for the new design of RC structures require that the shear demand needs to be calculated based on expected average material parameters, while the shear capacity is determined using design values incorporating a partial safety factor.

In [SIA2018] the requirements for existing structures are reduced to some extent, as the shear demand is to be calculated based on the lower *characteristic* material properties for the flexural strength in the plastic hinges. The shear capacity is supposed to be based on design values of the material strengths, as in the case of a new design, and shall be calculated according to [SIA262]. Considering that the shear capacity in [SIA262] is typically governed by the strength of the transverse reinforcement (and not the diagonal concrete compression struts), the design resistance includes only a partial safety factor of $\gamma_s = 1.15$. Numerically, this appears to provide only a comparatively low safety margin against brittle shear failure. Some allowance for an implicit conservatism of the shear strength model underlying the design equation of [SIA262] may be involved in the reasoning for this reduced safety margin in [SIA2018]. However, the level of conservatism related to the shear equation in [SIA262] is difficult to quantify and may not be constant for all cases. This is especially the case as its original field of application is the conventional static design and not the inelastic cyclic loading during earthquakes, which is known to influence the shear bearing capacity of RC members.

Generally, the displacement based assessment procedure is limited in [SIA2018] to structures which do not develop brittle failure mechanisms. The following four examples that would preclude its application are given in [SIA2018]:

(1) Shear failure in tension ($\rightarrow$ hoops).
(2) Shear failure in compression ($\rightarrow$ diagonal concrete compression struts).
(3) Flexural failure before yielding of the longitudinal reinforcement.
(4) Flexural failure due to fracture of the longitudinal reinforcement at small plastic strains.

For the last case, concerning the premature reinforcement rupture, in [SIA2018] a criterion is given which states that reinforcement steel having a strain hardening ratio of $(f_t / f_s) < 1.08$ should normally be considered to cause this unfavorable failure mode. In [Daz05] a further case is mentioned which limits the (stable cyclic) deformation capacity and thus creates problems for the application of the displacement based assessment procedure:

(5) Lap-splices in the inelastic region of RC members.

Although such lap-splices are not generally considered to inhibit the displacement based analysis, it is recommended in [Daz05] to limit the maximum allowable strains in the reinforcement based on a careful check of the splice length and the amount of confining reinforcement. However, aside from the recommendation to choose the maximum reinforcement strain conservatively, no further explicit guidance is given in [Daz05] on what basis this should be done.

The restrictions for the applicability of the displacement based assessment defined in [SIA2018] may rather be considered as precautions. There is no strict conceptual reason why any of the mentioned criteria would not allow a displacement based analysis. The influence of these particular failure mechanisms on the deformation capacity (and possibly on the demand as well) only need to be taken into account adequately. As this may not always be easy to quantify in a reliable manner, it was chosen to exclude those cases from the rather simplified and standardized displacement based assessment procedure outlined in [SIA2018].

In [Bim06] and [BD06] two studies are presented which apply the currently established principles of [SIA2018], as discussed above, to analyze the behavior of bridges under transverse seismic excitation. For piers of wall-type shape, the transverse bridge direction is typically more critical because their low aspect ratio in this direction limits the flexural displacement capacity and makes them more prone to shear problems. In the longitudinal bridge direction, such piers are comparatively slender which provides them with higher flexural deformation capacities. Possibly, sliding bearings in the longitudinal direction may even provide some form of seismic isolation, protecting the piers in this direction. It should be noted that for other parts of the bridge or for other types of piers the longitudinal direction can be more critical.

The analyzed bridge models have typical characteristics and deficiencies of Swiss structures from the 1960s and 1970s (see Section 2.2.2). For both studies the pier cross-section and the transverse reinforcement layout of the *Viadukt Untere Weid* as shown in Fig. 2.38 were used. The pier height was varied in order to study the influence of the absolute member length and the aspect ratio on the seismic behavior.

The rather small original spread footings, provided in the *Viadukt Untere Weid*, would result in significant flexibility of the soil-foundation system (see Section 3.5.1) which is likely to reduce the demand on the piers. This beneficial effect may not always be given and it was therefore disregarded in these analyses, as they rather aim at a general assessment of potential risks to Swiss bridges. Instead, the footings were modeled as rigidly fixed constraints which can be considered as a worst case assumption for the piers, approximating e.g. a very stiff pile foundation.

For similar reasons the span width of the superstructure was increased from 20 m in the original bridge to 40 m for the analyses. A length of 20 m was felt to be inadequately unconservative to represent the general case of Swiss bridges. This modification only influences the displacement demand of the piers as the increased tributary mass and the reduced stiffness (in case of a continuous superstructure) result in higher periods of the structure. Due to the open shape of its cross-section, no significant torsional stiffness was attributed to the superstructure, leaving the piers essentially unrestrained with respect to rotations at their tops. As a consequence, the piers could be modeled as cantilever columns.

The superstructure of the *Viadukt Untere Weid* consists of precast concrete girders which are interconnected on top of the piers by means of in-situ concrete cross-beams and a continuous deck-slab. The behavior of the superstructure for bending about the vertical axis (transverse seismic excitation) therefore is neither that of a real continuous superstructure nor that of individual simply supported girders. Assuming an elastic behavior of this superstructure under seismic loading would not be appropriate and only a more detailed analysis of its possibly inelastic response might be able to approximate the real behavior.
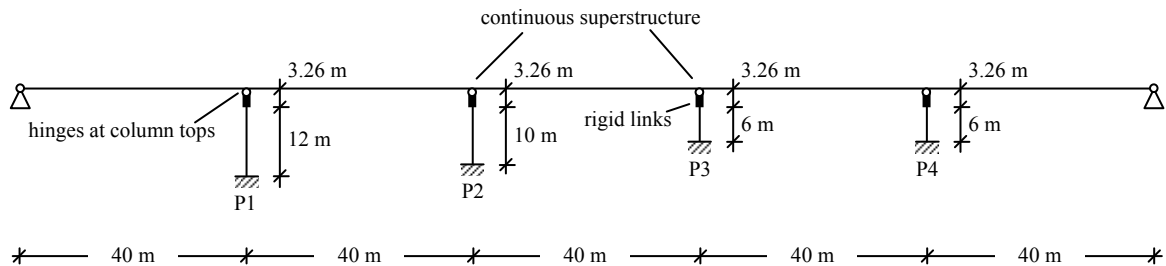
Fig. 2.46: Dynamic system of bridge with continuous superstructure [BD06]
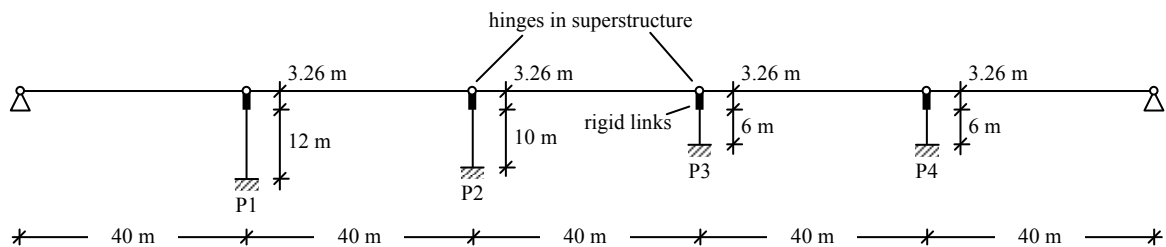
Fig. 2.47: Dynamic system of bridge with simply supported girders as superstructure [Bim06]

In the studies mentioned above, the two extreme cases of (a) a fully continuous superstructure [BD06] and (b) individual simply supported girders [Bim06] were analyzed. The first case (a), shown in Fig. 2.46, requires an integral seismic analysis of the entire bridge structure as a multi-degree-of freedom (MDOF) system due to the interaction of its members. For the second case (b), shown in Fig. 2.47, the hinges in the superstructure (for bending about the vertical axis) result in a decoupling of the transverse deformation behavior of the individual piers. Strictly speaking, this decoupling only exists under static loading, while under dynamic excitation the rotational inertia of the superstructure spans results in a certain interaction between neighboring piers. However, if the first mode dominates the vibrations, it can be expected that all pier tops are deformed in the same direction most of the time, thus limiting the rotation of the superstructure spans. As a consequence, the assumption of decoupled piers can serve as an approximation of the seismic bridge behavior with hinges in the superstructure. In this case, the piers can be analyzed as individual single-degree-of-freedom (SDOF) systems carrying tributary masses from the adjoining spans, as shown in Fig. 2.48.

Pier with clear height 12 m: | **Pier with clear height 10 m:** | **Pier with clear height 6 m:**

dynamic system | deformed shape & curvature distribution | plastic hinge model | dynamic system | dynamic system

Fig. 2.48: Dynamic systems of individual cantilever piers as SDOF [Bim06]

For the case of the pier with a clear height of 12 m, Fig. 2.48 also shows how the inelastic flexural behavior of the piers is approximated by a plastic hinge at its base. Along the length of this plastic hinge, as given by equation (2.3), the inelastic curvatures ϕ are considered constant and equal to the base curvature, while outside the plastic hinge an elastic behavior is assumed. This way, all inelastic flexural deformations of the piers are concentrated in the plastic hinges. As the piers are the same for the studies with continuous and hinged superstructure, their corresponding deformation behavior and displacement capacities do not differ between the two studies. Therefore, only the displacement demand is influenced by the different modeling of the superstructure and varies between the studies.

It has been mentioned above that certain structural characteristics are considered to preclude the application of the displacement based assessment procedure of [SIA2018]. The *Viadukt Untere Weid*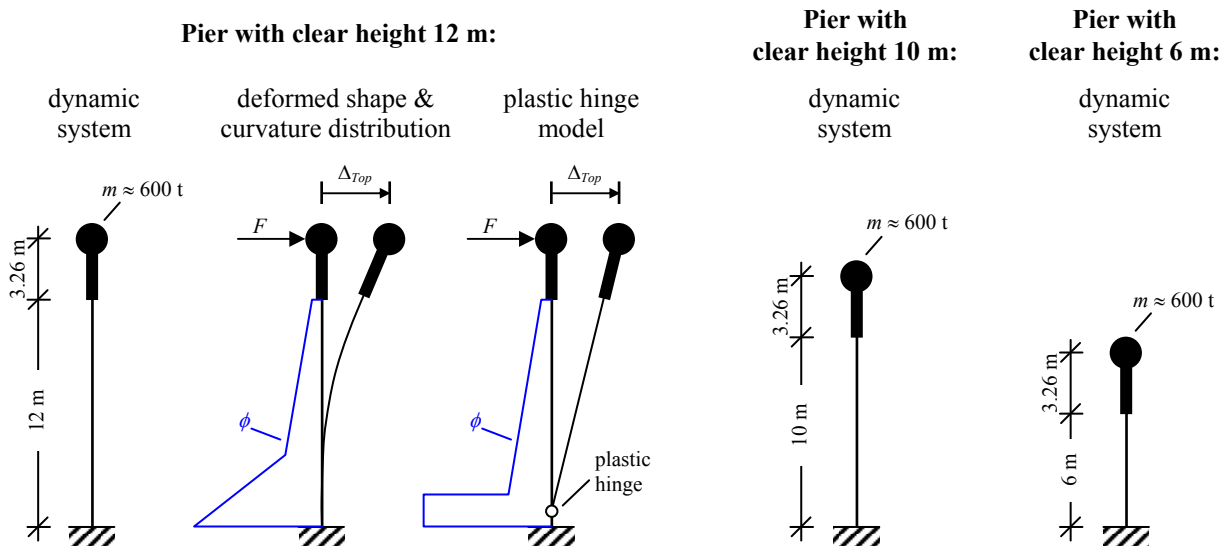 features some of these details and would therefore not be eligible for this type of analysis. Namely, the existence of lap-splices at the pier bases and – as will be seen below – the as insufficient predicted shear strength of one pier represent potential problems.

It should be noted that lap-splices are likely to be found at the bases of almost all existing bridge piers. Taking them as a criterion for a general disqualification of displacement based analyses would prevent the application of this method for existing bridges almost completely – and for building columns in many cases as well. Therefore, it appears more appropriate to allow the method for members with lap-splices, while introducing certain modifications of the deformation behavior in order to account for the adverse influence of the splices, as suggested in [Daz05]. Due to the current absence of any recommendations in [SIA2018], the issue of lap-splices is not further treated in this section where only the general concept shall be applied. A first approach to a potential handling of the problem, based on a model suggested in [PSC96], can be found in [BD06], and a more detailed discussion of the topic together with corresponding numerical and experimental results is given in Section 4.7.2.

Concerning the potential shear failure, the prohibition of the displacement based analysis in [SIA2018] does not appear to be compelling as long as the consequences on the deformation capacity are accounted for in an adequate manner. Therefore, in the current study the displacement based analysis method is applied despite the prediction of shear critical behavior in one case.

The flexural behavior of the pier cross-section can be described by means of a moment-curvature analysis. For the reinforcement a bilinear material behavior is assumed and the concrete in compression is modeled by the stress-strain relationship given in [SIA2018] which is based on [MPP88] and [Pop73]. According to [SIA2018], the analysis shall be based on characteristic material properties and not on average data. The corresponding moment-curvature curve based on the characteristic parameters of the *Viadukt Untere Weid* from Tab. 2.1 is shown in Fig. 2.49. The nominal yield curvature from this analysis results as $\phi_y = 1.39$ 1/km. As an alternative, [SIA2018] allows the direct approximate estimation of ϕ_y by means of equations which were developed in [Pri03] and

[PCK07]. Using the equation for wall cross-sections, a nominal yield curvature of ϕ_y = 1.5 1/km results, which compares favorably well with the result from the moment-curvature analysis. For the deformation limit, the ultimate strain of the concrete in compression ε_{cu} = 0.004, according to [SIA2018], governs and an ultimate curvature of ϕ_u = 6.2 1/km results which relates to a curvature ductility capacity of about 4.5. Using common principles outlined e.g. in [PSC96] and [Daz05] the nonlinear moment-curvature curve is further approximated by a bilinear relationship also shown in Fig. 2.49.
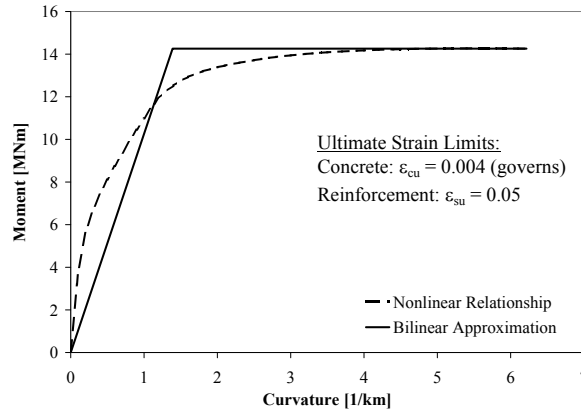
Fig. 2.49: Moment-curvature relationship of pier cross-section Viadukt Untere Weid for characteristic material parameters

Based on the plastic hinge model shown in Fig. 2.48 and the plastic hinge length as defined in equation (2.3), the bilinear approximation of the moment-curvature curve can be used to estimate a bilinear force-displacement curve for each of the piers in Fig. 2.48. The corresponding nominal yield displacements and ultimate displacements result from equations given in [SIA2018] and are based on simple kinematics of the plastic hinge model. The resulting force-displacement curves are shown on the left side of Fig. 2.50 together with the design shear capacity according to [SIA262]. Here it can be seen that the current models predict sufficient shear strength to develop the full flexural capacity for the piers with clear heights of 12 m and 10 m – corresponding to shear spans L_v of 15.26 m and 13.26 m, respectively. However, for the short pier with a clear height of 6 m (i.e. L_v = 9.26 m), the predicted shear strength is insufficient and a brittle premature shear failure would have to be assumed.
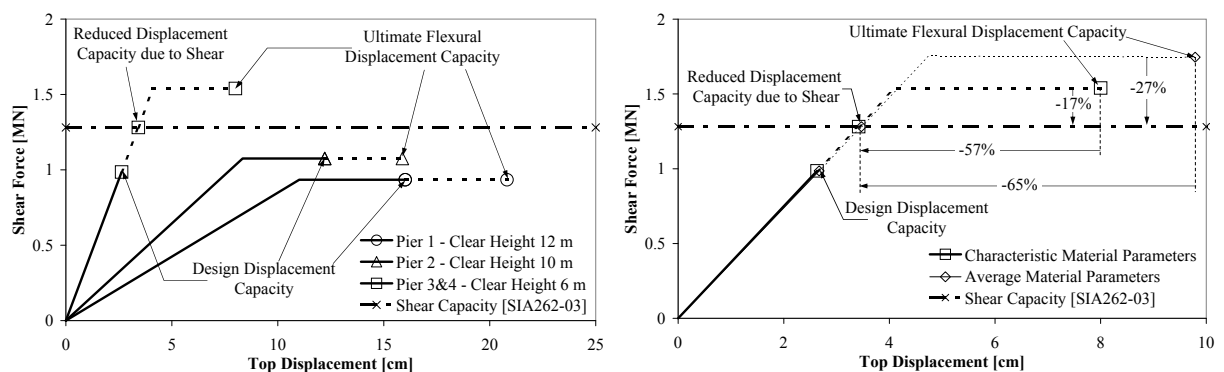
Fig. 2.50: Force-displacement relationships, shear capacity and displacement capacities
Left: Comparison between pier heights for characteristic material parameters,
Right: Comparison between characteristic and average material parameters for clear pier height of 6 m

The case of this short pier is analyzed on the right side of Fig. 2.50 in more detail. While the graph on the left side only contains the flexural capacity curves based on characteristic material parameters, as required by [SIA2018] for the check of shear capacity, on the right side the corresponding capacity curve is additionally shown for average parameters, as would be required for the more conservative overstrength calculations in [SIA262]. It can be seen that the deficiency of predicted shear capacity is

more pronounced in this latter case, resulting in a more critical picture of the situation. At the same time, the graph on the right side of Fig. 2.50 visualizes well the negative consequences of a premature shear failure. While the shear capacity corresponding to characteristic parameters only has a deficit of 17%, compared to the required strength for the development of the plastic mechanism, the resulting reduction of the deformation capacity amounts to 57%. With more realistic assumptions this effect may be even more pronounced as the flexural displacement capacity – here predicted for an ultimate concrete compression strain of $\varepsilon_{cu} = 0.004$ – in reality is likely to be significantly higher. If the shear capacity is not sufficient for the bending strength to develop, the total plastic range of flexural deformation capacity gets lost.

The ultimate displacement capacities Δ_u of the piers with clear heights of 12 m and 10 m result from the flexural behavior by reaching the compression strain limit of the concrete and amount to $\Delta_{u,flex} = 20.8$ cm and 15.9 cm, respectively. The shorter pier of clear height 6 m does not reach its flexural displacement capacity of $\Delta_{u,flex} = 8.0$ cm. Instead, its capacity Δ_u is rather limited by the premature shear failure to a reduced value of $\Delta_{u,red} = 3.4$ cm. The safety format of [SIA2018] requires that the characteristic displacement capacity shall be modified by a partial safety factor of $\gamma_D = 1.3$. The resulting design displacement capacities $\Delta_{ud} = \Delta_u/\gamma_D$ are shown in Fig. 2.50 and amount to 16.0 cm, 12.2 cm, and 2.6 cm for the clear pier heights of 12 m, 10 m, and 6 m, respectively.

The demand calculations in [Bim06] and [BD06] are based on a seismic zone 3b, soil type B and importance class III according to [SIA261]. For buildings, [SIA2018] recommends a viscous damping ratio of $\xi = 5\%$. The analyses presented in this section adopt the same value of $\xi = 5\%$, resulting in the elastic pseudo-acceleration spectrum as shown in Fig. 2.28. A more general discussion on the appropriate assumption of viscous damping for bridges can be found in Section 4.4 and in [BD06].

For the bridge system with the non-continuous superstructure (see Fig. 2.47 and Fig. 2.48), the displacement demand of the uncoupled piers acting as individual single-degree-of-freedom (SDOF) systems can be estimated directly using the *Equal Displacement Hypotheses* established in [SIA2018] for natural periods larger than 0.7 s. Fig. 2.51 shows the elastic displacement spectrum defined in [SIA2018] together with the elastic periods and resulting displacement demands for the three pier types of Fig. 2.48.
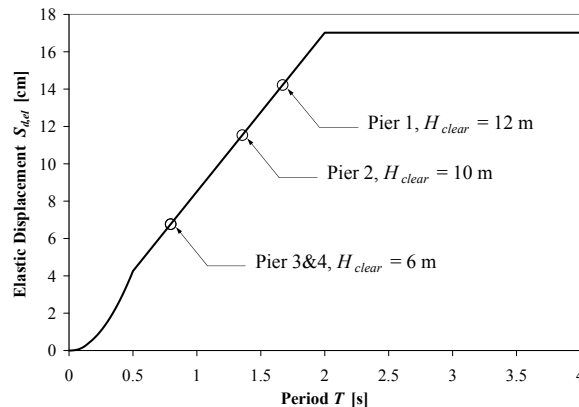
Fig. 2.51: Elastic displacement spectrum for demand calculations corresponding to [SIA2018]

The bridge with the continuous superstructure, shown in Fig. 2.46, requires an analysis of the entire multi-degree-of-freedom (MDOF) system. Several analysis approaches are discussed, applied and compared for this task in [BD06]. From this comparison it can be concluded that the various procedures give similar results for the comparatively low ductility demands reached in this example. Inelastic time history analysis (ITHA) can be considered to capture the seismic behavior in the most realistic way and it is therefore often used as a reference. Results from ITHA which were calculated with the software code SeismoStruct [SS06] for a spectrum compatible ground motion are shown in Fig. 2.52. For comparison purposes the nominal yield displacements and the design displacement capacity, as determined in Fig. 2.50, are also shown. It should be noted that for the MDOF analysis the abutments were modeled as rigidly pinned supports for the superstructure, not taking any flexibility

into account. This is a simplified assumption and the introduction of abutment flexibility would yield different results for the displacement demand of the piers. Especially for the outer piers 1 and 4, modeling of deformable abutments is likely to result in higher demands. A more detailed discussion on this topic can be found in Section 3.5.2.
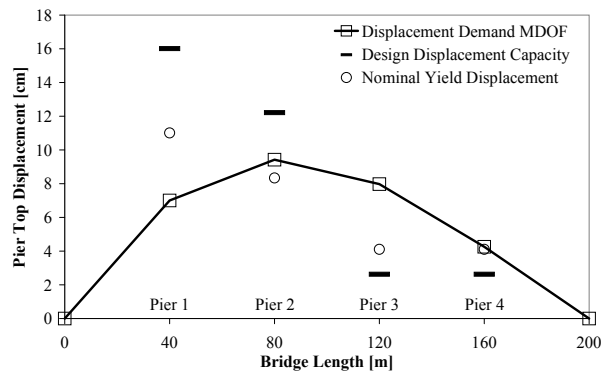
Fig. 2.52: Displacement demand of piers for bridge with continuous superstructure [BD06]

A complete comparison of the displacement capacities and demands of all the piers is shown in Fig. 2.53 for the two different modeling cases with hinged and continuous superstructure. It can be seen that for both types of superstructure modeling the longer piers 1 and 2 with clear heights of 12 m and 10 m fulfill the criteria of [SIA2018]. The lower demand values for these two piers in the case of the continuous superstructure are a result of the second load path which is provided by the elastic girder. Especially for the outer pier 1, the elastic superstructure – in combination with the rigid supports at the abutments – provides significant additional stiffness which limits the deformations. Obviously, this effect depends on a variety of parameters defining the second load path and can be completely different if e.g. the abutments are modeled differently or the distribution of pier heights along the bridge is changed. It should be noted that for the individual piers 1 and 2 on the left side of Fig. 2.53, despite their lengths, the corresponding design deformation capacities are just sufficient for the calculated displacement demands, resulting in compliance factors [7] according to [SIA2018] of $\alpha_{eff} = 1.13$ and 1.06, respectively.
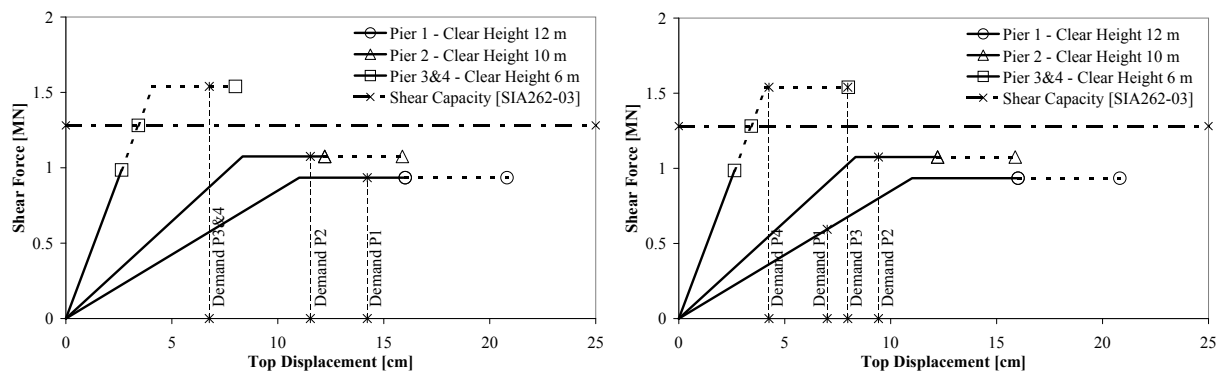
Fig. 2.53: Comparison between displacement capacity and demand for the four piers of the bridge
Left: Independent piers due to non-continuous superstructure,
Right: Coupled piers by continuous superstructure

A more critical situation is encountered for the shorter piers 3 and 4 with clear height 6 m (effective height 9.26 m). The premature shear failure according to [SIA262] and the consequential significant drop of displacement capacity result in a predicted failure of both piers, independent of the type of superstructure modeling. It is interesting to note that the model with continuous superstructure results in a higher displacement demand for the inner pier 3 compared to the model with individual piers. The

---

[7]   In the displacement based assessment approach of [SIA2018] the compliance factor α_{eff} is defined as the ratio between the design displacement capacity (including a partial safety factor) and the displacement demand.

continuous superstructure, in this case, forces the short pier 3 to follow the deformations of the integral structure which are higher than the demand on the independent pier with only its tributary mass. The opposite situation results for the outer short pier 4 which, due to its proximity to the rigidly modeled abutment, receives additional support from the continuous superstructure and thus experiences lower deformations than in the case of a hinged superstructure.

The generally lower displacement capacity of the short piers 3 and 4 is not sufficiently compensated by corresponding lower demands. Especially for the system with continuous superstructure (Fig. 2.53 right), the demand of the inner piers 2 and 3 does not differ very much, resulting in a critical behavior of pier 3 even if the full flexural displacement capacity could be reached. For the model with independent piers (Fig. 2.53 left), the design deformation capacity of piers 3 and 4 corresponding to flexure without shear problems would not be sufficient either if the partial safety factor γ_D according to [SIA2018] is applied. If the predicted shear failure is taken into account additionally, the lack of displacement capacity is substantial, resulting in compliance factors of $\alpha_{eff} = 0.33$ and 0.39 for continuous superstructure and individual piers, respectively.

This emphasizes once again the previously stated conclusion that short and squat piers can be expected to possess a more critical seismic behavior than longer and more slender columns. Furthermore, the results show that even in Switzerland, with its rather moderate seismicity, earthquake related damage to bridge piers cannot be ruled out. The presented simplified analyses suggest that the behavior may still be considered tolerable if no premature shear failure occurs, thus enabling at least the limited flexural displacement capacity to develop. Although the compliance factor α_{eff} might be found to be somewhat lower than unity in some cases, the provided seismic safety level may finally be accepted based on the cost-benefit considerations outlined in [SIA2018].

If, however, a predicted shear failure leads to a further significant reduction of the displacement capacity, as in the case of piers 3 and 4 in the presented example, it may occur that even the appraisal of cost-benefit aspects would not suggest an acceptable seismic performance of the pier anymore. This demonstrates that a reliable prediction of the shear capacity under cyclic inelastic loading is of particular importance for the assessment of reinforced concrete structures in Switzerland. Currently, [SIA2018] refers to [SIA262] for the estimation of the shear strength. The typically governing equation (37) of [SIA262] is based on a simple stress field, allowing inclinations of the concrete compression struts not lower than 25°. This equation is considered to provide sufficiently safe – and supposedly conservative – estimations of the shear strength for the purpose of new designs under static monotonic loading.

It is of particular research interest to investigate whether equation (37) of [SIA262] is really appropriate for the assessment of existing structures under seismic loading. The implicit proportionality between transverse reinforcement ratio and shear strength, according to equation (37), often leads to very low shear capacity predictions for existing older RC bridge piers with their typically low amounts of transverse reinforcement. In such cases, this simplified model may be overly conservative. On the other hand, it should be taken into account that cyclic inelastic loading can reduce the shear strength of RC structures, which may not be represented by a model that was calibrated on static monotonic test data only. It is therefore generally desirable to use possibly realistic shear strength predictions which are appropriate for the specific case and type of loading. If a more realistic shear capacity model is used which possibly incorporates less implicit conservatism, it should also be noted that the currently in [SIA2018] established way of estimating the shear demand without consideration of overstrength material properties may not be appropriate anymore. In either case, a sufficient safety margin between shear demand and capacity must always be guaranteed in order to preclude brittle failure in the elastic range of the piers.

A summary of the numerical results from the above example calculations can be found in Tab. 2.2. Further results, especially concerning the influence of lap-splices and reinforcement termination on the deformation behavior and capacity can be found in [Bim06]. These additional considerations which are not treated in [SIA2018] are based on models suggested in [PSC96]. A comparison of (alternative) procedures to estimate the displacement demand of MDOF bridge structures is included in [BD06], which also contains a discussion on the choice and influence of elastic viscous damping for seismic bridge assessment.

Pier Number			P1	P2	P3	P4
Clear Pier Height		H_{clear} [m]	**12**	**10**	**6**	**6**
Effective Pier Height		$H_{eff} = L_V$ [m]	15.26	13.26	9.26	9.26
Aspect Ratio		L_v/l_w [m]	5.09	4.42	3.09	3.09
Tributary Mass at Pier Top		m_{top} [t]	600	600	600	600
Capacity — Force	First Yield Force	F_y' [MN]	0.764	0.879	1.259	1.259
	Nominal Force Capacity	F_n [MN]	0.934	1.075	1.540	1.540
	Design Shear Capacity	V_{Rd} [MN]	1.281	1.281	1.281	1.281
Capacity — Displacement	First Yield Displacement	Δ_y' [cm]	9.01	6.82	3.36	3.36
	Nominal Yield Displacement	Δ_y [cm]	11.01	8.34	4.11	4.11
	Flexural Ultimate Displacement Capacity	$\Delta_{u,flex}$ [cm]	20.82	15.88	8.00	8.00
	Reduced Displacement Capacity [a]	$\Delta_{u,red}$ [cm]	20.82	15.88	3.42	3.42
	Design Displacement Capacity	Δ_{ud} [cm]	**16.01**	**12.21**	**2.63**	**2.63**
Displacement Demand — SDOF	Initial Stiffness	k_0 [MN/m]	8.49	12.89	37.48	37.48
	Elastic Period	T_0 [s]	1.67	1.36	0.80	0.80
	Elastic Spectral Displacement	S_d [cm]	**14.2**	**11.5**	**6.8**	**6.8**
	Compliance Factor [SIA2018]	α_{eff} [-]	**1.13**	**1.06**	**0.39**	**0.39**
Displacement Demand — MDOF	**Displacement Demand ITHA**	Δ_{ITHA} [cm]	**7.0**	**9.4**	**8.0**	**4.3**
	Compliance Factor [SIA2018]	α_{eff} [-]	**2.29**	**1.30**	**0.33**	**0.62**

[a] Takes into account potential reductions of the displacement capacity due to premature shear failure.

Tab. 2.2: Results for displacement capacity and demand of the two analyzed bridge configurations

2.2.4   Relevance of Seismic Risks to Infrastructure Systems

When assessing the adverse effects of earthquakes, it can generally be distinguished between, on one hand, personal injury and death of human beings and, on the other hand, economic damage resulting from the destructions. While the potential forms of harm to persons are rather easy to imagine, it is not always straightforward to consider all potential economic consequences. At first sight, one might primarily think of direct structural damage and the costs of repairing or reconstruction as economic consequences. In fact, for building structures, damage estimations after previous earthquakes suggest that this is a major contribution to the overall economic loss. However, for infrastructure, such as bridges, further secondary economic consequences can also play a significant role, which may even exceed the direct economic losses from structural damage considerably.

The importance of a bridge is accounted for in [SIA261] by means of three importance classes and corresponding modification factors γ_f influencing the required seismic demand. It can be expected that normally bridges that are part of major highways are classified at least into importance class II. The highest class III will usually be reserved for structures that are considered to be an essential part of so-called *lifelines*. Bridges which are necessarily required for the access to a certain region, to hospitals or other important emergency institutions are regarded to fall into this category. The reasoning behind this mainly refers to the need for immediate rescue and relief efforts after an earthquake.

However, experience from previous earthquakes has shown that the importance of the infrastructure, and the consequences of damage to it, can go well beyond these immediate requirements after an earthquake. Switzerland is a highly developed country in the center of Europe and its infrastructure is a vital and essential part of its national economy. Today's society relies on a stable flow of goods and unhindered movement of persons. Modern production processes are often based on just-in-time deliverance of components and resources, while international markets require the distribution of the products. Therefore, any severe malfunction of the infrastructure system which interrupts or limits this ability for reliable transportation can result in considerable secondary damage to the national economy.

Not only earthquakes can cause such problems but also other sources of halting, as e.g. strikes in the transportation sector, often visualize the great importance of infrastructure to our economic system. Although these consequences are always difficult to quantify reliably, in the context of a railway strike in Germany an attempt has been made to estimate the gross consequences on the German economy [KK08]. This study concluded that a strike of 3 to 4 days, which would halt about 80% of Germany's commercial railway transportation capacity without hindrance of passenger transport, could cost the national economy in the order of 70 million Euros per day. If the strike includes a significant part of the passenger transport, the damage could rise to 90 million Euros per day. It was further estimated that a longer strike of, say 2 weeks duration, would increase the daily costs to as much as 180 million Euros. Especially the latter number shows the importance of down time, which might be significantly longer than two weeks if bridges on important transportation routes suffer real structural failure.

Attempts to estimate the secondary economic costs to highly developed regions resulting from earthquake damage mainly started after the 1994 Northridge earthquake in California. Petak and Elahi [PE00], e.g., have attempted to quantify the total impact of the Northridge earthquake on society and economy including secondary effects. Seligson and Eguchi [SE05] have further found that loss estimates shortly after the earthquake underpredicted the full consequences, compared to later estimations. To some extent, this may be due to secondary effects which are not fully visible at short term after the earthquake, although different ways of analysis can certainly also play a significant role for the deviations.

Several studies have focused directly on the secondary economic consequences of damage to the transportation infrastructure which occurred after the Northridge earthquake. In one of these, Gordon *et al.* [GRD98] estimate the total economic loss from business interruptions to be in the order of $6.5 billion. Based on their research, they attribute more than $1.5 billion, i.e. around one quarter of the total business losses, to transport related interruptions. They identified mainly four sources of transportation disruptions which contributed to these costs:

1. Commute interruptions that impeded employee access,
2. Obstacles to customer access,
3. Interference with shipments of output,
4. Disruptions to the supplies of inputs.

Although these figures represent substantial economic damage, Gordon *et al.* emphasize that special circumstances limited such consequences for the Northridge earthquake, which in other cases could have been significantly more severe. Reasons for these limitations are related to the peripheral epicenter, focusing on residential zones which rather feature retail and service activities and not so much industrial or high-profile commercial locations. A second important factor for the limited consequences of transport related economic losses after the Northridge earthquake is attributed to a surprisingly low degree of damage to the highway system. This comparatively good behavior of the bridges is also related to the fact that at the time of the Northridge earthquake a large retrofitting program for a total of 860 bridges was just underway, which was initiated in the aftermath of the Loma Prieta earthquake five years earlier. This program proved its effectiveness as none of the 122 bridges that had already been retrofitted at the time failed during the Northridge earthquake [PE00]. In turn, all 9 bridges that collapsed on major interchanges had already been identified and scheduled for retrofit as part of the program, but the works were still due to be carried out. A report prepared for the California Department of Transportation concluded that these 9 bridges could have also survived the earthquake with little damage if they had been retrofitted in time [PE00].

Furthermore, Gordon *et al.* [GRD98] point out that the economic losses from the transportation disruption would have been much higher if there had not existed substantial redundancies within the Los Angeles highway system. The fact that even after the earthquake such redundancies remained may partly be attributed to the comparatively low damage to the highway system also resulting from the retrofitting efforts. However, the same amount of redundancy may not be provided in other regions of the world. Due to its alpine topography, part of the Swiss transportation infrastructure, e.g., is characterized by a limited number of highly important transportation lines. If any, or several, of these traffic routes had to be shut down for a longer period of time, this would significantly limit the transportation capacities and could not necessarily be compensated by redundancies as in the case of Los Angeles.

To illustrate that the economic consequences of the Northridge earthquake were still comparatively moderate, thanks to the alleviating circumstances mentioned above, Gordon et al. [GRD98] refer to estimates of an equivalent earthquake scenario located at the Newport-Inglewood Fault where more severe consequences would have to be expected. According to this study by the University of Southern California Planning Institute from 1992, the total loss due to business interruption is estimated as $33 billion, and thus much higher than the $6.5 billion experienced after the Northridge earthquake. Applying the same ratios resulting from the Northridge analysis, Gordon *et al.* generate a potential transport-related business interruption cost of $9.0 billion.

Another study by Boarnet [Boa98] also came to the conclusion that the transportation disruptions after the Northridge earthquake played an important role for the following economic costs. In his study he focused on the local and regional distribution of these business losses. Surprisingly, he found that no relationship existed between the distance from the transportation destruction and the business losses. While other types of damage are typically correlated with the distance to the epicenter, at least in the case of the Northridge earthquake, transportation-related business losses appeared to be an exception. This also means that such secondary economic damage can reach well beyond the actual region being struck by the earthquake.

While these economic consequences were limited in time, with a later recovery, there are also examples where this was not the case. Chang [Cha00] performed a study on the consequences for the transportation system of Kobe, and particularly for its port, after the earthquake that hit the city in 1995. She showed that, although previous literature typically assumed that earthquakes do not cause economic long-term effects, a clear influence could also be noted over the long run. The port of Kobe, which used to be the sixth largest container port worldwide in terms of cargo throughput before the earthquake, only ranked seventeenth in 1997, after repairs had been completed.

Chang concludes from this example that transportation infrastructure is crucial for secondary and long-term economic losses because of its comparatively long restoration times. While other lifelines, such as water and natural gas, were fully repaired within 3-4 months after the earthquake, the full restoration of the railway and highway system took 7 and 21 months, respectively. The full recovery of the port took even somewhat more than 2 years. Chang argues that such long transportation disruptions reduce the competitiveness of locations and regions.

Fig. 2.54: Damaged port of Kobe after the earthquake in 1995

Watanabe [Wat06] showed that the world wide importance of Kobe as a port kept dropping even after 1997. Based on its container throughput it ranked as 27th in 2001 and the total tonnage transferred in 2002 amounted to only 46% of the value before the earthquake in 1994. Based on data by the *American Association of Port Authorities* (AAPA), the downward trend of Kobe as a container port has continued until today since it has dropped globally to rank 41 in 2007. Watanabe explains these long-term consequences with the necessity of the shipping lines to search for alternative ports shortly after the earthquake. Once they had newly organized themselves there, they never came back even after the full repair of the Kobe port.

This drastic example visualizes the importance of earthquake related damage to transportation infrastructure and the potential economic consequences – possibly even in longer terms. This also illustrates that it may not be sufficient to consider only the costs from direct structural damage when assessing bridges, but also the potential wider consequences should be taken into account.

2.2.5   Formal Framework for the Seismic Assessment of Swiss Bridges

In the previous sections it has been shown that, due to a combination of circumstances, a sufficient seismic safety of Swiss bridges may not always be certain. The first contribution to this situation comes from the insufficient seismic code provisions in the past, based on which the vast majority of existing bridges has been built (see Section 2.2.1). Seismic input loads used in the design of the structures were therefore either much too low or simply non-existent. In Section 2.2.2, it has further been shown that the Swiss bridge stock contains a significant amount of structures featuring certain characteristics which can lead to critical seismic behavior. Aside from very low transverse-reinforcement ratios in the piers and lap-splices at their bases, it was also found that a high percentage of bridges features rather short piers that conceptually have low displacement capacities. If these piers additionally have low aspect ratios, they can also be shear critical. As a result, the simple analyses in Section 2.2.3, which follow currently established seismic assessment procedures for buildings, suggest that the seismic safety of existing Swiss bridges in some cases may be insufficient, especially in case of the aforementioned shear problems of the piers.

The ASTRA guideline [ASTRA05b] regulates the monitoring and maintenance of Swiss national highway bridges. Furthermore, the circular [ASTRA03] determines that evaluations of existing structures are to be based on the current *Swisscodes* together with the SIA guideline [SIA462]. Both guidelines demand that an assessment should be conducted if a changed or new risk situation for a structure has evolved, or if new findings cause doubts about the sufficiency of the current safety. Although [ASTRA05b] states that not every updating or new generation of codes requires a systematic assessment of the existing structures, the above situation – and in particular the severe increase of seismic loads over the last decades – should be considered as enough justification for the currently ongoing program for the seismic assessment of existing bridges.

Both guidelines also propose the use of a multiple-phase approach if the need for a safety assessment has been identified. In the first stage, a comparatively crude screening should be conducted which is supposed to answer the most crucial questions concerning the safety of the structure. According to [SIA462], this should essentially consist of gathering the existing documents on the structure, taking down its current condition, and only rough calculations on the key structural members. Based on these results it has to be decided whether a more detailed analysis needs to be carried out in a second assessment step. In such a second stage, the current condition of the structure would have to be figured out in more detail and a more complete structural analysis would be required taking the updated loads and actions into account.

For any analyses, [SIA462] requires that they should be based on the previously determined current condition of the structure. In particular, this refers to potentially existing flaws or pre-existing damages of the structure, any changes compared to the original structure, or signs of fatigue, aging, or corrosion. Furthermore, the support conditions and the bearings should be checked, and their current condition should be introduced into the structural analysis as boundary conditions.

For the assessment of existing structures, the guideline [SIA462] allows the use of other provisions than those from the SIA codes for new designs. This refers to possibly differing models representing the actions as well as the resistance of the structure, as long as a sufficient theoretical or experimental basis justifies these alternatives. However, the required structural safety in the end has to correspond to the same level as defined by the currently valid SIA codes for new structures. Only if additional safety measures are taken, it may be deviated from the principles of the SIA codes. These measures are to be determined taking (among others) cost-risk evaluations into account and considering the level of acceptable risk. Such acceptable risks would have to be agreed on with the owner of the structure and the responsible authorities. In special cases, where the provided safety appears insufficient but an acceptable level cannot reasonably be established without high costs, [SIA462] proposes the appointment of an expert committee. This group would be allowed to decide on a qualitative basis on the acceptability of the situation.

The current assessment procedure for existing national highway bridges, as established in [ASTRA05a], generally complies with the principles of [SIA462] and [ASTRA05b] as outlined above. The documentation [ASTRA05a] also builds on a two step approach for the seismic assessment and specifies the aforementioned principles in more detail. For the second step, containing the more

detailed structural analysis, [ASTRA05a] essentially refers to [SIA2018] and also adopts its procedure concerning the acceptability of risks. It therefore allows limited deficits of capacity compared to code provisions if justified by cost-benefit evaluations. Such an approach is not explicitly included in [SIA462] which normally requires full compliance with the safety level of existing codes, also for existing structures. However, [SIA462] does include the concept of acceptable risk in the context of additional safety measures which may serve as a substitute for full code compliance. It may therefore be said, that the principles of [SIA2018] – and thus also those of [ASTRA05a] – are not in contradiction to the general principles of [SIA462], but they rather add a quantitative concept to the qualitative principles of [SIA462].

Finally, it can be concluded that the current efforts for the seismic assessment of existing Swiss bridges appears justified. Risk is a two-dimensional quantity, consisting of (a) the probability of occurrence and (b) the extent of potential damage. Due to the development of codes in the past, the first component may represent a probability of damage that is higher than expected. Taking the importance of the national bridge stock into account, as outlined in Section 2.2.4, the potential damage consequences might not be acceptable. This situation should therefore not be ignored without further assessment.

3 Structural Modeling of Bridges

3.1 General Considerations

As in static analysis, the structural model of a bridge serves as a mechanical representation of the system, describing its relevant members and characteristics. The basis of such a modeling procedure is a profound qualitative understanding of the load carrying mechanisms – and for a seismic analysis also of the dynamic properties. For a given bridge the corresponding mechanical model is not unique and a variety of levels of detailing are conceivable. At first sight, one might think that the more detailed and complex a model is, the better should be the corresponding analysis results. In this context it is noteworthy that the authors of two very influential books from the field of bridge design as well as from seismic design have chosen the same quote by a former student and professor of ETH Zürich in their preface. In [BM03] and in [PCK07] the authors quote Albert Einstein's recommendation:

"Everything should be made as simple as possible, but not simpler."

Although Albert Einstein probably did not primarily think of seismic bridge analysis when making this statement, it can, in fact, also serve as a good general guideline for the development of structural bridge models. While it is already possible to create very complex and complicated models for static analysis, the amount of effort and complexity can even increase substantially for seismic analysis. This is not only true for the actual definition of the model (i.e. the data input), but may be even more so for the corresponding analysis results (i.e. the data output). While static analysis in normal cases is based on the assumption of linear elastic or ideal-plastic behavior, a realistic description of the seismic response typically requires the consideration of inelastic – possibly even cyclic-hysteretic – material behavior, plus the definition of dynamic characteristics, as e.g. damping properties and mass distribution. Furthermore, static analysis for a certain load case normally gives only one set of results, while a full dynamic time history analysis produces an entire set of results for every time instant of the response, increasing the amount of output data to be processed substantially.

The increased amount of required and produced data in a detailed seismic analysis can lead to additional error sources and may make the interpretation of the results rather cumbersome if an overly complex structural model is chosen. In particular, a very detailed model with respect to some issues may distract the attention from other important aspects whose relevance for a realistic description of the system response might not be recognized as a consequence. It is evident that the model must not be too simple either because this would lead to unreliable results. Therefore, it is recommended to start the modeling process by carefully analyzing (qualitatively) the system to identify its dynamic load carrying mechanisms. As seismic response is likely to be associated with at least some inelastic action, particular attention should be given to the correct identification of the possible plastic mechanisms and the order of their development. A fundamental error, like e.g. an incorrect plastic mechanism resulting from not recognizing possible positions of plastic hinges, can hardly be compensated by a complex modeling approach and it would make the entire analysis results of questionable value.

Therefore, it is strongly recommended to spend sufficient effort on understanding the system behavior qualitatively before developing the numerical model of the structure. In many cases, this previous qualitative analysis may help simplifying the actual computer model and thus speed up the numerical analysis, while also reducing potential error sources. Another common problem in seismic analysis is that not every modeling assumption can be made with sufficient certainty. Therefore, it may be recommendable to rather perform a variation of these uncertain assumptions in a number of analyses on a less complex model than using a very sophisticated model with only one set of assumptions. In some cases, the assumptions can influence the response very strongly and not investigating the consequences of their uncertainty by means of an appropriate variation may give a mistaken picture of the reliability of the results.

It appears noteworthy that several aspects of seismic bridge modeling may differ considerably from a corresponding bridge model for normal static load cases. This is related to the fact that under static load cases typically the vertical response is rather dominant, while for the seismic response mostly the horizontal behavior of the structure is more relevant. At the same time, in static analysis significant

effort is typically invested to investigate the elastic response of the superstructure under a variety of load cases. In contrast, for seismic analysis often the inelastic response of the substructure (e.g. the piers) is of much greater interest. These differing focuses should also be reflected in the chosen model for the individual case. As a consequence, a model that performs very well for static analysis under normal load cases may not yield realistic results in a seismic analysis – and vice versa.

Before going into the details related to the modeling of individual members, some initial decisions need to be made. A fundamental question in this context is whether a full three dimensional model should be chosen or whether a reduced dimensionality (typically 2D) is sufficient. Generally, an earthquake always excites the structure in all three directions so that the response is also three dimensional. Therefore, it may be appealing to use a 3D model which could be used for all three directions – possibly even in a single dynamic analysis. However, it should be kept in mind that a 3D model inevitably is significantly more complex than e.g. a 2D model. Every node in a 3D model has six degrees of freedom, compared to three in a 2D model. Likewise, every beam element in a 3D model has six internal force actions instead of three in a 2D model. This means that for every node more transitional and boundary conditions need to be defined and for every structural member a more complex load-deformation behavior has to be determined in the case of a 3D model. This requires special attention to ensure that no undesired actions occur in the members, as e.g. unwanted torsional moments in beams and columns due to mistakes in the boundary condition at the member ends.

Generally, it can be said that a 3D model features a substantially higher potential for errors in the system definition. Furthermore, the numerical solution in a 3D analysis is significantly more demanding, and the created output data is also much more complex than for a 2D analysis. The subsequent evaluation, interpretation, and verification of the results from a 3D analysis can therefore become a difficult task, bearing an increased risk of not detecting potential analysis errors.

At the same time, a full 3D analysis may not always be necessary. In many cases it will be sufficient to perform separate analyses for the three directions of seismic excitation and use a superposition rule, as e.g. the one from [EC8-2], Section 4.2.1.4 (see also [EC8-1], Section 4.3.3.5), in order to combine the individual response components. As different aspects of the bridge behavior are likely to be relevant for the individual directions of excitation, it may be sufficient to develop significantly simpler models incorporating only these governing characteristics for each of the analyses. For example, for the response in the horizontal transverse direction a more complex multi-degree-of-freedom system featuring inelastic piers may be necessary, whereas the horizontal longitudinal direction might only require a single-degree-of-freedom representation in case of a straight continuous superstructure. On the other hand, for the vertical direction of excitation a linear elastic analysis could already be sufficient, as the vertical loading is mainly relevant for the superstructure and it will normally not cause inelastic response.

Even if only a unidirectional excitation is applied, the bridge structure itself normally still represents a three dimensional system. However, in certain cases it may be possible to simplify and transform the system into a two dimensional model without changing its seismic response characteristics. As an example, in Fig. 3.1 the three dimensional model for the transverse seismic analysis of a 4-span girder bridge is shown. In this model the pier tops are connected to the superstructure via hinges. This representation may be appropriate if either justified by the arrangement of bearings or if the torsional stiffness of the superstructure is insignificantly low (e.g. in the case of an open superstructure cross-section). In this case, the piers serve as pure translational restraint to the superstructure and act as cantilever columns. The same behavior can be achieved in a model if the piers are (artificially) placed horizontally in parallel to the superstructure, as shown in Fig. 3.2. For transverse excitation this simplified two dimensional model is fully equivalent to the three dimensional model of Fig. 3.1. However, the definition of the structural properties, the numerical solution and the data evaluation is much simpler and less prone to errors. A further simplification of the system using inelastic springs for the piers is shown in Fig. 3.52. Here, in addition the influence of soil-structure interaction at the pier foundations is implemented in an efficient manner without increasing the complexity of the system significantly.

The shown simplifications are restricted to certain assumptions and may not always be possible (without modifying the response characteristics in an inadmissible manner). In Section 3.4 the influence of the superstructure rotational and torsional behavior on the system response is discussed,

which also influences the applicability of the simplifications described above. Despite the desirable reduction of the complexity of the model, it must be ensured that a potential simplification still captures the relevant aspects of the realistic system behavior.
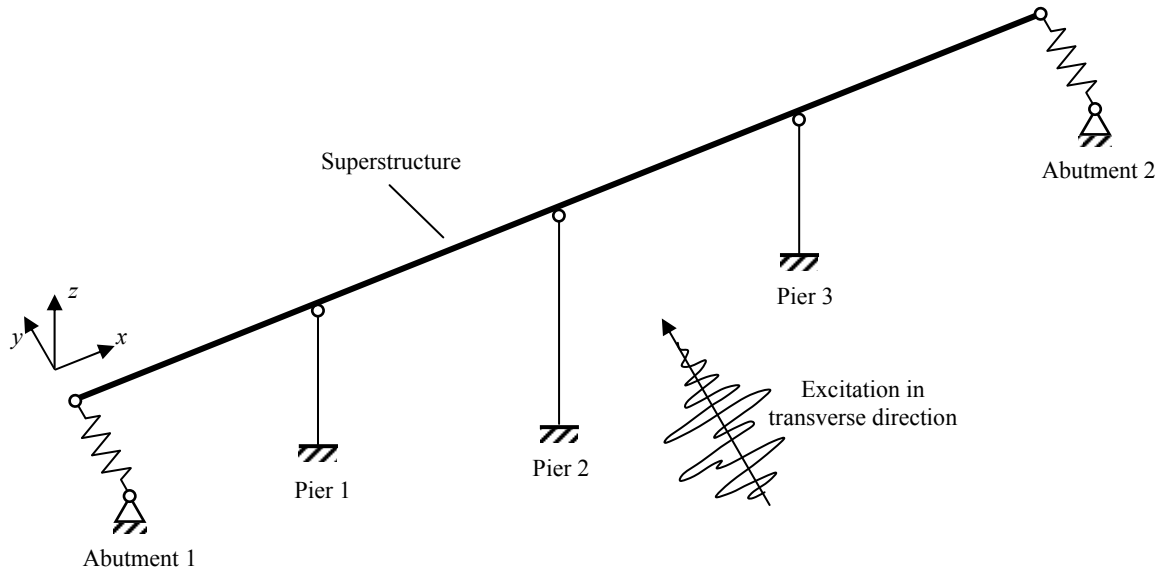
Fig. 3.1: Three dimensional bridge model for transverse seismic response analysis
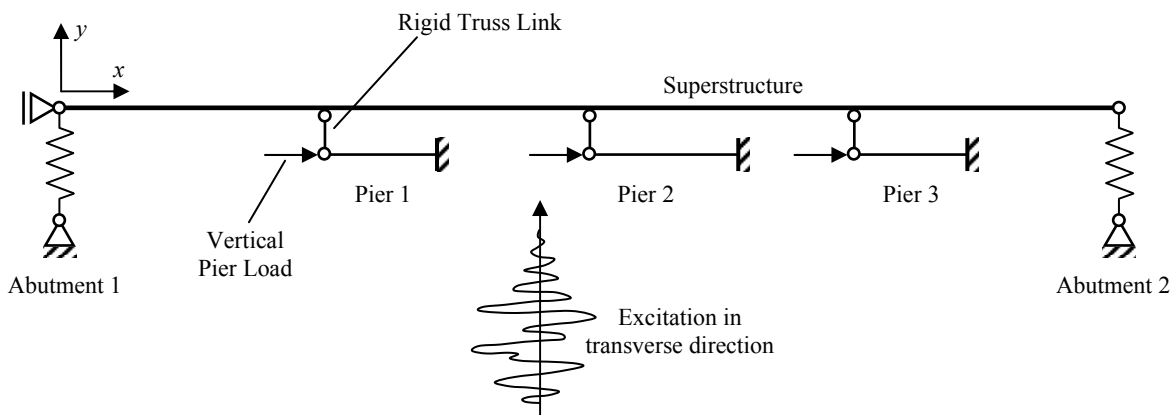
Fig. 3.2: Equivalent two dimensional bridge model for transverse seismic response analysis

Aside from the choice of the general dimensionality of the system, it needs to be decided how the individual members (e.g. beams, columns etc.) of the structure should be represented. Theoretically the members can be modeled e.g. using 3D solid, 2D shell or 1D beam-column elements. In some cases it may even be possible to represent an entire member by means of a single (inelastic) spring. For the seismic analysis of entire bridge structures, the use of a 3D solid representation can essentially be discarded. While 2D shell elements have already been used, e.g. for the modeling of box-girder superstructures [EGN06], their application in an inelastic (dynamic) analysis appears neither recommendable nor really necessary. As the primary focus of a seismic analysis typically is not on the superstructure itself (but rather e.g. on the piers), the girder rather represents the boundary conditions for the more relevant members. An overly complex modeling of the superstructure may therefore not be justified, especially if the consequence would be that then a less realistic modeling of more important bridge members needs to be chosen (e.g. because an inelastic analysis is not possible anymore).

Consequently, it can be concluded that beam-column elements in the majority of cases appear more appropriate for the member representation in seismic analyses. Further discussions on the representation of individual members will be given in the following sections. For a full dynamic characterization, the mass and damping properties are further required. Some aspects of mass modeling are discussed in Section 3.2. Under the expression "damping" all types of energy dissipation may be summarized. In general, it can be distinguished between *rate-independent* (also called *hysteretic*) damping and *rate-dependent* (also called *viscous*) damping [Cho01]. The *hysteretic damping* is related to the inelastic cyclic load-deformation response of the individual members and is therefore treated in this context. The *viscous damping* is typically used to take other forms of energy dissipation into account. It is discussed in Section 4.4 in connection with the recommendations on analysis procedures.

Another aspect that needs to be considered for the seismic modeling of bridges is the influence of soil-structure interaction which is treated separately in Section 3.5. In particular, recommendations on how to model the soil-flexibility at spread foundations of the piers are given in Section 3.5.1, while in Section 3.5.2 the response of bridge abutments and embankments is discussed.

3.2   Mass Modeling

The forces acting on the structure under seismic excitation are a result of inertia related to the acceleration of masses. As a consequence, the amount and distribution of these forces (as well as the general dynamic characteristics of the system) depend on the modeled distribution of masses. In the real structure the mass is continuously distributed along the individual parts of the superstructure, the piers, the abutment, and the embankment. Although it might be possible theoretically to use a corresponding mass distribution in the structural model, in many cases this may not be necessary. Instead, it may be sufficient to lump the continuously distributed masses in a limited number of discrete points. This way the number of dynamic degrees of freedom is reduced and the numerical solution as well as the interpretation of the results may be facilitated. It should be noted that in a finite element representation, even modeling a distributed mass on the members will implicitly be transformed to a discrete mass matrix based on the shape functions of the elements. In this case, the resulting mass discretization is automatically coupled to the mechanical discretization of the members.

In normal girder bridges the majority of the total mass is likely to be contributed by the superstructure. If lumped masses are to be used, these can be computed by means of tributary lengths along the superstructure, as shown in Fig. 3.3. The number of required masses, i.e. the density of the mass pattern, depends somewhat on the length of the bridge and the focus of the analysis. A rather crude pattern as the one shown in Fig. 3.3, where only one mass per span is concentrated at every pier top may not be sufficient for a short bridge of few spans. In this case, a finer distribution of masses, as e.g. shown in Fig. 3.4, is more recommendable to capture the dynamic behavior of the bridge realistically. However, for longer multi-span bridges the discretization based on one mass per pier top of Fig. 3.3 may already give a good representation of the main dynamic characteristics. In particular, if the primary focus of the analysis is on the displacement demand of the piers, the simple mass distribution shown in Fig. 3.3 can be sufficient for longer multi-span bridges. However, the resulting moment distribution along the superstructure is likely to be less accurate and an adequate representation of this aspect may call for a finer mass distribution, even for longer bridges.

Berweger [Ber09] performed a brief comparison between two different mass discretization schemes for two 5 span bridge models (one symmetric and one asymmetric system) of total length 168 m each (see also Section 4.6). The first discretization used only one mass per span being concentrated on top of the piers, comparable to Fig. 3.3. A second scheme was based on two masses per span, one at the pier tops and one at midspan between the piers. Berweger conducted modal analyses for the two bridges with two different mass discretizations each and compared the resulting natural periods, the effective modal masses and the mode shapes. He found that for the symmetric as well as the asymmetric bridge no significant difference occurred between the two mass distributions. For the relevant first and third mode in both bridges the periods differed only by about 0.6%. This deviation increased slightly for higher modes as these are more sensitive to the mass distribution, resulting in periods differing by up to 7.7% in the 5th mode. The effective modal masses varied by about 4.4% and

3.2 Mass Modeling

7.1% for the first and third mode, respectively, while the other modes were insignificant with respect to mass excitation. The mode shapes also agreed favorably well between the different mass discretizations. Therefore, it can be concluded that the dynamic behavior in these two cases was not strongly influenced by the choice between either of the two mass distributions. The cruder solution with only one mass per span at the pier tops would already be sufficient for the prediction of the pier displacement demands of these 5 span bridges. A further refinement of the mass pattern might only serve to improve the moment distribution along the superstructure if this is required.
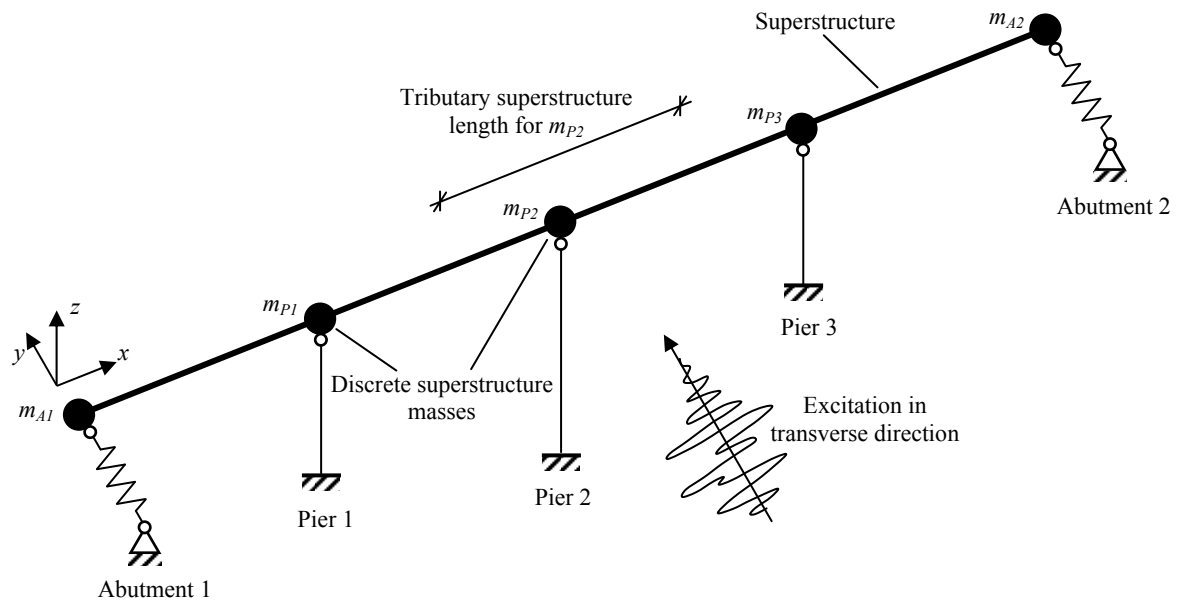
Fig. 3.3: Wide pattern of discrete lumped masses along bridge superstructure
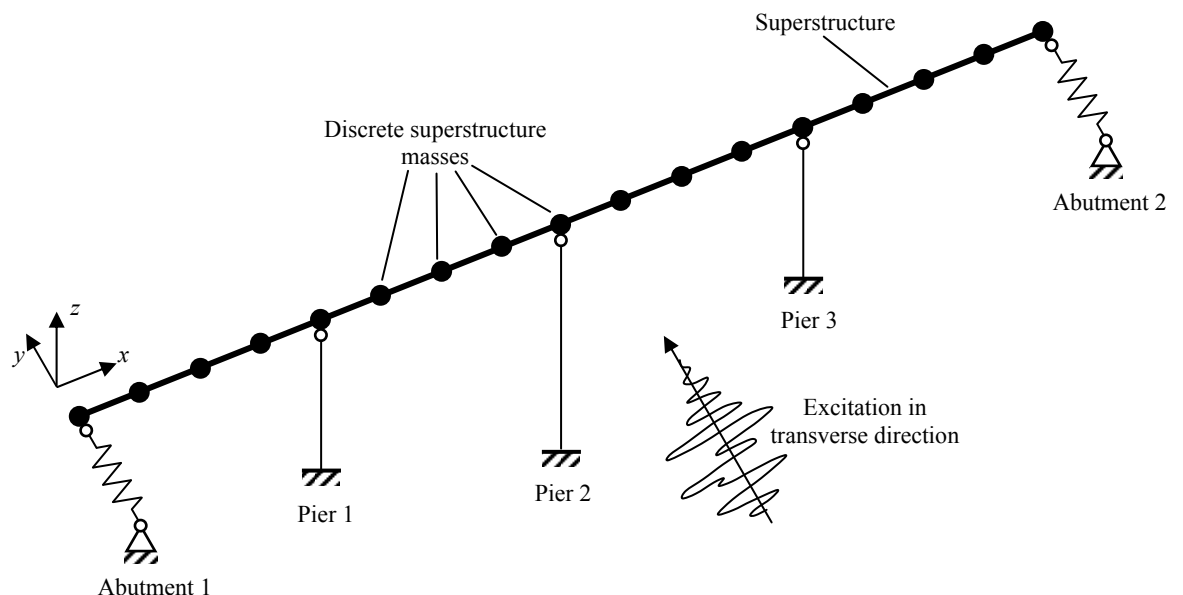
Fig. 3.4: Dense pattern of discrete lumped masses along bridge superstructure

Aside from the superstructure, other parts of the structure carry mass as well, which might have to be considered in the model. Normally, these are primarily the substructure (i.e. the piers) and the abutment-embankment system. According to [SIA260] no traffic loads need to be considered for the seismic load case. Concerning the masses associated to the piers, generally the same approach as for

the superstructure can be followed, i.e. the continuous mass can be lumped in a certain number of discrete points along the pier height. However, due to the typically low share of mass contributed by the piers, in normal cases it is likely to be sufficient if a certain share of each pier mass is simply added to the corresponding lumped superstructure mass at the pier top. Based on the recommendations given in [PSC96], adding a generalized mass equal to one third of the total pier mass can be considered as a reasonably accurate approximation for the majority of cases. Only in rather tall piers which can develop vibrations of their own, incorporating higher modes, it may be necessary to model several lumped masses along the pier height.

For transverse seismic response, the tributary mass related to the soil embankment can be taken into account based on the proposed model outlined in Section 3.5.2. Equation (3.41) gives an expression to estimate the effective embankment mass as the ratio α of the total mass within the tributary embankment length L_c, with L_c according to equation (3.34). The ratio α can be computed as a function of the embankment geometry using the expression given in the context of equation (3.41). However, as shown in Fig. 3.75, the ratio α is rather insensitive within the range of reasonable geometric parameters. Therefore, in many cases, it will be sufficient to assume α equal to about 0.3, i.e. approximately 30% of the total soil mass within the tributary length L_c of the embankment should be considered as effective. If displacements of the abutment are assumed to result entirely from the embankment flexibility, then abutment and effective embankment mass move together and can be summarized as one single lumped mass.

If further the superstructure is connected rigidly to the abutment – either monolithically or by means of sufficiently strong fixed bearings – the end of the superstructure also moves together with the soil-embankment system. In this case, the lumped mass of the soil-embankment system can simply be added to the discrete mass at the superstructure end. This summed up mass can be of considerable magnitude and it is likely to influence the bridge's seismic behavior, at least in the outer spans of the bridge. As a consequence, even a rather stiff abutment can in certain cases experience significant displacements, which may not be encountered if the embankment mass is not included in the model. Although the displacements of the abutments might not be the primary aspect of the analysis, they may have an important influence as boundary conditions at the bridge ends. As a consequence, they can nevertheless be important for the demand estimation of the outer piers adjacent to the abutments.

So far, the discussion in this section has focused on the amount of tributary mass and its (discrete) distribution for the model along the superstructure. In this context, it is noteworthy that a body of mass with a certain geometric extension generally has translational as well as a rotational inertia. As the mass of the superstructure in reality is not only concentrated along its axis, but rather transversely distributed over the dimensions of its cross-section, it does not only represent translational inertia but also rotational inertia about its longitudinal axis. The relevance of this aspect depends on the amount of rotational motion the superstructure experiences due to seismic excitation. If the superstructure is e.g. supported by multi-column bents, its rotational motion about the longitudinal axis due to transverse excitation will be negligible. In this case, it is dispensable to model the rotational inertia of the superstructure.

However, if a superstructure with low torsional stiffness is supported on cantilever piers, any top displacement of the piers is also associated with rotations at the pier tops. In this case, the rotational inertia of the superstructure is automatically activated with several potential consequences on the local and global seismic behavior. In particular, even if only transverse horizontal excitations and responses are considered in an analysis, every node at the pier tops receives an additional dynamic degree of freedom due to the rotational inertia of the superstructure. This can lead to modified dynamic characteristics and mode shapes, compared to a system without (consideration of) the rotational superstructure response. The relevance of this phenomenon and its potential consequences are discussed in more detail in Section 3.4 which treats the modeling of the superstructure.

3.3   Modeling Approaches for Inelasticity of Members

Is has been outlined in Section 3.1 that a realistic description of the response of reinforced concrete structures to severe earthquakes cannot be achieved without taking into account the inelastic behavior of the system. Generally, for the consideration of inelasticity in the flexural behavior of one-dimensional beam or column members two conceptual approaches are commonly used:

(i)   Spread plasticity
(ii)   Lumped plasticity

In spread plasticity elements the curvature at every point along the member results from an inelastic hysteretic moment-curvature relationship in combination with the locally acting moment. This concept is therefore the extension of classical beam theory to inelastic behavior, using either the Bernoulli or the Timoshenko hypothesis. These beam theories are based on the assumption that sections which are plane before the deformation remain plane in the deformed state. Furthermore, classical beam theory assumes that the deformation at a section is only dependent on the local actions at this section and that it is therefore independent from the response at other points along the member axis. Both assumptions are not justified anymore for reinforced concrete members being subjected to inclined shear cracking. The shear cracks cross a range of sections thus interconnecting their deformation behavior. Furthermore, the shear cracks also result in plane sections not remaining plane anymore. One consequence of this behavior is the shift of tension forces in the longitudinal flexural reinforcement which can strongly influence the flexural behavior of the member. These effects cannot be captured by classical beam theory based on the Bernoulli or Timoshenko hypothesis.

As discussed in detail by Yazgan [Yaz09], it is generally possible to compensate for some of these conceptual deficiencies, inherent to spread plasticity members, using an appropriate discretization scheme in a finite element representation. Such an approach is partly based on certain considerations underlying the plastic hinge concept which will be discussed below in the context of lumped plasticity. However, it should be noted that normally a finite element solution using beam elements (with sufficiently fine discretization) would attempt to approximate the analytical solution corresponding to the beam theory. If, in turn, a defined discretization scheme is used as mentioned above, this means that a conceptual deficiency of the beam theory is to be compensated by numerical means. In this case the goal is that the numerical results should not represent the solution according to the beam theory anymore. In order to produce meaningful results, a profound understanding of the element formulation and a reasonable concept for the intended numerical modifications are essential. The recommendations by Yazgan [Yaz09] can provide some guidance for the application of a finite element representation using beam-column members based on spread plasticity.

As an alternative, in a lumped plasticity approach the plastic deformations occurring in a beam or column element are considered as concentrated in a plastic hinge. While the member behaves elastically up to yield, once the yield moment is exceeded at one point, at this position a plastic hinge is activated with a defined moment-rotation relationship. While the inelastic flexural deformations in a spread plasticity model occur as curvatures over the range where the yield moment is exceeded, in the lumped plasticity model these curvatures are cumulated as a discrete rotation occurring in the plastic hinge. This plastic rotation is typically computed as the peak plastic curvature within the hinge region multiplied by a hypothetical plastic hinge length L_{pl}, which depends on the structural properties of the member. The plastic hinge concept has been implemented e.g. into [SIA2018], [EC8-2] (Annex B and E) and [EC8-3]. A general introduction into the approach can be found in [PCK07].

Obviously, the plastic hinge concept implies a certain simplification of the real deformation behavior of the member. Its capability of relating local deformations (e.g. strains and curvatures) to the global deformations (e.g. member end displacements and rotations) strongly depends on the choice of the plastic hinge length L_{pl}. Several recommendations concerning the definition of a reasonable value of L_{pl}, depending on various parameters of the member, have been proposed in the literature. A comprehensive summary of a number of proposals, as well as their historical development, has been compiled by Hines [Hin02].

While both the spread plasticity approach as well as the plastic hinge concept still represent the members explicitly as beams or columns, in some cases it may also be possible to further simplify the

entire member and its response as an inelastic spring with a hysteretic load-deformation characteristic. Such a representation may be feasible e.g. for cantilever piers that are connected to the superstructure via hinges and therefore only transfer forces but no moments. In this case, summarizing the inelastic behavior (which may have been determined using either of the two approaches discussed above) into a simple spring can be an efficient way to implement the member into the entire structural model.

Independent of the chosen form of representation for the inelastic behavior, it is often useful to define a bilinear relationship approximating the nonlinear load-deformation response under monotonic loading. Such a relationship can be defined on various structural levels, as e.g. for the moment-curvature curve, the deformation behavior of individual members, or the force-displacement relationship of an entire structure. An example for the latter case is depicted in Fig. 3.5. Although this curve shows the response under monotonically increasing loading, it is also useful for the definition of the seismic behavior as it is typically considered to represent the backbone curve under cyclic loading.
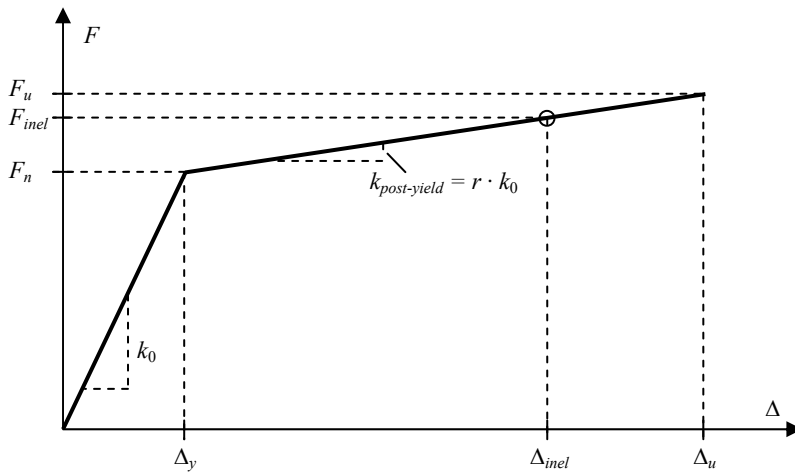
Fig. 3.5: Definition of characteristic force-displacement properties of inelastic SDOF system

The characteristic parameters defining the bilinear backbone of a force-displacement curve are given in Fig. 3.5. They are the nominal yield displacement Δ_y and the corresponding nominal force capacity F_n, as well as the ultimate displacement capacity Δ_u and the corresponding force F_u. The initial stiffness k_0 in the elastic range and the post-yield stiffness $k_{post-yield}$ after onset of yielding follow subsequently from the previously defined four parameters. Also the post-yield stiffness ratio r according to (3.1) follows automatically from the other parameters.

$$r = \frac{k_{post-yield}}{k_0} \tag{3.1}$$

In order to characterize the deformation state in the inelastic range, it is common practice to normalize the specific deformation to its corresponding yield quantity. The resulting normalized deformation measure is called *ductility*. For the case of a force-displacement curve, the definition of the *displacement ductility* μ_Δ is given in equation (3.2). It is also possible to define e.g. curvature or rotation ductilities in a similar way. However, it should be noted that, although the various ductility measures are interrelated, they are not equal. It is therefore always important to clearly state the type of deformation to which a certain ductility value refers (see e.g. [Bac02]).

$$\mu_\Delta = \frac{\Delta_{inel}}{\Delta_y} \tag{3.2}$$

A further discussion on the actual determination of appropriate models for the inelastic behavior of reinforced concrete members (i.e. primarily the bridge piers) is beyond the scope of this document. For practical assessment applications the recommendations given in [SIA2018], [EC8-2], [EC8-3], [PSC96], and [PCK07] provide further guidance.

3.4 Superstructure Modeling

In a new design of a bridge taking seismic aspects into account, the superstructure is typically designed to remain essentially elastic. But even in existing bridges without particular consideration of seismic loads during the design, the superstructure will normally not be subjected to significant inelastic actions. While reinforced concrete – and possibly even prestressed – superstructures may enter into the cracked state under more severe excitations, pronounced yielding of the longitudinal reinforcement might not be expected in the majority of cases. Nevertheless, it may be recommendable to check this assumption on an individual basis.

If a significant inelastic response can be ruled out, the superstructure may essentially be considered as an elastic beam. Its flexural stiffness should be estimated based on the expected state of cracking, e.g. by an appropriate reduction of the gross uncracked section properties if required. Care should be taken if the superstructure consists of precast segments which are, e.g., only connected by cast in-situ deck slabs or low amounts of reinforcement crossing the joints. In this case, the assumption of a continuous elastic beam may not be justified. Instead, potential concentrations of (inelastic) deformations in the joint regions should be considered and, if necessary, taken into account in the structural model.

Aside from the flexural characteristics, the superstructure behavior also depends on its torsional properties and on the boundary conditions. Although it would be convenient to model the superstructure as a simple beam along its axis ignoring the torsional and rotational behavior, as e.g. shown in Fig. 3.2, in some cases it is necessary to consider these phenomena – and be it only to ensure that the simplifications resulting from ignoring them are still acceptable. In the following Sections three aspects will be discussed which are related to the phenomena mentioned above. These are:

   a) The influence of the rotational superstructure inertia (Section 3.4.1)
   b) The definition of the superstructure axis for the structural model (Section 3.4.2)
   c) The influence of the torsional superstructure stiffness (Section 3.4.3)

While the rotational inertia of the superstructure always exists, the torsional stiffness strongly depends on the type of cross-section. While a closed box cross-section typically has a considerable torsional stiffness, that of an open cross-section (like e.g. a double T-beam section) may be rather negligible in many cases. But also the rotational inertia may not always be relevant for the response, as it is only activated if rotational motions – strictly speaking rotational accelerations – occur. Depending on the structural system, these rotational motions can in some cases either be negligible or at least rather limited. It will e.g. normally be justified to assume negligible rotations if the superstructure is supported on multi-column bents, in which the cap beam does not experience rotations under transverse deformations of the bridge. Limited rotations may be expected if a single-column bent supported superstructure features a high torsional stiffness and is restrained against rotations at the abutments. However, due to cracking of the concrete, the torsional stiffness can be reduced considerably and for longer bridges the influence of the restraint can diminish further away from the abutments. Aside from that, the boundary conditions for bearing supported superstructures also influence the torsional response, which subsequently influences the rotational motions and the activation of the rotational inertia. Hence, the relevance of the various aspects discussed in the following subsections depends on the particular configuration of any individual bridge. While in some cases disregarding these phenomena might not influence the response prediction significantly, in other cases neglecting them could lead to a conceptually mistaken picture of the seismic behavior.

3.4.1 Influence of the Rotational Superstructure Inertia

In Fig. 3.6 the elevation of part of a regular bridge is shown in the longitudinal direction. The superstructure shall have an open cross-section with rather negligible torsional stiffness (compared to the stiffness of the other parts of the structure) and all spans are assumed to have the same length. The piers are cantilevers rigidly fixed at their bases and also rigidly connected to the superstructure. For simplicity it is also assumed that all piers have the same height and the bridge is sufficiently long so that in the center of the bridge a region exists which is essentially uninfluenced by the restraints at the abutments. Further assuming a synchronous transverse excitation at every foundation (without time shift or loss of coherence), the response of all piers will be the same. In this case, for the center region of the bridge it is sufficient to analyze only a single pier with its tributary superstructure equal to one span width.
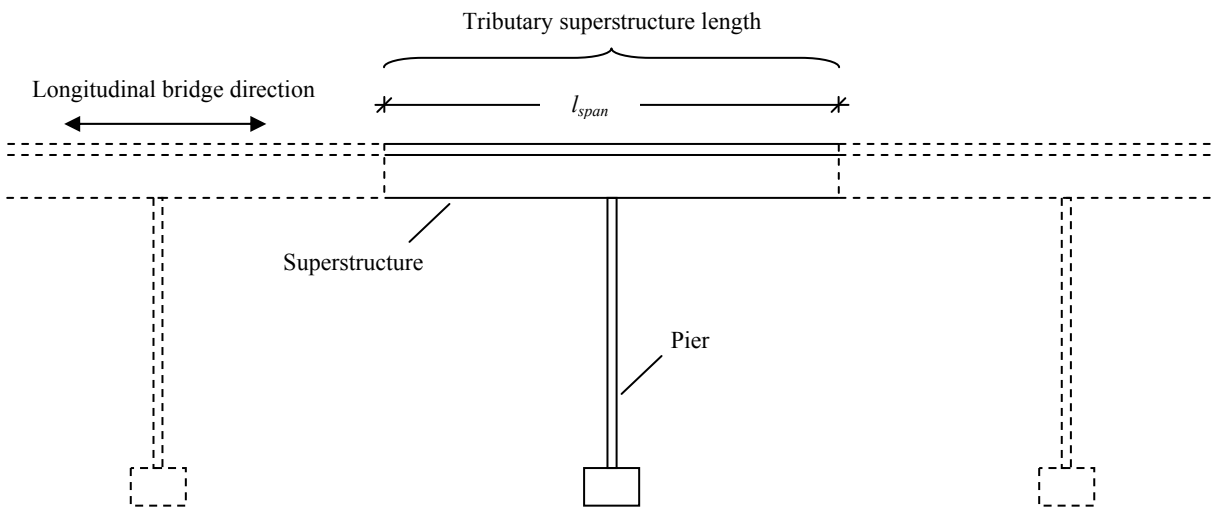
Fig. 3.6: Elevation of regular bridge in longitudinal direction
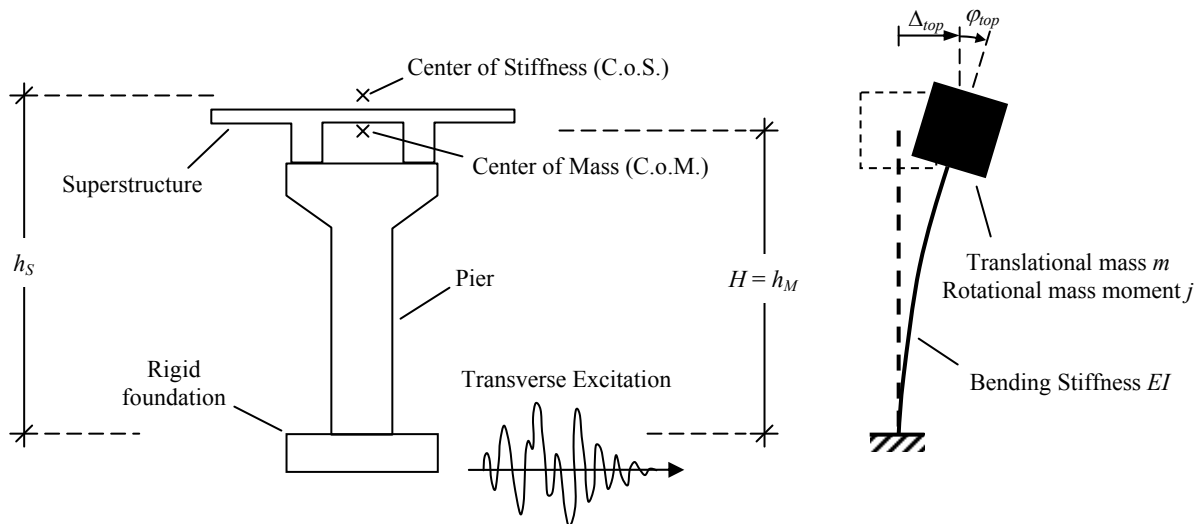
Fig. 3.7: Elevation of regular bridge pier in transverse direction
left: Pier with superstructure cross-section,
right: Corresponding structural model of single pier with tributary superstructure mass

Such an isolated single pier and the corresponding structural idealization are shown in Fig. 3.7. It can be seen that, if the cantilever is deformed, any top displacement will normally be associated with a rotation at the top as well. This will even occur without consideration of the rotational superstructure inertia. Under a pure horizontal force at the top, the top rotation φ_{top} and the top displacement Δ_{top} of a linear elastic cantilever are interrelated according to equation (3.3). If the deformation of the cantilever

results purely from a plastic hinge rotation at the base, a similar relationship exists according to equation (3.4). In either case, the ratio $\varphi_{top}/\Delta_{top}$ is related antiproportionally to the pier height. This means that under a pure horizontal top load the importance of the top rotation compared to the top displacement will reduce with increasing pier height.

$$\frac{\varphi_{top}}{\Delta_{top}} = \frac{3}{2H} \quad , \quad \text{for a linear elastic cantilever} \tag{3.3}$$

$$\frac{\varphi_{top}}{\Delta_{top}} = \frac{1}{H} \quad , \quad \text{for a cantilever with a plastic hinge at its base} \tag{3.4}$$

However, due to the existence of the rotational superstructure inertia, the behavior of the pier is somewhat more complex. While the pier-mass system has only a single independent degree of freedom Δ_{top} (in the transverse direction) if only the translational mass m is considered, taking additionally the rotational mass moment j into account, results in a second dynamic degree of freedom represented by φ_{top}. To study the general influence of this phenomenon, an elastic response spectrum analysis for the given system in Fig. 3.7 is performed. Based on this simple analysis, the cases with and without consideration of the rotational inertia (i.e. as a single-degree-of-freedom system and as a two-degree-of-freedom system, respectively) can be compared.

For an initial example case, stiffness and geometric parameters are chosen in rough accordance to the properties of the sample bridges presented in Section 2.2.2. The pier elastic bending stiffness is thus taken as $EI_{el} = 15\,000$ MNm^2, the translational mass of the tributary superstructure span is estimated as $m = 600$ t, and the rotational mass moment is assumed as $j = 5000$ tm^2. Taking the pier height as equal to $H = 6$ m, the natural periods result as given in Tab. 3.1 for the two-degree-of-freedom system (2-DOF) considering the rotational inertia, and the single-degree-of-freedom system (SDOF) neglecting it.

	2-DOF		SDOF
	1st Mode	2nd Mode	
T [s]	0.424	0.112	0.337

Tab. 3.1: Natural periods of 2-DOF and SDOF pier-superstructure models for a pier height of H = 6 m

The actual responses of the systems and the individual modes depend on the underlying response spectrum. To make the systems comparable without influence of the spectral shape, for this study it is assumed that all three periods shown in Tab. 3.1 happen to fall into the plateau of the elastic pseudo-acceleration spectrum. In this case, any response quantity can be normalized by the value of the peak spectral acceleration $S_{a,max}$. As a consequence, individual modes can be superimposed in a generalized way and the responses can be compared to each other.

In Fig. 3.8 the deflected shape of the cantilever is shown for the 1st and 2nd mode of the 2-DOF system, as well as the SRSS superposition of both modes. Furthermore, for comparison purposes the deflected shape of the corresponding SDOF system assuming the rotational mass moment as $j = 0$ is also shown in Fig. 3.8. In Tab. 3.2 the numerical values of the top displacements and rotations are given. From these results it can be seen that for the given set of parameters the 2-DOF system is clearly dominated by the 1st mode shape. The data also show that for this configuration the simplified SDOF system agrees reasonably well with the 1st mode of the 2-DOF system, both in terms of top displacement as well as top rotation. Due to the 1st mode domination of the 2-DOF system, the SDOF deformations also approximate the SRSS superposition well.
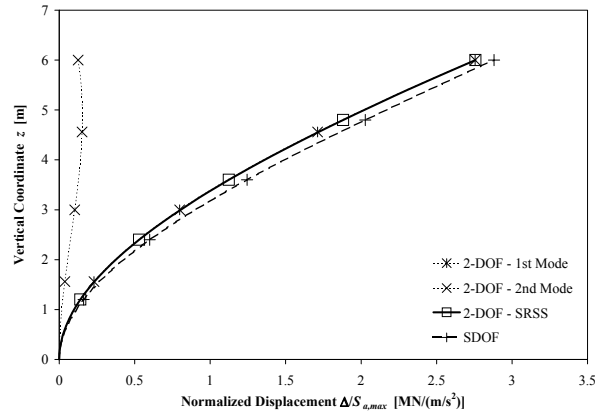
Fig. 3.8: Modal deformation shapes of elastic cantilever pier as 2-DOF and SDOF system for H = 6 m

	2-DOF			SDOF
	1st Mode	2nd Mode	SRSS	
$u_{top}/S_{a,max}$ [mm/(m/s^2)]	2.755	0.125	2.758	2.880
$\varphi_{top}/S_{a,max}$ [10^{-3}/(m/s^2)]	0.773	-0.053	0.775	0.720
φ_{top}/u_{top} [1/m]	0.281	-0.427	0.281	0.250

Tab. 3.2: Top deformations of 2-DOF and SDOF pier-superstructure models for H = 6 m

In an equivalent manner, the internal actions for the 2-DOF and the SDOF system are shown in Fig. 3.9, with the corresponding numerical data given in Tab. 3.3. It can be seen that, for the base moment M_{base}, the 1st mode of the 2-DOF system is also clearly dominant. Although the 1st mode domination is significantly less pronounced for the shear force V, due to the characteristics of the SRSS rule, the superimposed total SRSS shear force is only about 20% higher than the value of the 1st mode only. However, concerning the top moment M_{top}, no dominance of either mode exists. Instead, both modes contribute the same value to M_{top}, resulting in an SRSS superposition which is about 40% (factor square root of 2) higher than the value of the individual modes.
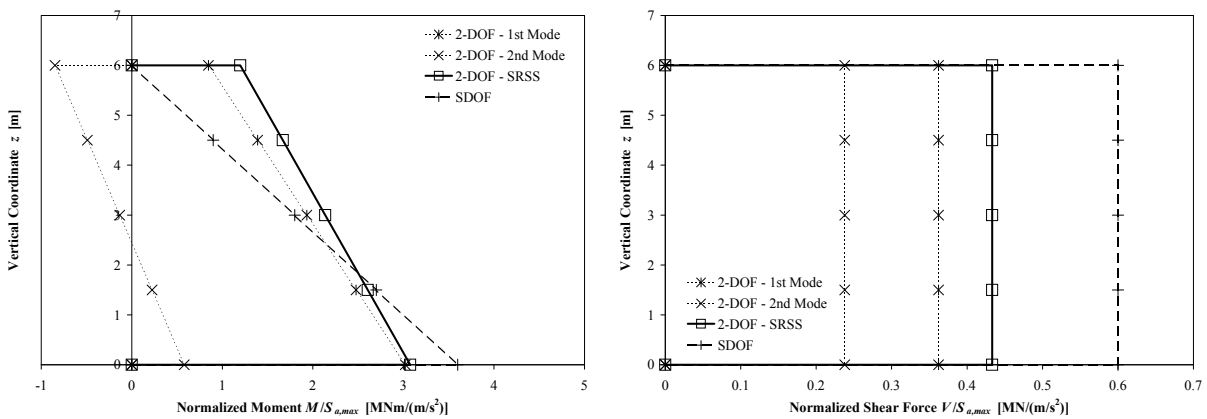

Fig. 3.9: Modal actions for elastic cantilever pier as 2-DOF and SDOF system for H = 6 m
left: Moment distribution, right: Shear force distribution

	2-DOF			SDOF	modified SDOF
	1st Mode	2nd Mode	SRSS		
$M_{top}/S_{a,max}$ [kNm/(m/s^2)]	847	-847	1198	0	1250
$M_{base}/S_{a,max}$ [kNm/(m/s^2)]	3020	580	3075	3600	see Fig. 3.10
$V/S_{a,max}$ [kN/(m/s^2)]	362	238	433	600	see Fig. 3.10

Tab. 3.3: Internal actions of 2-DOF and SDOF pier-superstructure models for H = 6 m

Compared to the 2-DOF results, the two actions M_{base} and V are overestimated by the SDOF analysis of this example (M_{base}: +17%, V: +39%), thus representing a conservative simplification. However, it is obvious that the SDOF system which experiences only a lateral inertia force at the top cannot reproduce the top moment M_{top} of the 2-DOF system. Therefore, the SDOF simplification is clearly unconservative for the moment demand in the top region of the pier.

This top moment in the 2-DOF system is a result of the rotational inertia being activated by the rotational acceleration at the top. Although this effect is not immediately included in the SDOF analysis, the simplified SDOF approach at least allows an estimation of the rotational top acceleration. As has been discussed above, the general deformation shape is predicted considerably well by the SDOF system – also with respect to the top rotation (see Fig. 3.8 and Tab. 3.2). Based on the finding that, for a linear-elastic cantilever under horizontal top force, the ratio between top rotation and top displacement is only dependent on the height *H*, double derivation of equation (3.3) with respect to time yields equation (3.5) for the rotational top acceleration of the SDOF system. Setting the translational top acceleration equal to $S_{a,max}$, the top moment $M_{top,modSDOF}$ of a *modified SDOF* solution can be estimated by multiplying the rotational acceleration with the rotational mass moment *j* according to equation (3.6). The resulting value for $M_{top,modSDOF}$, normalized by the pseudo-spectral acceleration $S_{a,max}$, is also given in Tab. 3.3 for the example configuration examined above.

$$\ddot{\varphi}_{top,SDOF} = \frac{3}{2H} \cdot \ddot{\Delta}_{top,SDOF} \tag{3.5}$$

$$M_{top,\text{mod}SDOF} = j \cdot \ddot{\varphi}_{top,SDOF} = \frac{3}{2H} \cdot j \cdot S_{a,\max} \tag{3.6}$$

It is important to note that the internal actions of such a *modified SDOF* solution, including the estimated top moment $M_{top,modSDOF}$, do not fully fit to the computed deformation shape of the original SDOF solution anymore (Fig. 3.8). Furthermore, the influence of $M_{top,modSDOF}$ on the equilibrium of the cantilever needs to be considered. On one hand, the base moment $M_{base,SDOF}$ and V_{SDOF} of the original SDOF solution were found to give reasonable and conservative estimations of the corresponding 2-DOF values. On the other hand, if these two values are kept unchanged, introducing an additional top moment $M_{top,modSDOF}$ would destroy the equilibrium. Therefore, it is necessary to consider how this apparent discrepancy should be treated. The following three interpretations are deemed possible solutions:

(i) *Adjust base moment*
    The cantilever can be considered as loaded by the horizontal top force $F_{top,SDOF} = m \cdot S_{a,max}$ and the top moment $M_{top,modSDOF}$ according to equation (3.6). This means that the top moment of the *modified SDOF* is combined with the shear force from the *original SDOF* solution. In this case, to achieve equilibrium the base moment from the original SDOF system needs to be adjusted as $M_{base,modSDOF(1)} = F_{top,SDOF} \cdot H + M_{top,modSDOF} = M_{base,SDOF} + M_{top,modSDOF}$. The shear force $V_{modSDOF(1)}$ of the *modified SDOF* solution would then remain equal to the corresponding value V_{SDOF} of the *original SDOF* system.

(ii) *Adjust shear force*

As an alternative, the base moment of the *modified SDOF* system can be taken the same as from the *original SDOF* solution, i.e. $M_{base,modSDOF(2)} = M_{base,SDOF}$, while additionally introducing the top moment $M_{top,modSDOF}$ according to equation (3.6). In this case, for equilibrium purposes, the shear force needs to be adjusted, resulting in $V_{modSDOF(2)} = (M_{base,SDOF} - M_{top,modSDOF})/H$. As for the underlying kinematic assumption (equation (3.5)) both moments at the top and the base have the same signs, the resulting modified shear force $V_{modSDOF(2)}$ is reduced in comparison to the shear force $V_{SDOF} = M_{base,SDOF}/H$ of the original SDOF solution.

(iii) *No adjustment*

The third possible interpretation of the problem might consist of not performing any adjustments, but rather assuming a joint occurrence of the actions $M_{top,modSDOF}$ according to equation (3.6), $M_{base,modSDOF(3)} = M_{base,SDOF}$, and $V_{modSDOF(3)} = V_{SDOF}$. This approximation would imply accepting a lack of equilibrium which at first sight appears inconsistent. However, it should be noted that the *modified SDOF* solution is intended to approximate the SRSS superposition of the 2-DOF system. In general cases, the several internal actions of a SRSS superposition are not in equilibrium either (compare e.g. Tab. 3.3), nor are they compatible to the SRSS deformation shape. They should rather be considered as an envelope of the possible distribution of peak actions which do not have to occur at the same time during a dynamic response. If the *modified SDOF* solution is interpreted in a similar way, the lack of equilibrium does not necessarily represent a drawback of this approach.

In Fig. 3.10 the distributions of moment and shear force resulting from the three possible interpretations of the *modified SDOF* solution are compared to the corresponding SRSS superposition of the 2-DOF analysis. It can be seen that, for this example configuration, the moment distribution of the approximation with *shear force adjusted* and the one with *no adjustment* appear to give the best approximation of the 2-DOF SRSS results. Concerning the shear force, the modified SDOF with *shear force adjusted* is closer to the 2-DOF SRSS result than the other two modifications (*base moment adjusted* and *no adjustment*) which are equal to the value from the original SDOF solution. However, the modification based on *shear force adjusted* gives an unconservative approximation. In the light of the importance the shear demand has on the seismic safety (especially with respect to potential brittle shear failure) such an underprediction of the shear force does not appear recommendable. Therefore, the solution with *no adjustment*, which does not formally fulfill the equilibrium criterion, is deemed the most appropriate solution in the given case. Its somewhat conservative character could be considered justified for an approximation.
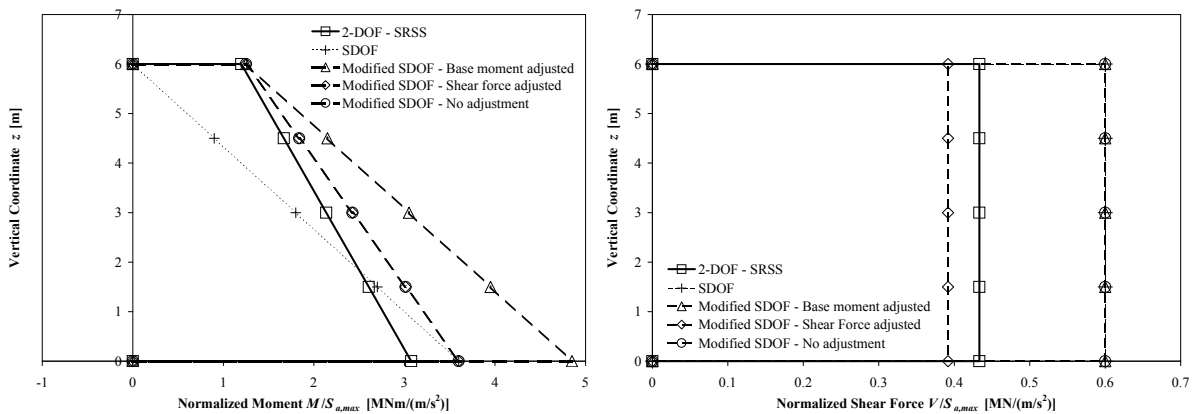
Fig. 3.10: Comparison of internal actions from 2-DOF and modified SDOF solutions for H = 6 m
left: Moment distribution, right: Shear force distribution

So far, the discussion on the influence of the rotational inertia has been based on the example configuration described above. To evaluate the problem more profoundly, it is necessary to consider other configurations as well, possibly in a way which reliably allows more general conclusions. The assumptions which are maintained for the following investigation are: (a) the system can be described as a single independent pier with translational and rotational mass at its top in accordance with Fig. 3.7, (b) the pier is a linear elastic cantilever, (c) the response of the 2-DOF system is described by a

response spectrum analysis using SRSS superposition of the two modes, and (d) for every mode of the 2-DOF system and for the simplified SDOF system it is assumed that the natural periods fall into the plateau of the pseudo-acceleration spectrum. Based on a normalization by the peak spectral acceleration $S_{a,max}$, the various responses then become comparable without further influence of the spectral shape.

When computing the ratio of any response quantity of the 2-DOF system (modal or SRSS) to the corresponding response quantity of the simplified SDOF system without rotational inertia, it can analytically be shown that this ratio is only dependent on the parameter α as defined by equation (3.7). Based on this finding, it can e.g. be shown that the fundamental period of the SDOF system always lies between the two natural periods of the 2-DOF system. Moreover, it can be shown that the natural period of the first mode $T_1 \rightarrow T_{SDOF}$ for $\alpha \rightarrow \infty$ and $T_1 \rightarrow \infty$ for $\alpha \rightarrow 0$, while the natural period of the second mode $T_2 \rightarrow 0$ for $\alpha \rightarrow \infty$ and $T_2 \rightarrow T_{SDOF}/2$ for $\alpha \rightarrow 0$ (with T_{SDOF} being the fundamental period of the SDOF system).

$$\alpha = \frac{H^2 m}{3j} \tag{3.7}$$

On one hand, the parameter α depends on the effective pier height H. On the other hand, it depends on the ratio between translational and rotational mass m/j. For a constant cross-section along the tributary length of the superstructure, this ratio m/j is equal to the ratio A/I_p between the cross-sectional area A and the second polar moment of the cross-section I_p. For a thin plate (e.g. a pure deck slab) with width b_{deck} and thickness $t_{deck} << b_{deck}$, the mentioned ratio results as $m/j = A/I_p \cong 12/(b_{deck})^2$. For other types of cross-section shapes common for bridge superstructures, as e.g. (multiple-) T-beams or box-girders, a somewhat more general expression can be used in the form of equation (3.8), where the parameter γ depends on the shape of the cross-section. A parametric analysis based on the sample bridges presented in Section 2.2.2 suggests that for the common types of cross-sections the parameter γ does not vary strongly. Values in the range of 10 to 15 tend to fit well for the majority of cases, with $\gamma = 12$ (as for the thin deck) being a reasonable average approximation. If pier heights in the range of $H = 5$ m to $H = 20$ m are considered[8], the reasonable values of the parameter α are likely to fall between 0.5 to 20. Therefore, this is the range of α on which the following evaluation will primarily focus.

$$\frac{m}{j} = \frac{A}{I_p} = \frac{\gamma}{b_{deck}^2} \tag{3.8}$$

In Fig. 3.11 through Fig. 3.13 comparisons of the internal actions (base moment M_{base}: Fig. 3.11, top moment M_{top}: Fig. 3.12, and shear force V: Fig. 3.13) as predicted by the 2-DOF analysis and the SDOF or modified SDOF approximations are shown. For each action, on the left side of the figures the demand according to the various approaches is presented as a function of the parameter α defined in equation (3.7). For this purpose, the moments and the shear force are normalized by the mass m of the system and the spectral pseudo-acceleration $S_a = S_{a,max}$. In this case, the absolute actions depend – aside from the parameter α – only on the pier height H, which has been chosen as $H = 6$ m for the graphs on the left side of Fig. 3.11 through Fig. 3.13. On the right side of the same figures, the ratios between the actions according to the SRSS superposition of the 2-DOF system and the corresponding SDOF or modified SDOF approximations are shown as functions of the parameter α. As outlined above in the context of equation (3.7), such ratios exclusively depend on the parameter α, and they are therefore valid for any value of the pier height H. If the SRSS superpositions of the 2-DOF actions are considered as a reference representing the target for the approximations by the (modified) SDOF solutions, the ratios shown on the right sides of Fig. 3.11 through Fig. 3.13 are measures for the accuracy of the approximations. Any ratio lower than unity stands for a conservative estimation, while for ratios higher than one the 2-DOF result is underpredicted by the (modified) SDOF solution.

---

[8] Higher piers are seismically rather less critical due to their higher natural deformation capacity. Furthermore, for them the relative influence of the rotational superstructure inertia – as compared to the translational mass – becomes also less significant. Focusing on shorter piers is therefore not a limitation of the investigation.
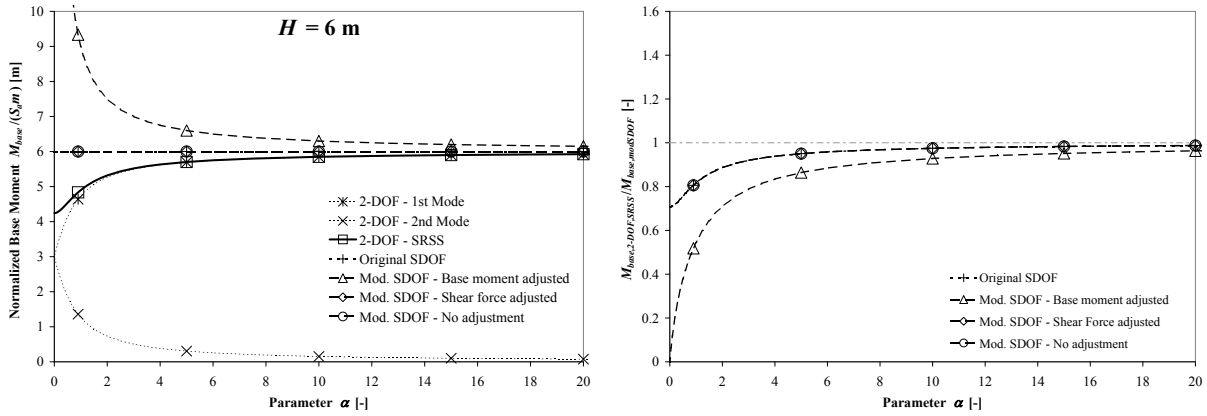
Fig. 3.11: Comparison of base moment from 2-DOF and modified SDOF system as a function of parameter α
left: Base moment normalized by spectral acceleration and mass for pier height H = 6 m,
right: Ratio between base moment from 2-DOF solution vs. SDOF or modified SDOF solutions
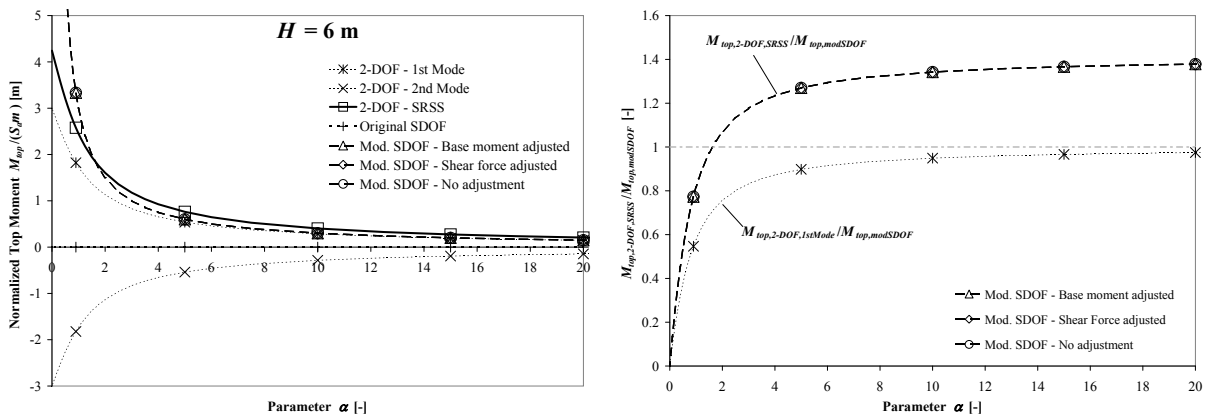
Fig. 3.12: Comparison of top moment from 2-DOF and modified SDOF system as a function of parameter α
left: Top moment normalized by spectral acceleration and mass for pier height H = 6 m,
right: Ratio between top moment from 2-DOF solution vs. SDOF or modified SDOF solutions
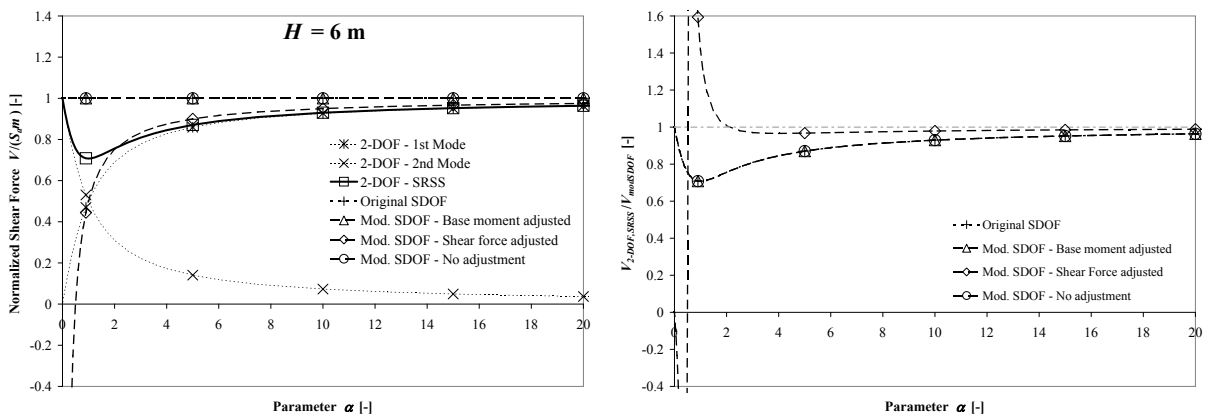
Fig. 3.13: Comparison of shear force from 2-DOF and modified SDOF system as a function of parameter α
left: Shear force normalized by spectral acceleration and mass for pier height H = 6 m,
right: Ratio between shear force from 2-DOF solution vs. SDOF or modified SDOF solutions

The data for the base moment M_{base}, presented in Fig. 3.11 (left), show that for large part of the relevant range of α the moment response of the 2-DOF system at its base is dominated by the first mode. Only for values of α lower than approximately one the second mode has a noticeable influence

on the SRSS result. This limit of $\alpha \approx 1$ is valid independently of the pier height H. According to equation (3.7), it corresponds to a mass ratio of $m/j \approx 1/(12\mathrm{m}^2)$ for $H = 6$ m. Using equation (3.8) together with a value of $\gamma \approx 12$, it can be concluded that for $H = 6$ m, the second mode has a rather insignificant influence on the base moment for superstructure deck widths $b_{deck} < 12$ m. For $\alpha \to \infty$, the first mode base moment converges to a value of $H \cdot S_a \cdot m$, while the second mode contribution converges towards zero. For $\alpha \to 0$ the base moments of both modes converge to $H/2 \cdot S_a \cdot m$.

Concerning the estimation of the base moment by the SDOF and modified SDOF models, Fig. 3.11 shows that all of the discussed simplifications yield conservative approximations throughout the entire range of α. In particular, all of the SDOF based solutions converge towards the 2-DOF result for $\alpha \to \infty$, which corresponds to either zero rotational mass j or infinite pier height H. At the same time, the graphs clearly show that the original SDOF estimation of the base moment $M_{base,SDOF}$ is a significantly better approximation than the modified value $M_{base,\mathrm{mod}SDOF(1)}$ resulting from the approach with the *base moment adjusted*. This is especially the case for low values of α, corresponding to a high influence of the rotational inertia, where the adjusted base moment $M_{base,\mathrm{mod}SDOF(1)}$ tends to strongly overestimate the 2-DOF result.

Equivalent comparisons as those above are shown in Fig. 3.12 for the top moment M_{top}. On the left side of the figure it can be seen that in the 2-DOF solution over the entire range of α the second mode contribution to M_{base} is exactly equal to the negative value of the first mode base moment. As a consequence, for any α the SRSS superposition is equal to the value of the first mode times the square root of two. For increasing α, corresponding to decreasing rotational mass j or higher pier lengths H, the 2-DOF top moments converge towards zero. In turn, for $\alpha \to 0$ the contributions of the two individual modes to the top moment converge towards $+H/2 \cdot S_a \cdot m$ (1st mode) and $-H/2 \cdot S_a \cdot m$ (2nd mode).

As all three *modified SDOF* solutions proposed above use the same expression for the estimation of the top moment $M_{top,\mathrm{mod}SDOF}$ (see equation (3.6)), the resulting ratio between the 2-DOF SRSS superposition and the *modified SDOF* approximation shown on the right side of Fig. 3.12 is the same for all three simplified approaches as well. It can be seen that the approximation is conservative for α values below about 1.6, while it becomes unconservative for higher α values. For $\alpha \to \infty$ the ratio converges towards the square root of 2, and it approaches zero for $\alpha \to 0$. To explain the unconservative character of the approximation, on the right side of Fig. 3.12 the corresponding ratio between the 1st mode result and the modified SDOF estimation is shown in addition. Here it can be seen that this ratio is conservative for any α and it converges towards unity for $\alpha \to \infty$. A possible interpretation of this phenomenon is that the modified SDOF estimation rather approximates the first mode response than the SRSS superposition of the 2-DOF system. Moreover, the problem that the modified SDOF solution does not converge towards the SRSS superposition for $\alpha \to \infty$ is related to the fact that the second mode contribution of the 2-DOF remains equal to that of the first mode. However, this does not represent too much of a problem for the approximate estimation of the top moment. At first, the unconservatism of the modified SDOF top moment develops in a range of α where the absolute top moment M_{top} already tends to diminish significantly (see Fig. 3.12 left). Furthermore, the unconservatism is generally not overly strong. In particular, the curve shown on the right side Fig. 3.12 could even be used to correct the estimation. For example, increasing the modified SDOF top moment $M_{top,\mathrm{mod}SDOF}$ calculated according to equation (3.6) by a factor of square root of 2 would in any case give a conservative approximation of the 2-DOF SRSS result.

The graphs in Fig. 3.13 show the equivalent comparisons as above for the shear force V of the pier. On the left side, the shear force normalized by the pseudo-spectral acceleration S_a and the mass m is shown for the various approaches discussed before. It is interesting to note that for α values up to one the shear force contribution by the second mode of the 2-DOF response is stronger than that from the first mode. For $\alpha \to 0$ the entire shear force comes from the second mode, with the first mode contribution being zero. For $\alpha \to \infty$ the relative contribution is just inverse. In either case, for the two extreme values of α the SRSS superposition of the shear force results as $V_{2\text{-}DOF} = S_a \cdot m$.

At $\alpha = 1$ the shear force contributions from both modes are equal to $V_{2\text{-}DOF,1st} = V_{2\text{-}DOF,2nd} = S_a \cdot m/2$, so that the corresponding SRSS superposition results as $V_{s\text{-}DOF,SRSS} = \sqrt{2}/2 \cdot S_a \cdot m$. This value also

represents the minimum of the SRSS shear force with respect to α. The original SDOF estimation predicts a shear force of $V_{SDOF} = S_a \cdot m$ independent of α, thus representing a conservative approximation of the 2-DOF SRSS superposition. In fact, the absolute sum of first and second mode shear forces in the 2-DOF solution also results in $V_{2\text{-}DOF,1st} + V_{2\text{-}DOF,2nd} = S_a \cdot m$ for any value of α. It can therefore be said that a discrepancy between the SDOF estimation and the 2-DOF solution is related to the statistical considerations underlying the SRSS rule and the corresponding probability of coinciding occurrence of first and second mode peak values.

Fig. 3.13 also shows that the *adjusted shear force*, corresponding to the modified SDOF approach (iii), gives a substantially worse estimation of the 2-DOF shear force. In fact, for small values of α this adjusted SDOF shear force estimation can be very unconservative and even change its sign. The fact that for large values of α it is slightly closer to the 2-DOF SRSS solution than the original SDOF shear force does not outweigh the unacceptable underprediction for small α values. For $\alpha \to \infty$ all of the solutions converge towards the same shear force being $V = S_a \cdot m$, but only the original SDOF estimation also converges towards $V_{2\text{-}DOF,SRSS} = S_a \cdot m$ for $\alpha \to 0$.

For the discussion so far, the response quantities were shown as a function of the parameter α defined in equation (3.7). This was chosen as the best representation for the generalized interpretation because this way the response ratios on the right sides of Fig. 3.11 through Fig. 3.13 were independent of other parameters. However, due to the somewhat abstract character of α, which combines the influence of three other parameters, the graphs may not be very illustrative. At the same time, based on the discussions above, it can be assumed that for normal road bridges the variation of the mass ratio m/j is considerably lower than that of the pier heights H (or especially their square value H^2) affecting α. Using equation (3.8) together with a value of $\gamma = 12$, for a deck width of $b_{deck} \approx 15.5$ m a reasonable value for the mass ratio can be estimated as about $m/j \approx 0.05$ $1/m^2$. Based on this mass ratio, relationships similar to those shown in Fig. 3.11 through Fig. 3.13 can be computed. In these relationships the pier height H is the only remaining parameter. The corresponding curves are shown in Fig. 3.14 through Fig. 3.16. Among the SDOF estimations discussed before, only that solution has been included into the graphs which has previously performed best in approximating the 2-DOF response. This is the modified SDOF solution (iii) corresponding to *no adjustment* of the actions to achieve equilibrium.

Although the graphs of Fig. 3.14 through Fig. 3.16 are only strictly valid for the chosen ratio of m/j, on a qualitative basis they are considered generally interesting as m/j is not expected to vary much more than by a factor of 2 for common cases of bridge structures. In contrast, the (square of the) pier heights varies significantly more. Therefore these graphs give a good (qualitative) impression of the strong influence of the pier heights on the relative importance of the rotational superstructure inertia and the subsequent relevance of multi-modal pier response. The curves of Fig. 3.14 through Fig. 3.16 show clearly that this influence is particularly strong for short cantilever piers, whereas it tends to diminish for longer piers.

This holds true for all three actions considered. Fig. 3.14 shows that the second mode contribution to the base moment becomes insignificant for long piers. At the same time, a SDOF representation appears to give a sufficiently accurate (and slightly conservative) estimation of the base moment for essentially all reasonable pier heights. While the relative contribution from the second mode to the top moment, shown in Fig. 3.15, remains the same for any pier height, the absolute value of the top moment reduces with an increasing pier height. As a consequence, the absolute influence of the rotational superstructure inertia here also diminishes for higher piers – especially if the top moment is compared to the base moment. Finally, for the shear force, presented in Fig. 3.16, the relationships are similar. While the second mode contributes a dominant part to the shear force for very short piers, its influence diminishes completely for longer piers. For the majority of reasonable pier heights, a first mode representation appears sufficient, which is also well approximated by the (slightly conservative) SDOF model. It can therefore be concluded that the explicit consideration of the rotational superstructure inertia is mainly necessary for rather short cantilever piers. But even in these cases a SDOF representation with the proposed modifications can give sufficiently accurate approximations in the typically occurring range of pier heights.

*Fig. 3.14: Comparison of base moment from 2-DOF and modified SDOF model
for mass ratio m/j = 0.05 and as a function of pier height H
left: Base moment normalized by spectral acceleration and mass,
right: Ratio between base moment from 2-DOF solution vs. SDOF or modified SDOF*

*Fig. 3.15: Comparison of top moment from 2-DOF and modified SDOF model
for mass ratio m/j = 0.05 and as a function of pier height H
left: Top moment normalized by spectral acceleration and mass,
right: Ratio between top moment from 2-DOF solution vs. SDOF or modified SDOF*

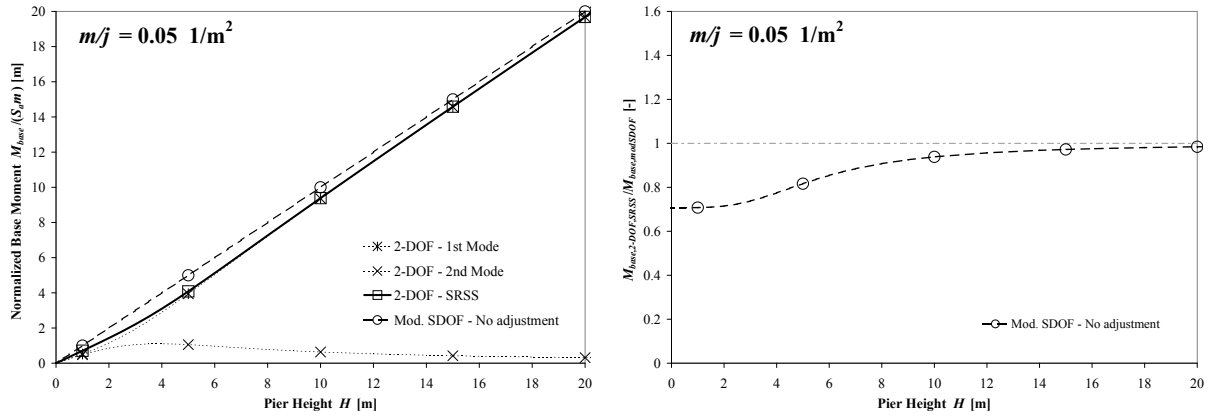*Fig. 3.16: Comparison of shear force from 2-DOF and modified SDOF model
for mass ratio m/j = 0.05 and as a function of pier height H
left: Shear force normalized by spectral acceleration and mass,
right: Ratio between shear force from 2-DOF solution vs. SDOF or modified SDOF*
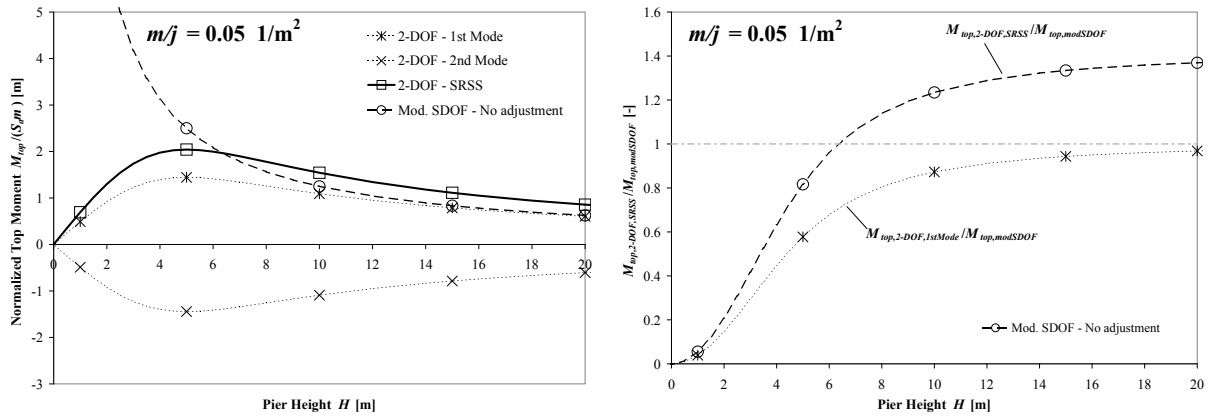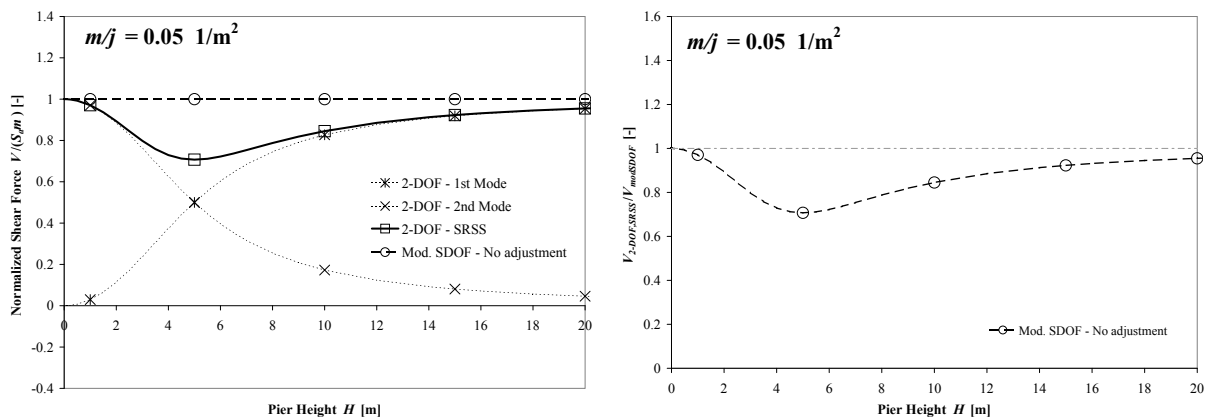
Summarizing the various comparisons discussed before, it can be concluded that the rotational inertia of the superstructure introduces an additional dynamic degree of freedom at every pier top. Generally, such degrees of freedom and the corresponding additional vibration modes must be considered in the model and the analysis of the structure. However, it has been shown that the relevance of this aspect is not the same for all types of systems. At first, the rotational inertia can be disregarded if significant rotational motions of the superstructure cannot occur due to structural reasons, as e.g. in the case of multi-column bents. Furthermore, even if rotational motions cannot be ruled out, the analyses presented above suggest – despite their simplifying assumptions – that certain structural properties influence the relevance of the phenomenon for the seismic response. It was found that the parameter α, as defined by equation (3.7), appears to have a strong influence on the response. Due to the limited variability of the mass ratio m/j, entering into α, the pier height H, being the third parameter in equation (3.7), is likely to control the relevance of the rotational superstructure inertia.

While for large values of α, corresponding to tall piers, a SDOF representation without consideration of the rotational mass j may be justified, for low α values (i.e. short piers) disregarding the rotational mass can give unrealistic results. In particular, the corresponding moment at the top of the cantilever pier cannot be captured by a SDOF model with translational mass m only. While a 3D dynamic model incorporating the rotational mass j can conceptually capture this effect, it has been shown that a certain modification of the SDOF solution might also serve as an approximation. Three possible alternatives to modify the SDOF response were considered for this purpose. Based on the comparisons with the 2-DOF results, it was found that the modification (iii) without any adjustments to achieve equilibrium performed best in approximating the SRSS superposition of the linear 2-DOF solution.

As a consequence, it is recommended that, if the rotational mass j is not explicitly considered in a 3D model although the superstructure can perform significant rotational motions, this deficit should be compensated by estimating the top moment $M_{top,\text{mod}SDOF}$ of the pier based on equation (3.6). This expression makes use of the kinematic relationship between the top rotation and the top displacement of a linear elastic cantilever corresponding to equation (3.3). If the pier develops a plastic hinge at its base with considerable plastic rotations, the relationship given in equation (3.4) might appear more appropriate. However, due to the underlying uncertainties and the fact that an inelastic response was not considered in the comparisons above, it is recommended to rather use the more conservative relationships of equations (3.3) and (3.6) even for inelastic response.

It was found that the thus determined approximation of the top moment $M_{top,\text{mod}SDOF}$ can underpredict the SRSS superposition of the 2-DOF analysis by up to a factor of $\sqrt{2}$. This only occurs for large values of the parameter α (see Fig. 3.12 right) which are typically associated with large pier heights (see Fig. 3.15 right). It might therefore be recommendable to increase the value of $M_{top,\text{mod}SDOF}$, determined using equation (3.6), by a factor of $\sqrt{2}$ for taller piers having effective heights H larger than, say, 8 m. Following the concept of SDOF modification (iii), the base moment $M_{base,SDOF}$ and the shear force V_{SDOF} coming from the SDOF analysis without consideration of the rotational mass are not changed. Instead, they are considered together with the top moment $M_{top,\text{mod}SDOF}$ in the sense of a response envelope which does not have to comply with equilibrium conditions.

When applying such an approximate solution, the underlying assumptions and simplifications should be kept in mind. While the proposed approach was shown to give reasonable (and conservative) results for the simplified cases considered here, for more general configurations this cannot always be guaranteed. Concerning the structural system, the simplifications mainly referred to the assumed linear elastic behavior and to the behavior of the individual pier which was modeled as independent from the rest of the structure. Both inelastic response as well as any coupling effect from other parts of the bridge – transferred by flexure or torsion of the superstructure – will influence the rotational seismic response of the superstructure. These effects were not considered by the analyses underlying the proposed simplified approach and therefore they cannot be covered by it either. Furthermore, the assumption that both natural periods of the 2-DOF system, as well as the fundamental period of the corresponding SDOF system, happen to result in the same spectral pseudo-acceleration will in general cases not always be fulfilled. Therefore, the actual response also depends on the spectral shape, which can lead to certain deviations from the behavior discussed above.

Since the observations discussed above are based on linear elastic behavior, it is recommendable to cover the related uncertainties by rather using a cautious approach. The fact that during inelastic response the base moment reaches it peak value (i.e. the nominal yield moment) not only at single time instants, but rather remains essentially constant in the plastic phases has consequences on the likely combinations of top and base moment. Based on inelastic analyses using typical configurations, Priestley *et al.* [PCK07] recommend assuming a top moment of $M_{top} = \pm \, 0.2 \, M_{base}$. It appears reasonable to follow this recommendation as a minimum requirement. In particular, it should be taken into account that under inelastic response double bending in the pier cannot be ruled out, with the corresponding consequences on the shear demand. Using the above recommendation for the top moment and assuming the nominal moment capacity M_n to act in the plastic hinge at the base, the shear demand in the plastic mechanism of a cantilever pier follows as $V = 1.2 \, M_n/H$.

Summing up, it can be said that whether the proposed simplified approach is applicable with sufficient reliability in a given case – or whether the effects of the rotational superstructure mass need to be modeled explicitly – should be decided on an individual basis. But even if the simplified approach is not considered sufficient, the findings and the conclusions of the discussions above may serve for a better understanding of the problem. As such, they can be valuable for the decision on how to best model the structure and also for the interpretation of the analysis results.

3.4.2 Definition of the Superstructure Axis for the Structural Model

For a conventional static analysis the definition of the beam or column axes in a structural model is rather straightforward. The behavior of a prismatic member is best represented if its axis is assumed along its center of stiffness (C.o.S.). However, for a seismic analysis the required structural representation does not only comprise the member stiffnesses, but also their masses. These masses are best represented along an axis passing through the cross-section's center of mass (C.o.M.).

As can be seen in Fig. 3.7, the center of mass of the superstructure cross-section does not necessarily coincide with its center of stiffness. While the eccentricity between the two points is zero for a solid rectangular cross-section and rather small for common box-girder shapes, a multiple T-beam, as e.g. the one shown in Fig. 3.7, can feature a certain distance between the centers of mass and stiffness. In such a case it is not fully accurate anymore to model the superstructure as a single beam which carries the masses along its axis. It would rather be more correct to model the beam itself in the C.o.S. axis and place the (lumped) masses in the C.o.M. axis, connecting them to the beam by means of (rigid) links. This modeling approach also visualizes that the eccentricity between the centers of mass and stiffness actually creates torsional moments in the superstructure independent of the rotational superstructure inertia or other torsional influences.

If nevertheless, as a simplification, the superstructure shall be modeled as a single beam with the masses along its axis (e.g. in a 2D model corresponding to Fig. 3.2), due consideration should be given to the positioning of this beam, as no fully correct solution exists. In particular, the choice will also influence the effective height of the piers. This question did not occur in the considerations concerning the rotational superstructure inertia discussed in Section 3.4.1, as for these analyses it was assumed that the superstructure did not have any coupling effect between the individual piers. This way the center of stiffness was irrelevant and the effective pier height H was simply chosen as the height h_M from the pier base to the center of mass. However, as soon as the superstructure provides some coupling between the piers, the behavior is not that simple anymore and the question about the best position for the beam and the masses arises. Due consideration to the relevance of the eccentricity between the centers of mass and stiffness, as well as to potential approaches to cover this aspect, should be given on an individual basis.

3.4.3 Influence of the Torsional Superstructure Stiffness

In Section 3.4.1 it has been assumed that the bridge is very regular and the response of its center region is rather uninfluenced by any restraints from the abutments, especially with respect to the rotational response of the superstructure. However, in many real cases such conditions may not be given, so that any rotational motion of the superstructure is also associated with torsional moments in the superstructure. While this effect may not be very pronounced in the case of an open cross-section having a rather low torsional stiffness, a closed box-girder superstructure features a considerable torsional stiffness GI_T which can provide significant torsional coupling between the piers and the abutments.

If the superstructure is connected to the piers and abutments either monolithically or by means of at least two bearings at each support (see Fig. 3.17), a moment transfer between pier and superstructure can occur. Under transverse seismic excitation this results in a torsional moment in the superstructure and a bending moment at the top of the pier. As a consequence, the pier does not behave as a pure cantilever anymore but is rather subjected to double bending, with subsequent effects on its transverse stiffness, the displacement and force capacity as well as on the inelastic shear demand.
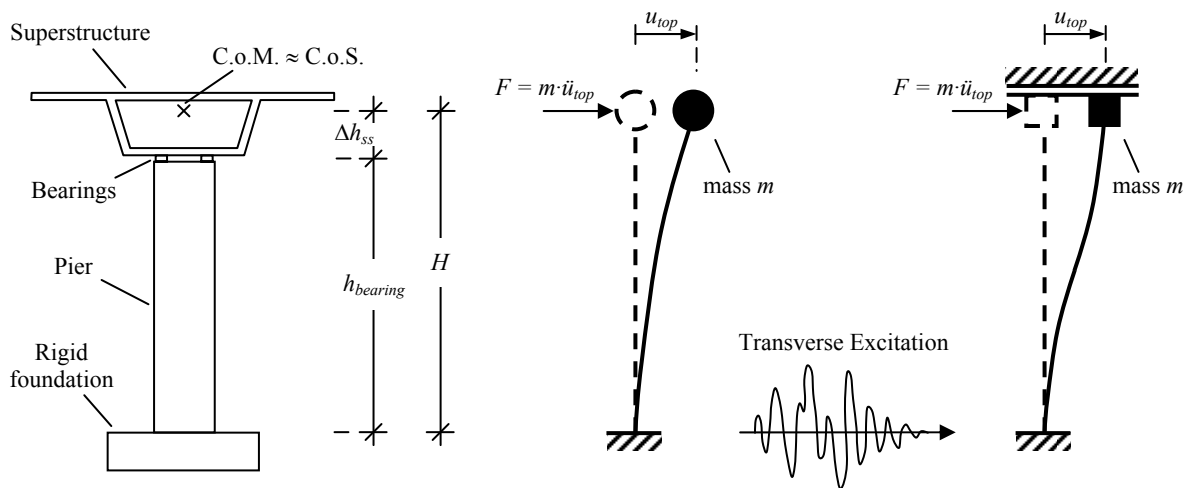
Fig. 3.17: Bridge pier with superstructure and simple modeling alternatives for the top boundary condition
left: Elevation, center: Model for fully released top rotation, right: Model for rigidly fixed top rotation

In Fig. 3.17 two simplified interpretations for the pier behavior under the two extreme cases of zero and infinite torsional superstructure stiffness GI_T are shown. The model in the center of Fig. 3.17 consists of a simple cantilever without any rotational restraint at the pier top, which may be representative for a negligible value of GI_T. As an alternative extreme case, an infinite torsional superstructure stiffness in combination with a rigid rotational fixation at the abutments would provide a rigid rotational restraint of the pier top as shown on the right side of Fig. 3.17. The translational restraint at the pier top due to flexure of the superstructure is nevertheless given in both cases, although not explicitly shown in Fig. 3.17.

While the conditions in a real bridge will normally lie somewhere between these to extreme representations, investigating them may give an impression of the possible range of responses. In Fig. 3.18 the corresponding distributions of moment and shear force along the pier are shown for both alternatives once a plastic mechanism has developed in the piers. While the cantilever, shown on the left side, needs to develop only one plastic hinge at its base, the rotationally restraint pier under double bending, shown on the right, requires two plastic hinges for a full plastic mechanism. For simplicity, the upper hinge is assumed at the very top of the pier model, although this would fall into the superstructure (see Fig. 3.17).

Assuming that all hinges have the same moment capacity $M_{y,pier}$, it can be seen from Fig. 3.18 that the shear force corresponding to the plastic mechanism in the double bending pier, on the right, is twice as high as that of the single bending cantilever, on the left. This shear force on one hand represents the

flexural force capacity of the pier, but also the shear demand that must be sustained by the pier. Especially the latter aspect may be of significant importance if the member is potentially shear critical, as such a brittle failure type could reduce its deformation capacity substantially. Another consequence of the double bending action is that the elastic translational stiffness is four times higher than that of the corresponding cantilever. Furthermore, it is likely that the displacement capacity of the pier on the right side of Fig. 3.18 is lower than that of the cantilever because of the higher moment gradient in double bending and the subsequent reduction of the plastic hinge length.
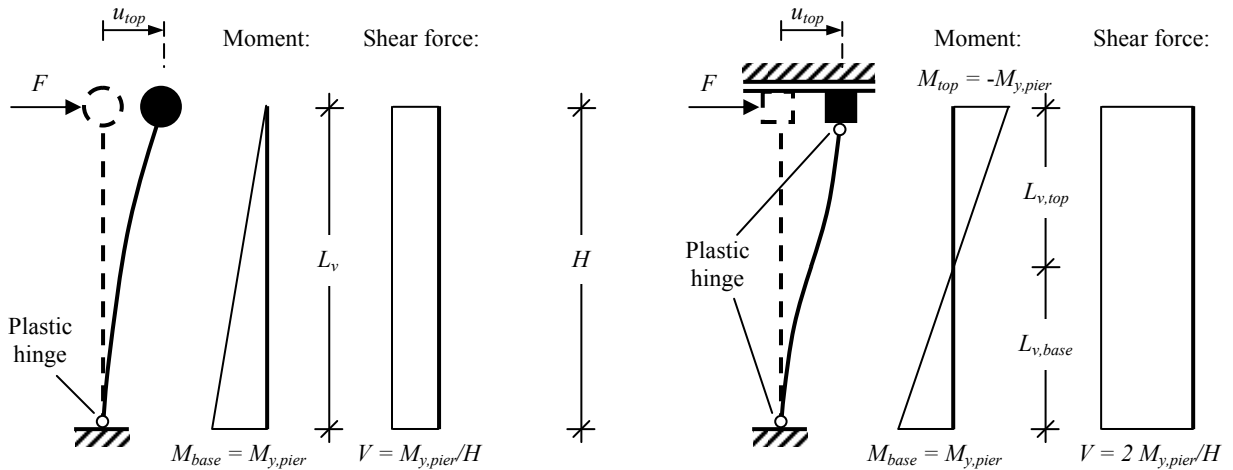
Fig. 3.18: Internal actions in piers developing a plastic mechanism for different boundary conditions left: Single bending for free top rotation, right: Double bending for fixed top rotation

As can be seen from the discussion above, the transition from a single bending cantilever to a double bending pier due to rotational top restraint can have a series of significant consequences on the pier behavior. Nevertheless, the (very) simplified pier models considered in Fig. 3.17 and Fig. 3.18 do not necessarily represent the real conditions in a realistic manner. If the superstructure is bearing supported on the pier top, as shown in Fig. 3.19, the moment that can be transferred by the pair of bearings is limited to a value of $\pm M_{y,bearing}$ at the seat level. It is rather likely that this moment capacity of the bearings is considerably lower than the moment capacity of the RC pier section. As a consequence, if the assumption of a rigid rotational top restraint by the superstructure is maintained, a plastic mechanism including a bearing hinge at the seat level results, as shown in Fig. 3.19.
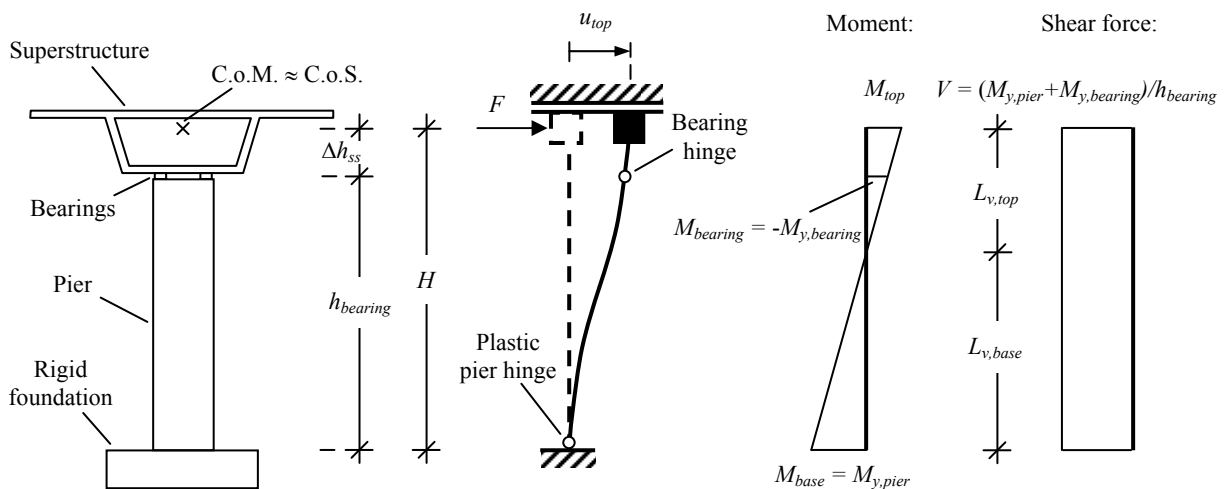
Fig. 3.19: Elevation of regular bridge in transverse direction left: Pier with superstructure cross-section, right: Corresponding structural model of single pier with tributary superstructure

The corresponding distributions of moment and shear force along the pier height are shown on the right side of Fig. 3.19. They lie between the two extreme cases discussed before in the context of Fig. 3.18. The potential plastic bearing hinge at the seat level thus results in a limitation of the shear demand in the plastic mechanism of the pier. As this upper boundary depends on the moment $M_{y,bearing}$ that can be transferred by the pair of bearings, some consideration shall be given to this detail and possible ways of modeling it. In normal bridge designs, the bearings will not be able to transfer vertical tension forces. In this case, any moment $M_{bearing}$ can only be transferred by the bearings in the form of (unequal) compression forces $R_{bearing}$ having a mutual distance of $d_{bearing}$ as shown in Fig. 3.20. The sustainable moment $M_{y,bearing}$ is then limited by the maximum eccentricity e_{Fv} of the vertical load F_v, with $e_{Fv} = d_{bearing}/2$, and can be computed according to equation (3.9).

$$M_{y,bearing} = \frac{1}{2} F_v d_{bearing} \tag{3.9}$$
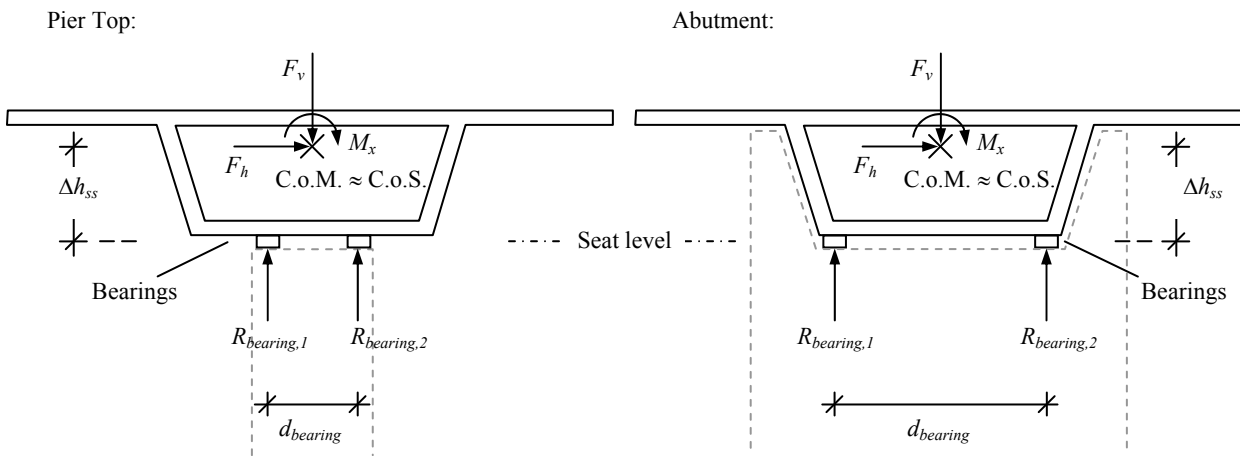
Fig. 3.20: Configuration of bearings and resulting reactions at superstructure supports
left: Situation at pier top, right: Situation at abutment
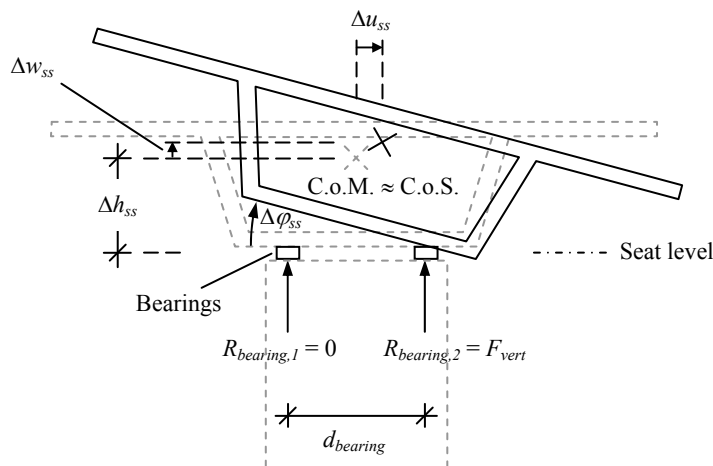
Fig. 3.21: Rocking motion of superstructure due to uplifting at bearing

If this upper limit to $M_{bearing}$ is exceeded, the superstructure will uplift at the unloaded bearing resulting in a rocking motion as shown in Fig. 3.21. Assuming that the bearings are rather undeformable under vertical compression loads, the moment rotation response becomes similar to that of a rigid plastic rotational spring as shown in Fig. 3.22. However, while a plastic behavior incorporates large hysteretic damping under cyclic loading, the rocking motion itself does not dissipate any energy. If energy

dissipation related to impact upon regaining contact between superstructure and bearing is neglected, it appears therefore reasonable to rather model a bilinear elastic behavior instead of a plastic response. In this approach, the unloading occurs along the same path of the moment-rotation relationship as the loading (see Fig. 3.22).
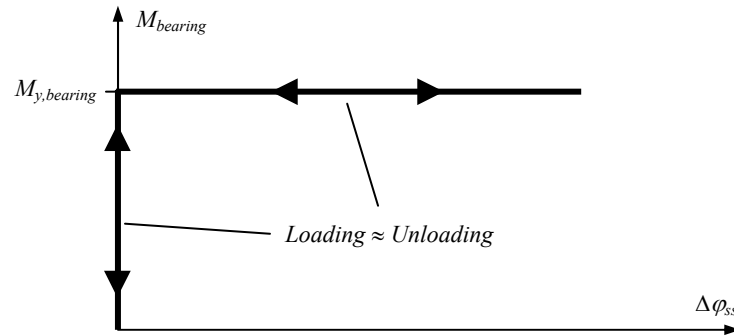
Fig. 3.22: Rigid-bilinear elastic moment-rotation behavior of the plastic bearing hinge at seat level

It should be noted that for large horizontal rocking motions Δu_{ss} the distance between the superstructure's center of mass (C.o.M.) and the loaded bearing, representing the lever arm for the vertical load F_v, is reduced. As a consequence the resisting moment $M_{bearing}$ also decreases, leading to a negative post-yield stiffness of the moment-rotation relationship. In Fig. 3.23 the influence of the effect is shown for two different configurations. It can be seen that this P-Δ-effect is more pronounced for small bearing spacings $d_{bearing}$ (left side of Fig. 3.23) while it may only be of secondary influence for a wide bearing spacing (right side of Fig. 3.23). In either case, for the range of moderate displacements shown in Fig. 3.23, it would appear sufficient to describe the superstructure motion based on linearized kinematics.
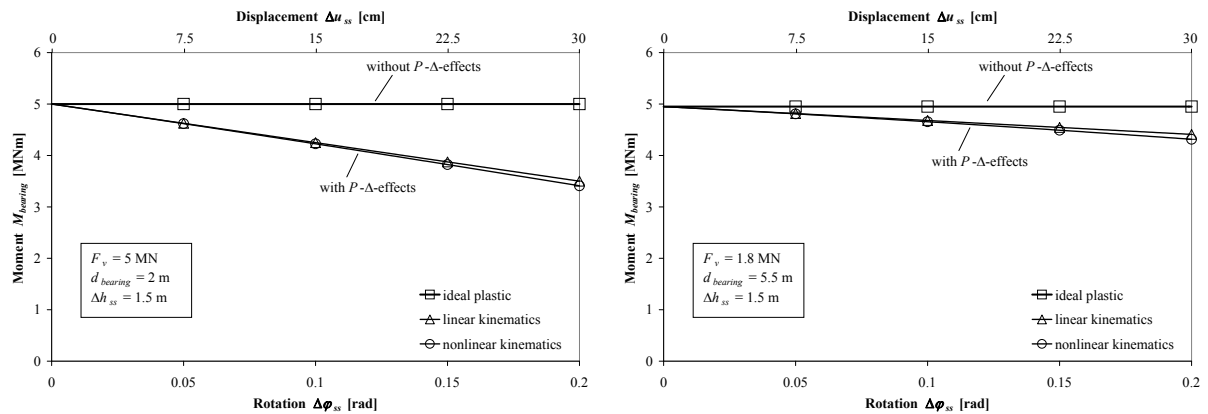
Fig. 3.23: Influence of P-Δ-effects on moment-rotation behavior of the plastic bearing hinge
left: Narrow bearing spacing configuration representative for seating on pier tops,
right: Wide bearing spacing configuration representative for seating at abutments

While a rocking motion of the superstructure may in some cases be acceptable, it can cause problems especially if only one of the two bearings is fixed against transverse displacements. If the fixed bearing uplifts considerably (left bearing in Fig. 3.21) at a certain point it will leave its horizontal guidance. Since the other bearing (right bearing in Fig. 3.21), due to its sliding interface, cannot provide any horizontal support, the superstructure can shift freely in the transverse direction. This motion can lead to an unlocking at the fixed bearing, so that even upon regaining contact on this side the (formerly) fixed bearing might not provide any horizontal support anymore either. When evaluating a rocking motion of the superstructure it should further be kept in mind that this type of response does not only incorporate horizontal displacements Δu_{ss} of the center of mass, but also implies vertical motions Δw_{ss}. The extent of this vertical response depends on the geometry of the system and it is related to the horizontal amplitudes by $\Delta w_{ss} = \Delta u_{ss} \cdot d_{bearing}/(2\Delta h_{SS})$.

So far, the discussion on the consequences of the torsional restraint from the superstructure have focused on the behavior of the individual pier, assuming that the superstructure would provide a near rigid rotational restraint to the pier top as long as the bearings do not uplift. This restraint would be based on a near infinite torsional stiffness of the superstructure and an equally near rigid as well as sufficiently strong rotational fixation at the abutments. As these assumptions are unlikely to be appropriate on a general basis, some consideration shall be given to these aspects.
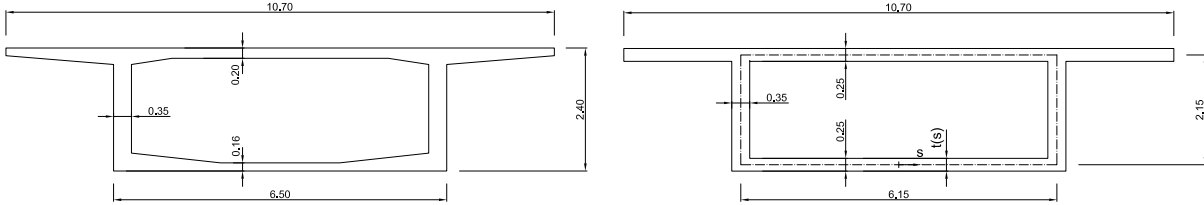
Fig. 3.24: Sample box-girder cross-section
left: Original geometry, right: Simplification including center line of box

A reinforced concrete superstructure with an open cross-section, as e.g. a multiple T-beam, has only a comparably low torsional stiffness. In many cases such a superstructure will only provide a negligible torsional restraint, especially if the concrete is cracked. In contrast, a closed box-girder cross-section, as the one shown in Fig. 3.24, can have a considerable torsional stiffness which may influence the response of the bridge. For a linear elastic material, the torsional stiffness due to St. Venant torsion results as GI_T, with G being the elastic shear modulus of the material and I_T being defined according to equation (3.10). A possible distortion of the cross-section can have an additional influence on the torsional stiffness of the superstructure [EGN06]. However, it is likely that in a prestressed concrete superstructure an adequate assumption of the elastic shear modulus G can have a significantly more pronounced influence.

$$I_T = \frac{4 \cdot A_m^2}{\oint_s \frac{1}{t(s)} ds} \tag{3.10}$$

with A_m: Area enclosed by the center lines of the box walls

Katsaras *et al.* [KPK09] have investigated the torsional stiffness of prestressed concrete superstructures considering cracked and uncracked conditions. While the stiffness of the uncracked superstructure can be estimated with reasonable accuracy using the shear modulus $G = E/2/(1+\nu)$ (ν: Poisson ratio) of the uncracked concrete, they found that the corresponding stiffness after cracking cannot only be reduced significantly, but also has a considerable variability and uncertainty. Based on theoretical considerations using a *softened space truss model* proposed by Hsu, they concluded that the torsional stiffness of a prestressed box girder after cracking tends to drop to values between 10% and 30% of the uncracked stiffness. After yielding of the transverse reinforcement, they even found a further reduction to only 8% to 12% of the stiffness before cracking. The actual relationship depends considerably on the amount of transverse reinforcement and the level of prestressing. It is further influenced to a lesser degree by the geometry of the cross-section and the longitudinal reinforcement.

Katsaras *et al.* [KPK09] compared the findings of their theoretical study to experimental results on the shear behavior of prestressed concrete panels by Marti and Meyboom. Based on these data they concluded that the experimental shear stiffness after cracking was in the range between 25% and 40% of the uncracked stiffness. The stiffness at first yield of the reinforcement was determined as 13% to 29%, and at last yield of reinforcement it amounted to 7% to 8% of the uncracked value. These experimental results therefore appeared to confirm the theoretical model with respect to the expected order of magnitude of stiffness reduction after concrete cracking.

For practical applications, Katsaras *et al.* [KPK09] suggest checking the principal tensile stress under combined actions including the prestressing, and comparing it to the tension strength of the concrete f_{ct} in order to determine whether the cracked or uncracked torsional stiffness should be used for an

analysis. However, on one hand the stress state is not known before the analysis and, on the other hand, some general uncertainty may exist in determining the exact stress state of the superstructure (as well as the tension strength). Due to the strong influence of the onset of cracking on the torsional stiffness GI_T, it may therefore appear justified to consider both, an uncracked value $GI_{T,uncracked}$ corresponding to the gross section and a cracked value $GI_{T,cracked}$ using 10% of $GI_{T,uncracked}$. If it is not possible to determine beforehand which assumption yields more conservative results, it may be necessary to perform two analyses using both alternative values for GI_T. Only if the first analysis using the uncracked stiffness suggests that the principal tensile stress lies considerably below the assumed value of the concrete tension strength, a further analysis based on the cracked torsional stiffness may be considered dispensable.

While the stiffness of the superstructure is one aspect influencing the torsional response, its boundary conditions at the abutments can be another controlling aspect for the behavior. If the superstructure is bearing supported at the abutments, as shown on the left side of Fig. 3.20, a similar situation results as discussed above for the bearing support on the pier tops. In comparison to other sources of deformations, the rotational stiffness of the support may be considered as rather rigid as long as no uplifting of the bearing occurs. However, as for the pier tops, the moment that can be transferred by the pair of bearings is limited by the maximum eccentricity e_{Fv} of the vertical support force being $e_{Fv} = d_{bearing}/2$. The maximum moment $M_{y,bearing}$ that the rotational fixation at the abutments can provide results according to equation (3.9). If this upper boundary is reached, a rocking response of the superstructure occurs as discussed above in the context of Fig. 3.20 through Fig. 3.23.

As a consequence, the rotational restraint of the pier tops shown in Fig. 3.19 is limited by (a) the torsional stiffness of the superstructure and (b) the limited moment capacity of the rotational fixity at the abutments. Generally, some rotational interaction can also result between different piers which are coupled by the superstructure. This effect may especially occur if the distribution of pier heights along the bridge is very irregular. It may be noted that the moment capacity provided by a pair of bearings according to equation (3.9) depends on the vertical support force F_v and the spacing $d_{bearing}$ between the two bearings. Both quantities are likely to differ between the abutments and the pier tops. On one hand, the support force F_v at the pier tops may be higher by a factor of more than two compared to the abutments. On the other hand, the distance $d_{bearing}$ at the abutments can be significantly larger than at the piers. While in the latter case, $d_{bearing}$ depends on the section depth of the pier, at the abutments the bearings are typically placed in the outer regions of the superstructure bottom plate (see Fig. 3.20). As a consequence, the two opposite influences on $M_{y,bearing}$, coming from the variations of F_v and $d_{bearing}$, can cancel each other out to some extent, and the resulting rotational moment capacity of the bearing supports at abutments and pier tops might result in a similar order of magnitude again.

To study the combined influence of all aspects discussed before, a pushover analysis on a symmetric three span sample bridge has been performed. Two general structural models are considered for this analysis: A simplified model shown in Fig. 3.25 and a more detailed model shown in Fig. 3.26. For the simplified model the torsional stiffness of the superstructure is taken as zero. Furthermore, the entire aspect of limited bearing moment capacity, as well as the vertical eccentricity Δh_{ss} between the superstructure axis and the seat level are neglected. As a consequence, the piers act as cantilevers being rigidly pinned to the superstructure at the height of its axis. The simplified bridge model of Fig. 3.25 therefore corresponds to the individual pier model shown in the center of Fig. 3.17 and on the left side of Fig. 3.18.

In contrast, the more detailed bridge model of Fig. 3.26 takes into account the various aspects discussed above. This includes the potential plastic bearing hinge at the pier tops and the abutments, having a rigid-bilinear elastic response according to Fig. 3.22. Further, the vertical eccentricity Δh_{ss} between the superstructure axis and the seat level is taken into account and a variety of assumptions for the torsional superstructure stiffness GI_T are considered in order to cover the range of possible values.

The structural properties of the systems are roughly based on the characteristics of the sample bridges presented in Section 2.2.2. The geometry of the two symmetric bridge models is defined as shown in Fig. 3.25 and Fig. 3.26. For both models the elastic bending stiffness of the piers is assumed as $EI_{pier,elastic} = 15\,000$ MNm^2. The nominal yield moment in the plastic hinges of the piers is estimated as

$M_{y,pier} = 20$ MNm, resulting in a yield displacement for the simplified cantilever representation of $\Delta_y \approx 19$ mm. These assumptions roughly correspond to a wall-type pier with a section depth of $l_w = 3$ m and a section width of $b_w = 0.7$ m. For the translational abutment-embankment springs, the concepts outlined in Section 3.5.2 are used to estimate an elastic stiffness of $k_{abut} = 225$ MN/m and a yield load of $F_{y,abut} = 2.7$ MN. The flexural stiffness of the superstructure for bending about the vertical axis is assumed as $EI_{z,ss} \approx 1.2 \cdot 10^6$ MNm^2.
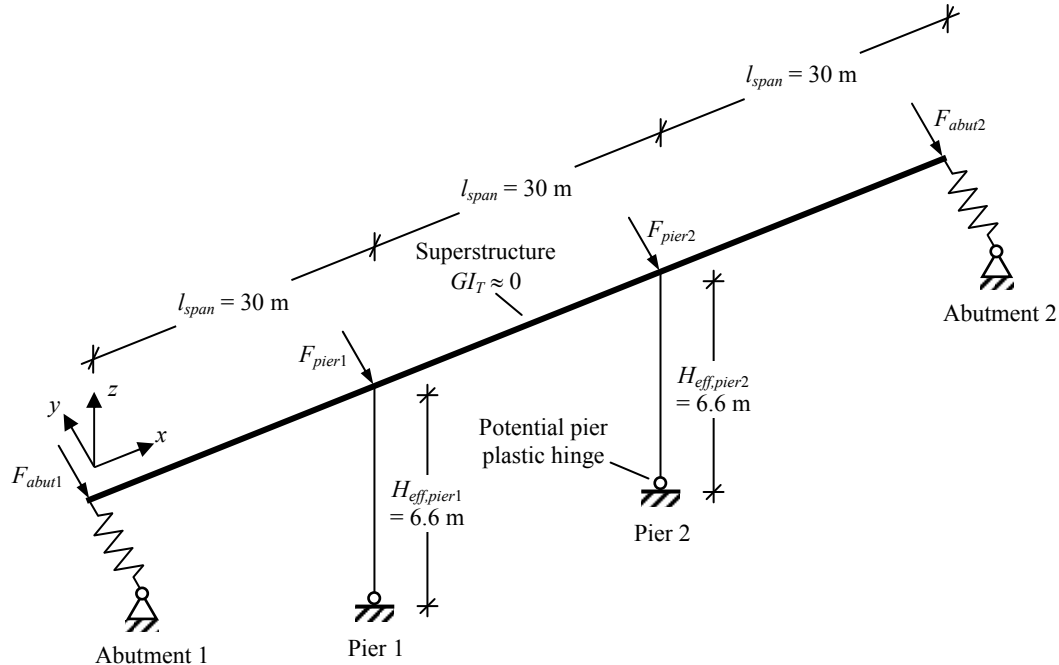

Fig. 3.25: Simplified 3-dimensional bridge model for transverse seismic response analysis
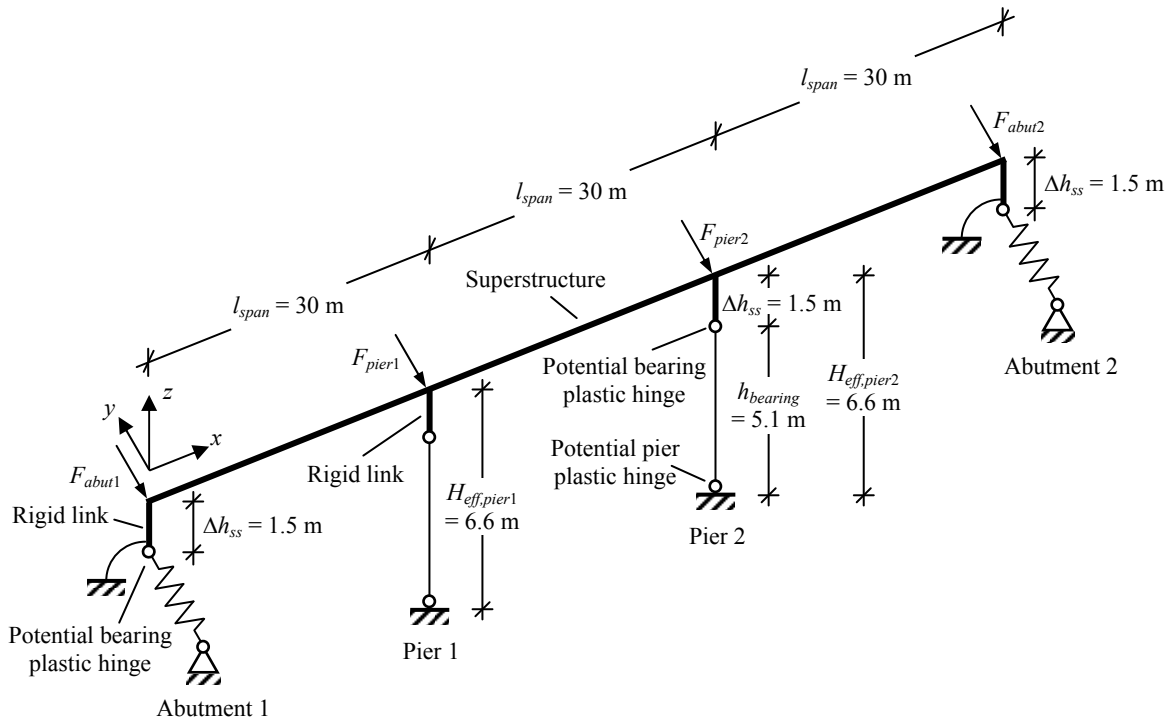

Fig. 3.26: Detailed 3-dimensional bridge model for transverse seismic response analysis

3.4 Superstructure Modeling

For the more detailed model of Fig. 3.26 the uncracked St. Venant torsional stiffness of the superstructure is estimated based on equation (3.10) as $GI_{T,uncracked} \approx 120 \cdot 10^3$ MNm^2 and the corresponding cracked stiffness is assumed as 10% of the uncracked value resulting in $GI_{T,cracked} \approx 12 \cdot 10^3$ MNm^2. These values roughly correspond to a prestressed box-girder cross-section having a geometry as the one shown in Fig. 3.24. For the determination of the moment capacity $M_{y,bearing}$ of the bearing supports the spacing $d_{bearing}$ between the axes of the individual bearings was assumed as 2 m and 5.5 m at the pier tops and the abutments, respectively. The corresponding support forces F_v for the superstructure were assumed as 5 MN at the pier tops and 1.8 MN at the abutments. As a consequence, using equation (3.9) for both types of bearing supports at pier tops and abutments similar moment capacities result as $M_{y,bearing} \approx 5$ MNm.

To study the influence of the torsional superstructure stiffness and the level of model detailing, a total of five system configurations were considered for the pushover analyses, being defined as follows:

System 1: Simplified model according to Fig. 3.25 without any consideration of superstructure torsion, uplifting of bearings or eccentricity of the seat level.

System 2: More detailed model according to Fig. 3.26 using the <u>cracked</u> torsional superstructure stiffness $GI_{T,cracked}$, including the bearing plastic hinges with yield strength $M_{y,bearing}$ at the eccentricity Δh_{ss} below the superstructure axis.

System 3: More detailed model according to Fig. 3.26 using the <u>uncracked</u> torsional superstructure stiffness $GI_{T,uncracked}$, including the bearing plastic hinges with yield strength $M_{y,bearing}$ at the eccentricity Δh_{ss} below the superstructure axis.

System 4: More detailed model according to Fig. 3.26 using an <u>infinite</u> torsional superstructure stiffness $GI_T \rightarrow \infty$, including the bearing plastic hinges with yield strength $M_{y,bearing}$ at the eccentricity Δh_{ss} below the superstructure axis.

System 5: More detailed model according to Fig. 3.26 using a <u>zero</u> torsional superstructure stiffness $GI_T = 0$, including the bearing plastic hinges with yield strength $M_{y,bearing}$ at the eccentricity Δh_{ss} below the superstructure axis.

These five systems were subjected to a nonlinear static pushover analysis applying a discrete force distribution as shown in Fig. 3.25 and Fig. 3.26. The forces were taken as proportional to assumed lumped masses being $m_{pier} = 500$ t at the pier tops and $m_{abut} = 180$ t at the abutments, thus implying an even distribution for the acceleration shape vector (see *Load Distribution 1* in Section 4.6.2c). On the left side of Fig. 3.27 the corresponding global pushover curves of all five systems are shown in terms of total base shear (= sum of all horizontal support forces) vs. top displacement of pier 1 (at the level of the superstructure axis). For each case, the occurrence of a new plastic hinge is visualized by a marker. On the right side of Fig. 3.27 and in Fig. 3.28 each graph shows a comparison between two of the curves at a time, also indicating the activated plastic hinges and their order of occurrence.

At first, on the right side of Fig. 3.27 the response of the simplified *System 1* is compared to the more detailed *System 2* using the cracked torsional superstructure stiffness. It can be seen that despite the considerable differences between the two models the pushover curves do not deviate very strongly. The additional rotational constraint from the superstructure only results in a slightly higher overall stiffness of *System 2*, compared to *System 1*. Both models predict the yielding at the pier base as the first plastic hinge at a top displacement of about 1.9 cm and a total base shear of about 10 MN. While in the response of the more detailed *System 2* the uplifting of the bearings at the abutments follows closely at a pier displacement of about 2.2 cm, this mechanism conceptually cannot occur in the simplified *System 1*. In this range, a somewhat softer behavior of the latter system is noticeable. Finally, both systems reach their ultimate force capacity when the abutment springs develop translational plastic hinges, thus resulting in a full plastic mechanism for both systems. The maximum base shear of System 2, $F_{tot,system2} \approx 11.75$ MN, is only insignificantly higher than that of System 1, being $F_{tot,system1} \approx 11.45$ MN. It appears that for the chosen bridge configurations, the torsional superstructure behavior does not have a very pronounced influence on the *global response* of the bridge.
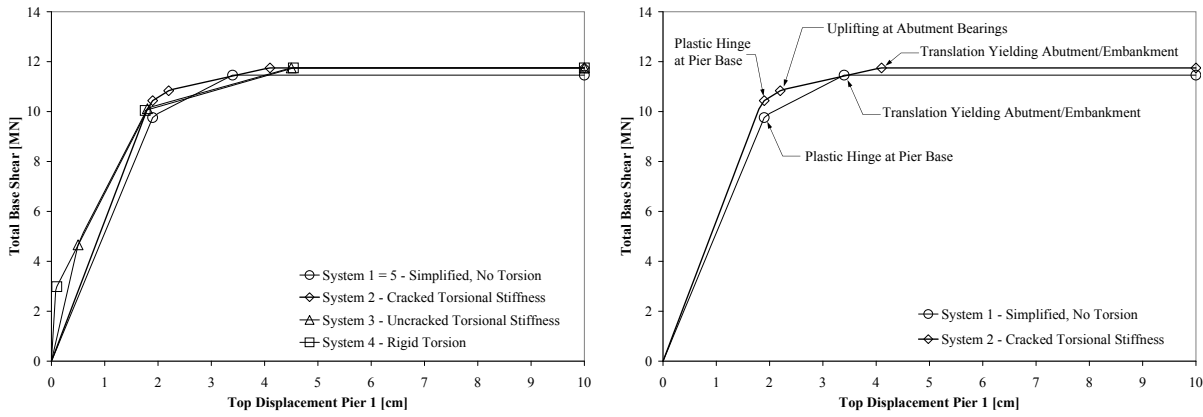
Fig. 3.27: Pushover curve in the form of total base shear vs. top displacement of pier 1
left: Overview of all system configurations,
right: Comparison between systems 1 and 2 with details of plastic hinge occurrence

On the left side of Fig. 3.28 a similar comparison is shown between the two detailed systems 2 and 3, featuring cracked and uncracked torsional superstructure stiffnesses. At first sight, the two curves again do not deviate significantly. However, looking at them in a more detailed manner, it becomes noticeable that the order of developing plastic hinges differs between the two models. While *System 2* with the cracked superstructure first develops a plastic hinge at the pier base, which is then followed by uplifting at the abutments, *System 3* featuring the torsionally stiffer cracked superstructure behaves in the opposite way. The latter system already shows uplifting of the bearings at a rather early stage, significantly before the development of a plastic hinge at the pier bases. The third plastic hinge finally occurs for both systems in the translational abutment spring at very similar pier displacements thus completing the same plastic mechanisms with the same ultimate base shear.
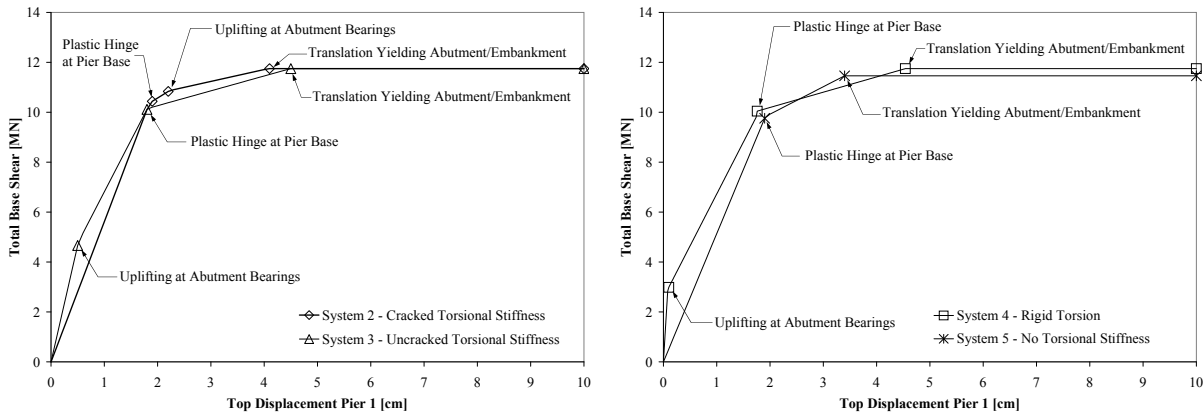
Fig. 3.28: Pushover curve in the form of total base shear vs. top displacement of pier 1
left: Comparison between systems 2 and 3 with details of plastic hinge occurrence,
right: Comparison between systems 4 and 5 with details of plastic hinge occurrence

The details of the two extreme systems 4 and 5, featuring infinite and zero torsional superstructure stiffnesses, are shown and compared to each other on the left side of Fig. 3.28. For the given geometry, *System 5* behaves exactly the same as the simplified *System 1*. This is related to the fact that, due to the zero torsional stiffness of the superstructure, moments at the bearing level of the abutments and the piers can only result from the shear forces in the rigid links times the eccentricity Δh_{ss} of the superstructure axis. At the abutments, as well as the piers, these shear forces are limited by the plastic hinges in the translational abutment spring and at the pier base to a level which does not suffice for uplifting of the bearings. Therefore, in this case, all comments on the behavior of *System 1* are also valid for the more detailed *System 5* where only the superstructure torsional stiffness is neglected. However, the equivalence of the two models is not warranted for any combination of Δh_{ss} and the strengths of other plastic hinges. *System 4*, featuring the torsionally rigid superstructure,

behaves similar to *System 3* with the uncracked superstructure. The uplifting moment at the abutments is already reached at marginal pier displacements. From then on, the response of systems 3 and 4 is basically the same (see Fig. 3.27 left). This similarity shows that the stiffness of the uncracked superstructure is already rather close to a rigid behavior (for such a rather short bridge). The fact that for larger deformations the pier tops are nevertheless not fully fixed rotationally, is a pure consequence of the limited moment capacity provided by the bearings at the abutments.

In general, the preceding comparisons have shown that the analyzed configurations hardly differ with respect to their global pushover curves. However, as the order in which the plastic mechanisms develop is not the same in all cases, the local demands may deviate more profoundly. To study this aspect, on the left side of Fig. 3.29 the internal moments of the piers at the base (M_{base}), the bearing level ($M_{bearing}$), and the level of the superstructure axis (M_{top}) are shown as defined in Fig. 3.19. In the same way, the shear force of the pier (V) is shown on the right side of Fig. 3.29. In both graphs the development of the actions is presented as a function of the top displacement at pier 1, thus providing a common parameter to define the system state, equivalent to the previous figures.

Fig. 3.29: Internal pier actions vs. top displacement of pier 1
left: Moments at base, bearing level and superstructure axis level, right: Shear force

While the development of the base moment M_{base} does not appear to be influenced very strongly by the various modeling alternatives, some differences can be noticed for the moments $M_{bearing}$ at the bearing level and M_{top} at the superstructure axis level. The bearing level response of *System 2* (cracked superstructure) at small deformations is rather close to that of *System 5* (no torsional stiffness), always experiencing positive moments $M_{bearing}$ (i.e. same sign as the base moment M_{base}). In contrast, systems 3 and 4, featuring the stiffer uncracked and the rigid superstructure, show negative bearing moments at small deformations. For larger deformations they reverse the sign of the bearing moment, which then converges towards the response of *System 2*. At this stage, all systems reach their highest bearing moments which approach the yield moment $M_{y,bearing} = 5$ MNm (especially *System 1*), but do not reach it completely. However, this shows that further small changes of the system properties could result in the development of other plastic mechanisms including uplifting of the bearings at the pier tops.

The moment M_{top} at the superstructure level has a negative sign throughout the entire response for all systems featuring torsional superstructure stiffness. It is noticeable that this top moment, especially for the torsionally stiffer systems 3 and 4, reaches rather high values for small deformations which later on reduce considerably to a residual value at large pier displacements. This shows that a small amount of double bending occurs along the effective pier height H, but the magnitude of the top moment is substantially lower than what would be expected from a rigid rotational response, as shown in Fig. 3.18 (right). This is an effect of the uplifting at the (abutment) bearings which acts like a fuse for the moment demand in the upper region of the pier. Within the actual pier (i.e. between its base and the seat level) the moment distribution is almost always positive for realistic torsional stiffness estimates of the superstructure.

As the shear force is equal to the moment gradient, the double bending along the effective height also influences the flexural force capacity, and thus the shear demand of the piers, as shown on the right

side of Fig. 3.29. As a consequence, systems 2 through 4, featuring torsional stiffness of the superstructure, result in a higher shear demand for the piers. It is interesting to note that the highest value of the shear force does not occur in the final plastic mechanism, but rather in an intermediate state where only two out of three plastic hinges have developed. This might at first sight appear somewhat surprising as the peak force capacity of the global system response is reached in the final mechanism when all plastic hinges are activated (see Fig. 3.27 and Fig. 3.28). This phenomenon also highlights that the differing plastic mechanisms resulting from varying modeling assumptions can influence the local demand situations, even in cases where the global behavior might not be altered very strongly.

The local demand situation at the abutments is shown in Fig. 3.30. Here, the actions in the rigid vertical link connecting the superstructure axis and the bearing level (see Fig. 3.26) are shown in a similar way as before for the pier. On the left side of Fig. 3.30 the moments at the bearing level ($M_{bearing}$) and the at the superstructure axis (M_{top}) are presented, while the right side shows the corresponding shear forces. Both graphs again show the actions as functions of the top displacement at pier 1, in order to maintain the same parameter defining the system state. This means that the inclinations of the curves in Fig. 3.30 do not represent the stiffnesses of the abutment, which were modeled equally in all systems.
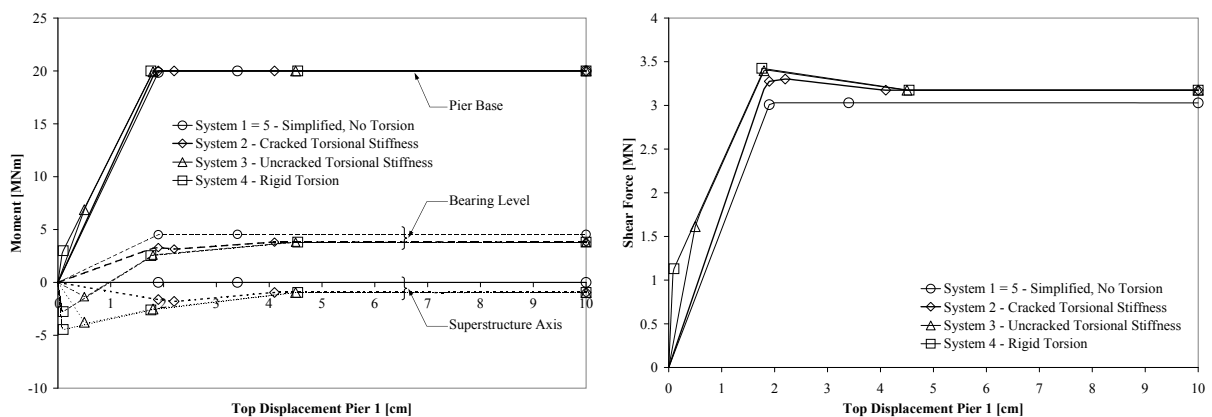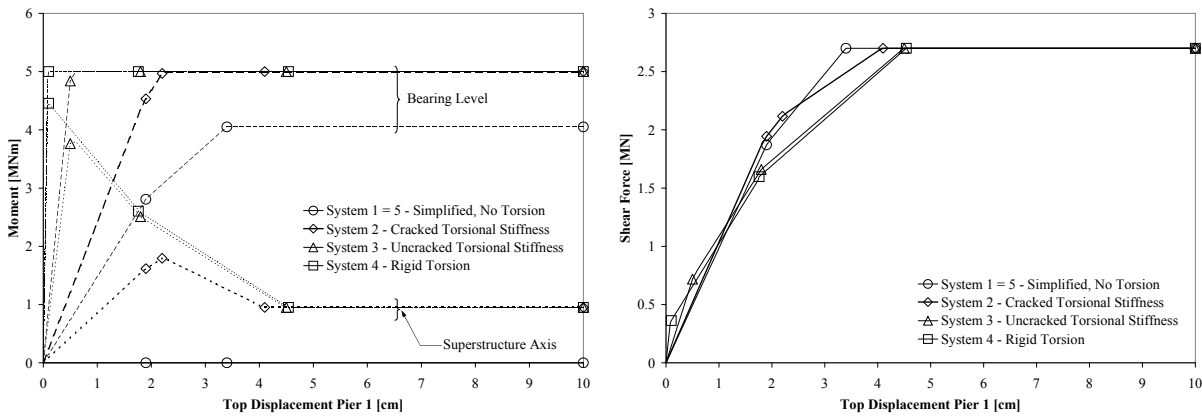

Fig. 3.30: Abutment actions vs. top displacement of pier 1
left: Moments at bearing level and superstructure axis level, right: Shear force

Concerning the moment $M_{bearing}$ at the seat level, the curves of all systems featuring a torsional stiffness of the superstructure only differ with respect to the top displacement of pier 1 at which the uplifting moment $M_{y,bearing}$ is reached. *System 5* without torsional stiffness does not reach this uplifting moment. As the superstructure of *System 5* does not introduce any torsional moment at the top, the moment at the seat level results only from the eccentricity Δh_{ss} along which the translational support force F_{abut} from the horizontal abutment spring is transferred. For the modeled value of $\Delta h_{ss} = 1.5$ m, the yield force $F_{y,abut} = 2.7$ MN of this spring only causes a bearing moment of $M_{bearing} = 4.05$ MNm, which is below the uplifting moment of $M_{y,bearing} = 5$ MNm. For a somewhat larger vertical eccentricity Δh_{ss} or a higher translational yield force $F_{y,abut}$ of the abutment, even *System 5* with the torsionally slack superstructure could experience uplifting at the abutment bearings.

The moment M_{top} at the superstructure level of the abutment link provides the restraining moment at the pier tops which is transferred by the superstructure via torsion. It can be seen on the left side of Fig. 3.30 that this moment increases, for all systems featuring torsional superstructure stiffness, up to the point where uplifting at the abutment bearings occurs. From then on it reduces again until a residual value is reached when the translational abutment spring starts yielding. For equilibrium reasons this residual value of M_{top} is equal to $M_{y,bearing}-F_{y,abut}\cdot\Delta h_{ss} = 0.95$ MNm. This explains why the largest (absolute) pier top moment – and thus the highest shear demand for the piers – is reached before the translational abutment spring yields.

The shear force in the vertical abutment link, shown on the right side of Fig. 3.30, is equal to the support force by the horizontal abutment spring. It can be seen that its yield force is reached

independent of the system modeling, also for zero torsional superstructure stiffness (*System 5*) and for the simplified model of *System 1*. Even the pier top displacement, at which the abutment spring starts yielding, does not differ strongly between the various modeling alternatives, with the simplified *System 1* reaching yield at first and *System 4* featuring the torsionally rigid superstructure reaching it last.

Summarizing the phenomena discussed above in the context of superstructure torsion, it should first be said that the details of the various findings strongly depend on the individual bridge system and its particular configuration, which can change significantly from one bridge to another. Therefore, the specific details of the behavior found in the investigated examples above should by no means be generalized. The example bridge systems were intentionally kept very simple in order to visualize the conceptual phenomena that can occur and to study the influences they may have on the global and local bridge behavior. For any other (possibly more realistic) bridge configuration these phenomena can cause significantly differing effects. In particular, more irregular and larger bridges are likely to result in a more complex behavior as well. At the same time, the conducted very simple pushover analyses cannot capture all dynamic effects that may occur during a seismic response. However, this simplified approach was chosen on purpose because it allows following the different stages of the response in a structured and better understandable way. Such a conceptual understanding may be very helpful for interpreting the response of more complex analysis results and may also serve as a means to decide which effects need to be included into a model, while others might be disregarded in an individual case.

Despite the limitations of this simplified study, some interesting and important conclusions can be drawn from it. One general finding is that the assumption of cantilever piers being subjected to only single bending under transverse excitation is not fully accurate if the superstructure has a non-negligible torsional stiffness while being connected to the abutments and the pier tops in a way which can transfer moments. On the other hand, it was found that the degree of this effect can strongly depend on the actual value of the torsional stiffness, and therefore also on the cracking state of the superstructure. Moreover, if the superstructure is bearing supported, the moment capacity at the seat level is typically significantly lower than that of a wall-type RC bridge pier or an abutment. As a consequence, this fuse-like behavior can limit the moment demand on the upper part of the pier by uplifting of the bearings. This results in a subsequent rocking motion of the superstructure, whose acceptability might have to be checked, especially if only one of the two bearings is transversely fixed and could therefore unlock upon uplifting.

Another important finding of the analyses is that the local effects of the investigated phenomena can be more pronounced than the influence on the global behavior. Therefore, it may not be sufficient to consider only the global pushover response in order to evaluate the necessity for a more detailed modeling. For example, the presented results have shown that, although the global force capacity of the system was hardly influenced by the various modeling alternatives, the shear demand on the individual piers could nevertheless be increased by the double bending. In the investigated cases this influence was still limited due to the fuse-like protection coming from the uplifting of the bearings. However, the amount of transferable moment at the seat level depends on the particular geometry and the vertical support force. Therefore, in other cases it cannot be ruled out that a more profound increase of the shear demand might be possible. Disregarding such an effect would be unconservative and could cause a brittle shear failure of the pier. It should further be noted that in the pushover analyses discussed above only translational forces representing the translational mass inertia were considered. As outlined in Section 3.4.1, an additional inertia moment can occur if the superstructure experiences significant rotational motions.

Finally, it should be noted that due to the diversity of possible bridge configurations the relevance of the previously presented phenomena can only be evaluated on an individual basis. The general discussions and conclusions presented above may aid for this task. Especially with respect to the global demand estimation, the torsional behavior of the superstructure does not necessarily need to have a dominant effect. However, at least when checking the local demand of the members, the influence of potential double bending and subsequently increased shear demand might have to be considered.

3.5 Soil-Structure Interaction

Significant research progress has been achieved in past decades with respect to the understanding of the seismic behavior of reinforced concrete (RC) members and structures. To some extent this has been motivated by the fact that many types of damage – especially the more severe life threatening ones – often occur in the concrete structure. At the same time, considerable research efforts have been invested into the understanding of soil under seismic loading, e.g. in the context of soil liquefaction. However, in many cases these two branches of research often tend to work rather separately from each other, as researchers typically are *either* experts in the field of reinforced concrete *or* experts in geotechnical engineering. In particular in earthquake engineering this separate approach may not always be justified as the RC structure can interact strongly with the soil during severe seismic excitation.

In new design situations this interaction can be limited to some extent. Current capacity design philosophy suggests that the soil-foundation system should rather be capacity protected, ensuring that it does not develop any inelastic deformations. As a consequence, only limited elastic soil deformations would be expected. These still influence the seismic behavior, e.g. by increasing the fundamental period of the structure, but it is unlikely that they change the system behavior completely.

In contrast, for an existing bridge where these capacity design principles had not been followed, it cannot be ruled out that the soil also develops inelastic deformations. In this case, the interaction between soil and structure can represent a significant influence on the seismic behavior of the system and in some cases may even be the dominant phenomenon governing the response [Gaz06], [WBL87], [KBD08]. Not allowing for these effects in a mechanical model of the structure might mean not capturing an important aspect of the structural behavior and could give a completely mistaken picture of the seismic response. Unfortunately, the inelastic behavior of an RC structure, as well as the inelastic response of the soil, are already rather complex phenomena each for themselves separately. The development of an adequate model which further includes the interaction between these two aspects can become very complex and demanding.

Especially for practical applications in an engineering company, in the majority of cases it will not be a realistic option to model the soil as an inelastic 3D continuum interacting with an inelastic model of the RC structure (possibly with gapping at the interface between the two subsystems). Aside from the significant effort and the computational power that would be needed, such a solution would also require a large amount of input data which may not always be available. The executing engineer would also have to possess in-depth specialized knowledge in the cyclic inelastic modeling of both reinforced concrete and soil. It appears therefore more realistic to use appropriate engineering models which take the most important effects of the soil into account while still being applicable with a reasonable effort.

In the following subsections, approaches are presented to model the soil-structure interaction (SSI) by means of inelastic springs representing the soil-foundation systems of spread foundations and abutments. The characteristics of the springs are determined using simplified models of the 3D soil continuum without complex finite element analyses but with consideration of nonlinearity and inelasticity. It is conceptually inherent to this approach that it cannot capture all effects with the same level of accuracy and reliability as a more complex analysis. It is therefore important to keep the underlying limitations in mind. Depending on the importance of the effects from SSI it may be recommendable to perform a parameter study varying the soil parameters and the modeling assumptions in order to allow for some of the uncertainties.

In Section 3.5.1 recommendations for the inelastic modeling of spread pier foundations are given. The numerical treatment of the seismic behavior of abutments is discussed in Section 3.5.2. The modeling of pile foundations of bridge piers is beyond the scope of this text. Some guidance on the seismic behavior of pile foundations can be found e.g. in [PSC96].

3.5.1 Spread Pier Foundations

The horizontal loads on bridges from wind or breaking are typically not very high. As a consequence, the base moment demands on cantilever bridge piers coming from these non-seismic loads are rather limited as well. If the local soil conditions allow it, spread foundations are a cost-effective solution to transfer the mainly vertical loads to the soil. As seismic loads in past decades either were not considered at all or were underestimated from today's perspective, these spread foundations were not necessarily designed to provide large base moment capacities. In particular, it is unlikely that they were designed to bear the full pier moment capacity at overstrength properties, as it might be required by modern capacity design principles.

As a consequence, the in-plan dimensions of such spread foundations of existing bridges may not be very large and, especially for wall-type bridge piers, they may be insufficient to transfer the yield moment of the pier to the soil. If this is the case, the pier will not be able to develop a plastic hinge at its base and a potential plastic mechanism will rather develop in the soil-foundation system instead. But even if the foundation is generally able to transfer the yield moment of the pier, considerable end-rotations of the footing can occur, especially if uplifting or soil yielding occur due to the limited dimensions of the foundation. For a realistic representation of the seismic bridge behavior these phenomena should be taken into account as they can influence the deformation demand on the piers significantly.

In the following subsections an engineering model will be presented which takes into account important effects of the nonlinear behavior of the soil-foundation system, while still being applicable with reasonable effort in an engineering company. This model is based on the assumption of a rigid foundation block on inelastic Winkler springs. First, the general concept of the model will be presented and some discussion and recommendations on the estimation of the characteristic model parameters will be given. After a comparison with experimental results, some guidance will be given how to efficiently introduce the soil-flexibility at spread foundations into a numerical bridge model. Finally, the relevance of the issue for the seismic behavior of existing bridges will be discussed and the influence on the seismic deformation demand of the piers will be investigated.

a) General Spread Foundation Model on Inelastic Winkler Springs

The use of Winkler springs to model the flexibility of soil layers underneath a foundation is a common approach in structural and geotechnical engineering. A possible model for the spread foundation of a cantilever pier on Winkler springs is shown in Fig. 3.31. While in common engineering cases the springs are often assumed as linear elastic, this does not necessarily have to be this way. Furthermore, if uplifting of the foundation occurs, it should be taken into account that the interface between foundation and soil cannot transfer any tension stresses and that a gap will consequently occur at this interface. This phenomenon creates a nonlinear behavior even if the soil is modeled as linear elastic in compression.

The assumption of linear soil behavior in compression is an approximation which may only be justified in a limited deformation range and which also depends on the previous load history. With increasing loading, the stress-settlement relationship will not only depend on the compressive behavior of the soil anymore, but will be influenced more and more by its shear behavior as well. Once the shear capacity of the soil is exceeded, the foundation reaches its vertical bearing capacity. At this point the vertical compression stresses at the soil-foundation interface will not be able to increase significantly anymore. This limitation of the vertical stresses can be interpreted as a form of yielding of the soil and can be modeled correspondingly in a Winkler spring approach.

A more generalized stress-settlement behavior of the Winkler springs supporting the spread foundation is therefore suggested in Fig. 3.32. It is characterized by a bilinear response without post-yield stiffness in compression and zero stress for tensile deformations. If this soil behavior is assumed, a spread foundation can generally be in four different stress states, as shown in Fig. 3.33. For a constant vertical load N_{fb}, only three of these four stress states will actually occur with increasing foundation rotation, as states 2a and 2b are mutual alternatives (see Fig. 3.33). Which one of the two cases occurs,

depends on the ratio between the vertical load N_{fb} and the vertical bearing capacity $N_u = \sigma_y L_f B_f$. For $N_{fb} < N_u/2$ only stress state 2a (elastic soil response with uplifting) occurs and state 2b (inelastic soil response without uplifting) does not exist, while for $N_{fb} > N_u/2$ the opposite situation results. For small rotations, the foundation will always start in stress state 1 (elastic without uplifting), while for very high rotations the system will always end up in stress state 3 (inelastic with uplifting), which is generally the last stage of the rotational soil-foundation response at constant vertical load N_{fb}.
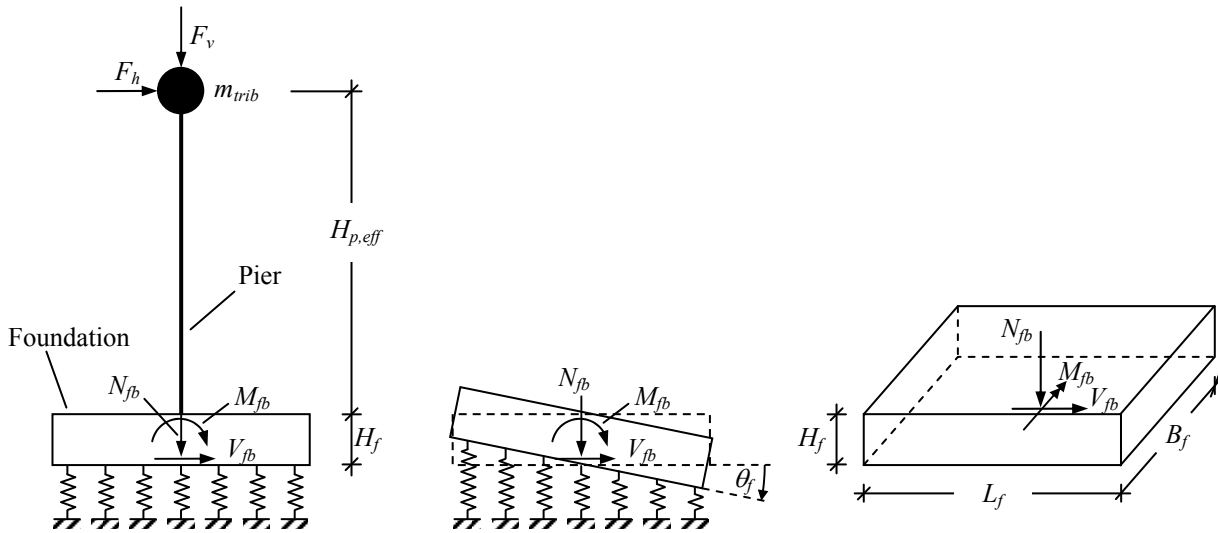
Fig. 3.31: Definition of actions, deformations and geometry of a spread foundation on Winkler springs
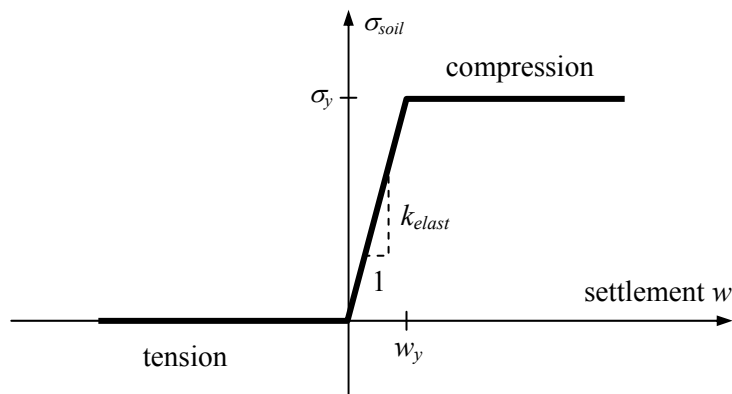
Fig. 3.32: Inelastic monotonic stress-settlement relationship for Winkler springs including uplifting in tension
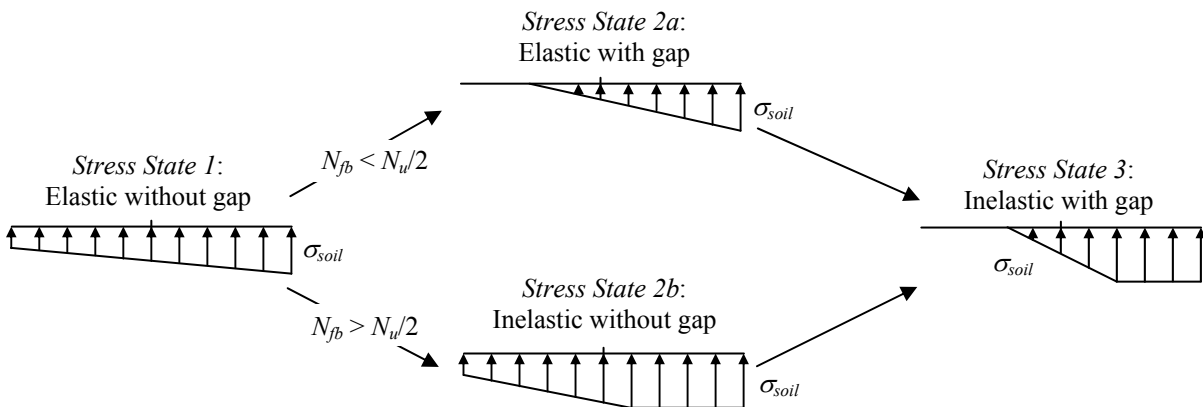
Fig. 3.33: Potential stress states of soil at increasing foundation rotation for constant vertical load

Stress State 1: Elastic soil response without gap

σ_{soil}

$$M_{fb} = \frac{1}{12} k_{elast} B_f L_f^3 \cdot \tan\theta_f$$

$N_{fb} < \frac{1}{2} N_u$ $N_{fb} > \frac{1}{2} N_u$

$$N_{fb} = \frac{1}{2} N_u$$

Limit 1a: Uplifting

$$\tan\theta_f \geq \frac{2N_{fb}}{k_{elast} B_f L_f^2} = \tan\theta_{f,1a}$$

Limit 1b: Soil yielding

$$\tan\theta_f \geq \frac{2\left(N_u - N_{fb}\right)}{k_{elast} B_f L_f^2} = \tan\theta_{f,1b}$$

Stress State 2a: Elastic soil response with gap

σ_{soil}

$$M_{fb} = N_{fb} \cdot \left[\frac{1}{2} L_f - \frac{1}{3} \sqrt{\frac{2N_{fb}}{k_{elast} B_f \cdot \tan\theta_f}} \right]$$

Limit 2a: Soil yielding

$$\tan\theta_f \geq \frac{N_u^2}{2k_{elast} B_f L_f^2 \cdot N_{fb}} = \tan\theta_{f,2a}$$

Stress State 2b: Inelastic soil response without gap

σ_{soil}

$$M_{fb} = \left(N_u - N_{fb}\right) \cdot \left(\frac{L_f}{2} - \frac{1}{3} \sqrt{\frac{2\left(N_u - N_{fb}\right)}{k_{elast} B_f \cdot \tan\theta_f}} \right)$$

Limit 2b: Uplifting

$$\tan\theta_f \geq \frac{N_u^2}{2k_{elast} B_f L_f^2 \cdot \left(N_u - N_{fb}\right)} = \tan\theta_{f,2b}$$

Stress State 3: Inelastic soil response with gap

σ_{soil}

$$M_{fb} = \frac{1}{2} N_{fb} L_f \left(1 - \frac{N_{fb}}{N_u} \right) - \frac{N_u^3}{24 L_f \left(k_{elast} B_f L_f \cdot \tan\theta_f \right)^2}$$

Limit 3: Full plastic response

$$M_{fb,3} = M_{fb,u} = \lim_{\theta_f \to \frac{\pi}{2}} M_{fb} = \frac{1}{2} N_{fb} L_f \left(1 - \frac{N_{fb}}{N_u} \right)$$

Fig. 3.34: Overview of M_{fb}-θ_f-relationship at different stress states

For each of the stress states shown in Fig. 3.33, an analytical moment-rotation relationship can be found corresponding to a given constant vertical load. Together with analytical equations for the limits between the various stress states, a continuous function $M_{fb}(\theta_f, N_{fb})$ for the moment-rotation relationship throughout the entire range of rotations can be developed. The equations describing the inelastic behavior of the soil-foundation system, based on the bilinear Winkler spring model with uplifting, are deduced in Annex A1. In Fig. 3.34 a summary of the resulting relationships is given, arranged by the sequential development of the various stress states at different rotation levels. Equivalent equations have also been presented in normalized form by Allotey and El Naggar [AE03].
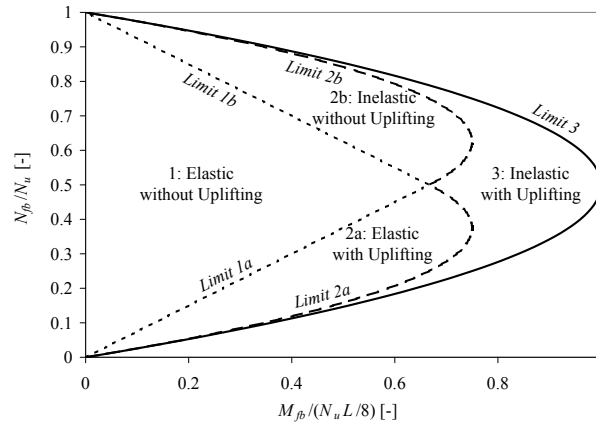
Fig. 3.35: Stress states and corresponding limit M_{fb}-N_{fb}-interaction curves for nonlinear Winkler spring model

The limits between the various stress states can also be interpreted as M_{fb}-N_{fb}-interaction curves[9] as shown in Fig. 3.35. The areas between the individual limiting interaction curves then represent the M_{fb}-N_{fb} combinations which fall into the different stress states. From the curves in Fig. 3.35, it can be seen that the vertical load level $N_{fb} = N_u/2$ has a particular significance with respect to the behavior of the nonlinear Winkler spring model. On one hand, as already mentioned above, it defines whether stress state 1 is followed by state 2a or 2b, depending on the question whether $N_{fb} < N_u/2$ or $N_{fb} > N_u/2$. On the other hand, at $N_{fb} = N_u/2$ the limiting curves for stress states 1 and 3 have their balance points, i.e. at this vertical load level the highest possible moment capacities of the two stress states are reached as resulting from the Winkler spring model. As N_u represents the bearing capacity of the foundation under centric vertical load, it can be expected that in existing pier foundations the present vertical load N_{fb} is considerably lower than N_u – at least by a certain margin defined by the safety factor. In the majority of cases it may therefore be expected that $N_{fb} < N_u/2$, with the corresponding consequences mentioned above.
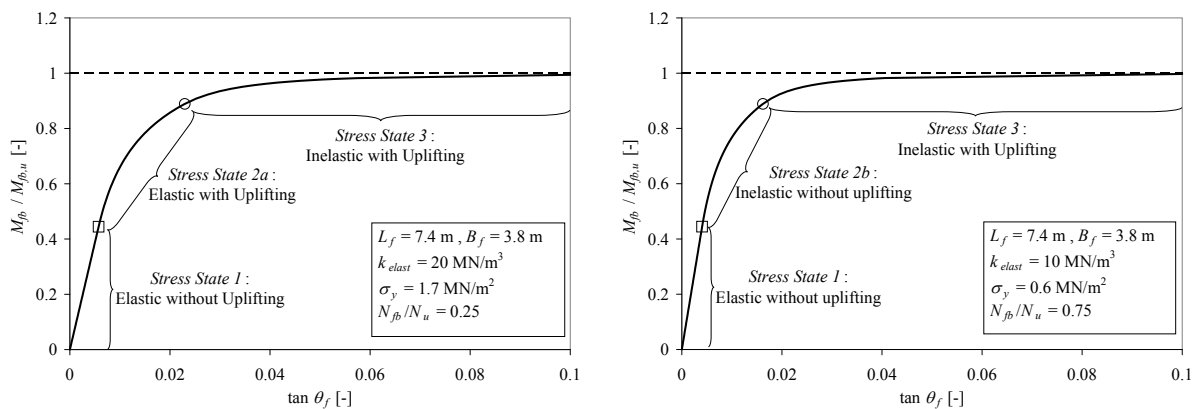
Fig. 3.36: Example M_{fb}-θ_f-relationships for two different parameter sets
left: Uplifting before soil yielding, right: Soil yielding before uplifting

---

[9]   The equations for the limit M_{fb}-N_{fb}-interaction curves are given in Annex A1.

In Fig. 3.36 the resulting numerical M_{fb}-θ_f-relationships for two sets of example parameters are shown. On the left side, a case with $N_{fb} < N_u/2$ is shown which features stress state 2a, i.e. elastic soil behavior with uplifting, while on the right side of Fig. 3.36 the alternative case with $N_{fb} < N_u/2$ is shown in which the soil first yields without uplifting (stress state 2b). It can be seen that in both cases the moment-rotation behavior is linear only in the first stress state, corresponding to elastic soil without uplifting of the foundation. As soon as the system enters into either one of the stress states 2a or 2b, the global foundation response becomes nonlinear. This shows that even if no yielding of the soil is taken into account, a linear rotational spring can only cover the deformation range corresponding to stress state 1. Potential uplifting that may not be untypical for common foundation sizes can result in nonlinear behavior similar to a global yielding. In particular, it results in an upper limit of the moment capacity of the foundation, as the value of $N_{fb}L_f/2$ cannot be exceeded even for infinitely strong soil (in compression). If the yield stress σ_y of the soil is taken into account additionally, then the maximum attainable moment is further reduced to $M_{fb,u} = N_{fb}L_f/2 \cdot (1-N_{fb}/N_u)$ (see Fig. 3.34). This value of $M_{fb,u}$ is used in Fig. 3.36 to normalize the moment response of the soil-foundation system.

As soil-structure interaction at the foundations generally provides additional flexibility, even linear elastic soil behavior makes the system softer, resulting in higher fundamental periods with corresponding influence on seismic forces and displacement demands. If the nonlinear behavior described above is taken into account, the global yielding behavior of the soil-foundation system may not only result in additional flexibility, but can in some cases even change the plastic mechanisms developing in the bridge structure. The nonlinear moment-rotation behavior of the footing, according to Fig. 3.36, can be interpreted as a potential plastic hinge at the foundation base. Consequently, two potential plastic hinges exist in the base region of the pier-foundation system, one at the pier base and one at the foundation base (see Fig. 3.37).
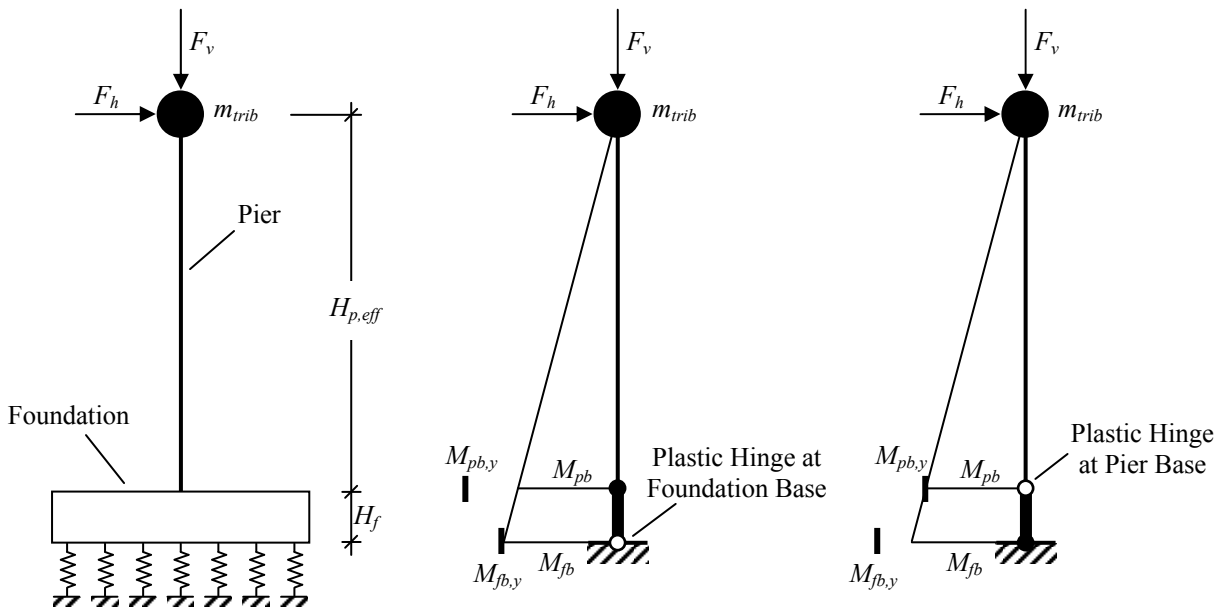
Fig. 3.37: SDOF cantilever pier model with two potential plastic hinge positions

If the moment M_{fb} at the foundation base reaches the corresponding yield capacity $M_{fb,y}$ before the moment at the pier base M_{fb} reaches its yield capacity $M_{fb,y}$, then the plastic hinge will first develop in the soil underneath the foundation (see Fig. 3.37 center). In the opposite case, the plastic hinge will develop at the pier base first (Fig. 3.37 right). In normal cases, the first plastic hinge will result in a capacity protection of the second hinge in the other member, so that typically only one of the two hinges will be activated. Only if the ratios $M_{pb}/M_{pb,y}$ and $M_{fb}/M_{fb,y}$ are rather close together and the moment-rotation relationship of the firstly activated plastic hinge has a significant post-yield stiffness, it may occur that the increase of moment demand in the post-yield range of the first hinge is sufficient to also activate the second hinge at larger deformations.

If the ratios $M_{pb}/M_{pb,y}$ and $M_{fb}/M_{fb,y}$ have similar magnitudes, the question which plastic hinge is activated first may to some extend depend on the definition of nominal yield capacities, i.e. on the chosen bilinearization of the curved moment-rotation relationships of both plastic hinges (see Fig. 3.48 in Subsection *d*) . In such cases it may also be useful to compare the maximum moment capacities. If, for example, even at the maximum moment capacity of the foundation, $M_{fb,u}$, the pier base does not reach its yield moment $M_{pb,y}$, then it is obvious that the plastic hinge at the pier base will not be activated at any deformation level and all inelastic deformations will be concentrated in the soil-foundation hinge. As a consequence, even before a dynamic analysis in some cases it may be possible to conclude that the deformation demand on the pier will not enter into the inelastic range if the pier is thus capacity protected by a plastic soil-foundation hinge.

If the maximum moment capacity at the foundation base is estimated according to Fig. 3.34 as $M_{fb,u} = N_{fb} L_f/2 \cdot (1 - N_{fb}/N_u)$, then some uncertainty is included related to the estimation of the soil yield stress σ_y and the corresponding ultimate vertical bearing capacity $N_u = \sigma_y L_f B_f$ (see Subsection *c* and Fig. 3.41 through Fig. 3.43). Assuming infinite soil strength, an upper limit max $M_{fb,u}$ can be estimated according to equation (3.11) which corresponds to the maximum possible eccentricity of the vertical load. This upper limit can be calculated very easily and quickly and it represents a reliable upper boundary for the moment capacity of the foundation that cannot be exceeded by any means.

$$\max M_{fb,u} = \frac{1}{2} N_u L_f \tag{3.11}$$

If this upper boundary max $M_{fb,u}$ is lower than the moment at the foundation base corresponding to yielding at the pier base, then it can be said with certainty that a cantilever RC pier cannot experience inelastic deformation demands (provided that the axial load is known with sufficient reliability). If max $M_{fb,u}$ at the foundation base would be sufficient to activate the plastic hinge at the pier base, then the maximum foundation moment $M_{fb,u}$ or a corresponding yield moment $M_{fb,y}$ are required to decide whether the yield moment of the pier can be reached. This decision can depend on the yield stress of the soil which is modeled for the inelastic Winkler springs. In this case, careful consideration of this issue may be required, and a variation of the relevant parameters may be justified in order to study their influence on the behavior.

b) Determination of Elastic Winkler Spring Stiffness

Generally, it appears reasonable to determine the elastic stiffness k_{elast} of the Winkler springs by means of a settlement calculation using standard geotechnical principles. This can, e.g., be done by modeling the soil as an infinite elastic half-space, if necessary taking layers of different soil types into account. However, even such an established and rather simple model is not quite as straightforward as it might appear. The spring stiffness k_{elast} should represent the ratio between the applied vertical soil stress and the resulting settlement. Using the model of the elastic half-space, this ratio will depend on the applied stress distribution underneath the footing (e.g. constant or triangular) and on the position of the point for which the settlement is computed.

This problem is related to a conceptual discrepancy between the Winkler spring model and the real soil-foundation interaction, only being approximated by the elastic half-space analysis. While the Winkler spring representation implicitly models an independent soil response for every point of the footing, in reality the soil stresses and deformations at different points are interrelated. One of the consequences is that a rigid foundation block on Winkler springs loaded with a centric vertical force results in evenly distributed constant soil stresses underneath the foundation. The more realistic model using the elastic half-space to represent the soil would rather predict an uneven stress distribution for a rigid foundation block with the same loading. In the latter model, stresses increase towards the foundation edges, and in particular they develop a significant concentration under the footing corners. In reality some of these stress concentrations will be averaged out due to local soil yielding, but nevertheless the stress distribution will remain uneven. This phenomenon, which also influences the foundation stiffness, cannot be captured accurately by the Winkler spring model. It should therefore be kept in mind that, even in the elastic range, the soil representation by Winkler springs can only be

considered as an approximation that is supposed to capture the most important effects of the general behavior, but it will not be able to give a fully accurate representation of the real soil response.
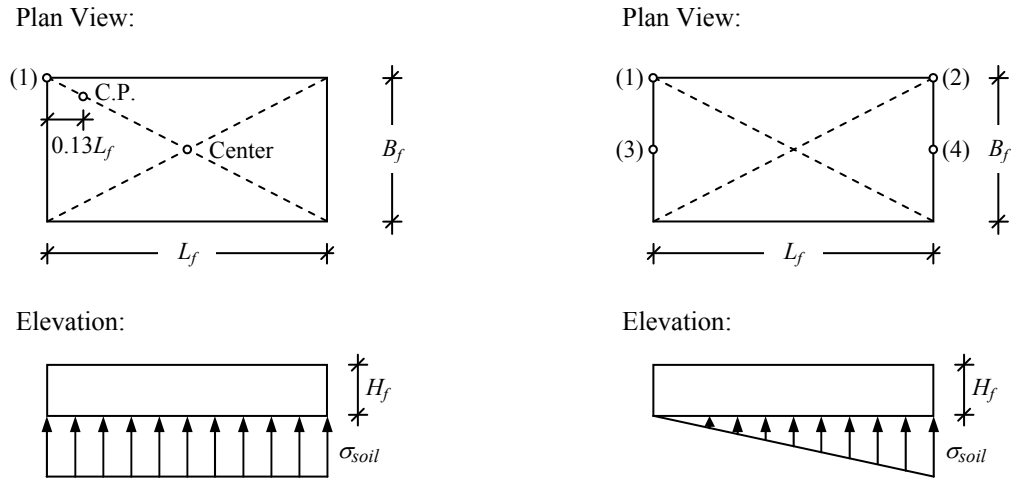
Fig. 3.38: Stress distributions and definition of points for settlement calculation
left: Constant stress distribution, right: Triangular stress distribution

The elastic Winkler spring stiffness can be determined by settlement calculations for a variety of stress distributions, e.g. according to [Lan+07]. In Fig. 3.38 two simple cases are shown representing a constant stress distribution (left) and a triangular stress distribution (right). In either case, the settlement w can be calculated for different points underneath the footing. From the settlement in each point an elastic Winkler spring stiffness can be estimated according to equation (3.12) and it is rather obvious that these values will differ from each other, even for the case of a constant stress distribution as shown on the left side of Fig. 3.38. If the characteristic point (C.P. in Fig. 3.38 left) is used for the settlement calculation, then the spring stiffness k_{elast} will correspond to a rigid foundation under centric vertical load. Using the corner point (1) or the center point (see Fig. 3.38 left), upper and lower boundary values for k_{elast} can be estimated for the same centric vertical load case.

$$k_{elast} = \frac{\sigma_{soil}}{w} \tag{3.12}$$

with σ_{soil}: soil pressure
            w: settlement at certain point due to σ_{soil}

These three values corresponding to different points are compared in Tab. 3.4 based on an example configuration. For this purpose, in-plan dimensions for the soil-pressure distribution of $L_f = 7.4$ m and $B_f = 3.8$ m have been used and the settlements in the various points were computed based on the solution for the elastic half-space according to [Lan+07]. The thickness of the elastic compressible soil layer was chosen to be $3B_f$ and within the entire layer a homogenous isotropic soil with constant stiffness characteristics was assumed. The Winkler spring stiffnesses given in Tab. 3.4 are normalized by the uniaxial confined stiffness modulus M_E of the soil layer which is related to its Young's Modulus E_{soil} and the Poisson ratio ν_{soil} via equation (3.13).

$$M_E = \frac{E_{soil}\left(1 - \nu_{soil}\right)}{\left(1 + \nu_{soil}\right)\left(1 - 2\nu_{soil}\right)} \tag{3.13}$$

Alternative estimations of the Winkler spring stiffness k_{elast} were also computed based on the triangular soil-pressure distribution shown on the right side of Fig. 3.38. In this case, settlements can be calculated for two points at opposite sides of the foundation, e.g. points (1) and (2) at the corners or points (3) and (4) at the center of the opposing footing edges. Based on the differential settlements on

the two sides of the foundation, a corresponding average rotation θ_f can be calculated according to equation (3.14). At the same time, the moment M_{fb} at the foundation base corresponding to the triangular soil-pressure distribution can be computed according to equation (3.15). Using these two values, an elastic Winkler spring stiffness k_{elast} can be determined according to equation (3.16). This solution corresponds to the Winkler spring model of Fig. 3.34 and results in the same relationship between average rotation θ_f and base moment M_{fb}. By combination of equations (3.14), (3.15), and (3.16), the expression for k_{elast} can be reduced to the one given in equation (3.17). The resulting estimates for k_{elast} are also given in Tab. 3.4 for the two pairs of points (1) - (2) and (3) - (4) as defined in Fig. 3.38.

$$\tan\theta_f = \frac{w_4 - w_3}{L_f} \tag{3.14}$$

$$M_{fb} = \frac{1}{12}\sigma_{soil} \cdot B_f L_f^2 \tag{3.15}$$

$$k_{elast} = \frac{12 M_{fb}}{B_f L_f^3 \cdot \tan\theta_f} \tag{3.16}$$

$\Rightarrow \qquad$ $$k_{elast} = \frac{\sigma_{soil}}{w_4 - w_3} \tag{3.17}$$

	Constant Stress Distribution			Triangular Stress Distribution	
	Corner Point (1)	Characteristic Point C.P.	Center Point	Rotation between corner points (1) - (2)	Rotation between edge center points (3) - (4)
k_{elast}/M_E [1/m]	0.54	0.30	0.27	1.07	0.74

Tab. 3.4: Comparison of various estimations of k_{elast} corresponding to different stress distributions and points for in-plan foundation dimensions of L_f = 7.4 m and B_f = 3.8 m

Comparing the results in Tab. 3.4, it can be seen that, depending on the chosen approach, quite a bandwidth of estimations for k_{elast} can be computed. Further approaches and thus other values are conceivable. The underlying uncertainty in the determination of k_{elast} is partly a result of the fact that the Winkler model with a constant spring stiffness will not be able to describe the settlement and rotation behavior of a foundation on an elastic halfspace accurately at various deformation levels – even in the linear elastic range without uplifting. This is further related to the fact that the Winkler model cannot capture the stress distribution underneath a stiff foundation as it would result from an analysis of the elastic half-space. While, e.g., a rigid foundation on the Winkler model will always result in a linear soil-pressure distribution in the linear elastic range, the same footing on an elastic half-space will result in stress concentrations towards its edges and corners.

As a consequence, none of the five approaches for the estimation of k_{elast} discussed above can be considered as "exact" and the variability can be interpreted as a sign of the uncertainties involved with the Winkler spring model. To allow for these uncertainties it may therefore be necessary to perform a set of analyses varying the parameters of the soil-foundation system if the soil-structure interaction affects the results significantly and if no conservative estimation can be found beforehand. If the focus of the analysis is on the deformation demand of the piers, in the majority of cases (but not always [Gaz06]) a stiffer soil-foundation system will rather yield conservative deformation demands on the piers. In this case, a rather high estimation of k_{elast} will be preferable and the approach using a triangular stress distribution according to Fig. 3.38 right, together with equation (3.17), may give an

estimation in the upper range of reasonable values. To avoid unnecessary over-conservatism, it appears more adequate to base the estimation of footing rotation θ_f on the differential settlement of points (3) and (4) in Fig. 3.38, instead of points (1) and (2). If a lower estimate of k_{elast} is required, it is recommended to use the constant stress distribution as shown on the left side of Fig. 3.38 and calculate the settlement in the characteristic point (C.P.) as this gives the same value as for a rigid footing on the elastic half-space. The corresponding estimation of k_{elast} follows from equation (3.12).

It should be noted that, independent of the uncertainties already discussed above, any estimate of k_{elast} can only be as accurate as the input parameters describing the soil behavior. Here, this is primarily the Young's modulus E_{soil} or the uniaxial confined stiffness modulus M_E of the soil. In this context it needs to be mentioned that, despite the nonlinear relationship between the base moment M_{fb} and the rotation $\tan \theta_f$ of the footing, in all four of the potential stress states (see Fig. 3.33 and Fig. 3.34) an antiproportional relationship exists between the rotation $\tan \theta_f$ and the stiffness k_{elast} of the Winkler springs. As a consequence, for a given moment M_{fb}, the rotational stiffness (secant or tangent) of the soil-foundation system is proportional to the Winkler spring stiffness k_{elast} – and this is the case in all stress states, i.e. also in the nonlinear range of the footing response. As the value of k_{elast} itself is proportional to the assumed value of the confined stiffness modulus M_E, the rotational stiffness of the soil-foundation system is also proportional to M_E.

If the primary focus of an analysis is on the seismic demand of cantilever bridge piers, an underestimation of the rotational stiffness of the soil-foundation system in many cases will not be conservative. As the value of the uniaxial confined stiffness modulus M_E strongly depends on the stress level and on the previous load-history, care should be taken with its determination. In particular, it should be kept in mind that the compressive first loading stiffness of the soil typically is considerably lower than the corresponding unloading and reloading stiffness. For the cyclic excitation during an earthquake it may be more appropriate to use the higher unloading/reloading value of M_E, which is also more likely to result in conservative deformation demands on the bridge piers. However, the appropriate choice of M_E should be determined on an individual basis with a certain level of caution. If a conservative estimation cannot be decided on right from the beginning, it is recommended to vary the stiffness modulus M_E in the possible range of values in order to account for the inevitable uncertainties. Aside from the stiffness of the soil material, it is also necessary to know the thickness of the relevant soil layers contributing to the settlements with sufficient accuracy.

c) Determination of the Soil Yield Stress

The elastic stiffness of the soil in the preceding subsection has been determined based on its compressive behavior. At high vertical loads the bearing capacity of the soil will be reached which represents a limit to the maximum vertical stresses that can be carried by the soil. In the following, the bearing capacity of the soil will be used to define the yield stress of the Winkler springs. Generally, the loss of bearing capacity is the result of a shear failure in the soil continuum which results in a sliding plane as shown in Fig. 3.39. A simplified solution to the problem has been developed by Terzaghi and is documented in [Lan+07].
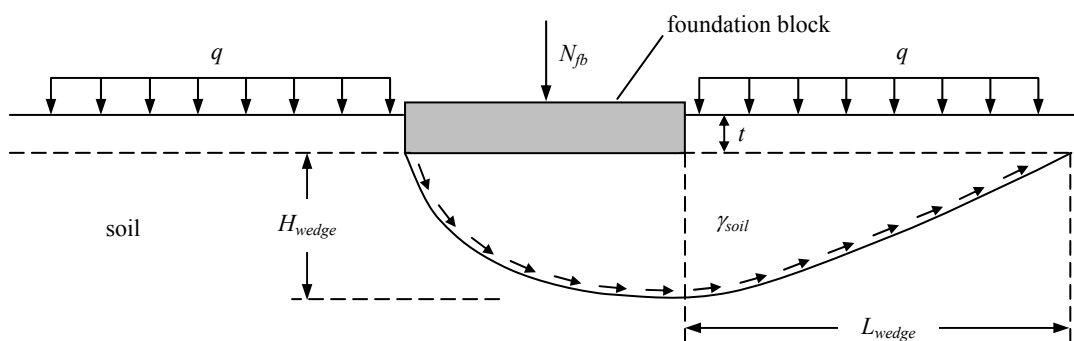
Fig. 3.39: Failure mechanism of a rigid foundation block on a soil half-space under centric vertical load

Based on this approach, the stress σ_y at loss of bearing capacity can be estimated according to equation (3.18) for a rectangular foundation under vertical load N_{fb}, horizontal load V_{fb}, and Moment M_{fb}. In this equation the eccentricity e_N of the vertical load N_{fb} due to the moment M_{fb} is taken into account by reducing the length L_f of the foundation to a reduced value $L_{f,red}$ as defined by equation (3.19). This reduction is based on an idealized constant stress distribution as shown in Fig. 3.40 and it treats the foundation with eccentric vertical load as a corresponding smaller footing with centric vertical load.

Fig. 3.40: Assumed soil pressure distribution for calculation of bearing capacity in case of eccentric vertical load

$$\sigma_y = \frac{N_u}{L_{f,red}B_f} = \frac{1}{2}L_{f,red}\gamma_{soil}N_\gamma s_\gamma i_\gamma + (\gamma_{soil}t + q)N_q s_q i_q + cN_c s_c i_c \tag{3.18}$$

with
$$N_\gamma \approx 1.8(N_q - 1)\tan\varphi \quad ; \quad N_q = e^{\pi\tan\varphi}\tan^2\left(\frac{1}{2}\varphi + \frac{\pi}{4}\right) \quad ; \quad N_c = \frac{N_q - 1}{\tan\varphi}$$

$$s_\gamma = 1 - 0.4\frac{L_{f,red}}{B_f} \quad ; \quad s_q = 1 + \frac{L_{f,red}}{B_f}\tan\varphi \quad ; \quad s_c = 1 + \frac{L_{f,red}}{B_f}\cdot\frac{N_q}{N_c}$$

$$i_\gamma = \left[1 - \frac{0.7V_{fb}}{N_{fb} + \dfrac{B_f L_{f,red}c}{\tan\varphi}}\right]^5 \quad ; \quad i_q = \left[1 - \frac{0.5V_{fb}}{N_{fb} + \dfrac{B_f L_{f,red}c}{\tan\varphi}}\right]^5 \quad ; \quad i_c = i_q - \frac{1 - i_q}{N_q - 1}$$

φ: Angle of friction of the soil in [rad]
c: cohesion of the soil
γ_{soil}:   specific weight of the soil

$$L_{f,red} = L_f - 2e_N = L_f - \frac{2M_{fb}}{N_{fb}} \tag{3.19}$$

The dimensions of the soil failure wedge, L_{wedge} and H_{wedge}, corresponding to the model by Terzaghi, as shown in Fig. 3.39, can be estimated according to [Lan+07] by means of equations (3.20) and (3.21).

$$L_{wedge} = L_{f,red}\tan\left(\frac{1}{2}\varphi + \frac{\pi}{4}\right)e^{\frac{\pi}{2}\tan\varphi} \tag{3.20}$$

$$H_{wedge} = L_{f,red}\frac{\cos\varphi}{2\cos\left(\frac{1}{2}\varphi + \frac{\pi}{4}\right)}e^{\left(\frac{1}{2}\varphi + \frac{\pi}{4}\right)\tan\varphi} \tag{3.21}$$

For a load case including gravity and seismic loads, normally the base moment M_{fb} and the shear force V_{fb} are not independent of each other. For a cantilever pier without influence of $P\text{-}\Delta$-effects, the relationship between M_{fb} and V_{fb} is linear and can be described by the rather simple expression given in equation (3.22) (with $H_{p,eff}$ and H_f according to Fig. 3.37). Using equation (3.19), V_{fb} can be expressed for cantilever piers also as a function of the reduced foundation length $L_{f,red}$, as given in equation (3.23).

$$V_{fb} = \frac{M_{fb}}{H_{p,eff} + H_f} \tag{3.22}$$

$$V_{fb} = \frac{L_f - L_{f,red}}{2\left(H_{p,eff} + H_f\right)} N_{fb} \tag{3.23}$$

Based on this, all parameters in equation (3.18) are either known or can be formulated as functions of $L_{f,red}$. Rewriting equation (3.18), it is thus possible to express the vertical bearing capacity N_u of the soil as given in equation (3.24) which only depends on the reduced foundation length $L_{f,red}$ as an unknown parameter. By iteration the nonlinear equation (3.24) can be solved to calculate the minimum possible value of $L_{f,red}$ for any given vertical load and by means of equation (3.25) the moment capacity $M_{fb,u}$ corresponding to this vertical load can be computed.

$$N_u = \left[\frac{1}{2}L_{f,red}\gamma_{soil}N_\gamma s_\gamma i_\gamma + \left(\gamma_{soil}t + q\right)N_q s_q i_q + cN_c s_c i_c\right] L_{f,red} B_f \tag{3.24}$$

$$M_{fb,u} = \frac{1}{2}N_u\left(L_f - L_{f,red}\right) \tag{3.25}$$

The principles outlined above can be used to compute $M_{fb,u}$-N_u interaction curves which give the moment capacity $M_{fb,u}$ at a given vertical load N_{fb} equal to N_u. In Fig. 3.41, two sets of $M_{fb,u}$ interaction curves are shown for the geometric dimensions of spread foundations representing two sample bridges (see Subsection f and Section 2.2.2). In both cases, the capacities were calculated for three different angles of friction φ of the soil, while the cohesion c was assumed to be zero. It can be seen that the angle of friction obviously has a very large influence on the resulting capacities and even rather small variations of φ can change the resulting bearing moment $M_{fb,u}$ at the given vertical load considerably. A possibly accurate knowledge of the soil characteristics is therefore important to limit the uncertainties with respect to the determination of the soil-foundation capacity.
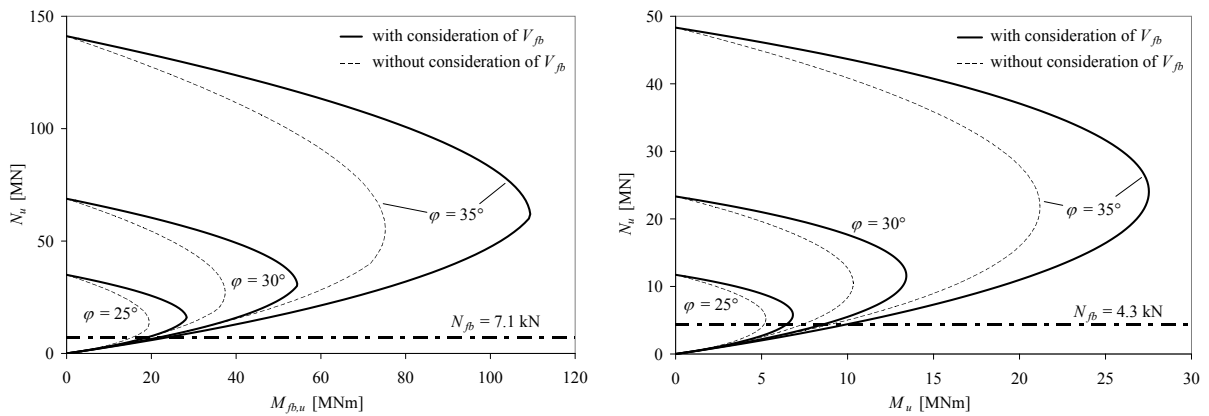

Fig. 3.41: $M_{fb,u}$-N_u-Interaction curves of two spread foundations for different soil conditions
left: Viadukt Mühle Rickenbach, pier 1, right: Viadukt Untere Weid, pier 3

For every angle of friction the $M_{fb,u}$-N_u interaction curves in Fig. 3.41 are shown once taking the influence of the shear force V_{fb} on the bearing capacity into account and once disregarding it[10]. From the resulting curves it can be seen that, according to the approximate approach by Terzaghi of equation (3.18), the influence of the shear force V_{fb} can be of significance as well. This influence will obviously be higher for rather short piers, as they result in a higher relative shear force demand. Pier 4 of the *Viadukt Untere Weid*, shown on the right side of Fig. 3.41, with an effective height $H_{p,eff}$+H_f of about 20 m (from center of mass to the base of the foundation) has only a limited influence of the shear force on the bearing capacity of the foundation. In contrast, the lower pier 1 of the *Viadukt Mühle Rickenbach*, shown on the left side of Fig. 3.41, has a corresponding effective height $H_{p,eff}$+H_f of about 12 m which results in a more pronounced influence of the shear force on the bearing capacity of the soil.

Using the approach by Terzaghi, according to equation (3.18), it should be kept in mind that the general concept is only approximate and intends to yield conservative results for normal static applications, where an underestimation of the bearing capacity will rather represent an estimation on the safe side. As a consequence, the modification factors i_γ, i_q, and i_c, that account for the influence of a shear force V_{fb}, always reduce the estimated bearing capacity, independent of the direction in which V_{fb} acts. This appears justified if the foundation is loaded only by a combination of N_{fb} and V_{fb} without additional moment M_{fb}. A centric load N_{fb} can lead to a failure of the soil in either direction (see Fig. 3.39) without preference so that an additional shear force can influence the failure direction in the way that causes the lowest bearing capacity corresponding to the direction of V_{fb}.

However, if N_{fb} and M_{fb} act together on the foundation, a preference for a certain direction of failure may already exist for these two loads. In this case, the influence of an additional shear force V_{fb} will depend on its direction, and especially on the question whether the preferred failure direction of the shear force coincides with that resulting from the combination of N_{fb} and M_{fb}. Depending on the direction of V_{fb}, this means that the additional influence of the shear force on the bearing capacity could in some cases either be less negative than predicted by the Terzaghi model, or even beneficial. The simplified approach by Terzaghi, according to equation (3.18), does not allow for such interaction effects that depend on the directions of the combined loads. Instead, it always attributes the same reducing influence on the bearing capacity to the shear force. This simplification is conservative, and therefore sufficient, for conventional static cases, where a lower bearing capacity normally represents the worst case.

In contrast, for the presented case of soil-structure interaction at seismic excitations, an underestimation of the bearing capacity is not necessarily conservative. A lower yield stress σ_y for the Winkler spring model of Fig. 3.34 results in a lower moment capacity of the soil-foundation system for a given vertical load N_{fb}. This can be seen in the interaction curves of Fig. 3.41, where the generally reducing influence of the factors i_γ, i_q, and i_c results in lower values of $M_{fb,u}$ if a shear force V_{fb} is taken into account. As shown in Fig. 3.37, if a plastic mechanism develops, a plastic hinge can only occur either at the pier base or in the soil-foundation system, and it depends on the ratio between the moment capacities of these two which hinge actually develops. Therefore, a reduction of the footing moment capacity rather results in a hinge within the soil, instead of the RC pier. As a consequence, an underprediction of the bearing capacity may result in the assumption that the RC pier is capacity protected by the soil-foundation system, although this might not be warranted by the real behavior.

Therefore, careful consideration should be given to the question whether rather an overestimation or an underestimation of the bearing capacity is likely to yield conservative results in an individual case. It would be unrealistic to assume that a simplified approach as the one by Terzaghi can give an accurate estimation of the real behavior for every case. If the primary focus of the analysis is on the deformation demand of cantilever piers, it is likely that rather an overprediction of the soil bearing capacity gives conservative results. Due to the simplified allowance for the shear force V_{fb} by the modification factors i_γ, i_q, and i_c in the Terzaghi model, which does not take into account any interactions with respect to the direction of V_{fb} (see above), it may therefore be more cautious not to

---

[10] The shear force V_{fb} influences the correction factors i_γ, i_q, and i_c in equation (3.18). For the case without influence of V_{fb}, these factors are set equal to one.

make use of these reduction factors in such cases, but rather compute the bearing capacity ignoring the influence of V_{fb} in the Terzaghi model. This decision should be made on an individual basis to ensure that really a conservative estimation of the real seismic behavior is achieved.

When determining the Winkler spring yield stress σ_y from the computed bearing capacity, it should be considered that every point of each curve shown in Fig. 3.41 is based on a different soil pressure σ_y, so that it will not be possible to define a single value of σ_y for a nonlinear Winkler spring model that would be valid for every loading case. The points in Fig. 3.41 with high values of N_u are related to low eccentricities e_N, and thus to larger reduced foundation lengths $L_{f,red}$. As a consequence, the dimensions of the sliding soil wedge H_{wedge} and L_{wedge} (see Fig. 3.39) are higher which results in high bearing pressures σ_y of the soil. At increasing eccentricities e_N, the vertical load capacity N_u is reduced due to lower values of $L_{f,red}$ and σ_y. It is therefore necessary to make a decision, which value of σ_y should be used as a yield stress in the Winkler model. If the vertical load N_{fb} is known, as will typically be the case for cantilever piers, it appears most reasonable to use the value of σ_y that corresponds to the given load N_{fb} in the $M_{fb,u}$-N_u-interaction curves.

In Fig. 3.42 this approach is being followed and the soil pressure at ultimate moment corresponding to the existing vertical loads N_{fb} is used as yield stress σ_y of the Winkler model. For the same two pier foundations as before, the interaction curves from Fig. 3.41, based on the Terzaghi model for $\varphi = 30°$ (here without the influence from the shear force), are shown in Fig. 3.42. Further, the resulting $M_{fb,u}$-N_u interaction curve from the Winkler spring model are shown, which use the same yield stress as it results from the Terzaghi model at the given vertical load N_{fb}. It can be seen that in both cases the value of N_{fb} lies well below the balance point of highest moment capacity at $N_u/2$. This might be expected because the foundations must have been designed with a certain safety factor against N_u.
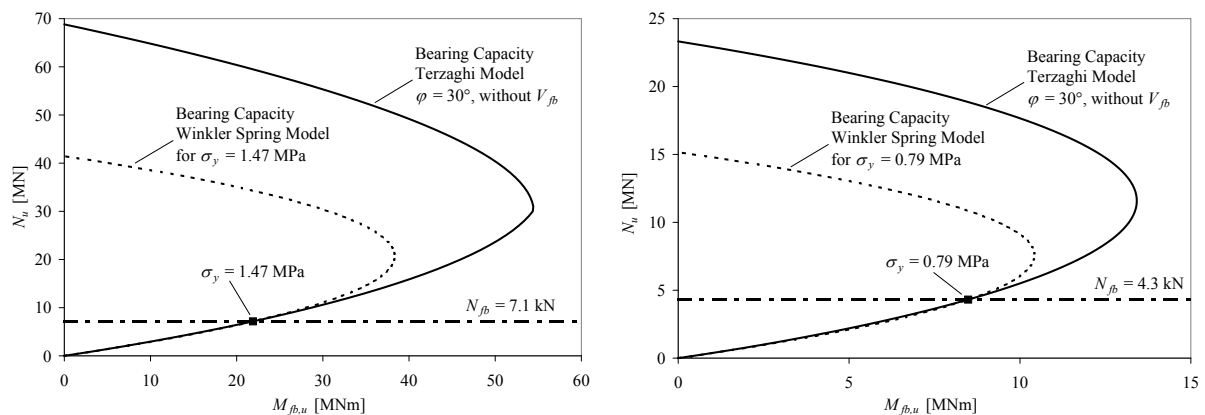
Fig. 3.42: $M_{fb,u}$-N_u-Interaction curves of two spread foundations for Terzaghi and Winkler models
left: Viadukt Mühle Rickenbach, pier 1, right: Viadukt Untere Weid, pier 3

From Fig. 3.42 it can be seen that in the proximity of the point for which the yield stress has been calibrated, i.e. at the existing vertical load N_{fb}, the Winkler spring model approximates the Terzaghi solution well. The same is true in the range of lower vertical loads where the two curves still agree well. At increasing vertical load, and in particular above the balance point ($N_{fb} = N_u/2$), a significant deviation between the two models develops. This is a result of the higher soil pressure at failure when the eccentricity of the vertical load reduces and the value of N_u increases. However, this is only of relevance if the vertical load level is not clearly defined, as e.g. in a multi-column bent with frame action, in which the axial load in the columns varies during horizontal seismic excitation. For cantilever piers, with mainly constant vertical load, the calibration process for the yield stress σ_y of the soil is sufficient as any deviations of the interaction curves at differing vertical load levels are not of relevance in this case.

It has been mentioned above that uncertainties concerning the angle of friction φ of the soil have a significant influence on the capacity of the foundations. However, as can be seen from Fig. 3.41, this influence is particularly pronounced at high vertical loads N_{fb} approaching or exceeding the balance

point. For lower values of N_{fb}, as they are typical for existing structures due to safety factors, the difference between various angles of friction is not quite as strong. Furthermore, in those cases with $N_{fb} < N_u/2$ stress state 2b (*inelastic without uplifting*) does not occur. As a consequence, the first time where the angle of friction φ, which controls the yield stress σ_y, has an influence is in stress state 3 (inelastic with uplifting). Depending on the vertical load N_{fb} and the elastic Winkler spring stiffness k_{elast}, in many cases stress state 3 will not be reached before considerable rotations $\tan \theta_f$. Up to this level, the moment-rotation behavior of a given foundation will be independent of the angle of friction φ of the soil and will rather only depend on the values of N_{fb} and k_{elast}.

In Fig. 3.43 the moment-rotation curves for the two previously discussed pier foundations are shown in the range of rotations up to $\tan \theta_f = 5\%$. For both footings the curves have been computed based on three different angles of friction φ equal to 25°, 30°, and 35° with a cohesion of $c = 0$ in all three cases. It can be seen that, in the investigated range of rotations, only for the case of $\varphi = 25°$ at pier 4 of the *Viadukt Untere Weid* (Fig. 3.43 right) a considerable deviation from the curves corresponding to higher values of φ occurs. This is related to the fact that for $\varphi = 25°$ the vertical load N_{fb} here is getting close to the balance point in Fig. 3.41. For the case of pier 1 at the *Viadukt Mühle Rickenbach*, shown on the left side of Fig. 3.43, the angle of friction φ does not appear to have a significant influence on the moment-rotation behavior, as the corresponding vertical load N_{fb} is well below the balance point for each of the friction angles in Fig. 3.41. It can thus be concluded that, despite the exponential influence of φ on the bearing capacity at high vertical loads with low eccentricities, for realistic cases, the influence on the moment-rotation curves may not be quite as pronounced in the rotation range of interest.
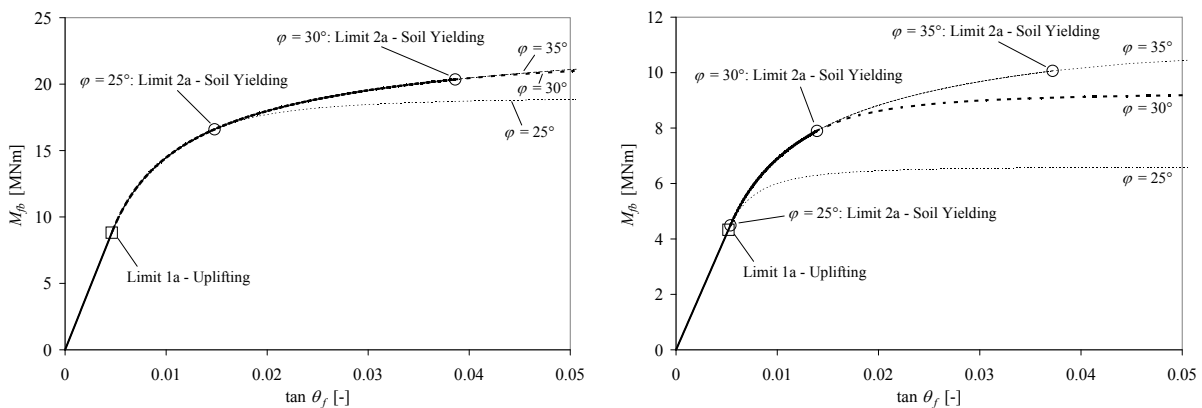
Fig. 3.43: Resulting M_{fb}-θ_f-relationships for different soil properties at sample bridges
left: Viadukt Mühle Rickenbach, pier 1, right: Viadukt Untere Weid, pier 3

This should, of course, be checked carefully on an individual basis and, if required, an appropriate variation of the parameters should be considered. In this context it is noteworthy that, if the primary focus of the analysis is on the seismic demand of the RC piers, a higher moment capacity of the foundations is more critical. This means that a rather high value of φ would result in conservative results for the RC pier. In contrast, a low value of φ with its corresponding low moment capacity of the foundation is more likely to result in a plastic mechanism in the soil thus capacity protecting the RC pier.

d) Energy Dissipation and Experimental Verification

So far, in the preceding subsections only the monotonic backbone of the moment-rotation relationship of the soil-foundation system has been discussed. For a complete description of the seismic behavior the knowledge of the response under cyclic loading and the related damping behavior is required. Generally, two types of energy dissipation can be found at a spread footing: (a) hysteretic material damping as a result of inelastic soil response and (b) radiation damping due to waves transporting energy away into the (theoretically infinite) 3D soil continuum.

The relative relevance of the two different types of energy dissipation depends on a variety of parameters. At first, it is frequency dependent, as the hysteretic damping occurs already under quasi-static loading, while radiation damping develops only under dynamic excitation. Furthermore, a dependency on the amplitudes of the deformations exists because significant hysteretic energy dissipation develops only under inelastic response of the soil. While purely compressive loading of over-consolidated soil causes a rather elastic response, a more pronounced hysteretic behavior develops once significant shear deformations occur at increased loading. The amount of radiation damping can also strongly depend on the arrangement of layers within the soil. If the soil layer carrying the spread footing is located on top of another layer with a significantly higher stiffness, the radiation damping can be reduced considerably. In particular, if the frequency of excitation is lower than the fundamental frequency of the top layer, hardly any radiation damping will occur because the spreading of the waves into the soil continuum is essentially inhibited [SK97], [Som85].

Radiation damping at spread footings has been an issue of research in the context of machine foundations for a long time. As a consequence, a variety of analytical and approximate solutions exist for common cases, typically assuming linear elastic behavior of the soil [SK97]. Generally, these approaches also allow the introduction of additional material damping, either in the form of viscous damping, which results in frequency dependent energy dissipation, or as rate independent hysteretic dissipation which is being achieved by means of a frequency dependent damping coefficient. However, if an inelastic time history analysis is performed, it may be more straightforward, to model any hysteretic energy dissipation directly by means of a cyclic-inelastic material law for the soil.

Somaini [Som85], [WS86] developed an equivalent substitute foundation model consisting of masses, linear elastic springs, and viscous dampers in order to represent the dynamic stiffness of the soil, including the influence of radiation damping. This substitute visco-elastic soil-foundation system was also incorporated into the model of an entire bridge in order to study the influence of multi-support excitation from travelling waves on the seismic behavior of the bridge structure. It should be noted that the chosen approach to determine the dynamic characteristics of the substitute foundation model assumes a perfect contact between the spread footing and the soil. At larger foundation rotations this assumption may not be fulfilled anymore due to partial uplifting of the footing. Further details on this substitute foundation model and the method to determine its dynamic characteristics can be found in [Som85] and [WS86].

Determining the hysteretic behavior of the soil-foundation system from theoretical considerations is a difficult task and may be subjected to considerable uncertainties. State-of-the-art inelastic finite element analysis using a 3-dimensional soil continuum with adequate models for the inelastic behavior of the soil may give some indications of a realistic behavior, but it will not be an appropriate approach for practical applications of bridge assessment in an engineering office.

To study the cyclic response of spread foundations on sand experimentally, the European Union funded a series of two tests in the framework of the TRISEE research project [Neg+00]. In these experiments a spread footing with in-plan dimensions of 1 m by 1 m was tested in a caisson filled with sand, as shown in Fig. 3.44. In each test, the foundation was first loaded by a vertical force F_v which from then on was kept constant. In the following, three phases of horizontal loading were conducted at increasing amplitude levels. The horizontal force F_h was applied at a height of 0.9 m above the base of the foundation creating a corresponding base moment of $M_{fb} = F_h \cdot 0{,}9$ m.

In both tests the same type of saturated Ticino sand was used with the primary difference between the two experiments being the relative density D_r of the soil. While for one test a low density (LD) with a value of $D_r = 45\%$ was chosen, in the second experiment a high density (HD) of $D_r = 85\%$ was used. These two cases were considered to represent upper and lower boundaries of reasonable densities for spread foundations. The constant vertical load was adapted to the sand properties, being $F_v = 100$ kN for the LD sand and $F_v = 300$ kN for the HD sand (see Tab. 3.5).

Despite the attempt to create possibly realistic conditions in these large-scale tests, Negro *et al.* [Neg+00] point out that the limited size of the caisson influences the test results and limits to some extent their generalization to real cases. Partly, this refers to the (elastic) settlement characteristics which depend on the thickness of the soil layer underneath the footing. However, with a thickness of three times the foundation dimensions, a reasonable behavior could be achieved. A thicker deformable

soil layer in a real case could easily be employed by simply modifying the corresponding settlement calculation.
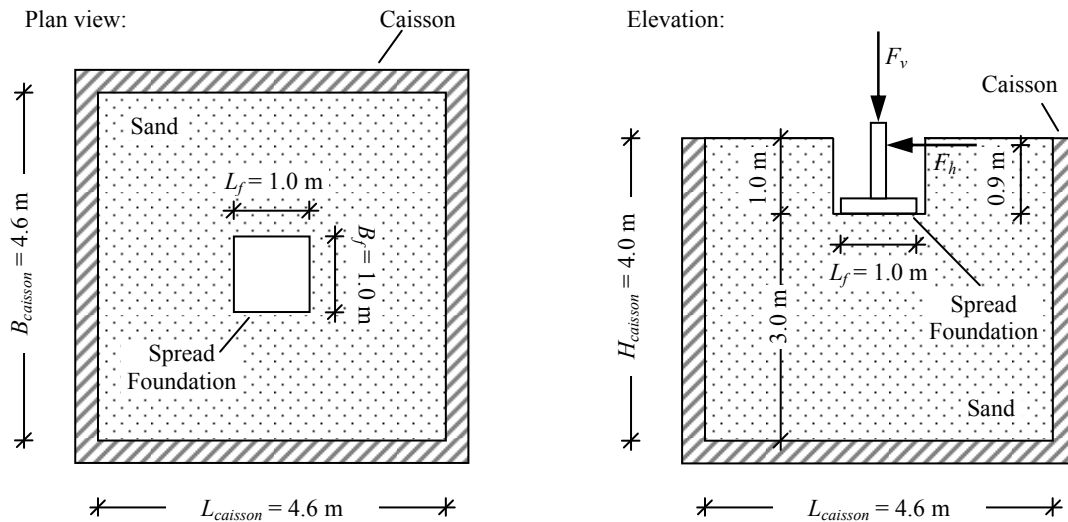

Fig. 3.44: Test set-up of TRISEE experiments featuring a spread footing on sand [Neg+00]

	Test with LD Sand	Test with HD Sand
Relative Density D_r	45%	85%
Vertical Load F_v	100 kN	300 kN

Tab. 3.5: Characteristics of the two different tests as part of the TRISEE project [Neg+00]

A stronger influence on the test results, resulting from the limited caisson dimensions, may be expected with respect to the possible failure mechanism. Using the model by Terzaghi, as shown in Fig. 3.39, the dimensions of the failure wedge in the soil can be estimated according to equations (3.20) and (3.21). For an angle of friction of $\varphi = 30°$, e.g., and under centric vertical load these dimensions would then result as $H_{wedge} = 1.6$ m and $L_{wedge} = 4.3$ m. The corresponding values for a vertical load of $F_v = 300$ kN and the associated ultimate moment capacity at failure, resulting in a reduced contact length of $L_{f,red} = 0.58$ m, are $H_{wedge} = 0.9$ m and $L_{wedge} = 2.5$ m. In both cases, the provided depth of 3 m underneath the footing is larger than the height of the estimated failure wedge H_{wedge}. However, the provided distance to the walls of the caisson, of 1.8 m, is lower than the predicted horizontal lengths of the failure mechanism L_{wedge}. Therefore, the geometric boundary conditions suggest that the normal free-field failure mechanism probably may not be able to develop. The likely consequence is that the failure loads experienced in the experiment might overpredict those under real conditions to a certain degree. For a comparison with the Winkler spring model proposed in Subsection a this would mean that the yield stress σ_y of the Winkler springs may not be fully realistic for the given combination of foundation, soil, and vertical load, while the settlement behavior and the uplifting of the footing were captured adequately.

In Fig. 3.45 the measured moment-rotation hystereses during the three phases of the experiments are shown for the two tests with different relative sand densities. It can be seen that at very small rotations (Phase I) an almost linear elastic behavior prevailed, with comparatively small hysteresis loops. For rotation angles in the range of about 0.3% to 0.6% (Phase II) a certain inelastic response developed which, especially for the LD sand (with somewhat higher rotation amplitudes), also involved considerable hysteretic behavior. In the last Phase III, with rotation peak amplitudes in the range of 2% to 3%, both experiments showed a pronounced inelastic behavior and some kind of global yield moment could be observed. In both cases, significant hysteretic energy dissipation developed, while the shape of the hystereses differed considerably between the two sand densities.
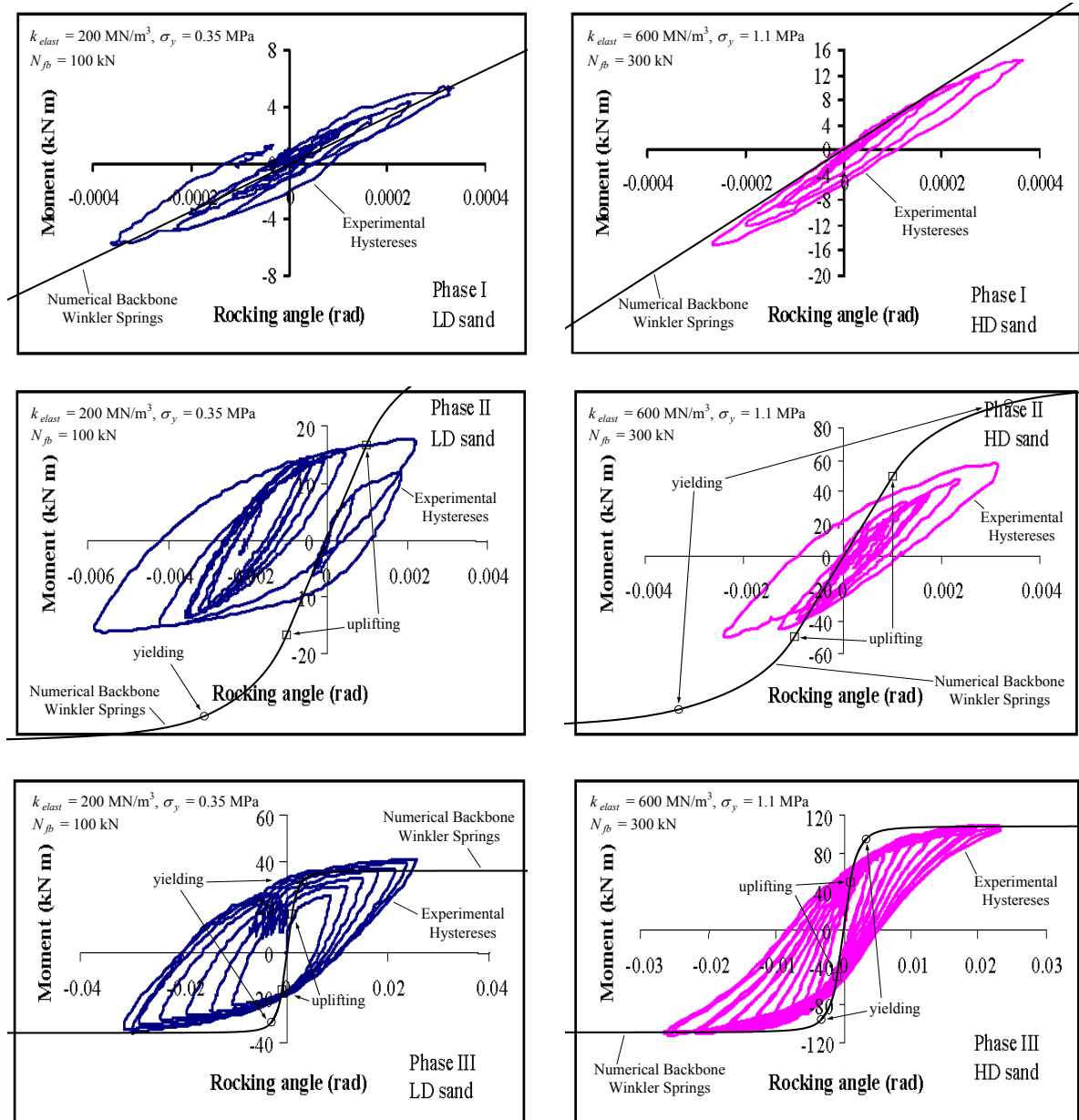
Fig. 3.45: Comparison between experimentally measured moment-rotation hystereses during three phases of TRISEE experiments [Neg+00] with increasing amplitude levels and numerically determined backbone curves using a Winkler spring model left: Test with low density (LD) sand, right: Test with high density (HD) sand

It is noteworthy that the yield moment of the high density (HD) sand remains rather constant throughout the cycles (with a certain post-yield stiffness), while the yield moment in the test with the low density (LD) sand appears to increase at every cycle. This cyclic strength enhancement of the LD sand can be explained by its initial low relative density which, especially during larger inelastic cycles, gradually gets compacted. This phenomenon can also be seen in Fig. 3.46 where the development of center settlements during phases II and III of the two experiments are shown. While both sand types show some increase in settlements, this cumulative compaction is significantly more pronounced for the LD sand during both experimental phases. Including such effects into a numerical model would be very difficult as they are essentially related to a change of soil properties during loading.

Aside from the experimentally measured hysteresis loops, in Fig. 3.45 corresponding numerically determined backbone curves are also shown for comparison purposes. These numerical backbone curves were computed based on the equations of Fig. 3.34. The parameters k_{elast} and σ_y defining the inelastic stress-settlement relationship of the Winkler springs were calibrated based on the measured

105

hystereses. This means, the elastic stiffness k_{elast} was determined in a way to approximate the essentially elastic behavior in Phase I of the experiments, while the yield stress σ_y was chosen to represent more or less the moment capacity of the soil-foundation system in Phase III of the experiments. Due to the changing soil properties of the LD sand and the corresponding cyclic increase of moment capacity, as discussed above, for this case the definition of σ_y is less clear, in particular since the cyclic behavior of the LD sand also resulted as somewhat unsymmetrical in the positive and negative directions. Due to the calibration of the stiffness and strength parameters, the comparison between measured cyclic and computed backbone response can obviously only refer to the general shape of the numerical curve and not to its magnitude.

Fig. 3.46: Development of center settlements during inelastic cycling of TRISEE experiments [Neg+00]
left: Phase II, right: Phase III

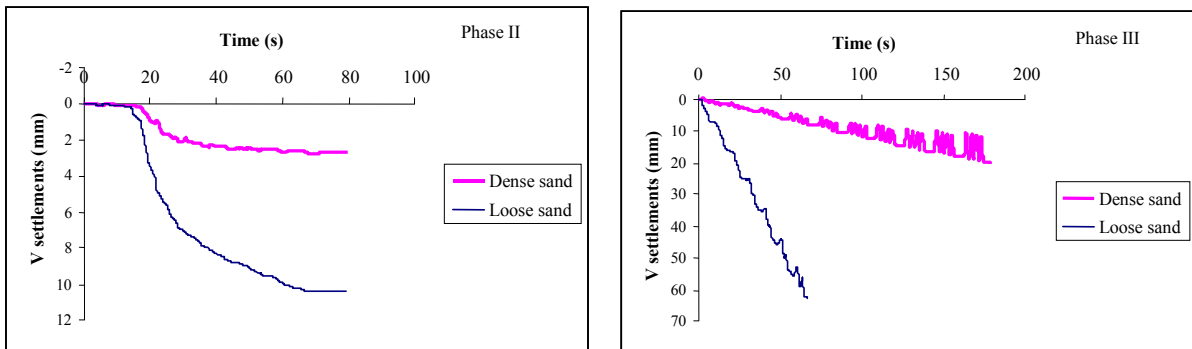From the comparison between numerical backbone curves and measured hysteresis loops it can be concluded that, provided the parameters can be determined sufficiently well, two general aspects of the response can be captured. These are, on one hand, the elastic rotational stiffness at small amplitudes and, on the other hand, the limited moment capacity of the soil-foundation system. While the first aspect influences the fundamental elastic period of the bridge system, the second aspect may be even more important as it can change the plastic mechanism by capacity protecting the pier from developing a plastic hinge at its base.

As mentioned before, a limit to the moment capacity will occur for any spread foundation, even in case of infinite soil strength σ_y, and a corresponding upper boundary max $M_{fb,u}$ can be determined according to equation (3.11). In many realistic cases, the influence of the yield strength σ_y on the moment capacity of the foundation may not be very strong. In the case of the LD sand shown in Fig. 3.45 and for the chosen yield strength of $\sigma_y = 1.1$ MPa, a response moment of $M_{fb} = 109$ kNm results at a rotation of $\theta = 2\%$. If instead a value of $\sigma_y = 4.0$ MPa is chosen, for which at the same rotation level the soil still remains elastic, the moment increases only by approximately 17% to $M_{fb} = 128$ kNm. A moderate underprediction of the yield strength in the form of $\sigma_y = 0.8$ MPa would in turn result in a moment capacity of $M_{fb} = 93$ kNm which corresponds to a reduction by 14%. Only a substantial underprediction of the soil strength, as e.g. $\sigma_y = 0.5$ MPa, would in this case result in an unacceptable moment strength prediction of $M_{fb} = 60$ kNm. It should be noted that an underprediction of the soil strength (and its stiffness) is likely to give rather unconservative results for the seismic response if the deformation demand on the piers is the primary objective of the analysis. In particular, an underprediction of the moment capacity $M_{fb,u}$ of the foundation, which could result in a plastic mechanism in the soil instead of the pier, might lead to a positive assessment result concerning the seismic safety of the pier that may not reflect the real behavior.

Aside from the stiffness in the elastic range (Phase I of the TRISEE experiments) and the ultimate moment capacity (Phase III), Fig. 3.45 also shows Phase II which can be considered a transitional deformation range between the other two bounding phases. Here, the shape of the backbone curve resulting from the numerical model does not fit the measured moment-rotation response very well. In both cases of sand densities, the numerical model overpredicts the stiffness in this transitional deformation range. This discrepancy may be the result of two phenomena: (a) The bilinear stress-settlement relationship for the soil (see Fig. 3.32) does not represent the real compressive deformation

behavior of the soil, and (b) the soil-pressure distribution under the foundation resulting from the independent Winkler springs does not correspond to the real behavior of a 3-dimensional soil continuum.

With respect to aspect (a), it would be more realistic to model a continuous stiffness reduction for the Winkler springs resulting in a more curved σ-w-relationship. Alternative computations based on a curved Ramberg-Osgood rule for the stress-settlement relationship indeed resulted in a numerical moment-rotation backbone with a shape somewhat closer to the backbone of the measured response, especially in Phase II of the experiments. However, even with the Ramberg-Osgood model the Winkler spring model is considerably stiffer than the measured response in Phase II.

This may be attributed to aspect (b), the unrealistic stress distribution under the rigid foundation block related to the representation by the independent springs. For linear elastic Winkler springs the model results in a linear stress distribution under the foundation, while for Ramberg-Osgood springs the stresses even increase less than linear towards the edge experiencing the larger settlement. In reality, however, there will be a pronounced stress concentration towards the edges and corners as long as the soil remains essentially linear elastic. These concentrations lead to an early onset of local soil yielding at the edges and corners which also influences the nonlinear moment-rotation behavior, especially in the deformation ranges where inelastic deformations start to develop, as in Phase II of the experiments.

As a Winkler spring representation with Ramberg-Osgood behavior is not possible using the basic equations of Fig. 3.34, but rather requires a complex numerical model with multiple discrete springs, the increase of accuracy by this additional effort is unlikely to be justified. Therefore, it is recommended to use the simpler bilinear σ-w-relationship of Fig. 3.32 for practical applications.

Generally, the Winkler spring model shown in Fig. 3.31 cannot only serve for the computation of the monotonic moment-rotation backbone, but it can also be used for cyclic response estimations if the σ-w-relationship is extended by a hysteretic rule. A comparatively simple extension to the bilinear law shown in Fig. 3.32 would, e.g., be given by an elasto-plastic hysteresis model which allows uplifting with zero stresses in tension. Such a model is implemented in the software code Ruaumoko [Car04] and it has been used to construct a numerical model of a rigid foundation on 25 discrete springs, approximating the continuously smeared Winkler springs.
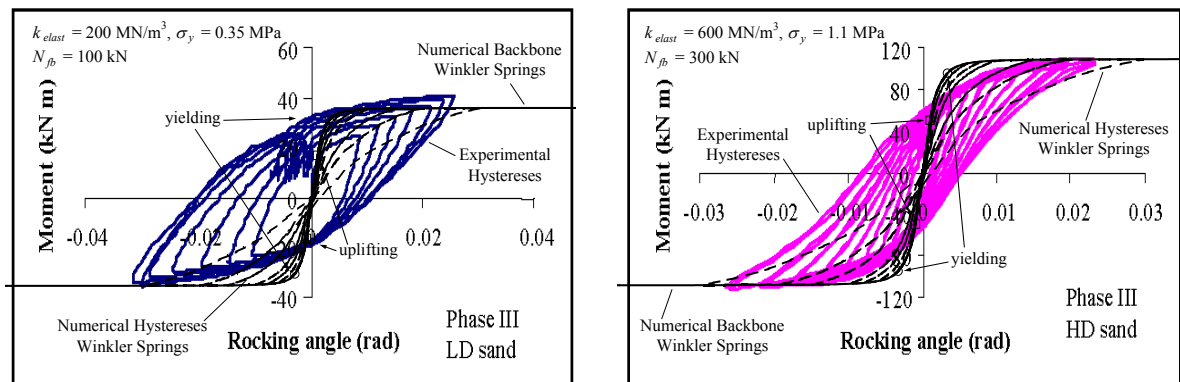
Fig. 3.47: Comparison between experimentally measured moment-rotation hysteresis
during phase III of TRISEE experiments [Neg+00] and
numerically determined hystereses using a Winkler spring model with elasto-plastic behavior in compression
left: Test with low density (LD) sand, right: Test with high density (HD) sand

Examples of corresponding hysteretic moment-rotation responses, based on the same parameters for soil stiffness and strength as before, are shown in Fig. 3.47. The comparison with the measured responses for the two sand densities reveals that the real cyclic behavior – and in particular the hysteretic energy dissipation characteristics – are not captured very well. The response of the HD sand on the right side of Fig. 3.47 fits somewhat better and the shape of the hysteresis loops is met closer. But even here, the loops are substantially too slim in the range of zero force, i.e. the residual rotation upon unloading is strongly underestimated.

While it has been stated above that limited modifications of the soil yield stress σ_y do not change the numerical moment-rotation backbone very strongly, this does not hold true for the corresponding hysteretic response. Here, changing the value of σ_y does have a considerable influence on the fatness of the hysteresis loops. In particular, it should be noted that nonlinear behavior due to uplifting only, numerically does not result in any hysteretic energy dissipation. This means that a yield stress of $\sigma_y = 4$ MPa, which has been shown above to modify the ultimate moment capacity only insignificantly, would result in a purely nonlinear elastic response for the deformation range shown in Fig. 3.47, as the onset of soil yielding is moved beyond the rotations considered in this case.

If the Winkler spring model is intended to represent cyclic hysteretic behavior, it should therefore be kept in mind that the choice of σ_y becomes a crucial part in determining the cyclic inelastic behavior of the foundations. The rather inadequate shape of the hysteresis loops may partly be related to the same aspects of the elasto-plastic Winkler spring model as discussed above in the context of the monotonic backbone response in Phase II of the experiments. These are namely the multi-linear shape of the hysteresis rule and the inappropriate stress distribution resulting from the independent springs. An attempt to model the same system cyclically using a Ramberg-Osgood rule for the springs appeared to bring some improvement of the hysteretic response, but did not run numerically stable in the analyzed cases.

Summarizing, it could be found that the inelastic behavior of spread foundations has three significant influences on the seismic response: (a) an additional flexibility in the elastic range which increases the initial fundamental period compared to a rigidly fixed foundation model, (b) a limitation of the moment capacity of the foundation which can change the plastic mechanism in the pier-foundation subsystem, and (c) considerable local energy dissipation from hysteretic soil response and radiation damping. If the seismic demand on the RC structure represents the primary focus of the analysis, then all three aspects are likely to have a beneficial influence on the seismic behavior[11]. The issues (a) and (b) are related to the backbone curve of the moment-rotation behavior and they can be captured reasonably well with the Winkler spring model presented above. In particular, it has been shown that the rather important aspect (b), which can completely change the plastic mechanisms, is not very sensitive to the modeling assumptions.

The energy dissipation characteristics, mentioned in aspect (c), are more difficult to capture with reasonable accuracy. The moment-rotation hystereses using the Winkler spring model with elasto-plastic spring behavior has been shown not to give a very good representation of the experimentally measured hysteretic loops. Furthermore, the hystereses computed with the Winkler spring model are rather sensitive to the choice of the soil yield stress σ_y, which is subjected to a considerable uncertainty due to its exponential relation to the soil's angle of friction φ. Apart from that, if the Winkler model is intended to be used cyclically, it is not possible to use the simple equations of Fig. 3.34 anymore, but it will rather be necessary to construct a more sophisticated numerical model using a number of individual springs, each being characterized by an elasto-plastic behavior in compression and uplifting in tension.

The second source of energy dissipation, the radiation damping, can generally be modeled by the principles presented by Somaini in [Som85] and [WS86]. However, these models assume a perfect contact between soil and foundation, thus loosing their validity if foundation uplifting occurs, which cannot be ruled out during severe seismic excitation for foundations of typically limited sizes. In such cases, very sophisticated numerical models representing the 3D soil continuum would become necessary, with particular focus on the boundary conditions of the soil to represent the radiation damping in an accurate manner. This type of analysis is unlikely to be appropriate for the practical assessment of existing bridges in an engineering office.

---

[11] Gazetas [Gaz06] has shown that cases exist where an increase of the fundamental period due to additional foundation flexibility can also have a negative influence on the seismic behavior. This is typically related to soft soil conditions which result in high characteristic periods of the response spectra. However, this phenomenon needs to be included in the spectral shape defining the seismic demand, which is not the case for the smooth average spectra that are used in [SIA261] and [EC8-1]. As a consequence, if the seismic demand is defined by the spectra of [SIA261], it can normally be assumed that system softening due to foundation flexibility will not have a negative influence on the seismic demand on the RC structure.

Taking into account that all three effects of soil flexibility mentioned above have a rather beneficial influence on the seismic demand of the RC structure, a conservative and simplified approach could be to consider only aspects (a) and (b), i.e. elastic softening and the limited moment capacity which can both be captured in the moment-rotation backbone, while disregarding the additional energy dissipation related to the foundation. In a practical application this can be achieved by modeling the soil-foundation system as a nonlinear elastic rotational spring with load-deformation properties as defined by the equations of Fig. 3.34, but without any hysteretic or radiation damping. This would mean that the spring features a nonlinear behavior including a global yielding-type response at large deformations, but unloading occurs along the same moment-rotation curve as during the loading phase.

Such an approach has also been applied in the studies by Kuhn in [Kuh07] and [KBD08] as a cautious modeling solution. The reasoning behind this decision is that the additional energy dissipation from the foundations could not be determined reliably with conventional engineering methods. As the effects resulting from the nonlinear elastic modeling already have a beneficial influence on the seismic behavior of the piers, it was considered potentially unconservative and thus unwise to model a certain amount of energy dissipation as an additional beneficial effect which cannot be determined with sufficient reliability. The chosen approach included the possibly most important effect, i.e. the potential change of the plastic mechanism due to development of a plastic hinge in the soil-foundation system, while maintaining a certain level of conservatism. At the same time, this solution can also be introduced easily into a numerical model of an entire bridge system. It thus limits potential error sources while numerically not being very demanding.

If the soil-foundation system is introduced into the numerical bridge model by means of a discrete nonlinear spring with properties as defined by the equations in Fig. 3.34, it may become necessary to use a bilinear approximation of the computed curved load-deformation relationship. In such a case it is recommendable to consider the expected deformation range in which the bilinear representation is supposed to approximate the curved moment-rotation relationship. In Fig. 3.48, the same numerical prediction of a moment-rotation relationship is shown for two different deformation ranges. In both cases, bilinear approximations are included which were determined in order to represent the computed curve in the corresponding ranges as good as possible.
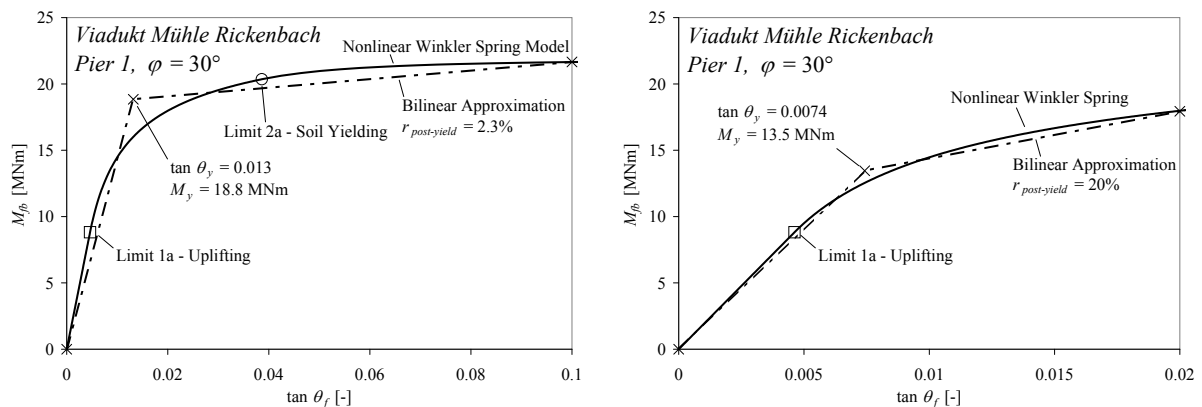
Fig. 3.48: Bilinear approximations of moment-rotation relationship for different ranges of rotations
left: tan θ$_f$ up to 10%, right: tan θ$_f$ up to 2%

It can be seen that the resulting parameters M_y and tan θ_y, as well as the post-yield stiffness ratio $r_{post-yield}$, defining the bilinear backbone representation differ considerably, although they are meant to approximate the same curve. While the approximation on the left side of Fig. 3.48, which is intended to be valid in the rotation range up to tan $\theta_f = 0.1$, may be a reasonable solution on average within this large range, on a local basis the deviations can be significant. For example, at the nominal yield moment $M_y = 18.8$ MNm the rotation according to the original relationship is tan $\theta_f = 0.025$ and the corresponding value of the bilinear approximation is tan $\theta_y = 0.013$. The original rotation at this moment level is thus 90% higher than that of the approximate one. At the same time, the tangent

stiffness of the original relationship at the origin is 33% higher than the initial stiffness of the bilinear approximation.

If the seismic deformation demand on the foundation is significantly lower than the upper limit of the rotation range for which a bilinear approximation has been developed, it is therefore recommendable to reduce this range in order to increase the accuracy. As shown on the right side of Fig. 3.48, in the given case the quality of the approximation for small deformations can be improved significantly if the rotation demand on the foundation does not exceed $\tan \theta_f = 0.02$ and the range for the bilinear approximation is adapted accordingly. As the total top displacement of a pier-foundation subsystem is composed of pier deformations and foundation rotations, the improved approximation influences the distribution of this total displacement between the two contributors, and it can thus influence the computed pier deformation demand in individual cases considerably.

Generally, once a bilinear approximation of the computed moment-rotation relationship has been determined, it would also be possible to define a corresponding hysteretic rule, e.g. using the modified Takeda model. However, as discussed above, the definition of the hysteretic energy dissipation characteristics (i.e. the fatness of the loops) is prone to large uncertainties and would therefore require a considerable amount of engineering judgment. It is therefore recommended to rather use a nonlinear elastic spring with the chosen bilinear characteristics as a conservative solution.

e) Introduction of Soil-Foundation Flexibility into the Bridge Model

In the preceding subsections the equations describing the moment-rotation relationship of a rigid foundation on Winkler springs have been presented and a set of procedures has been proposed to determine the necessary characteristic parameters. Based on these relationships, the soil-foundation system can be simplified to a single nonlinear rotational spring as shown in Fig. 3.49 (center). The moment-rotation relationship of this spring can be computed according to the equations given in Fig. 3.34 and can be further approximated by a bilinear relationship. This representation of the soil-foundation flexibility is particularly suitable if the reinforced concrete (RC) piers in the structural bridge model are represented by inelastic beam-column elements with fiber cross-sections (smeared plasticity) or by linear elastic beam-column elements with inelastic plastic hinges (lumped plasticity).
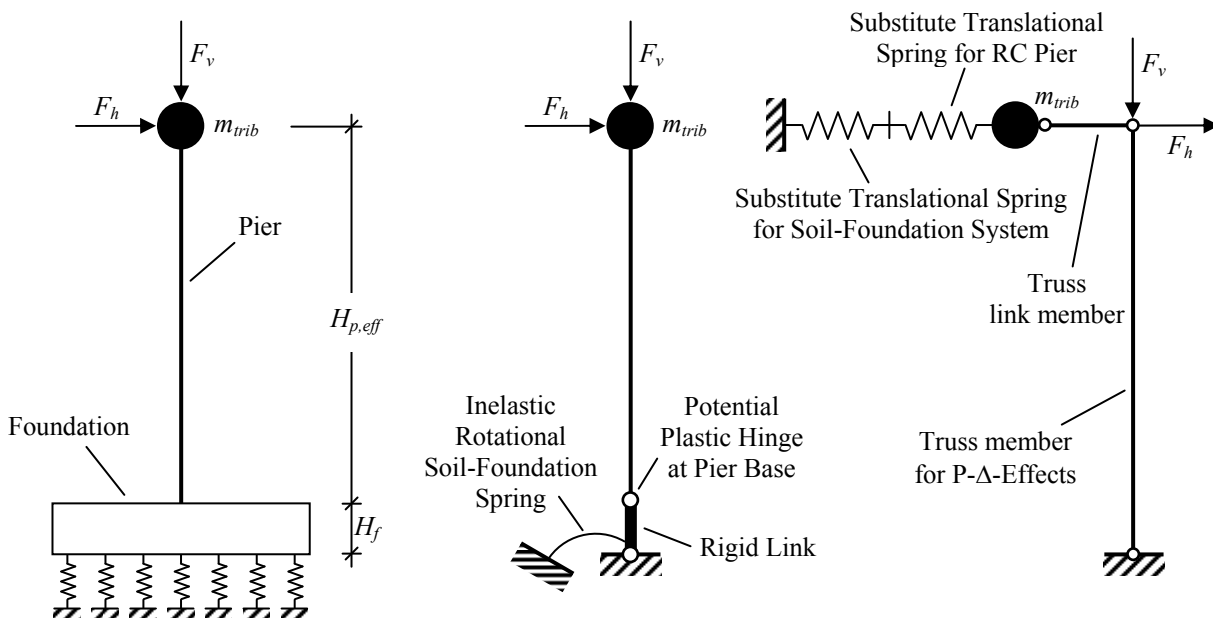

Fig. 3.49: Modeling alternatives for single cantilever bridge pier taking soil-flexibility into account
left: Pier on rigid foundation with Winkler springs, center: Pier with rotational spring for soil-flexibility,
right: Two substitute translational springs for pier and soil, complemented by truss members for P-Δ-effects

3.5 Soil-Structure Interaction

As an alternative solution, an entire cantilever pier can also be modeled by a single translational spring which represents the inelastic force-displacement relationship of the RC pier and features a hysteretic behavior, as e.g. defined by the modified Takeda rule. In this case, it is meaningful to transform the rotational soil spring into an equivalent translational spring as well. The conversion of any moment-rotation relationship (also cyclic) into a corresponding force-displacement relationship can be performed without significant effort by means of equations (3.26) and (3.27) which are based on the geometric and kinematic relations shown in Fig. 3.50. In Fig. 3.51 the resulting nonlinear force-displacement curves are shown which correspond to the moment-rotation relationships of Fig. 3.48 assuming an effective total pier height from the foundation base to the center of mass being $H_{p,eff} + H_f = 12$ m. These force-displacement curves represent the behavior of a rigid pier on a flexible foundation. The total load-deformation behavior of pier and foundation can be taken into account by implementing both translational springs for RC pier and foundation with their corresponding nonlinear force-displacement curves.

$$F_h = \frac{M_{fb}}{H_{p,eff} + H_f} \tag{3.26}$$

$$\Delta_{top,soil} = \theta_{f,soil} \cdot \left(H_{p,eff} + H_f \right) \tag{3.27}$$

As the horizontal shear force causing the deflections is the same in the RC pier and the soil-foundation system, while the top displacements from the two sources of deformations are added to each other, the combined system of pier and foundation can be represented by the two corresponding translational springs arranged in series, as shown on the right side of Fig. 3.49. It should be noted that with the two modeling alternatives shown on the left side and in the center of Fig. 3.49 it is possible to take P-Δ-effects directly into account if the solution strategy (i.e. the numerical software code) is capable of doing so. Using the simplified approach with only two translational springs in series this is not directly possible anymore. However, for cases where P-Δ-effects play a significant role, a possible solution is shown on the right side of Fig. 3.49. Here, an additional truss member with the length $H_{p,eff} + H_f$ of the original pier (including the foundation) is linked to the springs and is loaded by the vertical force acting on the pier (e.g. from gravity loads). When the system is deflected, the truss member experiences the same secant rotations as the original pier would for the same top displacement, thus creating the same P-Δ-effects.
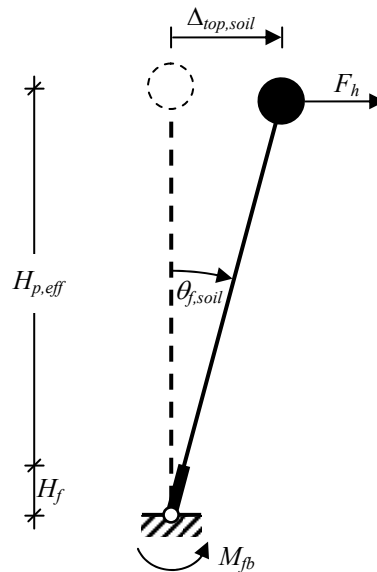
Fig. 3.50: Geometric relationships for conversion of rotational soil spring into equivalent translational spring

Such a simplified model of an individual pier-foundation subsystem can also be introduced into the model of an entire multi-degree-of-freedom (MDOF) bridge structure, as e.g. shown in Fig. 3.52 for

the transverse response of a four span girder bridge. This way of modeling has the advantage that the bridge can be represented as a 2-dimensional system, although the original structure has three dimensions. This simplification reduces the total number of degrees of freedom which makes it less prone to errors and numerically easier to handle.
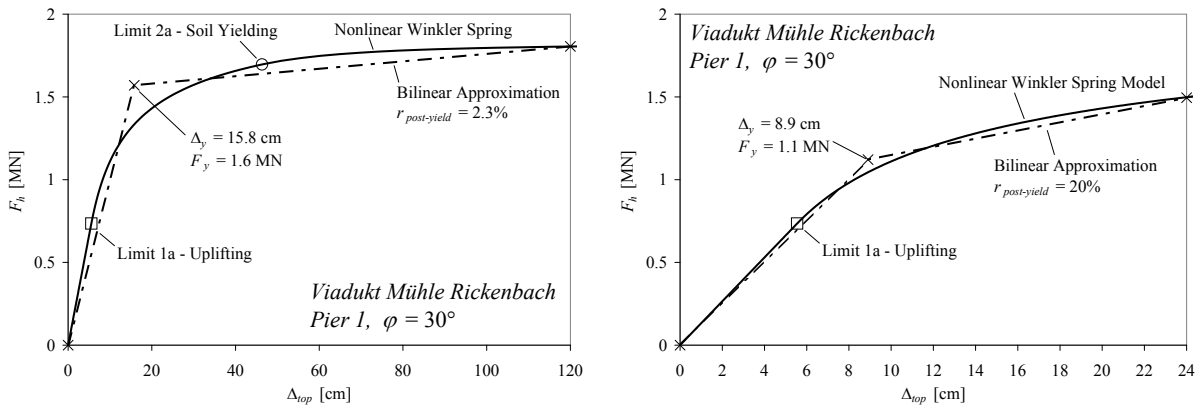
*Fig. 3.51: Bilinear approximations of force-displacement relationship
representing foundation related displacements only for different ranges of top-displacements
left: Δ_{top} up to 120 cm (tan θ_f up to 10%), right: Δ_{top} up to 24 cm (tan θ_f up to 2%)*
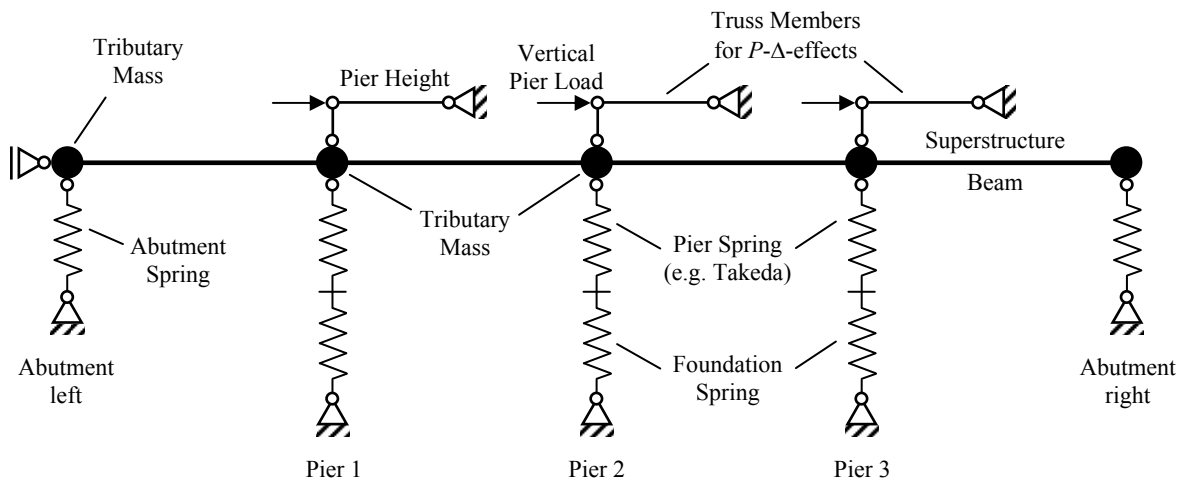
*Fig. 3.52: 2-dimensional MDOF model of bridge structure for transverse seismic response
taking soil flexibility and P-Δ-effects into account*

f) Relevance of Soil-Foundation Flexibility in Real Bridges

The relevance of soil flexibility at spread foundations for the assessment of the existing Swiss bridge stock depends on the relative occurrence of this footing type and on the size of typical spread foundations, as smaller footings have lower stiffness and strength properties. In Section 2.2.2 three existing Swiss bridges were presented which are used in this text as sample structures to work with realistic and possibly representative geometric and detailing assumptions. In Fig. 3.53 the geometry of the spread foundations found at piers 1 and 5 of the *Viadukt Mühle Rickenbach* is shown. In total, three of the five piers of the *Viadukt Mühle Rickenbach* are founded on spread footings. The highest two of the five piers, located in the center region of the bridge, are founded by means of multiple piles. Both piers of the second sample bridge, the *West-Bypass Gossau*, are founded on piles as well. All four piers of the third sample bridge, the *Viadukt Untere Weid*, feature spread footings with comparatively small dimensions. It can thus be concluded that, at least based on these sample bridges, spread foundations appear to have a relevant occurrence in existing Swiss bridges.

The dimensions of all spread footings mentioned above are summarized in Tab. 3.6 using the nomenclature of Fig. 3.53. Furthermore, the vertical loads N_{fb} acting on the footings at their base level and the resulting computed moment capacities $M_{fb,u}$ are also given in Tab. 3.6. The ultimate moments are computed based on equations (3.18) and (3.25) thus depending on the yield stress which is a function of the angle of friction φ of the soil. Therefore the moment capacities $M_{fb,u}$ in Tab. 3.6 are given for three different assumptions concerning the angle of friction, i.e. $\varphi = 25°$, $\varphi = 30°$, and $\varphi = 35°$. As an upper boundary for the maximum possible value of the ultimate moment the value max $M_{fb,u}$, as defined by equation (3.11) and corresponding to infinite soil strength, is also given. This value results if the vertical load has an eccentricity of half the foundation length and it cannot be exceeded by any means.

Plan view:

Section A-A:
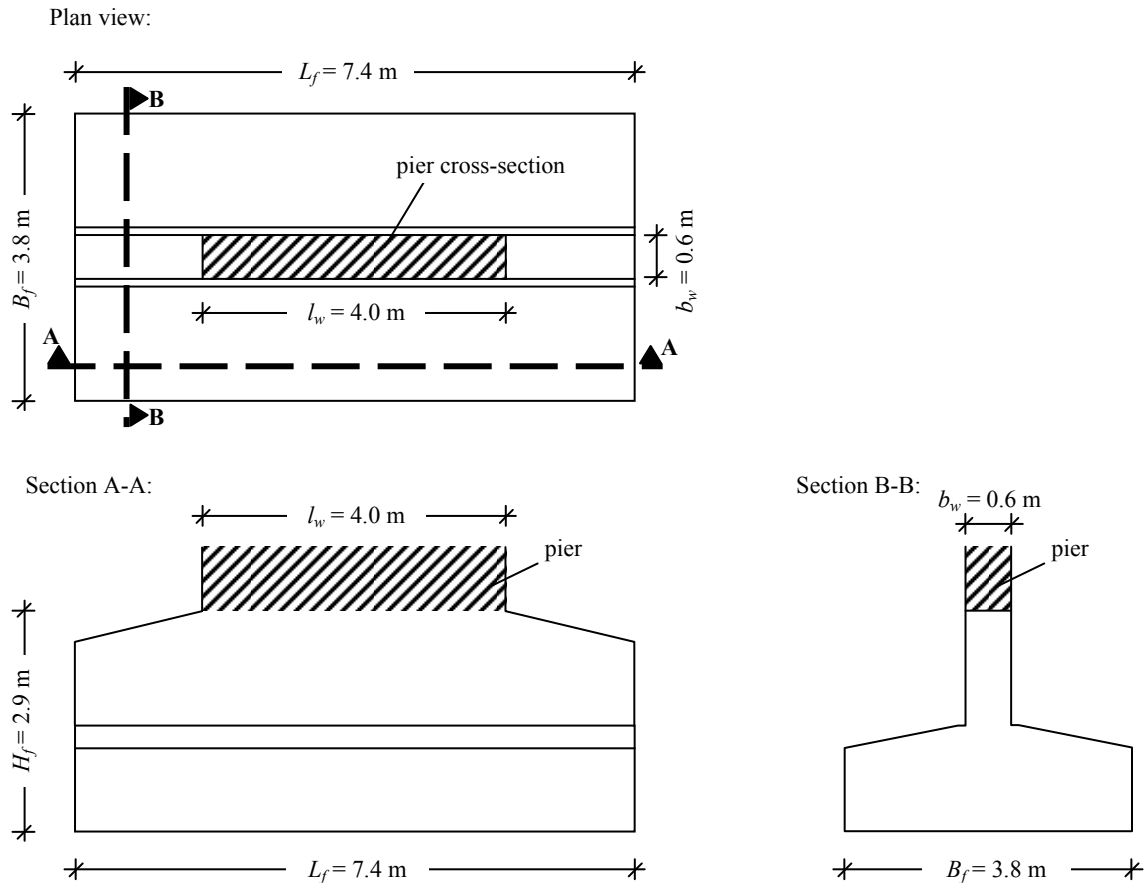
Section B-B:

Fig. 3.53: Geometry of spread foundation for piers 1 and 5 of sample bridge Viadukt Mühle Rickenbach (SG)

For the corresponding piers of each of the spread footings the moment capacities of the cross-sections at the pier bases can be estimated. In Tab. 2.1 the geometric data and the strength properties of the reinforcement and the concrete of all piers are given which were used to conduct moment curvature analyses of the pier cross-sections. In Tab. 3.7 the dimensions of the cross-sections, the axial load N_{pb} at the pier bases and the corresponding nominal moment capacities $M_{pb,pier,n}$ of the RC sections are summarized. The moment capacities of the foundation $M_{fb,u}$ and the capacities $M_{pb,pier,n}$ of the RC piers cannot be compared directly because one refers to the foundation base while the other acts at the pier base. Based on the relationships shown in Fig. 3.37, the moment at the foundation base $M_{fb,pier,n}$ corresponding to reaching the capacity of the RC cross-section $M_{pb,pier,n}$ at the pier base can be calculated according to equation (3.28). These values of $M_{fb,pier,n}$ are also given in Tab. 3.7 for each pier featuring a spread foundation.

$$M_{fb,pier,n} = M_{pb,pier,n} \cdot \frac{H_{p,eff} + H_f}{H_{p,eff}} \tag{3.28}$$

		Untere Weid				Rickenbach		
		Pier 1	Pier 2	Pier 3	Pier 4	Pier 1	Pier 5	Pier 2
Length of spread foundation	L_f [m]	5.5				7.4		8
Width of spread foundation	B_f [m]	3.5				3.8		5.6
Height of spread foundation	H_f [m]	1.2				2.9		3.9
Axial load at foundation base	N_{fb} [MN]	4.7	4.3	4.3	4.9	7.1	7.7	10.3
Moment capacity[a] of soil-foundation system for $\varphi = 25°$	$M_{fb,u}$ [MNm]	6.6	6.4	6.4	6.7	19.0	20.0	32.3
Moment capacity[a] of soil-foundation system for $\varphi = 30°$	$M_{fb,u}$ [MNm]	**9.0**	**8.5**	**8.5**	**9.3**	**21.9**	**23.3**	**35.8**
Moment capacity[a] of soil-foundation system for $\varphi = 35°$	$M_{fb,u}$ [MNm]	10.5	9.9	9.8	10.9	23.7	25.4	38.0
Moment capacity[b] of soil-foundation system for infinitely strong soil	max $M_{fb,u}$ [MNm]	**12.8**	**11.9**	**11.9**	**13.5**	**26.5**	**28.5**	**41.2**

[a] The moment capacities $M_{fb,u}$ of the soil-foundation system were calculated based on equations (3.18) through (3.25) but without consideration of the factors i_γ, i_q and i_c, which take into account the influence of a horizontal shear force. If these factors are used additionally, the resulting moment capacities of the foundations are further reduced.

[b] The moment capacity max $M_{fb,u}$ corresponding to an infinitely strong soil was computed using equation (3.11). It represents an upper bound to the attainable moment capacity for the given foundation size and axial load independent of the soil properties.

Tab. 3.6: Dimensions and moment capacities of spread foundations in sample bridges

		Untere Weid				Rickenbach		
		Pier 1	Pier 2	Pier 3	Pier 4	Pier 1	Pier 5	Pier 2
Section width of pier	b_w [m]	0.7				0.6		0.8
Section depth of pier	l_w [m]	3				4		4
Axial load at pier base	N_{pb} [MN]	4.2	3.8	3.8	4.4	6.1	6.7	8.5
Moment capacity of pier	$M_{pb,pier,n}$ [MNm]	13.8	13.4	13.4	14.1	16.9	17.7	25.9
Moment at foundation base corresponding to pier flexural capacity	$M_{fb,pier,n}$ [MNm]	**15.0**	**14.4**	**14.4**	**15.0**	**22.3**	**22.2**	**33.0**

Tab. 3.7: Dimensions and moment capacities of RC piers featuring spread foundations in sample bridges

Comparing the moment capacities of the footings and the RC piers, $M_{fb,u}$ and $M_{fb,pier,n}$ (both referring to the base level of the foundations), it can be seen that in a significant number of cases the foundations might not be able to transfer the entire moment capacity of the piers. In Tab. 3.8 the ratios $M_{fb,u}/M_{fb,pier,n}$ between the two capacities are shown for the various assumptions concerning the soil strength. From these data it can be seen that for none of the three angles of friction – $\varphi = 25°$, $\varphi = 30°$, or $\varphi = 35°$ – the resulting moment capacities of the footings used in the *Viadukt Untere Weid* would be sufficient to create the nominal moment in the RC piers. For $\varphi = 30°$, the deficit of the footing capacity is approximately 40%, which means that even at comparatively low excitation levels the soil-foundation system would be expected to develop a plastic hinge, while any inelastic response of the cantilever piers can be ruled out independent of the seismic loading.

		Untere Weid				Rickenbach		
		Pier 1	Pier 2	Pier 3	Pier 4	Pier 1	Pier 5	Pier 2
Moment ratio foundation capacity for $\varphi = 25°$ / flexural pier capacity	$M_{fb,u} / M_{fb,pier,n}$ [-]	0.44	0.45	0.44	0.44	0.85	0.90	0.98
Moment ratio foundation capacity for $\varphi = 30°$ / flexural pier capacity	$M_{fb,u} / M_{fb,pier,n}$ [-]	**0.60**	**0.59**	**0.59**	**0.62**	**0.98**	**1.05**	**1.08**
Moment ratio foundation capacity for $\varphi = 35°$ / flexural pier capacity	$M_{fb,u} / M_{fb,pier,n}$ [-]	0.70	0.69	0.68	0.73	1.06	1.14	1.15
Moment ratio foundation capacity for infinite soil strength / flexural pier capacity	max $M_{fb,u}$ / $M_{fb,pier,n}$ [-]	**0.86**	**0.83**	**0.82**	**0.90**	**1.19**	**1.28**	**1.25**

Tab. 3.8: Ratios between moment capacities of RC piers and spread foundations in sample bridges

Even based on the upper boundary of the footing capacity max $M_{fb,u}$, corresponding to infinite soil strength, a deficit of moment capacity of at least 10% remains for the foundations of the *Viadukt Untere Weid*. This means that independent of the uncertainties in the determination of the soil parameters, a plastic hinge in the RC piers could not occur and it would instead rather develop in the soil-foundation systems. Nevertheless, the validity of this statement depends also on the reliability with which the moment capacity of the RC pier can be estimated. This is also related to the general uncertainties in determination of the material parameters in existing structures.

For the three piers of the *Viadukt Mühle Rickenbach* featuring spread foundations, the situation concerning the relationship between moment capacities of footings and RC piers is less clear. As can be seen from the data in Tab. 3.8, for $\varphi = 30°$ the moment capacities of RC pier and foundation, with respect to the base level of the footing, are almost equal and the differences are well below the uncertainties related to the simplified models and the determination of the relevant parameters. Correspondingly, for $\varphi = 25°$ and $\varphi = 35°$ the capacity ratios $M_{fb,u}/M_{fb,pier,n}$ are slightly below and above unity, respectively. This means that for $\varphi = 25°$ a plastic hinge would rather be expected to develop in the soil-foundation system, while for $\varphi = 35°$ a plastic hinge at the base of the cantilever RC pier appears somewhat more likely. However, due to the underlying uncertainties in the estimation of the individual capacities – model and parameter uncertainties – in both cases a reliable statement concerning the expected plastic mechanism is hardly possible. Therefore, in this case it would appear reasonable to take both possibilities into consideration by varying the corresponding parameters accordingly for a set of analyses, unless a conservative assumption can be determined beforehand.

In either case, due to the relative proximity between pier capacity and foundation capacity and the curved shape of the load-deformation curves, it is likely that even the stronger one of the two (RC pier or soil-foundation system) will contribute a considerable share to the total deformations. Therefore, in this case, particular attention should be given to a potential bilinearization of the response curves, as discussed in the context of Fig. 3.48, in order to avoid that the seismic demand does not fall into a deformation range which is not approximated well by the bilinear curve.

Generally, from the discussions above, it can be concluded that in the presented cases soil-structure interaction at the spread foundations has a significant – if not dominant – influence on the seismic behavior of the bridge piers. Compared to a rigidly fixed pier foundation, the plastic mechanisms at the pier bases of the *Viadukt Untere Weid* are completely changed, with the corresponding consequences for the deformation demands on the RC piers. At the *Viadukt Mühle Rickenbach*, the proximity between the capacities of foundation and pier will result in a considerable contribution by the soil-foundation system to the total top displacement, even if the occurrence of a plastic hinge at the

base of the RC pier is assumed. However, the alternative development of a plastic hinge in the soil-foundation system cannot be ruled out either and should therefore be considered as a possible seismic response as well. It can be seen that, for both bridges, disregarding the influence of soil-foundation flexibility at the spread foundations is likely to give a completely mistaken picture of the seismic bridge behavior.

g) Influence of Soil-Foundation Flexibility on the Seismic Deformation Demand

In the preceding subsections, primarily the local deformation behavior, i.e. the *capacity*, of spread foundations and their potential interaction with the piers has been discussed on a member level. Generally, it may be assumed that the flexibility of spread foundations will also influence the displacement *demand* and the global behavior of the entire bridge structure. When looking at the effects on the displacement demand of the piers, it appears reasonable to make a difference between, on one hand, the displacement demand $\Delta_{top,pier}$ on the RC piers only, and on the other hand, the total top displacements $\Delta_{top,tot}$ at the pier tops, being composed of pier deformations and a displacement contribution from the foundations (see Fig. 3.54 for composition of total displacement at pier top). It is likely that the influence of a flexible foundation on the total displacement is different from that on the pier deformation only. In some cases, the influence on the two values may even be contrary, i.e., while the total top displacement $\Delta_{top,tot}$ might increase due to the flexible foundation and the corresponding overall softer system behavior, the pier deformation $\Delta_{top,pier}$ can nevertheless be reduced if the displacement share $\Delta_{top,found}$ provided by the foundation rotation is sufficiently large.
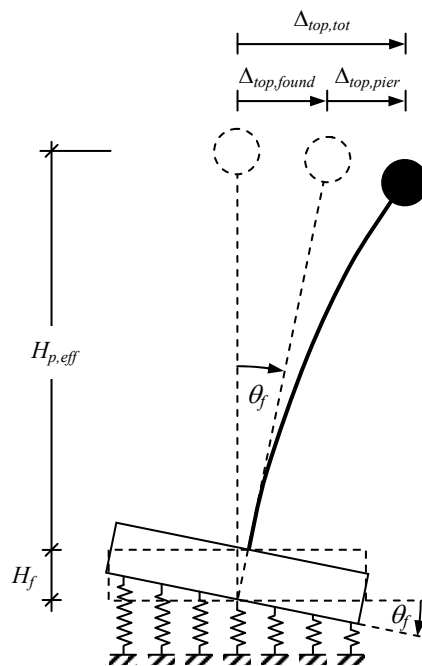
Fig. 3.54: Composition of the total top displacement for a cantilever pier on a flexible spread foundation

Based on the models for the flexibility at spread foundations, as presented above, the topic of a master thesis was developed in order to investigate the influence of soil-foundation flexibility on the transverse seismic behavior of multi-degree-of-freedom (MDOF) bridge structures. In the course of this master thesis, being co-tutored by the author, Kuhn [Kuh07] analyzed various configurations of MDOF bridge systems with characteristics that had been determined based on the sample bridges presented in Section 2.2.2. In this study, several modeling assumptions were varied in order to investigate their influence on the seismic response. Among these assumptions were the size of the spread foundations, the behavior of the abutments, and the distribution of the pier heights along the bridge. Typical results from this study are given in [KBD08] for a selected bridge configuration and will be summarized below.

The bridge presented in [KBD08] has a total length of 257 m and its general layout is shown in Fig. 3.55. The distribution of span widths, the superstructure cross-section, and the cross-section of the RC piers were chosen based on the properties of the *Viadukt Mühle Rickenbach* (see Section 2.2.2.*d*). For the numerical analyses, the transverse behavior of the abutments was modeled by a bilinear elastic spring with an initial stiffness of 30 MN/m and a yield force of 1.8 MN. The RC piers were modeled by inelastic translational springs having a hysteretic behavior according to the modified Takeda rule as implemented in the software codes Ruaumoko [Car04] and SeismoStruct [SS06]. The parameters defining the pier springs were determined by means of moment-curvature analysis and a plastic hinge model.
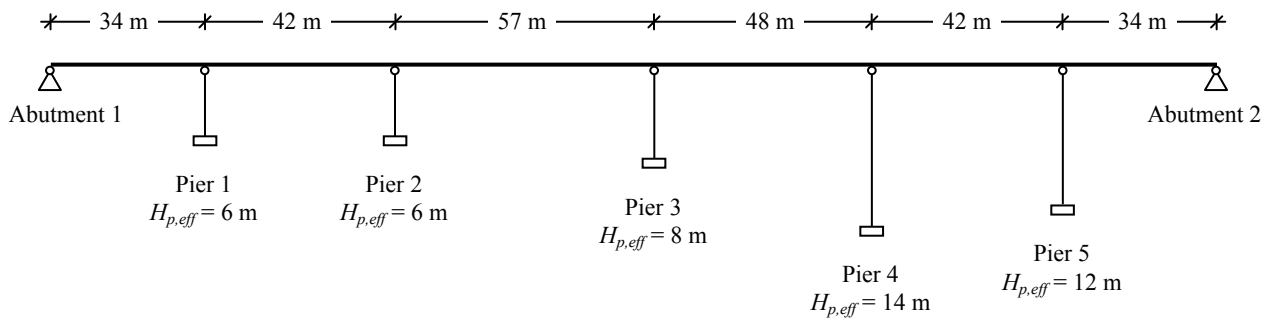
Fig. 3.55: Bridge system for dynamic analyses [KBD08]

Three different assumptions concerning the pier footings were considered: (i) a small spread foundation with in-plan dimensions of $L_f \times B_f = 7.4$ m x 3.8 m, (ii) a large spread foundation with dimensions of $L_f \times B_f = 10$ m x 5 m, and as a reference for comparison purposes, (iii) a rigidly fixed pier base which does not allow any end rotations. In each configuration, the same footing dimensions were used for all piers. The monotonic moment-rotation backbone of the spread foundations was computed using the equations given in Fig. 3.34 and the cyclic behavior was modeled as nonlinear elastic without any hysteretic energy dissipation. The numerical model for the rotational behavior of the foundations was represented by substitute translational springs as shown on the right side of Fig. 3.49, and the entire bridge system was assembled as a 2-dimensional model using the concept shown in Fig. 3.52. Further details of the modeling approach and the quantitative assumptions for the member behavior can be found in [KBD08] and [Kuh07].

Based on the chosen properties, it resulted that for the configuration with the small footings (7.4 m x 3.8 m) the yield strength of the foundations was lower than that of the piers, so that plastic hinges could only develop in the soil-foundation systems and not in the RC piers. In the case of the large footing configuration (10 m x 5 m), at the short piers 1 and 2 the yield strength of the foundations was also lower than that of the corresponding piers, while at the taller piers 3 through 5 the footings had higher yield strengths than the RC piers. As a consequence, for the large footing model, at piers 1 and 2 plastic hinges would develop in the soil, while at piers 3, 4, and 5 the plastic hinges would occur at the base of the RC piers (see Fig. 3.37).

The seismicity for the bridge analysis was defined by the elastic response spectrum of [SIA261] for seismic zone 3b, i.e. using a design peak ground acceleration of $a_{gd} = 0.16$ g. Due to modification factors of $S = 1.2$ for soil type B and $\gamma_f = 1.4$ for the highest structural importance class III, the effective peak ground acceleration was increased to a value of $a_g = 0.27$ g. Based on this elastic response spectrum, seven recorded ground motions were chosen and scaled to meet the spectral acceleration at the fundamental period of the bridge structure. The software codes Ruaumoko [Car04] and SeismoStruct [SS06] were used to perform inelastic time history analysis (ITHA) of the three bridge configurations using the seven scaled ground motions[12]. In the analyses a constant (i.e. mass proportional) elastic viscous damping ratio of $\xi_{el} = 2\%$ was modeled. For all three configurations the mean values and the standard deviations of the displacement demands at the pier tops were computed.

---

[12] Aside from minor difference in the inelastic small cycle response, the results from Ruaumoko [Car04] and SeismoStruct [SS06] agreed reasonably well with each other. Therefore, only the results computed with Ruaumoko will be presented below.

In the analyses it was distinguished between the total displacement demand and the deformation contribution from the RC piers only.

At first, in Fig. 3.56 the total peak displacements of the pier tops and the abutments are shown for the bridge structure with rigidly fixed pier bases. Aside from the mean values resulting from all seven accelerograms, the variation in terms of the standard deviation is presented. The corresponding results for the structures with the two types of spread foundations (small: 7.4 m x 3.8 m and large: 10 m x 5 m) can be found in Fig. 3.57. It can be seen that the total displacement demand of all piers is increased significantly by the flexibility of the spread foundations.
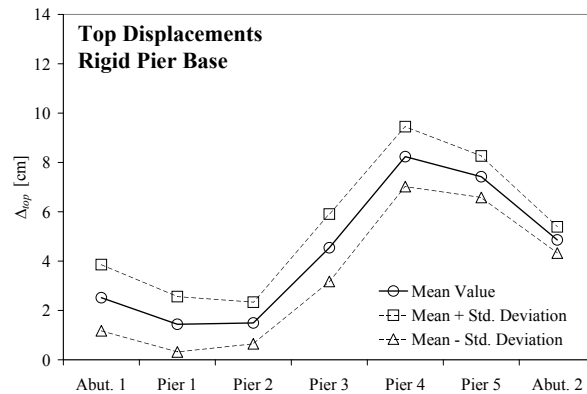
Fig. 3.56: Peak total displacements for rigidly fixed pier bases [KBD08]

In Fig. 3.58 the mean values for the three different systems are compared to each other. On the left side, the mean values of the *total peak displacements* $\Delta_{top,tot}$ resulting from pier and foundation deformations together are shown, while on the right side the *deformations of the piers only* $\Delta_{top,pier}$ are compared among each other. In the latter case, the corresponding yield displacements of the piers are also indicated, thus showing whether a pier experiences inelastic deformations or not. It can be seen that the *total displacement demand* $\Delta_{top,tot}$ in Fig. 3.58 (left) shows significant differences between the three systems. The small foundation system has the highest total displacements for most of the piers, while the fixed base system experiences the smallest total displacements. The response of the large foundation system lies between the two aforementioned configurations. This result could be expected as the small foundation system is the softest one and the fixed base system is the stiffest one of the three.
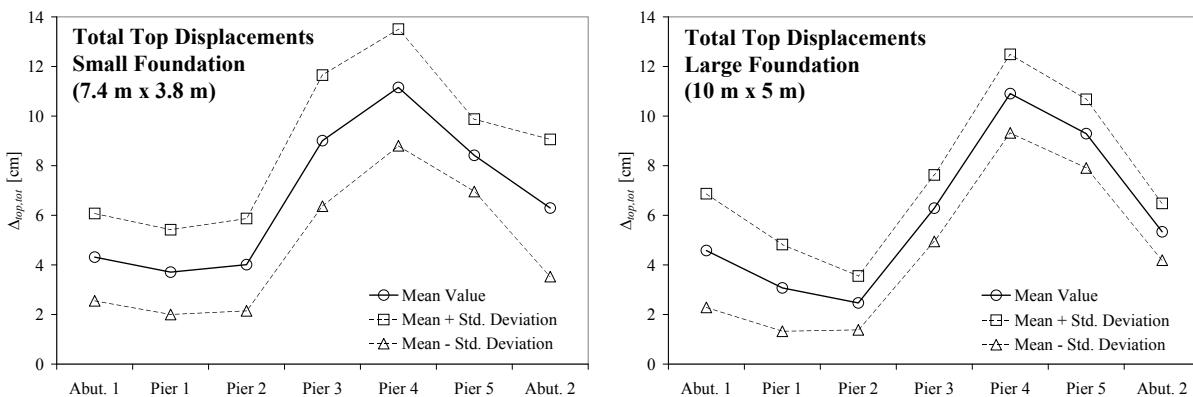
Fig. 3.57: Peak total displacements for piers founded on flexible spread foundations [KBD08]

Although the pure pier deformations $\Delta_{top,pier}$, shown on the right side of Fig. 3.58, also differ significantly among each other, the relationships are rather contrary to those of the total displacements $\Delta_{top,tot}$ on the left side of Fig. 3.58. For the pier deformations $\Delta_{top,pier}$, the small foundation system experiences the lowest deflections, whereas the fixed base system has the highest values, with the large foundation system being very close to the latter one. The rather small pier deformations in the

small foundation case are related to the low stiffness and strength properties of the foundations, which causes the footings to contribute a higher share to the total displacement demand and in some cases even protects the piers from yielding.
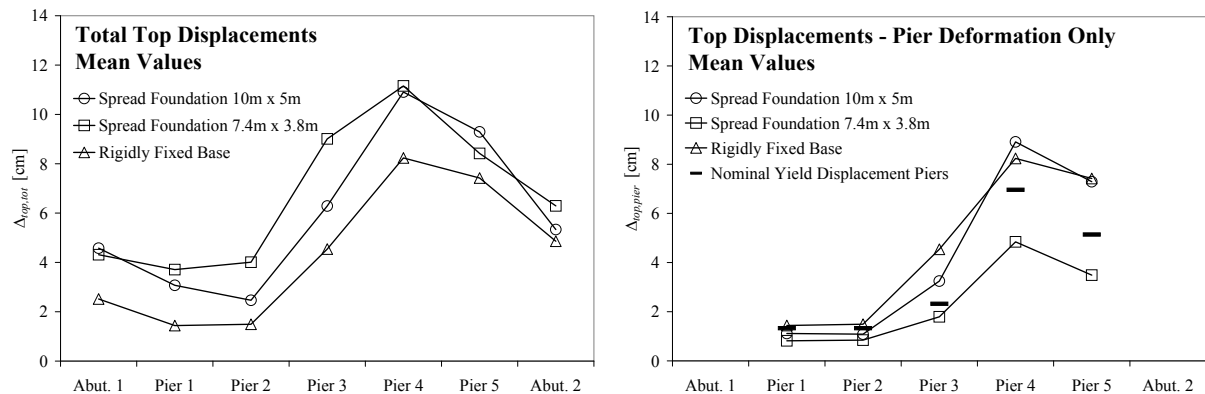
Fig. 3.58: Comparison of peak displacements for structures with different types of foundations [KBD08]

Comparing the response of pier 4 for the two systems with spread foundations, it can be seen in Fig. 3.58 (left) that the total deformations $\Delta_{top,tot}$ are almost the same in both cases. However, looking at the pure pier deformations $\Delta_{top,pier}$ (Fig. 3.58 right), the demand in the configuration with the large foundation is significantly higher. This difference is related to the relationships between pier and footing strengths and their influence on the developing plastic mechanisms. While the large foundation has sufficient capacity to cause yielding of the pier, the small foundation is not able to transfer the yield moment of the pier. As a consequence, in the large foundation configuration the plastic hinge has to develop in the RC pier, whereas in the case of the small footing the plastic hinge occurs in the soil-foundation system which capacity protects the pier. This way, the pier with the large foundation has to sustain the majority of the total displacement demand, while the pier with the small foundation remains in the elastic range and only contributes a minor share to the total top displacement.

For the case of the short piers 1 and 2, both footing configurations – the small one as well as the large one – have lower yield strengths than the RC piers so that the latter ones remain in the elastic range with small deformations. It should be noted that for a given combination of foundation size and pier cross-section it might be expected that the relation between the yield strengths is the same for all pier heights because the moment strengths of the piers and the foundations remain the same, independent of the pier height. However, for the yielding of the RC pier it is the moment demand at its base that governs, whereas the yielding of the soil-foundation system depends on the higher moment at the footing base. For constant foundation heights, the numerical difference between these two moments depends on the pier height and is more pronounced for shorter piers having a higher moment gradient (see Fig. 3.37).

Concerning the comparison between the different configurations and the magnitude of the influence coming from flexible pier foundations, it should be kept in mind that the presented results relate to a moderate seismicity level with limited total displacement demand. The differences in pier deformation demand between fixed and flexible base response can become significantly more pronounced for higher seismic loading, especially if the plastic hinge occurs in the soil-foundation system. It may also be noted that for the piers a longitudinal reinforcement ratio of $\rho_{sl} = 0.32\%$ was assumed which can be considered to rather represent the lower range of typical values. The increased moment capacity for higher reinforcement ratios would lead to an even larger influence of soil flexibility. At the same time, comparing the chosen foundation dimensions to the footing sizes of the sample bridges given in Tab. 3.6, it can be seen that especially the large footing configuration (10 m x 5 m) rather lies in the upper boundary region of realistic foundation sizes. As a consequence, many existing pier foundations which were mainly designed to support vertical loads may not have sufficient strength to cause yielding of cantilever piers. A very stiff and strong soil does not necessarily change this phenomenon as uplifting of the foundation can still cause nonlinear behavior and foundation dimensions on such soils can be expected to be rather small.

h) Conclusions and Recommendations

In the preceding subsections it has been shown that soil flexibility at spread foundations can have a significant influence on the seismic behavior of bridge structures in general, and on the deformation demand of cantilever piers in particular. A procedure for the modeling of the nonlinear footing behavior has been presented that is based on standard engineering methods. Despite its obvious simplifications and the related shortcomings in some details, this approach allows the estimation of the most important effects – namely the potential change in plastic mechanism due to the development of plastic hinges in the soil-foundation system and the increase of the initial period of the structure due to a softer behavior in the elastic range. For the assessment of existing bridge structures where the foundations have not been designed to be capacity protected, it can be crucial to consider the soil behavior for the analysis as it might change the seismic behavior completely. This refers especially to the local deformation demand at member level.

While conducting an analysis and interpreting its results, it is important to keep the immanent uncertainties in mind. On one hand, these are related to the simplifying nature of the model. On the other hand, incorrect soil parameters can also lead to an erroneous description of the behavior. It is therefore generally recommendable to perform a sensitivity analysis, varying the assumed parameter sets within a wider range. This appears particularly important if the yield strengths of the soil-foundation system and the RC piers are comparatively close together, so that it depends on the soil parameters which plastic mechanism will develop. In this context it is important to note that an underprediction of the foundation strength (and stiffness) can lead to unsafe results for the deformation demand on the RC pier. A typically conservative estimation for the moment strength of the soil-foundation system can be attained in any case by the upper boundary max $M_{fb,u}$ according to equation (3.11).

So far, the strength and deformation properties of the soil-foundation system have been determined exclusively based on the behavior of the soil. Concerning the flexibility properties, it appears justified to model the RC footing as a rigid block because it will normally be much stiffer than the soil underneath. However, despite the footing's high stiffness, it is certainly necessary to check whether it has sufficient strength to bear the loads acting on it during severe seismic excitation. It is likely that the footing was originally designed to carry an essentially centric load which results in a rather even distribution of soil pressure. The significantly different soil pressure distributions occurring at increased rotations, as shown in Fig. 3.33, can result in high bending moments and shear forces inside the RC footing, which were probably not considered in the design phase. It is therefore recommended to check the bearing capacity of these RC footings for the soil pressure distribution corresponding to the computed rotation demand of the soil-foundation systems. As no significant plastic deformations should normally be permitted inside the RC footing, this check of bearing capacity can be performed based on standard structural engineering concepts as for static monotonic loading.

Summarizing, it can be concluded that the presented engineering model for the soil-structure interaction at spread foundations bears some inevitable uncertainties, so that the computed analysis results should be interpreted with care and corresponding measures (e.g. a parameter variation) should be taken to avoid unsafe decisions. However, despite these uncertainties, disregarding the influence of soil flexibility is not recommendable, as it might give a completely mistaken picture of the seismic bridge behavior.

3.5.2 Abutments

The superstructures of bridges are supported at both ends by abutments which provide the transition between the bridge structure and the adjoining earth embankments. While in conventional bridge design the support of the superstructure for vertical loads may often be of primary interest, for seismic analysis the support provided in the horizontal directions – longitudinally and transversely – is of major importance. Although the geometries and structural details of abutments vary significantly between different bridges, a general distinction can be made between abutments which are monolithically connected to the superstructure and non-monolithic seat-type abutments which support the superstructure by means of bearings. The conceptual layout of these two types is shown in Fig. 3.59.
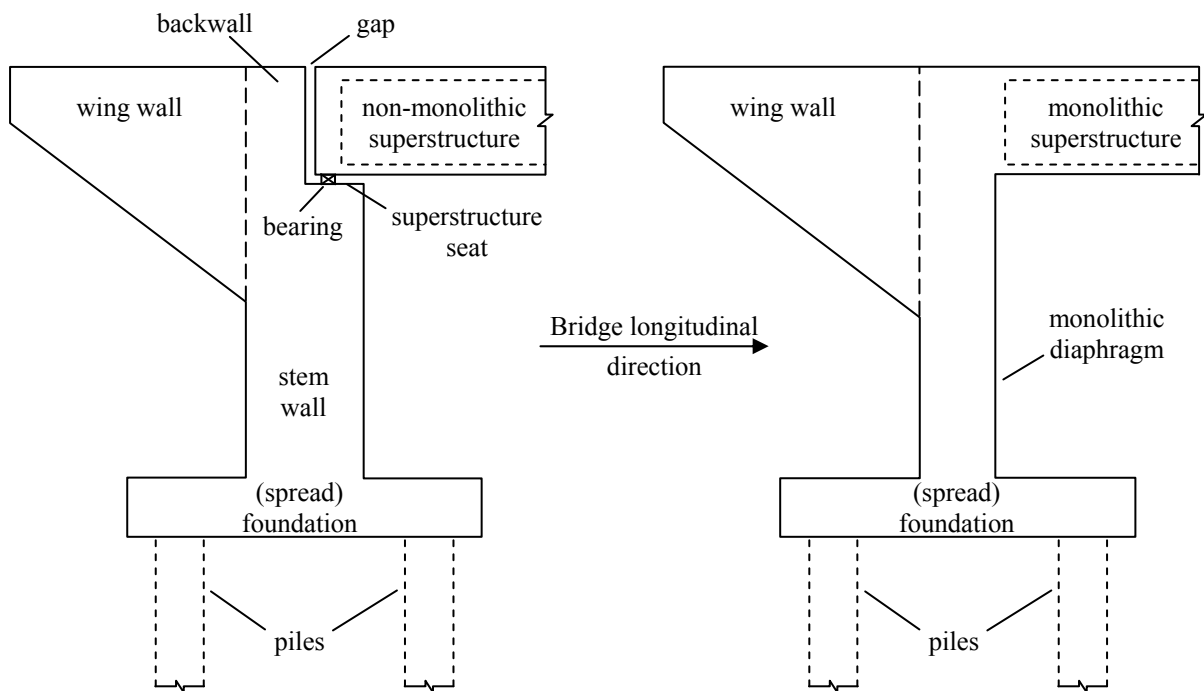
Fig. 3.59: Conceptual types of typical abutments
Left: Non-monolithic seat-type abutment; Right: Monolithic diaphragm abutment

In the case of a monolithic solution the transfer of forces between superstructure and abutment in all three directions will normally not be a problem. In contrast, in a seat-type solution any support force is transferred by the bearings, as long as they are intact. Seat-type abutments also bear the risk of superstructure unseating (Section Fig. 2.1.a) which is further discussed in Section 4.3.2. The following expositions in this section are limited to the force-displacement behavior of abutments, i.e. the interaction between the RC abutment and the soil at foundations, backfill and embankment. Potentially occurring relative movements and deformations between seat-type abutments and the superstructure need to be taken into account additionally.

a) Importance of Abutment Stiffness for Seismic Bridge Behavior

In the past, only limited attention has been given to the modeling of abutments for the seismic behavior of bridges. In part this may have been due to lack of reliable data on their behavior and, on the other hand, due to the notion that abutments are very stiff compared to the piers thus justifying the assumption of almost rigid behavior. While this assumption may even be approximately true for very small deformations (e.g. from small amplitude dynamic excitation), the behavior is likely to change substantially for larger deformations. Although a lot of experimental and numerical data exist on the behavior of concrete members, the amount of available data concerning seismic abutment behavior is

significantly scarcer. This may also be related to the very complex interaction between the concrete abutment and the embankment soil in which it is embedded.

Full-scale experimental testing of an entire abutment-embankment system is very costly and requires very high forces to be applied. On the other hand, scaling of soil systems requires an antiproportional increase of the acceleration of gravity for a realistic representation of the soil behavior. This can be achieved by centrifuge testing, but it typically only allows very small-scale testing. Numerical analyses intended to capture the behavior of the abutment-embankment system under large cyclic deformations are equally complex and need to take into account the pronounced inelastic behavior of the 3D soil continuum as well as the interaction between the concrete structure and the soil. This does not only require realistic mechanical models but also calls for significant computer power. Although current research is making good progress concerning the inelastic modeling of soil embankments, even for the most sophisticated and advanced numerical models, it would be desirable to verify and calibrate them on some kind of experimental or real behavior.

Two possible sources may be considered as realistic references for the deduction and calibration of models: (1) Large-scale experiments with a test setup that captures all relevant phenomena of the real abutment-embankment behavior, and (2) measurements on existing bridges during real earthquakes which allow calculating back the behavior during the earthquake. Some few examples exist for both approaches which provide interesting and valuable insight into the realistic behavior of abutment-embankment systems. While large-scale experimental testing (case 1) typically allows more detailed measuring and thus gives more detailed data, it bears some problems with respect to the realistic behavior of the system – e.g. due to scaling, loading-rate, or inadequacy in rebuilding all details of a real structure. On the other hand, measurements on existing bridges during real earthquakes give the best possible and most realistic representation of the seismic behavior for this particular structure, but the number of channels which are measured in such cases is normally very limited, thus not giving full insight into the complex behavior during the earthquake. In this case, it is necessary to conduct some numerical analyses and interpretation of the data to fill in the missing information needed for a complete description of the seismic behavior.
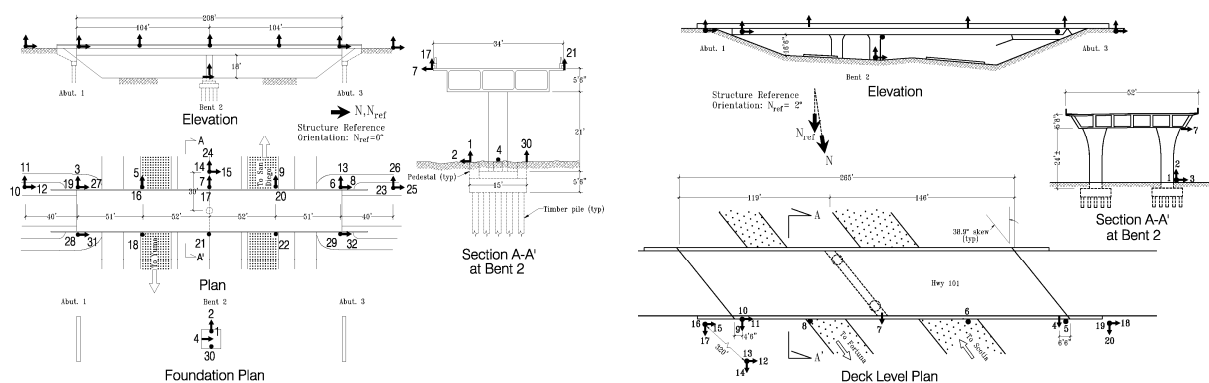
Fig. 3.60: Layout and sensor locations of instrumented short-span bridges in California
Left: Highway 8 / Meloland Overpass [CES09a]; Right: Highway 101 / Painter Street Overpass [CES09b]

Two rather short bridges that had been instrumented in California in the framework of the *Strong Motion Instrumentation Program* (SMIP) of the *California Division of Mines and Geology* (CDMG) have been the subject of extensive research. These are the *Meloland Overpass* over Highway 8 close to El Centro in Southern California and the *Painter Street Overpass* over Highway 101 close to Rio Dell in Northern California. The two bridges are shown in Fig. 3.60 together with an overview of the instrumentation that was applied to measure the seismic response (Meloland Overpass: 26 sensors, Painter Street Overpass: 20 sensors). Both structures are typical two-span highway overpasses having total lengths of 63 m and 81 m, respectively. While the Meloland Overpass is non-skew and its two spans have equal lengths of $L_{span} \approx 32$ m, the Painter Street Overpass has a skewness of 39° and unbalanced spans of length 36 m and 45 m. The Meloland Overpass is supported in its center by a single circular column, whereas the Painter Street Overpass features a two-column bent having the same in-plan skewness as the abutments (39°). As a result, the Meloland Overpass is somewhat shorter

and also more regular than the Painter Street Overpass which due to its skewness and the unbalanced spans represents to some extent a more complex seismic behavior. The characteristic data for the abutments and the embankments according to several literature sources are summarized in Tab. 3.9 using the definition of geometric dimensions as shown in Fig. 3.61.

		Meloland Overpass	**Painter Street Overpass**
Embankment Geometry	Crest Width W_c [m]	14.6 [WT90b] 10.36 [ZM02]	15.8 [IA04], [PE05] 15.24 [ZM02]
	Height H [m]	7.3 [WT90b] 7.92 [ZM02]	10.3 [IA04] 9.60 [ZM02] 8.8 [PE05]
	Side Slope S [-]	1:2 [ZM02]	1:2 [ZM02]
Embankment Soil Characteristics	Soil Type	Medium to stiff clay with traces of silt and sand [WT90b] Stiff clay [ZM02]	
	Plasticity Index I_p	5-10 [Ine02]	5-10 [IA04] 10 [PE05]
	Density ρ_s [kg/m^3]	1600 [WT90b] 1600 [ZM02] 1920 [Ine02]	1730 [IA04] 1600 [ZM02] 1760 [MR94], [PE05]
	Small Strain Shear Modulus G_{max} [MPa] [a]	7.2 [WT90b] 19.4 [ZM02] 76.8 [Ine02]	63.5 [IA04] 57.8 [ZM02] 75.8 [MR94] from borehole descriptions and standard formulae 55.2 [MR94] from seismic refraction studies by Heuze & Swift (1991)
	Poisson Ratio ν [-]	0.3 [WT90b]	0.4 [ZM02], [PE05]
	Shear Wave Velocity $v_{s,max}$ [m/s] [a]	67 [WT90b] 110 [ZM02] 200 [Ine02]	190 [IA04], [ZM02], [PE05]

[a] The values G_{max} and $v_{s,max}$ refer to the maximum shear stiffness of the soil corresponding to very small strains ($\gamma \le 10^{-6}$).

Tab. 3.9: Characteristic embankment data for instrumented highway overpasses

Fig. 3.61: Definition of geometric data for embankment cross-sections

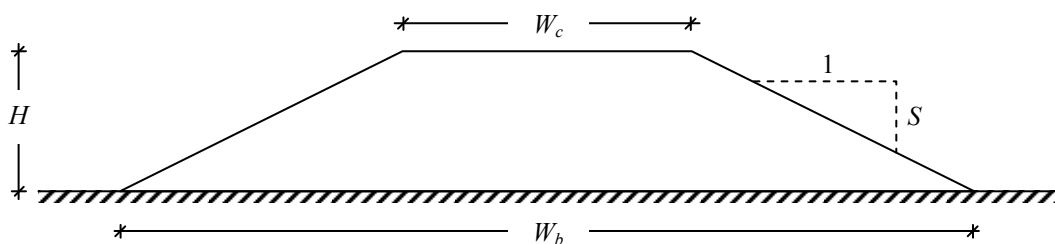Since the application of the instrumentation both bridges were subjected to several seismic events that have been recorded. The characteristic data of these earthquakes as given in several literature sources (not being fully consistent) are summarized in Tab. 3.10. The acquired data from the earthquakes has been used by several researchers for extensive analyses, trying to back-calculate the characteristics of the seismic behavior by means of different approaches.

Bridge	Date	Earthquake	Magnitude M_L	Distance [km]	Depth [km]	Peak Free Field Acceleration [g] [a]
Meloland	Oct 15, 1979	Imperial Valley	6.4	-	-	0.30 [WBL87]
Painter Street	Nov 21, 1986	Cape Mendocino	5.1	32	17	0.43 [GC97] 0.246 [IA01] 0.157 [PE05]
Painter Street	Nov 21, 1986 After Shock	Cape Mendocino	5.1	26	18	0.14 [GC97] 0.135 [IA01] 0.118 [PE05]
Painter Street	Jul 31, 1987	Cape Mendocino	5.5	28	17	0.14 [GC97] 0.096 [IA01] 0.089 [PE05]
Painter Street	Apr 25, 1992	Cape Mendocino/ Petrolia	6.4	24	15	0.54 [GC97] 0.472 [IA01] 0.550 [PE05]
Painter Street	Apr 26, 1992 After Shock 1	Cape Mendocino/ Petrolia	6.2	42	18	0.52 [GC97] 0.415 [IA01] 0.510 [PE05]
Painter Street	Apr 26, 1992 After Shock 2	Cape Mendocino/ Petrolia	6.4	41	21	0.26 [GC97] 0.206 [IA01] 0.196 [PE05]

[a] The differences between the given values in the case of the Painter Street Overpass may be a result of different directions for the corresponding accelerations. As the Painter Street Overpass is a skew bridge, the data also depends on whether the directions of the ground motion records are oriented on the bridge axis or on the skew direction.

Tab. 3.10: Overview of seismic events at instrumented overpasses in California

Werner, Beck and Levine [WBL87] performed *system identification*[13] on the Meloland Overpass response records for the 1979 Imperial Valley earthquake. They investigated two different subsystems consisting of (a) only the concrete structure (superstructure and pier) without abutment-embankment flexibility and (b) the entire bridge structure including the abutment-embankment system. From these analyses they concluded that the bridge structure without abutment flexibility had a significantly lower fundamental period of 0.27 s, compared to the period of the entire structure including the abutment flexibility which was estimated as 0.4 s. For the latter case they also computed a somewhat higher equivalent viscous damping of $\xi_{eq} = 7.2\%$, compared to $\xi_{eq} = 6.6\%$ for the concrete structure only.

The fundamental transverse mode shape for the superstructure in the entire bridge system, as determined by system identification, is shown in Fig. 3.62. Werner *et al.* concluded that the transverse response of the Meloland Overpass at this level of seismic excitation was mainly controlled by the motions of the abutments. While the structure provided only slight dynamic amplification of the transverse support motions, significant displacements occurred at the abutments. As a consequence, the abutments and embankments were seen to be the major contributors to the transverse response characteristics of the bridge.

---

[13] *System identification* is a systematic approach to find an equivalent linear elastic system with viscous modal damping that best represents the measured response. The resulting linear system is comparable to a model according to the *Substitute Structure Method* as proposed by Shibata and Sozen [SS76] (see Section 4.6.2*e*). It is characterized by an effective secant stiffness and an equivalent viscous damping ratio which are supposed to approximate the hysteretic behavior of the real inelastic structure.
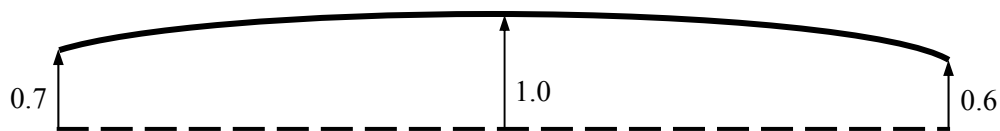
*Fig. 3.62: Fundamental transverse mode shape of Meloland Overpass
during 1979 Imperial Valley earthquake according to [WBL87]*

In a later study, Werner *et al.* [Wer+94] analyzed the Meloland Overpass again using system identification on the response records of the 1979 Imperial Valley earthquake. This time they used a somewhat more complex finite element model of the bridge and studied more sets of parameter assumptions. The general findings agreed well with the previous study [WBL87], resulting also in a fundamental period of the entire structure (including soil-structure interaction) of about 0.4 s, and similar fundamental mode shapes as the one shown in Fig. 3.62. A substantial difference between the results concerns the identified equivalent damping ratio ξ_{eq} for the entire structure including abutments and embankments. While the first study [WBL87] had identified a value of $\xi_{eq} = 7.2\%$, the later more detailed analyses [Wer+94] resulted in damping estimations in the range of $\xi_{eq} = 19\%$ to $\xi_{eq} = 26\%$. As will be discussed below, these higher values agree better with those found by other researchers and they are also more consistent with the strong influence of soil-structure interaction, especially at the abutments.

Wilson and Tan [WT90b] performed similar system identification analyses of the Meloland Overdrive embankment response during the 1979 Imperial Valley earthquake. This way they analyzed the dynamic characteristics of the embankment alone under seismic excitation. At first, they tried to find an equivalent linear system which would represent the inelastic behavior over 20 seconds of the strong motion record. The resulting solution gave fundamental periods T_{eff} for the two embankments in the range of 0.65 s to 0.69 s and equivalent viscous damping ratios ξ_{eq} as high as 43% to 62%. However, they found that the equivalent linear system could not describe the measured response very well, suggesting that the dynamic characteristics of the embankment changed during the earthquake.

Therefore, in a second analysis they performed the system identification on separate time windows of the record, having lengths of 4 seconds each. While the first and the third time window (0 to 4 s and 8 s to 12 s) contained low to medium shaking, the second time window (4 s to 8 s) represented the phase of most intense response. As can be seen in Tab. 3.11, during the strong shaking phase (4 s to 8 s) the effective period T_{eff} of the embankment increased considerably compared to the initial phase of lower excitation (0 to 4 s). This shows the significant softening of the soil at higher strains. It is interesting to see that after the strong shaking the embankment appears to recover large part of its initial stiffness again.

Time Window	North Embankment		South Embankment	
	T_{eff} [s]	ξ_{eq} [%]	T_{eff} [s]	ξ_{eq} [%]
0 to 20 s	0.68	62	0.65	51
0 to 4 s	0.41	55	0.38	47
4 s to 8 s	0.75	41	0.69	37
8 s to 12 s	0.48	31	0.49	47

*Tab. 3.11: Results of time window dependent system identification on the behavior of the embankments only
for Meloland Overpass during 1979 Imperial Valley earthquake [WT90b]*

Aside from the change in dynamic parameters discovered by the individual time window analysis, it was also found that the measure of fit between the equivalent linear system and the measured response improved significantly. While the equivalent linear system using constant parameters throughout the

longer 20 seconds record represented the measured behavior only moderately, the systems with the adjusted characteristics for every individual time window fit the measured response very well. This clearly shows that a single equivalent linear model has limitations in representing the real inelastic behavior at various levels of excitation occurring during an earthquake.

Generally, Wilson and Tan note that the equivalent viscous damping ratios they determined for the embankments are very high. Especially the values computed for the long time window (0 to 20 s) appears unreasonably high. It is further surprising that the equivalent viscous damping ratio found for the strong shaking time window (4 s to 8 s) is lower than that for the initial lower response phase (0 to 4 s). This is in contradiction to common understanding of soil behavior at increasing strains [SI70] (see also Fig. 3.68).

To study the influence of the damping ratio, Wilson and Tan conducted a sensitivity analysis on a linear elastic 2D finite element model of a cross-sectional embankment slice. They performed time history analyses for three different damping ratios of $\xi_{eq} = 43\%$, 25%, and 5% and found that for $\xi_{eq} = 43\%$ and 25% the computed behavior was quite similar to the measured response. In contrast, the lower damping ratio of $\xi_{eq} = 5\%$ resulted in a numerical behavior which deviated significantly from the recorded data, both in terms of peak displacement as well as response time history. Wilson and Tan concluded from these results that, due to the low sensitivity, the equivalent damping ratio cannot be determined with higher accuracy and recommended that for a comparable level of seismic excitation a value in the range of 25% to 45% (for the embankment only) might be reasonable. They compared this recommendation with standard curves for soil behavior at large strains by Seed and Idriss [SI70] which would result in damping ratios in the range of 10% to 30% for the determined average embankment shear strain of 0.7%. Wilson and Tan point out that these two ranges overlap, which they considered as a general confirmation of the values they found.

In addition to the system identification, Wilson and Tan [WT90b] conducted modal analysis on a comparatively simple elastic finite element model of the entire bridge representing the abutments as linear springs. From this analysis they found that in the fundamental transverse mode, the translations of the ends of the bridge deck contribute significantly to the total maximum displacement at the midspan. This is due to the relation between the stiffnesses of superstructure and abutments, which permits deformations in the first transverse mode to occur mainly in the abutment-embankment system. This subsystem consisting of abutment and embankment was found to be rather soft compared to the deck of such a short bridge. They concluded that a good estimation of the embankment soil properties (i.e. essentially the shear modulus) is crucial for the equivalent linear analysis as this represents the largest uncertainties.

In another study, McCallen and Romstad [MR94] performed analyses on the seismic behavior of the Painter Street Overpass during the 1986 Cape Mendocino earthquake and the 1992 Petrolia earthquake. For this purpose, they developed two different finite element models representing the entire bridge including abutment flexibility. The first system was a very simple linear stick model in which the abutments were modeled as elastic springs. In the second case, a detailed nonlinear 3D finite element model including soil-structure interaction was developed in which the superstructure was represented by shell elements and the embankment and foundation soils as 3D solid elements. Soil inelasticity was taken into account by transforming standard strain-dependent modulus reduction and damping curves by Seed *et al.* [SWI84] into a hysteretic shear stress-strain relationship based on the Ramberg-Osgood hysteresis rule.

The two models were used for a variety of analysis techniques ranging from simple modal analysis to complex inelastic time history analysis and the results were compared to the data from the response measurements on the real structure acquired during the corresponding earthquakes. From these analyses, McCallen and Romstad concluded a first order influence of the foundation and embankment soil on the seismic response of the bridge superstructure. In particular, they found that the dynamic behavior of the system becomes more sensitive to the soil stiffness when the soil becomes softer, as can be expected during strong earthquake shaking. In this case, the influence of the soil mass also becomes more pronounced. This can be interpreted in a sense that the stiff soil (at low strains) provides significant restraint for the abutments. As long as this restraint is given, a further increase of soil stiffness would not change the response much as the behavior will approach a quasi rigid behavior

asymptotically. However, at larger strains, differences in stiffness do change the dynamic behavior of the structure as they influence the flexible restraint provided by the abutments. In the same way, the soil masses do not have an influence as long as they do not experience significant motions. This changes at stronger excitations which are accompanied by softening of the soil.

Therefore, low level excitations of bridges, as e.g. related to ambient vibration measurements, are not appropriate to investigate the seismic characteristics of bridges – neither with respect to their natural periods nor concerning the mode shapes, as both will change at excitation levels corresponding to an earthquake. McCallen and Romstad used their complex 3D finite element model to study the influence of the soil shear modulus on the fundamental period of the entire system. They found out that the numerical period for a small strain shear modulus G_{max}, determined from the soil properties, agreed fairly well with the values observed by Gates and Smith from low amplitude ambient vibration measurements.

On the other hand, McCallen and Romstad had to reduce the soil shear modulus in their finite element model by more than 50% to compute the same fundamental period of the bridge structure as it was determined from the data of the recorded earthquake responses. A similar conclusion could be drawn from a comparison between recorded strong motion data with measurements by Werner, Beck and Nisar generated from low amplitude quick-release hydraulic ram excitation. Here, it was also found that mode shapes and periods differed between the two excitation levels. The period of the fundamental transverse mode was approximately 50% higher at the seismic excitation level, compared to the small amplitude measurements. Furthermore, the transverse modeshape at seismic excitation was dominated by embankment soil and abutment deformations, whereas the corresponding low-amplitude modeshape consisted of more prominent superstructure deformation with less abutment deformation.

Concerning the appropriate level of equivalent viscous damping, McCallen and Romstad concluded from their linear dynamic analyses that modal damping ratios in the order of 20% to 30% were required to represent the seismic responses during the 1986 and 1992 earthquakes adequately. These values, which are valid for the global modal damping of the entire Painter Street Overpass system including the soil embankment, are considerably higher than the comparable values identified by Werner, Beck and Levine [WBL87] based on their first system identification for the Meloland Overpass (see above). However, the damping ratios of McCallen and Romstad agree reasonably well with the corresponding values found in the second, more detailed, study by Werner *et al.* [Wer+94] which was also based on system identification. For comparison purposes, McCallen and Romstad also performed the same finite element analyses with a modal damping ratio of 5%, but found that the resulting numerical response did not comply with the recorded response from the real bridge, neither in terms of amplitude (which was overestimated) nor with respect to the frequency content.

Another approach for the analysis of the measured response of the Painter Street Overpass during seismic excitation was chosen by Goel and Chopra [Goe96], [GC97]. Assuming linear elastic behavior of the superstructure and the two-column bent at midspan, they used the recorded data from the 1986 Cape Mendocino earthquake and the 1992 Petrolia earthquake to calculate the displacement and acceleration responses of the bridge. Based on the dynamic differential equation of motion for the bridge system they back-calculated the force response time histories at the abutments, necessary to fulfill the differential equation at every time instant. They used the computed data to develop force-displacement hystereses of the abutments for the recorded earthquakes.

The resulting hysteretic behavior of the west abutment in the transverse direction during the entire earthquake is shown in Fig. 3.63. Based on this curve, Goel and Chopra estimated the maximum transverse capacity of the abutment as approximately 4.5 MN (1000 kips). They further attempted to determine effective secant stiffness values of the abutment at different deformation amplitudes. For this purpose they isolated individual hysteresis loops and approximated them by linear relationships up to peak response. In Fig. 3.64 the largest loop for the west abutment is shown together with the corresponding secant stiffness approximations in the positive and negative directions. Evaluating the calculated secant stiffness values and their relation to the corresponding displacement amplitudes resulted in the conclusion that the abutment stiffness varies with time and decreases significantly as the abutment deformation increases. This general, qualitative result agrees with the findings by other researchers (see above) using different analysis approaches.
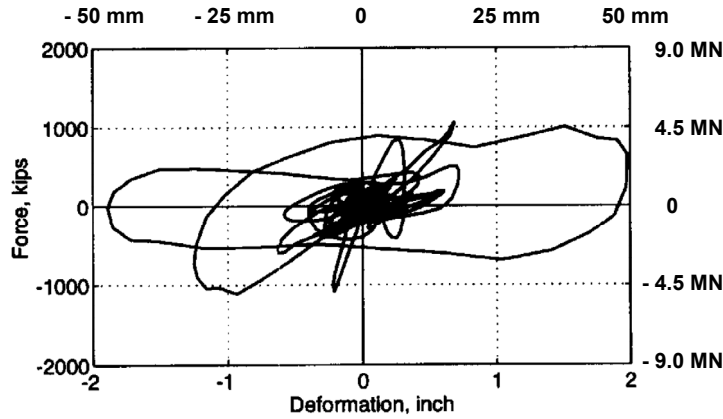
*Fig. 3.63: Force-displacement hystereses of west abutment at Painter Street Overpass
in transverse bridge direction during 1992 Petrolia earthquake [Goe96]*
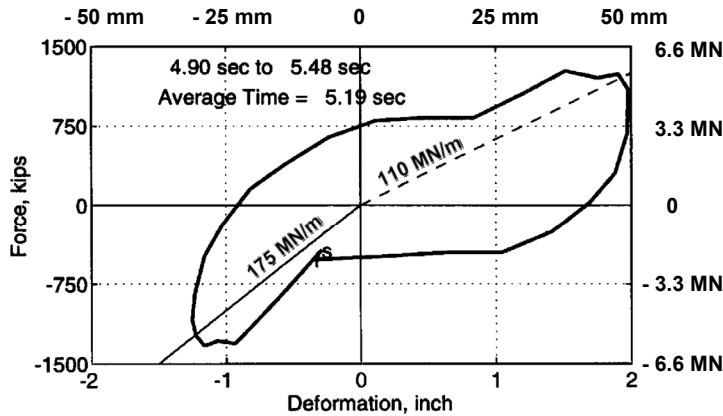
*Fig. 3.64: Isolated hysteresis loop of west abutment at Painter Street Overpass
in transverse bridge direction during 1992 Petrolia earthquake [Goe96]*

Inel and Aschheim [IA01] analyzed a total of seven earthquake responses recorded on the two aforementioned highway overpasses. They used a statistically-based technique called *Principal Component Analysis* (PCA) to identify the nonlinear response "mode" shapes from the measured earthquake motions. Their analysis results indicate that the bridge decks remained nearly undeformed for the seismic events with high peak ground accelerations (PGA), while in-plane deck deformations are more prominent for the cases with low PGA levels. They concluded from this finding that the deformation demands of the center bent are mainly dominated by the response of the embankments, particularly for stronger motions. These observations were found to be consistent with the general notion that the embankments are relatively stiff for small shaking intensities and soften considerably at higher response amplitudes.
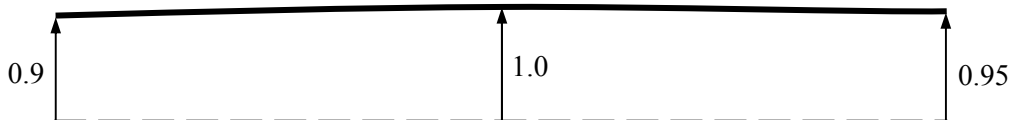
*Fig. 3.65: Fundamental transverse "inelastic mode shape" of Meloland Overpass
during 1979 Imperial Valley earthquake according to [IA01]*

The resulting inelastic mode shape determined by the *Principal Component Analysis* using the records of the Meloland Overpass during the 1979 Imperial Valley earthquake is shown in Fig. 3.65. It is noteworthy that the computed relative displacements of the abutments are even larger than those

determined by Werner, Beck and Levine [WBL87] using system identification for the very same case, shown in Fig. 3.62. The PCA results by Inel and Aschheim show an almost undeformed superstructure vibrating in a near rigid body translational mode. The determined abutment deformations are close to the top displacement of the column bent at midspan.

Finite element analyses of a short bridge model using different ways of abutment modeling, including an inelastic hysteretic abutment behavior, showed that the flexibility of the bridge embankment has a significant effect on the displacement demands sustained by the superstructure and the columns of short bridges, especially for strong excitations. In particular, Inel and Aschheim found that a rigidly pinned modeling of the superstructure support at the abutments would underestimate pier displacements of short bridges increasingly at higher intensities of shaking.

Zhang and Makris [ZM02] also performed various types of finite element analyses on the Meloland and Painter Street Overpasses. They studied both, the seismic behavior of the embankments only, as well as that of the entire bridge structures including soil-structure interaction at the abutments. Different levels of sophistication were applied for the modeling of the embankment behavior, ranging from a comparatively simple spring-dashpot damper representation up to a full 3D finite element model. The inelasticity of the soil was taken into account by the use of isotropic equivalent secant shear stiffnesses which were determined strain dependent from standard modulus reduction curves. The choice of the equivalent secant shear modulus was updated after the analyses as a function of the computed strains until convergence was reached.

They found reasonably good agreement between their numerical results using the converged shear stiffnesses and the recorded seismic responses of the real bridges and their embankments. Generally, the analyses confirmed the qualitative results of the other studies described above. In particular, Zhang and Makris emphasize that effective abutment stiffnesses during earthquakes are much lower and modal damping ratios much higher than those deduced from low-amplitude tests. They also point out that embankments – due to their mass and stiffness – reveal a significant dynamic earthquake behavior of their own, independent of the rest of the bridge structure. As a consequence, they amplify the free field motions noticeably and during moderately strong earthquakes embankments can reach (absolute) top displacements at their crest which are by a factor of 2 to 3 higher than the ground motions at their base. This means that a realistic representation of the soil-structure interaction at the abutments should not only comprise the embankment stiffness but rather the full dynamic characteristics, including the embankment mass and possibly its damping.

Summarizing the results of the studies mentioned above, it can be concluded that the seismic response of bridges can be influenced to a large degree by the behavior of the abutments and embankments. It may be noted that the concrete structure (bents and superstructure) of both overpass bridges discussed above were found to be essentially undamaged even after the most severe earthquakes that were recorded. Especially for short bridges the influence of soil-structure interaction at the abutments can have a dominating effect, where the response of the entire bridge can be controlled by the abutments at large seismic excitation levels. For longer bridges, it will particularly be the end zones of the superstructure and the outer piers that are influenced by the abutment response. In either case, disregarding the effects of soil-structure interaction at the abutments can give an erroneous picture of the seismic bridge behavior. For an appropriate representation of these effects it is necessary to take the inelastic behavior of the soil into account, e.g. by means of a deformation dependent equivalent linearization.

b) Modeling of Cyclic-Inelastic Soil Behavior

In the preceding subsection, it has been identified that for a realistic description of the seismic interaction at the abutments it is necessary to account for the inelastic behavior of the embankment soil. One way of doing so is the modeling of the full hysteretic behavior of the soil. Another simplified approach is the representation of the soil by its effective secant stiffness and an equivalent viscous damping. In the latter case, the stiffness is deformation dependent and the softening at increasing strain levels needs to be taken into account, possibly by iteration. Some of the studies on the two instrumented bridges mentioned in Subsection *a* used such an equivalent linearization of the systems,

including softening secant stiffnesses and corresponding viscous damping for the embankment soil. The soil parameters which were used or identified in these studies at increasing strain levels are summarized in Tab. 3.12.

		Meloland Overpass	**Painter Street Overpass**
		Imperial Valley Earthquake 1979	Petrolia Earthquake 1992
General Embankment Soil Description	Soil Type	Medium to stiff clay with traces of silt and sand [WT90b] Stiff clay [ZM02]	
	Plasticity Index I_p	5-10 [Ine02]	5-10 [IA04]
	Density ρ_s [kg/m^3]	1600 [WT90b] 1600 [ZM02] 1920 [Ine02]	1730 [IA04] 1600 [ZM02] 1760 [MR94]
Embankment Soil Parameters at Small Strains	Small Strain Shear Modulus G_{max} [MPa] [(a)]	7.2 [WT90b] 19.4 [ZM02] 76.8 [Ine02]	63.5 [IA04] 57.8 [ZM02] 75.8 [MR94] from borehole descriptions and standard formulas 55.2 [MR94] from seismic refraction studies by Heuze & Swift (1991)
	Poisson Ratio ν [-]	0.3 [WT90b]	0.4 [ZM02]
	Shear Wave Velocity $v_{s,max}$ [m/s] [(a)]	67 [WT90b] 110 [ZM02] 200 [Ine02]	190 [IA04] 190 [ZM02]
Embankment Soil Parameters at Large Seismic Strains	Effective Secant Shear Modulus G_{sec} [MPa]	2.4 @ γ_{avg} = 0.7% [WT90b] 1.5 @ γ_{avg} = 0.94% [ZM02] 2.2 @ γ_{avg} = 0.52% [ZM02]	9.4 @ γ_{avg} = 0.32% [ZM02] 7.8 @ γ_{avg} = 0.42% [ZM02]
	G_{sec}/G_{max} [-]	0.33 @ γ_{avg} = 0.7% [WT90b] 0.08 @ γ_{avg} = 0.94% [ZM02] 0.11 @ γ_{avg} = 0.52% [ZM02]	0.16 @ γ_{avg} = 0.32% [ZM02]
	Equivalent Viscous Damping Ratio ξ_{eq} [%]	25% - 43% @ γ_{avg} = 0.7% [WT90b] 28% @ γ_{avg} = 0.94% [ZM02] 26% @ γ_{avg} = 0.52% [ZM02]	24% @ γ_{avg} = 0.32% [ZM02] 25% @ γ_{avg} = 0.42% [ZM02]

[(a)] The values G_{max} and $v_{s,max}$ refer to the maximum shear stiffness of the soil corresponding to very small strains ($\gamma \leq 10^{-6}$).

Tab. 3.12: Material parameters of embankment soils at various strain levels
for Meloland Overpass and Painter Street Overpass as used by various researchers

In either case, be it a full hysteretic representation or an equivalent linearization, models are required which describe the response of the soil at various strain levels. Although a complete description of the soil as a 3-dimensional continuum with anisotropic inelasticity would generally require a sophisticated material model, an isotropic linear representation based on a standard modulus reduction relationship can already capture some of the most relevant effects for a simplified analysis. Several proposals for such modulus reduction relationships, in which the effective secant shear modulus is typically formulated as a function of the shear strain γ, can be found in the literature for different soil types [SI70], [SWI84], [SGS88]. A comprehensive summary on this issue is also given in [SK97]. Aside from the modulus reduction curves, these literature sources also provide curves for strain dependent

equivalent viscous damping ratios which, in connection with the modulus curves, serve as a basis for an equivalent visco-elastic linearization in the sense of the substitute structure method [SS76] (see Section 4.6.2*e*).

In Fig. 3.66 the ratio between the secant shear modulus G_{sec} at a certain strain level and the initial elastic shear modulus G_{max} is shown as a function of the shear strain corresponding to G_{sec}. The left curve refers to sand and also contains a range of expected values, while the curve on the right side of Fig. 3.66 is proposed for saturated clay [SI70]. If the shear modulus G_{max} at small strains ($\gamma \leq 10^{-4}$ %) is known from standard geotechnical examinations (or approximate equations[14]) the curves given in Fig. 3.66 can be used to estimate the softening behavior at increasing shear strain levels.

Generally, the ratio G_{sec}/G_{max} is subject to a considerable uncertainty and also depends on various parameters and the particular conditions of the soil. Two examples of influencing parameters and their effect are shown in Fig. 3.67 for clays. On the left side, the influence of the plasticity index I_p on the relative softening behavior is shown. It can be seen that increasing plasticity indices result in less relative softening at higher strain levels. On the right side of Fig. 3.67, the influence of the void ratio e on the shear modulus softening is shown in the same way, illustrating that lower void ratios result in more pronounced relative modulus softening.
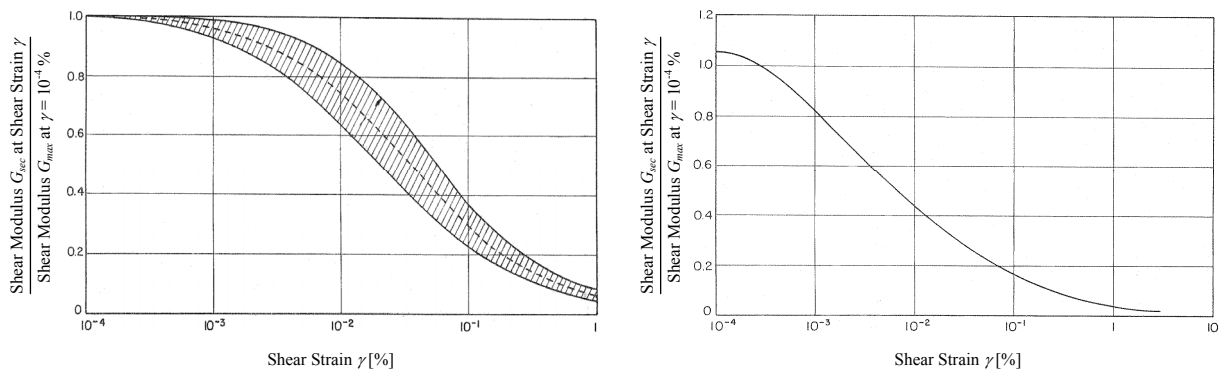
Fig. 3.66: Shear modulus ratio G_{sec}/G_{max} as a function of the shear strain γ according to [SI70]
Left: For sand, Right: For saturated clay
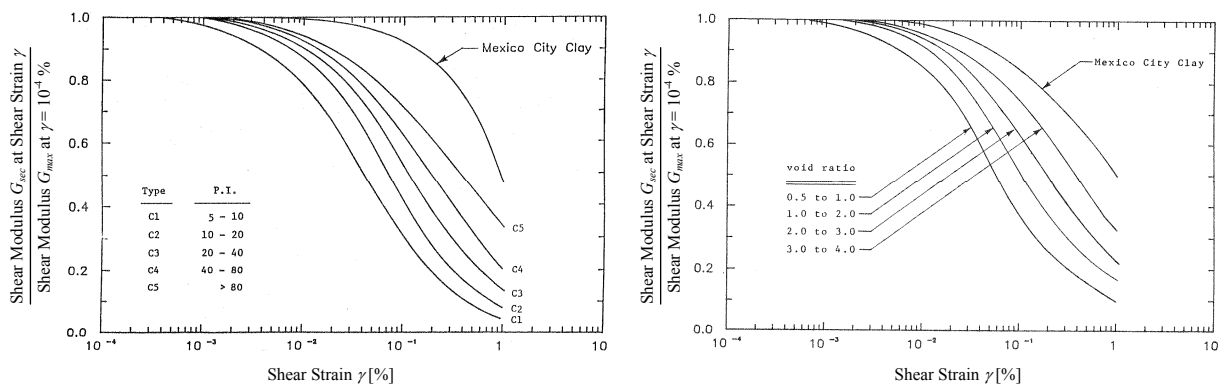
Fig. 3.67: Shear modulus ratio G_{sec}/G_{max} of clay as a function of the shear strain γ according to [SGS88]
Left: Influence of the plasticity index I_p (P.I.), Right: Influence of the void ratio e

Another parameter which is known to have an influence on the relative softening behavior of sand is the confining pressure. Increasing pressure typically reduces the relative modulus softening [SWI84]. For cohesive soils the confining pressure plays a significant role at low plasticity indices, while its influence diminishes almost completely at higher plasticity indices [SK97]. To some extent, the ratio

---

[14] The literature sources [SI70], [SWI84], and [SK97] also give some guidance on the estimation of the small strain shear modulus G_{max}.

G_{sec}/G_{max} also depends on the number of cycles during which the peak shear strain γ is being applied, with increasing cycle number resulting in more softening.

In Fig. 3.68 strain dependent equivalent viscous damping ratios ξ_{eq} for sand and saturated clay are given[15]. Together with the secant shear moduli according to Fig. 3.66 and Fig. 3.67 these damping ratios can be used for a representation of the soil by a linearized visco-elastic substitute structure. It can be seen that the range of observed values has quite a considerable bandwidth. In part, this is related to the general uncertainty and scatter in the description of the inelastic soil behavior. On the other hand, it is related to the fact that the equivalent damping ratio is not only a function of the shear strain. It can be assumed that the same parameters which influence the modulus reduction, as discussed above, also affect the damping behavior of the soil.

The equivalent viscous damping ratio has been found to be strongly dependent on the plasticity index I_p of cohesive soils, with increasing plasticity indices resulting in lower damping ratios [SK97]. An increase in the void ratio e, as well as a confining pressure, also tend to reduce the damping ratio ξ_{eq} of sands. Furthermore, it has been found that the damping ratio of dry clean sands is somewhat lower than that of saturated clean sands [SWI84].
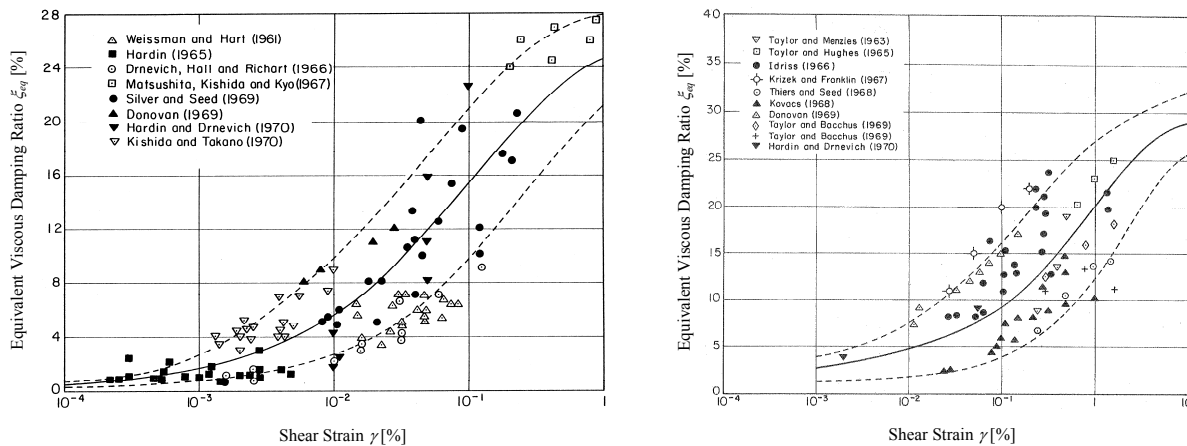
Fig. 3.68: Range of equivalent viscous damping ratios
Left: For sand according to [SWI84], Right: For saturated clays according to [SI70]

Taking into account that average shear strains in bridge embankments have been found to reach levels of around 0.3% to 1% (see Tab. 3.12) during moderate to stronger earthquakes, the presented curves show that significant softening as well as damping are likely to occur in such seismic events. The effective secant shear modulus G_{sec} can be reduced to as low as about 10% of the initial elastic shear modulus G_{max} at small strains. At the same time, the energy dissipation by the soil at these strain levels can reach equivalent viscous damping ratios of $\xi_{eq} = 20\%$ and more. These relationships emphasize the findings of Subsection *a* concerning the considerable inelasticity of the embankment soil and the subsequent need to take it into account for a realistic seismic analysis. As mentioned above, this can be done in a simplified manner by means of an equivalent linear visco-elastic representation using the secant shear modulus G_{sec} at a certain strain level. The corresponding equivalent viscous damping of the embankment can either be introduced as a weighted contribution to the global modal damping of the entire system, as in the substitute structure method [SS76] (see Section 4.6.2*e*), or for dynamic time history analysis a discrete dashpot damper can be modeled at the abutment to represent the local effects at the embankment in a more direct way. Some iteration may be required until the strain dependent equivalent visco-elastic parameters converge.

In reality the soil does not show a viscous – i.e. rate dependent – damping, but rather develops hysteretic loops under cyclic loading. In an inelastic time history analysis it is therefore more straightforward and more accurate to directly model this hysteretic behavior. Furthermore, this way of

---

[15] It should be noted that the given viscous damping ratios only refer to the soil at the embankments. When modeling a bridge structure including the embankments, it would not be correct to use this damping ratio on the entire bridge system.

soil representation does not require any iteration as the strain level directly influences the embankment response at every instant during a single analysis. In the same way as the real hysteretic soil response was converted for the development of the equivalent visco-elastic parameters given in Fig. 3.66 through Fig. 3.68, it is also possible to approximately re-transform the given relationships into hysteretic rules again.

As discussed in Section 4.5.2, depending on the type of excitation and dynamic response in the intended range of application, several approaches exist to convert hysteretic energy dissipation into equivalent viscous damping. When re-transforming an equivalent visco-elastic behavior into a hysteretic rule again, it is recommendable to use the same principles as applied for the initial conversion in order to prevent a distorting bias in the back and forth transformation process. Unfortunately, the literature sources of Fig. 3.66 through Fig. 3.68 do not state which concepts were used for the determination of the given equivalent viscous damping ratios. Due to the time of first publishing [SI70], it is assumed that the classical principles as suggested by Jennings (and also summarized by Chopra [Cho01]) were used.

This definition demands that the equivalent viscous damper should dissipate the same amount of energy in one cycle as a corresponding hysteresis loop of the original inelastic system. Assuming a steady state harmonic response of a linear system with secant stiffness G_{sec}, vibrating at its natural period, equation (3.29) can be deduced for the equivalent viscous damping ratio $\xi_{eq,hyst}$. The terms used in equation (3.29) are defined as shown in Fig. 3.69, with E_{hyst} being the energy (per unit volume) dissipated in one inelastic hysteresis loop to peak strain γ_{peak}. A further discussion on the assumptions underlying this approach to determine an equivalent viscous damping ratio can be found in Section 4.5.2.

$$\xi_{eq,hyst} = \frac{E_{hyst}}{4\pi \cdot E_{elast}} = \frac{E_{hyst}}{2\pi \cdot \tau_{peak} \cdot \gamma_{peak}} \qquad (3.29)$$
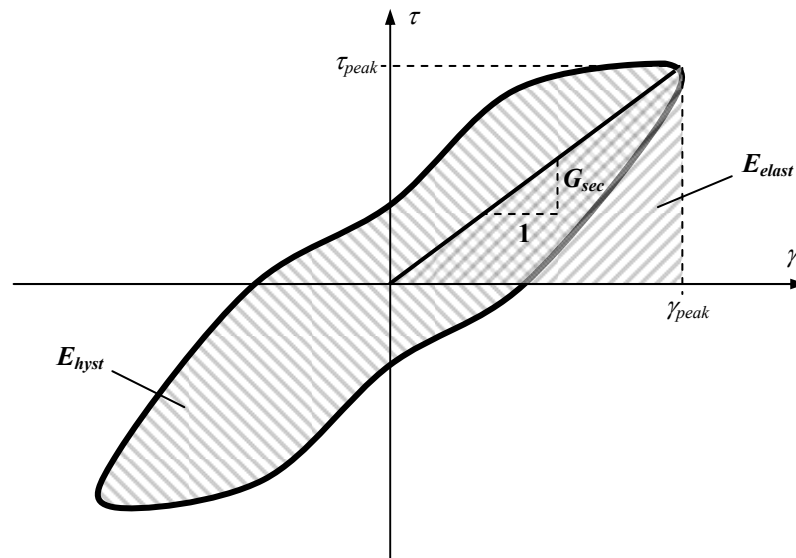
Fig. 3.69: Definition of hysteretically dissipated and elastic energy for a single hysteresis loop

To develop a hysteretic soil representation, the stiffness and energy dissipation characteristics should comply with the relationships shown in Fig. 3.66 through Fig. 3.68 (or other comparable curves). The left side of Fig. 3.70 shows the average G_{sec}/G_{max} vs. γ curve of Fig. 3.66 (left) by Seed and Idriss [SI70] for sand using linearly scaled axes. On the right side of Fig. 3.70, this relationship is converted into a shear stress vs. shear strain curve which can be interpreted as the target backbone of a hysteretic material representation. In Fig. 3.71, two possible hysteretic models are presented which were calibrated to approximate the visco-elastic behavior given by Seed and Idriss. On the left side, a modified Takeda rule has been used and the right side is based on a Ramberg-Osgood hysteresis. Both cases use the definitions of the implementation in the software code Ruaumoko [Car04].
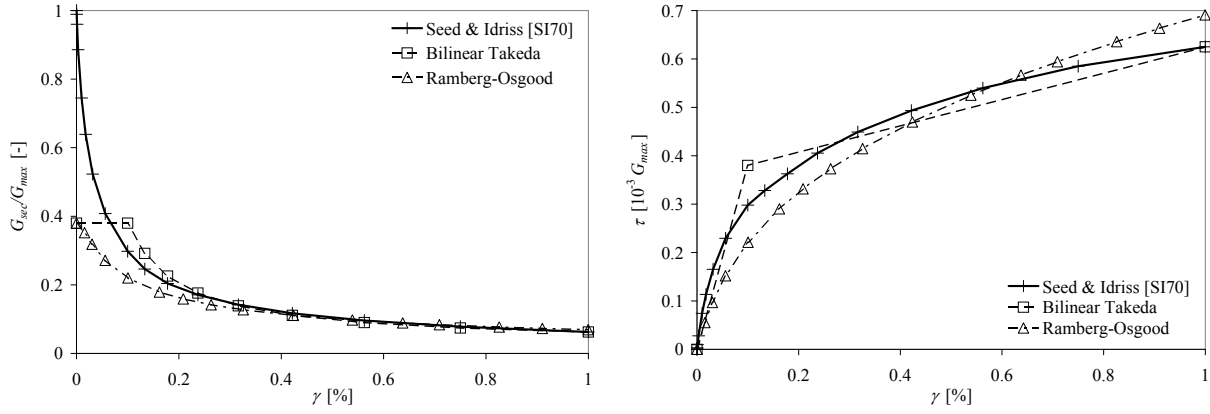
Fig. 3.70: Average strain dependent shear stiffness of sand
Left: Shear modulus ratio G_{sec}/G_{max} from [SI70] and from two numerical hysteresis approximations
Right: Backbone of inelastic shear behavior corresponding to [SI70] and to two hysteresis approximations
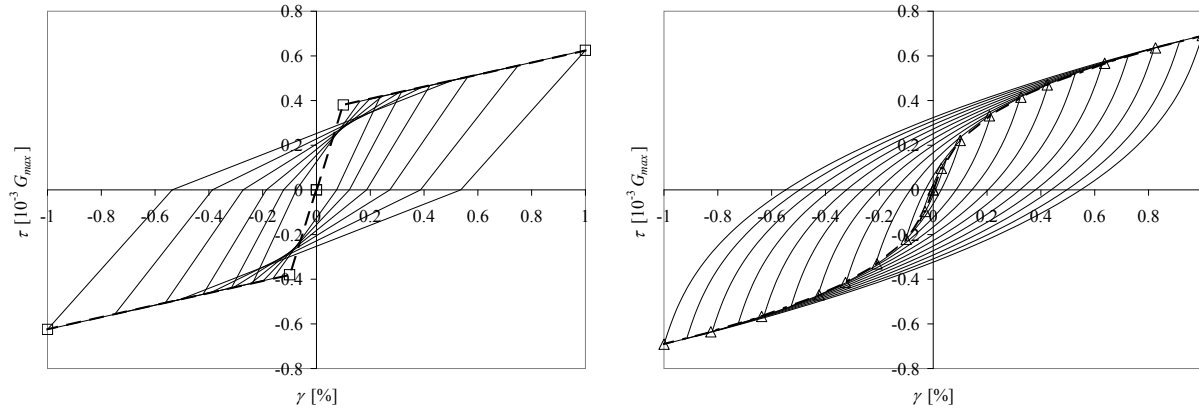
Fig. 3.71: Numerical hysteresis loops to approximate cyclic-inelastic shear behavior of sand
Left: Modified Takeda rule, Right: Ramberg-Osgood rule

For the modified Takeda model, the chosen backbone is defined by a yield strain of $\gamma_{y,Tak} = 0.1\%$, a yield stress of $\tau_{y,Tak} = 0.38 \cdot 10^{-3} G_{max}$ and a post-yield to initial stiffness ratio of $r_{Tak} = 0.072$. This results in an initial shear stiffness of $G_0 = \tau_{y,Tak}/\gamma_{y,Tak} = 0.38\,G_{max}$ for the bilinear representation of the Takeda backbone. The hysteretic unloading and reloading stiffnesses are defined by the corresponding chosen parameters as $\alpha_{unload} = 0.45$ and $\beta_{reload} = 0.55$ (see [Car04]). The hysteretic energy dissipation therefore lies between that of "thin" ($\alpha_{unload} = 0.5$ and $\beta_{reload} = 0$) and that of "fat" ($\alpha_{unload} = 0.3$ and $\beta_{reload} = 0.6$) Takeda loops, as suggested in [PCK07] for reinforced concrete columns and beams, respectively.

The Ramberg-Osgood model is defined by three parameters, the tangent stiffness $G_{tan,0}$ in the origin, the effective first yield stress $\tau_{y,RO}$, and the Ramberg-Osgood factor r_{RO} which controls the stiffness degradation with increasing deformations[16]. These parameters were chosen as $G_{tan,0} = 0.38\,G_{max}$, $\tau_{y,RO} = 0.27 \cdot 10^{-3} G_{max}$, and $r_{RO} = 2.6$. It should be mentioned that the original Ramberg-Osgood model, although describing large cycles well, can result in an inappropriate modeling of small cycles as these can leave the area bounded by the large cycles in some cases. For this reason, two modified Ramberg-Osgood rules were implemented into the software code Ruaumoko [Car04] which bound the small cycle response to the large cycle limits. Especially the implemented modification by Pyke which was developed for the modeling of soil behavior may be a worthwhile improvement to the original Ramberg-Osgood model. The changes do not influence the large cycle response so that the loops shown in Fig. 3.71 (right) remain the same for any of the mentioned versions of the Ramberg-Osgood rule.

---

[16] The Ramberg-Osgood factor r_{RO} is not related in any sense to the previously defined post-yield stiffness factor r_{Tak} used for the bilinear backbone of the modified Takeda rule.

3.5 Soil-Structure Interaction

For the two hysteretic models presented in Fig. 3.71 a related stress-strain backbone as well as a G_{sec}/G_{max} vs.γ curve can be computed. These curves are compared in Fig. 3.70 to the corresponding target relationships proposed by Seed and Idriss [SI70] for sand. In a similar way, strain dependent equivalent viscous damping curves can be computed for both hysteretic models using equation (3.29). The resulting relationships are compared in Fig. 3.72 to the corresponding target curve from Fig. 3.68 (left) using linearly scaled axes.
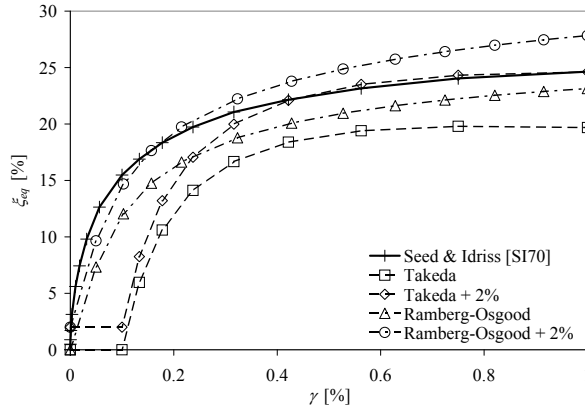
Fig. 3.72: Comparison between strain dependent equivalent viscous damping ratios
according to [SI70] and those corresponding to numerical hysteresis approximations

Normally, in dynamic analysis, aside from the hysteretic energy dissipation, a certain amount of elastic viscous damping is taken into account additionally in order to represent secondary damping effects not included in the inelastic model (see Section 4.4.1). Assuming that the target curve by Seed and Idriss already includes all relevant damping effects of the embankment part of the structure, it would be more appropriate to compare it to the sum of elastic and equivalent hysteretic damping, as defined in equation (3.30). As damping ratios refer to the critical damping coefficient c_{cr} which depends on the (secant) stiffness, the elastic viscous damping ratio needs to be modified as shown in equation (3.31) in order to model the same damping coefficient c at all strain levels. The resulting total equivalent viscous damping curves, based on equation (3.30), are also shown in Fig. 3.72, using an initial stiffness related elastic viscous damping ratio of $\xi_{el,0} = 2$ %.

$$\xi_{eq,tot}\left(\gamma\right) = \xi_{eq,hyst}\left(\gamma\right) + \xi_{el}\left(\gamma\right) \tag{3.30}$$

$$\xi_{el}\left(\gamma\right) = \xi_{el,0} \cdot \sqrt{\frac{G_0}{G_{sec}\left(\gamma\right)}} \tag{3.31}$$

with G_0:   Initial elastic shear modulus as modeled in the hysteretic model

      $G_{sec}(\gamma)$:   Secant shear modulus at shear strain γ

      $\xi_{el,0}$:   Elastic viscous damping ratio related to a critical damping coefficient based on the initial stiffness G_0

      $\xi_{el}(\gamma)$:   Elastic viscous damping ratio related to a critical damping coefficient based on the secant stiffness $G_{sec}(\gamma)$

From the comparisons shown in Fig. 3.70 and Fig. 3.72, it can be seen that the two hysteretic models shown in Fig. 3.71, using the chosen sets of parameters, result in a reasonable approximation of the target stiffness and damping curves by Seed and Idriss over a large range of shear strains. Especially, taking the uncertainties of the original curves in Fig. 3.66 and Fig. 3.68 into account, the deviations of the hysteretic models can be considered to lie within the range of experimental scatter for strain levels which are typical for moderate to stronger earthquakes (see Tab. 3.12). Only the modified Takeda hysteresis loops result in a significant underprediction of the damping at low shear strains ($\gamma \leq 0.2$%). This is related to the fact that the Takeda rule does not develop any hysteretic behavior in the elastic

range[17], i.e. in the presented example for $\gamma \le 0.1\%$. Although conservative, this deficiency may represent a certain drawback if large part of the seismic response takes place in this strain range. In this case, either the use of the alternative Ramberg-Osgood model or a different calibration of the Takeda rule, using a lower yield strain, may be a possible solution.

The Ramberg-Osgood hysteresis rule results in a comparatively good approximation of the target curves for stiffness and damping over the entire range of shear strains shown in Fig. 3.70 and Fig. 3.72. Here, hysteresis loops with corresponding energy dissipation already develop at very small strain levels, which results in a similar shape of the equivalent viscous damping curve compared to that of the target curve by Seed and Idriss. Generally, it can be said that, with an appropriate calibration of the parameters, the Ramberg-Osgood rule allows an almost perfect representation of either the target curve for stiffness or that for damping (Fig. 3.70, Fig. 3.72). Only if a possibly good approximation of both curves, stiffness and damping, is aspired, some compromise needs to be made. However, if e.g. a good representation of stiffness is considered more important for the response, some trade-off can be made between less damping accuracy for an improved stiffness representation. Nevertheless, in the majority of cases, an approximation as that shown in Fig. 3.70 and Fig. 3.72 will be satisfactory, taking the general uncertainties in soil modeling into account.

It can be concluded that the Ramberg-Osgood model may be somewhat more suitable for the representation of hysteretic soil behavior than the modified Takeda hystereses. This may also be the reason why McCallen and Romstad [MR94] used the Ramberg-Osgood rule for the embankment soil in their inelastic 3D finite element model of the Painter Street Overpass. However, if this type of hysteretic behavior is not implemented in a specific software code to be used, the modified Takeda rule – or another comparable hysteretic model – can also yield good results if the parameters are chosen properly to represent the stiffness and damping characteristics in the strain range of interest. Independent of the chosen type of hysteretic rule, it is always recommendable to calibrate the required parameters for a strain range which is not significantly larger than the actually expected deformations because increasing the calibration range inevitably results in less accurate approximations at the local level (see Section 3.5.1e and Fig. 3.51 for a similar discussion in the context of spread foundations). A somewhat less accurate representation can, of course, also be reached with the equivalent visco-elastic representation discussed before, in which the abutment is modeled using a linear elastic secant stiffness and a corresponding equivalent viscous damping.

c) General Approaches for the Modeling of Seismic Abutment Behavior

Assuming that for the response the largest part of the abutment displacements is related to rigid body movements of the concrete structure embedded in the embankment soil, generally six degrees of freedom exist – 3 translational motions and 3 rotations. When focusing on the abutment's influence on the global bridge behavior, i.e. especially on the displacement demands of the piers, the abutment rotations will normally be of subordinate importance. In the majority of cases, the vertical abutment response will also only be of secondary interest. Therefore, mainly the horizontal translational abutment behavior is required for the modeling of the bridge system including soil-structure interaction. Typically, the displacements at a height corresponding to the superstructure level are considered which allows disregarding the corresponding abutment rotations for the interaction with the superstructure. Although in some simplified approaches the longitudinal and transverse abutment behavior is treated in a similar way, with respect to some influencing effects significant differences may exist between the two response directions.

Aside from complex 3D continuum soil modeling approaches using inelastic finite element analysis, a variety of simplified methods for the abutment representation have been proposed in codes and literature, ranging from simple linear elastic springs to either visco-elastic or inelastic systems.

---

[17] The linear elastic behavior of the Takeda rule at small strains occurs only before the yield strain has been reached. Once the response has entered into the inelastic range during a previous cycle, even at small strains hysteretic energy dissipation will result. Therefore this drawback of the Takeda rule is likely to be limited to the initial phase of an earthquake, while during and after the strong shaking phase a more realistic representation of the hysteretic behavior will take place.

Furthermore, the possible introduction of a (tributary) embankment soil mass into the dynamic bridge model appears reasonable. However, it is not considered explicitly in all the approaches, and if so, it is not always treated in the same way. The existing models do not only vary in the types of simplifications they introduce for the estimation of the abutment stiffness, but can also differ fundamentally in the underlying concepts concerning the deformation mechanisms and thus the sources of abutment displacements.

Two general approaches can commonly be found in the literature for the simplified description of the abutment deformation behavior: (i) The abutment is considered as a rigid body being pushed horizontally into a soil continuum, with the corresponding displacements being related to the passive soil pressure-deformation behavior. The second notion, (ii), assumes that the abutment is a rigid block embedded into the embankment and performing the same motions as the embankment crest. In this case, the abutment displacements are not considered as movements *relative* to the soil, but rather *with* the soil, i.e. they are the result of deformations of the embankment as a whole. These deformations can be induced, on one hand, by interaction forces from the superstructure, while also being the result of (independent) vibrations of the soil masses, as the embankment also represents a dynamic system by its own which is excited by the earthquake ground motions.

The fundamental difference between the two conceptual modeling approaches shows the considerable amount of uncertainty which exists with respect to the seismic behavior of abutments. This discrepancy can further be illustrated by the fact that a quantification of stiffness characteristics will depend on completely different geometric parameters for the two cases. While interpretation (i) requires primarily the (effective) dimensions of the concrete wall that is pushed into the soil continuum, the second approach (ii) depends only on the geometry of the embankment. These model uncertainties add to the scatter related to the description of the cyclic inelastic behavior of the soil and thus result in rather vague estimations of abutment stiffnesses. Zhang and Makris [ZM02] conducted a comparison of stiffness estimations for three different abutments based on a variety of 13 approaches, using the same soil characteristics for every model. They ended up with a range larger than a factor of 10 between the highest and the lowest estimation. In some extreme cases, the discrepancy was even larger than a factor 100, which illustrates the substantial uncertainties related to the estimation of abutment stiffnesses.

Generally, it can be assumed that the real deformation behavior of an abutment-embankment system is not only the result of either of the two phenomena mentioned above, but will rather be related to the combination of both. This means that the abutment displacements are a result of motions relative to the embankment as well as deformations of the embankment itself. At the same time, the deformation behavior of the embankment is also influenced by the presence of the concrete abutment being embedded into the soil. The relative relevance of these various effects is likely to depend on the individual conditions, but can also be expected to differ between the directions of loading. For example, in the longitudinal bridge direction the displacements of the abutment relative to the embankment may be rather dominant. On the other hand, the significant dynamic motions of the embankment in the transverse direction measured on real bridges (see Subsection *a*) suggest that in the transverse direction the motion of the embedded abutment together with the embankment is likely to be more dominant.

In the following subsection the seismic behavior of the abutment-embankment system in the transverse bridge direction is discussed. Following the above considerations, a simplified engineering model will be presented which is based on the assumption that the dynamic embankment motions are dominant over the other effects and that the abutment is following these motions being embedded in the soil. Disregarding the relative displacements of the abutment with respect to the embankment can result in a certain over-prediction of the transverse abutment-embankment stiffness. On the other hand, disregarding the stiffening effect of the concrete abutment on the deformation behavior of the soil embankment will rather cause an under-prediction of the system stiffness. As a consequence, these two approximations counteract to each other to some extent. At the same time, as will be further discussed in the following subsection, any engineering model for the seismic abutment behavior will be prone to considerable uncertainties – both related to the soil behavior and to the model itself. The consequently necessary sensitivity analyses should also cover the approximations mentioned above.

The modeling of the abutment behavior in the longitudinal bridge direction is beyond the scope of this document.

d) Estimation of Transverse Abutment Stiffness Based on Embankment Behavior

Several authors have presented embankment models for the response in the transverse direction which are based on a simplified representation of pure shear deformations [WT90a], [ZM02], [IA04]. For this purpose, a tributary length L_c of the embankment is considered as shown in Fig. 3.73. When applying a transverse horizontal load F_{trans} at the top of this truncated wedge, it is assumed that it deforms exclusively due to horizontal shear stresses as shown in Fig. 3.74. The embankment is thus subdivided into horizontal layers with changing cross-sections and infinitesimal height dz, which experience individual shear strains $\gamma(z) = \tau(z)/G_{sec}$. By integrating these strains over the height H of the embankment, the top displacement u_{Top} corresponding to F_{trans} can be calculated, and subsequently a substitute spring stiffness $K_{trans} = F_{trans}/u_{Top}$ can be defined.
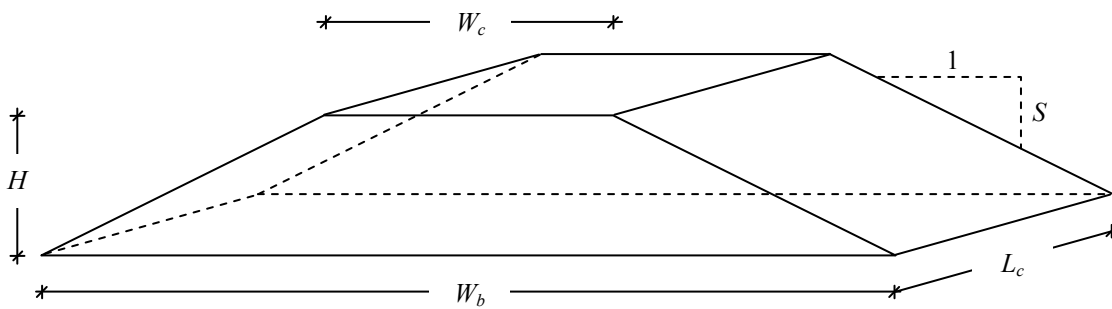
Fig. 3.73: Truncated shear wedge as 3 dimensional model of tributary embankment length
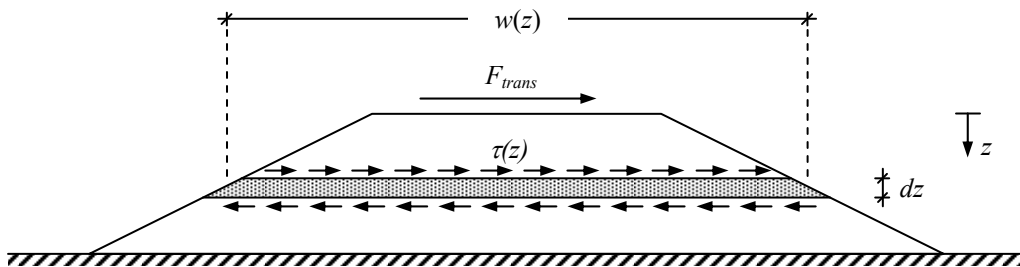
Fig. 3.74: Shear stresses in truncated shear wedge due to horizontal force at embankment top

Wilson and Tan [WT90a] have solved this problem analytically and present equation (3.32) for the transverse stiffness of an embankment with unit length. Zhang and Makris [ZM02] used the same general basis to deduce complex dynamic stiffnesses representing a linear elastic spring and a viscous dashpot damper. The corresponding equation is not quoted here as it requires the computation of the mathematical Bessel function and it may therefore be of limited use for practical applications in an engineering office. Zhang and Makris state that, if only the elastic stiffness is needed, their solution is equal to that of Wilson and Tan given in equation (3.32). In this text, energy dissipation of the embankment will rather be treated by hysteretic soil behavior as discussed in Subsection *b*, so that the more demanding computation of dashpot damper characteristics according to [ZM02] is unnecessary.

$$\hat{k}_{trans} = \frac{K_{trans}}{L_c} = \frac{2G}{S \cdot \ln\left(1 + \frac{2H}{S \cdot W_c}\right)} \tag{3.32}$$

Inel and Aschheim [IA01], [Ine02], [IA04] use the same general concept as Wilson and Tan to model the stiffness of the embankment. Instead of developing an analytical solution, they use discrete horizontal layers of finite thickness Δz. Each layer is represented by a lumped mass and a horizontal shear spring with a corresponding hysteretic rule. This way, the cyclic behavior and the dynamic characteristics of the embankment can be modeled. Generally, the monotonic stiffness according to Inel and Aschheim's approach will converge for decreasing layer thicknesses towards the analytical solutions by Wilson and Tan [WT90a] or Zhang and Makris [ZM02].

However, it should be noted that Inel and Aschheim define the deformable height of the embankment differently than the other authors. While the model according to [WT90a] and [ZM02] is based on the assumption that the abutment stiffness is related to the deformations over the entire embankment height H, Inel and Aschheim propose that the reinforced concrete abutment has a significant stiffening effect. Therefore, they suggest that over the abutment height the embankment should be modeled as rigid and only the soil deformations underneath the abutment should be used to calculate the system stiffness in the transverse direction. As a consequence, the stiffness estimation would have to be performed with a reduced embankment height $H' = H - h_{abutment}$ and a modified crest width which corresponds to the embankment width at the bottom edge of the abutment.

Although a certain stiffening effect of the abutment on the embankment deformation behavior cannot be ruled out, caution appears justified with respect to this modeling assumption. If the deforming force is introduced into the embankment via the abutment, then it is likely that not only abutment displacements *with* the soil occur, but rather also *relative to* the soil as a consequence of passive soil pressure-deformation behavior. This softening effect, which is contrary to the stiffening effect according to Inel and Aschheim, is not taken into account in the simplified shear wedge representation of the embankment. It might therefore be inappropriate – and for the adjoining piers possibly unconservative – to only model an additional stiffening effect without allowing for a counteracting softening aspect. The presented shear wedge model of the embankment can only be considered as a significant simplification of the real behavior. Any attempt for improvement should therefore be based on an integral analysis of additionally existing effects and their consequences to make sure that any possible modifications do not change the model in the wrong direction. As such modifications are beyond the scope of this text, the following discussion will be based on the shear wedge model with the full embankment height, and the stiffness estimation according to equation (3.32).

To calculate the transverse stiffness K_{trans} of an abutment, the unit stiffness given in equation (3.32) needs to be multiplied by a tributary embankment length L_c defining the part of the embankment which is effective in resisting horizontal loads introduced by the abutment. Wilson and Tan [WT90a] suggest using the embedded length of the abutment wing walls as L_c. Zhang and Makris [ZM02] discuss two possible formulations for L_c. The first proposal, given in equation (3.33), is based on a simplified analytical model of unit-width embankment slices interacting among each other in shear. The second approach consists of an empirical equation that has been calibrated on the results of 3D finite element analyses and is given in equation (3.34).

$$L_c = \frac{\sqrt{2}}{2} \cdot \sqrt{A \cdot S \cdot \ln\left(1 + \frac{2H}{S \cdot W_c}\right)} \qquad (3.33)$$

with $\qquad A = H \cdot \left(W_c + \frac{H}{S}\right) \qquad$ Area of embankment cross-section

$$L_c \approx 0.7 \sqrt{S \cdot W_c \cdot H} \qquad (3.34)$$

Inel and Aschheim [IA04] also give recommendations for the appropriate choice of L_c, which are the result of an empirical calibration procedure. They performed dynamic finite element analyses on models of the Meloland and Painter Street Overpass incorporating their abutment spring models and using a variety of values for the effective embankment length L_c. The analyses were conducted with measured ground motions of real earthquakes at the two bridges. For the calibration, the finite element results were compared to the corresponding recorded responses of the real bridges. Based on the rather

limited data set, Inel and Aschheim found that the best fit values for L_c depend on the intensity of seismic embankment response. For low intensity shaking, corresponding to crest amplitudes in the range of 0.2% to 0.5% of the reduced embankment height H' (see above), they recommend a best-fit length of $L_c = 8$ m. For moderate embankment amplitudes up to 1% of H', they found a lower value of $L_c = 4$ m. Additionally, they suggest lower boundary values of the effective embankment length, e.g. for conservative estimations of the displacement demand of adjoining piers. These lower bound embankment lengths are one half of the corresponding best-fit values for low and moderate shaking, respectively.

Another method for the estimation of an effective embankment length L_c has been proposed by Price and Eberhard [PE05]. Similar to the approach by Zhang and Makris [ZM02] for the deduction of equation (3.34), Price and Eberhard also used calibration on a 3D finite element model of the embankment to develop their relationships for L_c. While for the development of equation (3.34) the finite element model incorporated a constant linear elastic (secant) stiffness throughout the entire embankment, the model of Price and Eberhard [PE05] used varying secant stiffnesses based on standard modulus reduction curves and depending on the local strain level. As such, the latter model was able to capture varying stiffness distributions within the embankment as a result of soil inelasticity and corresponding changes of effective embankment length as a function of the deformation level.

Price and Eberhard recommend equation (3.35) for the estimation of the effective embankment length $L_{c,0}$ at very small deformation levels, in which the soil modulus is still essentially the same at every location. They found that the corresponding value L_c at higher deformation levels can be reduced significantly and propose an iterative procedure to estimate an appropriate value of L_c depending on the deformation level and the geometry of the embankment and the abutment. In this procedure, L_c corresponding to higher strains is estimated based on equation (3.36). As the abutment stiffness K on the right side of equation (3.36) depends on the resulting value for L_c, the relationship can be evaluated only iteratively for every individual strain level.

$$L_{c,0} = \left(2.0 + 0.53H\right)\left(\frac{W_c}{H}\right)^{0.15} \qquad \text{with } H,\ W_c \text{ in [m]} \qquad (3.35)$$

$$\frac{L_c}{L_{c,0}} = \frac{K}{K_{max}} + \ln\left(1 + \alpha_s\right)\left[\frac{1}{\alpha_s} - \frac{1}{\dfrac{K}{K_{max}}\sqrt{1+\alpha_s} - 1}\right] \qquad (3.36)$$

with K_{max} abutment stiffness at very low strains, corresponding to $L_{c,0}$
              K abutment stiffness at increased strain level, as a function of L_c
              α_s parameter depending on abutment and embankment geometry

It is interesting to note that, although the recommended relationships for the deformation dependent $L_c/L_{c,0}$ ratio, given in equation (3.36), have been deduced from a mechanical model without explicit empirical calibration, Price and Eberhard [PE05] discover a quite similar qualitative trend as Inel and Aschheim [IA04] with their purely empirical trial-and-error analyses. While Inel and Aschheim suggest a reduction of 50% for L_c when the shear strain of the soil is increased from a low range of 0.2-0.5% to a moderate level of 1%, the relationship by Price and Eberhard results in a continuous reduction of L_c. With respect to the value for very small strains ($\gamma \leq 10^{-6}$), relationship (3.36) can result in a decrease of more than 75%, depending also considerably on the geometry parameter α_s. For common geometric configurations, the approach by Price and Eberhard yields a 50% reduction of L_c, compared to $L_{c,0}$, at a stiffness ratio K/K_{max} in the range of 0.25. Taking into account that K/K_{max}, is a function of shear modulus reduction and decrease of L_c, a ratio of $K/K_{max} \approx 0.25$ is not unrealistic when increasing the shear strains from low 0.3% to moderate 1%. Therefore, the approach by Price and Eberhard [PE05] and the empirical findings by Inel and Aschheim [IA04] with respect to the reduction of the effective embankment length L_c generally support each, although some uncertainty will surely be included in the quantification of this phenomenon.

3.5 Soil-Structure Interaction

Generally, it should be noted that the empirical recommendations for L_c by Inel and Aschheim were calibrated in combination with their approach for the unit length shear wedge stiffness, based on a rigid embankment behavior over the height of the abutment. It would therefore be inconsistent to use their effective length proposals in combination with equation (3.32) but without the assumption of rigid response over the abutment height. Equation (3.32) should therefore rather be used in conjunction with the recommendations by Wilson and Tan [WT90a], Zhang and Makris [ZM02] or Price and Eberhard [PE05].

Wilson and Tan's proposal of setting L_c equal to the embedded length of the wing wall is not really mechanically deduced, but rather based on engineering judgment. Therefore, one of the other models that were either calibrated on 3D finite element analyses or deduced from mechanical considerations may be a little more soundly based. The approach by Price and Eberhard allows for the most influencing factors. However, due to its complexity and, especially, its iterative character, the required effort may not be justified in many practical cases. Instead, the two equations (3.33) and (3.34) by Zhang and Makris also give mechanically based solutions, but these do not require additional iterations and can be kept constant for any deformation level – and thus throughout a dynamic analysis.

As Zhang and Makris themselves rather recommend the use of equation (3.34) instead of (3.33), this recommendation is being followed here. For common geometric configurations, it is likely that at small strain levels the constant estimation of L_c according to equation (3.34) will result in somewhat smaller values for the effective embankment length than the variable solution based on equations (3.35) and (3.36). On the other hand, at higher deformation levels the approach by Price and Eberhard would yield somewhat lower effective embankment lengths than the proposal by Zhang and Makris, as the ratio $L_c/L_{c,0}$ in equation (3.36) decreases with increasing strains. In the light of the general uncertainties of the soil and embankment modeling, the expression according to equation (3.34) is nevertheless likely to give acceptable reasonable approximations which may be sufficient in many cases. For special structures, where the seismic abutment behavior has a dominant effect on the bridge response, a more sophisticated approach, possibly using the relationships of equations (3.35) and (3.36), might be justified.

Using equation (3.34) for L_c, the transverse abutment stiffness K_{trans} can then be estimated together with equation (3.32). These two expressions can also be summarized in the single equation (3.37). An alternative representation is given in equation (3.38), where the expression is split up into a purely geometry dependent term β and the shear modulus G standing for the material behavior of the soil which can vary as a function of the deformation level.

$$K_{trans} = \hat{k}_{trans} \cdot L_c = \sqrt{\frac{W_c \cdot H}{S}} \cdot \frac{1.4}{\ln\left(1 + \frac{2H}{S \cdot W_c}\right)} \cdot G \tag{3.37}$$

$$K_{trans} = \beta \cdot G \tag{3.38}$$

$$\text{with} \quad \beta = \sqrt{\frac{W_c \cdot H}{S}} \cdot \frac{1.4}{\ln\left(1 + \frac{2H}{S \cdot W_c}\right)}$$

It may be noted that in many cases the recommendations for L_c given in [WT90a], [ZM02], and [IA04] are likely to result in values which are at least in the same order of magnitude. The resulting range of values, which may easily have a bandwidth of a factor of 2, can to some extend also be interpreted as an indication of the inevitable model uncertainty associated with the stiffness estimation of the abutment.

As the model is based on deformations of the embankment, the motion of the corresponding embankment soil must also be accompanied by inertia effects of these masses. The exclusive modeling of abutment stiffness without allowing for a tributary embankment mass would therefore not describe

the real structural characteristics adequately. While the model used by Inel and Aschheim [IA04] automatically takes the soil mass into account, the proposal by Wilson and Tan [WT90a] as well as that by [ZM02] do not allow for soil inertia. However, in [WT90a] equation (3.39) is given for the estimation of the fundamental frequency of a unit width shear wedge slice. If the embankment (isolated from the bridge structure) is interpreted as an equivalent single-degree-of-freedom system in the transverse direction, the fundamental frequency relates the stiffness of this system to its tributary mass $m_{embank,trib}$. Solving this relationship for the mass, results in equation (3.40) and, substituting the unit stiffness according equation (3.32), leads to the expression of equation (3.41), where α is a geometry dependent parameter that relates the dynamic tributary mass $m_{embank,trib}$ to the total embankment mass $M_{embank,tot}$ within the effective length L_c.

$$f = 1.18 \cdot \left(\frac{H}{W_c}\right)^{0.08} \cdot \frac{1}{4H} \cdot \sqrt{\frac{G}{\rho}} \tag{3.39}$$

$$m_{embank,trib} = \frac{\hat{k}_{trans}}{4\pi^2 \cdot f^2} \cdot L_c \tag{3.40}$$

$$m_{embank,trib} = \alpha \cdot \rho_s \cdot A \cdot L_c = \alpha \cdot M_{embank,tot} \tag{3.41}$$

with $\quad \alpha = \dfrac{m_{embank,trib}}{M_{embank,tot}} = \dfrac{8}{\pi^2 \cdot \left[1.18 \cdot \left(\dfrac{H}{W_c}\right)^{0.08}\right]^2 \cdot \ln\left(1 + \dfrac{2H}{S \cdot W_c}\right) \cdot \left(\dfrac{S \cdot W_c}{H} + 1\right)} \quad$ tributary mass ratio

$M_{embank,tot} = \rho_s \cdot A \cdot L_c \quad$ total soil mass within tributary embankment length L_c

$A = H \cdot \left(W_c + \dfrac{H}{S}\right) \quad$ area of embankment cross-section

$\rho_s \quad$ density of soil

As shown in Fig. 3.75, for common configurations α is not very sensitive to the geometry of the embankment cross-section. Taking the general uncertainties of the simplified model into account, in the majority of cases it may be sufficient to choose the tributary mass ratio as $\alpha = 0.3$. This value corresponds e.g. to a height-to-width ratio $H/W_c = 0.5$ and a side slope of $S = 1:2$, which may serve as a reasonable typical configuration. This choice for α also lies rather close to the tributary mass ratio of a cantilever column with a hinge at its base, which has a value of 1/3 [PSC96].
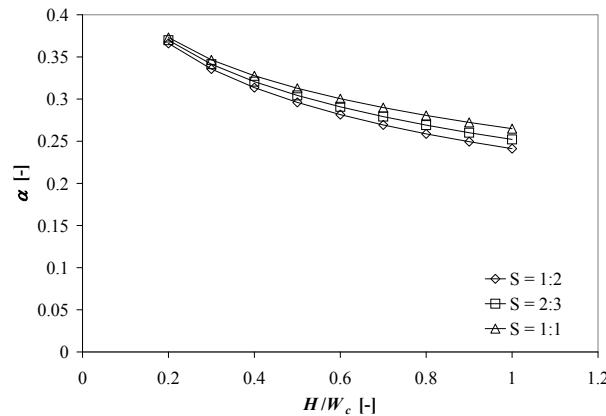

Fig. 3.75: Tributary embankment mass ratio α as a function of embankment geometry

3.5 Soil-Structure Interaction

Based on equations (3.38) and (3.41), the dynamic characteristics K_{trans} and $m_{embank,trib}$ of a linear elastic embankment representation can be determined. To allow for soil softening at increasing deformation levels, a secant abutment spring stiffness $K_{trans,sec}$ can be calculated by means of equation (3.38) employing the secant shear modulus G_{sec}. For the estimation of G_{sec} as a function of the average shear strain γ_{avg} in the embankment soil, standard modulus reduction curves, as those shown in Fig. 3.66 and Fig. 3.67, can be used. The relationship given in equation (3.42) can serve for the computation of the average shear strain γ_{avg} as a function of the transverse displacement u_{top} at the embankment crest.

$$\gamma_{avg} = \frac{u_{top}}{H} \tag{3.42}$$

On a similar basis, an equivalent viscous dashpot damper can be determined to represent the transverse abutment behavior together with the secant stiffness spring and the tributary embankment mass. The strain dependent equivalent viscous damping ratio $\xi_{eq,embank}$ for the embankment soil can be estimated based on the curves given in Fig. 3.68, and the corresponding damping coefficient $c_{eq,embank}$ of the dashpot damper follows from equation (3.43). It should be noted that the calculation of both values, the secant spring stiffness $K_{trans,sec}$ and the corresponding damping coefficient $c_{eq,embank}$, may require some iteration as it might not be possible to estimate the peak strain level of the embankment soil with sufficient accuracy before the dynamic analysis.

$$c_{eq,embank} = \xi_{eq,embank} \cdot c_{cr,eff} \tag{3.43}$$

with $\quad c_{cr,eff} = 2\sqrt{K_{trans,sec} \cdot m_{embank,trib}} \quad$ critical damping coefficient of embankment

Instead of a secant stiffness spring and an equivalent viscous dashpot damper, an alternative representation of the seismic force-deformation behavior of the embankment can be introduced into the model by means of a hysteretic spring, e.g. based on one of the two hysteretic shear stress-strain hysteresis models shown in Fig. 3.71. Such a model has the advantage that it does not require any iteration for the stiffness determination and it is essentially valid at every time instant during a dynamic analysis, whereas an equivalent linear visco-elastic representation is an approximation, being valid only at a certain amplitude (typically corresponding to the peak response).

Any given strain dependent shear modulus curve, as e.g. the ones shown in Fig. 3.66 and Fig. 3.67, can be turned into a relationship for G_{sec} as a function of the embankment top displacement u_{top} by means of equation (3.42). Based on the shear wedge model, described above, the $G_{sec}(u_{top})$ relationship can then be turned into a corresponding force-displacement backbone $F_{trans}(u_{top})$ according to equation (3.44).

$$F_{trans}\left(u_{top}\right) = K_{trans,sec}\left(u_{top}\right) \cdot u_{top} = \beta \cdot G_{sec}\left(u_{top}\right) \cdot u_{top} \tag{3.44}$$

If, further, the damping characteristics are to be taken into account, previously calibrated hysteretic models for the shear stress-strain behavior of soil, as e.g. those shown in Fig. 3.71, can be used as a basis for a hysteretic abutment spring. For any characteristic point i of the local stress-strain relationship, defined by the shear strain $\gamma_{avg,i}$ and the corresponding shear stress τ_i, a characteristic point of the global force-displacement curve ($F_{trans,i}$, $u_{top,i}$) can be calculated using equations (3.45) and (3.46). In the same way, a global spring stiffnesses K_{trans} (secant or tangent) can be computed from the corresponding local shear stiffnesses G according to equation (3.47).

$$F_{trans,i} = \beta \cdot H \cdot \tau_i \tag{3.45}$$

$$u_{top,i} = H \cdot \gamma_{avg,i} \tag{3.46}$$

$$K_{trans} = \frac{\Delta F_{trans}}{\Delta u_{top}} = \beta \cdot G \tag{3.47}$$

Using the parameters defining the modified Takeda and Ramberg-Osgood hystereses shown in Fig. 3.71, it is possible to estimate the parameters for a hysteretic spring which could represent the cyclic-inelastic behavior of the abutments at the Painter Street Overpass. Based on the geometric embankment data reported by Zhang and Makris [ZM02] (see Tab. 3.9), the effective length of the embankment can be estimated as $L_c = 6.0$ m. The purely geometry dependent stiffness parameter β of equation (3.38) results as $\beta = 19.0$ m and the maximum shear modulus at small strains is given in [ZM02] as $G_{max} = 58$ MPa.

For the modified Takeda rule, corresponding to the left side of Fig. 3.71, the yield displacement and the yield force can then be computed as $u_{top,y,Tak} = 9.6$ mm and $F_{trans,y,Tak} = 4.0$ MN, respectively. This corresponds to an initial spring stiffness of $K_0 = 420$ MN/m. The post-yield stiffness ratio and the parameters for cyclic unloading und reloading are the same for the global spring as for the local soil stress-strain hystereses, resulting in $r_{Tak} = 0.072$, $\alpha_{unload} = 0.45$, and $\beta_{reload} = 0.55$. In the same way, the parameters for the global force-displacement spring based on the Ramberg-Osgood hysteretic model, shown on the right side of Fig. 3.71, can be computed as $F_{trans,y,RO} = 2.86$ MN and $K_{tan,0} = 420$ MN/m. The Ramberg-Osgood parameter controlling the stiffness degradation of the spring is the same as that for the local stress-strain hystereses, and follows as $r_{RO} = 2.6$.

In Fig. 3.76, the resulting backbone curves for the modified Takeda and Ramberg-Osgood model are compared to the target force-displacement curve computed directly using equation (3.44) and the modulus reduction curve by Seed and Idriss [SI70] for sand (see Fig. 3.66 and Fig. 3.70). Taking the general uncertainties into account, the approximations appear acceptable over the shown displacement range.
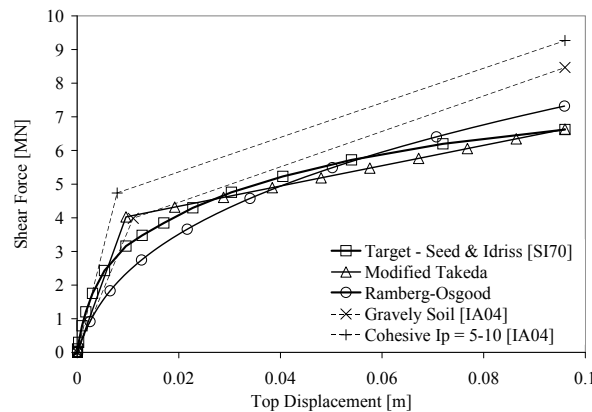
Fig. 3.76: Backbone curves of transverse inelastic spring models
for transverse behavior of Painter Street Overpass abutments

Inel and Aschheim [IA04] have presented unified pushover curves for transverse abutment response corresponding to several geometric configurations and soil types based on their embankment model. Using the data for the Painter Street Overpass, these curves have been evaluated and are shown in Fig. 3.76 additionally for gravelly soil and cohesive soil of low plasticity ($I_p = 5$ to 10). For this evaluation, the proposal of Inel and Aschheim to assume the embankment as rigid over the height of the abutment was ignored in order to make the curves comparable to those from the other models. Furthermore, the same effective embankment length L_c according to [ZM02] was used as for the other curves shown in Fig. 3.76. Although the unified embankment pushover curves by Inel and Aschheim are based on modulus reduction relationships from different sources than those used in this chapter for the other curves, the agreement is still quite reasonable. In particular for the gravelly soil curve, the nominal yield point is almost the same as that for the Takeda backbone determined above. Only the post-yield stiffness of the Inel and Aschheim curve is somewhat higher. However, taking the bandwidth of possible modulus reduction curves for sand, shown in Fig. 3.66, into account, this variation of post-yield stiffness is still well within the normal range of uncertainty for soil behavior at large strains.
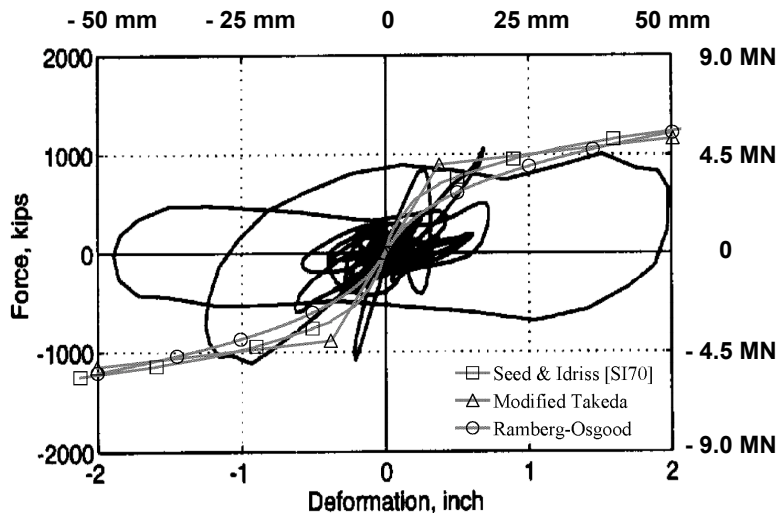
Fig. 3.77: Comparison between measured full hysteretic response of west abutment at Painter Street Overpass in transverse bridge direction during 1992 Petrolia earthquake [Goe96] and corresponding backbone predictions

As the Painter Street Overpass had an in-plan skewness of 39°, the estimated force-displacement backbones in the transverse direction are not fully comparable to the force-displacement hystereses in the skew direction determined by Goel and Chopra [GC97] from recorded seismic response. However, these hystereses, shown in Fig. 3.63 and Fig. 3.64 for the west abutment during the 1992 Petrolia earthquake, can at least serve for a rough comparison with respect to the general order of magnitude. Therefore, the measured hysteretic response during the 1992 Petrolia earthquake is repeated in Fig. 3.77 showing all cycles together with three of the numerical backbone predictions of Fig. 3.76. In the same way, the largest cycle of the measured response is compared in Fig. 3.78 with the same backbone predictions. It is noteworthy that the apparent yield load of $F_y \approx 4.5\text{-}5$ MN computed by Goel and Chopra agrees surprisingly well with the nominal yield load of the estimated backbone curves. Despite the somewhat higher post-yield stiffness of the modified Takeda and Ramberg-Osgood backbones, the estimated transverse force at the recorded peak displacement of $u_{top,peak} \approx 50$ mm is also still in an acceptable agreement with the large hysteresis loop in Fig. 3.78.
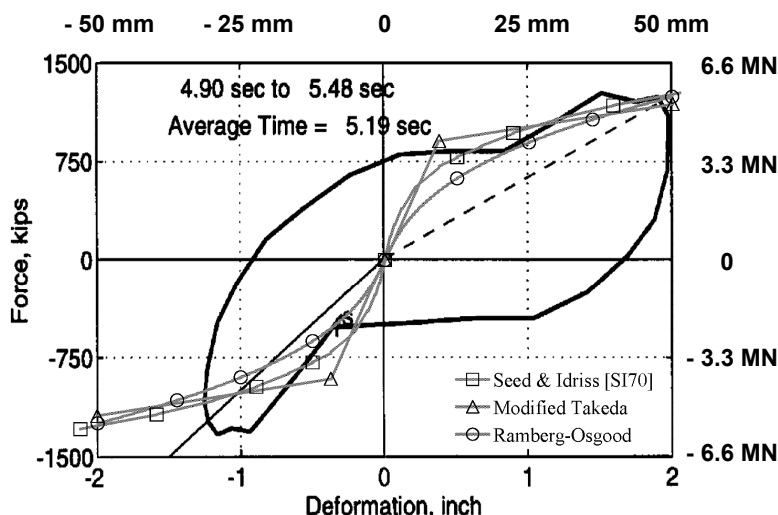
Fig. 3.78: Comparison between measured largest cycle of west abutment at Painter Street Overpass in transverse bridge direction during 1992 Petrolia earthquake [Goe96] and corresponding backbone predictions

Trying to determine an elastic stiffness in the pre-yield range of the hystereses shown in Fig. 3.77, results in estimations of approximately $K_0 = 580$ MN/m in the positive direction and $K_0 = 880$ MN/m in the negative direction. These values are higher than the model prediction of $K_0 = 420$ MN/m by

factors of 1.4 and 2.1, respectively. Partly, these differences might be explained by the use of the constant average value for L_c according to equation (3.34) in the numerical prediction. If the deformation influence on the effective embankment length was taken into account – e.g. by the model of Price and Eberhard [PE05] as defined by equations (3.35) and (3.36) – a somewhat higher elastic stiffness would result. For small strain levels, the maximum embankment length according to equation (3.35) can be computed as $L_{c,0} = 7.6$, resulting in an elastic stiffness of $K_{trans,0} = 530$ MN/m which compares favorably well, at least to the measured stiffness in the positive direction.

At higher strain levels, the model by Price and Eberhard predicts lower effective embankment lengths L_c, compared to the constant value based on equation (3.34) by Zhang and Makris [ZM02]. A variable consideration of L_c would therefore reduce the post-yield stiffness of the numerical abutment force-displacement backbones shown in Fig. 3.76, and might lead to a better approximation of the rather horizontal post-yield branch of the large cycle hysteresis loop shown in Fig. 3.77. The suggested variability of the effective embankment length can therefore be one potential explanation for the existing – rather minor – differences between the model backbones of Fig. 3.76 and the measured abutment response shown in Fig. 3.77, both in the elastic and the inelastic deformation range. However, taking the general uncertainties involved in cyclic-inelastic modeling of soil behavior into account, the additional effort related to the iterative procedure of equations (3.35) and (3.36) may not be justified. Especially, due to a lack of calibration data it may not be warranted that the quantification in general cases will really always yield better numerical results. Therefore, the constant value of L_c according to the simpler equation (3.34) may be sufficient in the majority of cases.

The comparisons above suggest that the shear wedge model for the embankment, together with standard modulus reduction curves, appears to result in estimations of the inelastic transverse abutment behavior which are at least not in contradiction to the response determined from real earthquake records. It would be unrealistic to always expect an agreement which is that close as in the case discussed above. However, if appropriate measures are taken to allow for inevitable uncertainties in the response estimation of such a complex soil-structure interaction problem (e.g. by parameter variation), even this rather simplistic model and its application as discussed above may be a reasonable means to model the seismic abutment behavior in the transverse direction.

It may be noted that Zhang and Makris [ZM02] suggest simply using the same spring stiffness – as determined for the transverse direction – also for the longitudinal behavior. However, due to a lack of underlying mechanical justification, it appears doubtful that this will lead to a reliable and appropriate response estimation in general cases.

e) Conclusions and Recommendations

In the preceding subsections it has been shown that the seismic behavior of the abutment-embankment system can have a significant influence on the transverse bridge response. While for longer bridges it mainly influences the response of the outer piers, measurements on existing structures have shown that for shorter bridges the behavior of the abutments can even be the dominating aspect for the transverse response of the entire system. Not allowing for this phenomenon can result in rather erroneous response predictions. In particular, modeling the abutments as rigidly pinned supports in the transverse direction is likely to produce unconservative displacement demand predictions for the piers adjacent to the abutments.

The measured response during real earthquakes has shown that not only the abutments are transversely displaced, but that rather the embankment itself experiences significant deformations as a result of its mass and flexibility. Based on this observation it can be assumed that large part of the abutment displacements is related to a motion together with the embankment soil. Therefore, it has been suggested to describe the transverse behavior of the combined abutment-embankment system as related to shear deformations of the embankment soil. Based on this simplification, analytical equations have been presented to estimate the transverse embankment stiffness as a function of the soil shear modulus. Furthermore, a relationship has been deduced to also estimate a tributary embankment mass.

It has been shown that established modulus reduction curves and equivalent viscous damping curves can serve as a means to take into account the inelastic behavior of the embankment soil. As a consequence, the abutment-embankment system can be modeled by a tributary mass, a simplified linear spring with secant stiffness to peak response, and a viscous dashpot damper representing the inelastic energy dissipation. It has further been shown that, as an alternative, the existing modulus reduction curves and equivalent viscous damping curves can also be used to calibrate hysteretic rules describing the shear deformation behavior of the soil. Based on these, it is then also possible to develop inelastic hysteretic springs for the transverse behavior of abutment-embankment systems. Such hysteretic springs can e.g. be introduced directly into dynamic models for inelastic time history analyses.

When using the concepts described above for the seismic modeling of abutments, it is important to be aware of the considerable uncertainties involved in such a simplified engineering model. This refers to both limitations of the conceptual model as well as to uncertainties related to the description of the cyclic-inelastic soil behavior. The range of these combined uncertainties can be rather large and it will normally require a sensitivity analysis to study the consequences of various assumptions on the seismic bridge response. The concepts outlined in the previous subsections should therefore not be interpreted as reliable means to compute the properties of the abutment-embankment system, but should rather serve as a starting point for the mentioned sensitivity analysis. If the primary focus of the analysis is on the response of the bridge piers, the variation of parameters for the abutment-embankment system should also primarily serve to study the consequences on the displacement demand of the piers. For simplicity, it will normally be sufficient to only vary the soil parameters, assuming that the model uncertainties can also be covered by a reasonably chosen range of variation.

4 Displacement Based Analysis Procedures

4.1 Fundamentals of Displacement Based Assessment

In seismic engineering, it is nowadays common to distinguish between so-called *force based* and *displacement based* analysis techniques. Although it is not always strictly defined what these two expressions comprise in detail, it appears justified to make a difference between these two conceptual approaches. Many existing seismic codes – including the current Swiss codes [SIA261], [SIA262] – can be considered as force based. The Eurocode 8 regulations for the design of new bridges [EC8-2] are primarily force based as well, but additionally they also include the possibility for a pushover analysis which represents a displacement based nonlinear static analysis technique. A similar analysis procedure is also included in Eurocode 8, Part 3 [EC8-3] for the assessment of existing building structures. In Switzerland, the displacement based analysis of buildings has been introduced by means of [SIA2018]. This document does not have the status of a code, but may rather be considered as a guideline. While force based analysis represents the more traditional approach, modern displacement based analysis methods bear some conceptual advantages. They may be considered as more accurate, but they are also somewhat more demanding with respect to the knowledge of the analyzing engineer. A brief discussion on the conceptual differences, as well as the pros and cons of the two approaches, will be given below.

In non-seismic static analysis the majority of load cases are related to some form of external forces acting on the structure. This is the reason why engineers are normally well familiar with the analysis of structures under such external forces. However, even under static conditions this is not the only potential form of loading. Instead, a structure can also be loaded by imposed deformations, as e.g. from uneven settlements or restrained deformations related to temperature variations or shrinkage. While a load case consisting of external forces must be equilibrated by internal force actions, an imposed external deformation does not necessarily require internal forces to cope with this type of external loading. In the latter case, any internal forces are rather a secondary consequence of the internal deformations and they depend on the stiffness of the system. Therefore, the resulting stresses can be controlled to some extent by an appropriate choice of the structure's load-deformation behavior. For example, if the system is made sufficiently soft, the internal forces are reduced correspondingly. For such a load case, consisting of externally imposed deformations, a reasonable failure criterion for fracture is not defined by the force capacity of the system but rather by its deformation capacity. This deformation capacity may also consist of inelastic deformations if these can be permitted with respect to other aspects (as e.g. serviceability).

Comparing static load cases to seismic excitations of structures, it can be found that a certain analogy exists between seismic actions on one hand and statically imposed deformations on the other hand. An earthquake causes dynamic, time-variant motions at the base of the structure, but it does not directly apply any external forces on the system. Instead, any resulting internal stresses are rather related to the dynamically arising relative displacements of the structure and to its resistance against them due to its stiffness. As a consequence, the resulting internal forces can also be influenced by the choice of the structure's load-deformation behavior – as in the case of statically imposed deformations – as long as the system has sufficient displacement capacity. And again it is also possible to make use of inelastic deformations in order to achieve a possibly large displacement capacity. One important difference between statically imposed deformations and seismic loading is that in the latter case the resulting deformation demand also depends on the load-deformation behavior of the system. Under static deformation loading a comparable dependency may not always exist or it might be less pronounced.

Nevertheless, it appears justified to consider the effect of seismic excitations on structures as rather comparable to statically imposed deformations than similar to static external force loading. For the limiting case of a very soft system with large mass, resulting in a very high natural period, this phenomenon is visualized in Fig. 4.1. In this example, the cantilever connects the system base with the mass at its top. During an earthquake the base of the pier is subjected to dynamic motions $u_g(t)$ while its top rather attempts to remain in its original position due to the inertia of the mass. As a result, the pier experiences deformations which create internal actions and subsequently accelerate the mass. If

the pier stiffness is very low, compared to the mass, hardly any motion of the pier top will occur and the mass will essentially remain in its original position. In this case, the pier will simply be subjected to the time-variant deformations imposed at its base as it would be under (quasi-) static conditions with a constraint at its top. The relative deformation $u_{rel}(t)$ of the pier top is equal to the negative value of the ground motion $u_g(t)$ at every time instant and the required deformation capacity of the cantilever equals the peak value of the ground displacement.
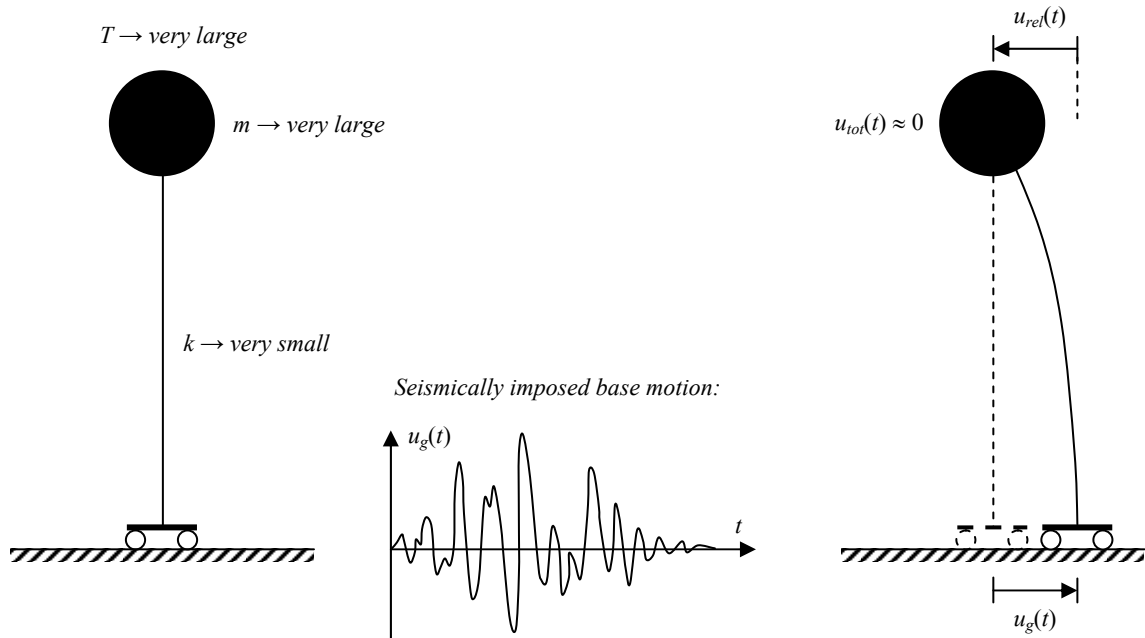
Fig. 4.1: Seismic deformation response of a system with a very long natural period

Although this simplified example is strictly correct only for the extreme relationship between stiffness and mass mentioned above, large part of the conclusions remain valid for more general cases as well. A higher ratio between stiffness and mass (with subsequent lower period) will result in a dynamic motion of the mass and thus influence the displacement demand on the pier. Nevertheless, in this case it is still more appropriate to characterize the system response in terms of displacements instead of forces. This is especially true as the beneficial effect of a potentially existing plastic displacement capacity can be accounted for in a more direct and more consistent manner if the behavior is described in terms of deformations. In particular, it is more appropriate to formulate the failure criterion in terms of deformations, i.e. by means of a comparison between *displacement demand* and *displacement capacity*.

In the traditional force based approach the deformations of the system are normally not computed, nor are they compared to the provided displacement capacity. Instead, the system is subjected to external substitute forces and the resulting internal forces and stresses are compared to the local strength capacities. As has been discussed above in connection with the analogy to the statically imposed deformations, this approach does not really describe the problem in an adequate manner for the given type of loading. Although, for a linear elastic behavior, it is possible to define substitute loads which create the same deformations and actions as the peak dynamic response (being determined e.g. by a response spectrum analysis), this is not possible for inelastic behavior anymore. In particular, in a force based approach the beneficial effect of plastic deformations cannot be directly taken into account. However, the additional displacement capacity provided by inelastic deformations is in many cases significant and not considering them would lead to unrealistic and especially uneconomic solutions.

The commonly adopted traditional approach to compensate for this problem in a force based analysis consists of artificially reducing the substitute forces which have been determined from a linear elastic analysis (e.g. response spectrum analysis) by means of so-called *behavior factors* or *force reduction factors*. This concept is e.g. followed in the current Swiss code [SIA261] in the form of the behavior

factor q, as well as in many other existing codes (e.g. Eurocode 8 [EC8-1], [EC8-2]). Normally, such behavior factors are implemented directly into the pseudo-acceleration response spectra defined in the codes and the thus reduced spectra are often being termed *design spectra* in order to distinguish them from the original spectra which are typically called *elastic spectra*.

It is important to note that the solution using such behavior factors is an attempt to artificially correct the deficiencies of an analysis approach which is conceptually not really appropriate for the given task. The underestimation of the system's deformation capacity related to its linear elastic representation is thus compensated by an artificial reduction of the seismic input loading. This means that a deficiency on the capacity side shall be counterbalanced by another "inaccuracy" on the demand side, instead of correcting the original problem related to the capacity characterization. In particular, the deformations being calculated from a reduced *design spectrum* in combination with a linear elastic system do not represent the expected seismic deformations of the system. This approach is therefore only to be used within its force based framework comparing internal stresses and forces to local strengths.

The quality of the thus determined results depends on the implementation of the concept in detail. A number of potential problems that can arise from a force based analysis have been discussed in depth in the literature (e.g. [Pri03], [PCK07]). Some of these problems can theoretically be overcome by certain adjustments and improvements, while others are immanent to the approach and its conceptual deficiencies. One important aspect in this context is the question how the *behavior factor* (or *force reduction factor*) is determined. As it is mainly supposed to allow for the plastic deformation capacity not considered in the linear elastic system model, it appears reasonable to make the allowed factor dependent on the available inelastic displacement capacity of the system. A large number of equations have been proposed that relate the force reduction factor to the provided displacement ductility capacity and other parameters (e.g. [NH82], [NK91], [VFF94], [MB94]).

However, in the majority of current codes an explicit computation of the structure's ductility capacity is not stipulated. Instead, most existing seismic codes either prescribe fixed behavior factors or define them dependent on certain structural parameters, but without including an explicit estimation of the actual deformation capacity. This rather strong simplification represents an obvious shortcoming of the method as the individual characteristics of the structure are not taken into account. In the best possible case, the codified behavior factors are sufficiently conservative for the majority of cases, which may unavoidably lead to rather uneconomic solutions. Nevertheless, as mentioned above, a considerable improvement of the method could be achieved if, instead, the inelastic displacement capacity of the structure was explicitly determined and an appropriate relationship were used to estimate the force reduction factor as a function of the ductility capacity.

Unfortunately, despite this possible improvement to the force based analysis concept, other problems remain which are more fundamentally linked to the approach. Although the method does not visualize it explicitly, the use of any force reduction factor implicitly makes use of the inelastic range of the structure. While the artificially reduced excitation may only load the system up to its yield point, the corresponding real earthquake would excite it far beyond that. Aside from the influence on the global displacement demand and capacity discussed above (which may be partly taken into account by the behavior factor), in the inelastic range the internal stiffness distribution of the system can also change due to local plastifications developing at different points during the loading phase. As the structural analysis in a force based approach is performed using a linear elastic system, these redistributions of stiffness – and consequently of internal actions and deformations – cannot be considered by this method. As a result, even if the global behavior could approximately be covered by means of an appropriate behavior factor, the demand estimation on the local member level can still be completely erroneous.

Some typical examples of cases where the linear elastic analysis leads to an unrealistic estimation of the local member behavior are given in [Pri03]. Among these are structures with a dual load path, as e.g. a bridge having an elastic load path along the superstructure to the abutments, and featuring a second inelastic load path involving plastification of the piers. Other problematic cases are structures in which the local plastifications develop at different load levels, as e.g. in bridges with strongly differing pier heights. A third typical problem of the linear elastic analysis is related to the superposition of the (reduced) seismic actions with the gravity loads. The internal force distribution in the real plastic mechanism is likely to deviate considerably from that of the assumed linear system.

The resulting errors concerning the flexural demands may still be acceptable in some cases as the system might have additional flexural deformation capacities which allow some redistribution of internal actions. As a result, the overall reduction of seismic capacity due to an inaccurate representation of the local flexural behavior might be limited. However, the flexural response of a member is always also coupled to its shear demand. Therefore, if a subsequent misconception of the local shear behavior results in an undiscovered potential for brittle shear failure, the seismic capacity of the structure may be reduced substantially. It is unlikely that this would still be considered as acceptable.

One possible alternative to traditional force based analysis is represented by an *inelastic time history analysis* (ITHA) which may be considered as the most complete analysis technique. In this method the inelastic behavior of the system is explicitly modeled – including the hysteretic response of the members under cyclic loading. Using this model, a real dynamic analysis is conducted in which the differential equation of motion is solved (numerically) for a given ground motion exciting the base of the structure. As ITHA is conceptually able to capture the important phenomena related to the seismic response of the system, the quality of the analysis results only depends on the accuracy of the inelastic structural model and the adequacy of the used input ground motions. The remaining uncertainties resulting from these two issues should not be underestimated so that even this advanced analysis technique does not necessarily guarantee a fully realistic assessment result.

As inelastic time history analysis gives a complete picture of the entire response, including the inelastic force and displacement time history of the individual members, it might be considered as superordinate to *force based* or *displacement based* analyses techniques. Therefore, ITHA is not only the conceptually most realistic analysis approach, but it also gives the most complete set of structural response data. These also allow the computation of the energy dissipated by individual members. Such data can theoretically be used for damage estimations taking the cyclic response into account (provided an appropriate damage model is available).

Despite these considerable advantages of ITHA, it may not be the best choice for the analysis of structures in ordinary cases, e.g. in an engineering company. Aside from the fact that ITHA can become computationally rather demanding, its application also requires advanced knowledge of the method. The sophisticated numerical solution strategies of the inelastic dynamic problem are sensitive to several aspects and convergence is not always guaranteed. Furthermore, the hysteretic modeling of the structure requires a considerable amount of additional data to fully characterize the inelastic system behavior, whose realistic determination might not always be straightforward. Other aspects, as e.g. the choice of adequate ground motions or appropriate viscous damping models, need to be considered in addition. The large amount of required data and the sophistication of the problem can make ITHA somewhat prone to errors, especially if the analyzing engineer is not sufficiently familiar with the potential sources of errors.

Therefore, it appears desirable to have an alternative analysis method available, which on one hand does not possess the typical deficiencies of force based analysis, but on the other hand is less complex and more readily applicable by engineers than an inelastic time history analysis. But even if ITHA is used for the analysis of a bridge structure, it is strongly recommended to apply additional, somewhat simpler, analysis techniques in order to verify the time history results. The complexity of the dynamic inelastic problem often does not allow a simple plausibility check which is indispensable due to the sensitivity of the method. The so-called *displacement based analysis* techniques unite certain characteristics which make them suitable as an alternative or a complement to the more sophisticated ITHA, while providing important improvements compared to the traditional force based analyses. It may be noteworthy that it is not always strictly defined which elements are comprised by the term *displacement based analysis* in detail.

The common characteristic of all of these approaches is that they focus on the deformations of the structure instead of the acting (or substitute) forces. This means that the demand estimation consists of a computation of expected local and global peak deformations, which are then compared to the estimated deformation capacities of the structure and its individual members. A satisfying behavior is anticipated if the deformation capacities exceed the corresponding deformation demands. By today, a large number of procedures have been proposed in the literature which may be considered to fall into this category and sometimes they consist of several modules which generally could also be

interchanged. To really provide a significant advantage over a force based method, the underlying structural analysis should somehow allow for the influence of the inelastic system response, both, on the global displacement demand as well as on the local member deformations.

The majority of the so far proposed displacement based approaches can be considered to fall into the category of *nonlinear static procedures*. These methods are often based on existing principles of classical elastic analysis, like e.g. the response spectrum analysis or the lateral force method, modifying them to account for the inelastic system behavior. As a result of these approximate modifications, typically an inelastic static analysis is performed to determine the structure's condition under peak seismic deformations. Alternatively, an iterative computation using secant stiffnesses of the members is also conceivable.

The probably most common method of this category is the so-called *pushover analysis* which has already been implemented into several international codes and guidelines, among them e.g. [EC8-2] and [SIA2018]. Strictly speaking, the expression *pushover analysis* does not define a single procedure, but rather an entire category of methods for which a large number of variations have already been proposed in the scientific literature (e.g. [Fre98], [FGD97], [Faj00] , [KS98], [CG02]). Aside from *pushover analysis*, other approaches exist which may be considered as *nonlinear static procedures* as well. Among them is e.g. the so-called *substitute structure method* [SS76] which also partly provides the basis for the principles of another nonlinear static concept termed *direct displacement based design* [PCK07].

A more detailed description of various displacement based analysis concepts is given in Section 4.6. Aside from an introduction into selected methods, several procedures are also evaluated with respect to their applicability and accuracy under different conditions. Based on this evaluation, recommendations are given concerning an appropriate choice and possible improvements of the methods to be applied for a certain task with given circumstances. Before that, in Section 4.2 a brief discussion on the general representation of the seismic input loading are given. In Section 4.3 some special implications related to multi-support excitation of bridges and to the risk of superstructure unseating are discussed. The subsequent Section 4.4 deals with the influence and the modeling of viscous damping in seismic analyses. In Section 4.5 the demand estimation of inelastic single-degree-of-freedom system is treated, which may be considered as a preparation for the displacement based MDOF analysis approaches outlined in Section 4.6. Finally, Section 4.7 deals with the problem of strength degradation and its influence on the seismic displacement demand.

4.2 Seismic Input

A displacement based seismic analysis aims at estimating the deformations that are imposed on the structure by a single or a set of earthquakes. For this purpose, the input loading corresponding to the earthquake needs to be represented in an appropriate way. Several approaches exist to describe this input and the question which one of them is the most suitable one also depends on the analysis method to be used. Generally, the real earthquake excites the structure in the form of ground motions in all three spatial directions. As the bridge is founded on this ground, the foundations of the piers and the abutments are forced to follow these motions, thus inducing the excitation into the structure.

A ground motion can be fully described in the form of a time history for the ground displacements, velocities or accelerations in three independent Cartesian directions. The different measures of the motion can mutually be transformed into each other by time integration or differentiation. However, due to measuring uncertainties and limitations of discrete numerical data representations, such a transformation can include certain inaccuracies. Although the ground motions generally can also include small rotations, these are normally not considered in the seismic analyses of structures. If a dynamic time-history analysis is conducted, the ground motion time-history can directly be used to characterize the input excitation. In this case, it is common to describe the motion in the form of ground accelerations, typically being called *accelerograms*.

A common alternative to define the seismic input on structures is the use of so-called *response spectra*, whose applications are wide spread in different analysis approaches. Strictly speaking, a response spectrum does not only define the input but to some extent already includes certain aspects of structural response. The conceptual idea of a response spectrum is that the seismic response of a linear elastic single-degree-of freedom (SDOF) system (with a certain amount of viscous damping) to a given earthquake can be fully characterized by the system's fundamental period T. This phenomenon is utilized for the establishment of response spectra which define certain response quantities of the system as a function of the natural period. As a consequence, it is possible to define (pseudo-) acceleration spectra, (pseudo-) velocity, or displacement spectra ([NH82], [Cho01]). A displacement spectrum, e.g., directly provides the peak relative displacement experienced by the SDOF system during the corresponding earthquake. The pseudo-acceleration spectrum represents a substitute external force, normalized by the mass, whose application on the system will result in the same internal actions and deformations as the peak values experienced during the earthquake.
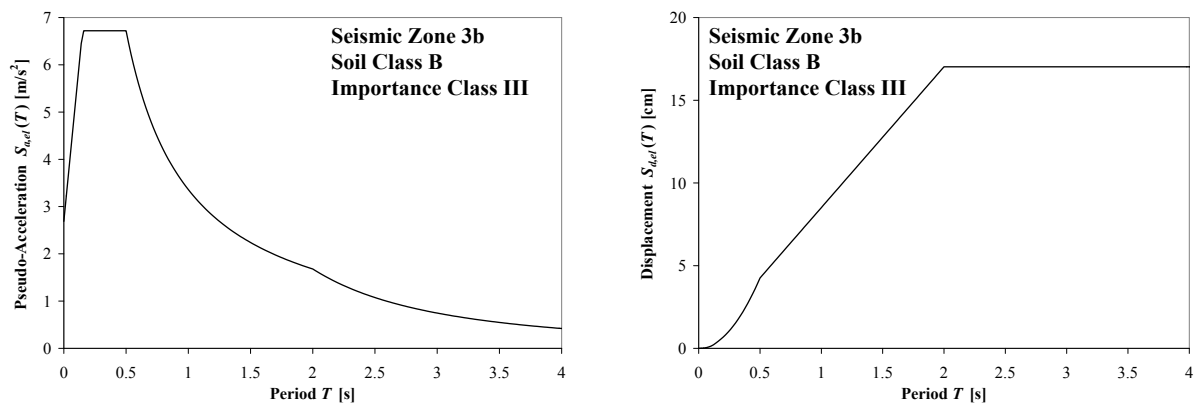
Fig. 4.2: Elastic response spectra according to [SIA261] and [SIA2018]
left: Pseudo-acceleration spectrum $S_{a,el}$, right: Displacement spectrum $S_{d,el}$

In Fig. 4.2 two corresponding examples of pseudo-acceleration $S_{a,el}$ and displacement $S_{d,el}$ spectra are shown, as defined by [SIA261] and [SIA2018][18]. Generally, the two elastic spectral quantities are mutually related to each other as defined by equation (4.1). The possibility to decompose the dynamic behavior of linear elastic multi-degree-of-freedom (MDOF) systems into individual modes, whose

---

[18] It should be noted that the elastic spectral pseudo-acceleration is denoted in [SIA261] as S_e, whereas it is named S_{ad} in [SIA2018]. The elastic spectral displacement is called S_{ud} in [SIA2018].

individual response can be described in a similar way as for SDOF systems, makes the response spectra applicable for such structures as well. In this case, the response quantities of the various modes need to be combined in an appropriate (approximate) manner, e.g. using a SRSS or CQC combination rule [Cho01].

$$S_{d,el} = \left(\frac{T}{2\pi}\right)^2 \cdot S_{a,el} \tag{4.1}$$

In the framework of a displacement based assessment approach, it is more straightforward to use the representation as displacement spectra $S_{d,el}$, instead of the corresponding pseudo-acceleration $S_{a,el}$. Therefore, in the displacement based framework of [SIA2018] the seismic demand is defined by elastic displacement spectra, which are essentially compatible to the elastic pseudo-acceleration spectra of [SIA261] (equation (4.1)). A difference between the definitions in the two documents is related to the inclusion of the factors γ_f accounting for the importance of the structure and η for the amount of viscous damping. While γ_f is included in the definition for the elastic response spectra of [SIA2018], it is not considered in [SIA261]. In turn, the correction factor η for viscous damping ratios other than $\xi = 5\%$ is only included in the elastic spectra of [SIA261], but it is ignored in [SIA2018] (i.e. in [SIA2018] the damping ratio is fixed to $\xi = 5\%$). Including the importance factor γ_f for the displacement based assessment of bridges appears mandatory. While a fixed damping ratio of $\xi = 5\%$ may be a generally reasonable assumption for building structures, this decision should be made on an individual basis for bridges (see discussion in Section 4.4.1). If it is concluded that a differing value for ξ should be assumed, the additional inclusion of the modification factor η into the spectra of [SIA2018] is recommended.

In [SIA261] the elastic spectrum is primarily intended for serviceability considerations, whereas the ultimate limit state design is based on so-called *design spectra* which are modified by a behavior factor q. It is important to note that these reduced spectra are exclusively applicable for the force based analysis which is incorporated for design in [SIA261] and [SIA262]. In particular, converting these *design pseudo-acceleration spectra* into corresponding displacement spectra, based on equation (4.1), would by no means be reasonable. Therefore, for the displacement based analysis only the elastic response spectra of [SIA261] and [SIA2018] can be used as a basis for the definition of the seismic input.

Generally, these elastic spectra are only correct for structures with linear elastic behavior. This is especially true for the pseudo-acceleration response spectrum. For inelastic systems, it is conceptually possible to develop inelastic displacement response spectra. For the determination of such a spectrum, a specific hysteretic rule describing the cyclic inelastic response of the system must be assumed. Strictly speaking, the resulting response spectrum then is only valid for this particular type of hystereses, while it would only be an approximation for other hysteresis forms. However, even for the displacement based analysis of inelastic systems a linear elastic displacement spectrum can be of significant value.

A variety of approximate modification approaches have been developed in order to estimate the inelastic displacement demand using an elastic response spectrum for the definition of the seismic input. Based on these concepts, the traditionally existing elastic response spectra can be used even for the more modern inelastic analysis methods. This is particularly useful as in the current generation of codes (e.g. [SIA261]) the seismic demand (as a function of seismic zone, soil type, importance of structure) is defined in the form of elastic response spectra. The various existing concepts for the required modifications of the elastic spectra will be discussed in detail in Section 4.5. It should be noted that these modifications only account for the influences of inelastic behavior in SDOF systems. Additional considerations are required to include further effects occurring in inelastic MDOF structures. These aspects will be discussed in Section 4.6.

It is generally possible to compute response spectra for any single earthquake ground motion, with the spectra corresponding to various seismic events possibly differing significantly due to the individual characteristics of real earthquakes. The peak amplitude as well as the shape of a response spectrum both depend on a variety of influences, such as e.g. earthquake magnitude, distance to epicenter, local

soil conditions etc. But even under similar conditions a considerable difference between two different spectra corresponding to real ground motions is to be expected. In fact, even ground motions coming from the same earthquake but recorded at different locations are likely to have individual characteristics influencing the response spectra. It is therefore not possible to define a single spectrum that would be representative for all conceivable seismic excitations at a certain location.

The common approach to resolve this problem, which is also the basis of the spectra given in [SIA261] and [SIA2018], is the definition of so-called smooth *uniform hazard spectra*. They represent an average demand taking into account several earthquake scenarios which are weighted based on probabilistic considerations. As a consequence, the response spectra of [SIA261] and [SIA2018] do not correspond to a single earthquake and due to smoothening effects, related to the averaging, their spectral shape to some extent deviates from what would be expected for an individual earthquake. However, if only one response spectrum is to be used for the demand definition, such a smooth *uniform hazard spectrum* is considered a reasonable compromise.

Although the representation of the seismic input in the form of response spectra is rather convenient, it is not directly applicable for every analysis type. It has been mentioned at the beginning of this section that a dynamic time-history analysis requires the input in the form of ground motions which are imposed on the foundation systems of the structure. To capture the seismic behavior in a possibly realistic way, normally an *inelastic time history analysis* (ITHA) will be required. The ground motion is typically described in the form of accelerograms, defining the soil accelerations as a function of time. As outlined above, every earthquake has its individual characteristics and the seismic excitations from different seismic events or at different locations can deviate considerably. Consequently, it is normally not considered sufficient to use only one ground motion as a seismic input.

Generally, it can be distinguished between recorded ground motions stemming from real earthquakes and artificially generated accelerograms. The latter solution has the advantage that the artificial ground motion can be generated in a way so that its corresponding response spectrum approximates a given demand spectrum defined e.g. in a code. This is particularly convenient if the level of intended seismic excitation is defined originally by a response spectrum. However, as discussed above, code specified spectra typically are smooth uniform hazard spectra whose shape does not fit to that of individual earthquakes, but rather represent an average of a set of ground motions. If a single accelerogram is supposed to approximate such an average spectral shape, its characteristics can only be considered as a compromise.

While the shape of a recorded ground motion is automatically given, other problems occur for such real earthquake accelerograms. In first place, this refers to the selection of appropriate recordings for a given task. In many cases, the definition of the selection criteria might not be straightforward. The situation becomes particularly complicated if the seismic input is initially defined by a (code specified) response spectrum whose shape conceptually does not fit to the shape of real ground motion spectra. Furthermore, sometimes it may be necessary to scale the original ground motions to a certain extent in order to make them more comparable to the desired demand level. Such a selection and scaling process can significantly influence the later analysis results and requires special consideration and knowledge of the potential consequences.

Independent of the type of ground motions, artificial or real recorded, it is always strongly recommendable to use a set of different accelerograms in a dynamic time history analysis. The various resulting system responses coming from the individual ground motions then need to be evaluated statistically to determine representative results. The minimum number of ground motions as well as the statistical evaluation procedure depends to some extent on the type and quality of the accelerograms and on the required reliability of the results. In any case, a considerable scatter between the various analysis results can be expected. Some guidance on ground motion selection and interpretation of the analysis results can be found in [EC8-2], Sections 3.2.3 and 4.2.4.

While many building structures are founded either on a single large base plate or on individual footings with limited mutual distance, bridges are always founded on several footings (for the piers and the abutments) with considerable distance between them. Each of these footings is subjected to an individual ground motion during an earthquake. Especially for very long bridges, or systems which are founded on different types of soil conditions, considerable deviations between the ground motions at

the various footings can occur, which is called *multi-support excitation*. Several sources for spatial variations of the ground motion input exist. These include:

- *Wave passage effect*
  Due to a limited velocity of the seismic waves, they arrive at the various foundations at different times, resulting in a time-shift between the individual ground motions.

- *Incoherence effect*
  Random reflections and refractions of the seismic waves along their path, as well as differences in superposition of waves arriving from an extended source, change the shape of the signals and lead to a loss of coherence between the individual motions.

- *Local site effect*
  Differences in the local soil conditions and corresponding mechanical properties can modify the ground motions between the foundations.

- *Attenuation effect*
  The amplitudes of the seismic waves are reduced with increasing distance from the source due to spreading and dissipation of energy along the path.

- *Soil-structure interaction effect*
  Different types of foundations, e.g. at the piers and the abutments, modify the ground motion input due to interaction of the structure with the soil.

It is likely that not all of these effects have the same relevance, and the importance of each one in a specific case depends on the individual situation. Conceptually, it is possible without any problems to impose a multi-support excitation in a dynamic time-history analysis by simply using different ground motions at each foundation of the structure. However, the determination of these differing accelerograms and their mutual relationships is a very complex task, associated with considerable uncertainties. Although the (approximate) inclusion of only the *wave passage effect* theoretically still appears comparatively straightforward, even for this aspect the angle of the incoming waves and a reasonable estimation of the relevant wave velocity along the path is required. At least the angle will normally not be known with certainty as it depends on the position of the epicenter, so that a set of analysis would be required varying the assumed direction. Allowing for the other effects is even more complex.

Although some general theoretical guidance on the development of spatially variable ground motions is given in [EC8-2], Annex D, its explicit inclusion into a dynamic analysis is hardly reasonable for normal assessment cases. Only for extraordinary bridges where at least one of the above mentioned effects is likely to control the seismic behavior, a more explicit consideration should be given to the topic. In more simplified analysis techniques, based on response spectra, a direct introduction of multi-support excitation is conceptually not as simple as for a time history analysis. Although approximate methods to take this aspect into account in more basic analysis approaches also exist (see e.g. [Cho01] and [EC8-2], Annex D), their use for ordinary cases may not be realistic.

Due to the complexity of the problem, a direct inclusion of multi-support excitation in the analysis of normal bridges, e.g. in the context of an assessment in an engineering company, will hardly be realistic. At the same time, in some cases the spatial variation of the ground motion can influence the response of a bridge to an extent which may not be disregarded anymore without distorting the real behavior. The influences multi-support excitation has on the bridge behavior and appropriate ways of taking it into account in a practical analysis will be discussed in Section 4.3. This includes the demand on the piers, as well as the consequences for the safety against unseating of the superstructure.

4.3 Effects from Multi-Support Excitation and Safety against Unseating

It has been outlined in Section 4.2 that due to the spatial variation of earthquake ground motions the seismic excitation of the various pier and abutment foundations of a bridge can vary to a certain extent. While several sources for differing ground motions have been identified in Section 4.2, not all of them need to have the same relevance. The importance of each one depends on the individual structure and possibly different characteristics of the entire situation. For example, the *wave passage effect* and the *incoherence effect* depend to a large extent on the length of the structure (and its spans), while the *local site effect* predominantly depends on potentially varying soil conditions at the various foundations.

In the following sections a more detailed discussion on the influence of multi-support excitation on the structural behavior is given. Section 4.3.1 focuses on the consequences for the deformation demands of the structure and on potential ways to allow for this aspect in the analysis. Section 4.3.2 is dedicated to the danger of superstructure unseating which is also influenced by the relative displacements between individual foundations as a result of the spatial variation of the ground motion.

4.3.1 Effect of Multi-Support Excitation on Seismic Deformation Demands

Generally, the response of a bridge subjected to multi-support excitation can be interpreted as a combination of (1) a *dynamic component* of the system related to the inertia of the masses and (2) a *pseudo-static component* as a result of the differential displacements at the supports of the structure. If instead only a synchronous excitation is considered in an analysis, the response consists merely of the dynamic component (1). However, the dynamic component resulting from a synchronous excitation will in general cases not be the same as that from a corresponding non-synchronous input. Nevertheless, splitting up the response to a multi-support excitation into the two components mentioned above helps interpreting the rather complex behavior. Furthermore, it is useful to distinguish between the various sources of spatial ground motion variability and their individual influence on the structure response.

A comprehensive overview of the current state-of-the-art concerning the seismic response of girder bridges to multi-support excitation is given in [fib07]. In this document a total of five studies ([MNP96], [MP98], [SSD00], [SKP03a], [SKP03b], [Lup+05]) are summarized which focus on the influence several aspects of spatial ground motion variability have on the seismic bridge behavior. The analyses conducted within these investigations include linear and nonlinear time history analysis, as well as random vibration analysis. As results, various measures for the deformation demands were considered and one study also computed failure probabilities and fragility curves for entire bridges. In the studies comparisons were conducted between, on one hand, simplified analyses using only synchronous input at all supports and, on the other hand, analyses using different levels of sophistication concerning the representation of the multi-support excitation. In particular, some works also investigated which consequences individual sources of spatial ground motion variability have on the bridge response. Primarily, the influences coming from the *wave passage effect*, the *incoherence effect*, and the *local site effect* were considered in the studies. The number of investigated configurations and excitations per study ranged between 12 and 972, and the total number of analyses within the five studies considered in [fib07] amounts to 1247.

It should be noted that despite the considerable number of analyzed configurations, a strict generalization of the results is not possible because too many effects come into play in an individual case. Furthermore, some assumptions, e.g. concerning the loss of coherency or the generation of correlated ground motions, are subjected to considerable uncertainty. Nevertheless, the findings of the studies show some common trends which may serve as an orientation for the treatment of this complex problem.

One conclusion that can be drawn from the various investigations presented in [fib07] is that if only the *wave passage effect* and the *incoherence effect* are present, statistically the expected response of *girder bridges* does not appear to differ very strongly from that of a corresponding synchronous excitation. However, it can be noted that the scatter of the results increases if multi-support excitation due to these two effects is included in the analysis. Although the expectation value of the response can

even be influenced slightly positively by multi-support excitation, due to the higher variability of the response, the same needs not necessarily be true for the overall failure probability. However, this variability was found to lie in a similar range as the general uncertainty typically included in the seismic analyses of structures. Based on this finding, the authors of [fib07] conclude that for girder bridges disregarding the influences of the spatial ground motion variability only related to the *wave passage effect* and the *incoherence effect* might be acceptable in design applications.

It should be noted that four out of the five studies summarized in [fib07] exclusively used bridge lengths equal to 200 m. This is somewhat unfortunate as it is known that the relevance of spatial ground motion variability tends to increase with the length of the structure. Only the study by Sextos *et al.* ([SKP03a], [SKP03b]) also considered bridges featuring lengths of 400 m and 600 m. When only taking *wave passage* and *incoherence effects* into account, this study suggests a slightly unfavorable trend for the deformation demands of such longer bridges, compared to analyses with synchronous input. However, in the presented analyses the negative influence still remained in the same order of magnitude as the uncertainties of the results. Nevertheless, for very long bridges a somewhat more cautious approach might be justified on an individual basis.

Aside from an empirical comparison between the results with and without the mentioned types of spatial ground motion variability, some conclusions can also be drawn from the way in which the multi-support excitation influences the bridge response. For this purpose, Monti *et al.* [MNP96] discuss the two extreme cases of fully incoherent and fully coherent ground motions. They found that for a fully incoherent motion the *wave passage effect* becomes completely irrelevant, which appears understandable as the motions at different supports are completely independent. Any additional time-shift between such independent motions does not make a difference any more. The structural response to such a fully incoherent multi-support excitation tends to be dominated by the *pseudo-static* component related to the differential displacements of the supports. The *dynamic component* corresponding to a vibration of the structure becomes of secondary importance, or even negligible.

For the alternative extreme case of fully coherent multi-support excitation, only the *wave passage effect* exists and the response becomes dependent on the wave velocity. Monti *et al.* [MNP96] state that, for the normal range of wave velocities (not less than 500 m/s), no significant contribution from the *pseudo-static* response component will be expected. Instead, the major influence on the response is related to a reduction of the *dynamic component* due to the lack of synchronism between the various supports. Only for very small wave velocities Monti *et al.* discovered a significant influence from the differential support displacements (i.e. *pseudo-static component*). In this case the dynamic contribution was also found to be significantly reduced, compared to a synchronous excitation.

The results by Lupoi *et al.* [Lup+05] show that if a combination of *wave passage* and *incoherence* effect occurs, the loss of coherence tends to dominate over the *wave passage* effect. The fragility curves computed by Lupoi *et al.* suggest that this loss of coherence actually can to some extent increase the failure probability, compared to a synchronous excitation. This probabilistic finding appears somewhat contradictory to the deterministic conclusions mentioned above, which did not suggest a negative influence on the expected response as a result of multi-support excitation. However, the increased failure probabilities may be a result of the higher scatter of the responses, rather than coming from a significant change of the expectation value. In this sense, the findings of the individual studies do not need to be in contradiction.

Although this text is primarily focusing on the seismic behavior of conventional girder bridges, due to the large relevance of multi-support excitation for suspension bridges and arch bridges, a brief comment shall be given on the consequences for these two bridge types. A study performed by Harichandran *et al.* [HHS96] investigated the response of the Golden Gate suspension bridge and two arch bridges to seismic multi-support excitation. Three types of ground motions were considered for the analyses: (1) an identical synchronous excitation at all supports, (2) a multi-support excitation taking only the *wave passage effect* into account, and (3) a multi-support excitation including both, the *wave passage* and the *incoherence* effect. To compare the consequences of the different assumptions, the various response quantities of the first two excitations were related to the corresponding quantities of the third excitation.

For the Golden Gate Bridge, having a 1280 m center span and 343 side spans, the results suggest that the multi-support excitation has a considerable influence on the response. Although, on average, the global demand is not necessarily higher than for synchronous excitation, the local member demands were found to differ significantly – both in the positive and the negative direction. This might be interpreted as a rather strong scatter which, can result in significantly unconservative demand estimations on the local level if multi-support excitation is not taken into account. Generally, including only the *wave passage effect* was found to improve the quality of the results already substantially in comparison to the pure synchronous excitation. However, the deviations compared to the more general excitation, including also the *incoherence effect*, are still significant and may not be acceptable for a design or assessment task. As a consequence, the findings discussed above for girder bridges (of medium length), saying that a multi-support excitation consisting of only the *wave passage* and the *incoherence effect* does not change the expected response in a substantial way, should not be transferred to long suspension bridges.

Concerning arch bridges, Harichandran *et al.* [HHS96] investigated the behavior of the New River Gorge Bridge (length 518 m) in West Virginia and the Cold Spring Canyon Bridge (length 213 m) in California. In both cases the same studies were performed as for the Golden Gate Bridge discussed before. The conducted analyses suggest that the assumption of a synchronous excitation tends to strongly underpredict the demand on important parts of the structure. Especially the demand on the arch itself under longitudinal excitation is not captured by the synchronous input loading at all. The magnitude of the underpredictions under transverse excitation are somewhat more comparable to those found for the Golden Gate Bridge, but still unacceptable. If at least the *wave passage effect* is taken into account, the results improve already considerably. However, the results by Harichandran *et al.* [HHS96] suggest that the *incoherence effect* should be included into the analysis additionally in order to achieve a reliable basis for design or assessment.

At first sight, it might appear somewhat surprising that the shorter Cold Spring Canyon Bridge resulted as even more sensitive to the longitudinal multi-support excitation than the significantly longer New River Gorge Bridge. However, as the predominant influence on the response of arch bridges under longitudinal multi-support excitation is likely to come from the *pseudo-static* component as a result of the differential displacements between the two supports, it is indeed possible that the shorter and thus stiffer bridge suffers more severely from this type of loading.

So far, the entire discussion has focused exclusively on spatial ground motion variability only related to *wave passage* and *incoherence* effects, whereas the influence of the *local site effect* has been disregarded. If, however, this latter effect comes into play due to varying soil conditions at the different supports, the response of the structure can be altered considerably compared to both, synchronous excitation as well as non-synchronous excitation from the other two effects discussed before.

Several of the studies reported in [fib07] (e.g. [SSD00], [SKP03b]) come to a similar conclusion, being that the *local site effect* can cause a significant increase of the displacement demands. In the investigated cases, ductility increments by a factor of about 1.5 to 2.5 have been found. Due to the inevitable model uncertainties and the almost unlimited number of configurations under real conditions, the influence from the *local site effect* need not be limited to the reported range of factors. However, the tendency for a generally rather negative influence from variable soil conditions is also confirmed by Lupoi *et al.* [Lup+05] who compared the failure probabilities resulting from *local site effects* only to those from *wave passage* and *incoherence* effects only. This comparison showed that, for the relevant cases, the failure probability related to the *local site effects* can be higher by a factor of 1.5 to 3 than that of the other two effects together.

It should be noted that, even if uniform soil conditions are modeled in an analysis, the response will be different for firm soil than for soft or medium stiff soil. When comparing the results of variable soil conditions to those of uniform conditions, a decision needs to be made which of the various soil types is considered in the uniform soil analysis. In the studies reported above, the uniform soil analyses were typically conducted with the stiffer soil types which yield lower seismic demands than the softer soils also included in the variable soil analyses. Therefore, Lupoi *et al.* [Lup+05] consider the local site effect as a 'global' demand increment coming partly from larger spectral ordinates of the softer soil and partly from the differences between the varying soil types.

The results of the various studies suggest that the influence of multi-support excitation can significantly influence the seismic bridge response (in a negative way) if *local site effects* occur and this phenomenon should therefore not be disregarded in an analysis. At the same time, the combination of all three effects discussed before is extremely complex and it is therefore hardly possible to include them directly into practical analyses, e.g. in an engineering company. The studies [MP98] and [SSD00] use the dominating influence of the *local site effect* for the proposal of a simplification. They found that the *local site effect* tends to mask the influence of the *wave passage* and *incoherence* effects and that therefore disregarding the latter ones is likely to still yield reasonable results. The authors of [fib07] follow this conclusion and recommend, as a simplification, to perform inelastic time-history analysis (ITHA) using independent ground motions for the individual supports. Each of these ground motions should be generated to represent the local soil conditions at the particular foundation.

It is important to note that this proposal is based on very limited evidence and for a reliable application further in-depth investigation of the approach is desirable. If the concept is nevertheless to be used (cautiously) for an assessment case, it is recommended to, at least, perform additional analyses using a uniform excitation corresponding to the worst of the soil conditions occurring at the various supports. The largest (also local) deformation demands resulting from the two sets of analyses should be used for the assessment. The second analysis using uniform excitation does not necessarily have to be an ITHA, but can rather also consist of one of the approaches presented in Section 4.6. The reasoning behind the additional uniform excitation analyses is that it needs to be avoided that the completely uncorrelated ground motions of the multi-support excitation ITHA do not excite the *dynamic component* of the response at all, but merely cause a *pseudo-static* response which could underpredict the real demand. The uniform excitation analysis will consider the dynamic response at least in a separate form.

Although the proposed approach by [fib07] simplifies the problem considerably, the fact that it can be used only in the context of ITHA still limits its applicability for practical purposes. The somewhat uncertain reliability outlined above should also be considered as a critical point. As an alternative, Eurocode 8, part 2 [EC8-2] (Section 3.3) contains a concept which is also applicable with other types of analyses, as e.g. nonlinear static procedures (see Section 4.6). This approach consists of separate analyses for the *dynamic component* and the *pseudo-static component* of the multi-support excitation response. Both components are then to be combined by means of the SRSS superposition rule. The *dynamic component* of the response is estimated based on a uniform excitation corresponding to the worst soil condition of all supports. It can be determined using any appropriate analysis approach, as e.g. the ones discussed in Section 4.6.

The additional *pseudo-static* component according to [EC8-2] is estimated by statically applying two different sets of differential support displacements. The first set corresponds to a linearly increasing ground displacement along the bridge, whereas the second set represents the possibly extreme differential displacement of one support with respect to its two neighboring pier (or abutment) supports. For every (local) response quantity the results of the more unfavorable one of the two displacement sets is to be combined with the corresponding results from the *dynamic component*. More detailed definitions of the two displacement sets can be found in [EC8-2].

Eurocode 8, part 2 [EC8-2] also gives guidance on when the consideration of the spatial ground motion variability is required. According to these provisions, the multi-support excitation needs to be taken into account for the analysis if either (i) the soil conditions at the various supports differ significantly or (ii) the bridge exceeds a certain limit length. For the first criterion, the soil classes defined in [EC8-1] are used. A significant difference between the local soil conditions at various supports shall be assumed if they fall into different soil classes. The second criterion uses the distance L_g from which on ground motions can be considered as essentially uncorrelated. Depending on the soil conditions, L_g according to [EC8-2] ranges between 300 m and 600 m. It is considered necessary to include multi-support excitation in the analysis if the bridge length exceeds $2/3 \cdot L_g$.

These two criteria conceptually comply with the findings discussed before concerning the question when spatial ground motion variability plays an important (and especially negative) role for the behavior of girder bridges. The same holds true for the way the effects from multi-support excitation are taken into account in the simplified Eurocode 8 approach. At the same time, considering the results

by Harichandran *et al.* [HHS96] discussed above, care should be taken with respect to an application of the simplified approach to arch bridges. For this type of bridges it might not be possible to apply the same limiting criteria defining from when on spatial ground motion variability needs to be taken into account. Furthermore, particularly the strong sensitivity of arch bridges to differential support displacements in the longitudinal direction might require special attention.

4.3.2 Unseating

In the previous subsection the influence of multi-support excitation on the displacement demands of the structural members has been discussed. A second aspect where spatial ground motion variability has a considerable influence is the potential for unseating of bearing supported superstructures. As outlined in Section 2.1*a*, this failure mode has been observed many times after past earthquakes and almost always its consequences are devastating. Therefore, ensuring that superstructure unseating cannot occur during an earthquake is a crucial aspect for the seismic safety of a bridge. According to Somaini and Bachmann [SB89], [Bac90b] it should be expected that ordinary fixed bearings on abutments are likely to fail under longitudinal seismic excitation. It is therefore not considered sufficient to rely on the restraint of such bearings for the prevention of superstructure unseating. Instead, Bachmann [Bac90a] argues that the failure of a fixed bearing might be acceptable as long as sufficient seat length is provided to ensure the vertical support of the superstructure even in a displaced position.

Unseating can occur wherever relative displacements between the superstructure and its supports occur to a degree that the overlap between the two can be exceeded. Typical locations are movement joints at the abutments or within the superstructure. But, as outlined above, unseating can also occur at fixed bearing supports although under static loads these would not be considered as movement joints. Care should be taken if precast girders are connected on top of the piers by means of cast in-situ concrete. Depending on the structural details of this connection, it may not always be warranted to consider this solution as a continuous superstructure for the issue of unseating.

It is generally possible to restrain the relative motion between superstructure and support by special seismic restraining devices in order to prevent unseating. However, the developing seismic forces in these restrainers can become extremely large, especially if an initial slack of the device exists (e.g. in order to allow thermal movements) [Bac90b]. The realistic demand estimation is rather difficult [PSC96] and, as can be seen in Fig. 2.3, even restrainers which were specifically designed for seismic purposes have already failed in past earthquakes. Therefore, the best measure to prevent unseating is still a sufficient overlap between the superstructure and its seat in order to ensure a vertical support even if (large) relative displacements occur between the two.

In the majority of cases the superstructure is more sensitive to unseating in the longitudinal bridge direction. The combined existence of superstructure cross-beams at the supports and large seat widths typically make bridges rather insensitive to unseating in the transverse direction. Therefore, in the majority of cases, it should be possible to rule out this type of failure just because of the geometrical conditions without any further analysis. Theoretically, a superstructure consisting of multiple T-beam girders with cross-beams over the intermediate supports could be sensitive to diagonal motions as a combination of longitudinal and transverse relative displacements if the bents consist of multiple columns without a connecting cap-beam. While a pure longitudinal motion would not result in unseating because the webs of the girders would still remain over the columns, the same holds true for a pure transverse motion because in this case the cross-beam would remain over the column. However, under a combined diagonal displacement both the cross-beam and the longitudinal girder could loose the support. The deck, being located considerably higher, can probably not substitute this support. Instead, the column might rather punch through the deck in such a case.

Despite these theoretical considerations, in the majority of cases unseating will be a phenomenon related to longitudinal motions (as confirmed by experience from past earthquakes). Therefore, the following discussion will concentrate on this aspect. The transverse (or diagonal) direction should be kept in mind and, if required in extraordinary cases, appropriate measures should be taken. The conceptual principals behind the approach for the longitudinal direction could then serve for the development of a conservative estimation of the behavior in other directions.

Theoretically it would be possible to approach the problem of unseating performing complex time-history analyses and using sophisticated models to describe the time-variant spatial ground motion variability as described in Section 4.3.1. However, this appears neither reasonably feasible, nor necessary in normal cases. Instead, it is common to treat the problem using simplified equations for minimum overlap lengths between superstructure and supports as shown in Fig. 4.3. The principals behind this approach are explained very comprehensively in [Bac90a] and a further discussion is included in [ASTRA05a]. The actual equations presented in [Bac90a] refer to the older code generation [SIA160-89], but the background of the general concept still remains the same also for the more recent regulations given in [SIA261] and [ASTRA05a].

It should be noted that, although not explicitly stated in the several documents, these rules have been developed based on the seismic behavior of straight non-skew bridges. Therefore, care should be taken with applying them directly on more general cases, such as e.g. curved or skew bridges. In Section 2.1*j* it has been mentioned that bearing supported skew bridges are prone to in-plan rotations about the vertical axis as a result of pounding against the abutments. This phenomenon being further discussed e.g. in [Mar85], [MJ87], [PSC96], [WK04] can also influence the possibility of unseating for skew bridges. Such additional effects are not covered by the simplified geometric requirements defined in [SIA261] and [ASTRA05a]. Therefore, the discussions in this section are limited to straight non-skew bridges, while other bridge shapes may require additional considerations to ensure a sufficient safety against unseating.
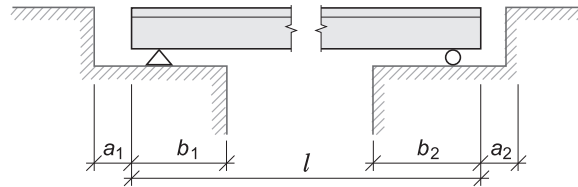

Fig. 4.3: Minimum overlap lengths at superstructure supports according to [SIA261] and [ASTRA05a]

Generally, a minimum seat length m between the superstructure and a support must be maintained to ensure a safe vertical force transfer even after relative displacements between the two have occurred. Such relative displacements can result from differential displacements between various foundations and from dynamic displacements of the superstructure relative to the foundations. The first aspect can be interpreted as corresponding to the *pseudo-static component* discussed in the previous Section 4.3.1, and the latter one corresponds to the *dynamic component* of the response to multi-support excitation. If the existing overlap lengths before the earthquake (b_1 and b_2 in Fig. 4.3) are sufficiently long to guarantee that the required minimum seat length m is still provided after the two displacement components have taken place, unseating cannot occur. Therefore, sufficiently conservative estimates of the minimum values for b_1 and b_2 are required. As the longitudinal bridge behavior is different for floating supported superstructures and for those with fixed bearings at an abutment, these two cases need to be distinguished in the treatment of the topic.

As the background for the commonly adopted approach to estimate the required overlap length is already explained elsewhere ([Bac90a], [ASTRA05a]), this will not be repeated here and the reader is referred to the given references. It should be noted that the formally valid current criteria given in [SIA261] were adopted from an older version of Eurocode 8-2. They are not considered as sufficiently conservative because they overestimate the length L_g (see Section 4.3.1), from which on ground motions are considered as fully uncorrelated. This can lead to an underestimation of the differential displacements of the foundations for short and medium length bridges. Therefore, in [ASTRA05a] modified equations are proposed which use the same values for L_g as the current version of Eurocode 8-2 [EC8-2]. It is recommended using this proposal due to its more consistent and more conservative character.

Examples of resulting values for the minimum overlap lengths b_1 and b_2 at abutments of floating supported bridges according to [ASTRA05a] are shown in Fig. 4.4. In both graphs the required values are presented as a function of the effective length L_{eff} between an abutment and the center of stiffness of the substructure (i.e. the piers). As outlined in [ASTRA05a], this center of stiffness is equal to the

point of the superstructure that does not experience displacements under thermal action. It can be seen that the required overlap length increases with L_{eff} because of loss of correlation between the ground motions at the piers and at the abutment, leading to an increase of the differential displacements between the corresponding foundations. When L_{eff} reaches L_g (see above), the ground motions are fully uncorrelated and the differential displacements do not increase any more, so that the required overlap lengths b_1 and b_2 also remain constant for higher values of L_{eff}.

From the comparison on the left side of Fig. 4.4 it can be seen that the level of seismic excitation obviously strongly influences the required minimum overlap length. The graphs on the right side of Fig. 4.4 show that the soil conditions can also have a considerable influence on b_1 and b_2. While the soil types B, C, and D, according to [SIA261], vary only slightly among each other, soil class A results in somewhat lower minimum overlap lengths. In contrast, the very unfavorable soil class E shows a significantly more critical behavior with respect to potential for superstructure unseating. It is noteworthy that, even for soil class B, long bridges can require overlap lengths at the supports of up to 0.65 m in the higher seismic zones.
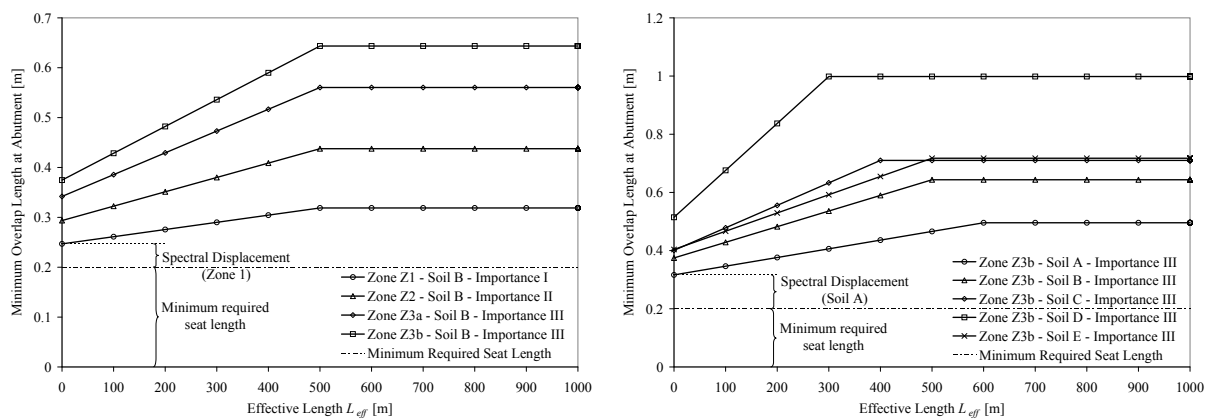
Fig. 4.4: Required minimum overlap lengths according to [ASTRA05a] for floating supported bridges
left: Influence of seismic excitation level for constant soil class,
right: Influence of soil class for constant seismic excitation level

Qualitatively similar trends result for bridges having longitudinally fixed bearings at one abutment, not shown in Fig. 4.4. It should be noted that the relative displacements occurring at intermediate movement joints in the superstructure can be larger than for supports at the abutments. This is related to the fact that at an intermediate movement joint both parts, the supported member as well as the supporting member, can experience dynamic displacements relative to the foundations. In contrast, at an abutment only the superstructure experiences such dynamic relative motions, while the abutment moves rather rigidly with its foundation. Therefore, at internal movement joints the required minimum overlap lengths given in [ASTRA05a] for end supports need to be increased according to [SIA261] by 30%.

A brief comment shall be given on the implicit estimation of the dynamic relative superstructure motion for bridges with fixed bearings at one abutment and longitudinally sliding bearings at the rest of the supports. While for floating bridges this relative displacement with respect to the foundations is estimated in [SIA261] and in [ASTRA05a] as the peak spectral displacement (compare Fig. 4.2), this approach is not possible for bridges with fixed bearings at one abutment. As long as these fixed bearings remain intact, they prevent any dynamic movement. But once they are destroyed (which should realistically be assumed in a major earthquake [SB89], [Bac90b]) no direct estimation of the relative superstructure movement is possible anymore, as the rest of the bearings are of the sliding type in the longitudinal direction. Due to this lack of connection with the substructure (i.e. the piers), the superstructure can perform rather free and arbitrary relative motions which are hard to predict in a reliable manner.

In order to nevertheless make a (possibly conservative) estimation of the maximum expectable relative superstructure motion, the underlying assumption in [Bac90b], [SIA261], and [ASTRA05a] is that it

cannot move further than until it reaches contact at the backwall of the opposite abutment. It should be noted that the resulting forces due to such a pounding between superstructure and abutment can be extremely large (especially for long superstructures having a very large mass). In new designs it will frequently hardly be possibly to design the backwall for such impact forces. As a consequence, current Caltrans bridge design guidelines [Cal06] e.g. rather recommend designing the backwalls deliberately as sacrificial parts which shall break off upon impact. This shall also serve to protect other parts of the abutment from more severe damage.

The fact that it is hardly possible to design the backwall for the impact forces also shows that a full reliance on the abutment as a blocking of the superstructure motion may not be warranted in every case. If the backwall breaks off upon pounding, only a rather limited amount of soil behind it will provide passive soil pressure. Compared to the large inertia of the entire superstructure a significant restraint by this passive soil pressure might be questionable. But even if the backwall does not break off, a certain amount of superstructure displacement or rotation due to the impact force cannot be ruled out completely. Such abutment displacements have been observed after several past earthquakes (compare Section 2.1c), even in cases where the superstructure was connected monolithically to the abutment, which reduces the interaction forces significantly due to the absence of pounding.

Without any doubt, pounding between the superstructure and an abutment will influence the motion of the former. As a consequence, it may be expected to have a beneficial effect on the risk of unseating at the opposite abutment. However, care should be taken with respect to completely relying on this mechanism. Especially, the assumption of a rigid restraint by the abutment which is impacted does not appear fully realistic. Furthermore, any longitudinal abutment displacements due to superstructure pounding will effectively reduce the seat lengths b_1, b_2 shown in Fig. 4.3. In this context it is also noteworthy that e.g. neither Eurocode 8-2 [EC8-2] nor the Caltrans design guidelines [Cal06] use pounding between superstructure and abutment as a restraint against unseating at the opposite abutment. Therefore, for bridges with fixed bearings on one abutment, where the criteria given in [ASTRA05a] are fulfilled only marginally, it is recommended to consider carefully whether the situation is really acceptable with respect to unseating. Due to the potentially severe and devastating consequences of this failure type, only very limited tolerance for deficiencies appears justified. In such a critical case, the structural details of the abutment and the mass of the superstructure might be taken into account to evaluate the anticipated behavior.

Generally, when applying the criteria against unseating, the required minimum overlap length according to [ASTRA05a] needs to be compared to the provided value at the individual supports. As the primary purpose of movement joints is to allow time-dependent relative displacements between the two joining members, the determination of the *provided* overlap length at a support may not be unambiguous. In particular, what counts is the provided overlap length when the seismic excitation starts, which cannot be predicted precisely beforehand e.g. because of thermal deformations of the superstructure. While [EC8-2] and [Cal06] include such time-dependent longitudinal deformations of the superstructure (in the *required* minimum overlap length instead of the *provided* overlap length), [SIA261] does not contain any regulation if or how this aspect should be considered in the evaluation.

Therefore, it is recommended to check on an individual basis if the longitudinal superstructure deformations are of a relevant magnitude, compared to the calculated minimum overlap length. Generally, contributions from pre-stressing, creep, shrinkage and temperature should be taken into account. While the first three will typically not change significantly anymore for older bridges, the temperature deformations remain subjected to variation. Following the regulations of [EC8-2] (Section 2.3.6.3), it is recommended to take into account the most unfavorable temperature deformation corresponding to the quasi-permanent load case. This implies that the combination factor ψ_2 can be applied on the temperature amplitude with respect to the average value. According to [SIA260], this combination factor can be chosen as $\psi_2 = 0.5$ for temperature actions on bridges.

It is therefore recommended to determine the provided overlap length taking into account the final deformations from pre-stressing, creep, and shrinkage, plus an unfavorable assumption for the temperature deformations corresponding to the quasi-permanent load case. The thus determined value needs to exceed the minimum overlap length according to the criteria given in [ASTRA05a].

4.4 Viscous Damping

It is known that real structures performing vibrations always tend to dissipate energy during such dynamic motions. This energy dissipation reduces the dynamic response of the system during an excitation and causes a decay of the motions after the excitation has ended. Many potential reasons for such energy dissipation may exist and it is common to summarize the several sources under the general term *damping*. As outlined by Chopra [Cho01], it is reasonable to distinguish the various types of energy dissipation as *rate dependent* and *rate independent* damping. While the former is a function of the motion velocity, the latter only depends on the displacement history while being independent of the speed of the motion. An example for *rate dependent* damping is the classical *viscous damping*, which incorporates a linear relationship between the velocity of motion and the corresponding damping force, as defined by equation (4.2). In contrast, the assumption of a *rate independent* damping is rather appropriate for hysteretic energy dissipation related to cyclic response of structures in the inelastic range, or for an (idealized) sliding response with a constant coefficient of friction.

$$F_{visc} = c \cdot \dot{u} \tag{4.2}$$

with F_{visc}:   Damping force
        c: Coefficient of (viscous) damping
        $\dot{u}$:   Velocity of motion

Traditionally, viscous damping has been the most common form of representation for energy dissipation – at least in more or less elastic analyses. This is not necessarily because the considered damping sources are really rate dependent and follow the corresponding law given in equation (4.2), but it is rather related to the fact that this way for a linear elastic SDOF system the dynamic motion can be described by a simple linear differential equation of second order[19]. This linear differential equation of motion is rather convenient for analytical solutions [Cho01], which represented a significant advantage over other possible representations in past times before the availability of powerful numerical solution tools. However, from the physical point of view, and depending on the source of energy dissipation, viscous damping may not always be the fully correct representation. In particular, in some cases viscous damping is also used to model *rate independent* sources of energy dissipation, which bears some conceptual problems, because the calibrated damping coefficient is only valid for a single velocity of motion (or on average for a single frequency of cyclic motion). If the real motion deviates from the assumed velocity or frequency, the resulting viscous damping effects inevitably over- or underestimate the real *rate independent* energy dissipation.

In practical applications, it is common not to define directly the damping coefficient c (or the damping matrix C in case of a MDOF system), but rather specify a certain *viscous damping ratio* ξ. The corresponding damping coefficient c then results as a fraction of the *critical damping coefficient* c_{cr}, according to equation (4.3). For a linear elastic SDOF system this critical damping coefficient c_{cr} is a function of the stiffness k and the mass m, as defined by equation (4.4). As a consequence, if the amount of viscous damping is defined by a certain damping ratio ξ, the subsequent damping coefficient c also depends on the stiffness and mass of the system. For linear elastic MDOF systems, equivalent relationships apply for the individual modes [Cho01].

$$c = \xi \cdot c_{crit} \tag{4.3}$$

$$c_{crit} = 2\sqrt{k \cdot m} \tag{4.4}$$

---

[19]   For a MDOF system with n degrees of freedom a system of n coupled linear differential equations of motion results.

4.4.1 Elastic Viscous Damping in Inelastic Systems

If the dynamic system response can be approximated by an essentially linear elastic behavior, it is common to combine all occurring energy dissipation effects into a single substitute viscous damping coefficient (or matrix). However, if the system experiences significant inelastic deformations a more detailed consideration should be given to an adequate representation of the energy dissipation related to the hysteretic response. In an inelastic time history analysis (ITHA) it is theoretically straightforward to allow for this aspect by defining hysteretic rules for those members which are loaded into the inelastic range. This is the most realistic way of modeling the hysteretic energy dissipation, as it includes the damping effects locally where they occur and in the form they develop, i.e. rate independent. The actual accuracy of the representation then only depends on how well the implemented hysteretic rules approximate the real inelastic behavior of the members. If any special seismic energy dissipation devices (e.g. viscous dashpot dampers, friction based devices or hysteretic dampers [PSC96]) are included in the bridge, these can also explicitly be modeled in an ITHA.

However, normally not only hysteretic energy dissipation will be encountered in systems responding inelastically. Therefore, it is common to model even in inelastic systems a certain amount of so-called *elastic viscous damping* which is intended to account for energy dissipation effects not included in the hysteretic models of the members. Priestley and Grant [PG05] identify essentially three main sources of energy dissipation which can require such an additional viscous damping:

- *Foundation damping*
  The system can loose energy due to radiation at the foundations (so-called *radiation damping*) or due to inelastic response of the soil.

- *Nonstructural damping*
  In building structures this typically relates to nonstructural members whose hysteretic response is not explicitly modeled. For bridges, nonstructural damping can e.g. be the result of friction in sliding bearings that are not explicitly modeled, or it can be related to an inelastic response of the pavement.

- *Small cycle hysteretic damping not included in the inelastic model of the members*
  Some (simplified) hysteretic models for the structural members approximate the inelastic behavior by multi-linear rules (e.g. the modified Takeda rule) which result in a linear elastic response as long as the force level has not reached the yield load for the first time. This is a simplification of the real behavior, as even during such pre-yield response a certain amount of small cycle hysteretic energy dissipation occurs. As a consequence, such simplified multi-linear hysteretic rules underpredict the energy dissipation in the pre-yield phase of the response.

The importance of each of these contributions can differ significantly between individual cases. Therefore it is rather difficult to quantify them on a general basis. The amount of foundation damping at piers and abutments, e.g., can reach considerable levels if inelastic deformations occur in the soil (see Section 3.5). Nonstructural damping in bridges is likely to remain below the level encountered in building structures, where nonstructural walls and installations can significantly influence the seismic response. The third aspect, the pre-yield hysteretic damping for simplified multi-linear hysteresis rules, considers not really a physical phenomenon but rather covers a modeling deficiency of the inelastic member response. Therefore its necessity depends on the chosen hysteresis models for the members. If these models already capture the entire response, including the initial elastic phase, in an adequate and realistic way, there is no real need to cover this aspect by additional viscous damping.

Generally, modeling any of the phenomena mentioned above as modal viscous damping in a multi-degree-of-freedom (MDOF) system results in a representation of the energy dissipation being smeared somehow over the entire structure. The individual distribution of the resulting damping forces and their effects on the seismic response depends on the details of how the damping matrix is determined (e.g. as Rayleigh damping [Cho01]). This smeared modeling of the damping might not be fully accurate if the energy dissipation in reality is a result of very localized mechanisms. If, e.g., the (considerable) damping corresponding to inelastic transverse embankment response (see Section 3.5.2) is smeared as modal damping over the entire structure, instead of modeling it locally at the abutments, this can change the displacement shape of the deformed bridge noticeably (see discussions in Section 4.6).

Therefore, it is recommended to model any significant contribution to the global energy dissipation in an explicit and direct way, wherever possible. This also avoids the need to model rate independent energy dissipation mechanisms as rate dependent viscous damping. However, it is recognized that such a direct introduction of individual damping mechanisms into the model will normally only be possible in an inelastic time history analysis. To use simplified analysis procedures, which may be more appropriate for normal applications in an engineering company, a certain trade-off between possibly accurate (local) damping modeling and efficiency of the analysis needs to be made. In many cases, where no extraordinary local damping mechanisms dominate the system behavior, summarizing the additional energy dissipation sources mentioned above altogether in a simplified smeared modal damping is likely to give an acceptable approximation.

When defining the elastic viscous damping ξ_{el} to be modeled in addition to the hysteretic energy dissipation in an inelastic system, care should be taken with respect to the stiffness representation of the system and the implicit consequences on the resulting damping coefficient c (or damping matrix C). According to equations (4.3) and (4.4), for a constant value of ξ_{el} the damping coefficient c of a SDOF system is proportional to the square root of the stiffness (similar relationships are valid for the modal properties of a MDOF system). In Fig. 4.5 three different (simplified) representations of the inelastic force-displacement relationship of a SDOF system are shown. These are (a) a curved hystereses, (b) a multi-linear hysteresis, and (c) a secant stiffness representation (in which the hysteretic energy dissipation needs to be taken into account by means of an additional separate *equivalent viscous damping*, see Section 4.5.2).
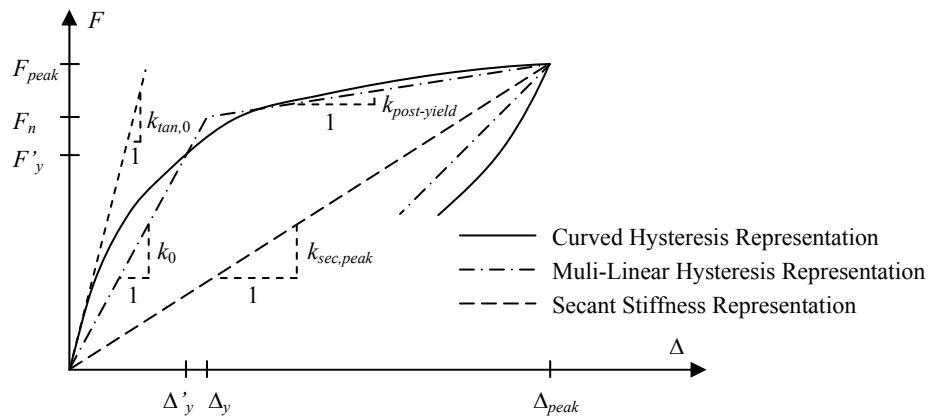
Fig. 4.5: Comparison of three different representations for the same cyclic inelastic SDOF behavior

From Fig. 4.5 it can be seen that in an inelastic system representation the unique definition of *one* stiffness is not possible anymore. The situation becomes further complicated if different representations are considered. This ambiguity also translates to the definition of a critical damping coefficient for inelastic systems[20]. In the majority of past studies the damping coefficient c has been determined assuming an elastic viscous damping ratio ξ_{el} and multiplying it with a critical damping coefficient c_{cr} corresponding to some form of initial elastic stiffness estimation (equations (4.3), (4.4)).

However, as can be seen in Fig. 4.5, the initial stiffness k_0 of the multi-linear hysteresis model can differ significantly from the initial (tangent) stiffness $k_{tan,0}$ of the curved hysteresis model. Consequently, assuming the same value for ξ_{el} would result in different damping coefficients, and thus in different actual damping forces, although both models are supposed to represent the same behavior. If, as an alternative, an equivalent visco-elastic secant stiffness representation is chosen (also shown in Fig. 4.5), the difference compared to the other two models becomes even larger. When defining or comparing viscous damping ratios to be used for inelastic systems, it is therefore important to clearly define on which stiffness the critical damping coefficient is based.

---

[20] It should be noted that the critical damping coefficient c_{cr} for inelastic systems loses its original meaning from linear elastic dynamics, where it defines the boundary for over-damped behavior. For inelastic systems it is rather used as an auxiliar quantity for the definition of the damping coefficient c as a function of an assumed viscous damping ratio ξ.

In each of the cases discussed above, the resulting viscous damping coefficient c has commonly been taken constant throughout the entire dynamic response of the system. More recent research, however, has focused on analyzing whether such a constant damping coefficient (or damping matrix in the case of MDOF systems) is a reasonable assumption. A theoretical study by Priestley and Grant [PG05] suggests that, instead of a constant damping coefficient, a *tangent stiffness proportional* damping coefficient might be a more reasonable assumption for many sources of energy dissipation in inelastic systems. This *tangent stiffness proportional damping coefficient* $c(k_{tan})$ is defined for SDOF systems according to equation (4.5), where c_0 is a constant damping coefficient being related to the elastic stiffness k_0, according to equations (4.3) and (4.4). The variable damping coefficient $c(k_{tan})$ is thus proportional to the instantaneous tangent stiffness k_{tan} during the system response. As a result of this approach, almost no damping forces develop during a response in the yield plateau if the post-yield stiffness of the inelastic system is low. The overall dissipated energy in a full inelastic cycle is therefore reduced significantly, compared to a model incorporating a constant damping coefficient of c_0.

$$c\left(k_{\tan}\right) = c_0 \cdot \frac{k_{\tan}}{k_0} \qquad\qquad (4.5)$$

As reasoning for their recommendation of a tangent stiffness proportional damping coefficient Priestley and Grant [PG05] discuss the three sources of additional energy dissipation mentioned above. Assuming that the foundations remain essentially elastic, they conclude that energy dissipation at the foundations only occurs while the support forces change. As long as the system responds in the yield plateau, these forces do no change (significantly) and therefore no viscous damping should be modeled during this phase of response either. In a similar way it can be argued that viscous damping which is intended to cover the energy dissipation during elastic cycles of simplified multi-linear hysteresis models should also be reduced once the system enters into the inelastic range, as the hysteretic damping in this response phase is already fully covered by the cyclic force-displacement rule.

Concerning the energy dissipation related to the hysteretic response of nonstructural elements or sliding between structural and nonstructural elements in building structures, Priestley and Grant [PG05] assume that these types of damping are dependent on displacements and are rather independent of the force level in the structure. Therefore, they conclude that nonstructural energy dissipation might be better represented by a constant damping coefficient instead of a tangent stiffness proportional damping. However, they estimate that in new building designs, following modern seismic design principles, the contribution of nonstructural damping to the total to viscous damping should be comparatively low. Therefore, Priestley and Grant [PG05] suggest (for new building structures) that the overall use of a tangent stiffness proportional damping coefficient should be considered most appropriate for the modeling of the mentioned additional energy dissipation effects not included in the hysteretic models of an inelastic system.

The situation with respect to individual contributors to such additional damping effects can, however, deviate somewhat for existing bridges, especially if they have not been designed following capacity design principles. For existing bridges, e.g., it cannot be ruled that the foundation response due to soil-structure interaction becomes inelastic (see Section 3.5). In fact, it is even possible that a footing experiences inelastic deformations, while the supported pier remains elastic due to the inelastic foundation response. In this case, the relevant part of foundation damping starts occurring just in the inelastic range and not, as assumed above for newly designed buildings, during the elastic part of the response. Generally, it is recommendable to model the energy dissipation related to such inelastic foundation behavior explicitly as a local mechanism (e.g. by a hysteretic rule or a discrete substitute dashpot damper). However, if as a simplification energy dissipation related to (limited) inelastic foundation response is taken into account in the form of a smeared viscous damping over the entire structure, tangent stiffness proportional damping would model the relevant damping effects just in the mistaken (i.e. elastic) phase of the response.

In normal cases, nonstructural damping in bridges may not be very large. The conceivable sources for nonstructural damping in bridges (e.g. friction in sliding bearings, hysteretic energy dissipation of the

pavement) may be better represent by a constant damping coefficient, as in the case of new buildings discussed above. Concerning viscous damping that is supposed to cover energy dissipation during the initial elastic response of multi-linear hysteresis models, the same relationships are valid as above for new buildings. This effect is therefore better represented by a tangent stiffness proportional damping. However, this is only of relevance if such simplified multi-linear hysteresis rules are used in inelastic time history analysis. A more complete curved hysteretic model being able to capture the energy dissipation in all response phases does not require additional viscous damping for this effect.

From the discussion above, it can be concluded that the decision which type of viscous damping representation is more appropriate for the analysis of existing bridges cannot be made on a general basis. Both, the structural characteristics of the bridge as well as the chosen modeling simplifications, influence the answer to this question. When performing inelastic time history analysis of an entire MDOF bridge system, another very practical issue comes into play. The study by Priestley and Grant [PG05] focuses primarily on SDOF systems which feature a single tangent stiffness k_{tan} and a single damping coefficient $c(k_{tan})$. For such cases the corresponding relationships are rather simple and fully described by equation (4.5). However, for MDOF systems the tangent stiffness is defined by a matrix K_{tan} and a relationship similar to equation (4.5) is rather difficult to define.

As discussed in [PG05], the use of Rayleigh damping using the instantaneous tangent stiffness matrix K_{tan} for the stiffness related component is not a reasonable solution for the modeling of tangent stiffness proportional damping in MDOF systems. At first, the tangent stiffness matrix influences only part of the damping matrix, while the other part is determined by the constant mass matrix. Second, the stiffness related component of the Rayleigh damping matrix influences mainly the damping ratio of the higher modes which are normally less relevant for the response. The damping of the typically predominant first mode is rather influenced by the mass component which does not change. Modeling only a stiffness proportional Rayleigh damping matrix, as proposed in [Pet+08], does not appear recommendable as this does not allow an adequate damping representation of several modes, but rather leads to substantial differences between the damping ratios of the various modes. This way, either the first mode would have to be underdamped or the higher modes might result artificially suppressed by an implicit overdamping. Therefore, an adequate representation of tangent stiffness proportional damping in MDOF inelastic time history analysis is difficult to achieve. This is a significant drawback of the concept, independent of its mechanical justification.

Aside from the conceptual choice for the viscous damping representation discussed above, a choice also needs to be made with respect to the amount of viscous damping to be modeled in the bridge analysis. This decision cannot reasonably be made without consideration of the different effects that shall be covered by such a smeared modal viscous damping. Therefore, similar discussions as before on the type of damping representation also apply for the amount of damping to be assumed. Obviously, the more effects need to be covered by the viscous damping, the higher it needs to be chosen. Generally, it appears recommendable to only cover rather secondary energy dissipation effects by the smeared viscous damping, wherever possible. Large individual damping mechanisms are always best represented locally in the form they occur (i.e. for example rate independent if necessary).

Due to the variety of effects potentially to be covered and the subsequently large number of influencing (and often uncertain) parameters, it is difficult to define an amount of viscous damping that would be generally valid. In particular, care should be taken with respect to values recommended in the literature for linear structural dynamics (e.g. [Bac+95], [Cho01]). These values are strongly amplitude dependent and may not represent the same damping effects that shall be taken into account by the elastic viscous damping in seismic ITHA. Care should also be taken in simply applying the same viscous damping ratios on bridges as commonly adopted for building structures. Some significant differences may exist in individual cases with respect to nonstructural elements, as well as with foundation damping.

Eurocode 8, part 2, [EC8-2] recommends using a viscous damping ratio of $\xi_{el} = 5\%$ if the significant part of the energy is dissipated in reinforced concrete members, and a ratio of $\xi_{el} = 2\%$ if the dissipation primarily occurs in prestressed concrete members. A weighted average ratio can also be estimated based on the deformation energy in the individual members (see e.g. Section 4.6.2e). The mentioned damping ratios refer to critical damping coefficients corresponding to the elastic secant

stiffness of the members up to first yield, i.e. k_0 of the bilinear backbone approximation in Fig. 4.5 (also see equations (4.3) and (4.4)). Eurocode 8-2 [EC8-2], however, neither states whether these damping ratios are considered as constant or tangent stiffness dependent, nor does it give any indication of which energy dissipation effects are supposed to be covered by these values. Therefore, in cases of reasonable justification it may be appropriate to deviate to some extent from these recommendations, based on individual considerations.

In the following, it is attempted to give a brief discussion on what aspects should be considered for such a decision. Generally, the damping related to nonstructural elements in bridges will normally be very low to negligible. Priestley and Grant [PG05] estimate that an appropriate damping ratio to cover nonstructural elements in seismically designed *building* structures is unlikely to exceed 0.5%. For bridges an appropriate value appears to be even significantly lower so that, in normal cases, an essentially negligible influence from nonstructural damping should be assumed. If – in special cases – a significant sliding response is to be expected, a corresponding contribution from friction can be estimated in the form of an equivalent viscous damping (see Section 4.5.2), which then can be smeared over the entire structure as a contribution to the weighted overall viscous damping ratio.

Concerning the requirement to model viscous damping to cover energy dissipation effects not included by the hysteretic member representation (i.e. primarily in the elastic range of multi-linear hysteresis models), the results from a study by Petrini *et al.* [Pet+08] can give some insight. In this study a shaking table test of a single cantilever RC bridge pier was numerically simulated using several modeling and damping approaches. For this purpose, two different hysteretic models for the pier behavior were calibrated on a preceding static-cyclic test of another equal pier. One of the models used a modified Takeda hysteretic rule, which defines a multi-linear approximation of the cyclic-inelastic behavior. This rule results in linear elastic response until the yield force is reached for the first time. Afterwards, the modified Takeda rule features hysteretic behavior (and thus energy dissipation) even in small cycles not reaching the yield force. The second model used for the simulation was based on a fiber-section finite element representation including hysteretic rules for the individual materials. This model results in a curved hysteretic response, which already features energy dissipation in small cycles below the yield load.

As damping models, constant viscous damping and tangent stiffness proportional viscous damping were considered. In both cases a value of $\xi_{el} = 5\%$ was assumed for the elastic viscous damping ratio. It should be noted that this viscous damping ratio referred to different initial stiffnesses (and thus different critical damping coefficients) in the two hysteretic models. In the modified Takeda model the initial stiffness was equal to the secant stiffness to first yield (corresponding to k_0 in Fig. 4.5), while in the fiber-section model the tangent stiffness at zero load (corresponding to $k_{tan,0}$ in Fig. 4.5) served as a reference. Due to a factor of 3 between these two stiffness values, the effective damping coefficient was roughly 70% higher in the fiber-section model than in the modified Takeda model. Aside from the constant and tangent stiffness proportional damping models using $\xi_{el} = 5\%$, both structural models (modified Takeda and fiber-section) were also analyzed without any viscous damping.

During the shake table test the pier developed significant strength degradation with subsequent failure. In the following, the comparison of the experimental results to the numerical analyses is limited to the part of the response before the onset of strength degradation, as the numerical analyses cannot describe the transitional phase to failure in a reasonable way. The time window up to onset of degradation consisted only of the first 3.5 s and during this phase only about 3 to 4 large inelastic cycles occurred.

Comparing the two analyses featuring a constant viscous damping coefficient based on $\xi_{el} = 5\%$ to the experimental results, it was found that the numerically computed displacements strongly underpredicted the measured shake table response. In the case of the fiber-section model the underprediction ($\approx$ -60%) was found to be even more severe than for the Takeda model ($\approx$ -30%), which may be related largely to the differing reference stiffnesses for the definition of the damping coefficient, as mentioned above. The strong underpredictions in both models show that a constant damping viscous damping corresponding to $\xi_{el} = 5\%$ overestimates the amount of required additional damping. This is to some extent not very surprising, as in the shaking table test conceptually no nonstructural damping can occur and also little to no foundation damping should be expected. Therefore, only structural damping not already covered by the hysteretic rules justifies any additional

viscous damping. Taking into account that a damping ratio of $\xi_{el} = 5\%$ is often assumed for real structures where all three of the mentioned effects occur altogether, this value might be expected as too high for a shaking table test under laboratory conditions. This appears especially true for the fiber-section model which is intended to already include the entire hysteretic energy dissipation throughout the response.

The analyses using the two alternative damping models (tangent stiffness proportional with $\xi_{el} = 5\%$ and zero damping) result in substantially lower viscous energy dissipation throughout the response. Comparing the corresponding numerical predictions to the experimental response, a significantly better agreement can be observed for both, the fiber-section model as well as the Takeda model. While the former tends to result in a slight underprediction, the latter was rather found to overpredict the experimental behavior slightly. However, the differences in peak displacements between experiment and analysis were limited to about ±20%. In fact, if the fiber-section model is combined with zero viscous damping and the modified Takeda model is combined with tangent stiffness proportional damping, the differences between analyses and experiment reduced to about ±10%. Based on the reasoning behind the various models discussed above, these two combinations also appear to be the most reasonable ones from the theoretical point of view which is being confirmed by the results.

From the presented results it can be concluded that a constant viscous damping with $\xi_{el} = 5\%$ should be considered as too high to represent only the structural damping not covered by (well calibrated) hysteresis models. For a fiber-section model that also captures the energy dissipation behavior in small pre-yield cycles, no additional viscous damping is required for this purpose. In the given case, the modified Takeda model also hardly required additional viscous damping to cover structural energy dissipation. To some extent this might be related to the fact that the chosen ground motion did not result in many relevant elastic pre-yield cycles but very quickly started with large inelastic cycles up to displacement ductilities in the range of $\mu_\Delta \approx 6$. Therefore, the elastic response phase where the Takeda rule requires additional viscous damping to correct the structural response hardly occurred. This is not necessarily always the case for seismic ground motions, especially not for moderate seismicity. It should be noted that the ground motion used in [Pet+08] was intentionally chosen to maximize the difference between constant and tangent stiffness proportional damping. Furthermore, the original ground motion was scaled by a factor of 8, which is rather high. Therefore, the characteristics of the chosen ground motion can be considered as rather extreme and the observed phenomena may not always be that pronounced for other ground motions. Nevertheless, the tangent stiffness proportional damping was found to be effective in reducing the additional energy dissipation in the inelastic range of the response.

At the same time, the evaluation of adequate models for the viscous damping representation cannot be conducted independently of the value chosen for the damping ratio ξ_{el}, nor can it be done independent of the energy dissipation characteristics of the hysteretic models. Obviously, any viscous damping in this context should compensate for lacking dissipation by the hystereses. If, e.g., the hysteretic damping on average already overpredicts the real structural dissipation, any additional viscous damping would be counterproductive. In the study by Petrini *et al.* [Pet+08] considerable effort was undertaken to calibrate the two hysteretic models to the antecedent quasi-static cyclic test. This level of accuracy would be impossible to reach in a practical assessment case of a real structure. But even for these ideal conditions, in [Pet+08] it is not explicitly reported how well the calibrated hysteretic models agreed with the tested pier response in terms of hysteretically dissipated energy.

Generally, the deviations between the hysteretic energy dissipation of a model and a real structure can be significantly larger than just the comparatively small part resulting from the pre-yield elastic response. In fact, in some of the tests on models of bridge piers performed by the author (see Section 4.7.2), significantly lower hysteretic energy dissipation than expected from common models was observed. For example, the *thin Takeda hysteresis* rule[21], typically recommended for RC piers and columns [PCK07], would have overpredicted the hysteretic energy dissipation of Test Unit VK1 by roughly 40% (see Section 4.7.2a). This appears especially noteworthy as the corresponding parameter configuration already represents the thinnest hystereses that can be achieved for the modified Takeda

---

[21]   Using an unloading parameter of $\alpha_{unload} = 0.5$ and a reloading parameter of $\beta_{reload} = 0$ in the nomenclature of Ruaumoko [Car04].

rule in the software codes [Car04] and [SS06]. On the other hand, the experimentally determined hysteretic energy dissipation of Test Unit VK3 was found to agree reasonably well with that of the corresponding model using the *thin Takeda hysteresis* rule. In the light of these large uncertainties with respect to the estimation of the general hysteretic energy dissipation, the influence of the elastic response phase on the required viscous damping should be put into perspective. This also influences the decision on the more appropriate viscous damping model.

The comparative results by Petrini *et al.* [Pet+08] are further influenced by the choice of viscous damping ratio as $\xi_{el} = 5\%$. The differences between constant and tangent stiffness proportional damping would have been less pronounced if a lower value for ξ_{el} had been chosen for the analyses. It cannot be ruled out that a similarly good agreement with the experimental results could have also been achieved if a constant viscous damping with a ratio of e.g. $\xi_{el} \approx 1\%$ (or less) had been used. Because of the absence of nonstructural and foundation damping, and in combination with the well calibrated hysteretic models, a value that low for ξ_{el} could also be justified from the theoretical point of view. For a good approximation, it may not be essential to represent the damping correctly at every time instant (this could not be achieved by a rate-dependent damping anyway), but rather to capture the average dissipation over several cycles in a reasonable way. It may be possible that this could also be achieved with constant viscous damping in combination with a correspondingly well chosen damping ratio. At the same time, the study by Petrini *et al.* [Pet+08] has shown that the error from not modeling any viscous damping for additional structural energy dissipation can be very limited. However, this may strongly depend on the accuracy of the chosen hysteretic representation.

Summarizing the above discussions on the various sources for elastic viscous damping, it can be concluded that non-structural damping and additional structural damping, intended to cover deficiencies of multi-linear hysteretic models, are likely not to contribute significant amounts of viscous damping in bridge structures. With respect to the additional structural damping, however, this strongly depends on the general success of capturing the relevant hysteretic energy dissipation characteristics of the structure. A considerable uncertainty may exist in this context. The factor that is likely to have the largest influence on the appropriate amount of elastic viscous damping may be the foundation behavior and its modeling. Especially if inelastic foundation response can occur that is not explicitly treated in the form of local energy dissipating mechanisms, foundation damping can contribute significantly to the overall required elastic viscous damping. However, it is impossible to estimate this on a general basis. At the same time, the foundation response can also strongly influence whether constant viscous damping or rather tangent stiffness proportional damping is more appropriate. The fact that energy dissipation at foundations increases in the inelastic range would rather contradict the use of tangent stiffness proportional damping for such cases. If, in contrast, the foundations remain elastic, the theoretical reasoning by Priestley and Grant [PG05] applies and tangent stiffness damping could be more appropriate.

For practical applications it is recommended to choose – for normal cases – elastic viscous damping ratios within the range recommended by Eurocode 8-2 [EC8-2], i.e. between $\xi_{el} = 2\%$ and $\xi_{el} = 5\%$. If all sources of damping are taken into account, it should not be necessary to consider total values lower than $\xi_{el} = 2\%$, as e.g. a certain amount of radiation damping at the foundations will always occur. On the other hand, if certain sources of energy dissipation would justify values higher values than $\xi_{el} = 5\%$, it might be worthwhile including these as discrete mechanisms in the model. It is important to note that the choice between a constant and a tangent stiffness proportional damping model equally influences the overall dissipated energy as the choice of the damping ratio. To result in a comparable behavior, for constant damping lower values of ξ_{el} would have to be chosen than for tangent stiffness damping.

For the actual decisions it may be important to keep in mind that the general energy dissipation characteristics (viscous and hysteretic) of real structures can hardly be determined with very high precision. This is especially true if significant foundation damping is to be expected, but it may also apply to the general hysteretic behavior of RC members. It is therefore questionable whether an overly sophisticated approach for the estimation and representation of viscous damping is justified in practical analysis applications. This holds true for the value of viscous damping ratio as well as for the chosen damping model (constant or tangent stiffness proportional). This should not be in contradiction to the findings presented in [PG05] and [Pet+08] that the choice of viscous damping can result in

considerable influence on the system response. Instead it rather calls for a cautious and sufficiently conservative approach.

For ordinary bridges and without specific consideration of the individual details, a reasonable first assumption for the elastic viscous damping might be a ratio of $\xi_{el} = 2\%$ if combined with a constant damping model or alternatively a value of $\xi_{el} = 5\%$ if combined with a tangent stiffness proportional damping model. In regions of moderate seismicity the expected number of large inelastic cycles is likely to be significantly lower than for the strong ground motion used in [Pet+08]. In this case the response differences between constant and tangent stiffness proportional damping are less pronounced [BD06]. The remaining deviations are expected to be roughly compensated on average by the two different damping ratios suggested above. Both values are also within the range of recommended damping ratios in [EC8-2].

The previous discussions may serve as an aid for potential adjustments to allow for specific characteristics of an individual bridge. In particular, a stronger influence from foundation damping may justify higher values for ξ_{el}. It might be reasonable to rather use a constant damping model in this case. It should be noted that, for a real structure, the chosen viscous damping ratio will always bear a certain amount of engineering judgment. If felt necessary, a parameter variation should be performed in order to study the sensitivity of the response and possibly choose a cautious and conservative solution.

It shall be mentioned that aside from the *elastic viscous damping* discussed in this subsection, viscous damping can also be used to cover – as an approximation – the entire hysteretic energy dissipation. This approach can only be used reasonably if the force-deformation behavior of the structure or its members is represented linearly using secant stiffnesses. This equivalent linearization is discussed in Section 4.5.2.

4.4.2 Influence of Different Viscous Damping Ratios on Seismic Demand

If a dynamic time history analysis is performed, the influence of the chosen viscous damping ratio is automatically taken into account and no further considerations are required. However, many simplified analysis techniques somehow make use of (elastic) response spectra to define the demand. These spectra are often defined in codes for a single viscous damping ratio, typically $\xi = 5\%$. If other viscous damping ratios are to be taken into account, the code specified spectra need to be modified correspondingly. Several researchers have proposed equations for a transformation factor η which can be applied on the elastic 5%-spectra in order to estimate spectral values corresponding to other damping ratios. Some of these equations have also been implemented into existing codes.

In the medium period range the 5%-spectra can simply be multiplied by η, so that the transformation factor in this case basically represents the relationship given in equation (4.6). However, based on theoretical considerations, the spectral ordinates corresponding to different damping ratios must converge to the same values for very short and very long periods. As a consequence, for periods smaller than T_B [SIA261] defines another relationship how the transformation factor η is to be applied. The very long period range is not covered by [SIA261], which might not be of major relevance for normal structures either. It should be noted that the guideline [SIA2018], which only focuses on building structures, does not allow for the transformation factor η in its definition of the spectra. Therefore, if damping ratios other than $\xi = 5\%$ are to be considered, rather the elastic acceleration spectra of [SIA261] should be used. The corresponding elastic displacement spectra can be computed based on equation (4.1). In this case, the importance factor γ_f needs to be taken into account additionally, as it is omitted in the elastic spectra of [SIA261].

$$\eta(\xi) = \frac{\Delta_\xi}{\Delta_{5\%}} \tag{4.6}$$

with Δ_ξ: Displacement demand for viscous damping ratio ξ
      $\Delta_{5\%}$: Displacement demand for viscous damping ratio 5%

When using any proposed equation for the transformation factor η, it should be noted that these relationships are purely *empirical* and can only give the *average* influence related to differing damping ratios. As a consequence, applying any transformation factor η on the displacement demand (or a response spectrum) from a single ground motion will rather not give a reasonable estimation. Instead, the factor η is only to be used on *average* spectra coming from a larger set of ground motions. The uniform hazard spectra typically defined in codes (also in [SIA261], [EC8-2]) fulfill this criterion so that the use of η in these cases is possible. Nevertheless, even when applied on average spectra, the resulting transformations can only be considered as rough estimations. This will also become clear from the variability between the various proposals discussed in the following.

Below, several proposals are summarized which define the correction factor η as a function of the viscous damping ratio ξ. At first, equation (4.7) represents the relationship given in the current version of Eurocode 8, part 1, [EC8-1]. The same expression has also been adopted in the Swiss code [SIA261]. The equation results in exactly the same values as recommended by Bommer and Elnashai [BE99] for the discrete damping ratios shown in Tab. 4.1. It should be noted that the lower boundary value of $\eta_{min} = 0.55$, defined in equation (4.7), is probably not mechanically justified but rather a cautious limitation. However, this boundary is unlikely to be relevant in the majority of cases as it governs only for damping ratios higher than 28%. Most probably it has been introduced because the study by Bommer and Elnashai [BE99] did not investigate damping ratios higher than 30%. Furthermore, it should be noted that Bommer and Elnashai only focused on damping ratios higher than 5%, i.e. only transformation factors η lower than unity. The performance of equation (4.7) for lower damping ratios, where η results in an increase of spectral values, may therefore be somewhat uncertain.

Eurocode 8-1 (2003) [EC8-1] & [SIA261]:
$$\eta(\xi) = \left(\frac{10\%}{5\% + \xi} \right)^{0.5} \geq 0.55 \qquad (4.7)$$

Eurocode 8-1-1 (1994) [EC8-1-1]:
$$\eta(\xi) = \left(\frac{7\%}{2\% + \xi} \right)^{0.5} \geq 0.7 \qquad (4.8)$$

Tolis and Faccioli [TF99]:
$$\eta(\xi) = \begin{cases} \left(\dfrac{7\%}{2\% + \xi} \right)^{0.5} , \ for \ \xi < 5\% \\[4mm] \left(\dfrac{15\%}{10\% + \xi} \right)^{0.5} , \ for \ \xi > 5\% \end{cases} \qquad (4.9)$$

Shibata and Sozen [SS76]:
$$\eta(\xi) = \frac{11\%}{6\% + \xi} \qquad (4.10)$$

ξ [%]	5	10	15	20	25	30
η [-]	1	0.82	0.71	0.63	0.58	0.53

Tab. 4.1: Transformation factors for various viscous damping ratios according to [BE99]

An earlier version of Eurocode 8 recommended a different relationship for η, given in equation (4.8). Concerning the lower boundary value of 0.7, similar comments as for the current Eurocode 8 equation apply as it is unlikely that its background is mechanically based. The relationship of equation (4.8) was adopted in a proposal by Tolis and Faccioli [TF99] for damping values lower than $\xi = 5\%$, given in equation (4.9). For higher damping values Tolis and Faccioli found another expression to be more appropriate, which results in more conservative response estimations for large damping ratios. They recommend a lower boundary value of 0.5 for η. However, this limit only governs for damping ratios

higher than 50% and is therefore unlikely to be relevant in real cases. It is therefore omitted in equation (4.9). Another, rather early, proposal for the relationship between η and ξ had been developed by Shibata and Sozen [SS76] in the context of the substitute structure method. This proposal corresponds to the expression given in equation (4.10).
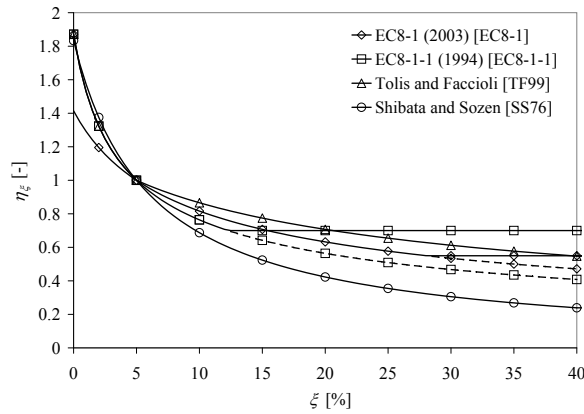

Fig. 4.6: Graphical comparison of proposals for transformation factors to account for the influence of various viscous damping ratios

A comparison of the various approaches is shown in Fig. 4.6 and a numerical evaluation for $\xi = 2\%$. and $\xi = 10\%$ is given in Tab. 4.2. The curves for the two Eurocode equations are shown in Fig. 4.6 with consideration of the boundary values defined in the codes. In addition, the same curves are also shown as dashed lines without these limiting values. From the comparison, it can be seen that the proposal by Shibata and Sozen [SS76] describes the strongest influence of the damping ratio on the elastic response. Especially for values higher than $\xi = 5\%$ this results in a decrease of η which is significantly stronger than that proposed by the other relationships. As the other, more recent, approaches are probably based on somewhat more in-depth investigation of the topic, care should be taken because equation (4.10) might be considered unconservative for viscous damping ratios higher than 5%.

	Transformation factors η	
	$\xi = 2\%$	$\xi = 10\%$
Eurocode 8 (2003) [EC8-1] Swisscode [SIA261]	1.20	0.82
Eurocode 8 (1994) [EC8-1-1]	1.32	0.76
Tolis and Faccioli [TF99]	1.32	0.87
Shibata and Sozen [SS76]	1.38	0.69
Priestley *et al.* [PCK07] near-field	1.15	0.87

Tab. 4.2: Numerical comparison of proposals for transformation factors η to account for the influence of various viscous damping ratios

When comparing equations (4.7) and (4.8) from the new and the old version of Eurocode 8 without consideration of the boundary values, it can be seen from Fig. 4.6 that the old relationship is significantly more conservative (by up to about 30%) for low damping ratios, while the new relationship is somewhat more conservative (by up to about 10%) for high damping ratios. If the

individual limiting values are taken into account, equation (4.8) from the older version of Eurocode 8 is more conservative over large part of the range of damping ratios.

In comparison to the two Eurocode approaches (without boundary values), the proposal by Tolis and Faccioli [TF99] appears rather conservative over the entire range. For low damping ratios it is equal to the more conservative old Eurocode expression (and also agrees reasonably well with the equation by Shibata and Sozen [SS76]). For higher damping ratios the relationship by Tolis and Faccioli results in even higher demand estimations than the new Eurocode 8 equation (without boundary value), which is the more conservative one of the two code proposals.

From these relative comparisons, it is not possible to draw any absolute conclusions concerning the appropriateness or accurateness of any of the proposals. It is also beyond the scope of this text to further evaluate the various approaches. Any evaluation result would most likely depend strongly on the set of ground motions to be selected and their characteristics. It is also likely that a considerable scatter of the results would be encountered. Therefore it might be difficult to say that either one of the proposals is really significantly better than the others on a general basis. In fact, it would be possible that, e.g., one equation performs better for low damping ratios while another one gives better results for highly damped systems.

When applying any of the presented equations, one should therefore be aware of the immanent uncertainties. It appears that for a rather cautious estimation the approach by Tolis and Faccioli [TF99] (equation (4.9)) would be best suited, although even this relationship does not guarantee a conservative result in every case. As stated above, it is recommended to rather not use the approach by Shibata and Sozen [SS76] on damping ratios higher than $\xi = 5\%$, because it deviates significantly from the other proposals in the unconservative direction. Choosing equation (4.7) might be appealing from a formal point of view because it complies with the current European and Swiss codified regulations.

In this context it may also be interesting that Priestley *et al.* [PCK07] rather recommend the use of the older Eurocode 8 equation (4.8) instead of the newer equation (4.7). As their comparisons are related to the equivalent visco-elastic linearization used in the direct displacement based design (DDBD) approach, this recommendation primarily focuses on damping ratios higher than $\xi = 5\%$. This recommendation appears somewhat surprising as just for this damping range Tolis and Faccioli found another expression more appropriate, while they also used the old Eurocode 8 expression for damping ratios lower than $\xi = 5\%$. This shows that some further investigation into the topic might be useful. However, possibly the differences might also simply be related to the inevitable scatter of these simplified expressions.

Finally, it should be noted that the influence of damping on the seismic response tends to differ between far-field and near-field ground motions. Damping becomes significantly less effective in reducing the seismic response if large velocity pulses occur, e.g. as a consequence of forward directivity in near-field ground motions. As a consequence, the overall influence of damping in such cases is lower. Therefore, Priestley *et al.* [PCK07] suggest that the exponent of 0.5 in the equations (4.7) through (4.9) might be too high for near-field ground motions and they recommend substituting it by 0.25 in such cases. Based on these considerations they tentatively propose the use of equation (4.11) for near-field ground motions. At the same time, it should be mentioned that near-field forward directivity also influences the spectral shape and amplitude and therefore requires further detailed considerations if this aspect is found to be necessary. This rather specialized topic, however, is beyond the scope of this text.

Priestley *et al.* [PCK07] for near-field:
$$\eta(\xi) = \left(\frac{7\%}{2\% + \xi} \right)^{0.25}$$
(4.11)

It should be noted that wherever either of the two equations (4.7) or (4.8) is further used throughout this text, the limiting values included in the equations will be ignored. This is related to the fact that they are not considered as founded on mechanical reasons. For a possibly realistic description of the dynamic behavior it is assumed that the pure equations without the limits are likely to give better results.

4.5   Simplified Demand Estimation of Inelastic SDOF Systems

Although bridges typically feature more than one relevant dynamic degree of freedom, the inelastic response of single-degree-of-freedom (SDOF) systems nevertheless gives valuable insight into the general seismic behavior of structures. This understanding is also one of the key elements of many nonlinear static procedures for the simplified displacement based analysis of structures. Generally, response spectra can be used to define the demand of individual SDOF systems subjected to a certain level of seismic excitation. Appropriate procedures and assumptions also allow estimating the response of multi-degree-of-freedom (MDOF) systems using the information on SDOF response. In the case of linear elastic behavior this is usually achieved using a modal decomposition as part of a response spectrum analysis. For inelastic behavior, the more generalized nonlinear static approaches outlined in Section 4.6 serve for a similar purpose in an approximate manner.

While it is conceptually possible to compute inelastic response spectra for a given hysteresis type, code specified response spectra are usually based on linear elastic behavior. Several approaches have been developed to modify these elastic spectra in order to estimate the corresponding response of inelastic SDOF systems. These concepts also give insight into the influence inelastic behavior has on the seismic demand, compared to the response of corresponding linear oscillators. Aside from the deviations in the overall global demand, inelasticity also influences the deformation shape of MDOF systems. This is due to the modified contributions of the several parts of the structure related to a change of the relative stiffness distribution in the inelastic system. Hence, compared to elastic response, inelastic behavior can be interpreted as having two separate effects on the demand: (i) a change of the global overall deformation demand, and (ii) a modification of the (relative) displacement shape for MDOF systems. While the latter will be the topic of Section 4.6, the former is discussed in this Section 4.5 in the context of the inelastic SDOF response.

Relating the inelastic seismic SDOF response to that of corresponding elastic systems has been the subject of intensive research throughout past decades. The works by Newmark and Hall summarized in [NH82] as well as by Gülkan and Sozen [GS74] have brought valuable insight into the general aspects of this problem and they have been the basis of many further developments in the following decades. At the same time, the two studies represent the two existing fundamental approaches to estimate the demand of inelastic SDOF systems based on the response of corresponding elastic systems. In the first concept, being related to the work by Newmark and Hall [NH82], the inelastic system is primarily characterized by its initial elastic stiffness and the corresponding natural period. The demand on the inelastic system is then estimated based on the peak response of a corresponding linear elastic system having the same period and viscous damping properties. This linear response can easily be determined provided the seismic input is defined by an elastic response spectrum. The difference between the responses of the elastic and the inelastic system is then typically considered in the form of empirical modification factors, or in certain conditions it is assumed to be negligible. The general approach of representing the inelastic system by a linear oscillator having the same elastic period and the same elastic viscous damping ratio, while the influence of inelasticity is taken into account by means of an adequate response modification, will be termed *initial period based method* in this text.

The alternative concept, corresponding to the general approach of Gülkan and Sozen [GS74], assumes that the nonlinear force-displacement relationship of an inelastic system can be represented by a reduced secant stiffness (depending on the deformation state) while the energy dissipation characteristics of the hysteretic behavior can be approximated by an equivalent amount of viscous damping. Based on these assumptions, a substitute linear elastic system with equivalent viscous damping can be defined and for this system the peak response can again be determined easily from an elastic response spectrum. As the mentioned adjustments concerning stiffness and damping are intended to take into account both, the softening and the hysteretic energy dissipation of the inelastic system, no further modifications of the elastic deformation demand need to be conducted. This means that the response of the substitute linear model is assumed to sufficiently approximate that of the original inelastic system. Any approach in which an inelastic system is represented by an equivalent linear oscillator, having a certain secant stiffness and an increased effective viscous damping, will be referred to as *equivalent linearization method* in this text. As an alternative, the approach may also be termed as *secant stiffness representation*.

In a practical application, some general differences result between the two concepts outlined above. The first difference is the natural period that is considered to best represent the inelastic system and for which the spectral value is determined. The first approach, corresponding to Newmark and Hall's work, assumes that the elastic spectral value at the initial stiffness based period is the best indicator for the response of an inelastic system, while the use of an equivalent linearized system implies that the spectral value should depend on a (higher) period corresponding to a secant stiffness. Another difference in the application of the methods is related to the fact that for the equivalent linearization method spectra with varying viscous damping ratios are required, whereas for the initial period based approach only one spectrum is needed. Furthermore, in an assessment case the initial period of the system is known right from the beginning and the spectral value for an initial period based method can thus be determined directly. In contrast, in the equivalent linearization method the equivalent viscous damping ratio, as well as the secant stiffness based effective period, depend on the deformation demand. Therefore, some iteration may be necessary in an assessment case, because the equivalent linear system properties are not known at the beginning.

Both approaches have in common that they rely on some form of approximate relationships that are typically determined empirically. For the initial period approach this empirical input consists of the relationship that is used to modify the elastically determined response, while for the equivalent linearization approach empirical equations are required to determine the equivalent viscous damping as a function of the peak demand. In some variants of the equivalent linearization approach an empirical relationship is also used for the determination of the effective period. It should therefore be noted that both concepts are only approximations and considerable uncertainties may exist in their application. The choice of the mentioned empirical relationships is likely to influence the quality of the results significantly. At the same time, the many existing variants and further developments of each of the approaches are mainly related to the assumed empirical relationships in either one.

For both approaches it may be said that the underlying empirical relationships are only strictly valid for the type of configurations used in their calibration. This primarily refers to the type of hysteretic behavior, but also to the viscous damping model that was used (e.g. constant or tangent stiffness proportional damping, see Section 4.4.1). As a consequence, if applying any of the empirical relationships on a system having e.g. a different hysteretic behavior then the one assumed during the calibration of the relationship, certain inaccuracies result in addition to the already existing general uncertainties. In the same way, the empirical relationships also depend on the type of ground motions used for their deduction. As a consequence, soil conditions, earthquake magnitude, and epicentral distance can influence to some extent the calibration process and the best results will be achieved if the empirical relationships were developed for similar conditions as those given in an application case.

But even under optimum conditions it should be noted that the resulting approximations are likely to fit only on a statistical basis, averaged over a set of ground motions. For an individual excitation, considerable deviations between the real inelastic response and the approximated demand using either of the two described approaches can occur. This inevitable uncertainty should be kept in mind for the interpretation of the results. However, it is also noteworthy that a considerable scatter generally exists between the individual inelastic responses to a set of various ground motions intended to represent the same seismic level, especially in the case of real records. Therefore, the uncertainty related to the prediction of an individual response using the simplified empirical approaches must be put into perspective. In fact, averaged smooth empirical relationships in the approximate methods can only be used reasonably in combination with the smooth averaged response spectra [VFF94]. However, for practical design or assessment cases, where the seismic input is defined by codified spectra, this aspect does not represent a limitation as codes typically define smooth uniform hazard spectra which fulfill this criterion.

In the following sections both general approaches outlined above will be discussed in more detail and for each conceptual approach a set of selected variants is presented. At first, in Section 4.5.1 the initial period based methods are discussed and then in Section 4.5.2 selected procedures for equivalent linearization are presented. The consequences for the actual demand estimations are subsequently compared and discussed in Section 4.5.3.

4.5.1 Initial Period Based Methods

In past times when seismic design was still predominantly force based, it was already discovered rather early that inelastic response has a beneficial influence on a structure's survival chance during a strong earthquake. This is related to the hysteretic damping as well as the additional plastic deformation capacity. However, due to the force based view at the time, the analyses did not directly focus on the displacements but rather on the required strength. In order to nevertheless allow for the beneficial effects from the inelastic response, reduced force demands were defined which depend on the provided deformation capacity. In this context, it is common practice to relate the displacement demand and capacity to the systems nominal yield displacement resulting in displacement ductilities μ_Δ, according to equation (3.2).

The reduced force demand is typically expressed in the form of a *force reduction factor R_y* which is defined as the ratio between the yield strength F_y of an inelastic system to the force demand of a corresponding linear elastic system F_{el}, according to equation (4.12). In this case, the linear elastic system has the same stiffness as the initial stiffness k_0 of the inelastic system, resulting in corresponding equal elastic periods as well. Furthermore, the same viscous damping ratio is considered in both cases. The possible force reduction factor R_y – also called *strength ratio* – depends on the provided ductility capacity of the inelastic system, with R_y typically increasing for larger ductility capacities. Furthermore, R_y can be influenced strongly by the elastic period of the system and to some extent depends on the hysteretic behavior, the viscous damping assumptions and the ground motion characteristics.

$$R_y = \frac{F_{el}}{F_y} \tag{4.12}$$

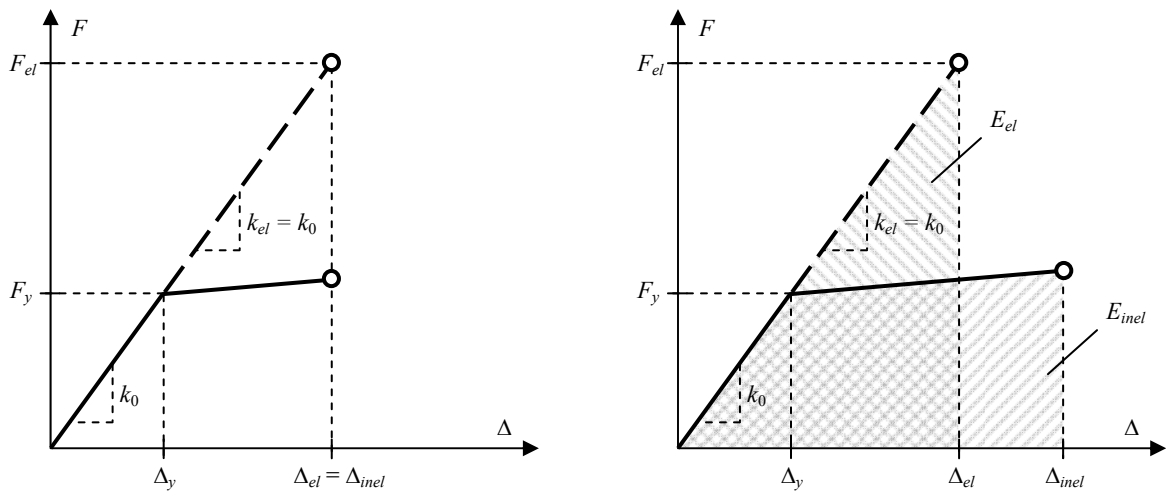with $\quad F_{el} = m \cdot S_{a,el}(T_0)$

Fig. 4.7: Comparison between the response of linear elastic SDOF and inelastic SDOF with equal initial period left: Equal displacement approximation, right: Equal energy approximation

A common simplified hypothesis which had been adopted already in the early stages of seismic design is the so-called *equal displacement rule* [NH82] (see also [Bac02]). This concept assumes that the displacement demand of the inelastic system and that of the elastic system with the same elastic period are roughly the same. Such a behavior is depicted on the left side of Fig. 4.7. In this case the force reduction factor R_y results equal to the ductility demand μ_Δ, as given by equation (4.13). However, it needs to be emphasized that the expression *equal displacement rule* is somewhat misleading, because there is no real physical reasoning behind this assumption. Empirically, it can be found that under certain circumstances indeed the peak response of the inelastic and corresponding linear elastic systems are statistically rather similar. However, this is on one hand a purely empirical finding, and on the other hand this statement is only valid on average over a larger set of ground motions. In an

individual case, considerable deviations between the two demands may exist. Therefore, it might be more appropriate to speak of an *equal displacement approximation* instead of a rule.

> *Equal displacement approximation:* $\qquad R_y = \mu_\Delta$ $\qquad\qquad\qquad\qquad$ (4.13)

The reasoning behind the *equal displacement approximation*, despite its lack of a strict physical basis, might be explained as the result of two counteracting effects which to some extent cancel each other out. On one hand, the inelastic system, once it yields, becomes effectively softer resulting in a period shift towards larger periods. This is likely to result in an increased deformation demand, compared to a linear system having the same initial elastic stiffness (and elastic fundamental period). On the other hand, the cyclic inelastic response results in considerable hysteretic energy dissipation which tends to reduce the response. The relative magnitude of these two opposite effects depends on the hysteretic behavior of the inelastic system, the assumed viscous damping model, and strongly on the relationship between the system's elastic period and the shape of the response spectrum.

In a study by Priestley and Grant [PG05] the *equal displacement approximation* was found to give an acceptable approximation of the response on average in the long period range, but only when a constant (initial stiffness proportional) elastic viscous damping with ξ_{el} = 5% was modeled. Performing the analyses with a tangent stiffness proportional elastic viscous damping model featuring the same damping ratio of ξ_{el} = 5%, the *equal displacement approximation* was found to give noticeably unconservative demand estimations for many hysteretic models. This shows the sensitivity of this empirical approximation to the specific conditions.

It is further important to note that the applicability of the *equal displacement approximation* is generally limited to the medium to long period range, while it may give completely unconservative demand estimations for systems with short elastic periods. Several literature sources give different recommendations for the limiting period up to which the *equal displacement approximation* can still be reasonably applied. Paulay *et al.* [PBM90] defines this limit at a period of $T_0 \cong 1.4$ s (f_0 = 0.7 Hz), while Bachmann [Bac02] recommends a limiting elastic period of $T_0 \cong 0.7$ s (f_0 = 1.5 Hz). The difference between the two values might primarily be related to different accepted tolerances against inaccuracies, as the *equal displacement approximation* does not suddenly loose its validity but rather tends to become increasingly inaccurate for decreasing periods. At the same time, it is also known that the limiting period depends on the ground motion characteristics, especially those related to the local soil conditions at the site. As a consequence, Newmark and Hall [NH82] do not define a fixed limit value but rather recommend using the characteristic period of the ground motion which separates the acceleration sensitive part of the elastic response spectrum from the velocity sensitive part. In a statistical study, Ruiz-García and Miranda [RM03] found that the limiting period for the application of the *equal displacement approximation* further depends on the strength reduction factor R_y, i.e. it increases as lateral strength ratio increases. Based on their empirical analyses, they also confirmed the influence of the soil conditions, stating that the limiting period tends to increase with decreasing average shear wave velocity in the upper 30 m of the site profile. Comparing several possible configurations, Ruiz-García and Miranda [RM03] found limiting periods for the *equal displacement approximation* in the range of 0.4 s to 1.0 s.

While for very short periods hardly any force reduction is possible anymore ($R_y \to 1$ for $T_0 \to 0$), a transitional zone in the short period range exists, where traditionally another approximate relationship for R_y has been assumed. This hypothesis, given in equation (4.14), is commonly called *equal energy rule*. As depicted on the right side of Fig. 4.7, it is based on the assumption that the seismic demand of inelastic and corresponding elastic system will cause the same deformation energy at peak displacement in both systems. As the inelastic system needs to be displaced more than the elastic system in order to retain the same deformation energy, based on the *equal energy rule,* a higher deformation demand is predicted for the inelastic system than for the corresponding elastic oscillator. Therefore, the equal energy hypothesis generally results in higher demand estimations than the equal displacement approximation.

> *Equal energy approximation:* $\qquad R_y = \sqrt{2\mu_\Delta - 1}$ $\qquad\qquad\qquad\qquad$ (4.14)

Concerning the validity and reliability of the equal energy hypothesis, similar statements can be made as before for the equal displacement approximation. The equal energy hypothesis is also essentially empirical and therefore limited in its range of application. Especially, despite its formal appearance, it is also lacking a strict physical basis. Therefore, similar to above, it might be more appropriate to speak of an *equivalent energy approximation* instead of a real rule. Any reasonable application of this approximation is also limited to a certain period range. Bachmann [Bac02] and Paulay *et al.* [PBM90] delimit this range between the elastic periods of $T_0 = 0.5$ s and $T_0 = 0.1$ s. Newmark and Hall [NH82] give expressions which relate the limiting periods to the spectral ground motion characteristics.

While the two presented hypotheses traditionally have a certain value by giving a rough indication of the inelastic SDOF demand, due to their empirical character it appears more consistent to directly use statistically developed relationships instead. By statistical optimization and regression analysis better approximations can be achieved, which are more generally applicable. It is also possible to develop separate relationships for various more specific configurations (e.g. type of hysteresis, ground motion characteristics etc.). A considerable number of studies have been dedicated to this topic over the last decades which resulted in a variety of empirical equations for the force reduction factor R_y as a function of the relevant parameters (e.g. [NK91], [Mir93], [VFF94]). An overview and evaluation of several proposed empirical approximations can be found in [MB94].

As has been stated at the beginning of this section, the use of force reduction factors R_y has been motivated primarily by the widely spread force based analysis approaches in the past. Furthermore, force reduction factors are only directly applicable in design cases, where the required strength is needed to limit the deformation demand to a certain predetermined acceptable level. In contrast, in a displacement based assessment application the situation is rather the other way around. Here, the strength (of an existing structure) is already given, and instead the expected seismic deformation demand is to be estimated. For this purpose, in recent studies *displacement modification factors* have been proposed which have a similar purpose as the previously discussed force reduction factors, but just for the modified question corresponding to displacement based application cases.

A displacement modification factor C_R relates the inelastic deformation demand Δ_{inel} to the displacement Δ_{el} of a corresponding elastic SDOF, having the same initial stiffness (and period), in the form defined by equation (4.15). In an assessment case, it is most useful to define the displacement modification factor as a function of the strength ratio R_y. This is straightforward because the expression in equation (4.12) can be evaluated right from the beginning of the analysis. The provided yield strength F_y can be estimated directly for an existing structure and the corresponding elastic force demand F_{el} can also be determined at the beginning using the initial stiffness based period and an elastic response spectrum. Alternatively, equivalent displacement modification factors C_μ as a function of the displacement ductility demand μ_Δ have also been developed in the literature. However, as the ductility demand is not known at the beginning of an assessment, this formulation is rather appropriate for design purposes (where in turn the strength is not known at the beginning).

$$\Delta_{inel} = C_R \cdot \Delta_{el} \qquad (4.15)$$

Generally, the displacement modification factor C_R, the ductility demand μ_Δ and the strength ratio R_y are not independent of each other for a given seismic response. Instead, they are rather mutually interrelated to each other as given by equation (4.16). Therefore, one quantity can conceptually also be deduced from the other two. This is also true for the ductility dependent displacement modification factor C_μ. The question if a transformation is possible in the form of an analytical closed-form solution depends on the individual mathematical format in which the empirical equations have been formulated. Nevertheless, at least in an implicit form a transformation from one empirical quantity to another is always possible.

$$C_R = \frac{\mu_\Delta}{R_y} \qquad (4.16)$$

From a deterministic point of view, it appears that such a transformation can be performed in a mathematically accurate manner, as long as no uncertainty in the underlying equations exists. However, from a statistical point of view the same is not true if the individual quantities are not deterministic values but rather represent expectation values of statistical distributions. In this case, the transformation relationship according to (4.16) is not fully correct for the individual expectation values.

Miranda [Mir01] has shown that estimating the inelastic deformation demand based on empirical equations for force reduction factors will introduce a statistical error. The magnitude of this error depends on the statistical uncertainty of the original relationship, i.e. the more scatter is involved in the prediction of R_y, the larger will be the statistical error of the transformation. Miranda therefore recommends that the regression analysis for the statistical determination of an empirical relationship should be performed directly on the quantity of interest. This means that if the inelastic displacement demand as a function of the provided system strength is needed, displacement modification factors C_R should be used which are the result of a regression analysis directly on this quantity. Ruiz-García and Miranda [RM03] have shown that estimating the inelastic displacement demand of a system with known strength indirectly based on empirical relationships for the modification factor C_μ, instead of using the statistically direct relationship for C_R, can lead to considerably unconservative results. They give the example of an inelastic SDOF with elastic period $T_0 = 0.2$ s and a strength ratio of $R_y = 3$, for which the indirect way of estimating the demand, based on C_μ, resulted in an underprediction of the peak response by more than 40%. It can therefore be concluded that, whenever possible, for the displacement based assessment of existing structures C_R relationships should be used which have been calibrated by a direct regression analysis on this quantity.

As research on the direct development of relationships for C_R has only started in rather recent years, the number of corresponding proposals is still limited. Especially the study by Ruiz-García and Miranda [RM03] as well as that by Chopra and Chintanapakdee [CC04] represent valuable contributions in this field, and will be summarized below. For comparison purposes, another study by Nassar & Krawinkler [NK91] will also be presented, in which relationships for the force reduction factor R_y had been calibrated by regression analysis. Although the subsequent derivation of equations for the displacement modification factor C_R introduces the statistical errors discussed above, this study will also be considered below for comparison purposes. Generally, a large number of further proposals on force reduction factors could be included in the same way. However, based on a preceding screening of various approaches the three studies mentioned above resulted as most promising for the given application of displacement based assessment. Therefore, the further discussion will focus on these three proposals as outlined below.

a) Ruiz-García and Miranda [RM03]

Ruiz-García and Miranda [RM03] used a total of 216 ground motions on firm soils and rock with average shear wave velocities of more than 180 m/s to study the influence of inelastic SDOF response on the displacement demand. These ground motions were grouped into three soil classes (B, C, and D) corresponding to the NEHRP classification[22] resulting in 72 ground motions in each category. The records came from 12 different earthquakes in California with magnitudes ranging from 5.8 to 7.7. As hysteretic rules of the inelastic SDOF, elasto-plastic behavior as well as bilinear response with post-yield stiffness ratios r of 3%, 5% and 10% were considered. Any stiffness degrading hysteretic models (e.g. modified Takeda) that would be more representative of reinforced concrete members were not considered in the study. In total, 64,800 displacement modification factors C_R were computed in this study using inelastic time history analyses (ITHA) on SDOF systems.

---

[22] NEHRP (National Earthquake Hazards Reduction Program) classification does not agree with that of Eurocode 8 [EC8-1] or SIA 261 [SIA261].
NEHRP class B: rock with $v_s \approx 760$ m/s ... 1500 m/s (roughly corresponds to class A of [EC8-1]).
NEHRP class C: dense soil with $v_s \approx 360$ m/s ... 760 m/s (roughly corresponds to class B of [EC8-1]).
NEHRP class D: stiff soil with $v_s \approx 180$ m/s ... 360 m/s (roughly corresponds to class C of [EC8-1]).

The computed distributions of the C_R factors were evaluated statistically, on one hand, separately for the three individual soil classes and, on the other hand, for all ground motions together without distinguishing between the soil classes. The resulting mean values and coefficients of variation (C.o.V.) are shown in Fig. 4.8. On the left side, the mean values are presented for various strength ratios R_y as a function of the initial period T_0. The curves show that for larger periods ($T_0 > 1.0$ s ... 1.5 s), the *equal displacement approximation* indeed appears to be a reasonable assumption *on average*, as the mean C_R factors are close to unity in this range. However, in the medium to low period range, the displacement modification factors increase substantially, in particular for higher strength ratios R_y. This shows that for such cases the assumption of the *equal displacement approximation* would be clearly unconservative.
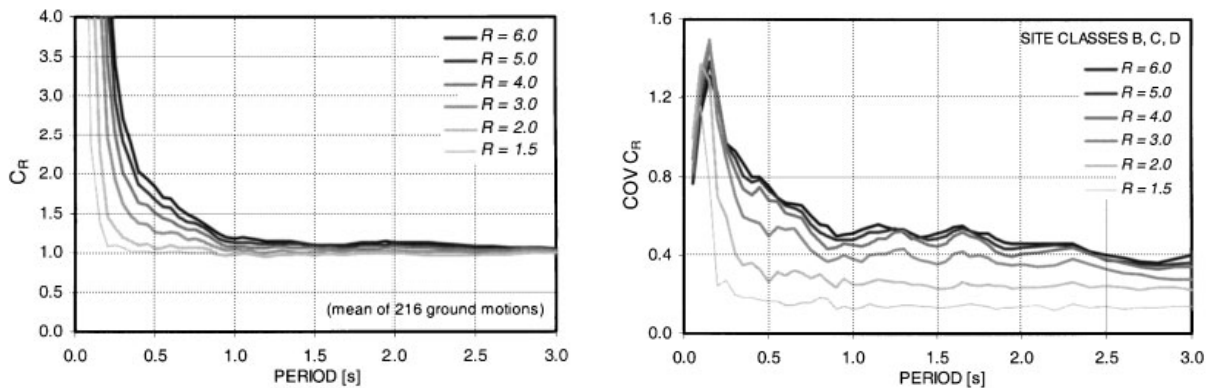

*Fig. 4.8: Statistical data for empirical C_R values computed by Ruiz-García and Miranda
based on ground motions for all soil classes together (Source: [RM03])
left: Mean values, right: Coefficients of variation*

The coefficients of variation for C_R, shown on the right side of Fig. 4.8, give an important indication of the considerable scatter in the results. It can be seen that in the long period range values for the C.o.V. in the range of about 40% must be expected if the response enters significantly into the inelastic range. For medium and short period systems the uncertainty increases even more and can reach values of up to 150%. This shows that the uncertainty in the use of C_R displacement modification factors can be substantial. For short period systems the scatter is so large that a reasonable application might even be questionable. A more or less acceptable demand prediction might still be considered possible for structures with elastic periods T_0 higher than 0.5 s, especially if the strength ratio R_y is not larger than 3. The corresponding uncertainty with C.o.V.s up to around 40% is still large, but in comparison to other uncertainties in seismic engineering it is not necessarily extraordinary.

It should be noted that in another comparative study by Miranda and Ruiz-García [MR02], in which different existing proposals for the inelastic demand estimation were evaluated, considerable scatter in the results was found as well. However, the extremely high dispersion shown in Fig. 4.8 (right) for short periods still exceeds the uncertainties found elsewhere. In particular, an equivalent statistical study by Miranda [Mir00] on displacement modification factors C_μ as a function of the ductility demand μ_Δ resulted in significantly more uniform coefficients of variation over the period range. In this case the scatter over almost the entire period range was more comparable to that of C_R in Fig. 4.8 (right) for very long periods, and for very short periods it even decreased. Even for displacement ductilities of $\mu_\Delta = 6$ the C.o.V. essentially did not exceed 40% for any period. This shows that the prediction of the inelastic displacement demand for a given system strength, as in an assessment case, represents a statistically particularly difficult task. The underlying uncertainties (and subsequent limitations) should be kept in mind when applying such an approach.

Furthermore, Ruiz-García and Miranda [RM03] investigated the influence of the post-yield stiffness ratio r on the displacement modification factor C_R for bilinear hysteretic models. In Fig. 4.9 the ratio between the inelastic displacement demand for $r = 3$ % and for $r = 0$ (i.e. elasto-plastic behavior) is shown. It can be seen that a moderate increase of the post-yield stiffness $k_{post-yield}$ reduces the displacement demand. For the medium to long period range this reduction is not particularly dominant,

especially for high system strengths (i.e. low force reduction factors R_y). However, in the short period range a substantial difference can be found. This shows that for a large part of the period range the post-yield stiffness of bilinear hysteretic models is not very relevant within the reasonable range of r values. Only for short periods an adequate representation of the post yield stiffness may be mandatory. However, it needs to be kept in mind that any bilinear model is a strong simplification of the real member behavior, which may also have a significant influence in such cases.

The statistical influence of soil conditions, earthquake magnitude and distance to rupture on the factor C_R was also investigated by Ruiz-García and Miranda [RM03]. Concerning the soil conditions, it was found that C_R increases in the short period range if the average shear wave velocity in the upper 30 m of the site profile decreases. Using the average C_R values calibrated on all soil classes together, as shown in Fig. 4.8 (left), tends to be slightly conservative for the two stiffer NEHRP soil classes B and C (i.e. A and B according to [EC8-1]), with the deviations from the mean values being rather insignificant for most periods. For the somewhat softer NEHRP soil class D (i.e. class C according to [EC8-1]) the average C_R values of Fig. 4.8 (left) can give slightly unconservative demand predictions, with underpredictions of up to about 20% (for part of the period range). However, for lateral strength ratios R_y smaller than 3, the errors produced by neglecting the effect of local site conditions was generally found to be smaller than about 10%. Based on the comparison between different soil types, Ruiz-García and Miranda also concluded that the prediction of C_R could generally be improved if the initial system period T_0 was related to a characteristic period of the soil class.
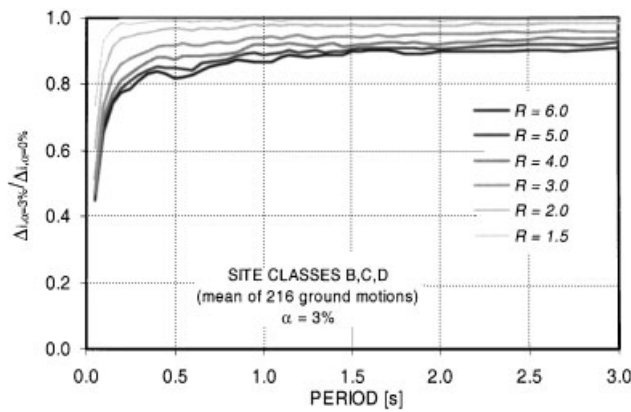

Fig. 4.9: Influence of the post-yield stiffness ratio r on the displacement modification factor C_R, expressed as ratio between inelastic displacement demand for r = 3 % and r = 0 (Source: [RM03])

Earthquake magnitude was found to have an influence on C_R only in the short to medium period range, combined with larger values of R_y. In such cases, stronger earthquakes tend to cause higher displacement modification factors. In other cases, no significant influence of earthquake magnitude was observed. For the ground motions considered, the distance to the rupture did not appear to have a significant statistical influence on C_R. However, no particular near-fault records featuring forward directivity were included in the ensemble. For such ground motions, higher displacement modification factors would be expected.

Based on the mean values of the computed C_R factors, Ruiz-García and Miranda [RM03] performed regression analysis to develop an empirical equation for the displacement modification factor as a function of the initial period T_0 and the strength ratio R_y. They propose a relationship having the general format given in equation (4.17), in which the initial system period T_0 is related to a characteristic period T_S of the soil type.

$$C_R = 1 + \left[\frac{1}{a \cdot \left(T_0/T_S \right)^b} - \frac{1}{c} \right] \cdot \left(R_y - 1 \right) \tag{4.17}$$

For the application of this equation, Ruiz-García and Miranda provide two sets of parameters. The first set, summarized in Tab. 4.3, consists of individual parameters for each soil class. Although these data

are expected to give the best approximation of the mean C_R value, it was found that a single set of parameters for a, b, and c can also give reasonably good results if only the characteristic period T_S is adjusted to the specific soil types. The corresponding simplified set of parameters is given in Tab. 4.4. In the light of the generally large dispersion, these simplified data are considered to provide a sufficient approximation.

Soil Class		Shear wave velocity	Parameters			
NEHRP	[EC8-1]	v_s [m/s]	a [-]	b [-]	c [-]	T_s [s]
B	A	760 ... 1500	42	1.60	45	0.75
C	B	360 ... 760	48	1.80	50	0.85
D	C	180 ... 360	57	1.85	60	1.05

Tab. 4.3: Parameters for the use of equation (4.17) according to [RM03], distinguished by soil classes

Soil Class		Shear wave velocity	Parameters			
NEHRP	[EC8-1]	v_s [m/s]	a [-]	b [-]	c [-]	T_s [s]
B	A	760 ... 1500				0.75
C	B	360 ... 760	50	1.80	55	0.85
D	C	180 ... 360				1.05

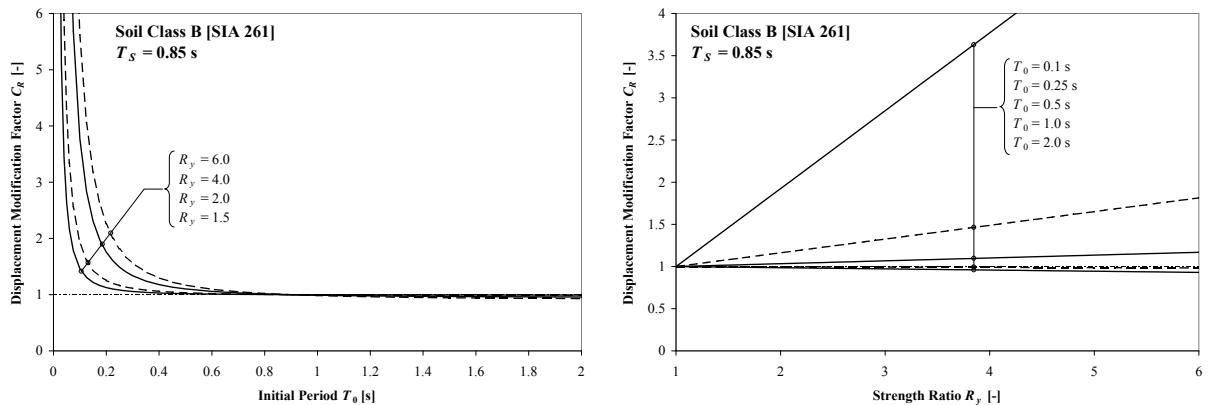Tab. 4.4: Simplified parameters for the use of equation (4.17) according to [RM03]

Fig. 4.10: Predicted C_R values according to equation (4.17) from [RM03] for soil class B [SIA261]
left: C_R as a function of initial period T_0, right: C_R as a function of strength ratio R_y

The resulting C_R curves applying equation (4.17) with the parameters of Tab. 4.4 for soil class B according to Eurocode 8 [EC8-1] and SIA 261 [SIA261] are shown in Fig. 4.10. Two different ways of visualization have been chosen here. On one hand, the left side shows C_R as a function of initial period T_0 for a variety of fixed strength ratios R_y. On the other hand, the right side of Fig. 4.10 presents the data as a function of R_y for various fixed periods T_0. Especially the latter curves show that the estimation of C_R results as a linear function of R_y, with the inclination depending on the initial period. For short periods, very large gradients can result. In contrast, for medium to long periods the predicted response corresponds essentially to the *equal displacement approximation*. It is noteworthy, that for periods larger than about 1 s even a negative gradient on the right side of Fig. 4.10 can be seen. This

means that for increasing strength ratios R_y a lower displacement demand than that of a corresponding linear system (with the same elastic period) is predicted. Although such a behavior actually may even occur, it may be recommendable not to make use of this demand reduction. Instead, as a cautious approach, a lower bound of $C_R = 1$ might be preferable for practical applications.
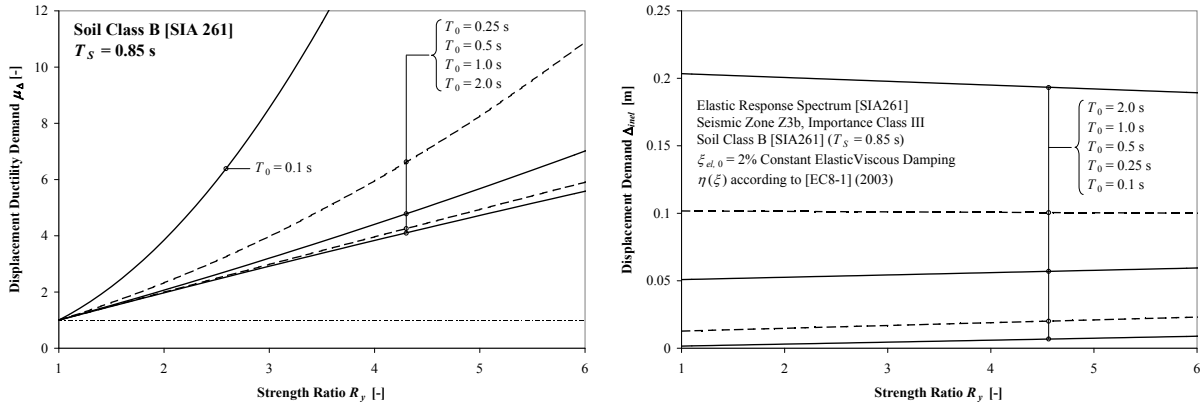

Fig. 4.11: Resulting deformation demand for elasto-plastic hysteretic behavior according to [RM03]
left: Displacement ductility μ_Δ, right: Absolute displacement Δ_{inel} for given elastic response spectrum

In Fig. 4.11 it is shown how the predictions of C_R according to equation (4.17) translate into actual deformation demands. On the left side, the displacement ductility demand μ_Δ is presented as a function of the strength ratio R_y for a set of initial periods T_0 and on the right side the corresponding absolute displacement demands Δ_{inel} are shown. While the relationships between strength ratio and ductility demand are independent of the actual excitation, this is not the case for the displacement demand curves. For these latter ones, an elastic response spectrum according to [SIA261] has been used having the properties given in Fig. 4.11 (right). It can be seen that for increasing strength ratio R_y the ductility demand increases. For the short periods the predicted increase is stronger than proportional to R_y. In contrast, the corresponding absolute displacement demand Δ_{inel} is comparatively uniform with respect to the strength ratio. While for short periods the displacement demand increases with increasing strength ratio R_y, for long periods, equation (4.17) even predicts a slight decrease of Δ_{inel}. However, if the previous recommendation of using a lower bound limit of $C_R \geq 1$ was followed, this decrease in the long period range would be replaced by a constant displacement demand with respect to R_y.

b) Chopra and Chintanapakdee [CC04]

A rather similar study to that described above has been prepared by Chopra and Chintanapakdee [CC04]. They used a total of 214 ground motions that were grouped into 11 ensembles, distinguishing the records by earthquake magnitude, NEHRP soil class, and distance to rupture – including near-fault ground motions. In total, earthquake magnitudes between 5.8 and 6.9 were considered and record-to-source distances ranged from 13 km to 60 km. Local site conditions corresponded to NEHRP soil classes B, C, and D (i.e. soil classes A, B, and C according to [EC8-1], respectively). As hysteretic rules, elasto-plastic and bilinear behavior with various post-yield stiffness ratios r were considered. Strength or stiffness degrading hysteretic behavior was not considered, nor any form of pinching. All analyses were conducted with a constant viscous damping ratio of $\xi_{el} = 5\%$. In the study [CC04] displacement modification factors were computed both, for predetermined strength ratios R_y and for given ductility demands μ_Δ, i.e. resulting in distributions of C_R and C_μ, respectively. Only the results on C_R will be further discussed below as these are more adequate for assessment applications.

In Fig. 4.12 median values of C_R are presented as a function of the initial period T_0 for ground motions corresponding to large magnitude earthquakes and short distance to rupture and for various combinations of strength ratio R_y and post-yield stiffness ratios r. It should be noted that the data in Fig. 4.12 are presented using double-logarithmic scales. By comparison with Fig. 4.8 it can be seen

that the general trends found by Ruiz-García and Miranda [RM03] are confirmed by the results from [CC04]. In particular, the good agreement with the *equal displacement approximation* for periods higher than about 1 s (representing the velocity and displacement sensitive regions of the elastic response spectra) and the significant increase of C_R in the medium to short period range (i.e. the acceleration sensitive period range) are also found by Chopra and Chintanapakdee [CC04].

The pronounced influence of the post-yield stiffness ratios r for very short periods appears noteworthy, although values of T_0 smaller than 0.1s are unlikely to have much relevance for the majority of bridges (especially when taking soil structure interaction into account). The influence of a variety of further parameters as well as the dispersion of computed C_R values is also studied in [CC04] (similar to [RM03]). However, the details of these results are omitted here for brevity. They essentially confirm the findings by Ruiz-García and Miranda [RM03] discussed above. Especially, it was also found that normalizing the fundamental system period by a characteristic period of the ground motion makes the shape of C_R curves rather insensitive to the specific ground motion properties (e.g. earthquake magnitude, distance to rupture).
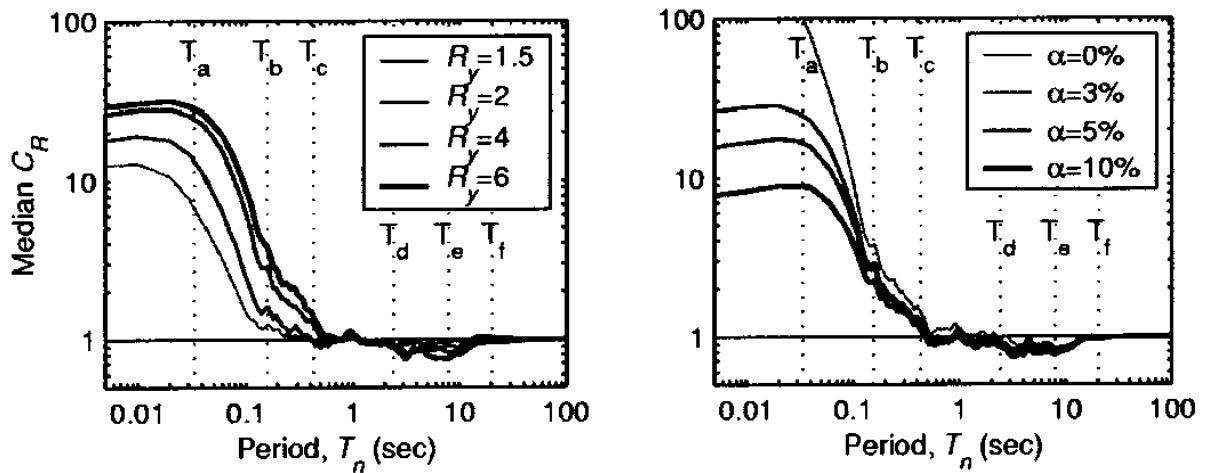

Fig. 4.12: Median C_R values for large magnitude / short distance to rupture ground motions (Source: [CC04])
left: For post-yield stiffness ratio r = 3% and various strength ratios R_y,
right: For strength ratio R_y = 4 and various post-yield stiffness ratios r

Based on regression analysis of the computed data, Chopra and Chintanapakdee also propose an empirical equation for the estimation of C_R (as well as a similar equation for C_μ). The general format for this relationship is given by equation (4.18). As in equation (4.17), C_R here is also defined as a function of the strength ratio R_y and the initial period T_0, with T_0 being normalized by a characteristic period of the ground motion. For a given elastic response spectrum, the chosen characteristic period, T_C, separates the acceleration- and the velocity-sensitive regions and corresponds to the value equally named in [EC8-1] and [SIA261].

$$C_R = 1 + \frac{1}{\dfrac{R_y \cdot r}{(R_y - 1) \cdot (1 - r)} + \left(\dfrac{a}{R_y^b} + c\right) \cdot \left(\dfrac{T_0}{T_c}\right)^d} \tag{4.18}$$

The parameters *a* through *d* specified in [CC04] for general applications are summarized in Tab. 4.5. According to Chopra and Chintanapakdee, these values should be valid for almost any ensemble of ground motions recorded on firm soil sites, independent of earthquake magnitude and source distance, within the range of conditions considered in the analyses (see above). This includes near-fault ground motion ensembles (both, fault-parallel and fault-normal). The parameters of Tab. 4.5 are not applicable for soft soil conditions. Values for the characteristic period T_C of the ground motions according to [SIA261] have been included in Tab. 4.5 as a function of the local site conditions.

Soil Class	Shear wave velocity	Parameters [CC04]				Characteristic Period [SIA261]
[SIA261]	v_s [m/s]	a [-]	b [-]	c [-]	d [-]	T_C [s]
A	760 ... 1500					0.4
B	360 ... 760					0.5
C	180 ... 360	61	2.4	1.5	2.4	0.6
D	150 ... 300					0.8
E	-					0.5

Tab. 4.5: Parameters a, b, c, d for the use of equation (4.18) according to [CC04],
characteristic period T_C for soil classes A through F according to [SIA261].

In Fig. 4.13 the resulting C_R estimations according to equation (4.18) are shown using the parameters given in Tab. 4.5 for soil class B according to [SIA261]. As before, the curves present the data separately as a function of the initial period T_0 (left) and as a function of the strength ratio R_y (right). Although the general trends are similar to those previously presented in Fig. 4.10 for the proposal by Ruiz-García and Miranda [RM03], the right side of Fig. 4.13 shows some considerable difference in the short period range. Here, the proposal by Chopra and Chintanapakdee [CC04] predicts significantly higher displacement demands. In the medium to long period range, the results shown in Fig. 4.13 approach the *equal displacement approximation* so that the differences between the different proposals in that part of the C_R spectrum tend to diminish. Due to its conceptual format, equation (4.18) will always yield C_R values larger than unity. As a consequence, even for very large periods it is not necessary to introduce an additional lower boundary for C_R, as suggested in Subsection a for the case of equation (4.17).
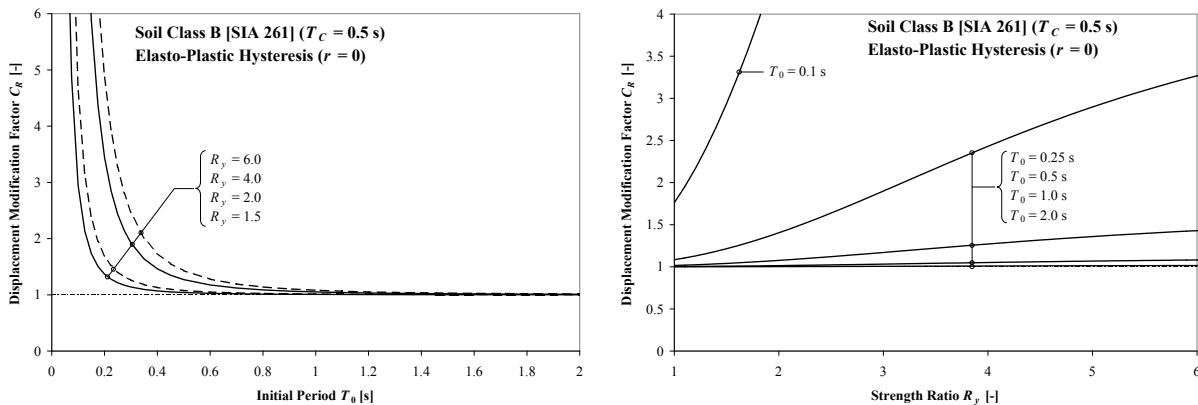

Fig. 4.13: Predicted C_R values according to equation (4.18) from [CC04] for soil class B [SIA261] and r = 0
left: C_R as a function of initial period T_0, right: C_R as a function of strength ratio R_y

It appears somewhat surprising that for short periods the C_R curves on the right side of Fig. 4.13 do not converge towards unity for $R_y \to 1$ if the post-yield stiffness ratio $r = 0$. It can be seen from equation (4.18) that the first summand in the denominator of the fraction is zero for $r = 0$. As a consequence, for $R_y \to 1$ the fraction does not become zero and $C_R \to 1+1/[(a+c)\cdot(T_0/T_c)^d]$. Such a behavior is counterintuitive as $R_y = 1$ represents linear elastic behavior and therefore no modification of the displacement demand determined from an elastic response spectrum is required. Instead, the modification factor should be $C_R = 1$. Chopra and Chintanapakdee [CC04] discuss this aspect and point out that for very short initial periods T_0, very slight strength deficits (i.e. R_y only slightly larger than one) already result in displacement demands that deviate considerably from the elastic displacements.

This phenomenon depends on the post-yield stiffness ratio and tends to diminish for increasing values of r. In fact, for $r > 0$ the displacement modification factor C_R according to equation (4.18) does converge towards unity for $R_y \rightarrow 1$. However, for small values of r, equation (4.18) results in a very large gradient of the C_R vs. R_y curve in the vicinity of $R_y = 1$. As a consequence, the displacement modification factor already reaches values significantly higher than one for R_y values only slightly above unity. In a similar way, the C_R vs. R_y curve according to equation (4.18) can be interpreted to have an infinite gradient at $R_y = 1$ if $r = 0$. As a consequence, it can be considered that $C_R = 1$ for $R_y \leq 1$, but the displacement modification factor directly jumps to a value of $C_R = 1 + 1/[(a+c) \cdot (T_0/T_c)^d]$ for any minimal increase of R_y above unity. This behavior, which at first sight appears to contradict common sense, is intended by the authors of [CC04] in order to cover the high sensitivity of short period systems to only slight strength deficits. For medium to long period systems, this phenomenon essentially does not occur, as can be seen in Fig. 4.13 (right). It also diminishes if the system has appreciable post-yield stiffness. Both aspects are captured by equation (4.18).
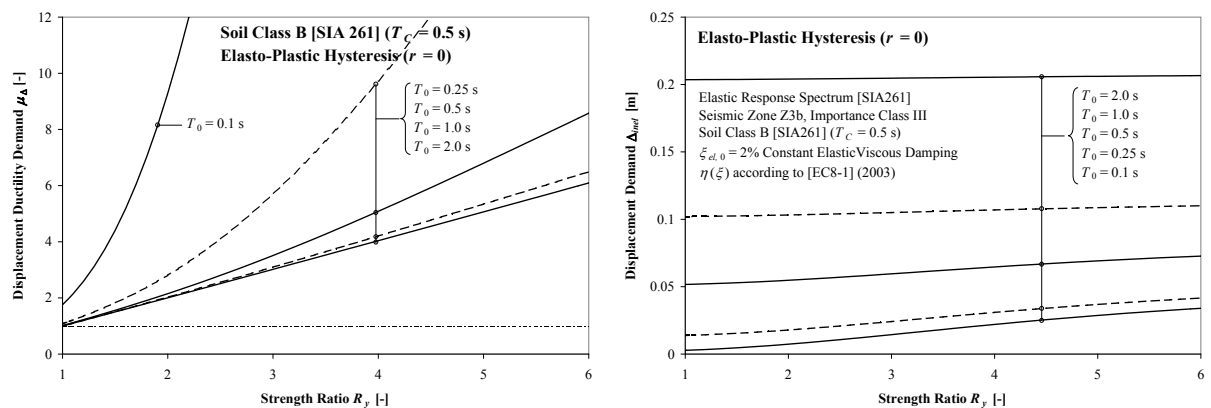

Fig. 4.14: Resulting deformation demand for elasto-plastic hysteretic behavior according to [CC04]
left: Displacement ductility μ_Δ , right: Absolute displacement Δ_{inel} for given elastic response spectrum

In Fig. 4.14 the corresponding ductility μ_Δ (left) and displacement demands Δ_{inel} (right) are shown for various periods T_0 as a function of the strength ratio R_y. The curves on the right side are based on an elastic response spectrum according to [SIA261] with the data given in the figure, whereas the μ_Δ vs. R_y curves (on the left side) are independent of the actual spectrum. It can be seen that the use of equation (4.18) results in a considerable increase of the predicted absolute displacement demand for increasing strength ratios R_y. For higher periods this increase is more and more diminished and in the long period range it turns into a displacement demand being essentially constant with respect to R_y. Displacement demand predictions that reduce with increasing strength ratio do not occur based on equation (4.18), independent of the period.

c) Nassar and Krawinkler [NK91], [KN92]

The third study presented here has been conducted by Nassar and Krawinkler [NK91], [KN92]. In contrast to the two previous ones, this work did not directly focus on displacement modification factors, but rather generated constant ductility force reduction factors R_y. They used a total of 15 ground motions from 9 different earthquakes in the Western US. Earthquake magnitudes ranged from 5.7 to 7.7 and source-to-record distances were between 12 km and 64 km. All ground motions were recorded on stiff soil or rock. As hysteretic models they considered bilinear behavior with strain hardening ratios of $r = 0\%$, 2%, and 10%, plus a modified Clough hysteresis as stiffness degrading behavior. Viscous damping was modeled with a damping ratio of $\xi_{el} = 5\%$.

The mean values of the computed R_y ratios for elasto-plastic behavior are shown in Fig. 4.15 as a function of elastic period T_0 for a set of fixed displacement ductilities μ_Δ. These values are not directly comparable to displacement modification factors, but are only an intermediate step for their subsequent derivation. Nevertheless, in Fig. 4.15 it can also be seen that in the medium to long period

range the results tend to support the *equivalent displacement approximation* as the force reduction factors approach the corresponding ductility values for increasing periods.
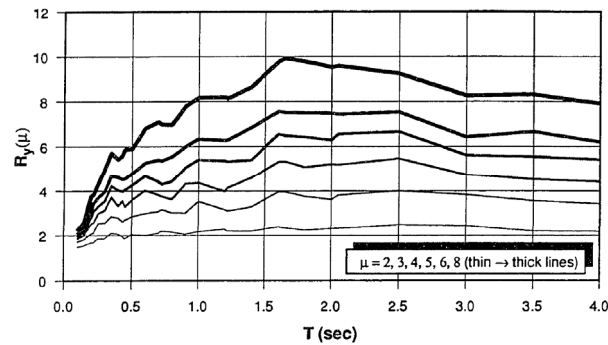

Fig. 4.15: Statistically determined mean strength reduction factors R_y for constant ductility μ_Δ (Source: [NK91]) based on elasto-plastic behavior (i.e. bilinear with r = 0)

In Fig. 4.16 the influence of various hysteresis types is shown. On the left side, the ratio between R_y values for bilinear behavior with post-yield stiffness ratio of $r = 0\%$ and $r = 10\%$ is presented. The right side shows corresponding ratios between R_y for a stiffness degrading modified Clough model and an elasto-plastic behavior (i.e. bilinear with $r = 0$). In the interpretation of these curves it should be kept in mind that, in contrast to C_R, large R_y values are beneficial. From Fig. 4.16 (left) can therefore be concluded that strain-hardening has a slightly positive influence on the seismic response of bilinear hysteretic systems, as also found in [RM03] and [CC04] above. The results on the right side of Fig. 4.16 suggest that the stiffness degrading model over large part of the period range appears to experience a slightly lower demand than the elasto-plastic model. In total, both sides of Fig. 4.16 do not show a very strong influence of the compared models on the seismic demand. Nassar and Krawinkler [NK91] conclude from this finding that strength reduction factors R_y, deduced from elasto-plastic behavior, could also be used, as an approximation, on systems featuring stiffness degradation. They expect the resulting demand estimations to be slightly conservative.
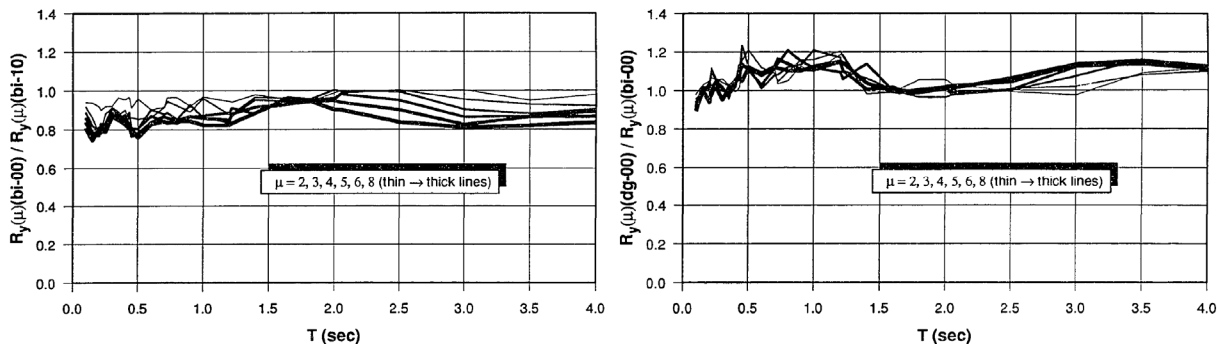

Fig. 4.16: Influence of hysteretic model on strength reduction factor R_y (Source: [NK91]), left: Ratio between R_y for elasto-plastic behavior (r= 0) and R_y for bilinear behavior with r = 10% right: Ratio between R_y for stiffness degrading hysteretic behavior and R_y for elasto-plastic behavior (r= 0)

Based on the statistical distribution of the computed data for the various bilinear hysteretic models, Nassar and Krawinkler [NK91] performed regression analysis to deduce empirical relationships for the strength reduction factor. Equation (4.19) gives the general format of their equation for R_y as a function of initial period T_0 and (predetermined) ductility demand μ_Δ. The required parameters for its application are given in Tab. 4.6 for three different post-yield stiffness ratios. It is noteworthy that Nassar and Krawinkler do not distinguish between soil types. This may be related to the rather limited number of ground motions they used which were all recorded on rather similar stiff soil conditions. As the previously presented studies [RM03] and [CC04] suggest a considerable influence of local soil type, care should be taken in the application of equation (4.19). It should not be applied on conditions that deviate significantly from those underlying its derivation.

$$R_y\left(\mu_\Delta\right)=\left[1+c\cdot\left(\mu_\Delta-1\right)\right]^{1/c} \tag{4.19}$$

with $\qquad c\left(T_0\right)=\dfrac{T_0^a}{1+T_0^a}+\dfrac{b}{T_0}$

Post-yield stiffness ratio	Parameters [NK91]	
r [-]	a [-]	b [-]
0.00	1.00	0.42
0.02	1.00	0.37
0.10	0.80	0.29

Tab. 4.6: Parameters a and b for the use of equation (4.19) according to [NK91]
for bilinear hysteretic behavior with different post-yield stiffness ratios

As discussed previously, for the assessment of existing structures with known strength, the use of displacement modification factors C_R is more convenient than that of force reduction factors R_y. Despite the statistical problems discussed above, equation (4.19) will be transformed here into a relationship for C_R. For this purpose, equation (4.19) is rewritten in the form of equation (4.20) expressing the ductility demand as a function of R_y. Using the relation between C_R, R_y, and μ_Δ given in equation (4.16), the expression for C_R according to equation (4.21) can be deduced. This relationship is conceptually comparable to the previously presented equations (4.17) and (4.18) as it allows the estimation of the displacement modification factor C_R as a function of R_y and T_0.

$$\mu_\Delta\left(R_y\right)=1+\frac{R_y^c-1}{c} \tag{4.20}$$

$$C_R=\frac{1}{R}\left[1+\frac{R^c-1}{c}\right] \tag{4.21}$$

with $\qquad c\left(T_0\right)=\dfrac{T_0^a}{1+T_0^a}+\dfrac{b}{T_0}$

In Fig. 4.17, equation (4.21) is evaluated for elasto-plastic hysteretic behavior (i.e. bilinear with $r=0$). On the left side, C_R is shown as a function of initial period T_0 for a set of strength ratios R_y. On the right side the same data is presented as a function of R_y for several fixed values of T_0. It can be seen that the general trends are the same as previously shown in Fig. 4.10 and Fig. 4.13 for the other two approaches. The displacement amplification for short periods lies between that predicted by Ruiz-García and Miranda [RM03] and that by Chopra and Chintanapakdee [CC04]. For long periods, the average response essentially corresponds to the *equal displacement approximation*, while here again C_R values (slightly) smaller than unity are computed. For conservatism it is recommended, as before, not to use such values lower than unity, but rather introduce a lower boundary of one. Although originally developed for bilinear hysteretic models, based on the comparisons by Nassar and Krawinkler it might by considered acceptable to apply equation (4.19) also on stiffness degrading systems if the parameters corresponding to $r=0$ are used.

In Fig. 4.18 the ductility (left) and displacement (right) demands are shown as they result from the use of C_R according to equation (4.21). The computed absolute displacements are based on a response spectrum according to [SIA261], with the data given on the right side of Fig. 4.18. It can be seen that for the periods $T_0=0.25$ s through $T_0=2$ s qualitatively similar trends result as those predicted using the proposal by Ruiz-García and Miranda [RM03]. For short periods, an increase of absolute displacement demand with increasing R_y is predicted. In the medium period range the displacements

are estimated to be essentially independent of the strength ratio, and for very long periods the approach by Nassar and Krawinkler [NK91] predicts a slight decrease of deformation demand with increasing R_y. This decrease will not occur if the previously recommended lower boundary of $C_R \geq 1$ is taken into account in addition to equation (4.21).
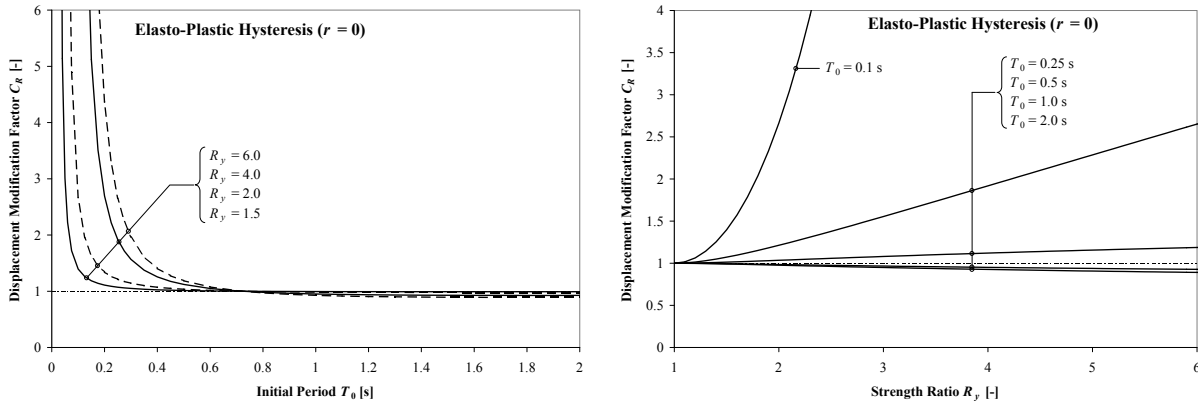

Fig. 4.17: Predicted C_R values according to equation (4.21) from [NK91] for elasto-plastic hysteretic behavior left: C_R as a function of initial period T_0, right: C_R as a function of strength ratio R_y
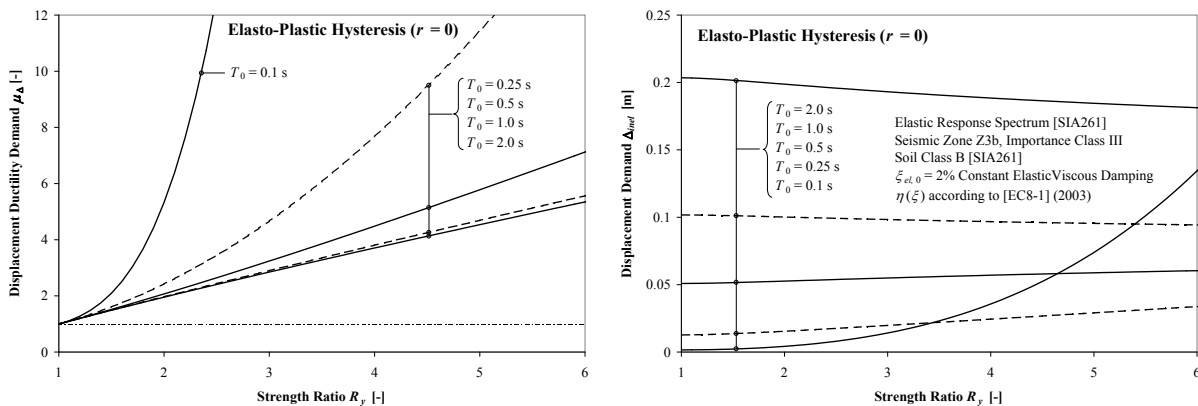

Fig. 4.18: Resulting deformation demand for elasto-plastic hysteretic behavior according to [NK91] left: Displacement ductility μ_Δ, right: Absolute displacement Δ_{inel} for given elastic response spectrum

A response prediction that deviates significantly from that previously shown in Fig. 4.11 and Fig. 4.14 can be found for the initial period of $T_0 = 0.1$ s on the right side of Fig. 4.18. While the estimated demand based on equation (4.21) still shows a qualitatively similar trend as the others in the range of up to $R_y \approx 2$, the curve in Fig. 4.18 increases very strongly for higher strength ratios. The progressive increase is so large that the predicted displacement demands for $T_0 = 0.1$ s, starting from a certain R_y value, even exceed the demands for higher periods. This extraordinary behavior is related to the very high gradient of the μ_Δ vs. R_y relationship for $T_0 = 0.1$ s shown on the left side of Fig. 4.18. Equations (4.19) through (4.21) do not seem to capture this range of parameter configurations realistically. This may be related to the fact that in the very short period range normally hardly any force reduction is considered possible (at reasonable ductility levels). Therefore, obviously no attempt has been made to cover the behavior for short periods combined with higher strength ratios R_y by the regression equation (4.19). The subsequently derived equation (4.21) should therefore not be used for such combinations of short periods T_0 and large strength ratios R_y. For many realistic cases this does not represent a major limitation, as such combinations would be related to extremely high ductility demands that might not be sustained by the majority of structures anyway. An application of equation (4.21) on such parameter configurations – which is not recommended – would at least yield (very) conservative results.

4.5.2 Equivalent Linearization Methods

The dynamic motion of a linear SDOF system with viscous damping can be described by a rather simple differential equation of second order. For certain types of excitation this allows a direct analytical solution and for earthquake loading the peak demand can be easily determined using elastic response spectra. These features have made linear visco-elastic systems interesting for dynamic problems already at early stages of research on this topic. Due to the advantages and the relative simplicity of the corresponding solution strategies, it has also been attempted to represent other energy dissipation effects in an approximate manner as some form of equivalent viscous damping. In particular, a considerable number of proposals have been developed for the representation of hysteretic energy dissipation by viscous damping. A variety of approaches exist how these two different forms of energy dissipation could be related to each other. An overview and comparison of some of these conceptual approaches has been provided by Iwan and Gates [IG79a] and an overview of some relationships for the determination of an equivalent viscous damping developed by various researchers has been given by Blandon and Priestley [BP05].

For the definition of an equivalent linear system, two parameters need to be defined: (1) the secant stiffness k_{sec} of the substitute system and (2) its equivalent viscous damping ξ_{eq}. The latter consists, on one hand, of an equivalent hysteretic damping $\xi_{eq,hyst}$ representing the energy dissipation related to the cyclic hysteretic response. On the other hand, the second contribution to ξ_{eq} comes from elastic viscous damping ξ_{el} covering other dissipation effects additionally modeled by viscous damping in an inelastic model as discussed in Section 4.4.1. As consequence, the total equivalent viscous damping ratio can be formulated in a general form as given by equation (4.22). As the mass of the linearized system is taken equal to that of the original inelastic system, the assumption of a certain secant stiffness k_{sec} can also directly be related to the determination of an effective period T_{eff} of the substitute system, corresponding to equation (4.23).

$$\xi_{eq} = \xi_{el} + \xi_{eq,hyst} \tag{4.22}$$

$$T_{eff} = 2\pi \sqrt{\frac{m}{k_{sec}}} \tag{4.23}$$
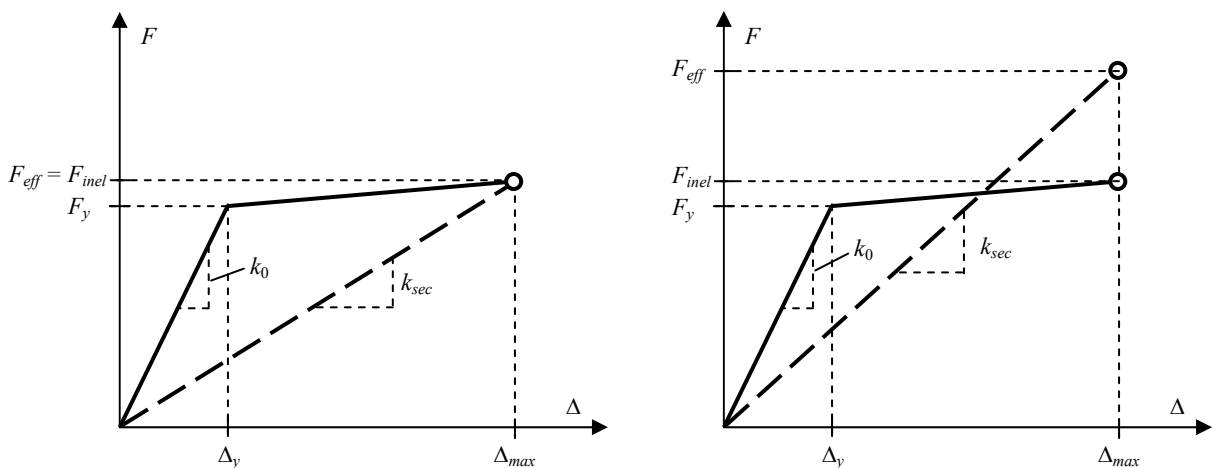
Fig. 4.19: Representation of an inelastic SDOF by a linear elastic SDOF with effective secant stiffness
left: Secant stiffness to peak response, right: Secant stiffness to less than peak displacement

Concerning the definition of the secant stiffness, several assumptions are conceivable as reasonable approaches, two of which are shown in Fig. 4.19. The possibly most obvious one is shown on the left side of Fig. 4.19. Here, the secant stiffness is defined to the point of the peak response Δ_{max} on the inelastic load-deformation curve. Expressing the deformation demand by the corresponding displacement ductility μ_Δ according to equation (3.2), the secant stiffness k_{sec} can then be related to the

initial stiffness k_0 of the inelastic system as defined by equation (4.24). Correspondingly, the effective period T_{eff} can be related to the initial period T_0 of the inelastic system as given by equation (4.25). From these two expressions, it can be seen that for low post-yield stiffness ratios r the secant stiffness k_{sec} is approximately antiproportional to the displacement ductility and the effective period T_{eff} is essentially proportional to the square root of μ_Δ.

$$k_{\text{sec}} = \frac{F_{inel}}{\Delta_{max}} = \frac{k_0}{\mu_\Delta} \cdot \left[1 + \left(\mu_\Delta - 1\right) \cdot r\right] \tag{4.24}$$

$$T_{eff} = T_0 \cdot \sqrt{\frac{\mu_\Delta}{1 + \left(\mu_\Delta - 1\right) \cdot r}} \tag{4.25}$$

Although this way of defining the secant stiffness and effective period is rather straightforward and also rather common in many proposals for equivalent linearization, it is not the only conceivable solution. As shown on the right side of Fig. 4.19, alternative definitions of the secant stiffness might also be assumed as appropriate for the substitute stiffness representation of the inelastic system. In fact, the peak displacement is only reached in a single instant throughout the entire response history of the system. Throughout the entire rest of the response, the value for k_{sec} according to the left side of Fig. 4.19 and equation (4.24) thus rather underestimates the secant stiffness. Corresponding to these considerations, it might be asked which period is most appropriate to characterize the system within an elastic response spectrum (together with an assumption for equivalent damping or subsequent modification). While the initial period based approaches, outlined in Section 4.5.1, and the assumption according to equation (4.25) represent essentially the extreme cases of appropriate stiffness representations, it might also be argued that a period somewhere between these two could be even more appropriate for the system characterization within a response spectrum.

Based on the premise that the effective period does not have to be defined as either of the two extreme cases mentioned above, Iwan and Gates [IG79a] proposed that an *optimum effective linear system* could possibly be achieved if both, the effective period T_{eff} and the equivalent viscous damping ratio ξ_{eq}, were introduced as free parameters into an optimization process. Allowing an optimization over two parameters might result in a better error reduction over a larger set of data than just a regression analysis optimizing the equivalent viscous damping for a predetermined effective period. In [IG79b], Iwan and Gates applied this approach to a set of selected hysteresis models and computed rather low root mean square (RMS) errors for the determined optimum parameters. The resulting effective periods indeed resulted as lying between the two extreme ones corresponding to initial stiffness and secant stiffness to peak displacement. It is important to note that any estimation of equivalent viscous damping is always related to the corresponding choice of effective period definition. Mixing parameters that do not correspond to each other in this sense would result in erroneous demand predictions and is therefore not permissible.

As mentioned above, several conceptual approaches have been used in the past for the determination of the equivalent viscous damping ratio $\xi_{eq,hyst}$ accounting for the hysteretic energy dissipation. A classical approach for this task consists of attempting to set the energy that is dissipated by viscous damping in the substitute structure equal to that dissipated hysteretically in the original inelastic system. For the case of a linearization with secant stiffness to peak response, this method is visualized in Fig. 4.20. In the literature this approach is often related to early works by Jacobsen, Housner, and Jennings from the 1930s and 1960s, and it is also discussed by Chopra [Cho01] in some detail. On the left side of Fig. 4.20, the steady state hysteretic response of an inelastic system to a given displacement amplitude Δ_{max} is shown. The dissipated energy $E_{inel,hyst}(\Delta_{max})$ per cycle of this system equals the area within the hysteresis loop as marked in Fig. 4.20.

On the right side of Fig. 4.20, the two corresponding contributors in a linearized substitute system are shown. The elastic spring having the secant stiffness k_{sec}, and shown in the upper part, does not dissipate any energy. Instead, in this system, all the energy is dissipated by the viscous damper. If the steady state response is harmonic (i.e. sinusoidal), the load deformation response of the viscous damper is elliptical as shown in the lower part on the right side of Fig. 4.20. As viscous damping is

rate dependent, the response of the damper depends on the circular frequency ω of the harmonic motion. It can be shown that the energy $E_{\xi,eq,hyst}(\Delta_{max})$ dissipated by the viscous damper during one cycle with displacement amplitude Δ_{max} is given by equation (4.26). This expression can be solved for the equivalent viscous damping coefficient $c_{eq,hyst}$, resulting in equation (4.27). The critical damping coefficient $c_{cr,eff}$ corresponding to the secant stiffness k_{sec} is given by equation (4.28) as a function of the effective fundamental circular frequency ω_{eff}. Based on these relationships, the equivalent viscous damping ratio $\xi_{eq,hyst}$ can be computed according to equation (4.29) for a given dissipated energy $E_{\xi,eq,hyst}$ per cycle.
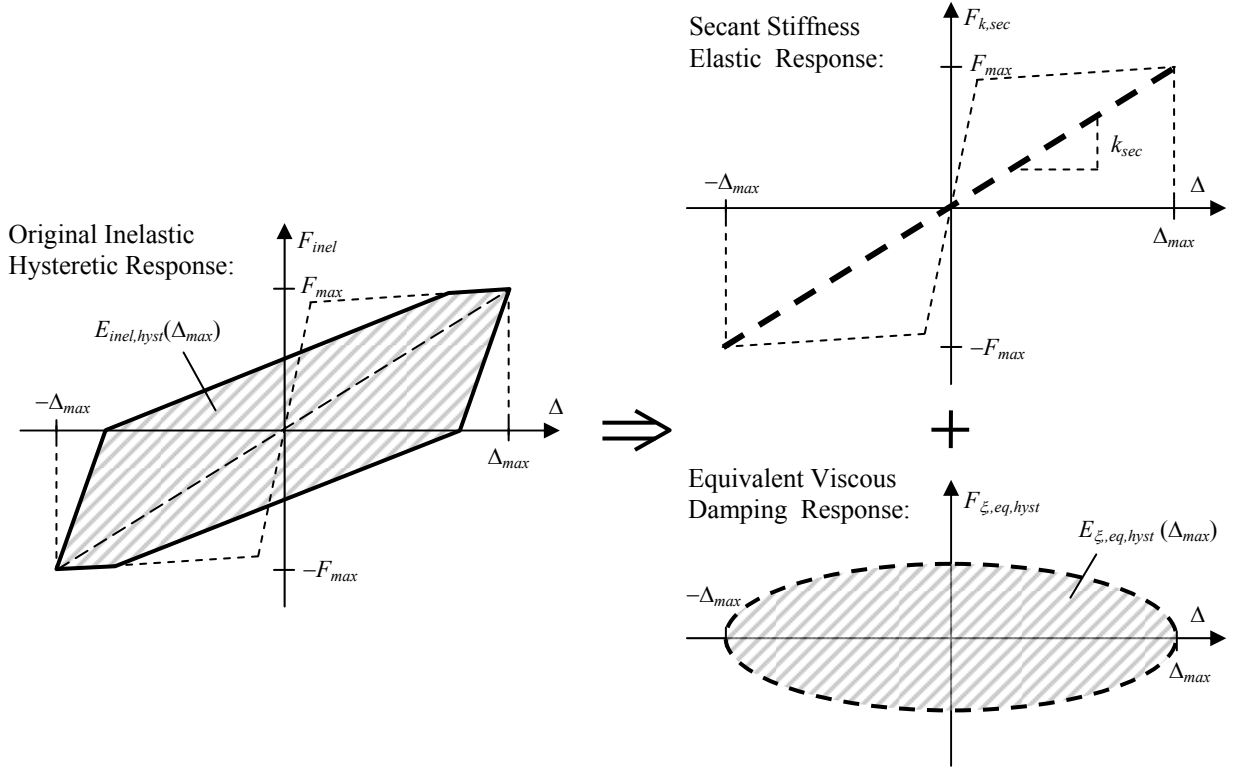

Fig. 4.20: Comparison between steady state responses of inelastic system and linearized substitute structure
left: Inelastic hysteresis, right: Individual contributions from secant stiffness and equivalent viscous damping

$$E_{\xi,eq,hyst} = \pi \cdot c_{eq,hyst} \cdot \omega \cdot \Delta_{max}^2 \tag{4.26}$$

$$c_{eq,hyst} = \frac{E_{\xi,eq,hyst}}{\pi \cdot \omega \cdot \Delta_{max}^2} \tag{4.27}$$

$$c_{cr,eff} = 2 \cdot \frac{k_{sec}}{\omega_{eff}} \tag{4.28}$$

with $\quad \omega_{eff} = \sqrt{\dfrac{k_{sec}}{m}}$

$$\xi_{eq,hyst} = \frac{c_{eq,hyst}}{c_{cr,eff}} = \frac{\omega_{eff}}{\omega} \cdot \frac{E_{\xi,eq,hyst}}{2\pi \cdot F_{max} \cdot \Delta_{max}} \tag{4.29}$$

with $\quad F_{max} = k_{sec} \cdot \Delta_{max}$

If the energy $E_{\xi,eq,hyst}$, dissipated by the viscous damper of the substitute model, is set equal to the energy $E_{inel,hyst}$, dissipated by the original inelastic system, equation (4.29) can be used to compute a corresponding equivalent viscous damping ratio $\xi_{eq,hyst}$ for the harmonic steady state motion of circular frequency ω. Analyzing the different factors in equation (4.29), several conclusions can be drawn. At

first, it is important to note that the energy $E_{\xi,eq,hyst}$ ($=E_{inel,hyst}$) in the numerator, as well as the peak force F_{max} and the peak displacement Δ_{max}, are amplitude dependent. In general cases, this will also be true for the ratio of the three. Therefore, the resulting equivalent viscous damping ratio $\xi_{eq,hyst}$ will normally be amplitude dependent as well, so that the definition of a unique $\xi_{eq,hyst}$ value for a certain hysteretic type, independent of the response, is not possible.

Second, the fact that equation (4.29) contains the ratio between the effective fundamental circular frequency ω_{eff} of the substitute system and the circular frequency ω of the harmonic motion shows that, strictly speaking, the value of $\xi_{eq,hyst}$ would only be valid for this type of motion. While the postulation of the *harmonic* character of the motion might be dropped as an approximation, the (inverse of the) frequency of motion still enters linearly into the expression for $\xi_{eq,hyst}$, resulting in a strong dependency on that parameter. This is related to the problem that hysteretic energy dissipation (i.e. $E_{inel,hyst}$) is rate independent, whereas viscous energy dissipation (i.e. $E_{\xi,eq,hyst}$) is rate dependent. It is therefore only possible to set these two equal for one specific rate of motion.

However, seismically caused motions are neither harmonic, nor steady state. And in particular, the rate or frequency of motion will not be known exactly beforehand. This makes it difficult to make a reasonable choice of the ratio ω_{eff}/ω, required in equation (4.29). The commonly adopted solution for this problem [Cho01] consists of the assumption that the system approximately vibrates at its natural effective frequency, thus resulting in $\omega_{eff}/\omega = 1$. As a consequence, the relationship for $\xi_{eq,hyst}$ reduces to the expression given in equation (4.30). On one hand, this assumption is reasonable in a sense that the natural effective frequency might be considered as the system's "preferred" frequency of response. On the other hand, as it is not a free vibration, the type and frequency of the (non-harmonic) excitation also strongly influence the characteristics of the response. Equation (4.30) can therefore only be considered as a rough compromise.

$$\xi_{eq,hyst} = \frac{E_{\xi,eq,hyst}}{2\pi \cdot F_{max} \cdot \Delta_{max}} \tag{4.30}$$

For the majority of realistic hysteresis models, the value of $\xi_{eq,hyst}$ computed by equation (4.30) will tend to increase with the amplitude Δ_{max}. As the seismic response of a system is not of the steady state type, various cycles with different amplitudes will occur during the time history. Due to the amplitude dependence of the equivalent viscous damping ratio, it is not possible to define a single value for $\xi_{eq,hyst}$ which would be appropriate for each of these different cycles. It might be considered determining $\xi_{eq,hyst}$ corresponding to the peak displacement demand of the seismic response history. However, although this could possibly be regarded as a reasonable assumption for this single cycle of peak response, it would overestimate the damping throughout the rest of the response. The energy dissipation during the entire time history would thus be overestimated, resulting in probably unconservative demand predictions.

An additional aspect in the evaluation of this model is that an inelastic system is not only characterized by its (secant) stiffness and its energy dissipation. Various hysteretic models have different recentering behavior after large excursions into the inelastic range. While, e.g., a flag-shaped hysteresis model (see [PCK07]) will always fully recenter after being released, a corresponding elasto-plastic hysteretic system shows very little recentering tendency. Stiffness degrading hystereses, more appropriate for normal RC members, typically lie between the two aforementioned models concerning recentering. This aspect has significant influence on the residual displacements after an earthquake, but it can also influence the maximum displacements. As a linearized substitute system has a perfect recentering behavior, it is likely that it might experience lower deformation demands than, e.g., a corresponding elasto-plastic model having similar energy dissipation characteristics.

Statistical studies (e.g. [Bla04]) have shown that the combination of the drawbacks outlined above results in typically unconservative results if the hysteretic part $\xi_{eq,hyst}$ of the equivalent viscous damping ratio is determined by equation (4.30) for the peak response. Therefore, especially in recent years, an alternative approach for the derivation of equations for $\xi_{eq,hyst}$ has been followed in several studies (e.g. [Guy04], [GBP05], [DKN07]). In this newer approach, empirical relationships are

developed from statistical regression analysis, somewhat comparable to the approach for the displacement modification factors presented in Section 4.5.1.

In these studies, either the equivalent viscous damping ratio only, or the effective period and the equivalent viscous damping together, have been optimized statistically in order to result in possibly good approximations of the corresponding inelastic peak displacement demand. While equations (4.29) and (4.30) were based on some postulated physical background, the alternative relationships are purely empirical. On the other hand, the statistically derived equations implicitly include – and to some extent solve – the previously discussed aspects representing drawbacks of the application of equation (4.30). For example, in the empirical approach the conceptual contradiction between rate-independent hysteretic energy dissipation and rate-dependent equivalent viscous damping remains. However, since the empirical studies are based on time history analyses using ground motions with realistic frequency content, this problem is implicitly covered by the calibration process.

The same is true for the potential influence related to the limited recentering behavior of certain hysteresis models. Moreover, the empirical approach does not rely on assumptions as steady-state or harmonic response, but rather directly considers realistic seismic response histories. As a consequence, such statistically optimized empirical relationships for the parameters of equivalent linearized models can be expected to yield more realistic results within the limits of conditions considered during the calibration process. However, it might not be justified to apply these parameters in case of completely different excitations, e.g. featuring strongly deviating frequency contents. The rate dependency of viscous damping might render erroneous results in such cases.

Two studies in which empirical relationships were developed for equivalent linear parameters will be presented in the following subsections. The first concept, developed by Priestley, Blandon, and Grant, is based on a secant stiffness to peak response and thus requires only the empirical determination of the corresponding equivalent viscous damping ratio. The second study, conducted by Guyader and Iwan, uses both parameters of the equivalent linearization, $\xi_{eq,hyst}$ and T_{eff}, to define a statistically optimum substitute system. Hence, they developed empirical equations for both parameters which correspond to each other and may only be used in pairs.

a) Priestley, Blandon, Grant [PCK07], [GBP05]

The inelastic demand estimations in the *direct displacement based design* approach developed by Priestley *et al.* [PCK07] relies on equivalent linearization using a secant stiffness to peak response. In this framework, two main studies have been performed for the estimation of appropriate equivalent viscous damping ratios. The first study by Priestley and Grant [PG05] was dedicated to the appropriate modeling of the elastic viscous damping ratio ξ_{el} (see Section 4.4.1) and the second study by Blandon and Priestley [BP05] investigated the equivalent viscous damping share $\xi_{eq,hyst}$ for the representation of hysteretic energy dissipation. The developed concepts were further developed in Grant *et al.* [GBP05] and are also summarized in Priestley *et al.* [PCK07]. The following summary refers primarily to the concepts as outlined in [PCK07] as this represents the latest version of the approach.

For both parts of the equivalent viscous damping ratio, ξ_{el} and $\xi_{eq,hyst}$, empirical equations have been proposed by Priestley and his co-workers. These relationships have been derived based on statistical regression of a large number of inelastic time history analyses (ITHA) performed on SDOF systems. The approach is therefore conceptually similar to that which was followed in the studies on displacement modification and force reduction factors [RM03], [CC04], [NK91] discussed in Section 4.5.1. For the derivation of the equivalent viscous damping ratios five artificial ground motion accelerograms were used which were developed to approximate the response spectra according to [ATC32]. The corresponding displacement spectra are continuously increasing in the period range up to $T = 4$ s. It is noteworthy that they differ in this respect from the elastic displacement spectra defined in [SIA261] which reach their peak value with a subsequent plateau at a period of $T_D = 2$ s (independent of soil type).

The studies were performed for a set of different hysteretic rules including the following models:

- *Elasto-plastic hysteresis*
  = bilinear with a post-yield stiffness ratio of $r = 0$
- *Bilinear hysteresis*
  with a post-yield stiffness ratio of $r = 0.2$
- *"Thin" Takeda hysteresis*
  with a post-yield stiffness ratio of $r = 0.05$
  unloading stiffness parameter $\alpha = 0.5$ (nomenclature according to [Car04])
  reloading stiffness parameter $\beta = 0$ (nomenclature according to [Car04])
- *"Fat" Takeda hysteresis*
  with a post-yield stiffness ratio of $r = 0.05$
  unloading stiffness parameter $\alpha = 0.3$ (nomenclature according to [Car04])
  reloading stiffness parameter $\beta = 0.6$ (nomenclature according to [Car04])
- *Ramberg-Osgood hysteresis*
  Ramberg-Osgood constant $r_{RO} = 7$
- *Flag-Shaped hysteresis*

For reinforced concrete piers, the *thin Takeda* model may be considered most representative. The *fat Takeda* having higher energy dissipation is rather appropriate for RC beams and frame structures. The *Ramberg-Osgood* hysteresis was shown to be useful for the modeling of inelastic soil-response in soil-structure applications (see Section 3.5.2). However, it should be noted that the analyses in [GBP05] are only strictly valid for a Ramberg-Osgood parameter of $r_{RO} = 7$. The *elasto-plastic* hysteresis is not really appropriate for RC members. However, due to its traditional significance in many earlier studies (see e.g. Section 4.5.1) it is considered here for comparison purposes. The *bilinear* model with post-yield stiffness ratio $r = 0.2$ and the *flag-shaped* model do not really have much relevance for ordinary RC structures. They are therefore not further considered in this section.

Based on theoretical considerations and on empirical ITHA results, it appears reasonable to assume that the equivalent viscous damping part $\xi_{eq,hyst}$, which is to cover the hysteretic energy dissipation, is a function of the ductility demand μ_Δ. The empirical evaluations also show that it depends statistically on the effective period T_{eff} (corresponding to the secant stiffness to peak demand). An empirical equation for $\xi_{eq,hyst}$ should therefore be formulated as a function of these two parameters in the form of $\xi_{eq,hyst}(\mu_\Delta, T_{eff})$.

As discussed in Section 4.4.1, the elastic viscous damping ratio ξ_{el} is normally defined with respect to the critical damping coefficient $c_{cr,0}$ corresponding to the initial stiffness k_0 of the inelastic system. In an equivalent linearized model, the critical damping coefficient $c_{cr,eff}$ according to (4.28) is a function of the secant stiffness k_{sec} and is therefore dependent on the ductility demand (see equation (4.24)). If the corresponding damping coefficient c_{el} is not supposed to vary in the same way, the damping ratio ξ_{el} must be modified accordingly. In Section 4.4.1 it was also discussed that, under certain conditions and based on certain assumptions, a variable elastic viscous damping coefficient c_{el} might be appropriate. Both aspects lead to the necessity to formulate an effective elastic viscous damping ratio as a function of the ductility demand in the form $\xi_{el,eff}(\mu_\Delta)$. This modified elastic viscous damping ratio, as well as the ratio $\xi_{eq,hyst}(\mu_\Delta, T_{eff})$ representing the hysteretic energy dissipation, then refers to the effective critical damping coefficient $c_{cr,eff}$ according to (4.28).

The total equivalent viscous damping ratio $\xi_{eq,tot}$, consisting of both parts mentioned above, then also becomes a function of μ_Δ and T_{eff}, so that equation (4.22) is therefore rewritten to define $\xi_{eq,tot}(\mu_\Delta, T_{eff})$ according to equation (4.31). For the elastic viscous damping part $\xi_{el,eff}(\mu_\Delta)$, Priestley *et al.* [PCK07] developed the general relationship given by equation (4.32). Furthermore, they recommend the general form of equation (4.33) for the hysteretic energy dissipation part represented by $\xi_{eq,hyst}(\mu_\Delta, T_{eff})$.

Based on regression analysis, Priestley *et al.* [PCK07] calibrated an individual set of parameters to be used with the above equations for each of the considered hysteretic models. These parameters are given in Tab. 4.7 for selected hysteretic models. Note that for the parameter λ two values are given for

each hysteretic rule. The upper value is to be used if a constant elastic viscous damping coefficient is considered appropriate in the original inelastic model, whereas the lower value corresponds to tangent stiffness proportional damping in the inelastic model, as discussed in Section 4.4.1. The positive λ value for the constant damping model results in an increasing damping ratio $\xi_{el,eff}(\mu_\Delta)$ with increasing ductility demand μ_Δ. It thus (partly) compensates for the decreasing critical damping coefficient $c_{cr,eff}(\mu_\Delta)$. In contrast, the negative λ value for the tangent stiffness proportional damping model yields a decreasing damping ratio $\xi_{el,eff}(\mu_\Delta)$ as the tangent stiffness proportional damping coefficient decreases stronger with ductility than the effective critical damping coefficient (see Section 4.4.1).

$$\xi_{eq,tot}\left(\mu_\Delta, T_{eff}\right) = \xi_{el,eff}\left(\mu_\Delta\right) + \xi_{eq,hyst}\left(\mu_\Delta, T_{eff}\right) \tag{4.31}$$

$$\xi_{el,eff}\left(\mu_\Delta\right) = \xi_{el,0} \cdot \mu_\Delta^\lambda \tag{4.32}$$

$$\xi_{eq,hyst}\left(\mu_\Delta, T_{eff}\right) = a \cdot \left(1 - \frac{1}{\mu_\Delta^b}\right) \cdot \left(1 + \frac{1}{\left(T_{eff} + c\right)^d}\right) \tag{4.33}$$

Hysteretic Model	Elastic Viscous Damping Model	Parameters				
		Eq. (4.32)	Equation (4.33)			
		λ [-]	a [-]	b [-]	c [-]	d [-]
Elasto-Plastic $r = 0$	constant	0.127	0.224	0.336	-0.002	0.250
	tang. stiff. prop.	-0.341				
Takeda "Fat" $r = 0.05, \alpha = 0.3, \beta = 0.6$	constant	0.312	0.305	0.492	0.790	4.463
	tang. stiff. prop.	-0.313				
Takeda "Thin" $r = 0.05, \alpha = 0.5, \beta = 0$	constant	0.340	0.215	0.642	0.824	6.444
	tang. stiff. prop.	-0.378				
Ramberg-Osgood $r_{RO} = 7$	constant	-0.060	0.289	0.622	0.856	6.460
	tang. stiff. prop.	-0.617				

Tab. 4.7: Parameter λ for the use of equation (4.32) and parameters a, b, c, and d for the use of equation (4.33) for various hysteretic models according to [PCK07]

An evaluation of equations (4.31) through (4.33) using the parameters from Tab. 4.7 is depicted in Fig. 4.21 for various configurations. On the left side, $\xi_{eq,tot}$ and $\xi_{el,eff}$ are shown as a function of μ_Δ for a constant effective period of $T_{eff} = 1$ s and assuming a *thin Takeda* hysteretic behavior. The contribution of $\xi_{eq,hyst}$ is implicitly depicted in the graph as the distance between the two curves for $\xi_{eq,tot}$ and $\xi_{el,eff}$. It should be noted that, for a given inelastic system, the effective period T_{eff} is not independent of the ductility demand μ_Δ. Keeping it constant in the figure therefore only serves for visualization purposes.

Two types of elastic viscous damping models are considered on the left side of Fig. 4.21. The first is a tangent stiffness proportional damping based on an initial damping ratio of $\xi_{el,0} = 5$ %, and the second is a constant damping coefficient model using $\xi_{el,0} = 2\%$. It has been discussed in Section 4.4.1 that under certain (but not all) conditions tangent stiffness proportional damping might be considered more appropriate. However, in inelastic dynamic analysis of MDOF systems it is hardly possible to define a reasonable damping model that would qualify for this purpose. It has therefore been argued in Section 4.4.1 that, as an approximation to the intended behavior, it might be a reasonable simplification to model a constant elastic viscous damping with a lower damping ratio in order to allow for the reduced energy dissipation in the plastic part of the response. The comparison in Fig. 4.21 (left) shows that a constant elastic viscous damping model with $\xi_{el,0} = 2\%$ can approximate the tangent stiffness

proportional model with $\xi_{el,0} = 5\%$ reasonably well over large part of the typically expected ductility range. Especially, with respect to the resulting total equivalent viscous damping ratio $\xi_{eq,tot}$ the remaining differences might be well acceptable.
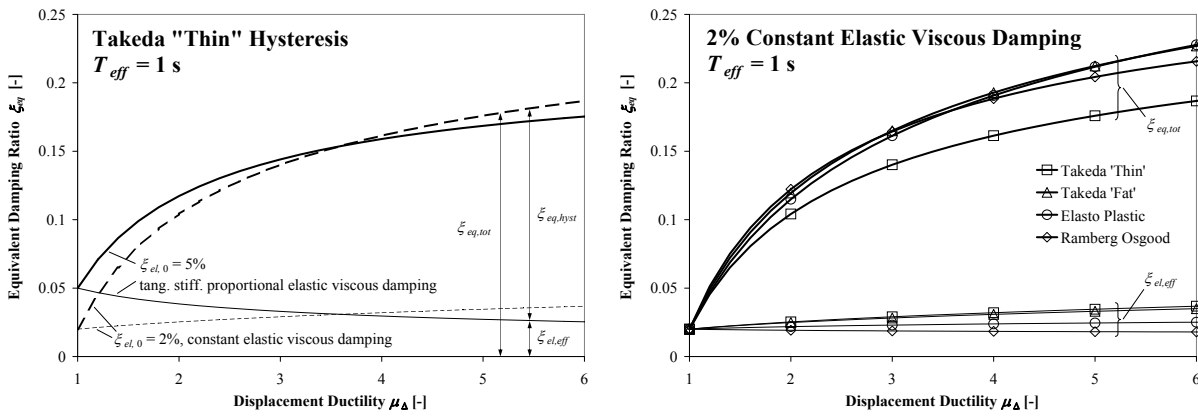

*Fig. 4.21: Equivalent viscous damping ratio $\xi_{eq,tot}$ and elastic viscous damping ratio $\xi_{el,eff}$
as a function of ductility μ_Δ for a constant effective period of $T_{eff} = 1$ s
left: For "Thin Takeda" hysteresis, distinguishing between two elastic damping models,
right: For various hysteresis types, corresponding to 2% constant elastic viscous damping*

On the right side of Fig. 4.21 the equivalent viscous damping curves for the four hysteretic models included in Tab. 4.7 are compared, based on a constant elastic viscous damping model with $\xi_{el,0} = 2\%$ and a fixed effective period of $T_{eff} = 1$ s. It can be seen that, despite the considerable differences between the individual parameter sets, the curves do not vary significantly for the given effective period. The curves for the *elasto-plastic*, the *fat Takeda* and the *Ramberg-Osgood* hystereses, having all rather high energy dissipation characteristics, result as almost equal over the considered ductility range. Only the *thin Takeda* rule, featuring less hysteretic energy dissipation, deviates somewhat resulting in lower $\xi_{eq,tot}$ values. At the same time, it should be taken into account that the differences in equivalent viscous damping ratios do not translate linearly to differences in displacement demand (see Fig. 4.6). The fact that the equivalent viscous damping ratio for the *thin Takeda* model at $\mu_\Delta = 6$ falls below the value for the *elasto-plastic* hysteresis by -22% therefore only results in a higher displacement demand estimate by +8.3% or +9.5% based on equations (4.7) or (4.8), respectively.

For practical applications of the equivalent viscous damping ratio $\xi_{eq,tot}$, in order to perform a displacement demand estimation, normally relationships for the transformation factor η will also be required. These $\eta(\xi)$ relationships transform elastic response spectra in order to allow for different viscous damping ratios. As discussed in Section 4.4.2, some uncertainties exist with respect to this transformation factor, resulting in several proposals for $\eta(\xi)$ relationships (see equations (4.7) through (4.10), and Fig. 4.6). For the practical application of the equivalent linearization approach according to [PCK07] therefore a variety of possible combinations of equivalent viscous damping relationships and transformation factors result. If the absolute demand estimations resulting from this approach are to be compared to those resulting from other concepts (see e.g. Section 4.5.1), a considerable diversity of conceivable permutations, related to the choice of hysteretic model, elastic viscous damping model, and relationship for the transformation factor $\eta(\xi)$, exists. It is therefore not possible to determine one unique demand value resulting from the equivalent linearization concept of [PCK07] which could be compared to the predictions from other approaches.

Furthermore, the general format of the equivalent linearization concept is conceptually not directly comparable to that using, e.g., displacement modification factors C_R as described in Section 4.5.1. As the results of the combined period shift and damping increase in the equivalent linearization concept depend on the spectral shape, a direct comparison with the demand predictions using C_R factors is only possible for a given elastic response spectrum. Although such a comparison is, strictly speaking, only valid for this particular spectrum, it appears interesting to investigate how the demand predictions from the equivalent linearization concept actually turn out in practical applications, compared to the

estimations resulting from other approaches. For this purpose, an elastic response spectrum according to [SIA261] and [SIA2018] will be assumed. The required parameters for its determination are chosen corresponding to a seismic zone Z3b (a_{gd} = 1.6 m/s^2), a soil class B (S = 1.2, T_B = 0.15 s, T_C = 0.5 s, T_D = 2.0s) and an importance class III (γ_f = 1.4). Elastic viscous damping is assumed as either constant with $\xi_{el,0}$ = 2 % or tangent stiffness proportional with $\xi_{el,0}$ = 5 %. For the transformation factor $\eta(\xi)$ the two approaches according to equation (4.7) ([EC8-1] version 2003 & [SIA261]) and equation (4.8) ([EC8-1-1] version 1994) are considered.

Based on this elastic response spectrum, inelastic displacement demand estimations can be computed using the equivalent linearization concept of [PCK07] with the equivalent viscous damping ratios according to equation (4.33). These demand estimations can be performed for a variety of systems featuring different initial periods T_0 and strength ratios R_y. Relating the determined predictions for the inelastic deformations to the displacement demand of the corresponding elastic systems having the same initial period T_0 and the elastic viscous damping ratio $\xi_{el,0}$, it is possible to compute equivalent displacement modification factors C_R which represent exactly the results from the equivalent linearization approach for the given response spectrum.
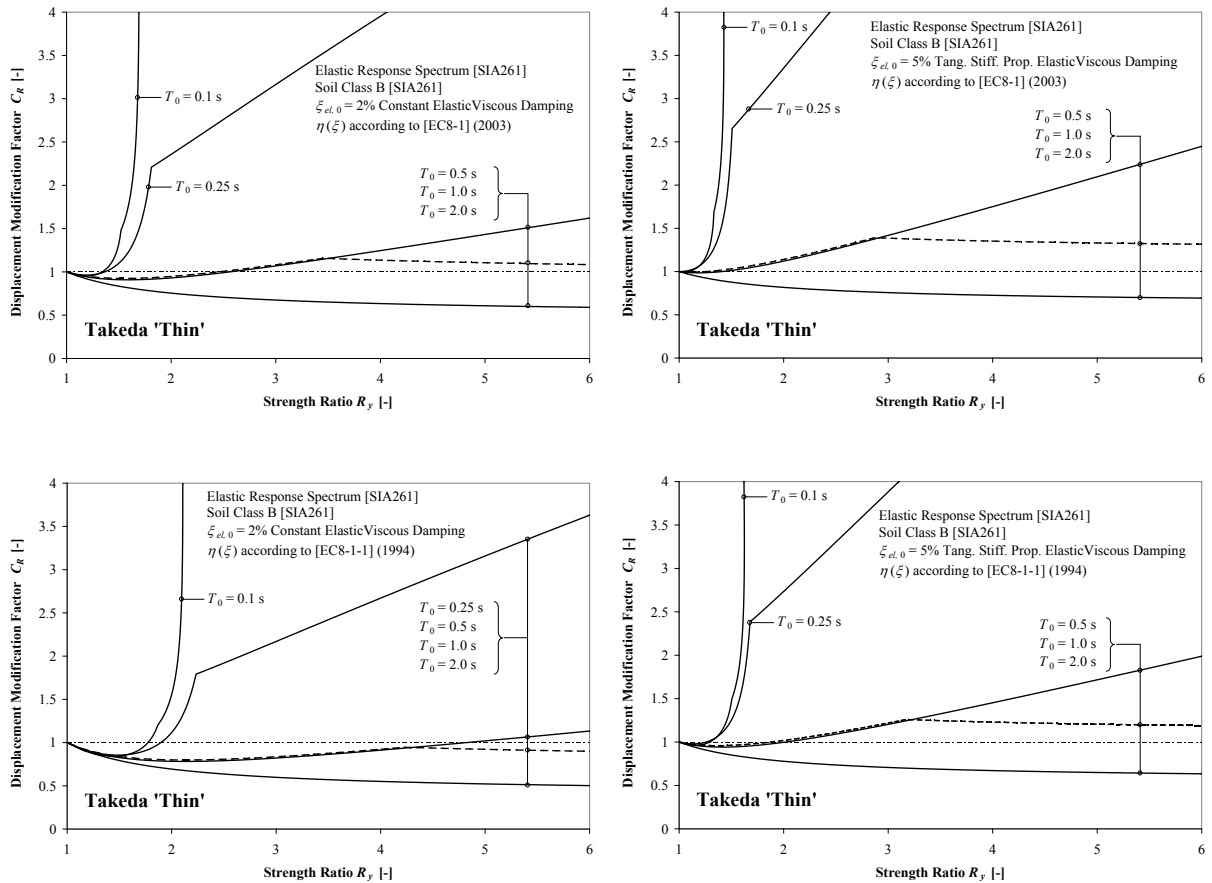

Fig. 4.22: Displacement modification factors resulting from equation (4.33) for "Thin" Takeda hysteresis upper row: Transformation factor η according to [EC8-1] & [SIA261], lower row: η according to [EC8-1-1] left column: 2% constant elastic viscous damping , right column: 5% tangent stiffness damping

Such an evaluation has been performed for several combinations of partial models as discussed above. The resulting equivalent C_R values are depicted in Fig. 4.22 for the *thin Takeda* hysteresis and in Fig. 4.23 for *elasto-plastic* behavior. In each case, they are shown as a function of the strength ratio R_y for a set of five different fixed initial periods T_0. On the left side of each figure, the elastic viscous damping has been assumed as constant with $\xi_{el,0}$ = 2%, while the right side shows the results for a tangent stiffness proportional damping with $\xi_{el,0}$ = 5%. In the upper row of each figure the displacement demands have been computed using the transformation factor $\eta(\xi)$ according to equation (4.7) as

given in [EC8-1] and [SIA261], and the results in the lower row are based on $\eta(\xi)$ according to equation (4.8) as defined in [EC8-1-1]. It can be seen that the general trends of C_R as a function of R_y are only roughly similar to those previously shown in Fig. 4.11, Fig. 4.13, and Fig. 4.17 corresponding to the initial period based procedures from [RM03], [CC04], and [NK91], respectively.
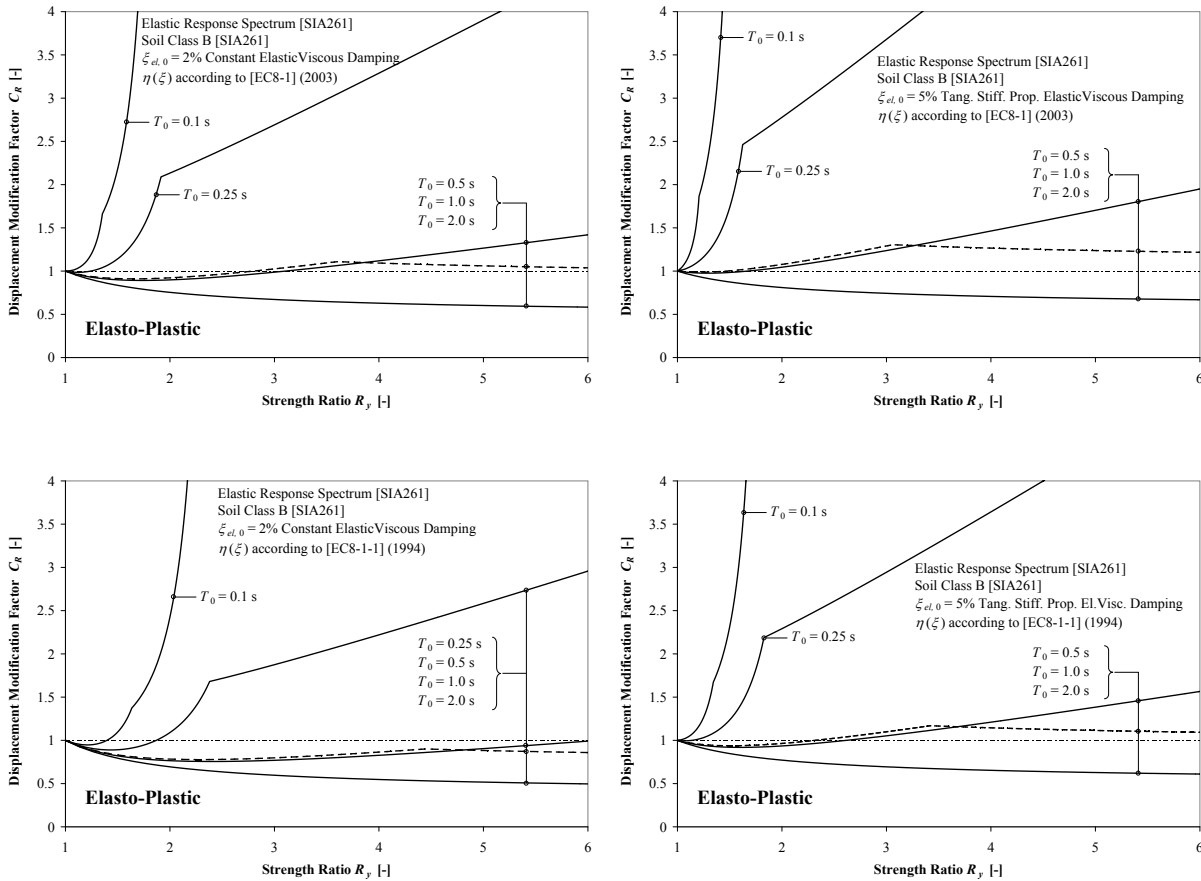

Fig. 4.23: Displacement modification factors resulting from equation (4.33) for elasto-plastic hysteresis upper row: Transformation factor η according to [EC8-1] & [SIA261], lower row: η according to [EC8-1-1] left column: 2% constant elastic viscous damping , right column: 5% tangent stiffness damping

The curves tend to agree in a sense that for short periods a very high gradient of the C_R vs. R_y curves can be found which results in extremely high displacement modification factors already at low to medium strength ratios. There is also agreement about the fact that C_R values are reduced significantly for increasing initial periods T_0, approaching a behavior close to the *equal displacement approximation* in the medium period range. However, in the long period range ($T_0 = 2.0$ s), a response prediction significantly lower than the *equal displacement approximation* can be found. Predicted inelastic deformations as low as only 50% of the corresponding elastic demands result in some configurations for strength ratios $R_y = 6$. Such low predictions were not found in Fig. 4.11, Fig. 4.13, and Fig. 4.17. The approaches from [RM03] and [NK91] also resulted in C_R values somewhat lower than unity for $T_0 = 2.0$ s, but they did not predict values as low as those from shown in Fig. 4.22 and Fig. 4.23.

The reason why the computed equivalent C_R values result so much lower than unity in the latter cases is related to the fact that the initial period $T_0 = 2.0$ s coincides with the corner period T_D of the elastic response spectrum. At T_D the displacement spectrum reaches its peak value and remains at a plateau for higher periods (see right side of Fig. 4.2). For lower periods, the equivalent linearization results in two separate effects which counteract each other and – in the range of the *equal displacement approximation* – to some extent cancel each other out. The first effect is the period shift towards the increased effective period T_{eff}, which results in a higher displacement demand as long as $T_0 < T_D$. On the other hand, the increase of the viscous damping ratio to $\xi_{eq,tot}$, as the second effect, reduces the

demand again. If, however, the initial period T_0 is equal to or higher than T_D, then the period shift does not lead to an increase of the displacement anymore and only the demand reduction by the increased damping ratio affects the result.

It can thus be seen that the equivalent linearization approach from [PCK07] will inevitably result in C_R values lower than unity in the period range $T_0 \geq T_D$ for displacement spectra that feature a peak value at T_D with subsequent plateau. It might be noteworthy that C_R would result differently if the response spectrum used for the comparison would feature similar characteristics as the spectra corresponding to the artificial ground motions used in the calibration of equation (4.33) and the parameters in Tab. 4.7. As mentioned previously, the artificial accelerograms had been developed in order to approximate displacement spectra which continuously increase for periods up to 4 s. For such a spectrum, even at $T_0 = 2.0$ s the counteracting effects of period shift and damping increase would still be effective and the resulting C_R values would not result as low as found in Fig. 4.22 and Fig. 4.23.

On the other hand, the fact that the equivalent linearization approach does not agree here with the initial period based concepts presented in Section 4.5.1 does not necessarily allow a conclusion about which approach should be considered as more realistic. It can be seen in Fig. 4.12 that Chopra and Chintanapakdee [CC04] also computed mean C_R significantly lower than unity in the period range $T_D \leq T_0 \leq T_F$ (note the double logarithmic scales in Fig. 4.12). The corresponding graph for the results by Ruiz-García and Miranda [RM03] in Fig. 4.8 only shows the period range up to $T_0 = 3$ s which for higher earthquake magnitudes might still be lower than T_D. At least qualitatively, it can therefore not be ruled out that the phenomenon of C_R values lower than unity for $T_0 \geq T_D$ represents a realistic behavior. Another question is how pronounced this phenomenon actually is, i.e. how low C_R can realistically become, and whether this displacement reduction (compared to a linear system with the same initial period) should be used in a possibly conservative practical application.

At the same time, these discussions show that it is meaningful to relate the periods (in empirical relationships for the inelastic demand estimation) to certain characteristic periods of the ground motions, and thus of the corresponding elastic response spectra. The expressions proposed for C_R in [RM03] and [CC04] already include a normalization of the initial period T_0 to a specified characteristic period T_s or T_C. It might be imaginable to also include additionally the period T_D, where the displacement sensitive part of the spectrum starts, in order to take into account possible effects as those discussed above. This might be a subject for future research.

Concerning the shape of the computed effective C_R curves in Fig. 4.22 and Fig. 4.23, it is noteworthy that they show corner-like changes of the gradient at certain points. This phenomenon is not really related to the equivalent linearization, but is rather an effect of the corresponding corners in the elastic response spectrum. Applying the approach on a continuously curved response spectrum would not result in such corners.

From Fig. 4.22 and Fig. 4.23 it can further be seen that the required choices of submodels for the practical application of the equivalent linearization approach influence the C_R curves to a noticeable degree. This refers to the choice of the elastic viscous damping model as well as to the selection of the transformation relationship $\eta(\xi)$ required to allow for different damping ratios in the elastic response spectra.

With respect to the elastic viscous damping model it should be noted that the elastic displacement demands corresponding to T_0, that were used to normalize the inelastic demand for the computation of the displacement modification factor C_R, were related to differing viscous damping ratios. In the constant elastic damping model, shown on the left side of Fig. 4.22 and Fig. 4.23, not only the inelastic demands were estimated using a viscous damping ratio of $\xi_{el,0} = 2\%$, but also the corresponding elastic demand was computed for $\xi = 2\%$. In a similar way, while the demand of the inelastic system with the tangent stiffness elastic viscous damping model (right side of the figures) was computed for $\xi_{el,0} = 5\%$, the corresponding elastic displacement was also determined for $\xi = 5\%$. As a consequence, the C_R values shown in Fig. 4.22 and Fig. 4.23 for the two different elastic viscous damping models are related to different elastic displacements. Therefore, differences between the curves on the left side and those on the right side of the figures partly result from the different elastic displacements used to normalize the inelastic demands. As will be shown below, the estimations of the absolute inelastic displacement demands differ significantly less between the two damping models.

However, a noticeable difference can also be found between the two curves in the upper rows and those in the lower rows of Fig. 4.22 and Fig. 4.23, corresponding to different $\eta(\xi)$ relationships. This difference is not due to different normalizations, but rather really reflects the differences in the inelastic demand estimations. This appears even more noteworthy as the two sets of curves physically should represent the same behavior, the only difference being the different choices for $\eta(\xi)$ reflecting the uncertainties related to the influence of differing damping ratios.

The rather limited differences between the two proposals concerning η for a given viscous damping ratio ξ, depicted in Fig. 4.6, translate into considerable deviations of the displacement demand for a given strength ratio R_y. For example, the displacement demand for a system with an initial period of $T_0 = 0.25$ s and a strength ratio of $R_y = 4$, as shown in Fig. 4.22 and Fig. 4.23, is between 25% and 50% higher for $\eta(\xi)$ according to equation (4.7) (i.e. [EC8-1] & [SIA261]) than for $\eta(\xi)$ according to equation (4.8) (i.e. [EC8-1-1]). For the initial periods $T_0 = 0.5$ s and $T_0 = 1.0$ s, in some cases the differing model for $\eta(\xi)$ can even result in a change between an increase of the demand (compared to the corresponding elastic response) – i.e. $C_R > 1$ – and a demand decrease – i.e. $C_R < 1$. It can thus be concluded that, for assessment cases with known fixed initial period and strength ratio, the uncertainties in the application of the equivalent linearization approach related to the choice of the $\eta(\xi)$ relationship can be significant.

In addition to the previously shown C_R values, in Fig. 4.24 and Fig. 4.25 the resulting ductility and absolute displacement demands are shown. These have again been evaluated for the two hysteretic models, *thin Takeda* (Fig. 4.24) and *elasto-plastic* (Fig. 4.25). In each case, the two differing elastic viscous damping assumptions, i.e. the constant model with $\xi_{el,0} = 2\%$ (left columns) and the tangent stiffness proportional model with $\xi_{el,0} = 2\%$ (right columns), were considered. For the $\eta(\xi)$ relationship only the expression from [EC8-1] and [SIA261] according to equation (4.7) has been used. Comparing the absolute displacement demands resulting from the two different damping models, a difference is noticeable, but it is somewhat less pronounced than the difference between the corresponding C_R curves. This suggests that part of the deviation between the C_R curves is indeed related to the varying elastic displacement demands that were used to normalize C_R, as mentioned above.
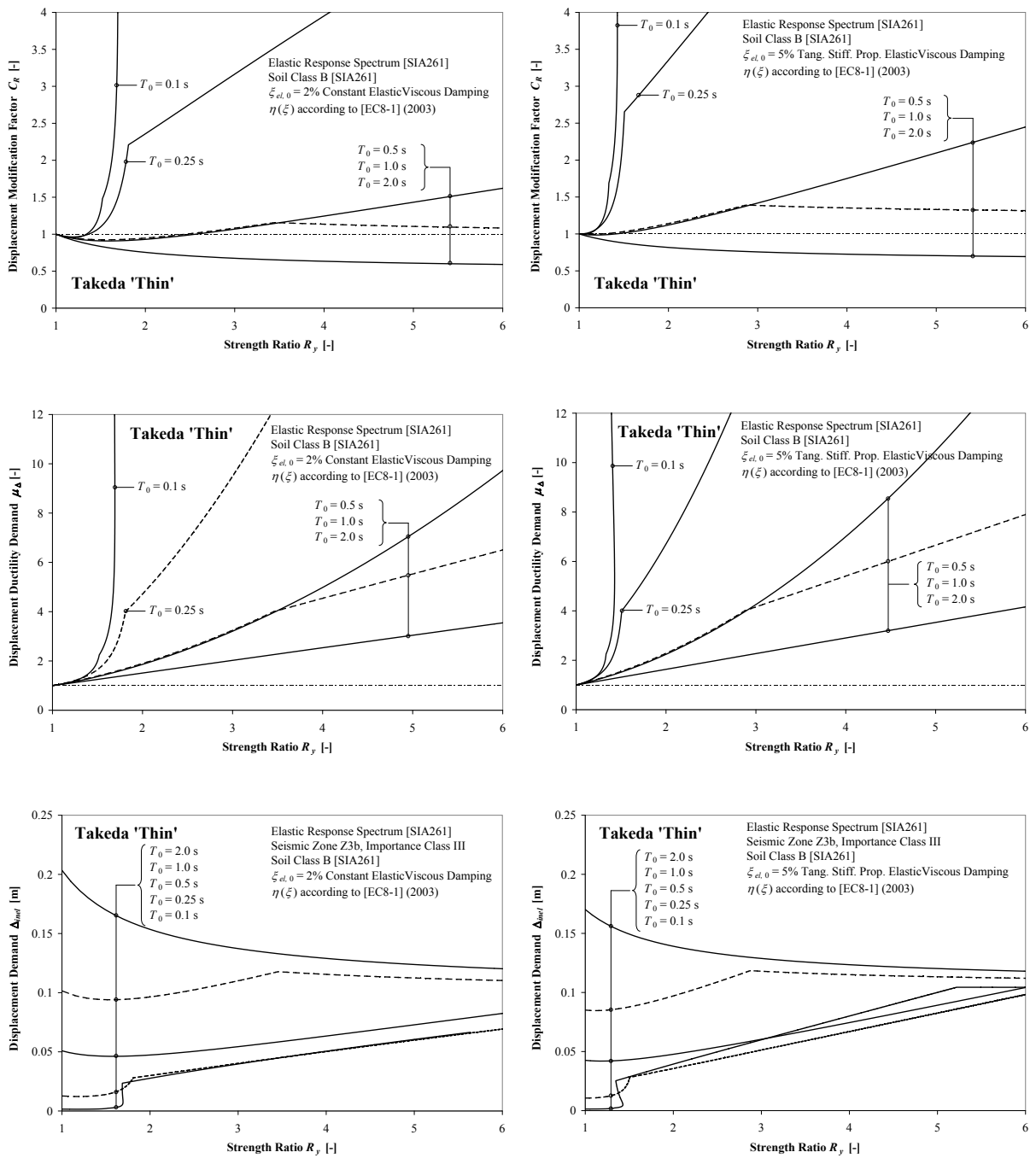
Fig. 4.24: Demand estimations resulting from equation (4.33) for "Thin" Takeda hysteresis [PCK07]
upper row: Displacement modification factor C_R, middle row: Displacement ductility demand μ_Δ,
lower row: Absolute displacement demand Δ_{inel}
left column: 2% constant elastic viscous damping , right column: 5% tangent stiffness damping
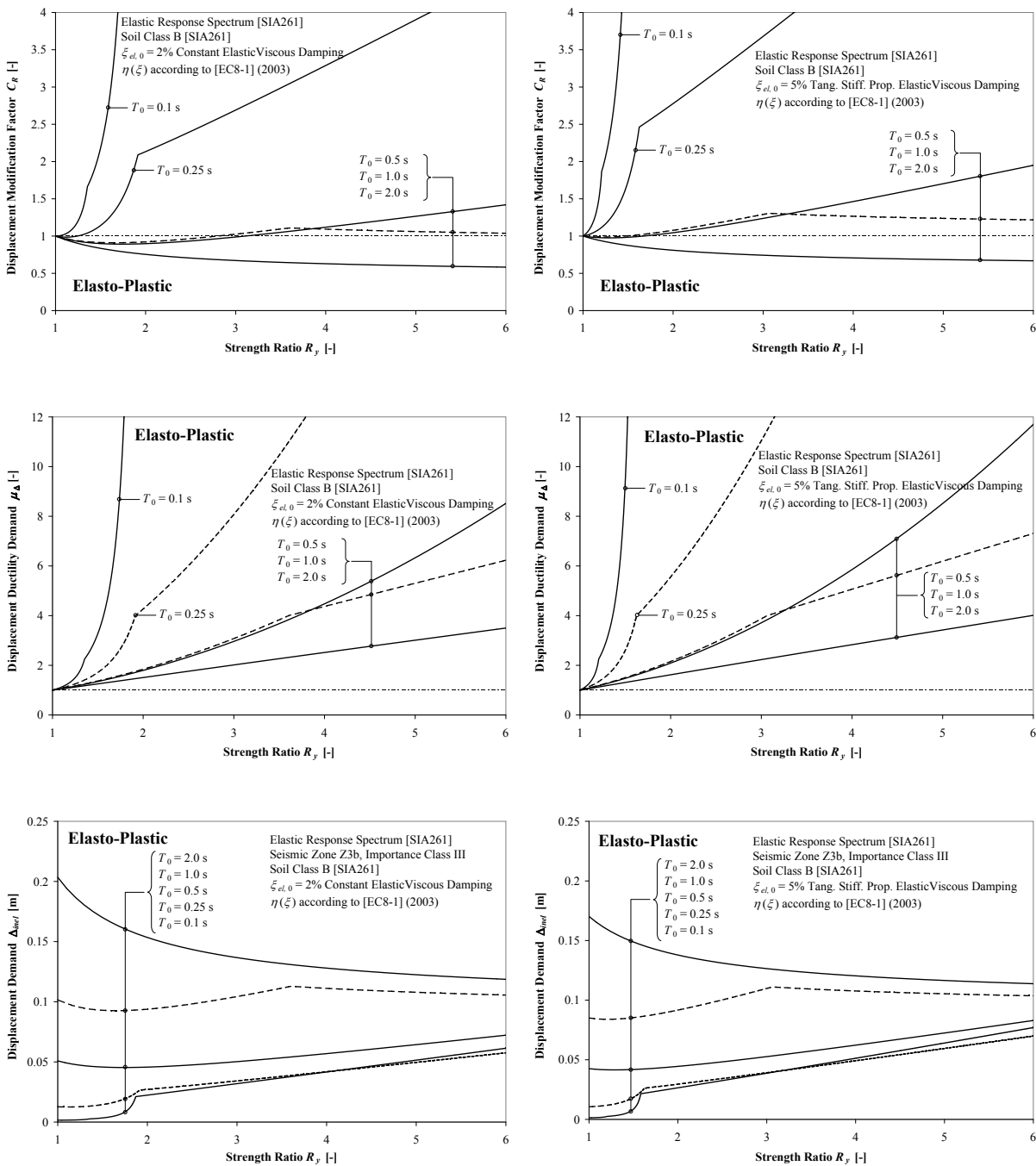
Fig. 4.25: Demand estimations resulting from equation (4.33) for elasto-plastic hysteresis [PCK07]
upper row: Displacement modification factor C_R, middle row: Displacement ductility demand μ_Δ,
lower row: Absolute displacement demand Δ_{inel}
left column: 2% constant elastic viscous damping , right column: 5% tangent stiffness damping

b) Guyader and Iwan [Guy04], [GI06]

A conceptually somewhat different approach for the definition of an equivalent linearized model has been proposed by Guyader and Iwan. Early works by Iwan and Gates [IG79a], [IG79b] suggested that a (statistically) "optimum effective linear system" could be achieved if both, equivalent viscous damping ratio ξ_{eq} and effective period T_{eff}, were taken as free parameters, for which optimized empirical relationships should be developed. In this case, the effective period T_{eff} would not be related to the secant stiffness to peak response anymore, as given by equations (4.24) and (4.25). Instead, T_{eff} would rather be determined independently and could be interpreted as related to a secant stiffness k_{sec} corresponding to some other displacement demand during the response history, not being the peak displacement.

Based on this conceptual approach, Iwan [Iwa80] suggested empirical equations for the optimum effective period T_{eff} and the corresponding equivalent viscous damping ratio $\xi_{eq,hyst}$ (covering hysteretic energy dissipation). The relationships were calibrated on inelastic SDOF time history analyses for a total of 12 recorded earthquake ground motions. In this context, it should be noted that Miranda and Ruiz García [MR02] evaluated a set of 6 approximate methods for the estimation of inelastic SDOF displacement demands by statistical comparison with results from inelastic time history analyses. One of the approximate methods considered in this review was the proposal by Iwan [Iwa80].

This study by Miranda and Ruiz García [MR02] evaluated, on one hand, the accuracy of the predicted mean values for the inelastic displacement demands. On the other hand, it also investigated the uncertainties and the scatter related to the predictions using the individual procedures. This scatter was expressed by the standard deviation of the relative errors. It should be mentioned that the comparison between inelastic time history results and approximate prediction in [MR02] was performed for predetermined ductilities μ_Δ and not for given strength ratios R_y, as it would be more representative for assessment cases. Nevertheless, the results might be considered of at least qualitative significance for this latter task as well.

According to the results by Miranda and Ruiz García [MR02], the proposal by Iwan [Iwa80] gave, on average, surprisingly good predictions of the inelastic displacement demand for three different hysteretic models considered in the review. Over large part of the period range (up to 3 s) the mean value of the ratio between approximate prediction and time history result was reasonably close to unity. Only in the (very) short period range, the approach tended to underpredict the mean ITHA response to some extent. Aside from the rather good performance with respect to the mean response prediction, Iwan's proposal was also found to result in comparatively low scatter of the results. The response predictions based on this approach resulted in standard deviations of the relative error being not higher than about 20% to 30%. Compared to the other methods considered in the review, which showed standard deviations in the range of about 30% to 40%, partly reaching up to 60%, Iwan's proposal thus resulted in significantly less uncertainty. Taking additionally into account the reasonably good prediction of the mean values, the proposal by Iwan [Iwa80] therefore tended to perform somewhat better than the alternative methods included in the study by Miranda and Ruiz García [MR02]. Only in the short period range, the approach by Iwan showed some deficits (which are also unconservative). It should be noted that none of the proposals presented in this text (Sections 4.5.1 and 4.5.2) had been included in the review by Miranda and Ruiz García [MR02] as these proposals have been developed more recently (aside from [NK91]).

While the procedure by Iwan [Iwa80] was already developed in 1980, the same general principles have been further developed more recently by Guyader and Iwan [Guy04], [GI06]. A conceptually similar approach as in [Iwa80] has been followed to calibrate empirical equations for the effective period T_{eff} and the equivalent viscous damping ratio $\xi_{eq,hyst}$ of a statistically optimum linearized system. For this purpose Guyader used a total of 28 recorded far-field ground motions to perform inelastic time history analyses (ITHA) on SDOF systems. As hysteretic rules he considered bilinear, stiffness degrading, in-cycle strength degrading and pinching models with a variety of post-yield stiffness ratios r for each model. As in the other studies presented above, the data of the ITHA results were statistically evaluated to develop empirical relationships for T_{eff} and $\xi_{eq,hyst}$.

A somewhat special feature of the approach followed by Guyader is that he did not only attempt to optimize the mean value of the response predictions, but also included the scatter in his optimization process in order to possibly reduce the uncertainties of the predictions. For this purpose he defined an error measure ε_D, being the relative error of the approximate prediction compared to the corresponding ITHA result. This parameter ε_D is a function of the chosen effective period T_{eff} and equivalent viscous damping $\xi_{eq,hyst}$. Furthermore, Guyader introduced an *engineering acceptability range* (EAR) that defines the limiting values within which ε_D could still be considered acceptable. In order to result in rather slightly conservative response predictions, it was chosen that the upper boundary for the EAR should be +20% (i.e. a response overprediction by a maximum of 20%) and the lower boundary of acceptability should be -10% (i.e. underpredictions by not more than 10%).

The optimization criterion adopted by Guyader was to minimize the probability of relative errors ε_D outside the thus defined *engineering acceptability range*. This means that the combinations of T_{eff} and $\xi_{eq,hyst}$ were determined in a way so that this probability reaches its minimum. Subsequently, empirical equations were developed to predict the thus defined optimum combinations of T_{eff} and $\xi_{eq,hyst}$. It should be noted that the approach does not necessarily yield the optimum parameters with respect to the mean values of the response predictions. However, it attempts to minimize the probability of large errors. In this sense, some implicit trade-off may result concerning the accuracy of the *average* prediction in order to reduce the *uncertainty* of the results.

From an engineering point of view, this approach appears reasonable because especially severe response underpredictions, as a result of large uncertainties, would have to be considered as potentially dangerous. In contrast, (more frequent) smaller errors, being combined with a higher reliability of the prediction, may be more acceptable for the safety of the analyzed structures. In fact, it is mostly not the mean accuracy of the simplified analysis procedures that makes the reliability of their response predictions questionable, but it is rather the considerable uncertainty often implied by their application. It therefore appears consequent to attempt to reduce the uncertainty instead of optimizing the mean response estimations by an additional small margin.

Based on the principles outlined above, Guyader and Iwan developed the two empirical equations (4.34) and (4.35) for the effective period T_{eff} and equivalent viscous damping ratio $\xi_{eq,hyst}$ (related to the hysteretic energy dissipation), respectively. A large number of parameter sets for the application of both equations is given in [Guy04], corresponding to the various combinations of hysteretic models and post-yield stiffness ratios r considered in the study. For elasto-plastic behavior (model BLH) and for the stiffness degrading model (KDEG) with $r = 0$ the required data are presented in Tab. 4.8 and Tab. 4.9.

$$T_{eff}\left(\mu_\Delta\right) = \begin{cases} T_0\left[1 + G\cdot\left(\mu_\Delta - 1\right)^2 + H\cdot\left(\mu_\Delta - 1\right)^3\right], & \text{for } \mu_\Delta < 4.0 \\[2mm] T_0\left[1 + I + J\cdot\left(\mu_\Delta - 1\right)\right], & \text{for } 4.0 \leq \mu_\Delta \leq 6.5 \\[2mm] T_0\left[1 + K\cdot\left(\sqrt{\dfrac{\mu_\Delta - 1}{1 + L\cdot\left(\mu_\Delta - 2\right)}} - 1\right)\right], & \text{for } \mu_\Delta > 6.5 \end{cases} \tag{4.34}$$

$$\xi_{eq,hyst}\left(\mu_\Delta, T_{eff}\right) = 1\%\cdot\begin{cases} A\cdot\left(\mu_\Delta - 1\right)^2 + B\cdot\left(\mu_\Delta - 1\right)^3, & \text{for } \mu_\Delta < 4.0 \\[2mm] C + D\cdot\left(\mu_\Delta - 1\right), & \text{for } 4.0 \leq \mu_\Delta < 6.5 \\[2mm] E\cdot\dfrac{F\cdot\left(\mu_\Delta - 1\right) - 1}{\left[F\cdot\left(\mu_\Delta - 1\right)\right]^2}\cdot\left(\dfrac{T_{eff}}{T_0}\right)^2, & \text{for } \mu_\Delta > 6.5 \end{cases} \tag{4.35}$$

It should be noted that the stiffness degradation of the KDEG model used by Guyader [Guy04] only refers to the reloading stiffness, whereas the unloading stiffness is equal to the initial elastic loading stiffness. This means that the large cycle response is equal to that of a modified Takeda model with

unloading parameter $\alpha = 0$ and reloading parameter $\beta = 0$ (in the nomenclature of Ruaumoko [Car04]). As a consequence, the hysteretic energy dissipation of the KDEG model exceeds that of the "thin" Takeda model, which is proposed by Priestley et al. [PCK07] as appropriate for RC piers and columns. Concerning its hysteretic energy dissipation characteristics, the KDEG model from [Guy04] is instead more comparable to the "fat" Takeda model, suggested by Priestley et al. [PCK07] for beams and frames (see Subsection a).

Hysteresis Model	Parameters for $\xi_{eq,hyst}(\mu_\Delta, T_{eff})$ according to equation (4.35)					
	A	B	C	D	E	F
Stiffness Degrading (KDEG, $r = 0$)	5.1261	-1.1090	12.1052	1.3622	20.66	0.62
Elasto-Plastic (BLH, $r = 0$)	3.1922	-0.6598	10.5687	0.1156	19.13	0.73

Tab. 4.8: Parameters for the computation of $\xi_{eq,hyst}$ according to equation (4.35) for stiffness degrading and elasto-plastic hysteretic models according to [Guy04]

Hysteresis Model	Parameters for T_{eff} according to equation (4.34)					
	G	H	I	J	K	L
Stiffness Degrading (KDEG, $r = 0$)	0.1725	-0.0317	0.1673	0.1767	0.85	0
Elasto-Plastic (BLH, $r = 0$)	0.1108	-0.0167	0.2794	0.0892	0.570	0

Tab. 4.9: Parameters for the computation of T_{eff} according to equation (4.34) for stiffness degrading and elasto-plastic hysteretic models according to [Guy04]

The total equivalent viscous damping ratio $\xi_{eq,tot}$, including the elastic viscous damping part ξ_{el}, follows according to equation (4.36). As outlined by Guyader [Guy04], in his approach the value $\xi_{el,0}$, referring to the initial stiffness related critical damping coefficient $c_{cr,0}$, is to be added directly to the hysteretic part $\xi_{eq,hyst}$. Any adjustments similar to those of equation (4.32), as included in the approach by Priestley et al. [PCK07], are not to be performed here. While the original calibration process for equations (4.34), (4.35) and the parameters of Tab. 4.8, Tab. 4.9 has been performed using a constant elastic viscous damping ratio of $\xi_{el,0} = 5\%$, Guyader [Guy04] also investigated how alternative damping ratios of $\xi_{el,0} = 2\%$ and 7% would influence the proposed relationships for T_{eff} and $\xi_{eq,hyst}$. From these analyses he concluded that the given equations and parameters could be used unaltered without significant errors, as long as $\xi_{el,0}$ remained within the range of considered values. As a consequence, he proposes the simple additive inclusion of the elastic viscous damping ratio $\xi_{el,0}$ according to equation (4.36). No consideration is given in [Guy04] to the difference between a constant and a tangent stiffness proportional elastic viscous damping model. It is therefore assumed that the proposed relationships are related exclusively to a constant damping model.

$$\xi_{eq,tot}\left(\mu_\Delta, T_{eff}\right) = \xi_{el,0} + \xi_{eq,hyst}\left(\mu_\Delta, T_{eff}\right) \tag{4.36}$$

An evaluation of equations (4.34) through (4.36) for the properties of the equivalent linearized system is depicted in Fig. 4.26, using the parameters given in Tab. 4.8 and Tab. 4.9 for the stiffness degrading and the elasto-plastic hysteretic models. On the left side of Fig. 4.26, the ratio between the effective period T_{eff} and the initial period T_0 is shown for both systems as a function of the peak ductility demand. For comparison purposes, the corresponding ratio that would result for the effective period T_{eff}, related to the secant stiffness to peak response, is also shown. It can be seen that a considerable difference exists between the two different definitions of T_{eff}. Taking into account that the effective

period is proportional to the square root of the corresponding secant stiffness k_{sec}, it becomes clear that the differences between the implicit secant stiffnesses are even more pronounced.
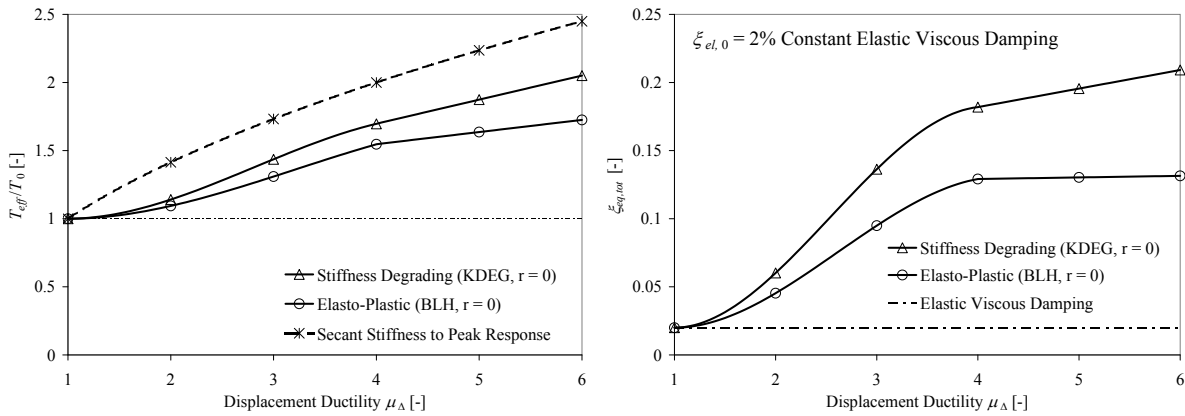

Fig. 4.26: Properties of equivalent linearized system according to equations (4.34) through (4.36) from [Guy04]
left: Ratio between effective period T_{eff} and initial period T_0, right: Equivalent viscous damping ratio $\xi_{eq,tot}$

On the right side of Fig. 4.26, the total equivalent viscous damping ratio $\xi_{eq,tot}$ according to equation (4.36) is shown as a function of the ductility demand μ_Δ. In this case, the elastic viscous damping ratio has been assumed as $\xi_{el,0} = 2\%$. Comparing the curves for the two different hysteretic rules, it appears somewhat surprising that the elasto-plastic model results in a lower equivalent viscous damping ratio than the strength degrading model, although the latter has lower large cycle hysteretic energy dissipation. However, it should be noted that the effective period for the elasto-plastic system is also lower than for the elasto-plastic system. As discussed by Guyader [Guy04] in more detail, these two differences cancel each other out to some extent. This also emphasizes that equivalent viscous damping ratios and effective periods always need to be considered as couples and interchanging single values between different models would lead to meaningless results.

It is also noteworthy that, for a given inelastic system and a single ground motion, the definition of an equivalent linearized system is not unique. Instead, a whole range of combinations of T_{eff} and $\xi_{eq,tot}$ values exist that result in the same peak displacement demand. Within this range, normally a higher effective period can be compensated by a certain increase of the equivalent viscous damping ratio without changing the peak response. It is therefore never possible to compare only the equivalent damping ratios of two different linearized systems. A unique combination of optimum values T_{eff} and $\xi_{eq,tot}$ will result if a set of ground motions is considered and the response to the whole set shall be approximated possibly well, as in the calibration process underlying the proposed equations (4.34) and (4.35).

As previously discussed in Subsection *a* for the approach by Priestley *et al.* [PCK07], it appears useful to investigate how the proposed equivalent linear parameters translate into demand estimations in an actual application. In this case, the same two aspects already discussed in Subsection *a* come into play. At first, for a practical application an additional relationship $\eta(\xi)$ of the type presented in Section 4.4.2 is required to transform elastic response spectrum to different viscous damping ratios. The implicit uncertainties in the selection and application of such relationships has already been discussed in Subsection *a* and in Section 4.4.2. The second aspect to be considered is that a comparison of the demand estimations from an equivalent linearization with those from an initial period based procedure (see Section 4.5.1) depends on the spectral shape of the seismic loading. It is therefore not possible to compare the two conceptual approaches on a general bases, but rather such a comparison will only be valid for the specific spectral shape considered.

In Fig. 4.27 and Fig. 4.28 similar evaluations of the demand predictions according to [Guy04] are shown as had been presented previously in Subsection *a* for the approach by [PCK07]. The underlying seismic input is again represented by the elastic response spectrum according to [SIA261] and [SIA2018] for a seismic zone Z3b, a soil class B, an importance class III and a constant elastic viscous damping ratio of $\xi_{el,0} = 2\%$. For the transformation factor $\eta(\xi)$ the relationships according to equation

(4.7), stemming from [EC8-1] and [SIA261], and equation (4.8) from [EC8-1-1] have been considered. Based on these assumptions, for the stiffness degrading as well as the elasto-plastic hysteretic model the resulting equivalent displacement modification factors C_R, the ductility demands μ_Δ, and the absolute displacement demands Δ_{inel} were computed for five different initial periods T_0.
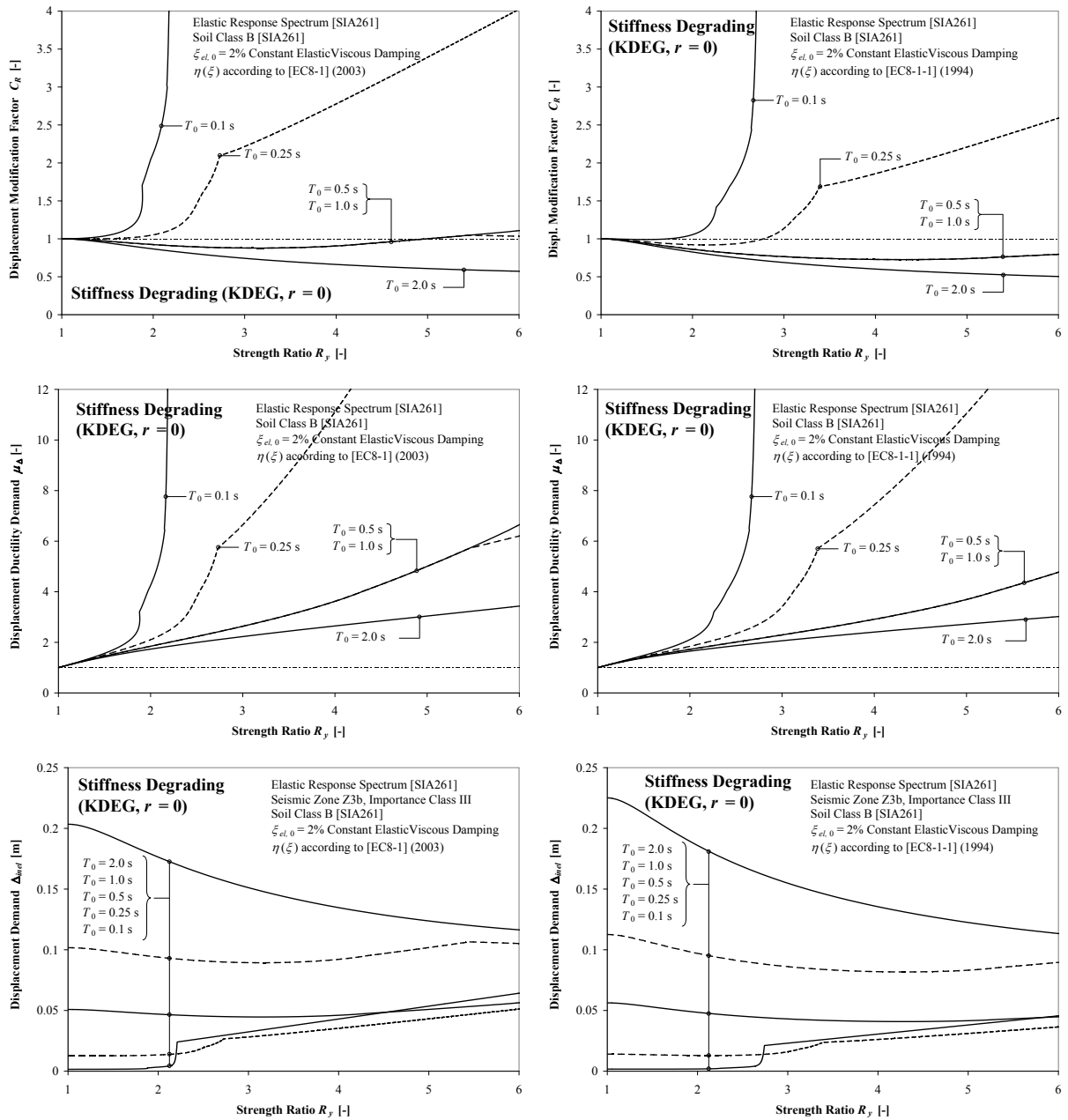

Fig. 4.27: Demand estimations resulting from equations (4.34), (4.35) for stiffness degrading hysteresis [Guy04]
upper row: Displacement modification factor C_R, middle row: Displacement ductility demand μ_Δ,
lower row: Absolute displacement demand Δ_{inel}
left column: $\eta(\xi)$ according to [EC8-1] & [SIA261], right column: $\eta(\xi)$ according [EC8-1-1]

The data shown in Fig. 4.27 and Fig. 4.28 thus essentially correspond to those previously shown in Fig. 4.24 and Fig. 4.25 for the approach by Priestley *et al.* [PCK07]. The primary difference is that in Fig. 4.27 and Fig. 4.28 a comparison between the two different relationships for $\eta(\xi)$ is included, whereas Fig. 4.24 and Fig. 4.25 contained a comparison between two different elastic viscous damping models, while keeping the relationship for $\eta(\xi)$ the same. Furthermore, it should be kept in mind that the stiffness degrading model KDEG from [Guy04], in terms of its hysteretic energy dissipation characteristics, is more comparable to the 'fat' Takeda model from [PCK07], whereas in Fig. 4.24 the results were shown for the 'thin' Takeda model.
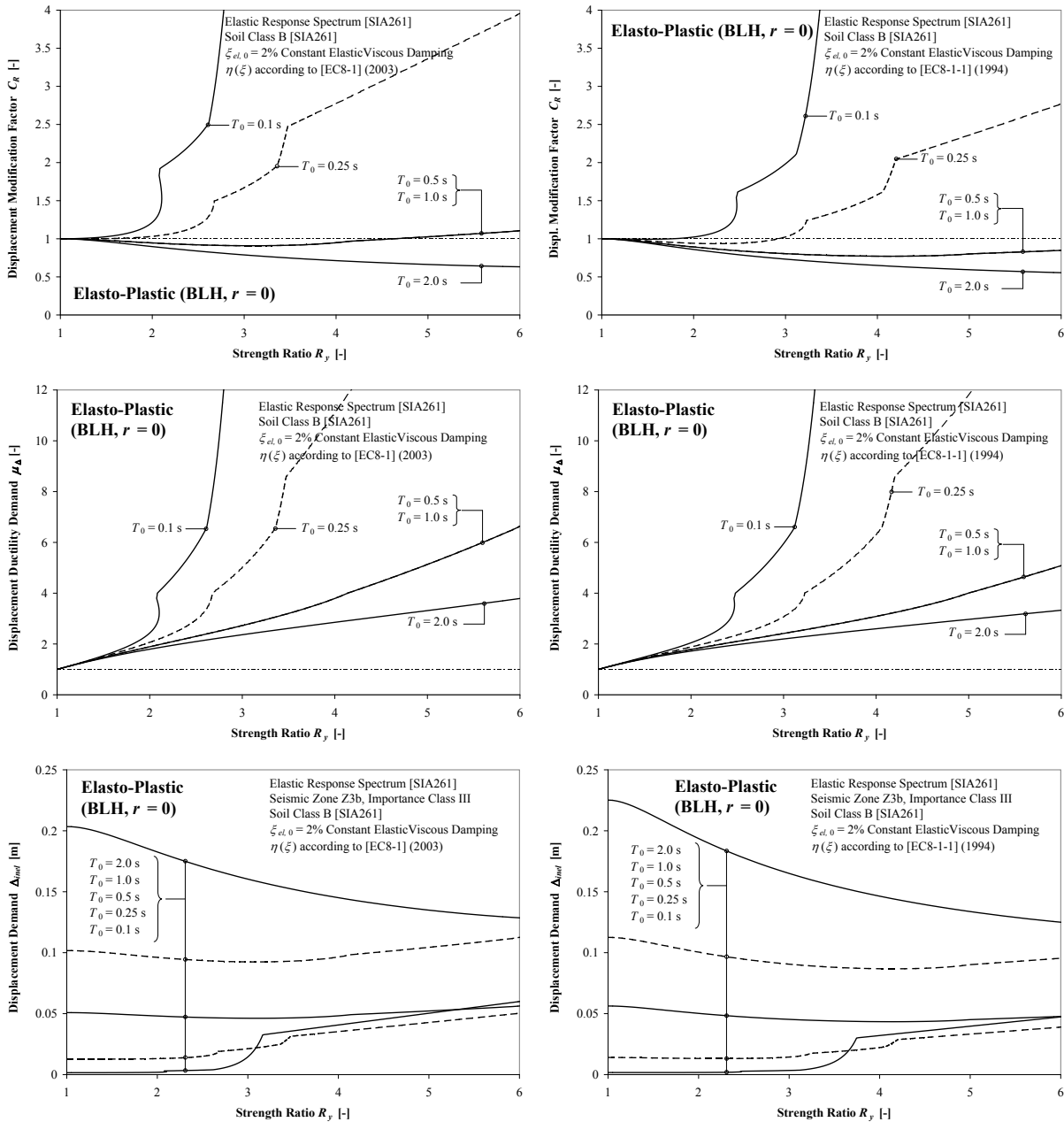
Fig. 4.28: Demand estimations resulting from equations (4.34), (4.35) for elasto-plastic hysteresis
upper row: Displacement modification factor C_R, middle row: Displacement ductility demand μ_Δ,
lower row: Absolute displacement demand Δ_{inel}
left column: $\eta(\xi)$ according to [EC8-1] & [SIA261], right column: $\eta(\xi)$ according [EC8-1-1]

The presented data show generally similar qualitative trends as those shown in Subsection *a* for the proposal from [PCK07]. In particular, it is noteworthy that the approach by Iwan and Guyader in the long (initial) period range also predicts demand values substantially lower than what would be expected from the *equal displacement approximation*. The corresponding discussion of Subsection *a* on this phenomenon is equally valid for the equivalent linearization approach by Guyader [Guy04]. At the same time, the data shown in Fig. 4.27 and Fig. 4.28 also confirm the previously observed considerable influence of the choice of the $\eta(\xi)$ relationship, which is required for the transformation between various viscous damping ratios. It can be seen that the relationship according to [EC8-1-1] consistently yields lower deformation demands than the corresponding equation from [EC8-1] and [SIA261].

4.5.3 Comparison of Various Methods

In the previous Sections 4.5.1 and 4.5.2 a total of five approximate procedures have been presented that can be used to estimate the displacement demand of an inelastic system based on an elastic response spectrum. Three of these methods fall into the category of *initial period based* approaches ([RM03], [CC04], [NK91]), while the other two procedures represent the concept of *equivalent linearization* ([PCK07], [Guy04]). So far, the various approaches have been presented individually and the evaluations concerning the possible results in a practical application have been performed separately. In this section it is intended to compare the various concepts among each other, especially with respect to the expected demand predictions resulting from them.

For this purpose, in Fig. 4.29, Fig. 4.30, and Fig. 4.31 the predictions from the five different approaches are compared to each other in terms of displacement modification factor C_R, displacement ductility μ_Δ, and absolute displacement demand Δ_{inel}. Wherever necessary, the seismic input has been assumed equal as in Section 4.5.2, i.e. defined by an elastic response spectrum according to [SIA261] and [SIA2018] for a seismic zone Z3b, a soil class B, an importance class III and a constant elastic viscous damping ratio of $\xi_{el,0} = 2\%$. It is important to note that, especially for the results from the *equivalent linearization* approaches, the comparison is only valid for this specific response spectrum.

To make the results from the various approaches comparable, in every case an elasto-plastic hysteretic behavior of the inelastic system has been assumed. A total of five different initial periods, being $T_0 = 0.1$ s, 0.25 s, 0.5 s, 1.0 s, and 2.0 s, have been considered for the evaluation. The two equivalent linearization methods have been applied for two different relationships for the factor $\eta(\xi)$ transforming the elastic spectra between different viscous damping ratios. On one hand, the results corresponding to the relationship according to equation (4.7), as given in [EC8-1] and [SIA261], are shown in the figures as continuous lines. On the other hand, an alternative relationship according to equation (4.8), as defined in [EC8-1-1], has been applied and the corresponding results are shown as dashed lines.

From the curves presented in Fig. 4.29 through Fig. 4.31, some general trends can be discovered. For example, it can be seen that a qualitative agreement between all of the considered approaches appears to exist with respect to the fact that the inelastic displacement demand in the short period range substantially exceeds the demand of a corresponding linear elastic system having the same initial period. This effect diminishes more and more with increasing initial period T_0. A conceptual difference appears to exist between the predictions from the *initial period based* procedures and the *equivalent linearization* approaches in the long period range. While all three proposals falling into the former category more or less predict a response similar to the *equal displacement approximation*, the two proposals of the latter type predict significantly lower peak displacement demands for $T_0 = 2$ s.

The best mutual agreement between all five methods was found at an initial period of about $T_0 = 1$ s. In the short period range, the *equivalent linearization* procedures tend to predict rather higher demands, while they result in lower displacements in the long period range, compared to the *initial period based* proposals. However, it should be mentioned that the actual results from the *equivalent linearization* methods strongly depend on the adopted relationship for the transformation factor $\eta(\xi)$. The differences between the two different assumptions for $\eta(\xi)$ applied on the same *equivalent linearization* model can be larger than the differences between two different demand prediction methods. This emphasizes the considerable importance of an adequate choice of the relationship for $\eta(\xi)$ and also visualizes the additional uncertainties introduced into the application of the *equivalent linearization* procedures by the required transformation factor $\eta(\xi)$.

Within the group of *initial period based* methods, the approach by Chopra and Chintanapakdee [CC04] consistently gives the most conservative results over the entire range of considered strength ratios R_y and initial periods T_0. Furthermore, this approach is the only one converging exactly to the *equal displacement approximation* for large periods. In the short period range the proposal by Ruiz-García and Miranda [RM03] yields the lowest demand predictions. The predicted displacement demands coming from [CC04] and [RM03] show considerable differences over the entire range of parameters. This appears rather surprising as both proposals had been developed in a very similar manner and in both cases the regression analysis for the calibration of the empirical equations were conducted directly on the displacement modification factor C_R. Due to these conceptual similarities a better agreement between the two methods might have been expected.
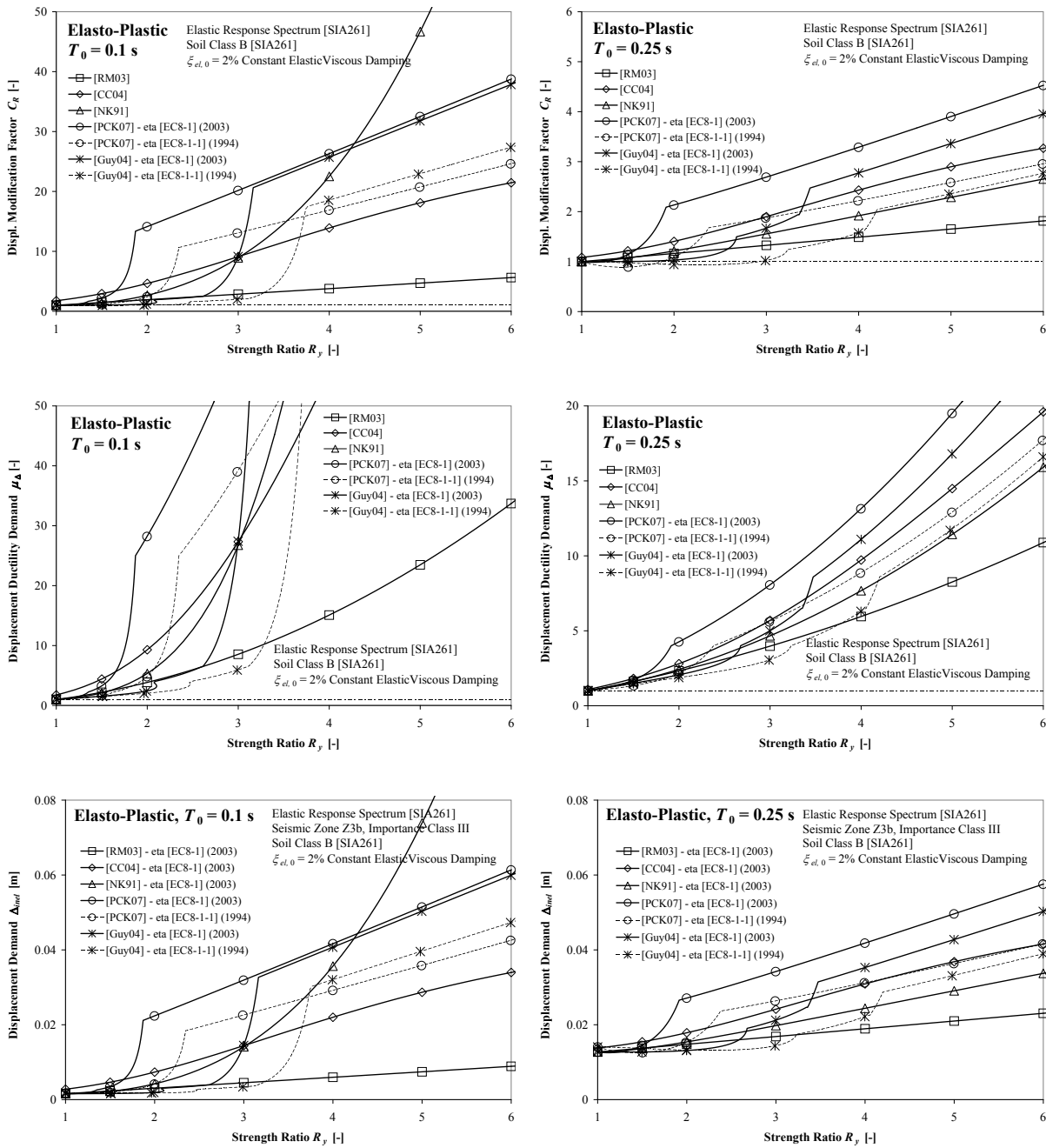
Fig. 4.29: Demand estimations resulting from different approximate approaches
upper row: Displacement modification factor C_R, middle row: Displacement ductility demand μ_Δ,
lower row: Absolute displacement demand Δ_{inel}
left column: System with initial period $T_0 = 0.1$ s, right column: System with initial period $T_0 = 0.25$ s

In the *initial period based* method deduced from the proposal by Nassar and Krawinkler [NK91] the calibration had not been performed directly on C_R, but was rather conducted for the force reduction factor R_y. The method therefore has the statistical drawbacks discussed in Section 4.5.1. In the short period range, it yields results that lie between those of [CC04] and [RM03]. For increasing periods the proposal by Nassar and Krawinkler [NK91] approaches the predictions of [RM03] and even undercuts them slightly in the long period range. As discussed in Section 4.5.1c, the results from [NK91] should not be considered as trustworthy in the very short period range ($T_0 = 0.1$ s), especially for strength ratios $R_y > 2$. The calibration process obviously did not cover this parameter range in a reliable manner, as it implies very high ductility demands.
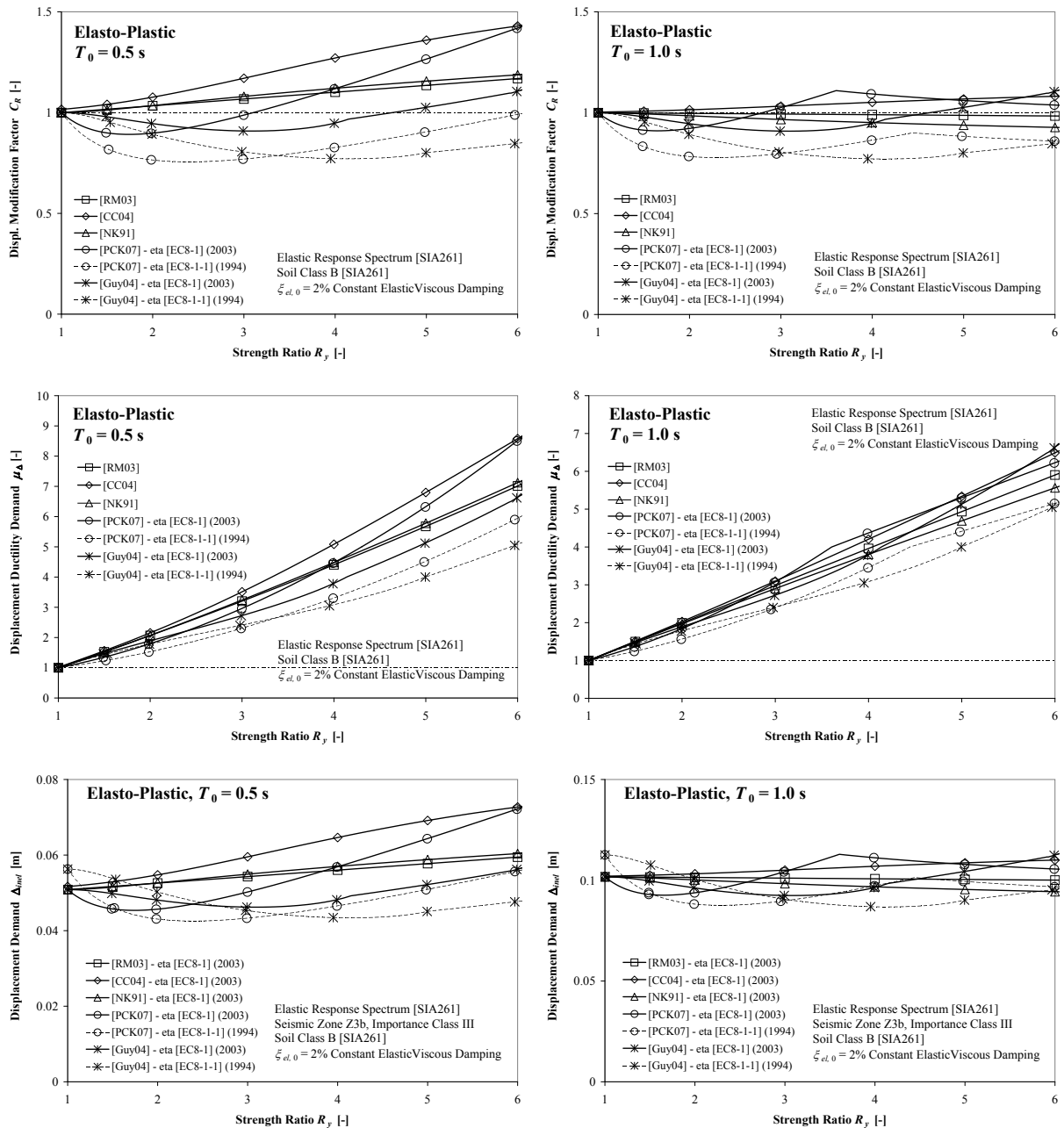
Fig. 4.30: Demand estimations resulting from different approximate approaches
upper row: Displacement modification factor C_R, middle row: Displacement ductility demand μ_Δ,
lower row: Absolute displacement demand Δ_{inel}
left column: System with initial period $T_0 = 0.5$ s, right column: System with initial period $T_0 = 1.0$ s

Generally, the relative comparisons between the various proposals do not allow any reliable conclusions about the appropriateness or accuracy of any one of them. Such an evaluation could only be done by comparison with the results from time history analyses as a reference. However, each one of the methods was actually calibrated on time history analyses and nevertheless such large differences result in the demand predictions. On one hand, this may be interpreted as an indicator of the general uncertainties involved in the problem. On the other hand, the type and selection of ground motions records for a calibration or an evaluation may also influence the results. This visualizes the complexity of the problem and also suggests that a *unique* best method might not exist. Instead, the appropriateness of any of the proposals might depend on a variety of circumstances. However, based on the existing information, it is not really possible to define reliable criteria for the choice between the presented concepts. Therefore, either one of them might formally be considered equally valid as the others.
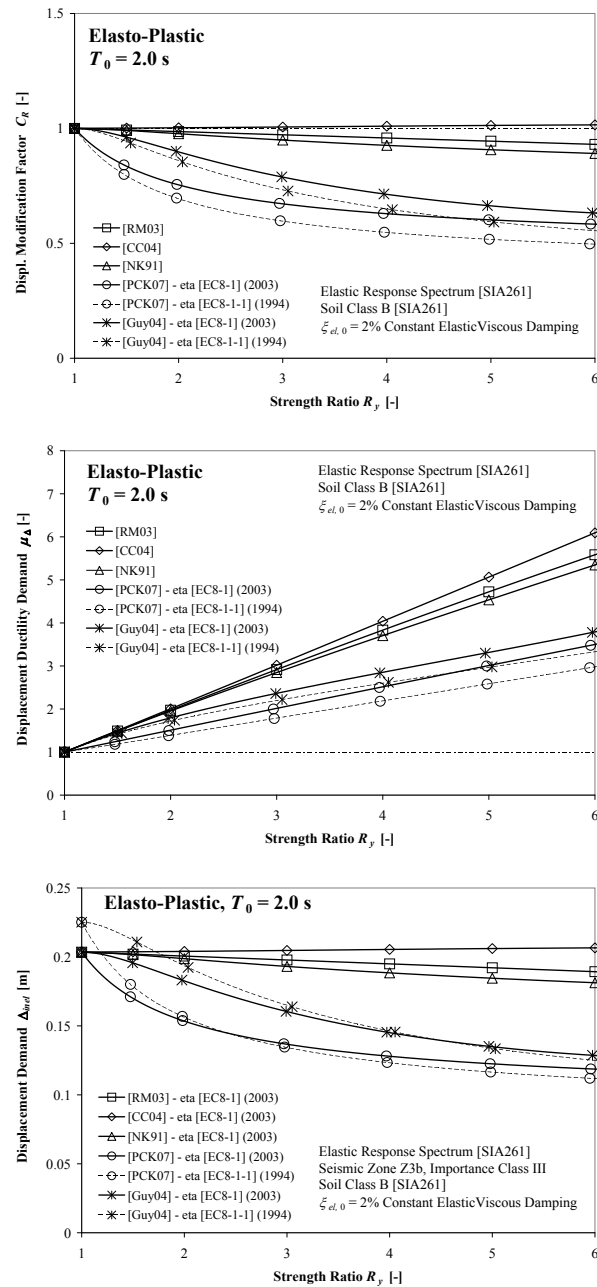
Fig. 4.31: Demand estimations resulting from different approximate approaches
for a system with initial period $T_0 = 2.0$ s
upper row: Displacement modification factor C_R, middle row: Displacement ductility demand μ_Δ,
lower row: Absolute displacement demand Δ_{inel}

Concerning the practical applicability of the different methods for a given assessment task, it should be noted that the *initial period based* procedures have some kind of an advantage over the *equivalent linearization* approaches. In an assessment case for an existing structure, the initial period and the strength of the structure are typically known right from the beginning of the analysis process. Therefore, all the input parameters for the *initial period based* procedures are readily available and the method can be applied without any iterations. While it has be shown that the *equivalent linearization* concept allows an equally efficient application in new design situations [PCK07], for the assessment of a system with fixed structural properties an iteration is required during the analysis. This is related to the fact that the characteristics of the equivalent system (T_{eff}, ξ_{eq}) depend on the demand estimation which is not known at the beginning of the process. Therefore, for the practical assessment of existing structures, the *initial period based* procedures have a certain advantage as their application is somewhat more convenient.

Within the *initial period based* methods, the relationship based on the proposal by Nassar and Krawinkler [NK91] has a certain formal disadvantage because it was not directly calibrated for the displacement modification factor C_R. Among the other two remaining proposals, the one by Chopra and Chintanapakdee [CC04] tends to result in more conservative demand estimations. In the light of the obvious uncertainties included in the task, it might be meaningful to rather adopt such a cautious approach. The proposal by Ruiz-García and Miranda [RM03] appears to yield surprisingly low demand estimations, especially in the short period range.

Similar considerations, at the other end of the period range, might call for caution with respect to the two *equivalent linearization* approaches by Priestley *et al.* [PCK07] as well as by Iwan and Guyader [Guy04]. The very low demand predictions for long periods ($T_0 = 2.0$ s) should be interpreted with care. Equivalent displacement modification factors reaching as low as $C_R \approx 0.5$, i.e. an undercut of the *equal displacement approximation* by 50%, might require additional verification before being adopted in practical applications. The second general problem associated with the *equivalent linearization* approaches is related to the requirement of a $\eta(\xi)$ relationship, which introduces additional uncertainties. The fact that the choice of this relationship can influence the demand estimation almost more than the choice of the general prediction method appears rather unsatisfying. It somewhat puts the efforts for the calibration of the equivalent linear parameters in question, as the quality of the final results might depend more on the accuracy of the η factor than on the actual equivalent linearized model.

In the light of these considerations and at the current state of knowledge, the approach by Chopra and Chintanapakdee [CC04] might represent a reasonable compromise for the assessment practice. It is, on one hand, rather simple and straightforward in its application and, on the other hand, also tends to yield somewhat well-balanced results. In the most relevant period range the demand predictions are rather conservative, compared to the other proposals, and at the same time the procedure does not seem to yield any particularly extraordinary results for any parameter configurations. The other four approaches can nevertheless serve for additional checking and may give an impression of the conceivable range of demand predictions being related to the inevitable uncertainties. The positive aspect is that the largest divergences between the various methods tend to occur in the very short and the very long period range. A somewhat better agreement between them can be found in the intermediate period range, which might be more representative for many real bridge structures.

Finally, some concluding remarks shall be given on the general *equivalent linearization* approach and potential modifications for its further improvement. The actual application of the *equivalent linearization* approach in connection with smooth code specified spectra does not differ very much from the *initial period based* procedures using displacement modification factors. The empirical equations for the equivalent viscous damping ratio ξ_{eq} can be combined with the relationships for $\eta(\xi)$ that transform smooth spectra for various damping ratios. Such a combined relationship, as defined by equation (4.37), basically also represents some kind of a displacement modification factor.

$$C_{R,eff}\left(\mu_\Delta, T_{eff}\right) = \eta\left[\xi_{eq,tot}\left(\mu_\Delta, T_{eff}\right)\right] \tag{4.37}$$

$$\Delta_{inel} = C_{R,eff}\left(\mu_\Delta, T_{eff}\right) \cdot S_{d,el}\left(T_{eff}, \xi = 5\%\right) \tag{4.38}$$

This *effective displacement modification factor $C_{R,eff}$* would have to be applied on the elastic spectral displacement corresponding to $\xi = 5\%$ at the effective period T_{eff}, as described by equation (4.38). In contrast, in the *initial period based* procedures the displacement modification factor is applied on the elastic spectral displacement for the elastic period T_0. The remaining conceptual difference between the two approaches is thus primarily related to the question which period best characterizes the response of the inelastic system – the initial stiffness based period T_0 or the secant stiffness based effective period T_{eff}. The elastic spectral displacement for either period is then multiplied by the corresponding (effective) displacement modification factor to result in the estimation of the inelastic deformation demand.

While the statistical calibration process in [RM03] and [CC04] directly focused on the displacement modification factor C_R, in the equivalent linearization proposals [PCK07], [Guy04] the calibration of

the developed empirical relationship was dedicated only to the equivalent viscous damping ratio ξ_{eq}. The latter approaches thus only optimized one part of the *effective displacement modification factor* $C_{R,eff}$ defined in equation (4.37). For the practical application then still another relationship $\eta(\xi)$ is required. This two-step solution is likely to add additional statistical uncertainties to the process. It might therefore be a worthwhile consideration to conduct regression analyses directly calibrating empirical equations for the *effective displacement modification factor* $C_{R,eff}$, also for the use with effective periods T_{eff}. If a secant stiffness based period – either related to peak demand as in [PCK07], or related to a lower demand as in [Guy04] – is considered to be more representative for the spectral displacement of the inelastic system, it would still be desirable to limit the statistical errors and uncertainties in the outlined manner. Based on the considerations discussed in Sections 4.5.1b and 4.5.2a, it is assumed that including characteristic periods of the ground motions into an empirical expression for $C_{R,eff}$ would improve its general validity. Especially the periods T_C and T_D separating the acceleration, velocity and displacement sensitive regions of the response spectra are recommended as normalizing parameters for the fundamental period of the system. The development of such optimized equations for an *effective displacement modification factor* $C_{R,eff}$ might be a promising subject of future research.

4.6 Simplified Demand Estimation of Inelastic MDOF Systems

A large variety of concepts has already been developed for the seismic analysis of MDOF structures. These approaches range from very simple and easy to apply procedures, as e.g. the equivalent lateral force method, to highly sophisticated techniques requiring considerable knowledge and computing power, such as e.g. inelastic time history analyses. When considering the application in an engineering office for the practical assessment of a (larger) number of structures, the required accuracy of the assessment results is not the only criterion for the selection of the appropriate analysis technique. Other aspects, as e.g. the efficiency of its application, required knowledge, sensitivity or susceptibility to errors, and required information about the details of the structure also play an important role. Furthermore, the question which analysis concept is best suited may also depend on the individual application. Especially simplified procedures conceptually cannot capture every conceivable phenomenon. They were typically developed, calibrated and verified for a certain field of application, consisting e.g. of type of structure, level of seismicity, or required accuracy.

As a consequence, an analysis approach which performs just well in one case, can be considered unnecessarily complex for another task, while it might provide an insufficient accuracy in a third situation. For example, the level of inelasticity experienced by the system is a function of the seismicity. In regions of low to moderate seismicity the ductility demands are likely to be lower than in high seismicity zones. Consequently, under moderate seismic conditions it may not be necessary for a satisfying accuracy to use an analysis procedure which is particularly capable of covering very high inelastic demands. On the other hand, the relevance of higher modes depends to some extent on the irregularity of the bridge (and on its fundamental period). Therefore, for very regular systems it may not be necessary to use an approach which has been developed to particularly capture higher mode effects, as the structure might be controlled predominantly by its first mode response.

As can be seen, a single procedure which is on one hand universally applicable, while on the other hand also satisfying efficiency requirements may not exist. The choice of an appropriate analysis technique for a specific task requires careful consideration in order to ensure that the relevant aspects of the seismic response are captured in a sufficient way. As a consequence, the task is to select an analysis method which is, on one hand, efficient and well applicable in regular practice, while, on the other hand, being able to capture the relevant influences on the seismic behavior to a sufficient degree of accuracy.

At the same time, it is also desirable to have not only one method at hand. The more complex an analysis procedure is, the more susceptible it typically becomes to errors and the more difficult is the interpretation and verification of its results. Therefore, even if a rather sophisticated approach is chosen, it appears important to have simpler methods at hand which may not be able to capture all detailed effects of the response, but which can be applied quickly, and whose results are easy to interpret. In fact, the results of such simple analyses are typically more straightforward to follow and therefore also aid the conceptual understanding of the system's dynamic behavior. It is generally recommendable to always check and verify a complex analysis by at least one simpler method.

It is conceptually inherent to a simplified analysis procedure that it cannot fully capture all aspects of the dynamic response of an inelastic MDOF structure during an earthquake. For the appropriate choice of an adequate analysis procedure it is therefore necessary to consider which particular response characteristics are relevant in a given application case and how capable various analysis approaches are in capturing these aspects. Although the following discussions will focus exclusively on the transverse response of bridges (being the more complex one of the two horizontal directions), the general findings can also be applied in a similar way to the longitudinal behavior. For the inelastic response of MDOF structures, in particular three phenomena are potentially relevant for an accurate representation of the behavior:

(1) *Influence of inelasticity on the global displacement demand*
    In analogy to the response of inelastic SDOF systems, discussed in Section 4.5, the displacement demand of an inelastic MDOF system can differ on a global level from that of a comparable linear elastic system. The effective loss of stiffness, together with the hysteretic energy dissipation in the inelastic range, change the global response characteristics. In case of a demand increase, this can result in higher displacements at (almost) every node of the

inelastic system if the deformed (relative) shapes of the inelastic and the elastic system are more or less similar. The global seismic deformation demand of an MDOF structure can e.g. be expressed by the displacement of a reasonably chosen *reference point*.

(2) *Influence of inelasticity on the displacement shape*
The inelastic response will not only reduce the global stiffness, but it may also change the relative stiffness distribution within the system. As a consequence, the shape of the deformed structure is likely to differ between the inelastic and a corresponding elastic system. The degree, to which this redistribution occurs, depends on the question how uniformly the inelasticity develops throughout the different members of the structure at increasing lateral load levels. It is therefore more pronounced in very irregular structures in which the individual members (especially the piers and abutments) feature significantly differing load-deformation characteristics.

(3) *Influence of higher modes*
Although the concept of eigenmodes is, strictly speaking, only valid for linear elastic systems, a somewhat similar behavior can often be observed also during inelastic response. Several simplified analysis procedures are based on the assumption that the dynamic response of a MDOF structure is largely governed by a predominant first mode. In such cases, the quality of the corresponding analysis results will obviously depend on the appropriateness of this assumption. The larger the influence of higher modes is, the less accurate a single mode based analysis will become. If higher modes play a significant role for the seismic response, this needs to be accounted for in the analysis, typically making the approach more complex. It can be expected, that a rather regular structure is more likely to respond with a predominant first mode, while increasingly irregular structures tend to be more susceptible for higher modes. Furthermore, the ground motion characteristics also influence the relevance of higher modes to some extent. In particular, the relationship between the natural periods of the individual modes and the spectral values of the ground motion at these periods influences the degree to which those modes are excited.

It becomes clear from the above discussion that the relevance of each of the mentioned phenomena is not the same in all cases. Two important aspects which influence their significance are the level of inelasticity – i.e. the ductility demand – that is sustained by the structure and its degree of regularity. The ductility demand, on one hand, depends on the structural properties, but, on the other hand, is also strongly correlated to the seismicity, i.e. to the expected level of loading. As a consequence, the choice of the appropriate analysis procedure to some extent also depends on these mentioned boundary conditions. For example, for a very irregular structure with pronounced higher mode effects, being located in a region of low to moderate seismicity, it would probably not be reasonable to choose an analysis approach which is capable of taking into account severe inelastic response, but which is hardly able to capture the influence of higher modes. In such a case, a simpler technique with respect to inelastic behavior – possibly even a linear elastic procedure – would most likely yield more realistic results if the approach, in turn, can reproduce the higher mode effects in a sufficiently accurate manner. This shows that even the use of very conventional linear analysis methods may still be appropriate under certain conditions.

To investigate the pros and cons of a variety of simplified analysis approaches – especially with respect to the three aspects outlined above – the topic of a master thesis was developed. In the course of this master thesis, which was co-tutored by the author, Berweger [Ber09] prepared a comprehensive investigation comparing several existing displacement based analysis methods. In this study, a set of (hypothetical) sample bridges was analyzed using several displacement based methods under three different levels of seismic excitation. As a reference for the evaluation of the simplified analysis methods, Berweger also performed inelastic time history analyses (ITHA) on the same bridges, using a set of spectrum compatible artificial ground motions. The mean displacement demands from ITHA were then used to judge the quality of the various simplified analysis techniques on an empirical basis and to give recommendations on their applicability under certain conditions.

Based on Berweger's analysis results, the considered procedures were subsequently subjected to a further detailed reinterpretation. In this process, a detailed evaluation was conducted with respect to the question why specific analysis procedures were empirically found to perform rather well or badly

under certain conditions. On the basis of the theoretical background of the various methods, some of them were modified in order to mitigate the identified deficiencies and thus improve the approaches. The modified procedures were used to reanalyze the sample bridges developed by Berweger [Ber09] and the results were compared to the mean displacement demands determined by ITHA.

The most relevant results of this evaluation process will be presented in the following sections. At first, in Section 4.6.1 the various bridge configurations and the corresponding models analyzed by Berweger [Ber09] will be presented. This section also contains the results from the inelastic time history analyses, serving as a reference for the evaluation of the simplified analysis approaches. Subsequently, in Section 4.6.2 five different concepts are presented which can generally be used for a displacement based analysis of bridge structures. Aside from a brief description of the procedures, the corresponding analysis results computed by Berweger are presented and compared to the reference ITHA data. The findings from this evaluation, together with theoretical considerations, serve as a basis for a proposal of modified analysis procedures presented in Section 4.6.3. Using these modified analysis procedures, the same bridge configurations are reanalyzed. By comparison with the ITHA data, it can be shown in Section 4.6.3 that the proposed modifications result in important improvements of the seismic demand predictions.

4.6.1 Reference ITHA Analysis

In this section, the bridge models analyzed by Berweger [Ber09] and the corresponding ITHA results are summarized. A total of 9 different bridge configurations were considered in this study. Six of them were five-span bridges having the same total length of 168 m and the same span width distribution. They differed only in the distribution of pier heights along the bridge, corresponding e.g. to different valley shapes. To complement the set of configurations, two longer 8-span bridges with a total length of 276 m and a rather short 3-span bridge with a total length of only 96 m were analyzed in addition.
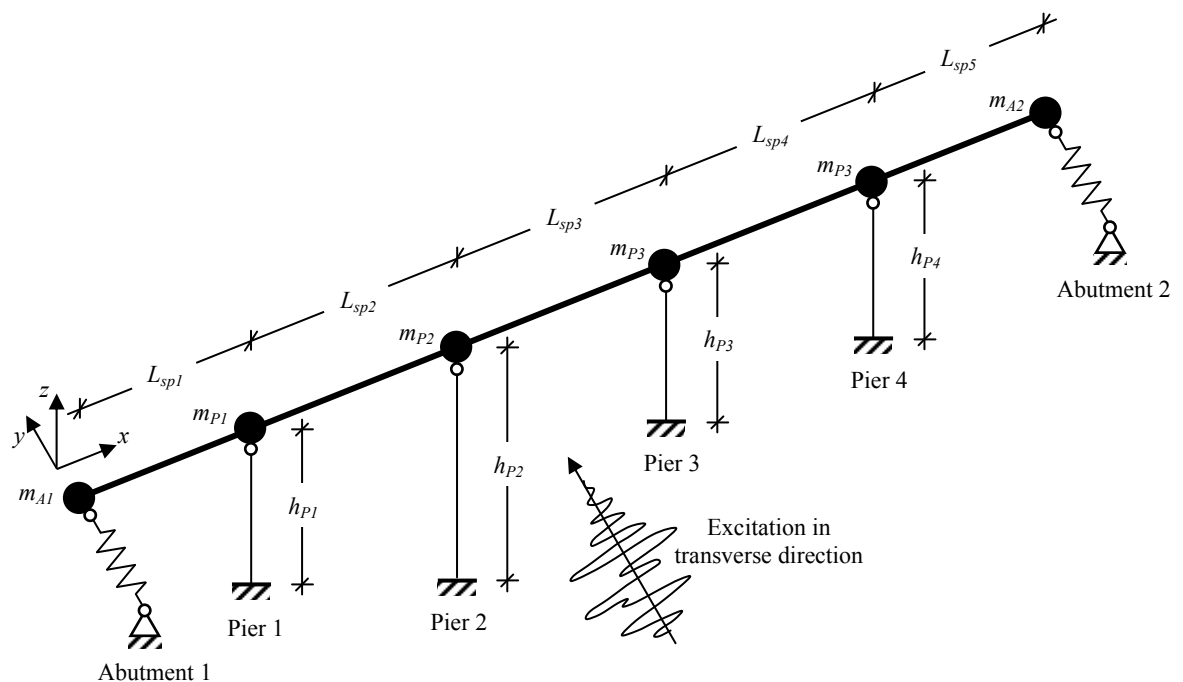

Fig. 4.32: General conceptual layout of bridge models used by Berweger [Ber09]

The general conceptual layout of the bridge models is shown in Fig. 4.32 for the case of a 5-span configuration. The bridge piers were assumed as wall-type RC cantilever columns rigidly fixed at their bases and pinned to the superstructure at their tops. In this study, neither soil-structure interaction nor P-Δ-effects were included. The focus of the investigation was not necessarily on describing the behavior of real bridges as accurately as possible, but rather on performing a relative comparison

between different analysis methods. The modeling of certain pier types therefore only serves as means to create different roughly reasonable stiffness distributions. As the same stiffness distributions are used in the simplified procedures as in the reference inelastic time history analyses, it is not of primary relevance where the modeled member stiffnesses come from. Instead, the stiffness distributions are only used to create structures of different levels of regularity and irregularity. As long as they are roughly within the range of reasonable values for real bridges, the resulting models fulfill their purpose.

The abutments were modeled as inelastic springs in the transverse direction and the superstructure was assumed as an elastic beam. Discrete masses were modeled at the pier tops and the abutments, where the tributary masses from the neighboring superstructure spans, the piers, and – in the case of the abutments – also an effective mass from the embankment were lumped together. As discussed in Section 3.1, for the given configuration of Fig. 4.32 it is possible to simplify the system to a 2-dimensional model without loss of accuracy. In Fig. 4.33 a corresponding 2-d model is shown, in which the individual piers are represented by inelastic translational piers.
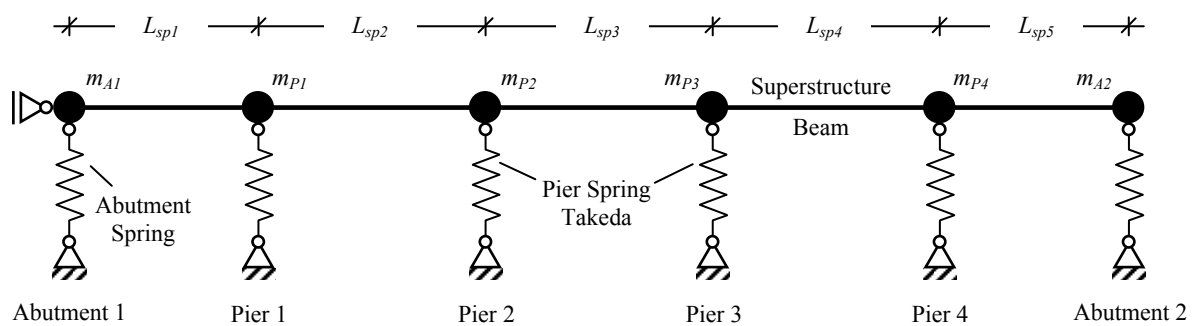

Fig. 4.33: Simplified structural bridge model as analyzed by Berweger [Ber09]

The hysteretic behavior of each pier was modeled by a modified Takeda rule, as implemented in Ruaumoko [Car04]. In total, piers with four different heights, all having the same wall-type cross-section, were considered in the various bridge configurations analyzed by Berweger [Ber09]. The load deformation behavior of each of these piers was estimated and bilinearized using a plastic hinge approach as described e.g. in [PSC96] and [PCK07]. The characteristic data of the resulting force-displacement curves are given in Tab. 4.10. The unloading and reloading parameters, α and β, of the Takeda rule correspond to the "thin Takeda" model, suggested in [PCK07] as suitable for RC columns and piers. The flexural stiffness of the elastic superstructure beam about the vertical axis (i.e. for bending under horizontal transverse loading) was chosen as $EI_{ss} = 1.2 \cdot 10^9$ MNm^2. Further details about the underlying assumed geometry of the members for the computation of the stiffness properties can be found in [Ber09].

	Pier Modeling Data			
Pier Height [m]	6	10	12	18
Nominal Yield Displacement Δ_y [cm]	2.0	5.5	7.9	17.7
Nominal Yield Force F_n [MN]	3.3	2.0	1.6	1.1
Initial Stiffness k_0 [MN/m]	165	36	21	6.1
Post-Yield Stiffness Ratio r [-]	0	0	0	0
Takeda Unloading Parameter α [-]	0.5	0.5	0.5	0.5
Takeda Reloading Parameter β [-]	0	0	0	0

Tab. 4.10: Modeling data for the wall-type piers considered in the sample bridges by Berweger [Ber09]

Based on an assumed embankment geometry, Berweger used the principles outlined in Section 3.5.2 to estimate the inelastic behavior of the abutments. For the majority of analyses, a Ramberg-Osgood rule was used to describe the hysteretic behavior. The characteristic data of the model, the resulting backbone curve, and a corresponding example hysteresis loop are shown on the left side of Fig. 4.34. To study the influence of abutment modeling, an alternative modified Takeda hysteresis rule was developed for the same type of abutment. The corresponding properties as well as the resulting monotonic and hysteretic behavior are visualized on the right side of Fig. 4.34. While all bridge configurations were analyzed using the Ramberg-Osgood abutment model, some selected bridges were reanalyzed with the Takeda model, in order to investigate the influence of the differing models on the overall system response. It should be noted that both hysteretic rules were meant to represent the same abutment-embankment system, so that any deviations only result from the different mathematical implementation. In all analyses, both abutments of each bridge configuration were always modeled equally.
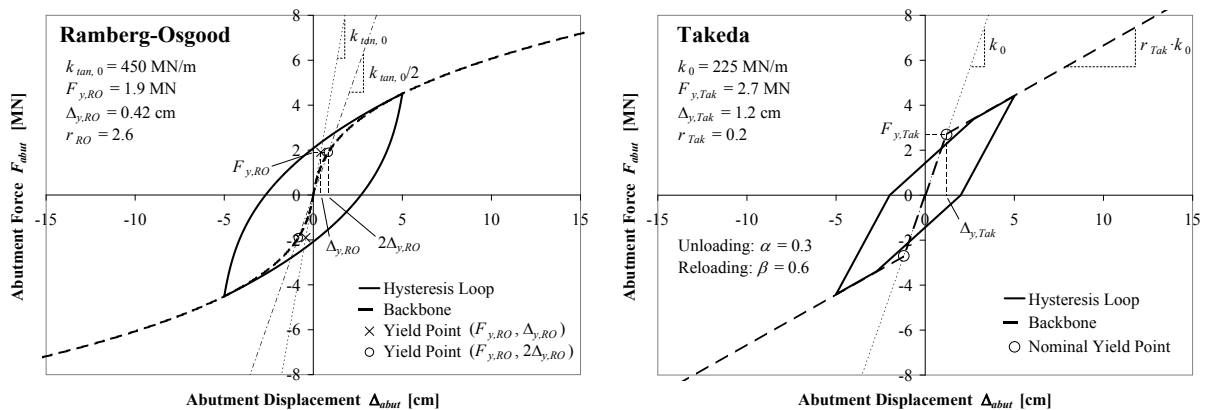

Fig. 4.34: Inelastic behavior for transverse abutment response as modeled by Berweger [Ber09]
left: Ramberg-Osgood hysteresis rule, right: Modified Takeda hysteresis rule

Preliminary analyses showed that the choice of the initial stiffness k_0 for the Takeda model was not fully straightforward if a similar behavior as with the Ramberg-Osgood model was intended. The latter is typically defined by a "yield force" $F_{y,RO}$ and by either the tangent stiffness $k_{tan,0}$ in the origin of the force-displacement curve or a "yield displacement" $\Delta_{y,RO}$. These three parameters are mutually interrelated, with only two of them being independent quantities. As can be seen in Fig. 4.34 (left), it is important to note that the point defined by the "yield displacement" $\Delta_{y,RO}$ and the "yield force" $F_{y,RO}$ does not lie on the backbone curve, for the way these two parameters are specifically defined in the Ramberg-Osgood model. Instead, this point is rather related to the tangent stiffness $k_{tan,0}$ in the origin.

In contrast, the initial stiffness k_0 of the Takeda model is normally considered to be a secant stiffness to a "nominal yield displacement" Δ_y, due to the linear response in the pre-yield region. Choosing the nominal yield displacement $\Delta_{y,Tak}$ and the yield load $F_{y,Tak}$ for the Takeda model equal to the corresponding values $\Delta_{y,RO}$ and $F_{y,RO}$ of the Ramberg-Osgood model would implicitly result in setting the initial stiffness k_0 for the Takeda rule equal to the tangent stiffness $k_{tan,0}$ in the origin of the Ramberg-Osgood hysteresis. As the Ramberg-Osgood model is continuously curved right from the beginning, while the Takeda rule is linear up to yield, setting these two stiffness values equal would effectively result in a considerable overestimation of k_0 for the Takeda model.

As confirmed by preliminary analyses, it is more reasonable to choose a certain *secant* stiffness from the Ramberg-Osgood rule to define k_0. Due to the continuously curved shape of the Ramberg-Osgood backbone, the definition of the section point for this secant is not straightforward. For the study by Berweger [Ber09] it was chosen to use a secant stiffness being half the value of the origin tangent stiffness $k_{tan,0}$ in order to define k_0 for the Takeda model. This choice has the advantage that it intersects the Ramberg-Osgood curve at its yield load $F_{y,RO}$ for any value of the Ramberg-Osgood parameter r_{RO}. This implicitly means that the "nominal yield displacement" of the Ramberg-Osgood model should rather be defined as $2\Delta_{y,RO}$ because the point $(2\Delta_{y,RO}, F_{y,RO})$ always lies on its force-

displacement curve and it corresponds to the better choice for the initial stiffness k_0 being set equal to $k_{tan,0}/2$.

Using the various member representations described above, the nine bridge configurations depicted in Fig. 4.35 were assembled by Berweger [Ber09] (abutment springs and lumped masses not shown). The first three systems have five spans and a symmetrical distribution of pier heights, resulting in a rather regular behavior. In particular, only symmetrical eigenmodes are excited by an earthquake, so that the seismic response is always symmetrical as well (also in the inelastic range). While having the same distribution of span widths, bridge configurations 3 through 6 are unsymmetrical and, consequently, also more irregular. For these systems all modes are excited (to some degree) thus resulting in a more complex response as that of the previous symmetrical configurations.
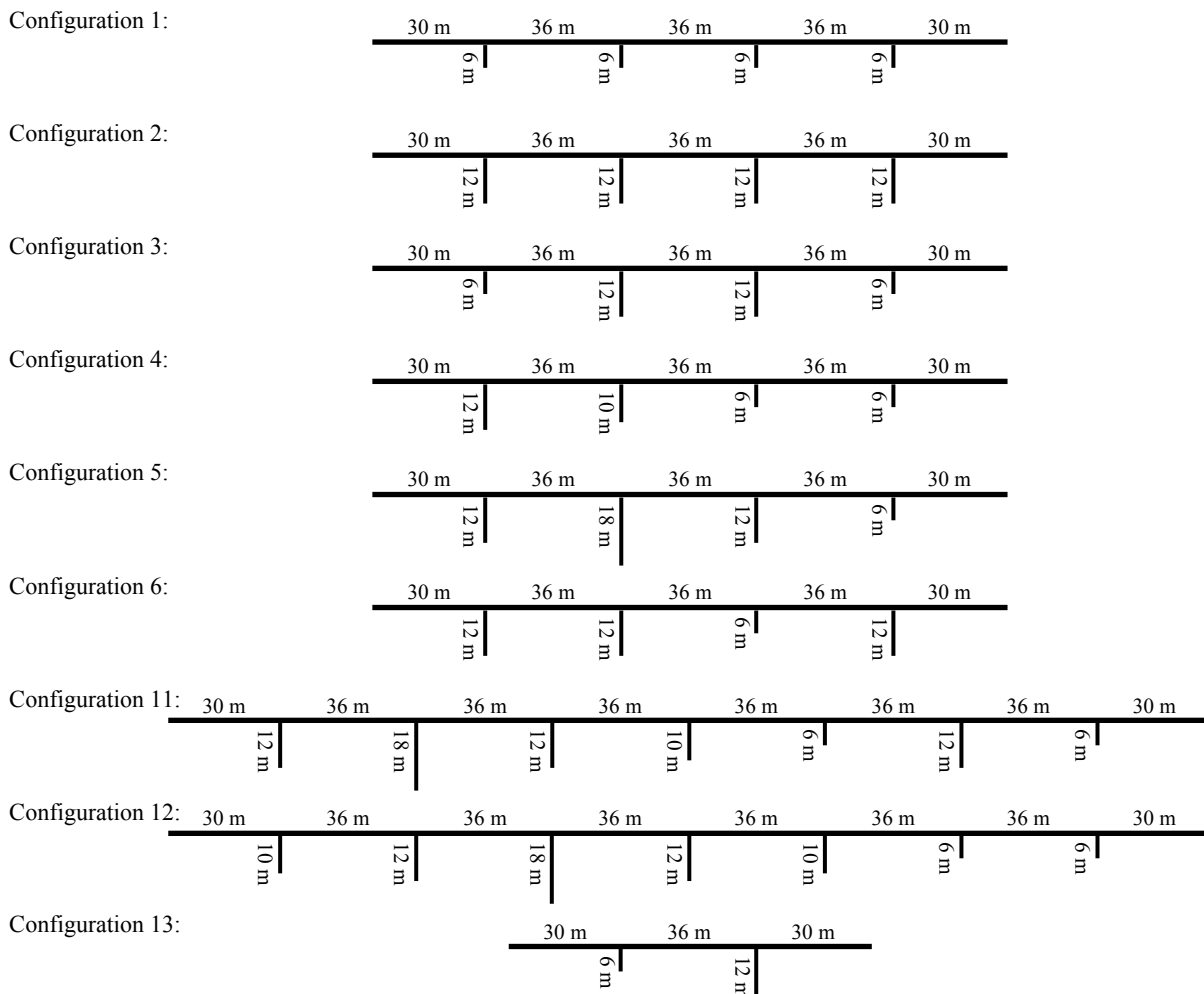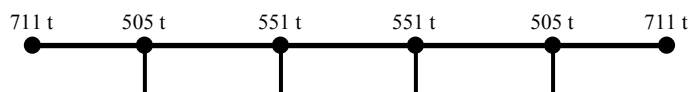

Fig. 4.35: Geometry of bridge configurations analyzed by Berweger [Ber09] (shown as elevations)

Configurations 11 and 12 are significantly longer, having a total of eight spans. While both systems are unsymmetrical, configuration 11 might be considered as somewhat more irregular because it features a short (and stiff) pier between two taller (and softer) piers in the right half of the bridge. The larger length of configurations 11 and 12 has the consequence that the abutment response becomes less significant for the overall system response. A certain influence will certainly still exist towards the ends of the superstructure and at the outer piers However, it may be expected that in the inner part of the superstructure a region exists which is rather controlled by the pier behavior and less influenced by the abutments. The opposite extreme is represented by the rather short bridge of configuration 13. Based on theoretical considerations and practical experience from past earthquakes (see Section 3.5.2a) it appears reasonable to assume that this bridge is controlled to a large extent by the response of the abutments related to soil-structure interaction.
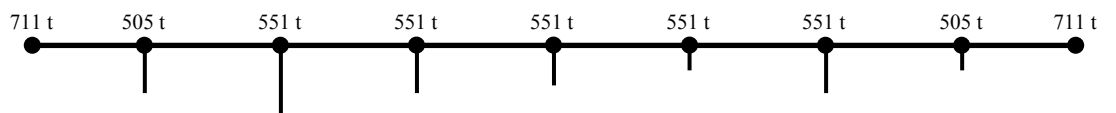
The distributions of the lumped masses for the three different bridge lengths are shown in Fig. 4.36. It is noteworthy that the tributary mass of the embankments, which had been estimated based on the concepts outlined in Section 3.5.2, results in total lumped masses at the bridge edges being higher than those along the inner part of the superstructure. Neglecting this contribution from the embankments, the edge masses resulting only from the part of the adjoining superstructure span would be less than half of the lumped masses at the pier tops. Including the embankment mass contribution subsequently increases the inertia forces acting on the abutments, which also influences the deformed shape of the superstructure towards higher displacements at the abutments. This relative difference becomes even more pronounced if considered together with the (inelastic) flexibility of the abutments. A model without or little (elastic) abutment flexibility and also without consideration of the embankment mass contribution would probably yield a significantly differing displacement shape than an inelastic abutment model also including the inertia effects of the embankment masses. These effects also influence the demand on the outer piers so that a realistic modeling of the abutments is not only relevant for their own behavior.

Configurations 1-6:

711 t 505 t 551 t 551 t 505 t 711 t

Configurations 11&12:

711 t 505 t 551 t 551 t 551 t 551 t 551 t 505 t 711 t

Configuration 13:

711 t 505 t 505 t 711 t
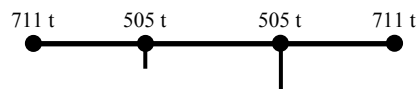
Fig. 4.36: Discrete mass distributions of bridge configurations analyzed by Berweger [Ber09]

Bridge Configuration	Elastic period T_0 of the first mode
1	0.36 s
2	0.91 s
3	0.65 s
4	0.58 s
5	0.89 s
6	0.61 s
11	0.97 s
12	1.02 s
13	0.44 s

Tab. 4.11: First mode elastic periods of bridges using an abutment stiffness of $k_0 = 225$ MN/m (Source: [Ber09])

The elastic natural periods of the first mode of each bridge configuration are summarized in Tab. 4.11. They were computed using the initial stiffnesses k_0 of the Takeda springs for the piers, as given in Tab. 4.10, and an initial stiffness of $k_0 = 225$ MN/m for the abutment springs. Furthermore, the relative effective modal masses $m^*_{i,eff}/m_{tot}$ (defined by equations (A2.4) and (A2.5) in Annex A2) are

summarized in Tab. 4.12 for the various bridge configurations[23]. These values give an indication of the relevance of higher modes for the (linear) response of the systems. It should be noted that effective modal contributions to the displacement demands also depend on the shape of the response spectra and the individual modal periods. It was found that the elastic displacement demand in the center region of all considered bridges is governed by the first mode response. However, towards the bridge edges higher modes can have a considerable influence on the response, many times even dominating it at the abutments. The relevance of higher modes is likely to be influenced by the abutment modeling and the superstructure stiffness.

Bridge Configuration	Relative Effective Modal Mass $m^*_{i,eff}/m_{tot}$ [%]					
	Mode 1	Mode 2	Mode 3	Mode 4	Mode 5	Mode 6
1	90	0	10	0	0	0
2	60	0	40	0	1	0
3	42	0	57	0	1	0
4	48	0	44	8	0	0
5	50	1	46	3	0	0
6	50	24	24	0	1	0
11	39	6	28	1	25	0
12	46	0	28	19	4	2
13	67	20	13	0	-	-

Tab. 4.12: Effective modal mass contributions from individual modes for different bridge configurations [Ber09]

The seismic loading was defined by elastic target spectra according to [SIA2018] (equivalent to [SIA261] if additionally the importance factor γ_f is taken into account). These spectra were determined for a soil class B ($S = 1.2$, $T_B = 0.15$ s, $T_C = 0.5$ s, $T_D = 2.0$ s), an importance class III ($\gamma_f = 1.4$), and a viscous damping ratio of $\xi = 5\%$. A total of three different spectra were defined representing different levels of seismicity. The lowest seismicity level was based on a design peak ground acceleration (PGA) of $a_{gd} = 0.16$g, corresponding to seismic zone Z3b of [SIA261]. To study the influence of higher seismicities, and thus higher ductility demand levels, further two spectra corresponding to $a_{gd} = 0.35$g and $a_{gd} = 0.50$g were considered. It should be noted that, while a_{gd} represents the *design peak ground acceleration* according to [SIA261], due to the modification factors S and γ_f for soil and importance class, higher actual peak ground accelerations a_g result. The three seismicity classes with $a_{gd} = 0.16$g, 0.35g, and 0.50g therefore correspond to effectively higher peak ground accelerations of $a_g = 0.27$g, 0.59g, and 0.84g, respectively. However, as the seismic zones in [SIA261] are linked to the *design peak ground accelerations*, in the following discussions the values of $a_{gd} = 0.16$g, 0.35g, and 0.50g will be used to identify the three different seismicity levels, keeping in mind that the actual values a_g corresponding to the elastic spectra are higher.

While the seismic input for the simplified procedures is fully defined by the spectra, the dynamic time history analyses require ground motions as input loading. For this purpose, the software SIMQKE [GV76] was used to generate 8 artificial accelerograms approximating each spectrum (i.e. in total 24 ground motions). For the case of the seismicity level with $a_{gd} = 0.16$g, the elastic displacement spectra corresponding to the individual ground motions are depicted in Fig. 4.37. For comparison purposes, the mean spectrum from the 8 ground motions, the mean +/- standard deviation spectra, and the target spectrum according to [SIA2018] are shown additionally. It can be seen that, while individual ground motion spectra can deviate considerable from the target spectrum at certain periods, the average of all ground motions represents a fairly good approximation.

---

[23] For bridge configuations 11 and 12 only the values for the first six modes are presented. The higher modes, not shown in Tab. 4.12, are of negligible influence.
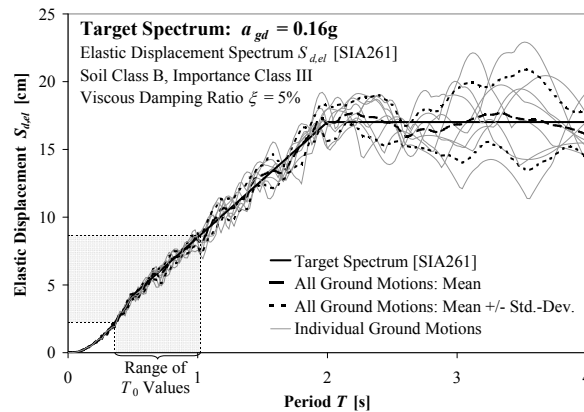
*Fig. 4.37: Elastic displacement spectra computed from 8 artificial ground motions,
the corresponding mean spectrum, and the target spectrum according to [SIA261], [SIA2018]*

Furthermore, in Fig. 4.37 the range of first mode elastic periods is shown, corresponding to the 9 different bridge configurations as given in Tab. 4.11. This suggests that rather the low to medium period range of the spectra might be relevant for the analyses. However, taking into account potential period shifts related to inelastic response (see Section 4.5.2), spectral values at higher periods may also be relevant for the response characterization. Due to the linear elasticity underlying the spectra of Fig. 4.37, the shapes of the elastic spectra for the higher seismicity levels remain the same[24]. The ground motions and corresponding spectra for $a_{gd} = 0.35$g and 0.50g therefore result simply by scaling with the PGA ratios.

In Fig. 4.38 and Fig. 4.39 the results of the inelastic time history analyses in terms of displacement demand at the pier tops and abutments along the bridge are shown for the bridge configurations 1 through 6 (Fig. 4.38) and 11 through 13 (Fig. 4.39). The analyses were conducted for uniform transverse excitation using the 8 artificial ground motions described above for each of the three seismicity levels. The graphs show the mean response of the individual ground motion sets, as well as the corresponding mean +/- standard deviation displacements. For all analyses shown in Fig. 4.38 and Fig. 4.39, the abutment model based on the Ramberg-Osgood hysteresis rule of Fig. 4.34 (left) was used. A constant elastic viscous damping ratio of $\xi_{el} = 5\%$ was modeled in the ITHA. No attempt was made to model a damping behavior similar to tangent-stiffness proportional damping because of the corresponding difficulties in MDOF systems (see discussion in Section 4.4.1).

For every bridge configuration in Fig. 4.38 and Fig. 4.39, the nominal yield displacements of the individual piers according to Tab. 4.10 are also shown. By comparison with the displacement shapes, it can be seen that in many systems the piers hardly enter into the inelastic range for a design peak ground acceleration of $a_{gd} = 0.16$g. Those bridges where a short pier is located between two taller piers (configurations 6 and 11) represent a certain exception, as the short piers experience somewhat more inelastic action in such cases. However, even in these cases the ductility demand of the piers remains rather limited. It should be noted that for a lower elastic viscous damping ratio of, e.g., $\xi_{el} = 2\%$, displacement demands being higher by approximately 20%-30% might be expected. Consequently, somewhat more inelastic action throughout the structures would result.

It should also be kept in mind that the structural models for the piers are rather basic, not considering e.g. soil-structure interaction at the foundations. The real behavior of piers with the given heights might therefore be a little more complex, so that a full generalization of the findings concerning the computed demand levels may not be possible. Nevertheless, they give a certain impression of the rough level of inelasticity to be expected at the various seismicity levels. Especially, the rather low displacement demands at $a_{gd} = 0.16$g may be of relevance for the choice of appropriate simplified analysis strategies in such moderate seismicity conditions.

---

[24] For real ground motions, the spectral shape also depends on the earthquake magnitude, as stronger earthquakes tend to result in higher spectral values especially in the long period range. However, this effect is not included in the spectrum definitions of [SIA261] and [SIA2018]. It is therefore neglected here for simplicity as well.
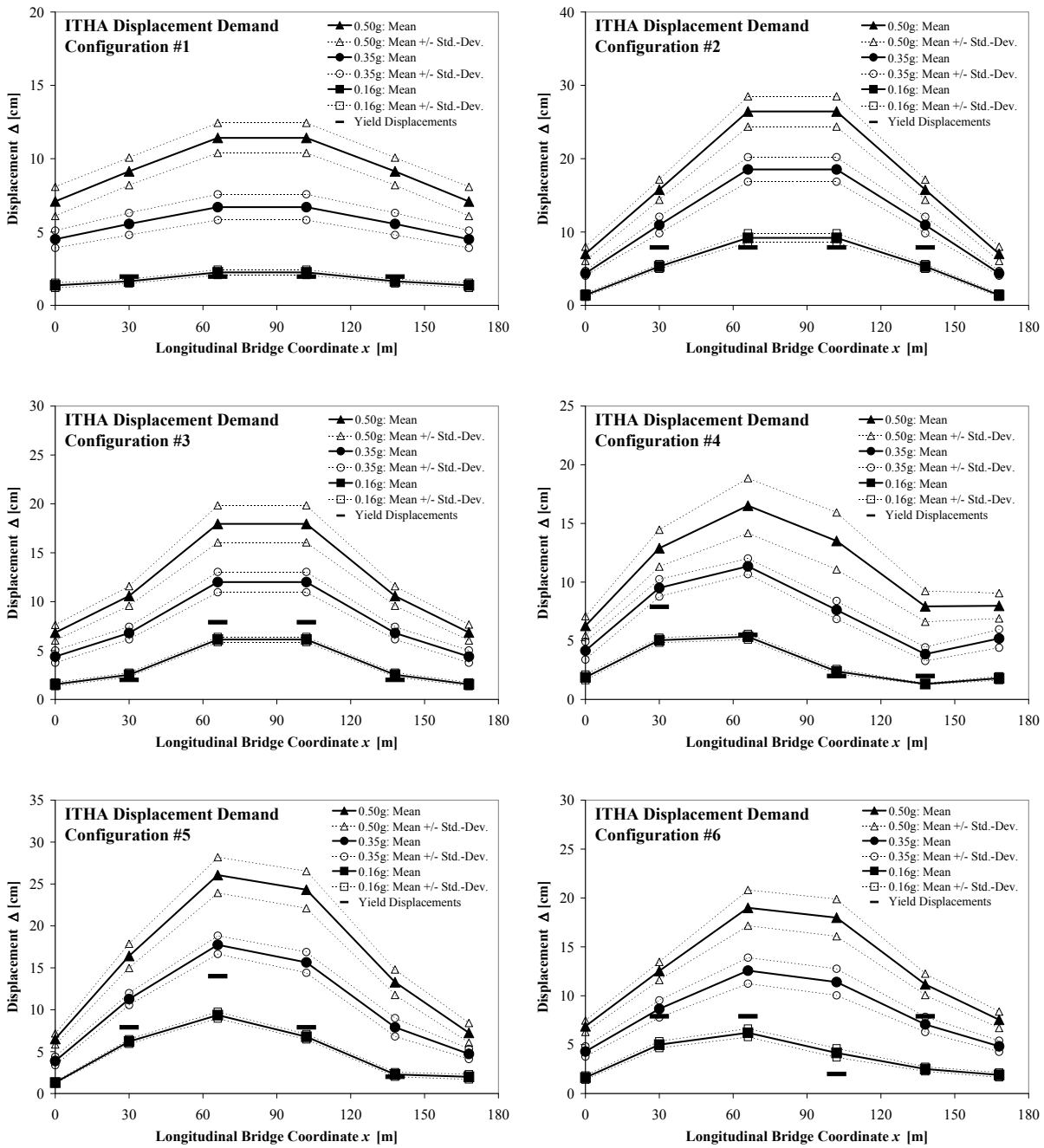
Fig. 4.38: Displacement demands for bridge configurations 1 through 6 from ITHA for transverse excitation at seismicity levels a_{gd} = 0.16g, 0.35g, and 0.50g (Source: [Ber09])

As can be seen in Fig. 4.38 and Fig. 4.39, significant inelastic actions develop at the higher seismicity levels represented by design PGAs of a_{gd} = 0.35g and 0.50g. This is especially true for the shorter piers. For the tall piers, the inelastic demand at a_{gd} = 0.35g is still rather limited, whereas at a_{gd} = 0.50g the piers of all heights included in the analyses have to sustain noticeable inelastic deformations. Comparing the (relative) displacement shapes of the individual bridges at the various PGA levels, it can be seen that, despite certain qualitative similarities, the peak deformation shapes change with increasing ductility demand. This corresponds to "phenomenon (2)" described above in Section 4.6. The extent of deviation depends on how the relative stiffness changes occur at different piers and abutments with increasing load level.

It has been outlined in Section 4.6 that the global demand level of the bridge can e.g. be characterized by the displacement of a certain defined *reference point*. Common choices for this reference point comprise the center of mass of the superstructure or the point of largest displacement. It should be

noted that for all but one bridge configuration shown in Fig. 4.38 and Fig. 4.39 the point of maximum displacement remains the same at all three PGA levels considered in the study. Only for configuration 11 the corresponding point changes from pier 2 in the (almost) elastic range of $a_{gd} = 0.16g$ to pier 3 at the higher demand levels.
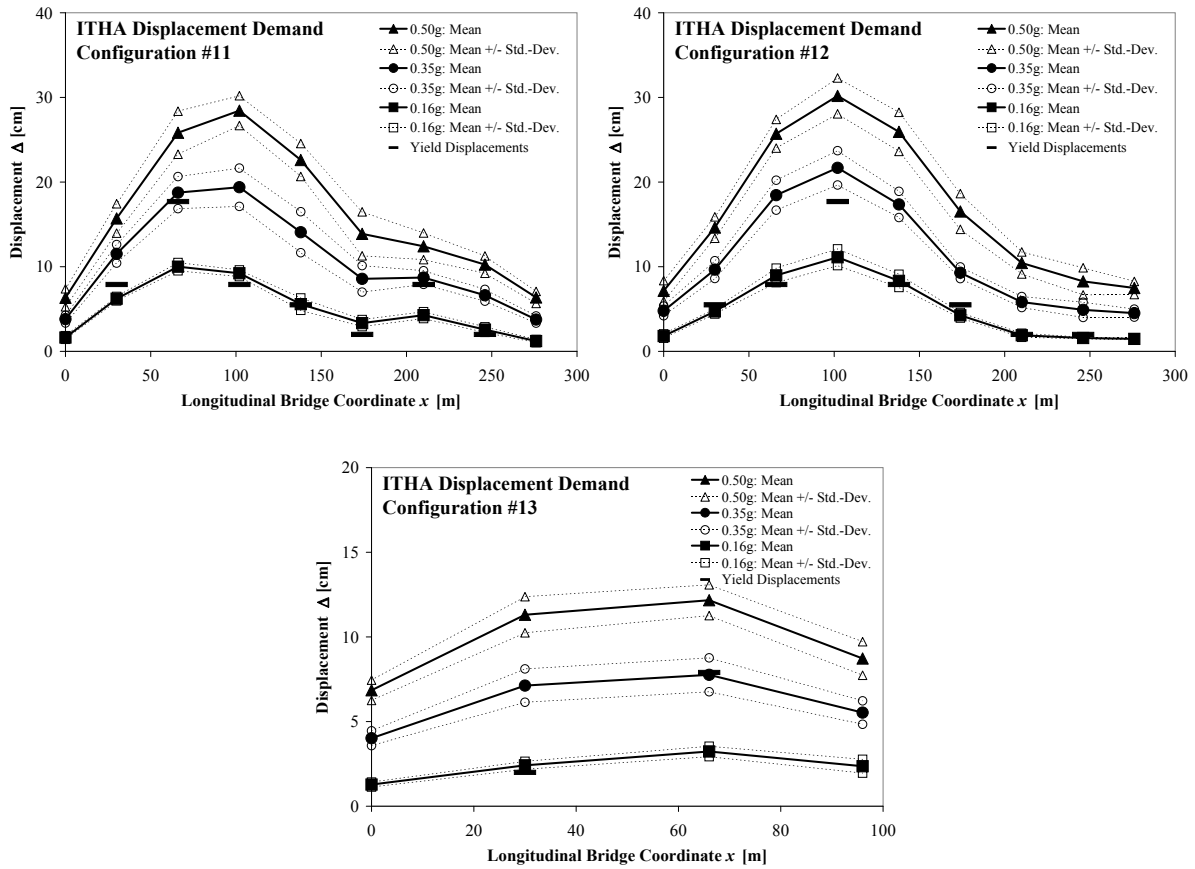

Fig. 4.39: Displacement demands for bridge configurations 11, 12 (top row), and 13 (bottom) from ITHA for transverse excitation at seismicity levels a_{gd} = 0.16g, 0.35g, and 0.50g (Source: [Ber09])

Defining the reference point as the point of largest displacement in the elastic range, it is possible to compute the ratio between the displacement at higher PGA levels and the one at $a_{gd} = 0.16g$. These values are presented in Tab. 4.13 for all bridge configurations. For comparison purposes, the corresponding ratios between the PGA values a_{gd} are also shown. If the systems responded linearly elastic at all seismicity levels, the displacement demands would be simply scaled by the PGA values. As a consequence, the ratios between the displacement demands at different seismicity levels would be equal to the corresponding PGA ratios. The same holds true (approximately) if an inelastic response occurs that fulfills the *equal displacement approximation* (see Section 4.5.1).

As can be seen from the data in Tab. 4.13, for the bridges with an elastic first mode falling into the medium period range (e.g. configurations 3, 4, 6), the displacement ratios of the reference point agree reasonably well with the corresponding PGA ratio, thus confirming the *equal displacement approximation* for these cases. At the same time it needs to be emphasized that the ITHA have been performed with a constant (i.e. initial stiffness proportional) elastic viscous damping of $\xi_{el} = 5\%$. As outlined in Section 4.5.1, this assumption corresponds to the damping configuration for which Priestley and Grant [PG05] had also found reasonable agreement with the *equal displacement approximation*. However, it was shown that this cannot be generalized as for other configurations (e.g. tangent stiffness proportional viscous damping) the *equal displacement approximation* may not give acceptable results anymore.

For the bridges with the elastic first mode rather approaching the short period range (e.g. configuration 13, and especially configuration 1), the displacement ratios can exceed the corresponding PGA ratios

considerably for higher values of a_{gd}. This means that, at higher levels of inelasticity, the global displacement demand exceeds the elastic demand increasingly. This corresponds to the behavior that was identified for inelastic SDOF systems in Section 4.5. In contrast, for longer first mode periods (e.g. configurations 2, 5, 11, 12) the inelastic displacement demand for the reference point rather tends to be somewhat lower than that of a corresponding elastic system. A similar behavior was empirically found for inelastic SDOF systems in Sections 4.5.1 and 4.5.2. It can thus be concluded that the global behavior of inelastic MDOF systems, represented by the response of the reference point, appears to be qualitatively similar to that of inelastic SDOF systems described previously.

| | | Design Peak Ground Acceleration a_{gd} | |
		0.35g	0.50g
Peak Ground Acceleration Ratio	a_{gd}/0.16g [-]	2.19	3.13
Bridge Configuration	Elastic period of the first mode	Reference Point Displacement Ratio	
	T_0 [s]	$\Delta_{ref,0.35g}/\Delta_{ref,0.16g}$ [-]	$\Delta_{ref,0.50g}/\Delta_{ref,0.16g}$ [-]
1	0.36	2.98	5.08
2	0.91	2.01	2.87
3	0.65	1.96	2.93
4	0.58	2.12	3.09
5	0.89	1.90	2.79
6	0.61	2.02	3.06
11	0.97	1.87	2.58
12	1.02	1.95	2.71
13	0.44	2.4	3.76

Tab. 4.13: Ratio of mean reference point displacements between higher seismicity levels and a_{gd} = 0.16g as well as corresponding PGA ratios (based on data by Berweger [Ber09])

For three bridges (configurations 1, 4, and 13) Berweger [Ber09] also performed analyses using the Takeda rule depicted on the right side of Fig. 4.34 for the abutments. This way, the influence of different modeling assumptions on the response of the abutments and the entire bridge can be studied. In Fig. 4.40 a comparison is presented between the displacement demands using the Ramberg-Osgood abutment model and those based on the Takeda abutment model. It can be seen that, although both models were intended to represent the same type of abutment-embankment system, a noticeable difference exists between the corresponding responses. For the chosen parameter sets (see Fig. 4.40), the Takeda model consistently results in larger abutment displacements for all three bridge configurations and at each PGA level considered.

To understand the reasons for these differences, it is necessary to interpret the characteristics of the two models. At small displacements, up to Δ_{abut} = 1.2 cm, the Takeda model still remains in its linear elastic range. In this phase it therefore does not dissipate any energy. Up to Δ_{abut} = 0.84 cm, the Takeda model is additionally softer than the Ramberg-Osgood representation. For larger displacements, the backbones of the two models become quite similar and, starting from about Δ_{abut} = 6 cm, the Takeda backbone is even slightly stiffer than the Ramberg-Osgood curve. Considering the levels of displacements experienced by the abutments, as shown in Fig. 4.40, the differing behavior in the elastic range cannot explain the higher demands sustained by the Takeda model.

In this context it is noteworthy that, although the Takeda model also develops a significant hysteretic response in the inelastic range, its energy dissipation still remains smaller than that of the Ramberg-

Osgood model. For the chosen parameter sets, the large cycle dissipation of the Takeda spring tends to converge to about 65% of the hysteretic energy dissipated by the Ramberg-Osgood model at large amplitudes. As the differing responses cannot be explained by the stiffnesses of the backbone curves, the results suggest that the localized differences in energy dissipation behavior appear to be the reason for the higher displacements occurring for the Takeda abutment model.
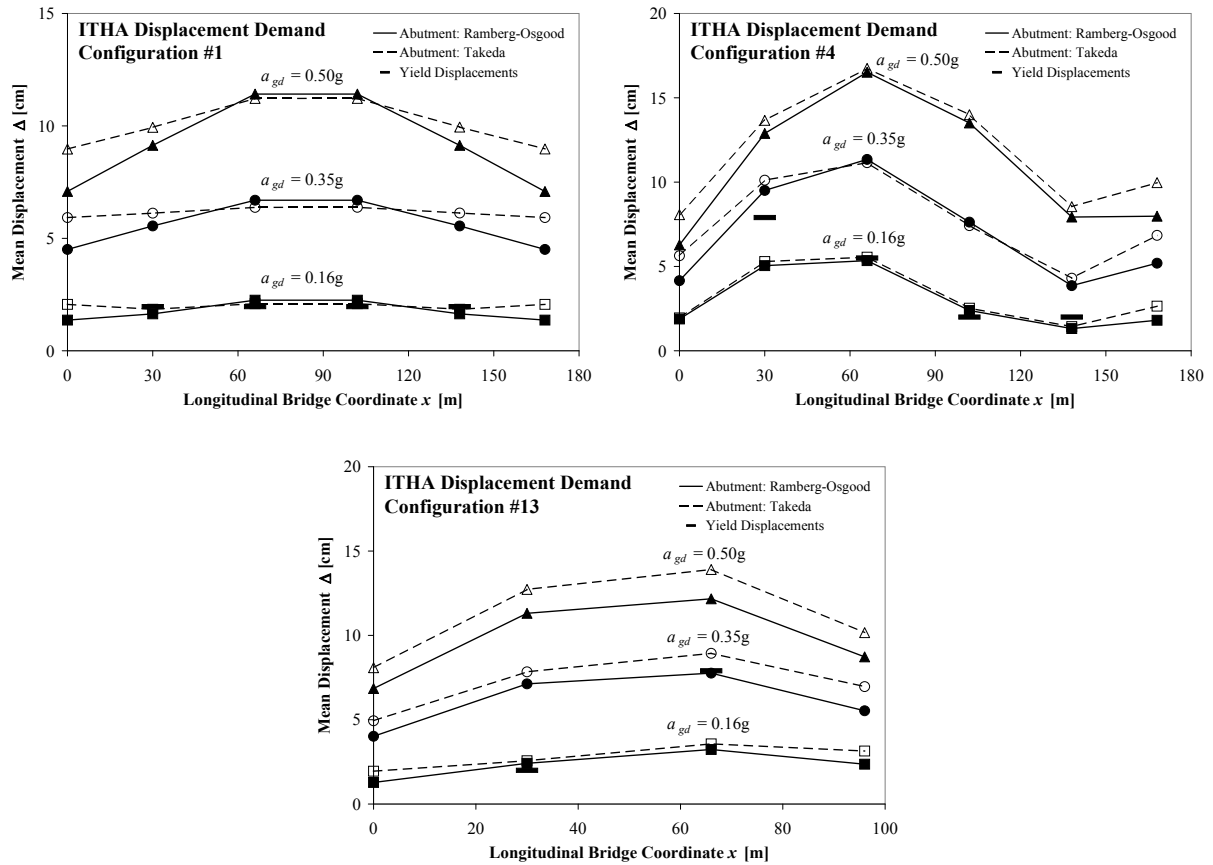

Fig. 4.40: Mean displacement demands for bridge configurations 1, 4, and 13 from ITHA
for transverse excitation at seismicity levels a_{gd} = 0.16g, 0.35g, and 0.50g (Source: [Ber09])
here: Comparison between Ramberg-Osgood and Takeda model for abutment springs

The displacement shapes in Fig. 4.40 show that for the longer five span bridges the influence of the differing abutment modeling is rather limited to the edge regions of the superstructure. While in configuration 1 the first outer piers are still affected by the abutment modeling, in configuration 4 hardly any influence on the piers exists, limiting the response differences essentially to the abutments themselves. This is different for the shorter bridge configuration 13. Here, the response differences of the abutments translate almost completely to the entire bridge. This finding complies with the general notion outlined in Section 3.5.2a that such rather short bridges are controlled to a large extent by the abutment response.

It can thus be concluded that, on one hand, the response of the abutments shows a considerable sensitivity to the (rather uncertain) modeling approach. This does not only refer to the stiffness representation, but also to the energy dissipation characteristics. On the other hand, for longer bridges this influence appears to be essentially limited to the abutments themselves and possibly to the outer piers. Therefore, if the primary focus of the analysis is on the pier response, while the abutment behavior is only considered relevant as a boundary condition for the rest of the system, then the sensitivity and uncertainty related to the abutment modeling may not be overly relevant in many cases. However, for short bridges a reasonable choice of the abutment model is likely to be crucial for the response prediction of the entire structure. This shows that in such cases a sufficiently conservative assumption concerning the abutment properties is necessary and some variation of the relevant parameters may be recommendable in order to get an impression of the sensitivity to the assumptions.

4.6.2 Overview of Simplified Procedures

In this section an overview of several simplified analysis concepts is given that were also applied in the comparative study by Berweger [Ber09]. The presented approaches comprise different levels of simplification with respect to the three aspects (1) *influence of inelasticity on the global displacement demand*, (2) *influence of inelasticity on the displacement shape*, and (3) *influence of higher modes* as outlined in Section 4.6. A discussion on the applicability in certain cases will be given below, as well as a summary of the corresponding analysis results computed by Berweger [Ber09].

It should be noted that for some of the methods not only one form of application is possible as not all of them are uniquely defined in every detail. As a consequence, during the application certain decisions and choices may be required which influence the final results. When comparing the simplified analysis results to those from the reference ITHA, it is therefore necessary to keep in mind that the quality of the approximation may not be independent of the individual interpretation of the methods and the specific choices made during its application. The study by Berweger [Ber09] was limited to applying the simplified procedures based on certain decisions and comparing the results empirically to the reference ITHA displacement demands. An attempt to further explain some of the differences encountered by Berweger and subsequently suggest improvements to the methods can be found in Section 4.6.3.

a) Response Spectrum Analysis

The response spectrum analysis is a classic and well established method for seismic applications. It is based on modal analysis and can, strictly speaking, only be applied on linear elastic systems. However, as outlined in Section 4.1, it has been common in force based design to allow for inelastic behavior by means of force reduction factors while conducting the actual analysis on a linear elastic representation of the system. On this basis, the response spectrum analysis can be used in an approximate manner to determine the corresponding internal (force) actions of the structure. In the framework of established codes the force reduction factor (or *behavior factor*) is often directly incorporated in the so-called design spectra which may only be used in this particular context.

As an alternative, it is also conceivable to use the response spectrum analysis to estimate the displacement demand, instead of internal (force) actions. In this case, the elastic (unreduced) response spectrum must be used to define the input loading. Applying the linear response spectrum analysis on an inelastic system implicitly implies that the first two aspects mentioned above – i.e. (1) *influence of inelasticity on the global displacement demand* and (2) *influence of inelasticity on the displacement shape* – are neglected. Not allowing for the influence on the global displacement demand essentially corresponds to assuming the *equal displacement approximation* as valid. As discussed in Section 4.5.1, such an assumption may be acceptable in the medium period range and possibly slightly conservative in the long period range. However, for systems with short elastic periods of the first mode, the *equal displacement approximation* can yield considerably unconservative results. Aside from the natural period, the validity of this approximation is also influenced by the level of inelasticity experienced by the structure. For rather small ductility levels the subsequent error will be less pronounced than for high ductility demands, even for shorter periods.

With respect to neglecting the influence of inelasticity on the displacement shape, the ITHA results presented in Fig. 4.38 and Fig. 4.39 can give some indication of the quality of this approximation. These curves show that the inherent error tends to increase with the level of inelasticity sustained by the structure. While the displacement shape at rather low ductility demands is still essentially the same as that of a linear elastic system, some noticeable deviations can develop at high ductility demands. The degree of deviation also depends on the properties of the individual structure, especially its regularity. Structures in which the individual members yield at significantly different load levels are more likely to show stronger changes of the displacement shape at increasing deformations. An example for this can be short (and stiff) piers being located between adjacent tall (and soft) piers

While the two influences related to the inelastic system response can not be covered accurately, the third aspect – i.e. the *influence of higher modes* – is captured by the response spectrum analysis almost

perfectly. For linear elastic systems, the only inaccuracy inherent to the response spectrum analysis is related to the superposition of the individual modes, which is typically done using either the SRSS or the CQC rule. Aside from this approximation, the response spectrum analysis reproduces the results of a linear time history perfectly if the ground motion fits the elastic response spectrum.

Hence, it can be concluded that the method is well suited for systems with considerable higher mode effects, but without strong influences from inelasticity on global displacement demand and deformation shape. Considering the ITHA results presented in Fig. 4.38 and Fig. 4.39, it may be expected that for moderate seismicity levels – as those encountered in Switzerland with design PGA values not higher than $a_{gd} = 0.16g$ – the mentioned criteria might be fulfilled in many cases. In fact, under these conditions a reasonable representation of higher mode effects may be more relevant for a realistic demand estimation than the capability to cover large levels of inelasticity.

But even if the ductility demands become larger, e.g. due to increased input loading, a linear response spectrum analysis can still serve in some cases for approximate demand estimations. The extent to which the errors resulting from not allowing for the two effects of inelasticity mentioned above can still be considered as acceptable may also depend on the required level of accuracy. If only a rough estimation of the demand is needed, the displacements from the linear elastic response spectrum analysis might still be sufficient. This may, e.g., be the case if the response spectrum analysis is only used to check another more sophisticated analysis. It should be noted that Eurocode 8, part 3 [EC8-3], providing provisions for the seismic assessment of existing buildings, also allows the response spectrum analysis in the described form for the computation of the displacement demand of building structures.

As the application on inelastic systems implicitly relies on the *equal displacement approximation*, the stiffness representation in this case must be given by the initial elastic stiffnesses k_0 of the members, in analogy to the principles outlined in 4.5.1. The viscous damping to be assumed for the linear elastic response spectrum analysis then needs to be equal to the elastic viscous damping ratio ξ_{el} of the inelastic system. As mentioned above, the seismic input loading is correspondingly defined by the *elastic* response spectrum, and <u>not</u> by any modified *design spectrum* (as e.g. defined in [SIA261] for the force based analysis). As a consequence, the forces computed from the corresponding analysis have no specific meaning (equivalent to the force F_{el} of an inelastic SDOF in Fig. 4.7, which does not have a mechanical meaning either). Instead, only the computed displacements are accessible to a meaningful interpretation and to a demand-capacity comparison.

A summary of the most important equations underlying the response spectrum analysis is given in Section A2.1.1 of Annex A2 without a detailed deduction. A further discussion on the background of the response spectrum analysis or on its application will not be given here as the method can be considered as well established and well documented in the common literature on structural dynamics (e.g. [Cho01]). It should be noted that attention needs to be given to the adequate choice of the modal superposition rule. Based on the criteria given in [EC8-2], 4.2.1.3, and complemented by selected linear time history analysis, Berweger [Ber09] found that for some of the bridge configurations considered in his study the SRSS rule was not sufficient and needed to be replaced by the more general CQC rule. In these cases, considerable differences between SRSS results and the displacement demands from linear time history analysis (LTHA) were encountered. However, using the CQC rule the LTHA results could be reproduced with good accuracy.

Another issue found to have a considerable influence on the results is the appropriate choice for the elastic stiffness of the abutments. As already mentioned in Section 4.6.1, the continuously curved backbone of the Ramberg-Osgood model does not directly suggest a specific choice for such an initial elastic stiffness k_0. Berweger [Ber09] investigated two different choices for k_0 to be assumed in the response spectrum analysis. These were on one hand the tangent stiffness in the origin of the Ramberg-Osgood model, i.e. 450 MN/m, and on the other hand half this value, i.e. 225 MN/m (see Section 4.6.1 for a further discussion on the background of these two values). The analyses showed that the stiffer assumption resulted in rather bad estimations of the abutment response, which might be expected as this tangent stiffness is only valid in a single point, i.e. zero deformation. For any non-zero abutment displacement it overestimates the stiffness of the abutment. Therefore, in the following discussion only the results based on an elastic abutment stiffness of $k_0 = 225$ MN/m will be considered.
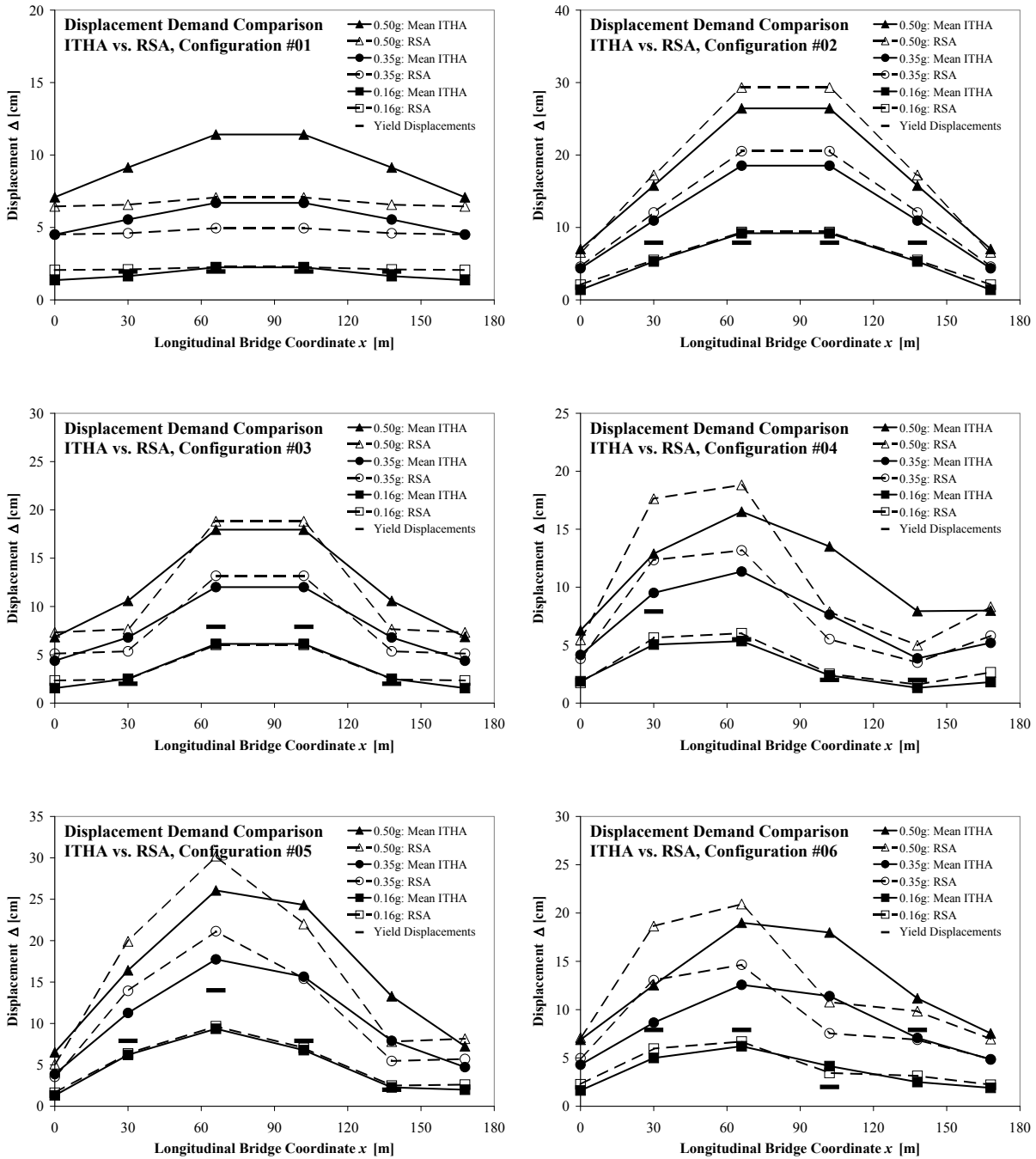
Fig. 4.41: Displacement demands for bridge configurations 1 through 6 from RSA and ITHA for transverse excitation at seismicity levels a_{gd} = 0.16g, 0.35g, and 0.50g (Source: [Ber09])

In Fig. 4.41 and Fig. 4.42 the corresponding results from [Ber09] using the response spectrum analysis (RSA) are compared to the reference displacements from inelastic time history analysis (ITHA). As can be seen, the approximation at the design PGA level of a_{gd} = 0.16g is fairly good for essentially all bridge configurations. This could have been expected as the ITHA here predicts rather low ductility demands and thus close to linear elastic response. In this case, the only approximations introduced by the response spectrum analysis are related to the modal superposition rule (SRSS or CQC) and to the linearization of the abutment behavior. If the abutments had been modeled in the ITHA by the alternative Takeda rule also outlined in Section 4.6.1, the second approximation would be dropped for displacement demands below the nominal yield displacement.
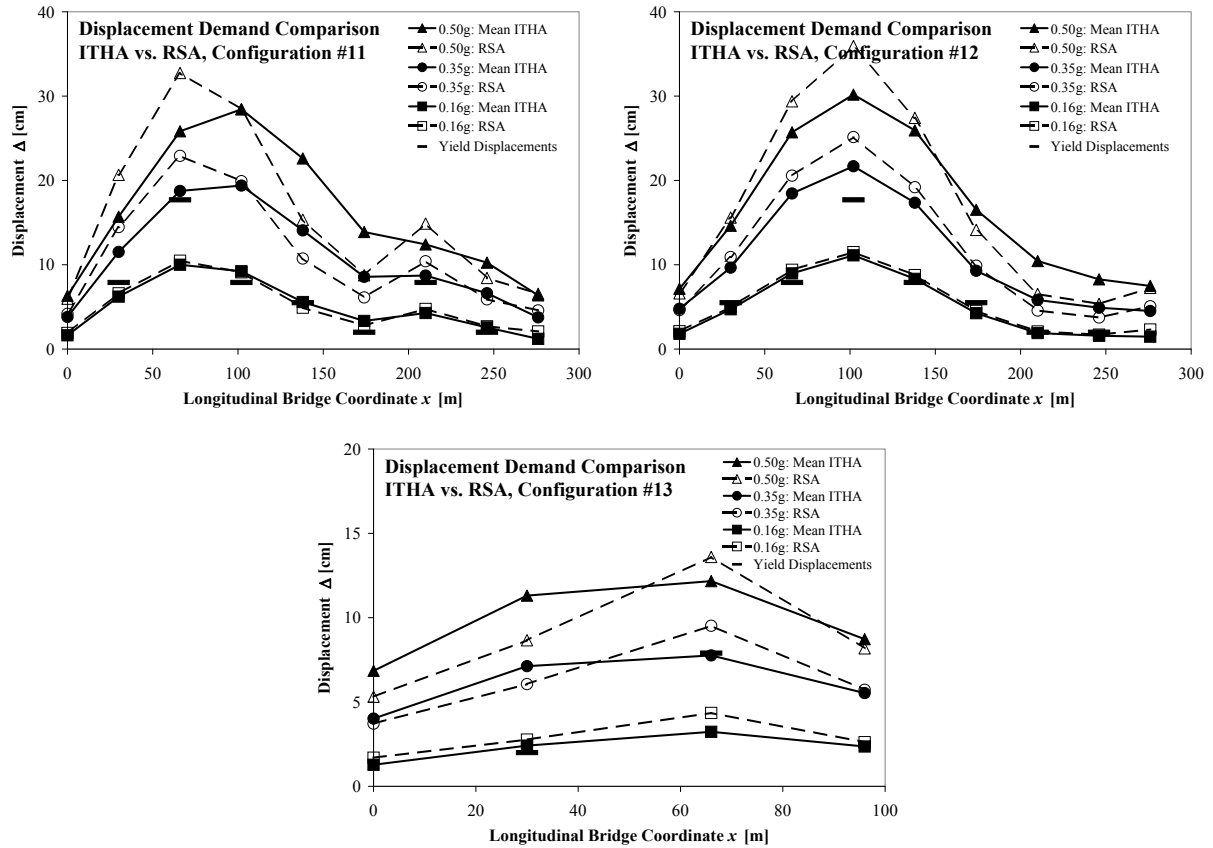
Fig. 4.42: Displacement demands for bridge configurations 11, 12, and 13 from RSA and ITHA
for transverse excitation at seismicity levels a_{gd} = 0.16g, 0.35g, and 0.50g (Source: [Ber09])

At higher PGA levels, and consequently higher ductility demands, for some bridges the response prediction by the response spectrum analysis becomes increasingly worse. This is partly related to inaccuracies in the estimation of the global displacement demand, and partly it is coming from deviations in the predicted deformation shape. Deficiencies in the estimation of the global displacement demand are very noticeable for bridge configuration 1 at a_{gd} = 0.35g and 0.50g. Such an effect was already noticed in the context of Tab. 4.13, where a more than linear increase of the reference point[25] deformation demand with respect to a_{gd} was encountered. As the response spectrum analysis results can be scaled linearly with PGA, this also explains why RSA underpredicts the reference point displacements compared to inelastic time history analysis. The reason for this effect is related to the short first mode period of bridge configuration 1, being only T_0 = 0.36 s, at which the *equal displacement approximation* cannot be reasonably assumed anymore. As suggested by the relationships presented in Section 4.5.1, this value of T_0 already lies in a region where displacement modification factors C_R larger than unity would result for inelastic response (see e.g. Fig. 4.13).

Inaccuracies in the deformation shape estimated by means of the response spectrum analysis can be attributed largely, on one hand, to yielding of individual piers at different load levels and, on the other hand, to differing stiffness development between the curved Ramberg-Osgood abutment model and the bilinear Takeda backbones of the piers. The former influence can be seen especially in those bridges were short piers are located next to rather tall piers. The small yield displacement of the short piers results in an inelastic response already at a rather early stage, while the taller piers still remain elastic. The yielding of the short piers represents an effective softening, resulting in a disproportionate increase of their top displacements (see e.g. configuration 6 in Fig. 4.41 or configuration 11 in Fig. 4.42). As can be seen from the displacement demands at a_{gd} = 0.35g and 0.50g, the inelastic action tends to somewhat smoothen out the deformation shape as a consequence of the stiffness redistributions after yielding. While the elastic displacement shape reflects significantly more the

---

[25] Here, the reference point is defined as the point experiencing the largest displacement demand in the elastic range. For bridge configuration 1 this is the top of pier 2 (having the same displacement demand as pier 3).

strong differences between initial stiffnesses of the piers with different heights, with increasing inelasticity of the piers the deformation shape becomes more uniform or smoothly curved. This is also related to the influence of the second (elastic) load path via the superstructure to the abutments, which becomes more important as the effective stiffnesses of the inelastic piers reduce.

An example for stiffness redistributions between the piers and the abutments due to the conceptually different shapes of the Ramberg-Osgood and the Takeda backbone is represented by bridge configuration 1 shown in Fig. 4.41. The response spectrum analysis predicts a rather uniform displacement shape for this bridge, as the ratio between mass and assumed elastic stiffnesses happens to be similar at the piers and the abutments. At a loading level of $a_{gd} = 0.16$g, the displacement shape of the bridge according to ITHA is also close to uniform. At this load level the piers remain essentially elastic and the effective stiffness of the abutments also coincides roughly with the assumed elastic value of $k_0 = 225$ MN/m.

At higher PGA levels, both, piers and abutments soften in the ITHA. While the Takeda pier models have no post-yield stiffness ($r = 0$, see Tab. 4.10), the Ramberg-Osgood abutment model features a considerable tangent stiffness even at higher displacement demands. The corresponding further increase of the force resistance at the abutments – while the resistance of the piers remains at their nominal capacity – results in a relative stiffness redistribution from the piers towards the abutments. As a consequence, at larger PGA levels the displacements at the piers increase stronger than those at the abutments, thus changing the deformation shape from uniform to more parabolic as shown in Fig. 4.41. The response spectrum analysis, however, cannot capture this redistribution as it is based on the same elastic stiffnesses for every PGA level. It therefore also predicts the same uniform deformation shape at all loading levels.

A rather unsatisfactory and also worrying effect of the deficient deformation shape in the RSA is that especially the demand on the short piers tends to be underpredicted. This effect appears most pronounced for short piers between or adjacent to longer piers. The former already yield at a rather early stage and therefore they are strongly subjected to stiffness redistributions, which are not captured by the displacement shape of the RSA. At the same time, this effect also causes particularly high ductility demands for those short piers. As a result, they are likely to be the most critical piers within the structure. Therefore it is especially problematic if the simplified analysis underpredicts the response exactly for these members. The situation may become even more critical as short piers are more susceptible to potential shear failure than taller piers.

Summarizing, it can be said that the ability of the response spectrum method to realistically capture higher modes results in reasonably good displacement estimations at the elastic and low ductility demand level. The quality of the approximation at higher levels of inelasticity depends on the amount of stiffness redistribution occurring within the inelastic structure and on the initial period of the system. The former influences the change of the deformation shape, while the latter determines to what extent the global displacement demand deviates from the *equal displacement approximation*. In the medium to long period range, the global displacement demand is typically represented reasonably well by the *equal displacement approximation*, or the displacement prediction for the reference point is even slightly conservative (see Fig. 4.41 and Fig. 4.42). In the short period range, a certain correction of the expected global demand underprediction could possibly be achieved by introducing a period dependent displacement modification factor, as presented in Section 4.5.

If this way a reasonably good estimation of the global displacement demand can be achieved, only the conceptual deficiency related to a potentially incorrect deformation shape remains. This, to a considerable extent, depends on the irregularity of the structure and the level of seismicity. Hence, it might be possible to estimate qualitatively whether the elastically determined deformation shape may be used, as an approximation, also in the inelastic range. The considerations outlined above, will serve for a proposal to modify – and possibly improve – the use of the response spectrum method as a displacement based analysis procedure, as presented in Section 4.6.3.

b) Lateral Force Method

The lateral force method (LFM) is another well established linear elastic analysis procedure which is commonly used in force based analysis. It is included in many codes, as e.g. in [SIA261], [EC8-1], and [EC8-2], and is typically considered to be an approximation of the response spectrum analysis. Its practical application is simpler and more accessible to hand calculations as it does not require a modal analysis. As a consequence, higher mode effects cannot be represented as realistically as by the response spectrum analysis. Instead, an acceleration shape for the distribution of the equivalent lateral forces must be assumed, which might be chosen to approximate the first mode shape. Furthermore, the fundamental period of the first mode must be estimated by some means as it does not automatically result from any modal analysis.

A summary of the principles underlying the lateral force method is given in Section A2.1.3 of Annex A2. In particular, it should be noted that the activated mass used to compute the lateral inertia forces is artificially increased in the LFM. While in the response spectrum analysis the sum of all inertia forces in the first mode is equal to the product of the corresponding effective modal mass $m^*_{eff,1}$ times the spectral acceleration $S_{a,el}(T_1)$ (see equation (A2.10)), the sum of the forces in the lateral force method is computed based the total mass m_{tot} of the structure (see equation (A2.20)). This increase is intended to compensate for neglecting the influence of higher modes and for the implicit inaccuracies in the estimation of the acceleration shape used to determine the distribution of the lateral forces.

As the lateral force method represents an approximation of the response spectrum analysis, the limitations of and comments on the latter also apply for the LFM. As outlined in Subsection *a*, in common seismic codes (e.g. [SIA261], [EC8-1], [EC8-2]) these two approaches are normally used in a force based framework. This means that, based on (reduced) *design response spectra*, internal force actions are computed which are used for the structural design. The deformation demand, however, is not considered explicitly in this context. Instead, the beneficial influence of the plastic deformation capacity is supposed to be accounted for by means of behavior factors included in the design spectra.

On the other hand, equivalent to the case of the response spectrum analysis outlined in Subsection *a*, it is generally also possible to use the lateral force method in a displacement based framework. In this case, the method is not used to compute internal force actions, but rather to estimate the displacement demand of the structure. For this purpose, the seismic input must be represented by the unreduced elastic response spectrum, instead of the design spectrum as the latter would not yield reasonable deformation demands. It should be noted that a corresponding approach is also included in Eurocode 8, Part 3 [EC8-3] for the assessment of existing building structures. In this case, as for the response spectrum analysis in Subsection *a*, the behavior of the individual inelastic members must be represented by their initial elastic stiffnesses k_0.

For the practical application of the LFM, an estimation of the (1st mode) fundamental period and an appropriate assumption for the acceleration shape vector $\tilde{\phi}_{LFM,a}$ are required. As outlined in Section A2.1.2 of Annex A2, the Rayleigh quotient can be used to estimate the fundamental period. For the computation of the Rayleigh quotient an assumption for an (independent) acceleration shape vector $\tilde{\tilde{\phi}}_{RQ,a}$ is required. While several different assumptions for this vector are conceivable, and it is also possible to iteratively improve it (see Section A2.1.2), Eurocode 8, Part 2 [EC8-2] suggests using a uniform acceleration shape $\tilde{\tilde{\phi}}_{RQ,a} = \vec{1}$ resulting in a mass proportional distribution of the lateral forces $\tilde{\tilde{F}}_{RQ}$ to compute the Rayleigh quotient. This proposal was followed in the study by Berweger [Ber09] and the fundamental periods of all bridge configurations in the context of the lateral force method were determined by the corresponding Rayleigh quotient.

A separate acceleration shape $\tilde{\phi}_{LFM,a}$ and corresponding force distribution $\tilde{F}_{LFM}$ are required for the actual application of the lateral force method. Several potentially reasonable choices for $\tilde{\phi}_{LFM,a}$ are presented and discussed in Section A2.1.3 of Annex A2. While for building structures a common assumption is to use a triangular acceleration shape [SIA261], [EC8-1], for bridges, Eurocode 8, Part 2

[EC8-2] suggests using the displacement shape $\tilde{\vec{\phi}}_{RQ,u}$ resulting from the lateral forces $\tilde{\vec{F}}_{RQ}$ of the Rayleigh quotient as the acceleration shape vector for the determination of the forces $\tilde{\vec{F}}_{LFM}$ in the lateral force method. This assumption might be considered as an approximation of the 1st mode shape of the structure. As a consequence, following this recommendation the lateral force method could be expected to yield a displacement shape roughly similar to the first mode shape. However, due to the increased mass contribution used in the lateral force method (see above), the absolute displacements should be larger than the actual first mode response.

While this increase of the deformations is intended to provide some conservatism, this is not guaranteed for every local deformation. If the higher modes contribute significantly to the response, or if the approximate shape vector coming from the Rayleigh quotient represents an unsatisfactory estimation of the 1st mode shape, the increase of the activated mass included in the lateral force method is unlikely to compensate for an insufficient shape estimation. No particular consideration to this potential problem is given in [EC8-2]. In Section A2.2.1 of Annex A2 it is shown that a certain analogy exists between the lateral force method and a conventional pushover analysis applied on a linear elastic system. In the pushover analysis described in [EC8-2] Annex H, it is required to consider two different acceleration shapes for the determination of the force distribution. On one hand, a first mode proportional shape shall be used and, on the other hand, a uniform acceleration shape is required which results in a mass proportional force distribution. In the pushover analysis, the overall demand to be assumed for the design is the envelope of the results from the two different analyses. This approach obviously does not aim at a realistic best estimate of the response, but rather on a possibly conservative solution.

Independent of the question whether the envelope of two analyses with different force distributions should be used, it appears reasonable to consider not only one shape vector. Therefore, Berweger [Ber09] conducted the lateral force method based on the following two different acceleration shape vectors, in analogy to the pushover analysis of [EC8-2] Annex H:

- *Load Distribution 1*:

  Based on uniform acceleration shape vector $\tilde{\vec{\phi}}_{LFM,a} = \vec{1}$.

- *Load Distribution 2*:

  Based on acceleration shape vector $\tilde{\vec{\phi}}_{LFM,a} = \tilde{\vec{\phi}}_{RQ,u}$ equal to the resulting displacement shape vector from the Rayleigh quotient.

In both cases, the corresponding lateral forces can be computed from equation (A2.21) or (A2.22) given in Annex A2 of this text. Although *Load Distribution 2* does not exactly agree with the first mode shape, here it is considered to correspond roughly to the load distribution in the fundamental mode. As discussed in Subsections *a* and *c* of Section A2.1.3, the application of *Load Distribution 1* in the LFM becomes very simple in the given configuration because the same acceleration shape is already used for the computation of the Rayleigh quotient. As a consequence, it is not necessary to perform a new static analysis under these loads. Instead, it is possible to simply scale the displacement results from the Rayleigh quotient according to equation (A2.47) given in Section A2.1.3.

For bridge configurations 1 through 6, the displacement demands resulting from the lateral force method (LFM) based on *Load Distribution 1* (LD1) and *Load Distribution 2* (LD2) are compared in Fig. 4.43 to the mean responses from inelastic time history analysis (ITHA). For the additional bridge configurations 11 through 13, the lateral force method was only applied using *Load Distribution 1* (LD1) in [Ber09]. These results are compared to the corresponding ITHA data in Fig. 4.44. All linear analyses using the lateral force method were conducted with an elastic stiffness for the abutments of $k_0 = 225$ MN/m.

From the curves shown in Fig. 4.43 it can be seen that in many cases a considerable difference exists between the results coming from the two different load distributions. For configurations 2 through 6, *Load Distribution 2* substantially overpredicts the demand in some parts of the structures. If the pier top experiencing the largest displacement in the elastic range is defined as a reference point, then this reference point displacement is significantly overpredicted for configurations 2 through 6 at all three

PGA levels. This effect is clearly related to the artificial increase of the forces in the LFM by assuming the entire system mass m_{tot} as activated in the approximated first mode. Considering that the effective modal masses of the first mode, given in Tab. 4.12, only range between 42% and 60% of m_{tot} for these configurations, implicit amplification factors for the first mode between 2.38 and 1.67 result (see Section A2.1.3 of Annex A2 for details on the underlying principles). Based on these data, the strong response overpredictions for the reference points, shown in Fig. 4.43 for *Load Distribution 2*, are not surprising.

Fig. 4.43: Displacement demands for bridge configurations 1 through 6
from lateral force method (LFM) and ITHA
for transverse excitation at seismicity levels a_{gd} = 0.16g, 0.35g, and 0.50g (Source: [Ber09])

However, despite the large implicit amplification factors, the analyses for *Load Distribution 2* can still result in considerably unconservative local demand estimations. For example, the displacement predictions for the right edge of bridge configuration 4 can hardly be considered satisfactory. These underpredictions are related to a combination of insufficient higher mode representation and inability to capture the stiffness redistributions at higher levels of inelasticity. Taking into account the rather

strong demand overestimations in large parts of the structures, while nevertheless in other parts of the structures significant underpredictions cannot be ruled out, the results from the *Load Distribution 2* cannot really be considered as acceptable.

Bridge configuration 1 represents a special case in this context. Not only that in this case hardly any difference exists between the results of the two load distributions, but furthermore, here, *Load Distribution 2* does not overpredict the displacement demand of the reference point. This rather extraordinary behavior, compared to that of the other configurations in Fig. 4.43, is related to a large extent to the fact that, for configuration 1, the displacement shape vector $\tilde{\tilde{\phi}}_{RQ,u}$ does not approximate the first mode shape well. Instead, it essentially also represents a uniform shape as for *Load Distribution 1*. Therefore, *Load Distribution 2*, in this case, simply does not serve as an approximation of the anticipated first mode shape. It should be noted that bridge configuration 1, despite its very regular structure and its close to uniform elastic response, actually shows a very complex behavior in the elastic range. This is because the almost uniform elastic response is not coming from a single dominant mode, but is a rather a composition of the first and third mode, having almost the same natural period. For further details see [Ber09], where a detailed analysis of this special behavior is given.
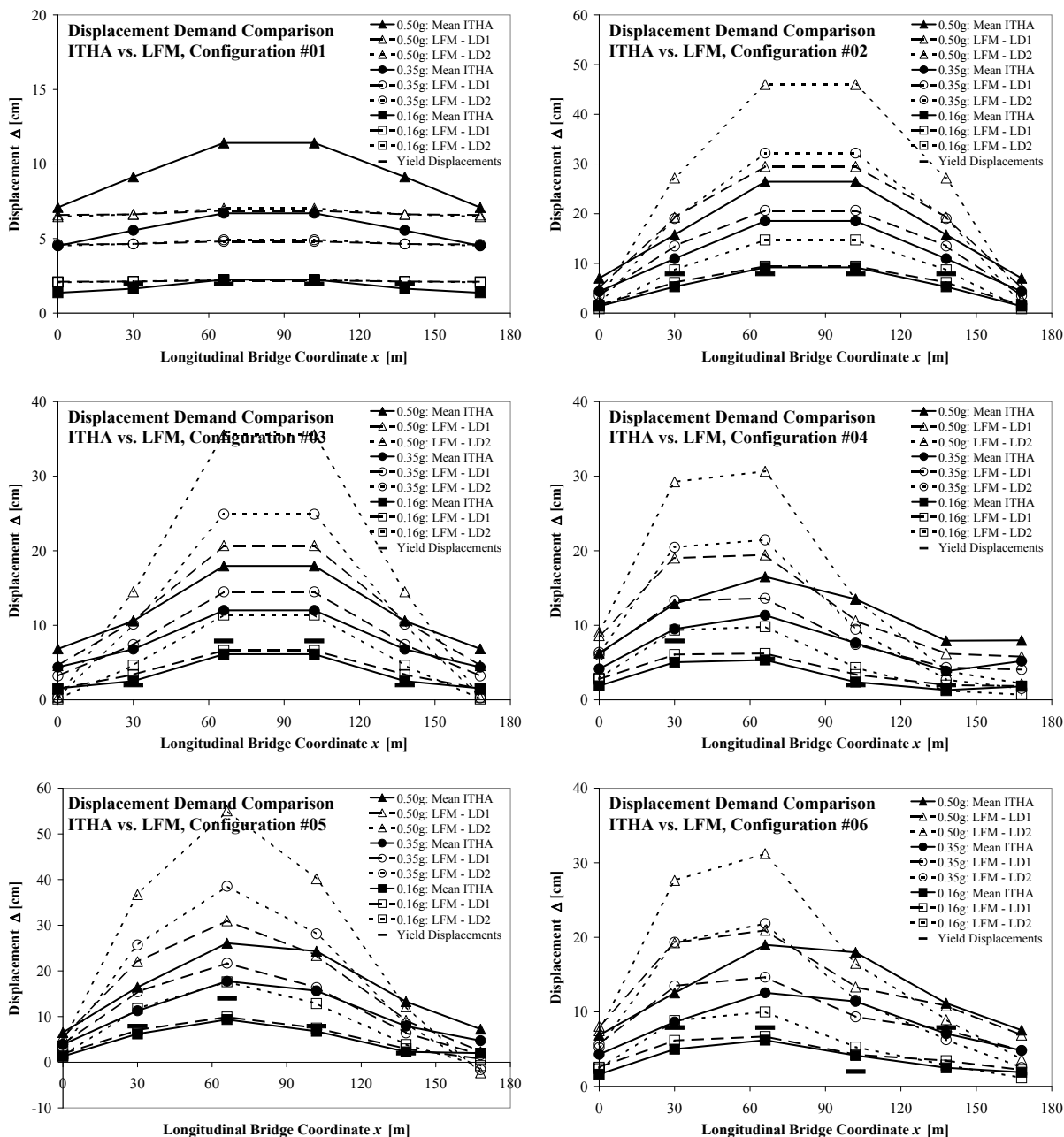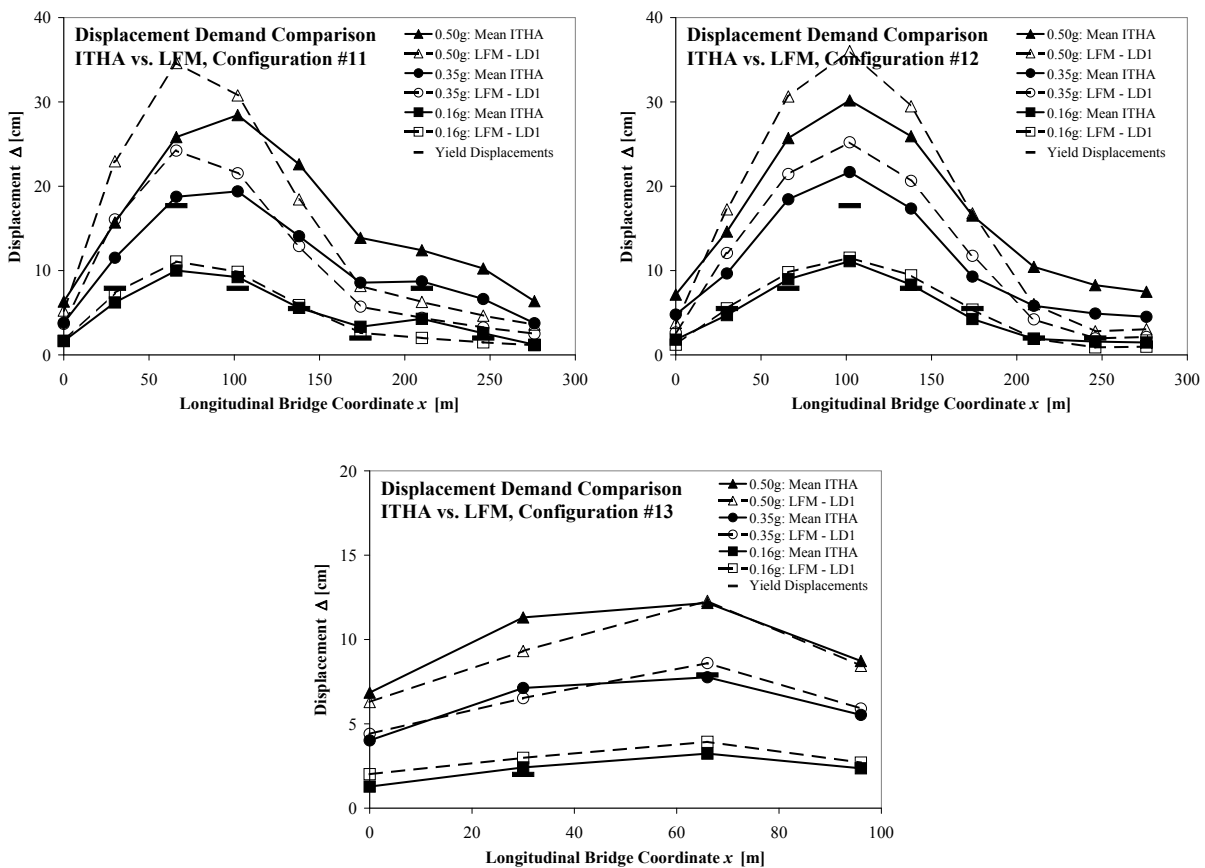

Fig. 4.44: Displacement demands for bridge configurations 11, 12, and 13
from lateral force method (LFM) and ITHA
for transverse excitation at seismicity levels a_{gd} = 0.16g, 0.35g, and 0.50g (Source: [Ber09])

As can be seen from Fig. 4.43 and Fig. 4.44, the displacement demands based on *Load Distribution 1* represent a significantly better approximation of the mean ITHA results than those from *Load Distribution 2*. As a matter of fact, the LD1 results even show some similarities to those from the response spectrum analysis presented previously. The comments made on the RSA results in Subsection *a* with respect to the global deformation demand (represented by the displacement of a reference point), are essentially also valid for the LFM results based on *Load Distribution 1*. As a consequence, the underprediction of the global demand for bridge configuration 1 can mainly be

attributed to the invalidity of the *equal displacement approximation* due to the rather short elastic period of the first mode.

With respect to the displacement shape, the LFM with *Load Distribution 1* conceptually cannot fully capture the elastic higher mode effects as the response spectrum analysis does. However, as discussed in Subsection *a*, the elastic deformation shape becomes invalid with increasing level of inelasticity anyway. It was found that the inelastic action tends to smoothen out the displacement shape, compared to that in the elastic range. In this context it is noteworthy that the uniform acceleration shape of *Load Distribution 1* also results in a somewhat smoother response shape right from the beginning. As a result, this simpler analysis technique in some cases even yields deformation shapes which approximate the mean ITHA response in the inelastic region better than the response spectrum analysis. Examples for such a better approximation at PGA levels of a_{gd} = 0.35g and 0.50g are the bridge configurations 3, 4, and 6. On the other hand, for the configurations 11 and 13, the lateral force method with *Load Distribution 1* performs rather worse than the response spectrum analysis. This is especially pronounced for the right halves of these two bridges, where the response is predominantly controlled by higher modes. Obviously, these cannot be captured well by the lateral force method with LD1. For bridge configurations 1, 2, 5, and 13 the quality of the results from *Load Distribution 1* is more or less comparable to that from the response spectrum analysis.

Summarizing the results from the two load distributions considered by Berweger [Ber09] for the lateral force method, it can be concluded that *Load Distribution 2* is rather inappropriate for a realistic estimation of the displacement demand, independent of the PGA level and the corresponding level of inelasticity. The fact that LD2 is typically overly conservative in some parts of the structures, while it can nevertheless be significantly unconservative in other parts of the same structure, disqualifies it for the given task. *Load Distribution 1* performs significantly better, resulting in a similar overall quality of approximation as the response spectrum analysis. At a_{gd} = 0.16g, the near elastic response of almost all bridges is captured reasonably well. Only in bridge configuration 11 it results in a noticeable demand underestimation for pier 6, where the response spectrum analysis performs better. At higher load and thus inelasticity levels, the lateral force method with *Load Distribution 1* in some cases gives a somewhat better approximation than the response spectrum analysis, while in other cases it performs somewhat worse. The overall quality of the results can be considered as comparable in the two methods, with the deficiencies partly occurring in different configurations and locations.

Due to the poor performance of *Load Distribution 2*, using an envelope of the displacement demands coming from both load distributions, similar to the requirements in the pushover analysis of Eurocode 8, Part 2, Annex H [EC8-2], cannot be recommended. The benefits from such an envelope would be particularly questionable as in many cases the points where *Load Distribution 1* tends to underpredict the demand are the same points where *Load Distribution 2* also yields results which are too low. Therefore, hardly any improvement with respect to avoiding unconservative results would be achieved, while an exaggerated over-conservatism would be introduced at those points which are already predicted well by *Load Distribution 1* alone. If the lateral force method is to be used as an approximate analysis tool, it is therefore recommended to use only *Load Distribution 1*, related to a uniform acceleration shape and a corresponding mass proportional force distribution.

As a concluding remark, it should be mentioned that the above disqualification of the envelope of the two load distributions for the lateral force method cannot be transferred to the original application in the pushover analysis of [EC8-2], Annex H. As shown in Section A2.2.1 of Annex A2, conventional pushover analysis converges towards the lateral force method, when applied on linear elastic systems, but without the artificial increase of the activated mass included in the lateral force method. Therefore, the substantial overestimation of the global deformation demand by *Load Distribution 2* would not result in a conventional pushover analysis. Furthermore, in the specific interpretation of the pushover analysis given in [EC8-2] Annex H, the target displacement is determined from a response spectrum analysis, while the load distributions only influence the (relative) deformation shape. In this form of application, a global demand overestimation from *Load Distribution 2*, comparable to that found in the lateral force method, will not occur either. Therefore, determining the overall displacement demand for design from the envelope of two load distributions in a pushover analysis, might be more reasonable than in the case of the lateral force method discussed above. This aspect will be further discussed in the following Subsection *c*.

c) Conventional Pushover Analysis

The conventional pushover analysis, in some sense, represents an equivalent to the lateral force method, extended for the application on inelastic systems. In this analysis procedure, also an acceleration shape vector is assumed in order to define a (relative) distribution of lateral forces which are to represent the inertia effects of the masses. In contrast to the lateral force method, these lateral forces do not serve for the definition of the global displacement demand, but only for the determination of the inelastic deformation shape. The global deformation demand, expressed by the displacement of a reference point, is determined separately by an appropriate approach. Based on these data, an incremental nonlinear static analysis is performed, in which lateral forces, with the relative distribution outlined above, are incremented until the reference point reaches its target displacement. The resulting displacement shape at this load level defines the deformation demand throughout the entire structure.

Several criteria for the selection of the reference point are conceivable. The provisions of Eurocode 8, Part 2, Annex H [EC8-2], for example, define the reference point for bridges as the center of mass of the superstructure. For building structures it is common practice (e.g. [EC8-1], Annex B) to use the roof level as a reference point, as this is where the largest displacements are to be expected. Generally, the pushover procedure can be applied with any choice for the reference point. However, it appears reasonable to choose a point of rather large displacement as this might be most representative for the global response of the structure. In this text, it is therefore chosen that the reference point is defined as the point of largest displacement at linear demand levels, which can e.g. be determined by means of the response spectrum analysis and using an appropriate superposition rule of the modal responses (SRSS or CQC).

For the estimation of the displacement demand Δ_{ref} of the reference point, several conceptual approaches exist. A common method consists of transforming the multi-degree-of-freedom (MDOF) bridge model into an equivalent single-degree-of-freedom (SDOF) system. For this SDOF model it is possible to estimate the inelastic displacement demand e.g. based on the concepts outlined in Section 4.5. Using the same principles as for the transformation from MDOF to SDOF system, it is then possible to retransform the inelastic SDOF displacement demand to the original MDOF structure and thus estimate the inelastic deformations of the entire structure. The theoretical principles and the underlying approximations of the corresponding transformations between SDOF and MDOF system are outlined in detail in Section A2.2.1 of Annex A2. The practical application can be summarized as follows (see Section A2.2.1 for further details):

(i)   Choose an acceleration shape $\tilde{\tilde{\phi}}_{PO,a}$ in order to define the relative lateral load distribution.

(ii)   Perform a nonlinear static analysis under increasing lateral forces $\tilde{\tilde{F}}_{PO,MDOF}(\beta) = \beta \cdot M \tilde{\tilde{\phi}}_{PO,a}$, with M being the mass matrix of the MDOF system and β being a load increment factor. From this analysis, the corresponding displacement distribution $\tilde{\Delta}_{PO,MDOF}$, including the displacement $\tilde{\Delta}_{PO,MDOF,ref}$ of the reference point, results as a function of the parameter β.

(iii)   Draw the pushover curve of the MDOF system showing the total base shear $V_{b,PO}$ versus the reference point displacement $\tilde{\Delta}_{PO,MDOF,ref}$, as shown on the left side of Fig. 4.45, with the total base shear $V_{b,PO}$ being the sum of the individual forces in the vector $\tilde{\tilde{F}}_{PO,MDOF}$.

(iv)   Define the force $F_{SDOF}(\beta)$ of the equivalent SDOF system as equal to the total base shear $V_{b,PO}(\beta)$ of the MDOF structure. Further, define the displacement $\Delta_{SDOF}(\beta)$ of the equivalent SDOF system according to equation (4.39), where $\tilde{\phi}_{PO,a,ref}$ is the component of the assumed acceleration shape vector $\tilde{\tilde{\phi}}_{PO,a}$ corresponding to the reference point and $\tilde{\Gamma}_{PO,a}$ is the participation factor related to $\tilde{\tilde{\phi}}_{PO,a}$. This way, the force F_{SDOF} and the displacement Δ_{SDOF} of the equivalent SDOF system are known as functions of the parameter β, so that the pushover curve

of the SDOF can be drawn as shown on the right side of Fig. 4.45. This pushover curve represents the nonlinear force-displacement relationship of the equivalent SDOF system.

$$\Delta_{SDOF}(\beta) = \frac{\tilde{\Delta}_{PO,MDOF,ref}(\beta)}{\tilde{\phi}_{PO,a,ref}\tilde{\Gamma}_{PO,a}} \tag{4.39}$$

with
$$\tilde{\Gamma}_{PO,a} = \frac{\vec{1}^{T}M\tilde{\tilde{\phi}}_{PO,a}}{\tilde{\tilde{\phi}}_{PO,a}^{T}M\tilde{\tilde{\phi}}_{PO,a}}$$
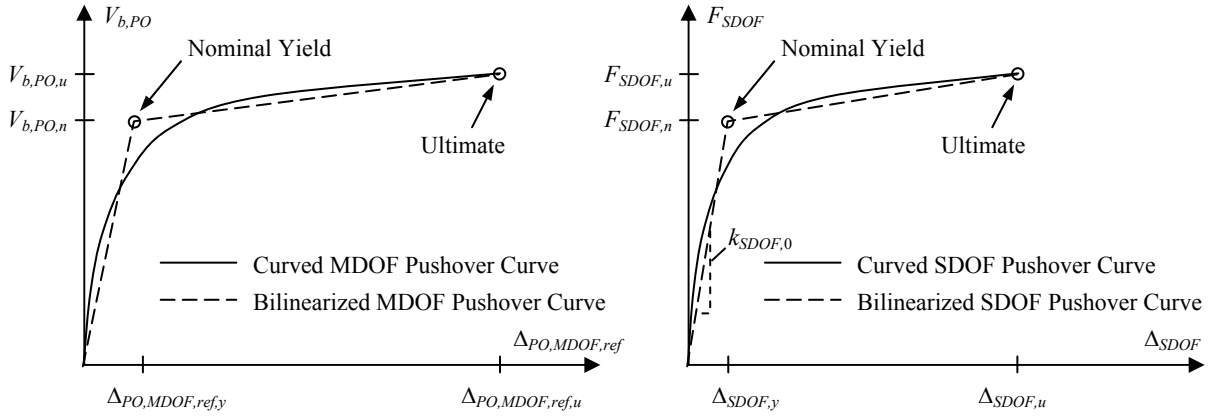

Fig. 4.45: Inelastic pushover curve and corresponding bilinearization
left: Total base shear vs. reference point displacement for MDOF system, right: Equivalent SDOF system

(v) Define the mass m_{SDOF} of the equivalent SDOF system as equal to the effective modal mass $\tilde{m}^{*}_{eff,a}$ of the MDOF structure for the assumed shape vector $\tilde{\tilde{\phi}}_{PO,a}$, as given by equation (4.40).

$$m_{SDOF} = \tilde{m}^{*}_{eff,a} = \tilde{\Gamma}_{PO,a} \cdot \vec{1}^{T}M\tilde{\tilde{\phi}}_{PO,a} \tag{4.40}$$

(vi) Estimate the inelastic displacement demand Δ_{SDOF} of the equivalent SDOF system, having the nonlinear force-displacement relationship and the mass as determined during steps (iv) and (v), respectively. This can, e.g., be done using one of the approaches presented in Section 4.5. For this purpose, it may be necessary to bilinearize the inelastic force-displacement relationship of the SDOF system as indicated by dashed lines in Fig. 4.45. The initial stiffness $k_{SDOF,0}$ can then be used to compute an elastic period $\tilde{T}_{SDOF,0}$ of the equivalent SDOF system. As outlined in Section A2.2.1, the periods of SDOF and MDOF are supposed to be equal so that $\tilde{T}_{SDOF,0}$ can also be estimated using the Rayleigh quotient for the MDOF structure, with the individual members being represented by their initial stiffnesses k_0.

(vii) Retransform the inelastic displacement demand Δ_{SDOF} of the equivalent SDOF system to the MDOF demand of the entire structure. For this purpose, the value of the parameter β is determined at which the SDOF displacement $\Delta_{SDOF}(\beta)$ occurs in the pushover curve. The displacement vector $\tilde{\tilde{\Delta}}_{PO,MDOF}(\beta)$ for the MDOF system then corresponds to the same value of β and follows from the nonlinear static analysis performed in step (ii). All other response quantities, as e.g. internal shear forces, also follow from this nonlinear static analysis under the lateral forces according to $\tilde{\tilde{F}}_{PO,MDOF}(\beta) = \beta \cdot M\tilde{\tilde{\phi}}_{PO,a}$.

The pushover analysis, in the form presented above, does not have a strict mechanical background. However, as outlined in Section A2.2.1, it is theoretically based on principles coming from the response spectrum analysis and the lateral force method. In particular, it is interesting to investigate how the pushover analysis is related to these two approaches if applied to a linear elastic system. As shown in Section A2.3, if the first mode shape of a linear elastic MDOF system is used for the acceleration shape vector $\tilde{\tilde{\phi}}_{PO,a}$ and the displacement demand of the equivalent SDOF is estimated from an elastic response spectrum, then the pushover analysis will exactly reproduce the displacement demand of the elastic first mode. This means that the pushover analysis, in this case, converges towards the first mode displacements from the response spectrum analysis, but fully neglects any higher modes. On a general basis, this result should be considered as rather unconservative.

If any other choice is made for the acceleration shape vector $\tilde{\tilde{\phi}}_{PO,a}$, not being an eigenvector in the modal analysis, then the pushover analysis develops some similarity to the lateral force method being applied with the same acceleration shape vector. As shown in Section A2.3, the pushover results in this case converge to a solution which coincides with the lateral force method if the lateral forces are not increased artificially. This means that the force level in the pushover analysis is implicitly based only on activated masses equal to the effective modal mass $\tilde{m}^*_{eff,a}$ related to the assumed shape vector $\tilde{\tilde{\phi}}_{PO,a}$ as defined in equation (4.40). In contrast, the lateral force method assumes the entire system mass m_{tot} as activated and thus artificially increases the lateral forces. This increase is introduced as an additional safety measure to compensate for higher modes not covered by the analysis and other simplifications inherent to the lateral force method. The pushover analysis, as presented above, in this respect is less conservative than the lateral force method as it does not feature a comparable safety measure.

Berweger [Ber09] applied the pushover analysis according to steps (i) to (vii) on the bridge configurations 1 through 6, using two different assumptions for the acceleration shape vector $\tilde{\tilde{\phi}}_{PO,a}$. The two cases basically correspond to the two load distributions also used in Subsection *b* for the lateral force method. The only difference is that, for the pushover analysis, *Load Distribution 2* is defined using the exact first mode shape and not the approximation coming from the computation of the Rayleigh quotient.

For the estimation of the inelastic SDOF displacement demand, Berweger [Ber09] considered three of the five general approaches presented in Section 4.5. These are the displacement modification factor approach by Ruiz-García and Miranda [RM03] and the two equivalent linearization approaches by Priestley *et al.* [PCK07] and Guyader [Guy04]. As outlined in Section 4.5.2, for the practical application of the equivalent linearization approaches several variants exist as they additionally require a relationship $\eta(\xi)$ to transform elastic response spectra between different viscous damping ratios. In the study by Berweger [Ber09] only the relationship according to equation (4.7), as defined in [EC8-1] and [SIA261], was used. For the approach by Priestley *et al.* [PCK07] further permutations of practical applications exist as the method distinguishes between constant and tangent stiffness proportional elastic viscous damping. Berweger here only considered constant damping with a viscous damping ratio of $\xi_{el} = 5\%$ as in all the other analyses as well.

Due to the large number of data related to different load distributions and various procedures for the SDOF demand estimation, the corresponding quantitative results will not be reproduced here. For detailed information on these results the reader is referred to the original study by Berweger [Ber09]. As shown in Section 4.5.2, the choice of the $\eta(\xi)$ relationship for the spectrum transformations in the equivalent linearization approaches can influence the results significantly. Therefore, empirically comparing the results of only one (rather arbitrary) choice for $\eta(\xi)$ to the ITHA reference demands does not allow substantiated conclusions about the two equivalent linearization methods anyway. Instead, in Section 4.6.3 a more detailed evaluation is presented, including also other methods for the inelastic SDOF demand estimation discussed in Section 4.5. For the proposals that are developed based on this evaluation, quantitative results will be presented in Section 4.6.3.

An alternative implementation of the pushover concept, slightly differing from the steps (i) through (vii) summarized above, is given in Eurocode 8, Part 2, Annex H [EC8-2]. In this procedure, the displacement demand of the reference point is not determined by transformation into an equivalent inelastic SDOF system. Instead, it is taken equal to its displacement resulting from the linear elastic response spectrum analysis, conducted with the initial stiffnesses k_0 of the individual members, as discussed in Subsection a. The actual pushover analysis therefore only serves for the estimation of the (relative) displacement shape by means of a nonlinear static analysis, while the global deformation demand, represented by the displacement of the reference point, is taken from the response spectrum analysis.

As a consequence, only the first two steps of the general concept outlined above remain. In step (ii) the loads are then incremented until the reference point reaches its already known target displacement (from the response spectrum analysis). It should be noted that this target displacement is not only based on the first mode response, but is a result of the modal superposition in the framework of the response spectrum analysis. For the practical application, [EC8-2] Annex H prescribes that the two load distributions mentioned above are to be considered for the nonlinear static analysis, i.e. on one hand a uniform acceleration shape (resulting in a mass proportional force distribution) and on the other hand a first mode proportional acceleration shape. The design shall then be based on the envelope of the two resulting deformation shapes, i.e. the maximum of both demand estimations at each point.

The reasoning of the provisions in [EC8-2] Annex H for the determination of the target displacement can be explained best by considering the application of the approach on a linear elastic MDOF structure. As mentioned previously, it is shown in Section A2.3 that the implementation according to the above steps (i) through (vii) results in a reference point displacement equal to that of the first mode in the response spectrum analysis if the corresponding first mode shape is used as an acceleration shape vector. This means that, for a linear elastic system with *Load Distribution 2* (LD2), steps (i) through (vii) result in a similar response prediction as the [EC8-2] approach. The only difference is that in the latter case the displacement demand of the reference point additionally includes the contributions from higher modes. This aspect appears more consistent in the [EC8-2] provisions as the implicit neglect of the higher modes in the above steps (i) through (vii) is unconservative.

For the case of *Load Distribution 1* (LD1), in the application of steps (i) through (vii) the demand estimation of the reference point and the nonlinear static analysis defining the displacement shape are based on this same load distribution. This is different in the [EC8-2] approach, where the target displacement of the reference point is still kept the same as before, coming from the modal superposition in the response spectrum analysis. Here, only the nonlinear static analysis for the determination of the displacement shape is performed with the alternative *Load Distribution 1*.

As there is no strict theoretical background for the pushover analysis in general, it is not necessarily required that the load distribution for the estimation of the reference point displacement must be the same as that used in the nonlinear static analysis for the determination of the deformation shape. Therefore, it may be a reasonable approach to use two different load distributions for the two parts of the analysis, with each one chosen to be best suited for the individual task. A similar concept is essentially followed by the provisions of [EC8-2] Annex H. If the convergence of the procedures, being applied on linear elastic systems, is considered as a plausibility check, then the way of defining the target displacement Δ_{ref} of the reference point in [EC8-2] Annex H appears superior to that according to the above steps (i) through (vii) based on an equivalent SDOF system. Including the contributions of higher modes is necessary for a consistent estimation of Δ_{ref}.

Using the target displacement, coming from the response spectrum analysis, also for inelastic response, implicitly corresponds to the application of the *equal displacement approximation* for Δ_{ref}. This assumption bears all the inherent consequences outlined in Section 4.5.1, being also discussed in Subsection a for the application of the response spectrum analysis on inelastic systems. Especially, this refers to the likely unconservative demand estimations for structures with an elastic first mode in the short period range. It may conceptually be possible to allow for these effects by introducing a displacement modification factor as described in Section 4.5, but this is not included in [EC8-2] Annex H. With respect to this aspect, the procedure defined by the above steps (i) through (vii) may therefore be considered as superior if the demand estimation for the equivalent SDOF system includes

the effects from inelastic response in an appropriate manner. However, a combination of both procedures, using the reference point target displacement from the response spectrum analysis, as in [EC8-2] Annex H, but including additionally a displacement modification factor to account for potential demand increases related to the inelastic behavior, could be a very promising solution. Such an approach will be further developed in Section 4.6.3 in order to propose an improved method.

The original pushover (PO) procedure of [EC8-2] Annex H, using the two different load distributions in combination with the (unmodified) reference point target displacement from the response spectrum analysis, has been applied by Berweger [Ber09] on all nine bridge configurations considered in his study. The corresponding results are compared in Fig. 4.46 and Fig. 4.47 to mean displacement demands computed by ITHA.
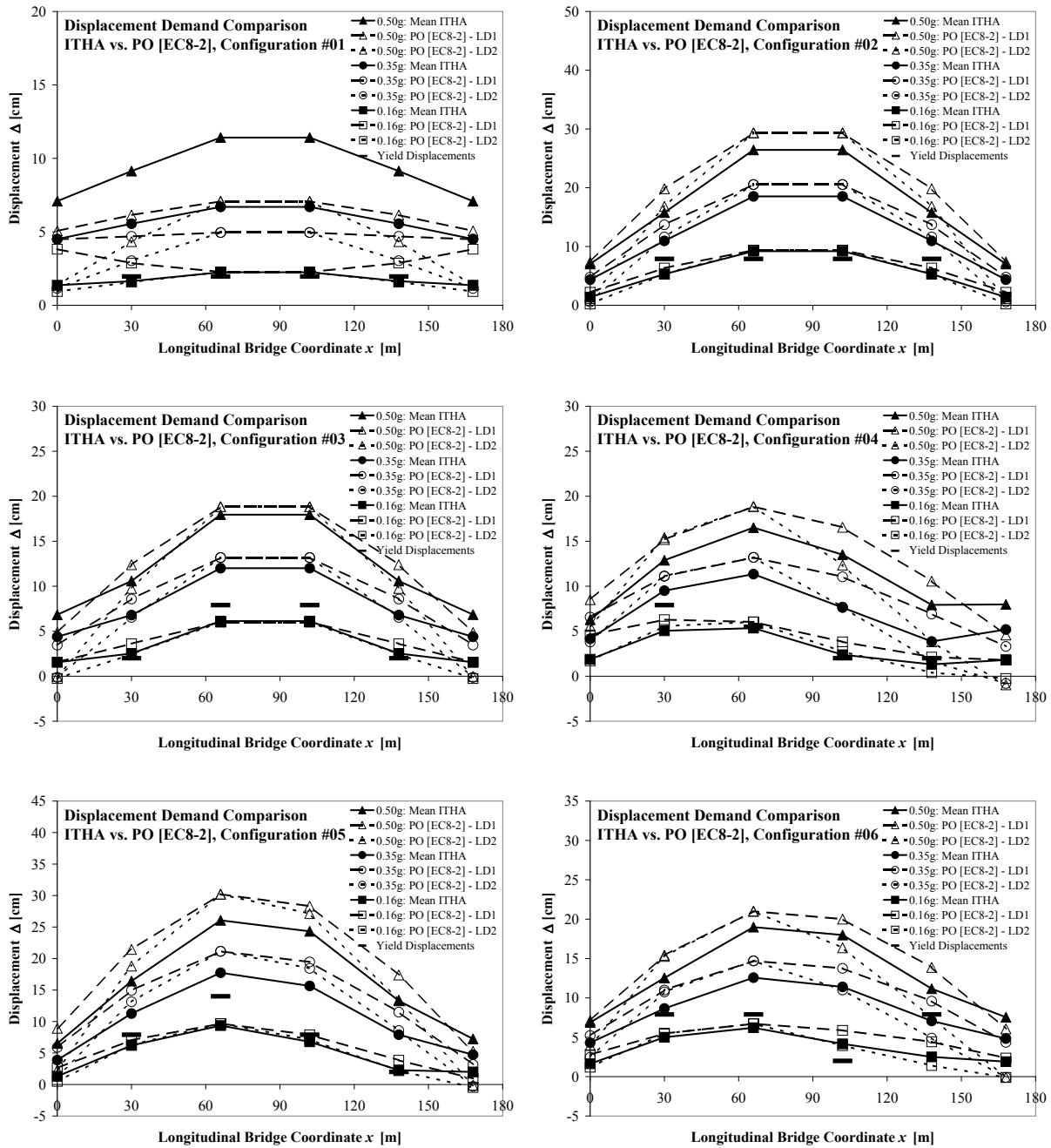

Fig. 4.46: Displacement demands for bridge configurations 1 through 6
from pushover analysis (PO) according to [EC8-2] Annex H and ITHA
for transverse excitation at seismicity levels a_{gd} = 0.16g, 0.35g, and 0.50g (Source: [Ber09])

4.6 Simplified Demand Estimation of Inelastic MDOF Systems

The presented curves show that, in this form of pushover analysis, the substantial global demand overestimations previously encountered for *Load Distribution 2* in the lateral force method (Subsection *b*) do not occur. This is related to the fact that, by definition, in the approach of [EC8-2] Annex H the target displacement of the reference point is determined separately based on the response spectrum analysis, thus resulting equal for any load distribution. As a consequence, all comments made in Subsection *a* with respect to the global displacement demand of the reference point in the context of the response spectrum analysis equally apply for the pushover analysis according to [EC8-2] Annex H.
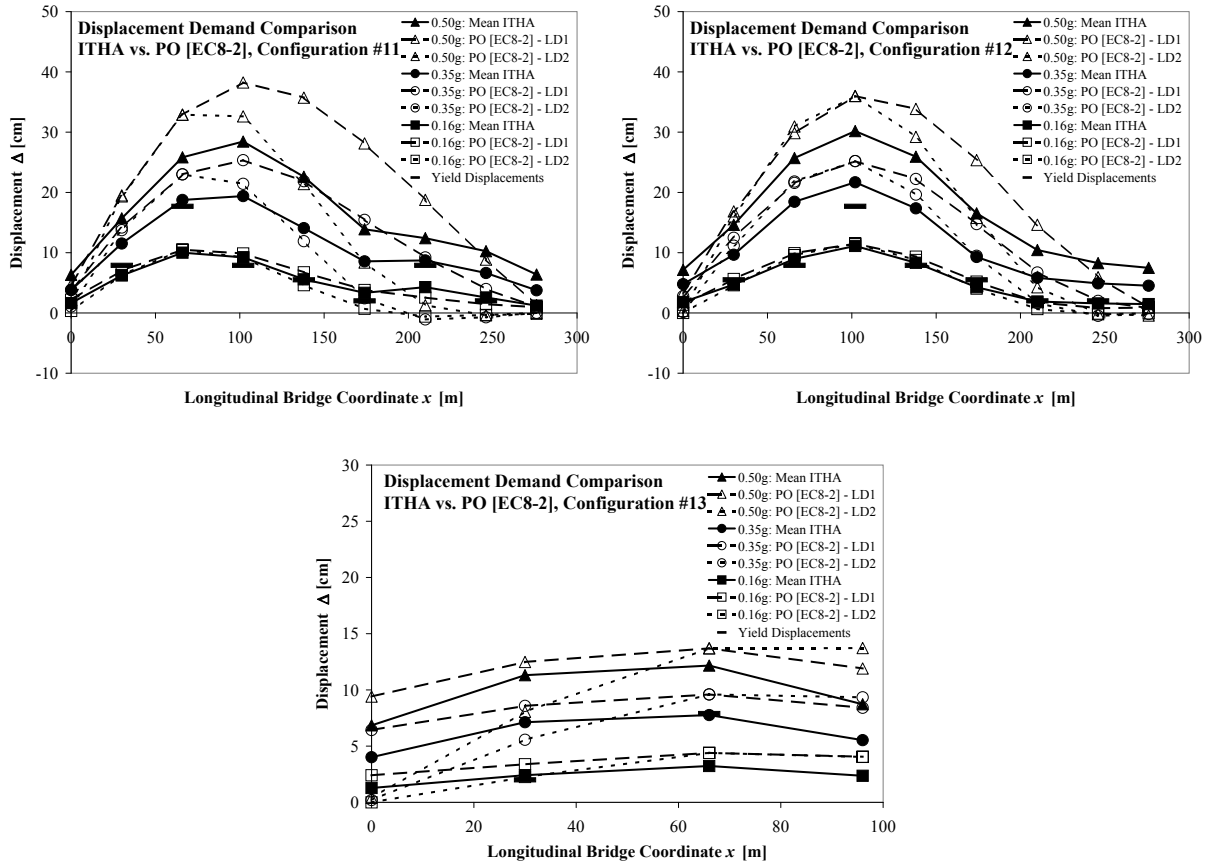

*Fig. 4.47: Displacement demands for bridge configurations 11, 12, and 13
from pushover analysis (PO) according to [EC8-2] Annex H and ITHA
for transverse excitation at seismicity levels a_{gd} = 0.16g, 0.35g, and 0.50g (Source: [Ber09])*

As can be seen in Fig. 4.46 and Fig. 4.47, for many bridge configurations the implicit *equal displacement approximation* tends to result in rather reasonable and slightly conservative demand estimations for the reference point (e.g. configurations 2, through 6 and 13). For the two longer bridge configurations 11 and 12, the overestimation of the reference point displacement is somewhat more pronounced, which may be attributed to the longer fundamental periods (see Tab. 4.11). Clearly problematic is again the substantial underestimation of the reference point displacement for bridge configuration 1. This deficiency, already encountered in Subsection *a*, is related to the rather short fundamental period of the bridge and the corresponding invalidity of the *equal displacement approximation* (see Section 4.5.1). Potential ways to improve the response prediction for such cases will be discussed in Section 4.6.3.

With respect to the choice of an appropriate load distribution, the results in Fig. 4.46 and Fig. 4.47 suggest that *Load Distribution 1* (LD1) based on a uniform acceleration shape in the majority of cases tends to result in a better approximation of the relative deformation shape than the first mode proportional *Load Distribution 2* (LD2). This effect is largely related to the fact that LD2 cannot cover higher mode effects nor is it able to capture the change of the displacement shape at increasing levels of inelasticity. *Load Distribution 1* does not explicitly account for either of these two aspects.

However, its less concentrated force distribution comes closer to that which typically develops under the influence of higher mode effects and inelastic stiffness redistributions. In particular, LD2 may be considered more "effective" in causing large deformations of the reference point.

As the target displacement of the reference point by definition is equal for both load distributions, LD2 typically reaches this value with a lower sum of all forces (i.e. total base shear) than LD1. In contrast, LD1 displaces other points of the structure further than LD2 for the same target displacement of the reference point. This effect tends to compensate somewhat for the deficiencies related to higher mode effects and stiffness redistributions not covered by LD2. As a consequence, in many cases *Load Distribution 1* results in a more conservative displacement shape than *Load Distribution 2*. This is confirmed by the curves shown in Fig. 4.46 and Fig. 4.47 where the displacement shapes related to LD1 often represent some kind of envelopes by themselves.

One case where the pushover analysis with LD1 results in a rather erroneous deformation shape occurs for bridge configuration 1 at a_{gd} = 0.16g. Here, the displacements at the abutments are largely overestimated by the pushover analysis with *Load Distribution 1*. This effect can be attributed largely to the chosen Ramberg-Osgood abutment model. The ITHA captures its very specific continuous stiffness change and the hysteretic energy dissipation characteristics already at small displacements, which mutually counteract and therefore cancel each other out to some extent. In contrast, the pushover analysis can only cover the continuous softening of the curved Ramberg-Osgood model, while the hysteretic energy dissipation, developing concurrently, is not captured. This effect results in an overestimation of the abutment displacements by the pushover analysis with LD1. However, as this error does not cause any unconservative results, it might be considered as still acceptable.

Comparing the results of the two load distributions shown in Fig. 4.46 and Fig. 4.47, it appears that LD2 does not really result in good demand estimations. For the nine bridge configurations considered by Berweger [Ber09], LD1 provides a significantly better representation of the mean response determined by ITHA for almost all PGA levels. Building an envelope of the results from LD1 and LD2, in the majority of cases hardly changes the results, compared to LD1 only, as the latter load distribution is almost always more conservative than LD2 (see discussion above). As a result, the response estimations using LD1 can be considered as reasonably good for bridge configurations 2 through 6 and 13. The demand underpredictions for bridge configuration 1 are related to the deficiencies in the estimation of the target displacement for the reference point and are therefore independent of the load distribution. But even in this case, the relative deformation shape for LD1 in the inelastic range can be considered as acceptable. For the two longer bridge configurations 11 and 12, *Load Distribution 1* gives conservative results over large part of the structure. However, at the edges of both bridges, where the response is mainly controlled by higher modes, some demand underpredictions can be found also for LD1. Here, the simplified load distribution, based on the uniform acceleration shape, somewhat reaches its limits.

Summarizing, it can be said that for the application of the pushover analysis according to [EC8-2] Annex H, *Load Distribution 1* was found to provide better demand estimations than *Load Distribution 2*. In some cases, the quality of the results is somewhat better for the inner part of the bridge than at the edges. If the primary focus of the analysis is only on the deformation demand of the piers, while the abutment models only serve as (possibly realistic) boundary conditions, then some deficiencies in the displacement prediction for the abutments may still be acceptable.

d) Multi-Modal Pushover Analysis

In more complex and irregular bridges, higher mode effects can have a significant influence on the response of the structure, as also confirmed by the results presented in the previous subsections. As the conventional pushover analysis is based on a single constant acceleration shape, it rather approximates the response of only one mode. Therefore, it cannot capture realistically the demand at every location in more complex systems. To improve the response predictions of structure where higher mode effects play a significant role, Chopra and Goel [CG02] have proposed an enhanced approach being called *multi-modal pushover analysis*. The procedure can be considered as a combination of principles coming from the pushover analysis outlined in Subsection *c* and the response spectrum analysis discussed in Subsection *a*.

The *multi-modal pushover analysis* (MMP) by Chopra and Goel [CG02] consists of performing several pushover analyses corresponding to the individual modes of the structure and combining the results by means of a modal superposition rule. For this purpose, at first a modal analysis is conducted in order to determine the modal shape vectors based on the initial elastic stiffnesses of the members. Then separate pushover analyses, i.e. nonlinear static analyses, are performed, in which each time the acceleration shape vector for the determination of the relative force distribution is set equal to a different elastic mode shape. The selection of the reference points and estimation of the corresponding target displacements are also determined independently based on the individual mode shape vectors using the same principals as in the conventional pushover analysis described in Subsection *c*. As a consequence, each pushover analysis is supposed to provide some form of inelastic response estimation to a single mode. As in the response spectrum analysis, these individual modal responses then are superimposed by the SRSS or CQC rule.

Berweger [Ber09] applied the concept of the multi-modal pushover analysis on his nine bridge configurations. For each individual mode, he defined the reference point as the point of largest elastic displacement, i.e. equal to the degree of freedom with the largest value in the mode shape vector. For the determination of the target displacements of these reference points, he followed the general principles of the pushover analysis according to [EC8-2] Annex H. This means that the target displacements are taken from the response spectrum analysis, implicitly presuming the validity of the *equal displacement approximation*. While the original pushover analysis of [EC8-2] Annex H (as discussed in Subsection *c*) requires that the target displacement is equal to the SRSS or CQC superimposed value from the response spectrum analysis, for the various modal pushover analyses in the MMP, only the corresponding individual modal displacements of the reference points are to be used.

It should be noted that, theoretically, for every elastic mode of the structure an individual pushover analysis has to be performed for a complete description of the system response. However, in order to reduce the amount of effort in larger systems with several degrees of freedom, it should be sufficient to include only a limited number of the most relevant modes as is also common practice in response spectrum analyses. In the study by Berweger [Ber09], e.g., only two modes were used for bridge configurations 1 through 6 and 3 modes were considered for the configurations 11 through 13. For more complex structures with several relevant modes, it might become necessary to make a trade-off between, on one hand, required accuracy of the analysis and, on the other hand, efficiency of application, i.e. the intention to limit the number of pushover analyses.

In this context it should be noted that performing several separate nonlinear static analysis for the individual modes appears mechanically somewhat questionable. The purpose of the inelastic analysis is to reproduce the change and redistribution of the stiffnesses within the structure. However, these effects depend on the *total* member deformations resulting from all modes together and not only on the deformations of the single modes, as implicitly modeled by the separate pushover analyses performed in the framework of the MMP according to [CG02]. Assuming that one mode exists which is rather dominant for the response (typically the first mode), two possibilities result for the higher modes. Either their deformations are so small that the corresponding modal response remains essentially in the elastic range, or the developing plastic mechanisms are likely to be erroneous because under consideration of the entire response probably other combinations of plastic hinges would develop.

Therefore, especially for the higher modes, the nonlinear analyses are lacking a strict mechanical justification. The MMP approach can nevertheless provide good approximate results, but it appears questionable if the effort for the nonlinear static analyses in the higher modes is really justified. The difference between a (simpler) linear elastic analysis and a nonlinear analysis is only related to the different stiffness assumptions. If the *equal displacement approximation* is considered to be roughly appropriate, then the difference between linear and nonlinear analyses will even be limited to the shape of the modal displacements, while the global level of deformations is assumed to be similar. Taking into account that the internal stiffness distributions in the higher modes are not captured correctly by the isolated modal pushover analyses anyway, it appears that the effort for the nonlinear – instead of a simple linear – analyses might not really improve the quality of the approximation. In this case, the extra effort for conducting such nonlinear analyses in the higher modes as well would not be justified.

This is even more so as linear analyses for the higher modes do not even have to be performed explicitly if a response spectrum analysis has been conducted previously. As such a response spectrum analysis is required anyway for the determination of the individual modeshapes and the target displacements, the linear displacement demands of all modes are already available without further analysis. Based on these considerations, it is possible to modify the MMP approach by Chopra and Goel [CG02] in a sense that only for the first (dominant) mode an inelastic pushover analysis is performed, while the higher modes are taken directly from the linear elastic response spectrum analysis. Aside from this amendment, all other steps in this modified approach remain the same as in the original procedure according to [CG02]. This means that for the first mode pushover analysis, the target displacement of the reference point is still taken equal to the corresponding first mode displacement according to the response spectrum analysis. The resulting displacements are then superimposed with the elastic RSA higher mode displacements using either the SRSS or the CQC rule to compute the total displacement demand. This procedure is equal to a proposal by Chopra *et al.* [CGC04] and will be referred to as *modified multi-modal pushover analysis* (mod MMP) in the following text. The underlying notion that inelastic behavior primarily influences the first mode response, while the higher mode behavior can be approximated well by linear elastic models, is inline with similar findings and concepts by other researchers (e.g. [EK88], [RRC02], [Pri03], [Alv04], [PCK07]).

It should be noted that, for the reference point of the first mode, the modified multi-modal pushover analysis, the conventional pushover analysis according to [EC8-2] Annex H and the response spectrum analysis, all result in the same displacement demand. For the original multi-modal pushover analysis according to [CG02] this is true only approximately as the individual modes are likely to have different reference points. It might further be noted that in the modified approach it is easily possible to include the response of all modes, even for very complex structures with a large number of dynamic degrees of freedom. As no pushover analyses are required for the higher modes, the trade-off between accuracy and efficiency, as in the original MMP procedure, is not necessary anymore. In some cases, this might improve the quality of the demand estimations in practical applications.

Berweger applied both approaches, the original MMP according to [CG02] and the modified MMP, in his study [Ber09]. The results of these analyses are compared in Fig. 4.48 and Fig. 4.49 to the mean ITHA displacement demands. Due to the equality of the reference point displacements with results from the RSA and the conventional pushover analysis according to [EC8-2] Annex H, all comments made in Subsections *a* and *c* with respect to this aspect also apply here. This is especially the case for the considerable underprediction found in bridge configuration 1. The corresponding discussions and the considerations to potentially overcome this problem will not be repeated here (see Subsections *a* and *c* instead).

The conceptual differences between the results presented in Fig. 4.48 and Fig. 4.49, on one hand, and those from the response spectrum analysis (Fig. 4.41 and Fig. 4.42) and the pushover analysis according to [EC8-2] Annex H (Fig. 4.46 and Fig. 4.47), on the other hand, are therefore limited to the displacement shapes. Comparing the curves for the two variants of the multi-modal pushover analysis, it can be seen that in the majority of cases only small differences exist between the two sets of results. This can be attributed to the fact that the nonlinear analyses for the higher modes in the original MMP according to [CG02] often hardly enter into the inelastic range. As long as the response in the

individual modes remains elastic, no difference between the pushover analyses and the linear RSA modal displacements result. In this context the continuously curved Ramberg-Osgood model used for the abutments becomes noticeable as it does not feature an initial linear elastic range. As a consequence, at the abutments, a little more pronounced response differences between the two MMP interpretations can be encountered in some cases.
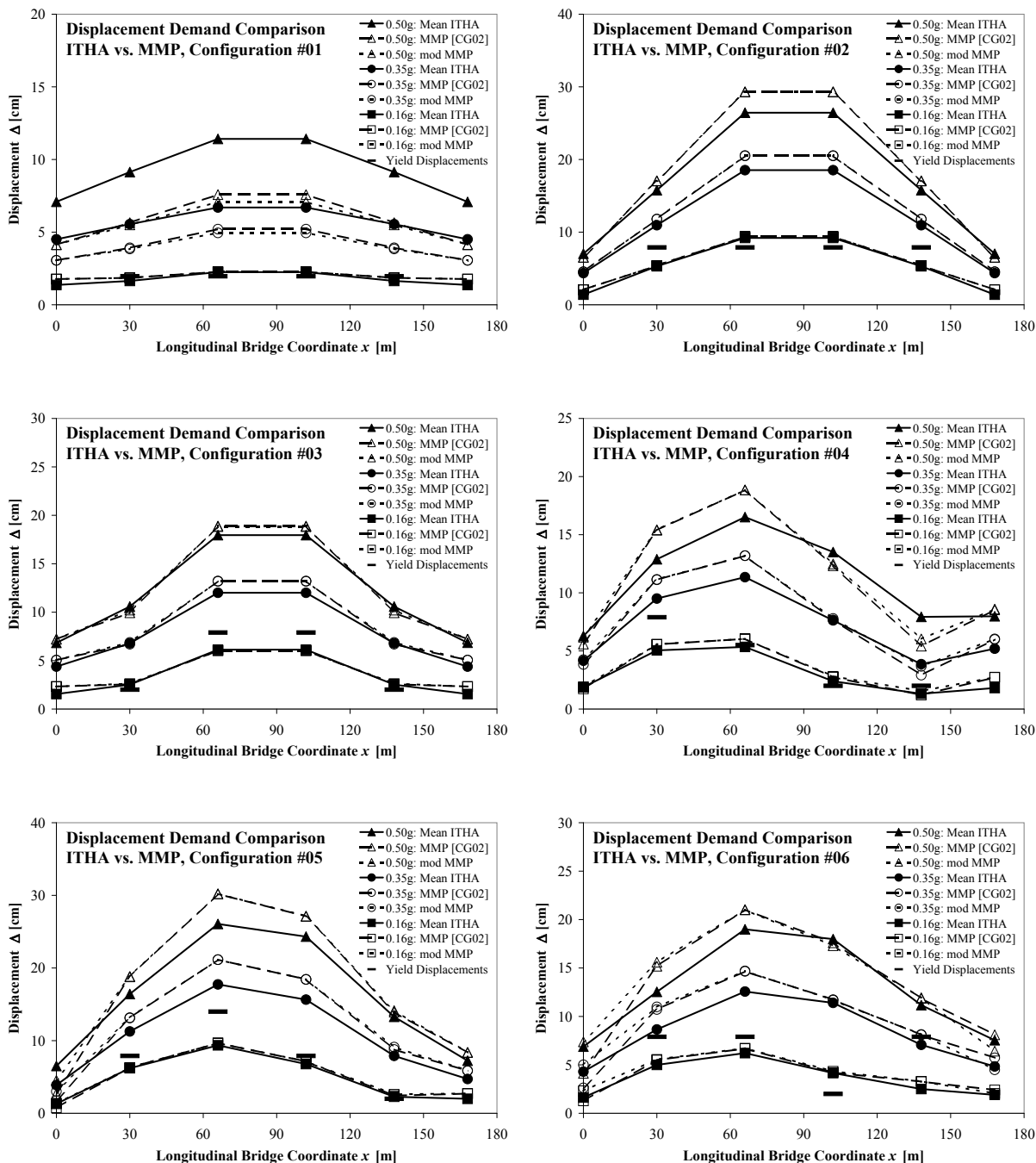

Fig. 4.48: Displacement demands for bridge configurations 1 through 6
from multi-modal pushover analysis (MMP) and ITHA
for transverse excitation at seismicity levels a_{gd} = 0.16g, 0.35g, and 0.50g (Source: [Ber09])

Another case where the two MMP approaches give somewhat different results can be found in the right third of bridge configuration 12 at PGA levels of a_{gd} = 0.35g and 0.50g. The different demand predictions in these cases are related to the fact that in this region the response is strongly controlled by higher modes which deform the piers into the inelastic range at the mentioned PGA levels. As a consequence, this is a case where using the elastic higher mode displacements from the response

spectrum analysis cannot capture the behavior adequately. The original MMP according to [CG02] appears more appropriate for this special case, as it attempts to reproduce the inelastic higher mode response. However, although the original MMP really gives a somewhat better approximation of the mean ITHA results, it also still underestimates the response considerably, especially at $a_{gd} = 0.50$g.
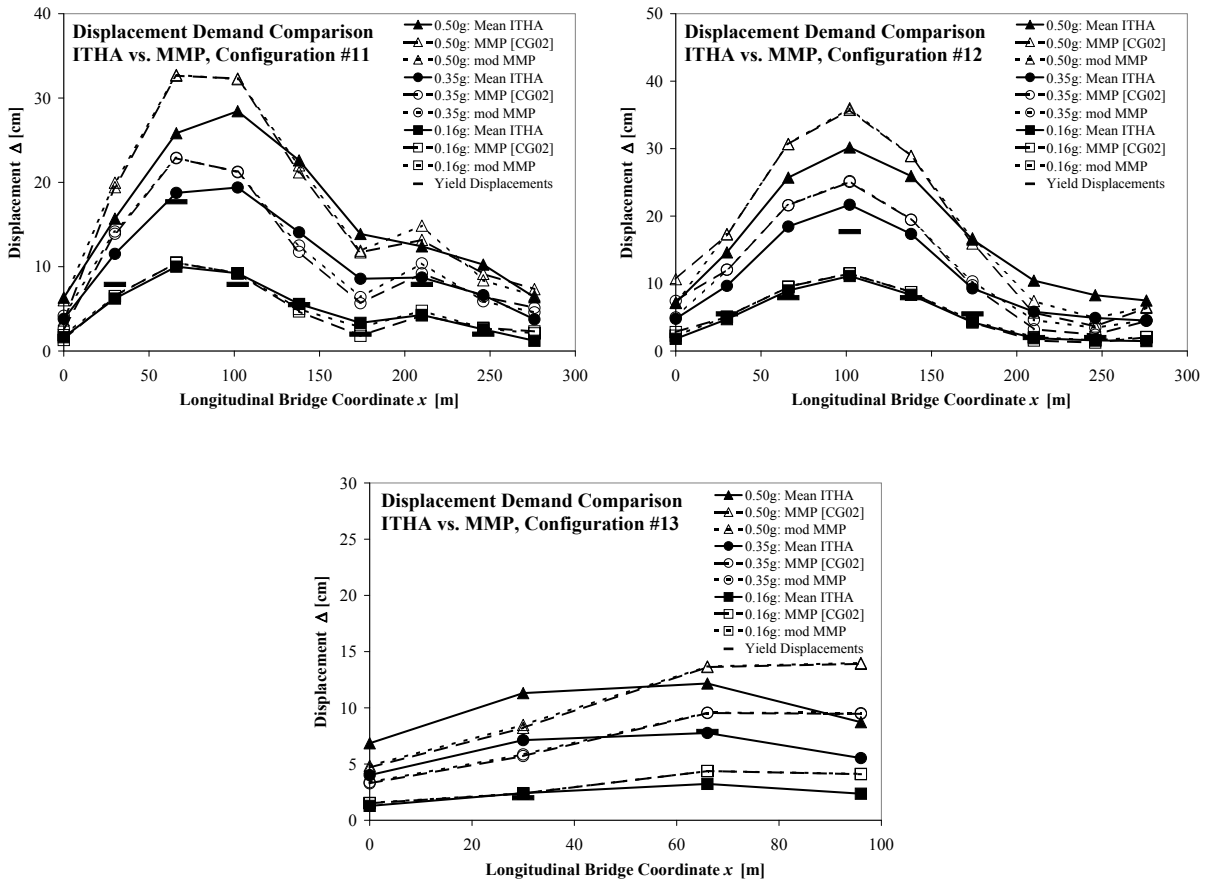

Fig. 4.49: Displacement demands for bridge configurations 11, 12, and 13
from multi-modal pushover analysis (MMP) and ITHA
for transverse excitation at seismicity levels a_{gd} = 0.16g, 0.35g, and 0.50g (Source: [Ber09])

Comparing the results of both MMP procedures to those from the conventional pushover analysis according to [EC8-2] Annex H or those from the response spectrum analysis, significant improvements of the response predictions can be found. The MMP solutions reproduce the general deformation shapes fairly better than the other two methods. It can be seen that the MMP is really capable of mitigating the individual deficiencies of the two alternative procedures. Compared to the response spectrum analysis, the MMP is able to partly correct the errors related to the neglect of inelasticity and the subsequent change of the deformation shape due to the internal stiffness redistribution. At the same time, it essentially maintains the capability of the response spectrum analysis to capture higher mode effects. Comparing the MMP solutions to the conventional pushover analysis according to [EC8-2] Annex H, the situation is just the other way around. Here, the MMP introduces the allowance of higher mode effects, missing in the [EC8-2] approach, while maintaining the capability to consider the influence of inelastic behavior.

As a consequence, comparing the response curves from the MMP approaches to those of the other two concepts, it can be seen that the improvements found in the MMP solutions really appear to come from a mitigation of the mentioned deficiencies in the RSA and conventional pushover procedure. Although the MMP results can therefore be considered as a significant improvement over the procedures discussed in previous subsections and the response predictions often represent reasonably good approximations to the mean ITHA results, some cases still exist where the MMP deformation shapes are, at least locally, unconservative. It may be noted that, for the configurations considered in the study

by Berweger [Ber09], at almost all points where the MMP estimation is unconservative, the corresponding solution from [EC8-2] Annex H using the uniform *Load Distribution 1* tends to be conservative.

If a rather conservative response prediction is required, it might therefore be an option to perform a MMP as well as a conventional pushover analysis according to [EC8-2] Annex H (with LD1) and use the envelope of both sets of results for the assessment. This approach would be similar to that currently adopted in [EC8-2] Annex H, only that the pushover analysis using LD2 would be replaced by a multi-modal pushover analysis. In this case, it might be considered sufficient to use the simpler *modified multi-pushover analysis* outlined above, which only requires a single nonlinear static analysis. At least for the bridge configurations considered in [Ber09], the response prediction at the only points where the modified MMP really performed noticeably worse than the original MMP version according to [CG02] (i.e. the right edge region of configuration 12) would be governed by the second analysis according to [EC8-2] Annex H with LD1.

The combination of the modified MMP with the conventional pushover analysis results here in a safer response estimation compared to the more demanding original MMP. For the combined application of the modified MMP and the conventional pushover analysis with LD1, a response spectrum analysis and two nonlinear static analyses have to be conducted. This represents the same effort as required by the current provisions of [EC8-2] Annex H. However, the data shown in Fig. 4.46 through Fig. 4.49 suggest that the modified envelope is likely to result in a more reliable demand estimation. A strategy to resolve the considerable underprediction of the global response of bridge configuration 1, which is related to the invalidity of the *equal displacement approximation*, will be proposed in Section 4.6.3.

e) Substitute Structure Method

The *substitute structure method* (SSM) can be considered as an extension of the equivalent linearization principles, outlined in Section 4.5.2, to multi-degree-of-freedom systems. Its theoretical background is based on the works by Gülkan and Sozen [GS74] on the visco-elastic representation of inelastic SDOF systems and that by Shibata and Sozen [SS76] on the equivalent visco-elastic modeling of inelastic MDOF structures. Conceptually, the approach is able to take into account all three aspects relevant for an adequate representation of the inelastic MDOF response, as identified above in Section 4.6, i.e. the influence of inelasticity on the global deformation demand as well as on the displacement shape and the influence of higher modes.

The concept applies the same principles of the equivalent linearization presented in Section 4.5.2 for SDOF systems in an equivalent manner to the individual members of an MDOF structure. This means that the inelastic load-deformation relationship of each member is replaced by the secant stiffness up to peak response. To take into account the hysteretic energy dissipation of the inelastic system, an equivalent viscous damping ratio for each member is determined. This equivalent viscous damping ratio depends on the ductility demand in the individual member and can be determined using the same principles as those presented in Section 4.5.2. Shibata and Sozen [SS76] suggest that a smeared average viscous damping ratio for the entire MDOF system can be computed by weighting the various damping ratios by the deformation energy of the individual members. In this case, the deformation energy in the members is computed based on the linearized secant stiffness representation and not on the original nonlinear load-deformation relationship.

Using the linearized member stiffnesses and the average viscous damping ratio, as determined above, a linear dynamic MDOF model of the structure can be assembled. While it is conceptually possible to analyze this model using any appropriate technique (as e.g. a linear time history analysis), the considerable advantage of the substitute structure representation lies in the applicability of the response spectrum analysis, which is very efficient and furthermore also implemented in many software codes. Despite this efficiency of the analysis method, the practical application of the substitute structure method in an assessment case can still require considerable effort. This is related to the fact that both, the secant stiffnesses as well as the equivalent viscous damping, depend on the deformation demand which is only known after the analysis. As a consequence, the procedure can only be conducted iteratively requiring several linear analyses to achieve a satisfying convergence.

Berweger [Ber09] used the principles of the substitute structure method and applied the response spectrum analysis on models of bridge configurations 1 through 6 which had been linearized correspondingly. While Shibata and Sozen [SS76] provide a relationship to determine the ductility dependent viscous damping ratio, based on the recommendations by Gülkan and Sozen [GS74], Berweger [Ber09] used the more recently developed equations by Priestley *et al.* [PCK07] presented in Section 4.5.2*a*. The seismic input for the substitute structure method, conducted by a response spectrum analysis, is defined by an elastic response spectrum related to the previously determined average viscous damping ratio. As discussed in Section 4.4.2, several different proposals exist for the transformation of response spectra between different viscous damping ratios. This aspect introduces some additional uncertainty into the application of the method. In the study by Berweger [Ber09], only the transformation relationship according to equation (4.7), as defined in [EC8-1] and [SIA261], was considered. Therefore, all results are related only to this approach and any conclusions from the interpretation of these results are limited to this particular form of application.

The results computed by Berweger [Ber09] for the bridge configurations 1 through 6 using the substitute structure method (SSM) are compared to the mean ITHA displacements in Fig. 4.50. The data show that in most cases the (relative) deformation shapes are predicted reasonably well by the substitute structure method. It can be seen that the representation using the secant stiffnesses indeed provides better estimations of the deformation shape than the response spectrum analysis using initial elastic stiffnesses, as presented in Subsection *a* (see Fig. 4.41). This suggests that the relative redistribution of internal stiffnesses is more or less captured by the substitute structure method. On the other hand, comparing the SSM results to the data shown in Fig. 4.48, it appears that the multi-modal pushover analysis in the majority of cases tends to provide an even better estimation of the (relative) deformation shape. Especially for bridge configuration 1, where the substitute structure method fails to give a good estimation of the displacement shape, the multi-modal pushover analysis provides a significantly better prediction.

It may appear somewhat surprising that the SSM solution differs noticeably from the mean ITHA results even for the (near) elastic response developing at a PGA level of $a_{gd} = 0.16$g. This is primarily related to the fact that the Ramberg-Osgood abutment models do not feature a real linear elastic range. Obviously, the substitute structure method is not capable of fully reproducing the dynamic abutment response computed by the inelastic time history analyses. This effect appears more pronounced at small demand levels as the prediction of the displacement shape rather tends to improve for higher values of a_{gd}. Probably, the unsatisfying reproduction of the Ramberg-Osgood abutment behavior at small demand levels comes from the way the effective softening and the hysteretic energy dissipation in individual members are represented in the substitute structure method.

While the softening of the abutments with increasing deformations is taken into account locally, the corresponding damping in the SSM is smeared over the entire structure. In the real behavior, which is captured better by the ITHA, these two effects both occur locally and thus tend to balance each other out to some extent. However, in the SSM this mutual compensation cannot develop as softening and damping do not occur at the same locations. As a consequence, the local softening of the abutments increases their deformations noticeably, while the smeared damping slightly reduces the (global) deformations of the entire system. In fact, it can be seen in Fig. 4.50 that for $a_{gd} = 0.16$g the response of the rest of the structure (i.e. the piers) is rather slightly underpredicted by the SSM, while the abutment response is often overpredicted. At higher PGA levels, where the piers are also deformed into the inelastic range, this one-way redistribution of equivalent damping from the abutments to the piers does not occur anymore, or it becomes less significant. As a consequence, the predicted deformation shapes in the inelastic range tend to improve. compared those in the (near) elastic range.

Despite the promising estimation of the relative displacement shapes by the SSM, considerable errors can be found with respect to the prediction of the global deformation demand, expressed for example by the displacement of the reference point. For all configurations shown in Fig. 4.50, a rather strong overprediction of the global deformation demand can be encountered in the inelastic range ($a_{gd} = 0.35$g and 0.50g). In this context, it should be recalled that the application of the substitute structure method requires a ductility dependent relationship $\xi_{eq}(\mu_\Delta)$ for the equivalent viscous damping ratio and a second relationship $\eta(\xi)$ for the transformation of the elastic response spectrum at different

damping ratios. Hence, the results presented in Fig. 4.50 – and particularly the global deformation demand – depend on the specific choice for these two relationships.
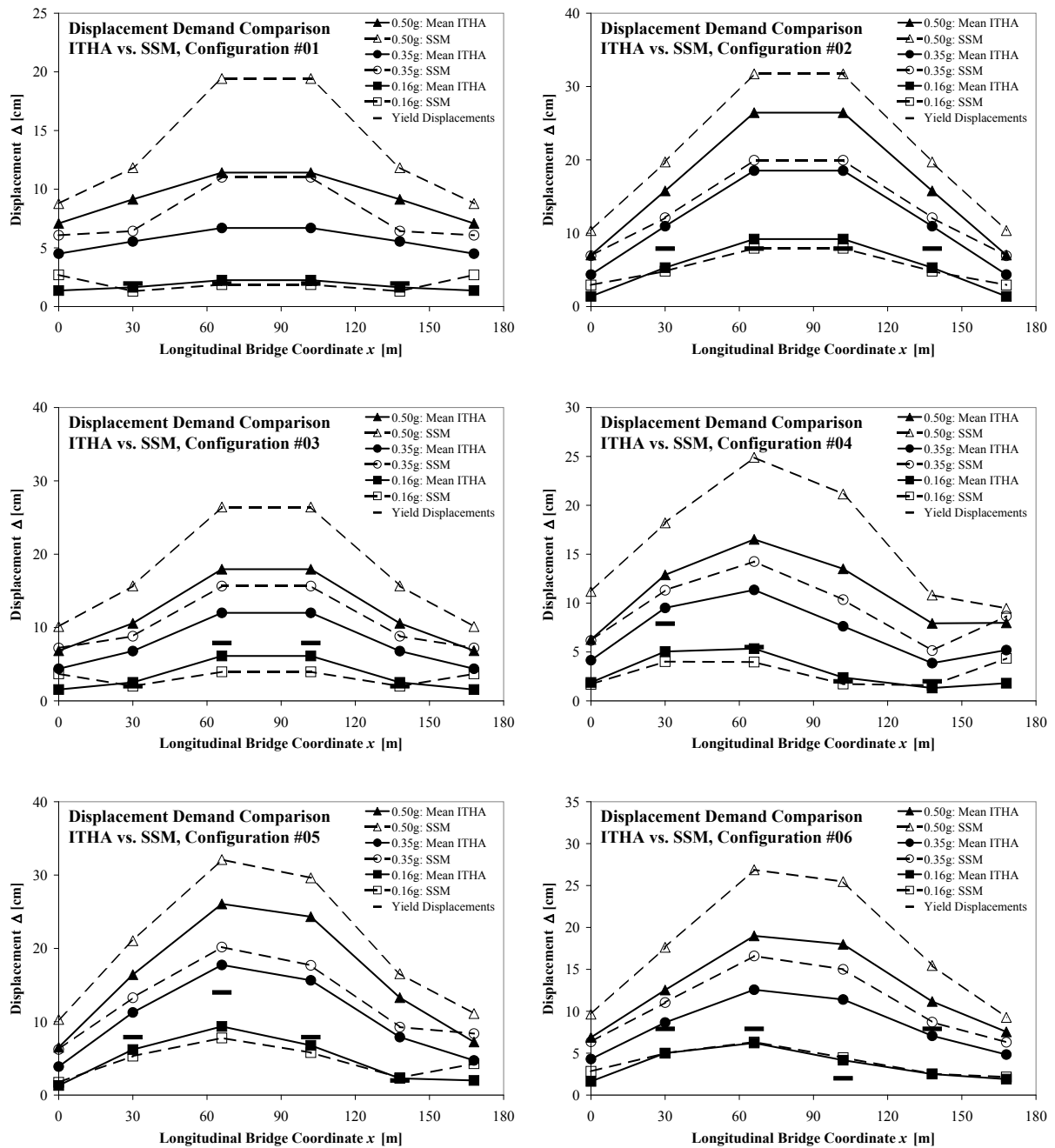

Fig. 4.50: Displacement demands for bridge configurations 1 through 6
from substitute structure method (SSM) and ITHA
for transverse excitation at seismicity levels a_{gd} = 0.16g, 0.35g, and 0.50g (Source: [Ber09])

As can be seen in Fig. 4.6 or the comparisons shown in Fig. 4.29 through Fig. 4.31, a noticeably lower demand prediction could be expected from the SSM if the alternative $\eta(\xi)$ relationship according to equation (4.8) from [EC8-1-1] had been used for the transformation of the response spectra to different damping ratios. Therefore, the overestimation of global deformation demand shown in Fig. 4.50 is not a systematic problem generally inherent to the substitute structure method. Instead, it shows the considerable influence of the choice of submodels which need to be introduced into the SSM. Aside from using an alternative equation for $\eta(\xi)$, it might also be conceivable to consider further relationships for the ductility dependent equivalent viscous damping $\xi_{eq}(\mu_\Delta)$.

4.6.3 Proposal for Improved Procedures

In Section 4.6.2, several approximate analysis procedures have been presented featuring different levels of simplification. The pros and cons in terms of accuracy, required effort, and applicability have been discussed. The evaluation of the quality of the approximate results in Section 4.6.2 is limited to the specifically chosen interpretation of the simplified approaches as applied by Berweger [Ber09]. From the above discussions, a variety of conclusions could be drawn and in some cases it was possible to identify certain reasons for deficits in the demand prediction. In this section, these conclusions will be used to modify some of the analysis approaches and propose procedures which show improved characteristics in some key aspects. Numerical results will be presented based on these modified analysis procedures in order to study their capabilities. Furthermore, it will be discussed under which conditions the individual procedures can be expected to perform satisfactory for a seismic demand estimation.

Based on the findings of Section 4.6.2, the following approaches will be considered for the establishment of potential improvements:

(i) *Response Spectrum Analysis with Multi-Modal Superposition (RSA)*
The response spectrum analysis is included in the considerations as a linear elastic analysis procedure, in which the influence of the higher modes is taken into account by means of the SRSS or CQC superposition rules.

(ii) *Lateral Force Method with Load Distribution 1 (LFM - LD1)*
The lateral force method is included as a second linear elastic procedure, which aims at approximating the results of the response spectrum analysis. Only the *Load Distribution 1* corresponding to a uniform acceleration shape will be considered, as the alternative first mode proportional acceleration shape (*Load Distribution 2* in Section 4.6.2*b*) has been found to give conceptually unsatisfying results, which can be overly conservative for some parts of a structure, while nevertheless predicting unconservative results in other parts of the structure. In contrast, *Load Distribution 1* was found to give more realistic and less extreme demand estimations which tend to be closer to the mean ITHA results.

(iii) *Conventional Pushover Analysis according to* [EC8-2] *Annex H with Load Distribution 1 (PO - LD1)*
Among the conventional pushover analyses, discussed in Section 4.6.2*c*, the version as given in [EC8-2] Annex H is considered. In this procedure, the target displacement of the reference point is set equal to that from the response spectrum analysis. This definition has the advantage that it includes the contribution of higher modes to the displacement of the reference point. As discussed in Section 4.6.2*c*, the alternative approach of defining the target displacement by means of an equivalent single-degree-of-freedom system rather corresponds to a single mode contribution which may result in an underestimation of the demand. For the following improved proposal, only *Load Distribution 1* corresponding to a uniform acceleration shape will be considered, as this has been shown to give a better approximation of the general displacement shapes than the first mode proportional *Load Distribution 2*.

(iv) *Modified Multi-Modal Pushover Analysis (mod MMP)*
Only the modified multi-modal pushover analysis according to [CGC04], as described in Section 4.6.2*d*, will be included in the subsequent considerations. The analyses by Berweger [Ber09] suggest that the higher effort involved in the original multi-modal pushover analysis, according to [CG02], does not appear to be justified in the light of hardly improved demand predictions. Instead, the modified procedure, which requires only a single nonlinear static analysis, provides almost the same quality of the displacement shape at a greatly reduced computational effort.

The substitute structure method, presented in Section 4.6.2*e*, will not be included in the following considerations. Although it was found to provide reasonably good estimations of the (relative) displacement shapes, it did not really perform better than the multi-modal pushover analyses with respect to this issue. On the other hand, due to the required rather complex iterations, the effort in a

practical assessment application of the approach is considerably larger than that of the modified multi-modal pushover analysis. This drawback lets the substitute structure method appear less appropriate for practical applications. This does not mean that the approach is conceptually inferior to the other procedures. However, the following discussion will primarily focus on the establishment of procedures which are particularly suitable for practical applications in engineering companies. For this purpose, an appropriate relationship between expected accuracy and required effort is the primary criterion for the selection.

For the evaluation of the considered approaches it is useful to distinguish between, on one hand, the prediction of the global deformation demand, expressed e.g. by the displacement of a reference point, and, on the other hand, the predicted (relative) displacement shape. The overall accuracy of the deformation demands throughout the structure then is the combined result of these two aspects. Consequently, for the selection or the modification of any of the various approaches a separate evaluation with respect to the two mentioned aspects can give valuable insight into the reasons for strengths and weaknesses of the individual methods.

Therefore, the following Subsection *a* will focus only on the prediction of the (relative) displacement shapes. The corresponding conclusions may serve for the selection of an appropriate analysis approach, depending on the given circumstances. Afterwards, in Subsection *b* the prediction of only the global displacement demand, in terms of target displacement of the reference point, will be investigated. For this aspect, improvements of the demand estimations will be proposed based on the principles outlined in Section 4.5. Finally, in Subsection *c* the two different aspects will be joined together again and numerical results will be presented for the modified approaches. An evaluation of the proposed modifications will be performed based on the mean ITHA results by Berweger [Ber09] and conclusions will be drawn with respect to the potential applicability of the modified procedures and the expected level of accuracy.

a) Estimation of the Relative Displacement Shape

To isolate the prediction of the relative displacement shape from that of the global displacement demand, it is useful to assume that the target displacement of the reference point could be estimated accurately within a simplified analysis procedure. For this purpose, for each of the four methods mentioned above, it is assumed that the displacement of the reference point is equal to the corresponding mean displacement from the inelastic time history analysis. This means that the two linear analysis methods (response spectrum analysis and lateral force method) are simply scaled to meet the mean ITHA displacement at the reference point. For the two inelastic procedures (pushover analysis according to [EC8-2] Annex H and modified multi-modal pushover analysis) the target displacement for the nonlinear static analysis is determined using the corresponding mean ITHA value. As a result, all four simplified approaches and the ITHA reference have the same displacement demand of the reference point and any differences throughout the rest of the structure can be attributed to differences in the relative displacement shape.

A comparison of these displacement shapes predicted by the four simplified analysis procedures and the corresponding mean ITHA deformation shape can be found in Fig. 4.51 and Fig. 4.52 for each bridge configuration at the three PGA levels $a_{gd} = 0.16g$, $0.35g$ and $0.50g$. For better visibility, the same curves are reproduced in Annex A3, showing the results corresponding to the individual PGA levels in separate graphs. As in Section 4.6.2, the reference point of each individual bridge is defined as the point which experiences the largest displacement in the elastic range (as determined by the response spectrum analysis). For all bridges, but one, the reference point is located at the top of pier number 2. Only for bridge configuration 12, the top of pier number 3 represents the reference point.

The form of the displacement shape, and also the quality of its prediction by the various simplified approaches, depends primarily on (1) the influence of higher modes and (2) the amount of relative stiffness redistribution in the inelastic range. Normally, for the near-elastic responses at $a_{gd} = 0.16g$, only the first aspect should have a significant influence, while with increasing loading level, and thus increasing inelasticity, the second aspect becomes more important. For the given way of abutment modeling by means of Ramberg-Osgood springs, a third phenomenon occurs which, to some extent,

might be considered a special feature of the second aspect mentioned above. The fact that the Ramberg-Osgood model does not feature a linear elastic response, even at small deformations, causes in some cases that even at $a_{gd} = 0.16g$ the displacement shape is not predicted correctly. This is related to the uncertainty in representing the Ramberg-Osgood springs by an initial elastic stiffness in this range. The results therefore depend on the individual choice for this initial stiffness. On the other hand, these effects might not occur in the same way if the abutments had been modeled differently in the ITHA – e.g. also using a modified Takeda hysteresis rule. As a consequence, some of the deficiencies in the prediction of the displacement shape at small excitation levels are not primarily related to the capabilities of the simplified analysis methods, but are rather a combined result of several effects.
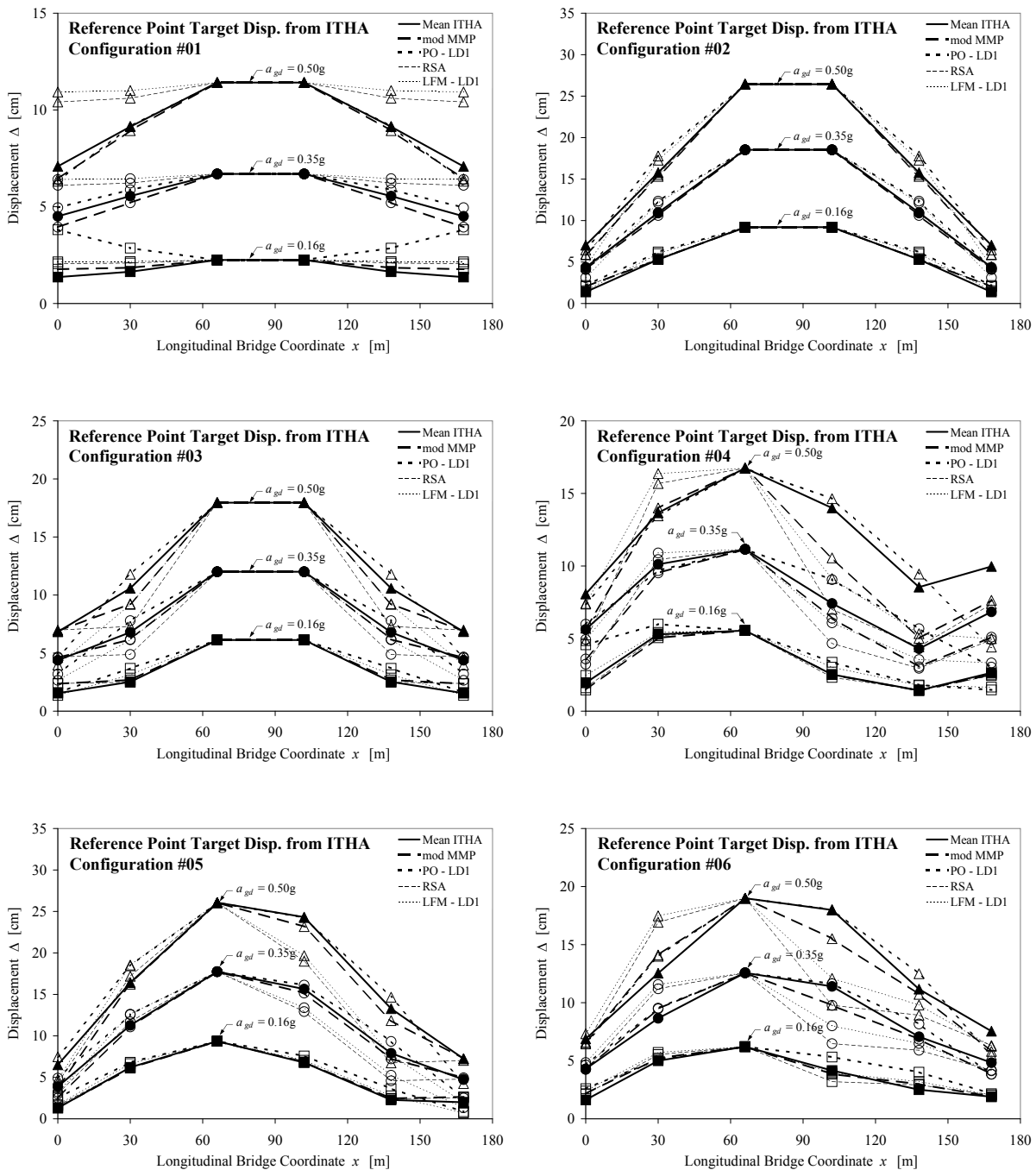

Fig. 4.51: Displacement shapes of bridge configurations 1 through 6
for target displacements of the reference point determined from mean ITHA
at transverse excitation levels $a_{gd} = 0.16g$, 0.35g, and 0.50g

Aside from these effects related to the abutment modeling, the comparisons presented in Fig. 4.51 and Fig. 4.52 show that at the low PGA level of $a_{gd} = 0.16g$ the displacement shapes are typically predicted reasonably well by the response spectrum analysis (RSA). Only for those structures where very short piers are located between longer piers, i.e. especially in configuration 6 (pier number 3), the prediction is somewhat unsatisfying (and unconservative). This is related to the fact that in such a configuration the short pier experiences noticeable inelastic actions already at $a_{gd} = 0.16g$, while its neighboring piers remain elastic. The related redistribution of stiffnesses is not captured by the response spectrum analysis, causing the inaccurate estimation of the displacement shape.
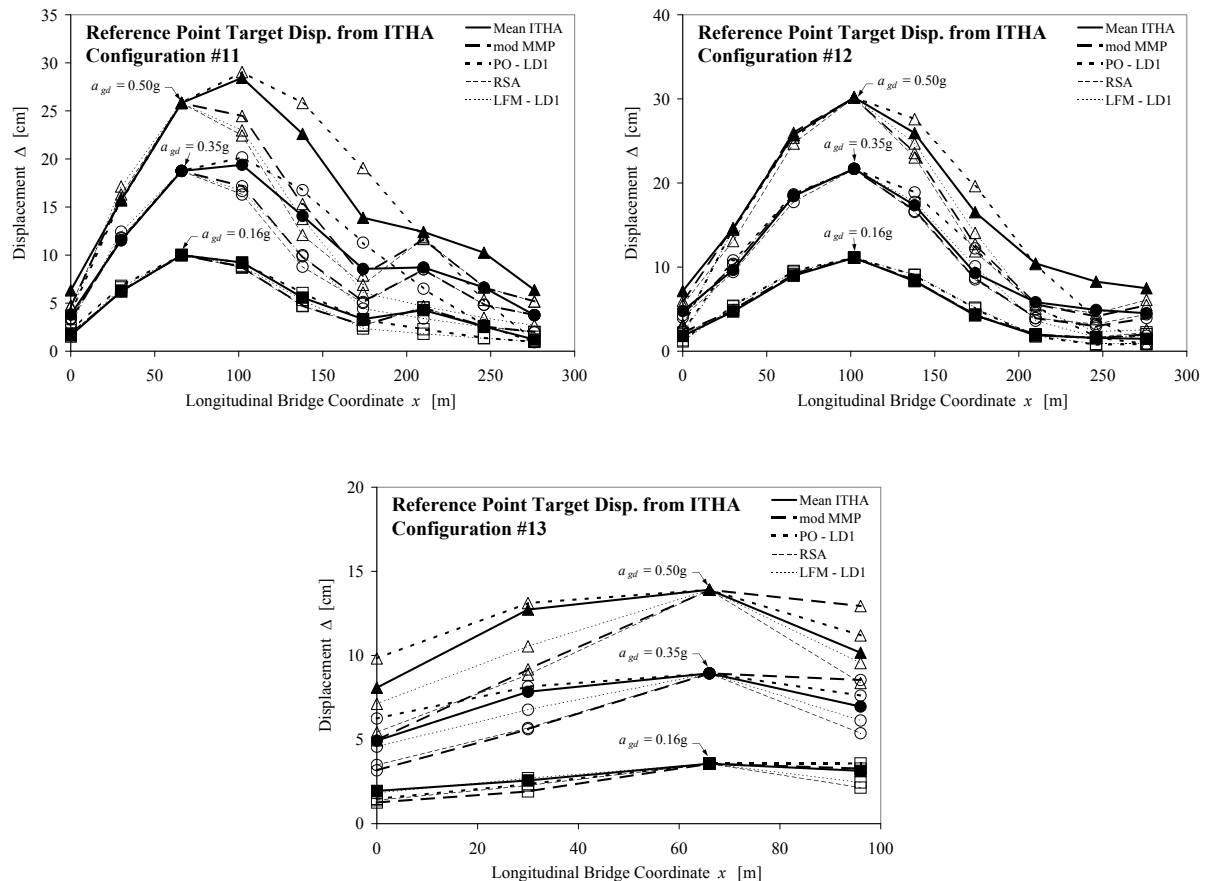

Fig. 4.52: Relative displacement shapes of bridge configurations 11, 12, and 13
for target displacements of the reference point determined from mean ITHA
at transverse excitation levels a_{gd} = 0.16g, 0.35g, and 0.50g

Whenever significant inelasticity occurs, and especially if the inelastic action does not develop uniformly over the entire structure, the (modified) multi-modal pushover analysis (mod MMP) performs better with respect to the predicted deformation shape. This generally holds true for the demand situations corresponding to higher PGA levels, but also for very irregular structures at lower seismicity levels, as is the case for configuration 6 at $a_{gd} = 0.16g$ mentioned above. The lateral force method (LFM - LD1) and the conventional pushover analysis (PO - LD1), both using the *Load Distribution 1*, can be considered as simplified approximations of the response spectrum analysis and of the (modified) multi-modal pushover analysis, respectively.

As the lateral force method and the conventional pushover analysis do not explicitly take into account higher mode effects, the quality of their deformation shape prediction tends to reduce if such effects play a major role for the seismic response of a bridge. On the other hand, due to the characteristics of the chosen *Load Distribution 1*, the deviations compared to the results from the response spectrum analysis or the multi-modal pushover analysis are often rather conservative. Therefore, the simpler procedures may still serve as approximate analysis approaches. With increasing complexity, however, as e.g. in the cases of configurations 11, the lateral force method and the conventional pushover

analysis may noticeably fall behind their multi-modal counterparts (RSA and mod MMP). It cannot be ruled out that in such cases significantly unconservative demand predictions may result from the two simpler approaches (as e.g. in the case of bridge configuration 11).

At the same time, it should not be ignored that even the (modified) multi-modal pushover analysis, being the most sophisticated one of the four approaches, in some cases predicts unconservative deformation demands for the given target displacement at the reference point (see e.g. configuration 12 at a_{gd} = 0.35g and 0.50g). Due consideration to the generally inevitable uncertainties of any simplified approach should therefore be given during the analysis and the interpretation of the results.

b) Improved Target Displacement of the Reference Point

For the response spectrum analysis, for the conventional pushover analysis according to [EC8-2] Annex H, and for the (modified) multi-modal pushover analysis, as presented in Section 4.6.2, in each case the target displacement of the reference point was determined by Berweger [Ber09] in the same way. In all three cases the displacement demand of the reference point was equal to the corresponding displacement stemming from the response spectrum analysis. The target displacement resulting from the lateral force method differed somewhat, but it is also intended to approximate the value of the response spectrum analysis. Therefore, all four procedures, in the form as applied by Berweger [Ber09], used the same principles for the determination of the reference point displacement. It has been outlined in Section 4.6.2 that taking the target displacement equal to the corresponding value resulting for a linear system (with same initial stiffnesses) implicitly represents the application of the *equal displacement approximation*.

Although this approach complies with the requirements of [EC8-2] Annex H and it is also in line with the provisions of [SIA2018] and [EC8-3], the relationships presented in Section 4.5 for single-degree-of-freedom systems show clearly that the validity of this approximation is limited to certain circumstances. Especially for structures with short fundamental periods (based on the initial elastic stiffnesses), it must be expected that the *equal displacement approximation* is likely to result in unconservative demand estimations[26]. A potential solution to this problem is included in the seven steps outlining the conventional pushover analysis using an equivalent single-degree-of-freedom system in Section 4.6.2c. In this approach, the displacement demand of the inelastic SDOF is used to determine the target displacement of the reference point. For the estimation of the inelastic SDOF displacement any appropriate method can be used, including those presented in Section 4.5. Hence, by applying a displacement modification factor C_R, as outlined in Section 4.5.1, or by using the equivalent linearization principles described in Section 4.5.2, the estimation of the displacement demand can be greatly improved compared to the rather simple *equal displacement approximation*.

Conceptually, it is also possible to apply a displacement modification factor C_R on the target displacement coming from a response spectrum analysis. In the relationships, presented in Section 4.5.1, C_R depends on the initial period T_0 of the (equivalent) SDOF system and the strength ratio R_y. As outlined in Section 4.6.2c and in Section A2.2.1 of Annex A2, the initial period T_0 of the equivalent SDOF system essentially approximates the natural first mode period of the MDOF structure with initial elastic stiffnesses k_0 of the individual members. Therefore, the period T_0 for the determination of C_R can be computed either using the Rayleigh quotient (see Section A2.1.2 of Annex A2) or it can simply be taken directly as the first mode period from the response spectrum analysis.

The strength ratio R_y of the equivalent SDOF system is defined according to equation (4.12). It represents the spectral pseudo-acceleration $S_{a,el}(T_0)$ times the mass m_{SDOF} of the SDOF divided by its nominal yield force $F_{y,SDOF}$. Both SDOF properties, m_{SDOF} as well as $F_{y,SDOF}$, depend on the assumed acceleration shape used to perform the transformation between original MDOF and equivalent SDOF systems (see Section 4.6.2c and Section A2.2.1 of Annex A2). They are therefore not uniquely defined. Furthermore, $F_{y,SDOF}$ also depends on the chosen bilinearization of the generally curved or multi-linear pushover curve for the MDOF structure.

---

[26] This is why [SIA2018] limits the application of this approach to structures with a fundamental period higher than 0.7s, while no provisions are included in [SIA2018] for structures with shorter fundamental periods.

If a uniform acceleration shape (corresponding to that of *Load Distribution 1)* is assumed for the transformation between MDOF and SDOF, the mass m_{SDOF} becomes equal to the total mass of the MDOF structure and can be easily computed. The yield load $F_{y,SDOF}$ can then be determined based on a pushover analysis using the same uniform acceleration shape. For this purpose, the transformation according to step (iv) in Section 4.6.2c can be performed (see also Section A2.2.1 of Annex A2) and an appropriate bilinearization of the pushover curve for the SDOF system needs to be chosen. This approach for the determination of $F_{y,SDOF}$ does not represent any significant extra effort if a pushover analysis (using a uniform acceleration shape corresponding to *Load Distribution 1*) is performed anyway. If, e.g., only a linear analysis procedure (RSA or LFM) is to be used, $F_{y,SDOF}$ can be approximately estimated as the sum of the yield forces of the piers and abutments in the MDOF structure.

Based on an estimation for the strength ratio R_y and the initial fundamental period T_0, any of the procedures presented in Section 4.5 can then be used to estimate a displacement modification factor C_R. This value of C_R can subsequently be multiplied with the reference point displacement from the response spectrum analysis in order to compute an improved target displacement which takes into account the influence of inelasticity on the global deformation demand of the MDOF system. This approach has been applied on the nine bridge configurations originally analyzed by Berweger [Ber09]. For this purpose, the three proposals for C_R presented in Section 4.5.1 and the two equivalent linearization concepts outlined in Section 4.5.2 have been used. For each of the latter two methods, two relationships $\eta(\xi)$ for the transformation of elastic spectra corresponding to different viscous damping ratios ξ have been considered. As a consequence, a total of seven different combinations for the estimation of the inelastic displacement demand of the reference point have been included in this evaluation, as follows:

(1) Displacement modification factor C_R according to Chopra and Chintanapakdee [CC04] (see equation (4.18) in Section 4.5.1b) using the parameters for soil class B given in Tab. 4.5

(2) Displacement modification factor C_R according to Ruiz-García and Miranda [RM03] (see equation (4.17) in Section 4.5.1a) using the parameters for soil class B given in Tab. 4.4

(3) Displacement modification factor C_R deduced from the proposal by Nassar and Krawinkler [NK91] (see equations (4.19) through (4.21) in Section 4.5.1c) using the parameters for a post-yield stiffness ratio of $r = 0$ as given in Tab. 4.6

(4) Equivalent linearization based on the proposal by Priestley *et al.* [PCK07] (see equation (4.31) through (4.33) in Section 4.5.2a) using the parameters for the "*Thin Takeda*" hysteresis rule and constant elastic viscous damping as given in Tab. 4.7
in combination with the $\eta(\xi)$ relationship given in the 1994 version of [EC8-1-1] (see equation (4.8) in Section 4.4.2)

(5) Equivalent linearization based on the proposal by Priestley *et al.* [PCK07] (see equation (4.31) through (4.33) in Section 4.5.2a) using the parameters for the "*Thin Takeda*" hysteresis rule and constant elastic viscous damping as given in Tab. 4.7
in combination with the $\eta(\xi)$ relationship given in the 2003 version of [EC8-1]
(see equation (4.7) in Section 4.4.2)

(6) Equivalent linearization based on the proposal by Guyader [Guy04] (see equation (4.34) and (4.35) in Section 4.5.2b) using the parameters for the "*Stiffness Degrading*" hysteresis rule (KDEG) as given in Tab. 4.8 and Tab. 4.9
in combination with the $\eta(\xi)$ relationship given in the 1994 version of [EC8-1-1] (see equation (4.8) in Section 4.4.2)

(7) Equivalent linearization based on the proposal by Guyader [Guy04] (see equation (4.34) and (4.35) in Section 4.5.2b) using the parameters for the "*Stiffness Degrading*" hysteresis rule (KDEG) as given in Tab. 4.8 and Tab. 4.9
in combination with the $\eta(\xi)$ relationship given in the 2003 version of [EC8-1] (see equation (4.7) in Section 4.4.2)

Based on the various concepts mentioned above, for every bridge configuration and at every PGA level seven different estimations of the inelastic displacement demand for the reference point result. For each demand estimation the relative error with respect to the mean ITHA solution has been computed. These error values are presented as percentages in Fig. 4.53 and Fig. 4.54, in which a positive value represents an overestimation of the target displacement by the simplified approach (compared to the mean ITHA result).

Fig. 4.53: Relative error of simplified displacement demand estimation for reference point compared to mean results from ITHA for bridge configurations 1 through 6 at transverse excitation levels a_{gd} = 0.16g, 0.35g, and 0.50g

In Section 4.5.3 mutual comparisons between the various approaches for the demand estimation of inelastic SDOF systems were presented. While these comparisons gave some impression about the relative tendency of the individual procedures to yield higher or lower demand estimations than the other approaches, no absolute evaluation concerning the accuracy or conservatism of the methods was

possible based on these comparisons. In contrast, the results presented in Fig. 4.53 and Fig. 4.54 allow a certain evaluation of the individual approaches by relating them to the independent demand predictions from ITHA, taken as a reference. However, in the interpretation of the data it should be kept in mind that, due to their origin from MDOF analyses, further influences come into play, which go beyond the simpler case of inelastic SDOF behavior. This holds true for the ITHA analyses as well as for the response estimation using the simplified methods.

The more complex MDOF behavior influences the response, especially if higher mode effects play a significant role. Furthermore, the decision of determining the elastic displacement demand based on the response spectrum analysis or the chosen way of estimating the strength ratio R_y for the MDOF system are not unique and also have an influence on the results. Finally, even the choice of ground motions for the ITHA may play a role for the demand predictions and it cannot be ruled out that the use of scaled recorded accelerograms might, e.g., yield somewhat different results. Therefore, the data shown in Fig. 4.53 and Fig. 4.54 do not necessarily serve for a general evaluation of the approaches presented in Section 4.5 with respect to their capability of predicting the response of inelastic SDOF systems. On the other hand, in practical applications it is the final response prediction for the MDOF structure that matters. In such cases, all the influences mentioned above enter into the results so that the data presented in Fig. 4.53 and Fig. 4.54 are more representative for the given task.
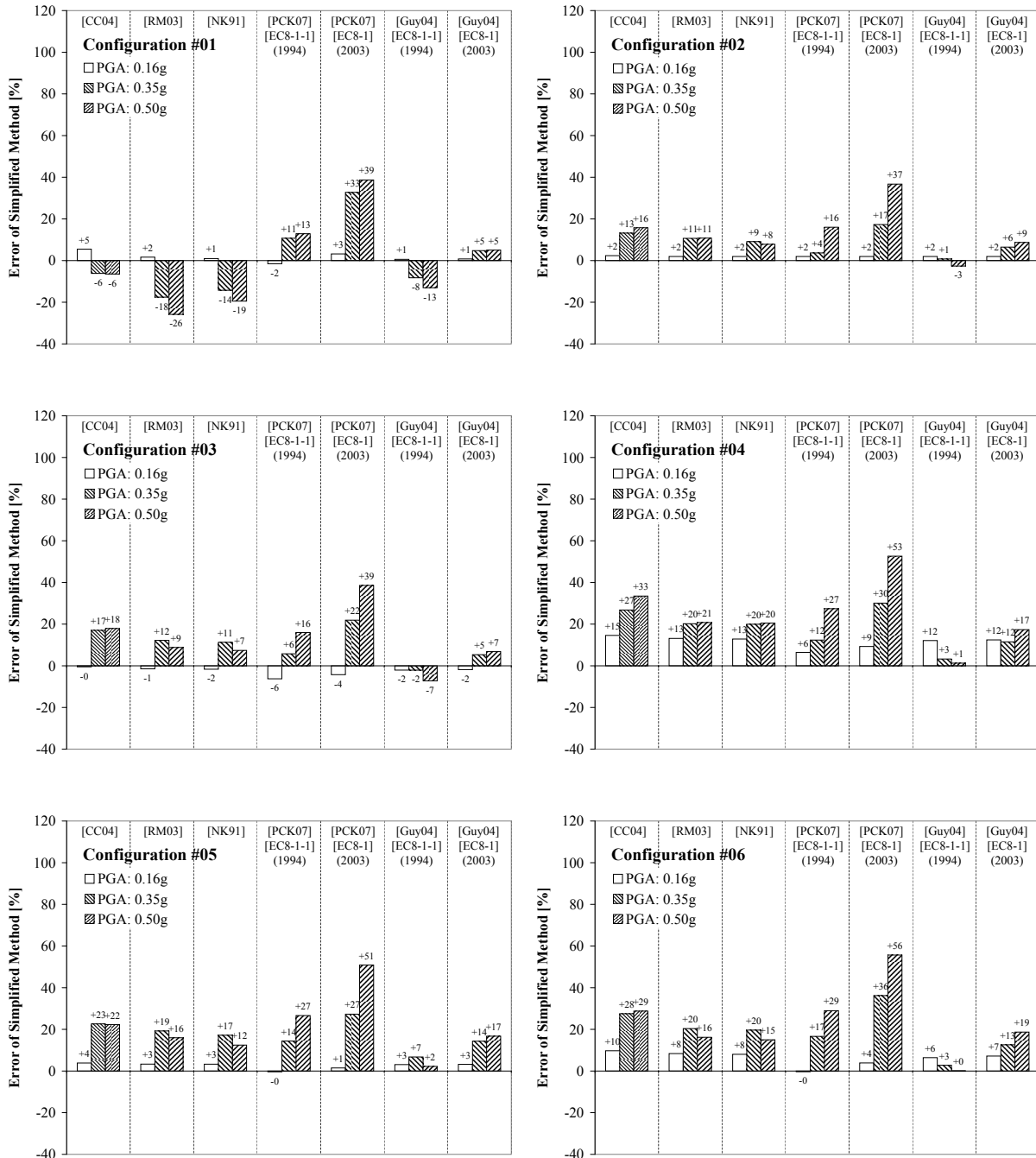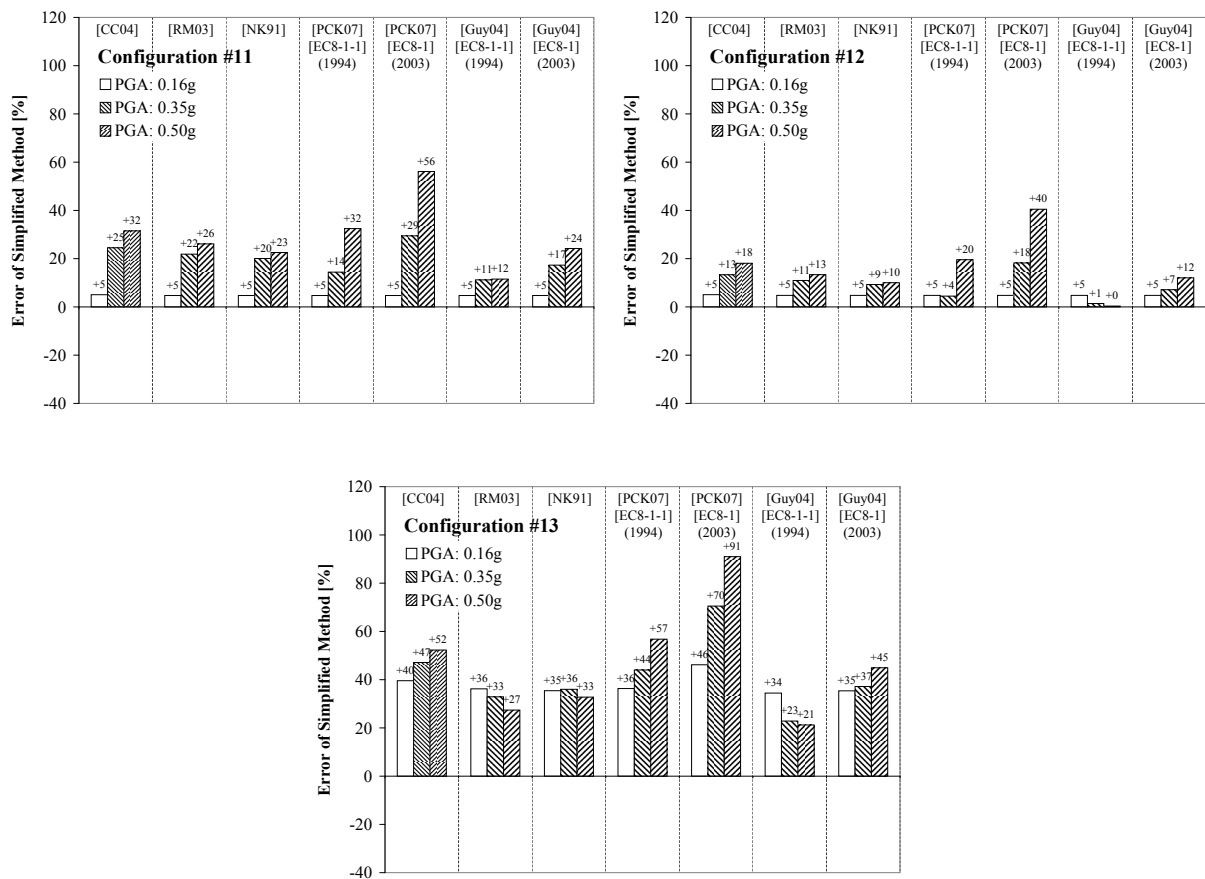
Fig. 4.54: Relative error of simplified displacement demand estimation for reference point compared to mean results from ITHA for bridge configurations 11, 12, and 13 at transverse excitation levels a_{gd} = 0.16g, 0.35g, and 0.50g

In Section 4.6.2 it has been shown that especially for bridge configuration 1 the global displacement demand in the inelastic range is severely underestimated if the target displacement of the reference point is determined from the unmodified response spectrum analysis. This is related to the fact that, due to its elastic first mode period of T_0 = 0.36 s, the *equal displacement approximation* cannot reasonably be applied on this bridge. Therefore, it is particularly interesting to see how the various modification approaches mentioned above perform in this case. The data for configuration 1,

presented in Fig. 4.53, show that all of the considered approaches result in an increase of the target displacement. While the unmodified prediction coming from the response spectrum analysis (see Fig. 4.41) underpredicts the displacement of the reference point by 26% and 38% for PGA levels of $a_{gd} = 0.35g$ and $0.50g$, respectively, none of the results shown in Fig. 4.53 for configuration 1 represents such a strong underprediction.

Despite a certain mitigating effect, the approaches according to [NK91] and [RM03] are not able to compensate sufficiently for the underprediction by the response spectrum analysis. Especially the modified prediction resulting from [RM03] might rather not be considered acceptable for bridge configuration 1, as a remaining underprediction by 26% at $a_{gd} = 0.50g$ is still considerably unconservative. A reasonably good prediction of the target displacement is achieved by application of the displacement modification factor according to [CC04]. The resulting underprediction by 6% in the inelastic range may be considered as rather negligible, especially in comparison to the general uncertainties inherent to seismic demand estimations.

As found before, the results from the two equivalent linearization approaches according to [PCK07] and [Guy04] depend strongly on the chosen relationship $\eta(\xi)$ to transform elastic spectra of different viscous damping ratios (see Section 4.4.2). As the approach from [PCK07] conceptually yields higher equivalent viscous damping ratios ξ_{eq} than the proposal by [Guy04][27], the influence of the choice of $\eta(\xi)$ is also more noticeable for the former method. Using the $\eta(\xi)$ relationship according to the 1994 version of [EC8-1-1], as recommended in [PCK07], the equivalent linearization according to [PCK07] yields a reasonably good, slightly conservative, demand estimation for the reference point. However, if the $\eta(\xi)$ relationship according to the 2003 version of [EC8-1] (also adopted by [SIA261]) is used, the [PCK07] proposal results in a considerable overprediction of the inelastic deformation demand.

The demand estimations for bridge configuration 1 based on the equivalent linearization according to [Guy04] are lower than those from [PCK07] for both $\eta(\xi)$ relationships considered in the evaluation. To some extent this might be attributed to the fact that for the [PCK07] approach the parameters corresponding to the "Thin Takeda" hysteretic behavior have been used, which features a lower hysteretic energy dissipation than the stiffness degrading model underlying the proposal by [Guy04]. Generally, the inelastic target displacements resulting from the equivalent linearization according to [Guy04] are rather close to the mean ITHA predictions for both $\eta(\xi)$ relationships. While the use of $\eta(\xi)$ according to [EC8-1] (2003) yields slightly conservative demand estimations, the $\eta(\xi)$ relationship from [EC8-1-1] (1994) results in a somewhat more pronounced underprediction. In the latter case, the unconservatism by -13% for $a_{gd} = 0.50g$ might be at the limit of what can still be considered acceptable.

For the other bridge configurations (2 through 6 and 11 through 13) shown in Fig. 4.53 and Fig. 4.54, the majority of demand predictions tends to be rather conservative. It appears noteworthy that the equivalent linearization according to [Guy04] combined with the $\eta(\xi)$ relationship from [EC8-1-1] (1994) gives demand predictions which are very close to the mean ITHA results throughout these configurations. The same equivalent linearization from [Guy04] applied together with $\eta(\xi)$ according to [EC8-1] (2003) still results in reasonably good predictions of target displacement, which are somewhat more conservative than those from the alternative $\eta(\xi)$ relationship. The approach by [PCK07] gives conservative demand estimates in almost all cases. While the results based on the $\eta(\xi)$ relationship from [EC8-1-1] (1994) can also be considered as reasonably good, those coming from $\eta(\xi)$ according to [EC8-1] (2003) tend to be overly conservative in many cases.

The two proposals for displacement modification factors by [NK91] and [RM03] perform significantly better for the bridge configurations 2 through 6 and 11 through 13. In these cases, generally conservative results are computed, which might be considered as sufficiently good approximations to the mean ITHA values. Application of the displacement modification factor according to [CC04] also

---

[27] The two approaches use different definitions of the effective period T_{eff} for the equivalent linearized system. As the required equivalent viscous damping ratio ξ_{eq} also depends on the choice of the effective period, consequently, different values for ξ_{eq} must be used. The fact that the approach according to [PCK07] always results in higher effective periods than those from [Guy04] requires that the equivalent viscous damping ratios according to [PCK07] will also tend to be higher than those from [Guy04].

yields generally conservative results for these bridge configurations, with a somewhat stronger overprediction than by the other two proposals for displacement modification factors. Generally, the estimates based on [CC04] tend to be of similar magnitude as those resulting from [PCK07] together with $\eta(\xi)$ according to [EC8-1-1] (1994).

It is noticeable that all approaches result in a considerable demand overestimation for the short bridge configuration 13. In this context it should be noted that already in the elastic range ($a_{gd} = 0.16g$) the response spectrum analysis overpredicts the mean ITHA result for the displacement of the reference point by 35% (see Fig. 4.42). Therefore, the strong overpredictions shown in Fig. 4.54 for configuration 13 should not primarily be attributed to the deficiencies of the various proposals for displacement modification factors or equivalent linearization. Instead, the deviations are rather related to very special problems of the response spectrum analysis in predicting the (elastic) displacement of pier number 2. If, instead, pier number 1 of configuration 13 had been chosen as the reference point, this severe overprediction would not have occurred in the same way.

Summarizing the above discussion, it can be concluded that any of the approaches provides at least an improvement over the implicitly assumed *equal displacement approximation* underlying the provisions of [EC8-2] Annex H, [SIA2018], and [EC8-3]. Nevertheless, noticeable differences could be encountered with respect to the performance of the various approaches. The fact that the two proposals according to [NK91] and [RM03] still resulted in significant demand underpredictions, especially for bridge configuration 1, where the correction is most needed, lets these two concepts appear less appropriate for the given task. On the other hand, the substantial demand overpredictions by the equivalent linearization of [PCK07] together with $\eta(\xi)$ according to [EC8-1] (2003) lets this combination appear less favorable as well.

The remaining approaches might be considered as generally qualified for the task. Rather close overall predictions, compared to the mean ITHA results, were achieved with the equivalent linearization according to [Guy04]. While the combination with the $\eta(\xi)$ relationship according to [EC8-1-1] (1994) on average gave predictions which were closest to the mean ITHA results, some minor underpredictions cannot be ruled out for this approach. The alternative combination between [Guy04] and $\eta(\xi)$ from [EC8-1] (2003) results in slightly worse agreement with the mean ITHA results but bears less likelihood for unconservative demand predictions.

If somewhat more conservative estimates for the target displacement of the reference point are preferred, either the displacement modification factor according to [CC04] or the combination of equivalent linearization according to [PCK07] with $\eta(\xi)$ from [EC8-1-1] (1994) might be considered as appropriate. As has been shown in Subsection *a*, even for a perfect prediction of the target displacement, the various simplified analysis procedures may result in underpredictions of the demand in other parts of the structure due to inaccurate representation of the (relative) displacement shape. As these deficiencies can never be ruled out completely – even for the more sophisticated analysis methods – a somewhat more conservative estimation of the reference point displacement might be useful to compensate for some of the deficits related to the prediction of the deformation shape. Therefore, the more conservative approaches according to [CC04] or [PCK07] with $\eta(\xi)$ from [EC8-1-1] (1994) might be more preferable for practical applications than the possibly somewhat more accurate solutions for the reference point resulting from [Guy04].

For a practical application, the effort involved in the analysis also plays a significant role for the choice of the appropriate procedure. In this context it should be noted that the equivalent linearization approaches always require iteration for the computation of the target displacement when applied in an assessment case with known structural properties. In contrast, the approaches using a displacement modification factor do not require an iteration but can rather readily be applied in an assessment situation. Therefore, the displacement modification factor according to [CC04] might be considered as somewhat more expedient for the given task. Taking into account that for many cases the results from [CC04] tend to be similar to those from [PCK07] with $\eta(\xi)$ from [EC8-1-1] (1994), choosing [CC04] instead of the alternative equivalent linearization does not appear to have a significant influence on the resulting response predictions.

c) Proposal of Modified Analysis Procedures

Based on the considerations presented in Subsections *a* and *b*, it is possible to modify the four MDOF analysis procedures mentioned at the beginning of this section. For this purpose, the following modifications to the individual methods are proposed:

(i) *Response Spectrum Analysis with Multi-Modal Superposition (RSA)*
The response spectrum analysis is performed using a linear elastic model of the structure, in which every member is represented by its initial elastic stiffness k_0 (see Section 4.6.2a). To allow for the influence of inelasticity on the global deformation demand, the elastically determined deformations throughout the structure are multiplied by a displacement modification factor C_R as discussed in Subsection *b*. The value of C_R can either be determined directly from a corresponding proposal (e.g. [CC04]) or indirectly by means of an equivalent linearization (e.g. [PCK07] or [Guy04], see Section 4.5.2). If additionally a pushover analysis is performed using *Load Distribution 1*, corresponding to a uniform acceleration shape, then the nominal yield load required for the computation of the strength ratio R_y should be determined by an appropriate bilinearization of the pushover curve of the equivalent SDOF system (see Subsection *b*). Otherwise, the nominal yield load of the equivalent SDOF system can be estimated as the sum of the yield loads of all piers and abutments. In both cases, the mass of the equivalent SDOF system is taken as the sum of the masses in the MDOF system.

(ii) *Lateral Force Method with Load Distribution 1 (LFM - LD1)*
The lateral force method is performed on the same linear elastic model as for the response spectrum analysis. *Load Distribution 1* corresponding to a uniform acceleration shape is used for the transverse forces (see Section 4.6.2b). As for the response spectrum analysis, the deformation results of the lateral force method are multiplied by a displacement modification factor C_R which is determined in the same way as described under (i).

(iii) *Pushover Analysis with Load Distribution 1 (PO - LD1)*
A conventional pushover analysis is performed as described in Section 4.6.2c. For the nonlinear static analysis, *Load Distribution 1* corresponding to a uniform acceleration shape is used. The target displacement of the reference point is taken equal to the corresponding displacement resulting from the modified response spectrum analysis as described under (i). The strength ratio R_y, required for the estimation of the displacement modification factor C_R, should be determined from the bilinearized pushover curve of the equivalent SDOF system.

(iv) *Modified Multi-Modal Pushover Analysis (mod MMP)*
The modified multi-modal pushover analysis is conceptually performed in the same way as described in Section 4.6.2d. This means that only one pushover analysis corresponding to the first mode response is performed, while the higher mode displacements are taken directly from the linear response spectrum analysis. They are superimposed on the first mode pushover analysis results using the SRSS or CQC rule. The target displacement of the reference point in the pushover analysis is taken as the corresponding first mode displacement from the modified response spectrum analysis including a displacement modification factor as described under (i). The linear higher mode displacements are also multiplied by a displacement modification factor C_R. Generally, it would be possible to determine individual values of C_R for each mode, e.g. based on modal period and an appropriate definition of a strength ratio R_y. However, a strict mechanical reasoning for individual modal displacement modification factors does not really exist. Therefore, it is proposed to use the same value of C_R for the linear higher modes as for the first mode pushover analysis. This has also the advantage that the same displacement of the reference point results as from the response spectrum analysis and the conventional pushover analysis, as described in (i) and (iii), respectively. Generally it is possible to determine the required strength ratio R_y on an equivalent SDOF system coming from the first mode pushover analysis with a corresponding first mode proportional acceleration shape for the load distribution. In this case it is important that both, the nominal yield load and the mass of the equivalent SDOF system, are computed based on the same acceleration shape (see Section

A2.2.1 of Annex A2). However, for consistency with the other three analysis methods it might also be worthwhile considering the use of the same strength ratio, and thus displacement modification factor, determined on an equivalent SDOF system based on *Load Distribution 1*, like in procedure (iii).

The four modified analysis approaches, as described above, have been applied on the nine bridge configurations originally used by Berweger [Ber09]. The performance of the four procedures has been evaluated by comparison of the corresponding analysis results to the mean displacement predictions from ITHA. For the estimation of the inelastic target displacement of the reference point, the following three of the seven approaches discussed in Subsection *b* have been considered for this further evaluation:

(1) Displacement modification factor C_R according to Chopra and Chintanapakdee [CC04]

(4) Equivalent linearization based on the proposal by Priestley *et al.* [PCK07] with $\eta(\xi)$ according to [EC8-1-1] (1994)

(6) Equivalent linearization based on the proposal by Guyader [Guy04] with $\eta(\xi)$ according to [EC8-1-1] (1994)

It should be noted that, while the application of the equivalent linearization concept on a SDOF system is straightforward, several possible ways of application exist for MDOF systems. As discussed in the context of the *substitute structure method* in Section 4.6.2*e*, for a MDOF structure both the secant stiffness representation as well as the determination of the equivalent viscous damping ratio can be done locally on the member level. A global modal damping ratio can then be defined as a weighted average over the whole structure, while the secant member stiffnesses are used to assemble an entire MDOF model. As an alternative, the *direct displacement based design* concept presented in [PCK07] uses an equivalent SDOF system for the demand estimation, but still determines the equivalent viscous damping ratios locally at the member level which are then averaged in the same way as in the *substitute structure method*. For the analyses presented in this section, a third approach has been followed by applying the equivalent linearization exclusively on the equivalent inelastic SDOF system. This means that both, the secant stiffness and the equivalent viscous damping ratio, are determined directly on the equivalent SDOF. As a result, the indirectly computed displacement modification factors computed for the two equivalent linearization approaches, as shown in Fig. 4.22 through Fig. 4.25 and Fig. 4.27, Fig. 4.28, could directly be applied. This way the same relationships between the various concepts exist as found for inelastic SDOF systems in Section 4.5.3. It would, however, also be possible to compute the equivalent viscous damping ratio as a weighted average over the individual members, like in the *direct displacement based design* approach of [PCK07]. It is not believed that this difference would influence the final results very strongly.

Comparisons between the results from the four simplified analysis procedures, as proposed above, and the mean ITHA displacement demands of the MDOF bridge configurations are depicted in Fig. 4.55 through Fig. 4.60. The data based on the displacement modification factor according to [CC04] are shown in Fig. 4.55 and Fig. 4.56. The corresponding results using the equivalent linearization according to [PCK07] are given in Fig. 4.57 and Fig. 4.58 and those based on [Guy04] are included in Fig. 4.59 and Fig. 4.60. In addition, all these results are also reproduced for better visibility in Annex A3, separated by PGA levels.

The presented data show that the modified multi-modal pushover analysis (mod MMP), being the most sophisticated one of the four methods, yields reasonably good demand predictions for the considered bridge configurations if an appropriate choice of displacement modification factor or equivalent linearization is included. The results show that the two somewhat more conservative choices, i.e. [CC04] and [PCK07] with $\eta(\xi)$ from [EC8-1-1], are more likely to yield reliable and conservative results throughout the MDOF structure than the alternative use of [Guy04] with $\eta(\xi)$ from [EC8-1-1]. Although it has been found in Subsection *b* that the predictions of the target displacement for the reference point resulting from the latter approach are rather close to the mean ITHA values, any deficiencies in the representation of the (relative) displacement shape can immediately lead to unconservative results on the local level if the approach according to [Guy04] is adopted. In contrast, the slight conservatism inherent to the approaches by [CC04] and [PCK07] may

lead often to a certain overprediction of the reference point displacement, but they are likely to better compensate for inaccuracies related to the displacement shape. As a consequence, these two approaches are more likely to result in acceptable demand predictions, also on the local level throughout the structure.
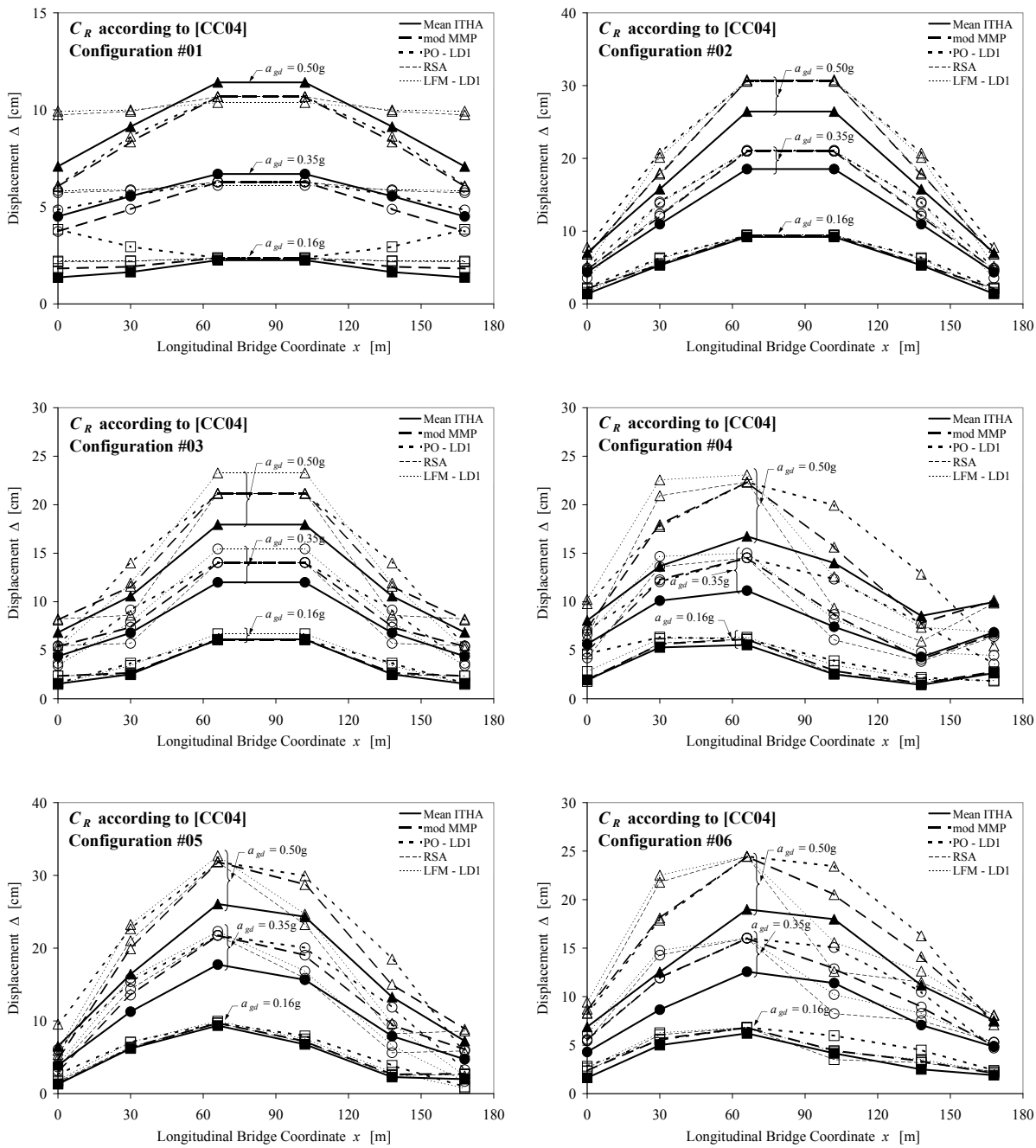

Fig. 4.55: Displacement demands based on proposed modified analysis procedures
using displacement modification factors according to [CC04]
for bridge configurations 1 through 6 at transverse excitation levels a_{gd} = 0.16g, 0.35g, and 0.50g

Generally, the results using the modifications according to [CC04] and [PCK07] are rather similar for the majority of bridges. It may be noteworthy that for bridge configuration 1 the modified multi-modal pushover analysis with [PCK07] yields slightly conservative demand estimations, whereas the same procedure with [CC04] results in a slight underprediction of the displacements. Although this underprediction may not be severe, the fact that it occurs at bridge configuration 1, where the correction by a displacement modification factor is most relevant, might attribute some advantage to the solution by [PCK07] with $\eta(\xi)$ from [EC8-1-1]. On the other hand, the fact that the equivalent

linearization according to [PCK07] requires an iterative solution for the target displacement, whereas the displacement modification factor approach based on [CC04] does not require any iteration, lets the latter approach appear more appropriate for practical applications.
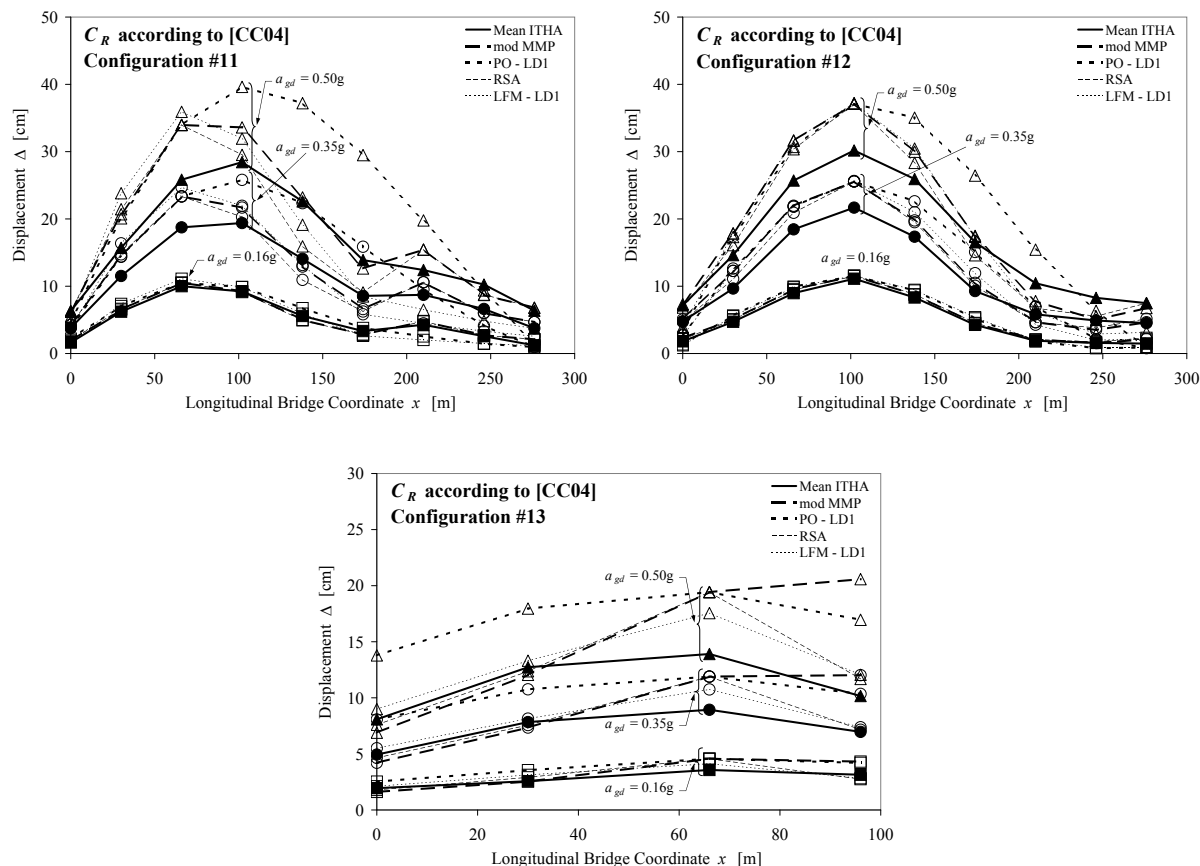

Fig. 4.56: Displacement demands based on proposed modified analysis procedures
using displacement modification factors according to [CC04]
for bridge configurations 11, 12, and 13 at transverse excitation levels a_{gd} = 0.16g, 0.35g, and 0.50g

The quality of the results from the other three analysis procedures (RSA, LFM - LD1, and PO - LD1) depends on the degree to which higher modes and stiffness redistributions in the inelastic range control the response. Both aspects are influenced by the level of irregularity of the individual bridges. The two linear analysis methods (i.e. RSA and LFM - LD1) are conceptually best suited for low ductility response cases, typically resulting at low to medium PGA levels (e.g. $a_{gd} \leq 0.16g$). As the results by Berweger [Ber09] (presented in Section 4.6.2) show, in such cases even the introduction of a displacement modification factor might be dispensable. However, care should be taken with structures in the very short period range as in these cases even low ductility demands can already cause significant demand increases.

For rather simple and regular structures, the linear analysis methods may still result in rather reasonable demand estimations even for moderate ductility levels (if applied with some form of displacement modification factor as discussed above). However, the reliability of the results reduces with increasing degree of inelasticity so that in these cases the linear methods should rather only be used as a rough orientation or for a plausibility check of more sophisticated nonlinear analysis results. Empirically, the presented data suggest that – especially in the inelastic range – the lateral force method with *Load Distribution 1* (LFM - LD1) may even yield somewhat better and more conservative results than the response spectrum analysis (RSA). This phenomenon, which might appear surprising at first sight, is related to the fact that the inelastic response tends to smoothen out the sometimes very uneven modal distribution of inertia forces represented by the RSA. This effect is captured better by the *Load Distribution 1* of the lateral force method being based on a uniform acceleration shape.

*Fig. 4.57: Displacement demands based on proposed modified analysis procedures
using equivalent linearization principles according to [PCK07] with η (ξ) from [EC8-1-1] (1994)
for bridge configurations 1 through 6 at transverse excitation levels a_{gd} = 0.16g, 0.35g, and 0.50g*

The conventional pushover analysis, using *Load Distribution 1* (PO - LD1), may be considered as an approximation of the multi-modal pushover analysis, or could also be considered as an extension of the lateral force method to the inelastic range. As a consequence, it is related to the multi-modal pushover analysis in a similar way as the lateral force method is related to the response spectrum analysis. To some extent, this is also reflected by the response predictions achieved with the pushover analysis using *Load Distribution 1*. The field of application for the pushover analysis is primarily in the inelastic response range as this analysis method is capable of allowing for stiffness redistributions as a result of ductile behavior. However, the conventional pushover analysis is conceptually not able to capture the influence of modal response (especially higher modes) in a realistic way. Therefore, the predicted displacement shapes are less accurate than those from a multi-modal pushover analysis. To some extent this deficit is compensated by the fact that the conventional pushover analysis with *Load Distribution 1* often rather overpredicts the results of a multi-modal pushover analysis over large part

of the structure. Some similarity may be discovered in this context with the tendency of the lateral force method to rather overpredict the results from a response spectrum analysis.

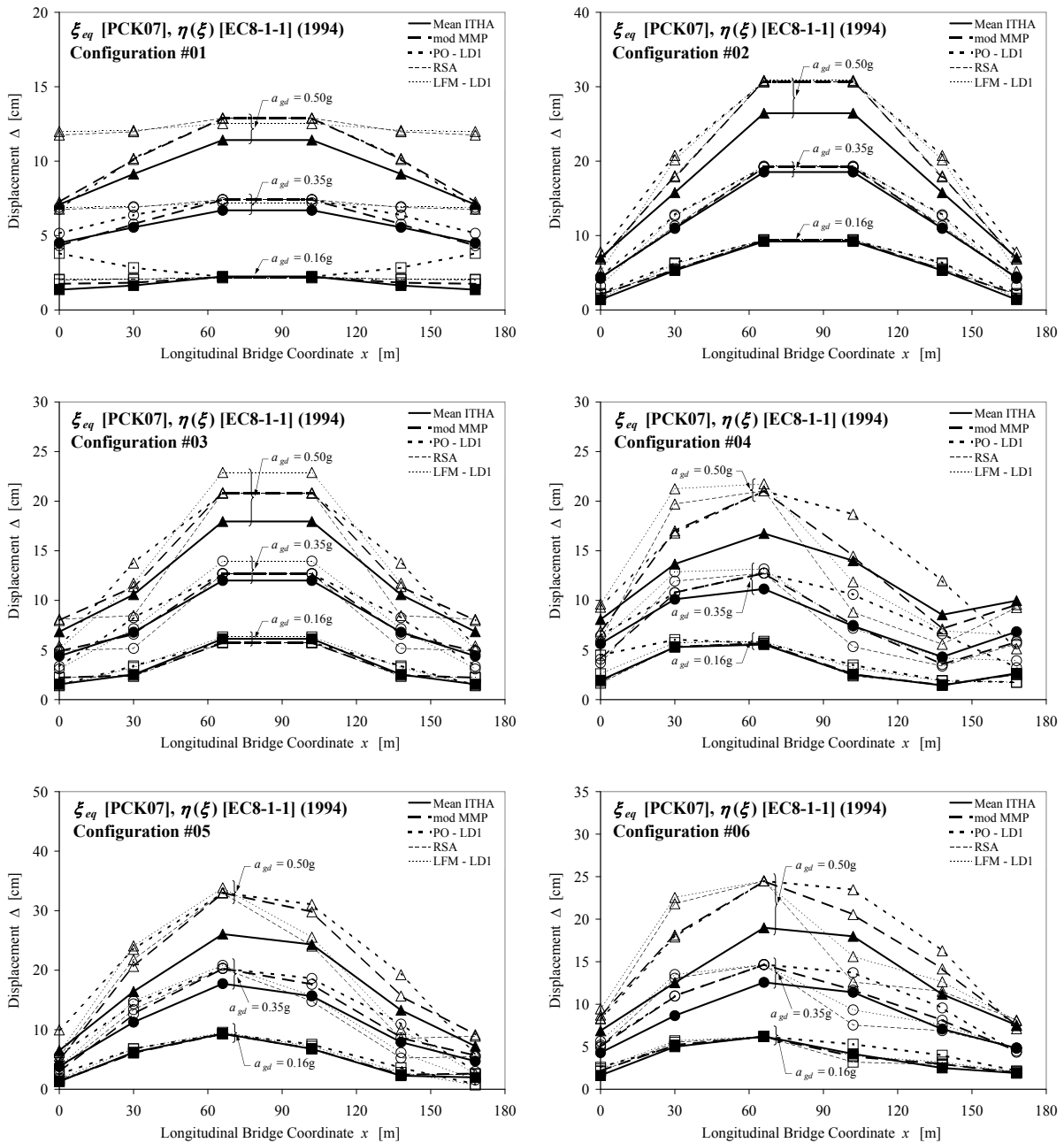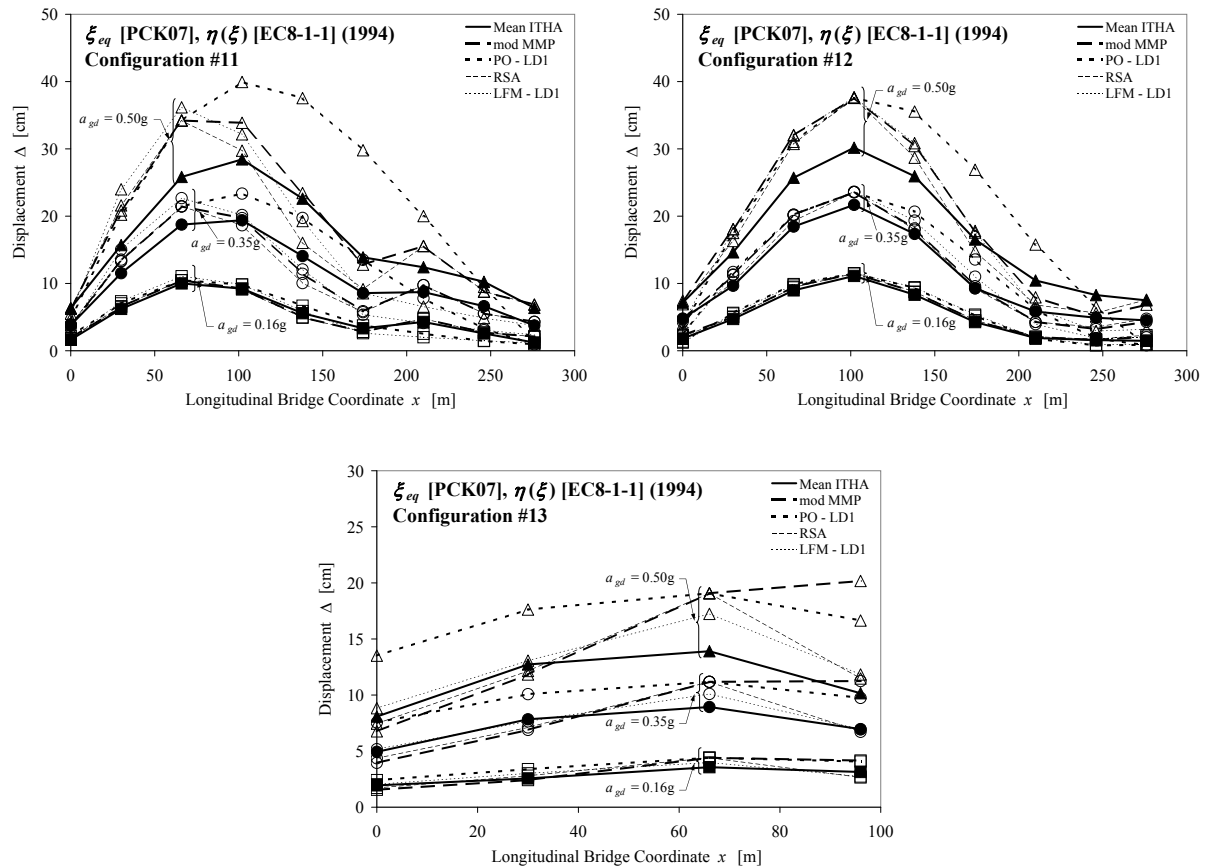*Fig. 4.58: Displacement demands based on proposed modified analysis procedures using equivalent linearization principles according to [PCK07] with η (ξ) from [EC8-1-1] (1994) for bridge configurations 11, 12, and 13 at transverse excitation levels a_{gd} = 0.16g, 0.35g, and 0.50g*

In those parts of a structure where the response is strongly controlled by higher modes, the inherent conservative tendency of the conventional pushover analysis may not be sufficient anymore to compensate for the lack of modal representation. As a consequence, in some of the analyzed bridge configurations the displacements in the edge regions – especially those of the abutments – are underpredicted by the conventional pushover analysis. As long as this unconservatism remains limited to the abutments, it might still be considered as acceptable if the primary focus of the analysis is on the response of the piers (while the abutment behavior is only considered as a boundary condition). However, care should be taken as similar underpredictions might generally also occur in other parts of the structure, especially in the case of more complex and irregular bridges. Aside from these potential problems, the proposed form of the conventional pushover analysis in the majority of cases gives rather reasonable and conservative demand estimations in the inelastic range.

Summarizing the findings from the above evaluations, it can be concluded that all four proposals for the modified analysis procedures can give reasonable demand estimations if applied under appropriate circumstances. Generally, it is recommended to allow for the influence of inelasticity on the global deformation demand by computing the target displacement of the reference point either based on the displacement modification factor according to [CC04] or based on the equivalent linearization principles of [PCK07] together with the $\eta(\xi)$ relationship from [EC8-1-1] (1994). If significant inelastic action is expected, then the (modified) multi-modal pushover analysis is likely to yield the most realistic results. However, even this rather sophisticated method cannot guarantee a reliable demand prediction in every case. With increasing complexity of the structure at least local response underpredictions cannot be ruled out even for the multi-modal pushover analysis (see e.g. right end region of bridge configuration 12 at a_{gd} = 0.35g and 0.50g).

Fig. 4.59: Displacement demands based on proposed modified analysis procedures
using equivalent linearization principles according to [Guy04] with η (ξ) from [EC8-1-1] (1994)
for bridge configurations 1 through 6 at transverse excitation levels a_{gd} = 0.16g, 0.35g, and 0.50g

Therefore, it might be a cautious approach to complement the MMP with an additional conventional pushover analysis using *Load Distribution 1*. The displacement envelope from both analyses should then be used for the assessment. Such a solution would conceptually correspond to the provisions of [EC8-2] Annex H, where the pushover analysis using a first mode proportional acceleration shape (required by [EC8-2] Annex H) would be replaced by the modified multi-modal pushover analysis. This alternative proposal does not really represent noticeably more effort than the original provisions of [EC8-2] Annex H. The modified multi-modal pushover analysis also requires a nonlinear static analysis using a first-mode proportional load distribution. The additional superposition of the linear elastic higher modes in the modified multi-modal pushover analysis is of little extra effort because the required response spectrum analysis needs to be performed anyway for the determination of the target displacement of the reference point according to [EC8-2] Annex H.

The additional use of a displacement modification factor (or equivalent linearization principles) to modify the target displacement represents some limited additional effort. However, the analyses by Berweger [Ber09] have shown that this modification is imperatively necessary because otherwise the global deformation demand can be severely underpredicted – especially for structures in the short period range (see configuration 1 in Fig. 4.46). For the bridge configurations considered in this evaluation, the use of an envelope as described above results in essentially conservative demand predictions in almost all cases. Only for one pier, a significant underprediction of the displacement demand remained (pier 7 in bridge configuration 12: ≈ -30% at a_{gd} = 0.35g and ≈ -20% at a_{gd} = 0.50g). However, taking into account that even the ITHA results feature a significant coefficient of variation (see Fig. 4.38 and Fig. 4.39)[28], these underpredictions might still be accepted in exceptional cases as a form of inevitable uncertainty in any seismic analysis.
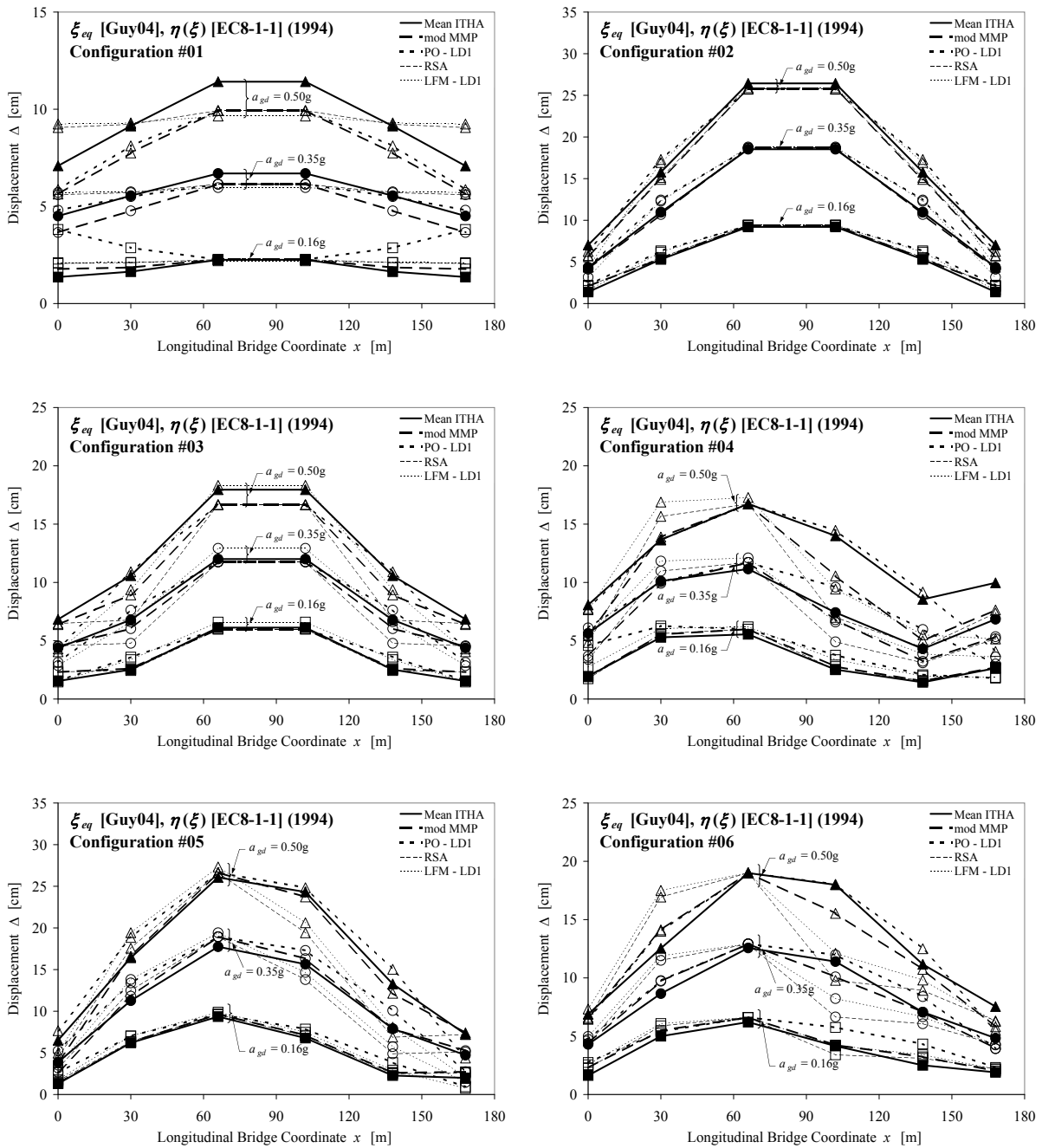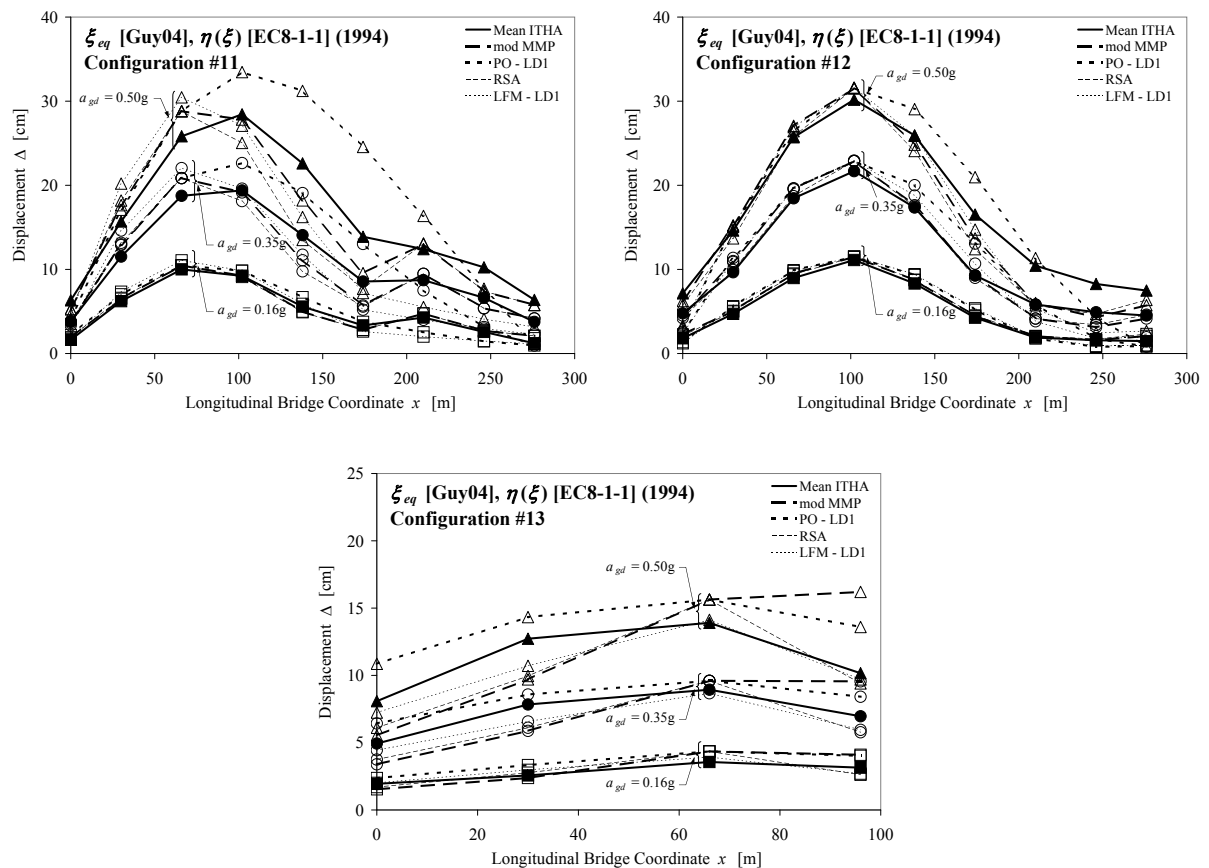

Fig. 4.60: Displacement demands based on proposed modified analysis procedures
using equivalent linearization principles according to [Guy04] with η (ξ) from [EC8-1-1] (1994)
for bridge configurations 11, 12, and 13 at transverse excitation levels a_{gd} = 0.16g, 0.35g, and 0.50g

In the almost-elastic or low-ductility range, often encountered in low to medium seismicity regions (e.g. a_{gd} ≤ 0.16g), the use of one of the elastic analysis procedures (RSA or LFM - LD1) can be a very efficient alternative to the more demanding inelastic pushover analyses (conventional or multi-modal). Especially for structures with the first mode falling into the low period range the modifications proposed in this subsection, i.e. the use of a displacement modification factor (or equivalent linearization), is recommended. The analysis results presented above suggest that the modified elastic methods can give a reasonable representation of the seismic bridge response as long as no significant redistribution of internal stiffnesses occurs. Such redistributions (already at limited global inelasticity) are likely to occur especially in very irregular bridges where short piers are located next to or between taller piers. As a result, the short pier can already experience significant inelastic actions while the

---

[28]   It should be kept in mind that the ITHA results presented in Fig. 4.38 and Fig. 4.39 are based on artificial ground motions which approximate the target spectrum rather closely. Real recorded ground motions would result in significantly higher scatter between the various ITHA results.

longer piers still remain elastic (see e.g. bridge configuration 6 at $a_{gd} = 0.16g$). Although this behavior might not be reproduced correctly by the linear analysis procedures, the corresponding results in such a case are at least likely to show that the short pier is deformed into the inelastic range. By critically checking the analysis results of rather irregular structures it might therefore be possible to detect such cases where a further inelastic analysis appears recommendable.

Furthermore, if some limited inelastic action in (parts of) the structure is detected by one of the linear analysis procedures, it may be recommendable to apply both, the response spectrum analysis and the lateral force method (with *Load Distribution 1*). It can then be considered as a somewhat cautious approach to use the envelope of the two sets of analysis results for the assessment, in a similar way as for the two types of pushover analyses discussed above. Although the lateral force method may formally be considered as the less accurate procedure (compared to the RSA), if applied with *Load Distribution 1*, it tends to result in somewhat smoother deformation shapes which empirically tend to approximate limited stiffness redistributions better. As can be seen e.g. from the results for bridge configuration 6 at $a_{gd} = 0.16g$, the suggested use of an envelope covering both sets of linear results would reduce the risk of unconservative results for the short pier number 3. Nevertheless, in case of strong irregularities or significantly differing ductility demands between adjacent piers, it should be considered complementing the demand estimations by additional inelastic analyses.

Aside from their application in low-ductility demand situations, the two modified linear methods may also be useful in more general cases. Although it is not recommendable to solely rely on their results in medium or high ductility demand situations, they can nevertheless represent valuable means for checking the results of more sophisticated analyses. Any inelastic analysis – be it a pushover analysis or a dynamic ITHA – bears the potential to errors due to its complexity. Therefore, simpler analysis procedures are required which are, on one hand, applicable without excessive effort and which, on the other hand, may be more accessible to plausibility checks based on general engineering understanding, due to their simplicity. The response spectrum analysis and the lateral force method appear well suited for this purpose. Although they may not be able to fully reproduce the local behavior at every part of an inelastically responding structure, the above results show that the global response can be captured satisfactorily if the proposed use of displacement modification factors (or equivalent linearization) is included in the linear analyses. This general check of the global response can be very valuable and may serve to decide whether the more complex inelastic analysis results can be trusted. It should be noted that, if the two types of pushover analyses are used for the inelastic analyses in the form as proposed above, then an additional check by a response spectrum analysis does not represent any extra effort at all because both RSA and displacement modification factor are computed anyway during the course of the pushover analyses.

Generally, it should be kept in mind that any of the simplified analysis procedures can only produce approximate results. A certain amount of uncertainty and potential for unconservative results therefore always remains. On the other hand, due to variations between individual ground motions and general modeling uncertainties, some scatter is also involved in ITHA. Nevertheless, the advantage of having different analysis methods at hand, at least provides a means for mutual checking of the corresponding results. At the same time, it should be noted that even the simpler of the discussed analysis methods could be improved by the modifications proposed in this section, compared to the originally unmodified versions included in [EC8-3], [SIA2018], or [EC8-2] Annex H. The problem of model uncertainties, inevitable in any analysis method, can typically only be covered by variation of the corresponding modeling assumptions and structural properties within the range of potential values.

For practical cases, it is recommended to apply the available analysis methods stepwise with a hierarchy of increasing sophistication (i.e. LFM, RSA, PO, MMP, ITHA). This way, the understanding of the load carrying mechanisms is improved and a constant checking of the results is possible right from the beginning. This stepwise application also serves for deciding whether further analyses using the next more sophisticated approach is still required. Finally, it should be noted that the above discussions only focused on the response in the seismic load case. It might be necessary to take into account additional actions, e.g. from gravity loads, which act together with the seismic loads. It may not always be possible to satisfactorily represent the combined action using a linear analysis method. Such cases can call for an inelastic analysis although the seismic loading alone might be covered sufficiently by a linear elastic analysis.

4.7   Influence of Strength Degradation

It is known that structures can loose part of their strength under increasing seismic demand levels. In this context it is common practice to distinguish between two different ways how this strength degradation develops. On the left side of Fig. 4.61, an example of the so-called *in-cycle strength degradation* is shown which is characterized by a negative tangent stiffness in the inelastic range resulting in a loss of strength *within* individual cycles. A typical cause of in-cycle strength degradation can e.g. be *P*-Δ effects in combination with low post-yield stiffness of the structure, which together can result in a global negative tangent stiffness in the inelastic range.

For comparison purposes, on the right side of Fig. 4.61 an example of the so-called *cyclic strength degradation* is shown. In this case, no loss of strength occurs *within* the individual cycles but rather *between* two successive hysteresis loops. One typical cause of cyclic strength degradation can be related to lap-splices of the longitudinal reinforcement in the plastic region of flexural members which fail under increasing cyclic deformations.
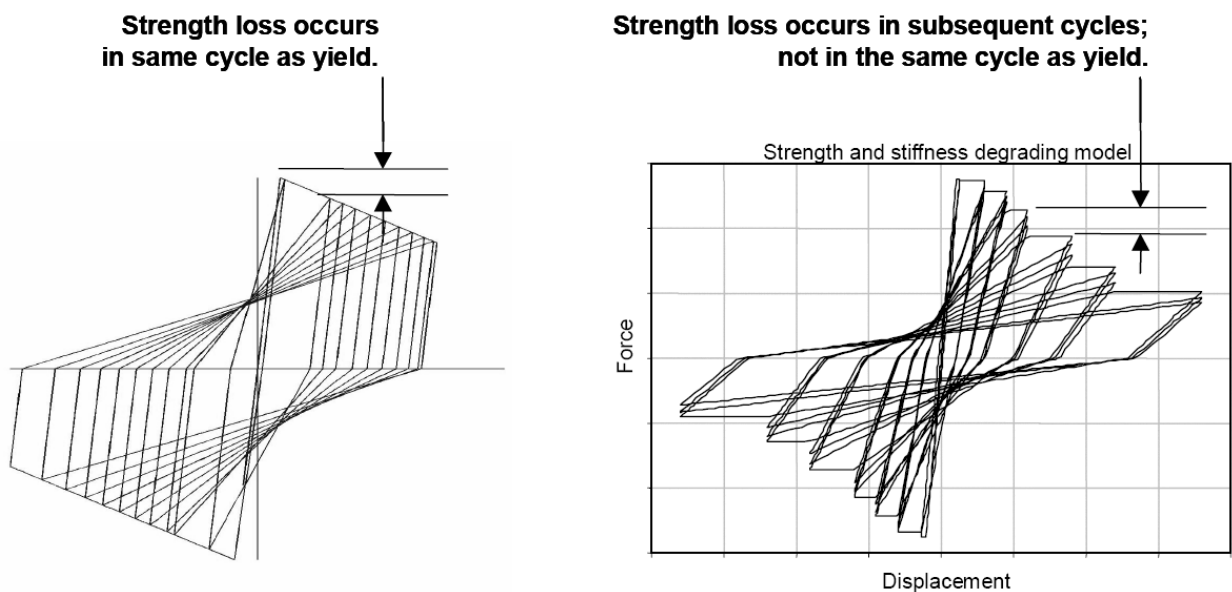
*Fig. 4.61: Definition of different types of strength degradation according to [FEMA440],
left: In-cycle strength degradation, right: Cyclic strength degradation*

While both types of strength degradation can influence the displacement demand of a structure under seismic excitation, the consequences and the type of influence are likely to vary for both cases, so that it is necessary to treat them separately. In an inelastic time history analysis (ITHA), it is theoretically possible to introduce both types of strength degradation directly into the hysteretic model, provided the software code contains adequate modeling options. In this case, any effect on the displacement demand is automatically taken into account within the analysis.

If, however, the analysis technique does not allow the explicit inclusion of strength degradation, as e.g. in the case of an approximate pushover analysis, the dynamic effects should at least be taken into account by further considerations. This means that the primary analysis could be performed with a non-degrading system and any increase of the deformation demand due to strength degradation – be it in-cycle or cyclic – would have to be included approximately in a separate step. A discussion on the behavior of strength degrading systems and their effects on the seismic displacement demand can be found in the following Sections 4.7.1 and 4.7.2 for in-cycle and cyclic strength degradation, respectively.

4.7.1 In-cycle Strength Degradation due to P-Δ Effects

In structures with members carrying significant axial compression forces the equilibrium conditions change with increasing deformations due to the development of P-Δ effects. It is known that under static conditions these effects must be taken into account as they can cause the development of a local or global instability of the system. In a similar way, P-Δ effects can also play an important role under seismic loading, although their influence on the dynamic response of structures is more complex than for static cases. The influence of the P-Δ forces can be interpreted as an effective change of the load-deformation behavior as depicted in Fig. 4.62 for the bilinear backbone of a single-degree-of-freedom (SDOF) cantilever column. While the horizontal force resistance $F_h^I(\Delta)$ without consideration of P-Δ effects results directly from the base moment M_{base} as given by equation (4.41), the load-deformation relationship is modified to $F_h^{II}(\Delta)$ according to equation (4.42) if the equilibrium conditions are formulated for the deformed system.
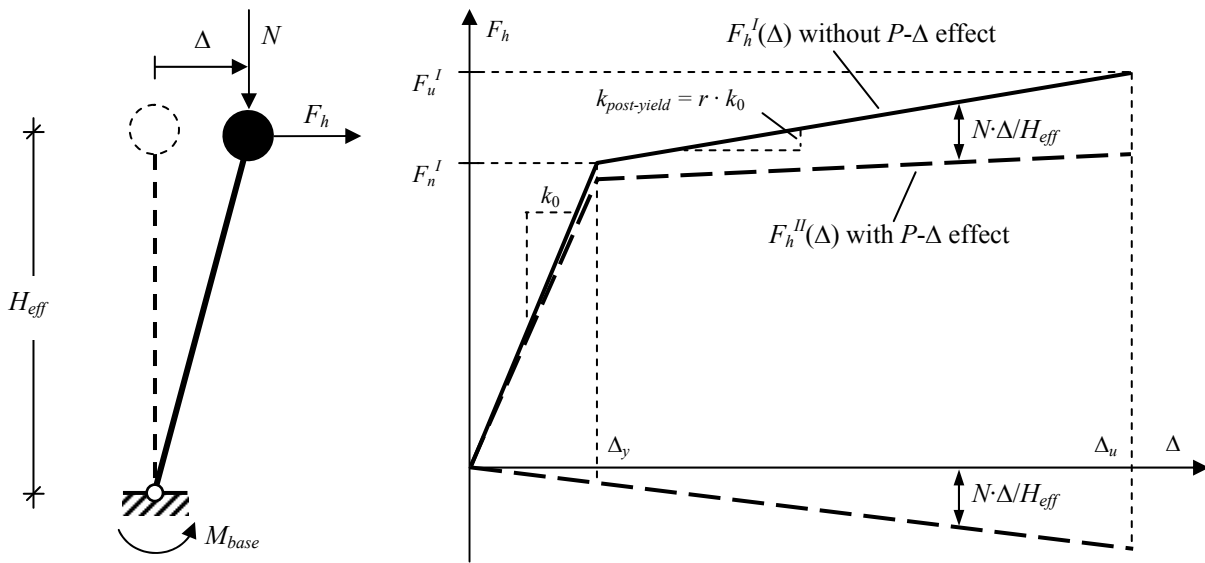

Fig. 4.62: Influence of P-Δ effects on effective force-displacement behavior

$$\text{without } P\text{-}\Delta \text{ effect:} \qquad F_h^I(\Delta) = \frac{M_{base}(\Delta)}{H_{eff}} \qquad\qquad (4.41)$$

$$\text{with } P\text{-}\Delta \text{ effect:} \qquad F_h^{II}(\Delta) = \frac{M_{base}(\Delta)}{H_{eff}} - N \cdot \frac{\Delta}{H_{eff}} \qquad\qquad (4.42)$$

The term $N \cdot \Delta / H_{eff}$ being subtracted in equation (4.42) causes a softening of the system in the elastic and the inelastic range. In a corresponding way, the entire hysteretic response is modified thus changing the dynamic properties of the system. The reduction of the elastic stiffness k_0 causes a (typically slight) increase of the initial period T_0 which can result in a subsequent increase of spectral displacements. The reduction of the post-yield stiffness and the corresponding change of the cyclic hystereses is likely to have a noticeably more pronounced influence on the response modification due to P-Δ effects [Mac94]. In total, the displacement demand of such a modified dynamic system can be increased compared the response without P-Δ influence. In certain cases this aspect can be dominant causing a dynamic instability. In contrast to unstable behavior under static loading, the dynamic instability typically does not consist of a single unlimited excursion in one direction. Instead, unstable response under seismic loading rather causes the system to successively crawl off in one direction over several cycles. While a dynamically stable system will largely cycle about its initial center position, unstable systems tend to cumulate residual displacements resulting in the center point of the vibration to veer off in one direction. As a consequence, the extent of such dynamically unstable behavior also

depends on the number of large inelastic cycles and the duration of the strong motion phase of an earthquake.

The susceptibility to P-Δ effects and especially to potential for dynamic instability depends on a variety of characteristics. Aside from the magnitude of the axial compression load, the type of hysteretic shape was found to have a considerable degree of influence (see e.g. MacRae *et al.* [MPT93], Fenwick and Davidson [FD94], Tremblay *et al.* [TDL98]). Results from inelastic time history analyses (ITHA) performed in these studies have shown that systems with elasto-plastic or bilinear hysteretic behavior are influenced much stronger by P-Δ effects than e.g. stiffness degrading systems which are more representative for the behavior of reinforced concrete structures. The better recentering tendency upon unloading of stiffness degrading systems reduces the residual displacements after large inelastic cycles and thus limits their tendency to crawl in one direction. Therefore, especially the degradation of the unloading stiffness plays an important role, with lower unloading stiffnesses causing better behavior. A concept to take into account the P-Δ related behavior of general hysteresis types has been proposed by MacRae *et al.* [MPT93]. In this approach a "hysteresis centre curve" is defined whose characteristics allow the definition of a corresponding substitute bilinear hysteresis featuring a similar behavior.

An important parameter concerning the likelihood of a crawling behavior is the post-yield stiffness $r \cdot k_0$. If the reduced post-yield stiffness under the influence of P-Δ effects results as negative (see Fig. 4.62), the system becomes prone to dynamic instability (Bernal [Ber87], MacRae *et al.* [MPT93], Miranda and Akkar [MA03]). Some studies also found an influence of the fundamental period of the system and the frequency content of the ground motion on the relevance of P-Δ effects ([TDL98], [MA03]).

The most direct way of taking into account all these aspects is by performing inelastic time history analysis using a model that explicitly includes the P-Δ effects. Examples of how to include their influence on the pier behavior in simplified 2D models are shown in Fig. 3.49 and Fig. 3.52 for single piers and entire bridge structures, respectively. Alternatively, approximate approaches have been proposed in the literature to account for P-Δ effects in a simplified way without having to include them explicitly in the analysis. One possible strategy is to perform the analysis without P-Δ effects and subsequently increase the deformation demand based on empirical equations. Such an approach is e.g. included in [FEMA356]. However, a review of these provisions in the framework of [FEMA440], based on the work by Miranda and Akkar [MA03], replaced the modification relationship for the displacement demand of [FEMA356] by a relationship for a minimum strength in order to prevent dynamic instability. If this minimum strength is provided, no further modifications of the demand are required by [FEMA440]. In this context, it should be mentioned that the underlying investigation by Miranda and Akkar [MA03] was based exclusively on the response of systems with bilinear hystereses, not considering stiffness degrading models which are more representative for reinforced concrete structures.

An alternative approach consists of performing a simplified analysis without consideration of P-Δ forces and subsequently increasing the system strength in order to approximately compensate for the influence of the related effects. The empirical relationships for the required strength increase are calibrated so that the modified system with P-Δ effects experiences the same displacement demand as the original system without their consideration. Such an approach has been used e.g. by Bernal [Ber87], MacRae *et al.* [MPT93], Fenwick and Davidson [FD94], Tremblay *et al.* [TDL98], as well as Pettinga and Priestley [PP07]. It should be noted that, due to the complex dynamic behavior, considerable scatter must be expected when approximately accounting for P-Δ effects by means of any of the simplified approaches ([FD94], [MA03]). Therefore, Caltrans *Seismic Design Criteria* [Cal06] e.g. require that, if P-Δ effects are considered relevant, they can only be captured accurately by means of an inelastic time history analysis.

At the same time, as common for static loading cases, it appears reasonable to define limits below which the influence of P-Δ forces can be neglected. Due to their dependence on the deformations, especially in low to moderate seismic conditions with corresponding limited displacement demands P-Δ effects may not always be relevant. Corresponding limit criteria have been proposed using the

stability index θ_{max} at peak displacement Δ_{max} as defined in equation (4.43)[29]. Based on a literature review, MacRae [Mac94] has found proposed limits for neglecting P-Δ effects in the range of $\theta_{max} \leq 0.15$ to $\theta_{max} \leq 0.2$. Presuming a rather strong post-yield strength increase in well-confined RC columns, Caltrans *Seismic Design Criteria* [Cal06] also allow a limiting value of 0.2 in connection with a similar criterion. Priestley *et al.* [PCK07] propose the use of stricter limits for neglecting P-Δ effects, being $\theta_{max} \leq 0.05$ for steel structures and $\theta_{max} \leq 0.1$ for reinforced concrete structures. Considering the inevitable uncertainties due to the complex dynamic behavior and the various influencing factors not entering into such a simple criterion, it is recommended to use the more cautious proposals by Priestley *et al.* [PCK07].

$$\theta_{max} = \frac{N \cdot \Delta_{max}/H_{eff}}{F_n^I} \tag{4.43}$$

It appears likely that the use of the above criteria in low to moderate seismic regions, and considering the typically limited displacement capacities of older existing structures, may often allow neglecting P-Δ effects in the analyses. In those cases, where the criteria are not fulfilled, an approximate consideration of the influences from P-Δ forces can be achieved using the previously mentioned concept of strength modification. In a new design the strength of the system would be amplified by a certain margin after the simplified analysis without P-Δ effects has been performed, in order compensate for their influence. In an assessment situation, the strength of an existing structure cannot be increased anymore. Therefore, the simplified analysis must be performed on a system with the strength being artificially reduced by a corresponding margin. Based on the findings from the study by Pettinga and Priestley [PP07], Priestley *et al.* [PCK07] propose reducing the base shear capacity F_n^I for the analysis by ΔF_n according to equation (4.44). The modified force-displacement relationship with the reduced strength for the analysis is shown in Fig. 4.63. For the constant C, Priestley *et al.* [PCK07] recommend a value of $C = 1$ for steel structures and $C = 0.5$ for reinforced concrete structures. Since the expression for ΔF_n depends on the peak displacement Δ_{max}, which is not known before the analysis, an iterative solution can become necessary. However, conservatively Δ_{max} could also be replaced by the ultimate displacement capacity Δ_u, thus avoiding an iteration.

$$\Delta F_n = C \cdot N \cdot \frac{\Delta_{max}}{H_{eff}} \tag{4.44}$$
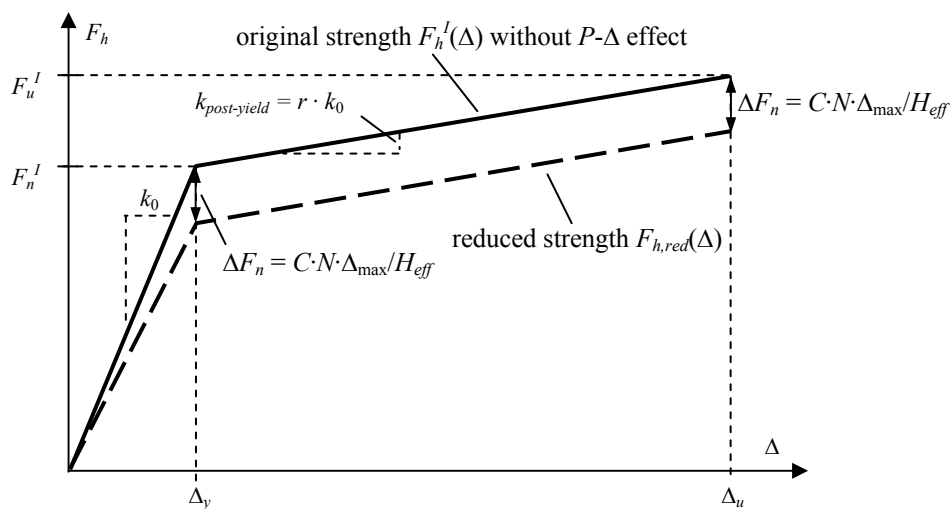

Fig. 4.63: *Artificially reduced strength to account for P-Δ effects in assessment cases*

---

[29] Note that in some literature sources the stability index θ is defined with respect to the yield displacement Δ_y instead of Δ_{max}. The two different definitions must be distinguished in corresponding equations.

4.7.2 Cyclic Strength Degradation from Lap-Splice Failure

Several experimental studies have shown that flexural RC members with lap-splices of the longitudinal reinforcement in the plastic hinge region can develop cyclic strength degradation under cyclic inelastic loading [CPS91], [Lyn+96], [MWC03]. These findings are also confirmed by a test series on models of existing bridge piers carried out at ETH Zürich by the author. This test campaign also included two test-units which were almost identical, the only difference being that one unit, VK1, had continuous longitudinal reinforcement from the foundation to the pier top, while the other unit, VK2, featured a lap-splice of the longitudinal bars at the pier base. The details of the test units and the experimental results can be found in Section 5.

It is noteworthy that previous test campaigns conducted in the US [CPS91], [Lyn+96], [MWC03] always featured splice lengths l_s of about 20 bar diameters (d_{bl}), which are representative of older compression splices according to past US practice. In contrast, in Switzerland already in older code generations significantly longer splice lengths were required. For an adequate representation of this Swiss practice, a splice length of $l_s = 43\ d_{bl}$ was chosen for test unit VK2. As might be expected, the test results suggest that this increased length provides a somewhat better behavior of the lap-splices under cyclic loading than that found in the US studies. However, cyclic strength degradation was still found to occur also for these longer splices. While the splice length does have an influence on the point where degradation starts, and possibly also on the gradient of degradation, at least within the range of tested splice lengths, the degradation could not be prevented. Therefore, also for the Swiss situation it is necessary to study the influence that cyclic strength degradation can have on the seismic displacement demand of structures.

This investigation can be conducted best by response comparisons between structures with and without lap-splice, while the seismic demand is estimated based on inelastic time history analysis. For this purpose, hysteretic rules for both models are required. While for the non-degrading system without lap-splice standard plastic hinge approaches and established hysteretic models, as e.g. the modified Takeda rule, can be used, the system with lap-splice further requires a rule for the description of the cyclic strength degradation. A model for the backbone estimation of bridge piers with cyclic degradation due to failing lap-splices in the plastic hinge region is proposed in [PSC96] as a function of member deformations, expressed as strains and ductilities. However, this model was rather calibrated on shorter US lap-splices as mentioned above. Therefore, the longer lap-splices typically found in existing Swiss bridge piers may not be described adequately when applying the model of [PSC96] without further consideration or modification.

For the current study, it was rather chosen to calibrate the hysteretic models directly on the measured static-cyclic response of test units VK1 and VK2 mentioned above. The calibration process leading to numerical models for the cyclic behavior of bridge piers with and without lap-splices in their potential plastic zones is described in the following Subsection *a*.

a) Calibration of Hysteretic Models for Piers with and without Lap-Splices

In Fig. 4.64, the results from the calibration of two different hysteretic models for test unit VK1 without strength degradation are shown using the software codes Ruaumoko 2D [Car04] and IDARC 2D [RVK06]. In Ruaumoko, it was intended to choose the modified Takeda hysteresis rule for the numerical representation. However, it was found that even for the thinnest possible Takeda loops that can be modeled in Ruaumoko, i.e. using an unloading parameter of $\alpha_{unload} = 0.5$ and a reloading parameter of $\beta_{reload} = 0$, the experimentally determined energy dissipation was significantly lower than the corresponding energy of the numerical model, using the same displacement load history as in the experiment. To improve the agreement between the experiment and the numerical model, two weighted inelastic springs were used in parallel. The first spring is a modified Takeda spring with the parameters mentioned above providing a share of 70% of the total response, while the second spring has an origin-centered hysteresis with the same backbone curve. This origin-centered spring shows only very low energy dissipation and it was chosen to represent 30% of the full response. The hysteresis loops of the numerical model shown in Fig. 4.64 (left) represent the resulting combined spring model consisting of 70% modified Takeda and 30% origin-centered response contribution. The

corresponding development of dissipated energy applying the displacement load history from the test on the numerical model is compared in Fig. 4.65 (left) to the experimentally determined dissipation history of unit VK1. Both curves almost coincide, showing that the energy dissipation characteristics of the numerical model represent the behavior of the test unit fairly well.
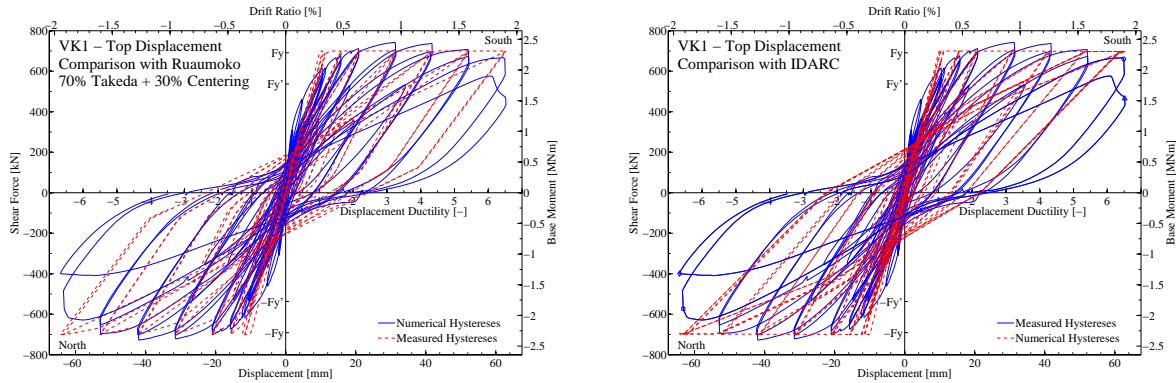

Fig. 4.64: Comparison between measured and numerical hysteresis loops for Test Unit VK1 without lap-splice
left: Numerical model using software code Ruaumoko [Car04],
right: Numerical model using software code IDARC [RVK06]

In the same way, a hysteretic model for test unit VK1 was developed using the *three parameter Park model* [PRK87], [Val+96] as implemented in the software code IDARC [RVK06]. With this model it was directly possible to capture both, the stiffness and the energy dissipation characteristics, of test unit VK1 sufficiently well. The resulting hystereses and energy dissipation history using the displacement history from the experiment are shown on the right sides of Fig. 4.64 and Fig. 4.65, respectively.

Fig. 4.65: Comparison between measured and numerical energy dissipation for Test Unit VK1 without lap-splice
left: Numerical model using software code Ruaumoko [Car04],
right: Numerical model using software code IDARC [RVK06]

In addition to the steps described above, the calibration of hysteretic models for test unit VK2 with the lap-splice at the base requires the development of a rule defining the cyclic strength degradation. For this purpose, an assumption needs to be made with respect to which parameters are considered to control the degradation. The proposed degradation model by Priestley *et al.* [PSC96] for short lap-splices is formulated as a function of strains and ductilities, i.e. depending on deformation states without direct consideration of influences from repeated cyclic loading. Melek *et al.* [MWC03] studied the influence of the load history on the degradation behavior of lap-splices in RC columns. Within their experimental campaign they tested two equal columns, one using a static-cyclic history (test unit 2S20H), while applying almost monotonic displacements to the second column (test unit

2S20HN)[30]. Although both test units exhibited strength degradation with increasing deformation, it became clear that the cyclically loaded column (2S20H) degraded significantly faster. This shows that the degradation of lap-splices is not only a function of the applied peak deformation but is further influenced by cyclic loading.

As the strength degradation can be interpreted as some form of damage, it appears reasonable to take generally established concepts of damage modeling into consideration for the description of lap-splice failure. According to Park and Ang [PA85], e.g., damage can be assumed as a weighted linear combination of peak deformation and dissipated energy, with the latter term allowing for the effects of repeated cyclic loading. From only one test with a single displacement history (as in the case of test unit VK2) it is not possible to determine how the two aspects, peak deformation and dissipated energy from cyclic hystereses, contribute to the total damage, i.e. to the strength degradation. At the same time, the capabilities of the available software codes also limit the possible modeling options to some extent.
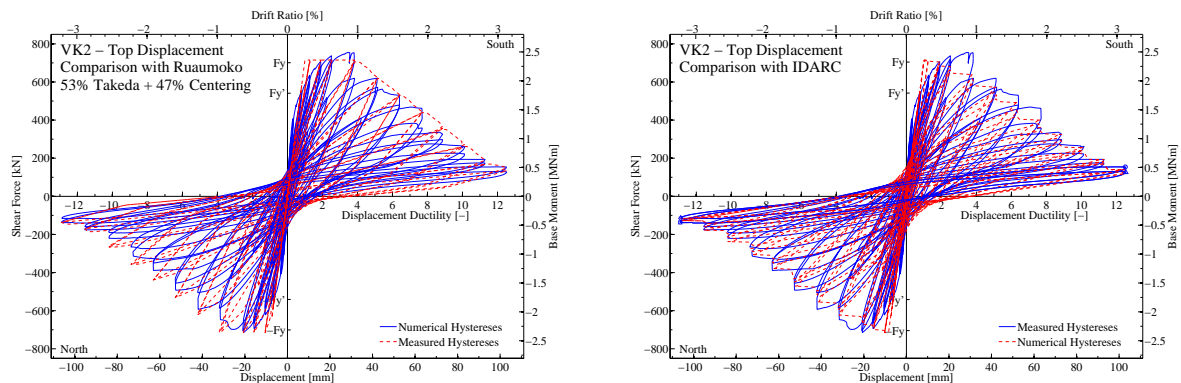
Fig. 4.66: Comparison between measured and numerical hysteresis loops for Test Unit VK2 with lap-splice left: Ductility-dependent cyclic strength degradation model using software code Ruaumoko [Car04], right: Dissipated energy dependent cyclic strength degradation model using software code IDARC [RVK06]

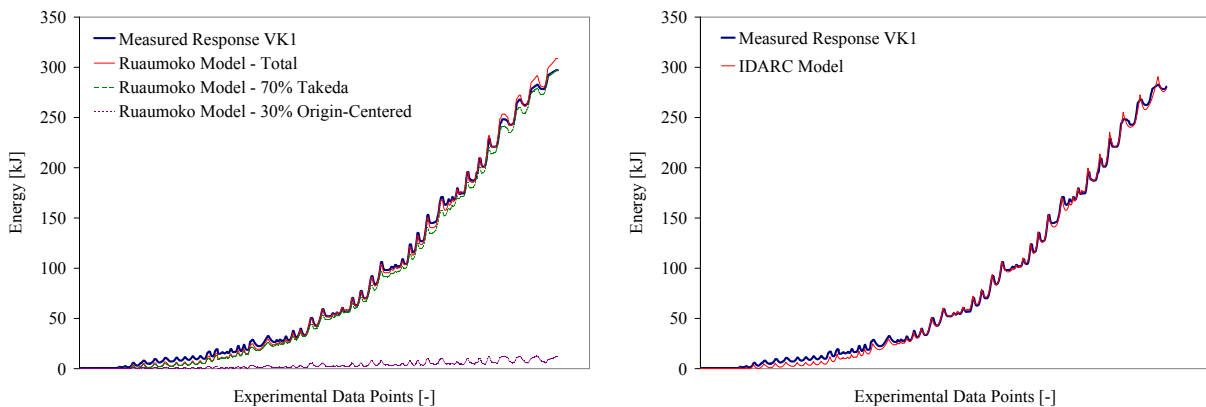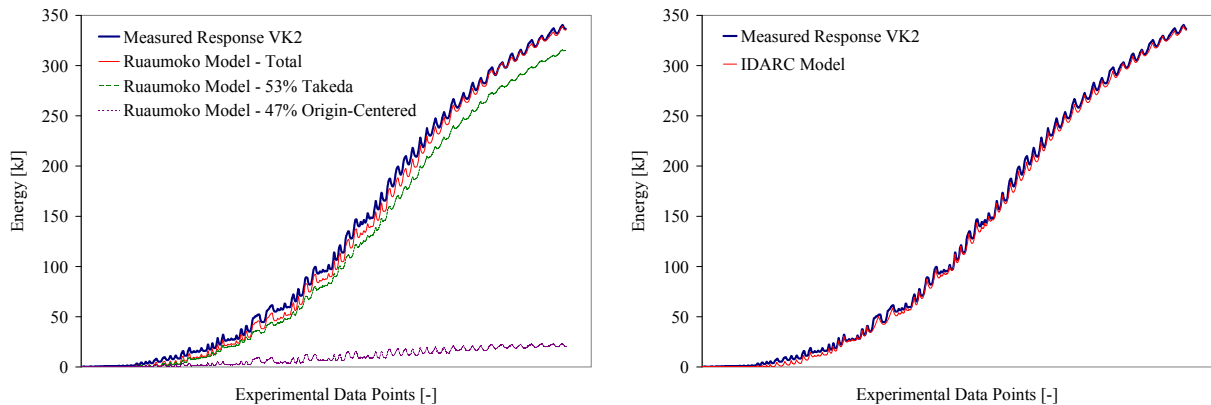*Fig. 4.67: Comparison between measured and numerical energy dissipation for Test Unit VK2 with lap-splice left: Ductility-dependent cyclic strength degradation model using software code Ruaumoko [Car04], right: Dissipated energy dependent cyclic strength degradation model using software code IDARC [RVK06]*

Several calibration alternatives have been tested to approximate the response of VK2 that had been measured during the experiment. Reasonable agreement has been reached with a model in Ruaumoko [Car04] that formulates the strength degradation due to lap-splice failure as a function of the peak deformation expressed by the displacement ductility μ_Δ. A comparison between the measured

---

[30] The loading of test unit 2S20HN was meant to represent a near fault displacement history. After initial cyclic loading up to drift ratios of 1% ($\mu_\Delta = 1.7$) and a half-cycle at 1.5% ($\mu_\Delta = 2.6$), the column was monotonically deflected up to a drift ratio of a about $\delta = 12\%$.

hystereses of VK2 and the corresponding numerical loops from the numerical Ruaumoko model with ductility dependent strength degradation is shown on the left side of Fig. 4.66. The corner ductilities of the multi-linear degradation backbone were chosen to fit the measured hysteretic response from the experiment. As in the case of VK1, it was necessary to model a combination of a Takeda spring and an origin-centered spring in parallel, as the energy dissipation of a pure Takeda spring was too high, even for the unloading and reloading parameters representing the thinnest possible loops. For VK2, the two springs were weighted by ratios of 53% and 47% for the Takeda and the origin-centered share, respectively. The resulting dissipated energy applying the displacement history from the experiment to the numerical model is compared to the measured energy dissipation of test unit VK2 on the left side of Fig. 4.67, showing that the chosen combination of Takeda and origin-centered springs represents the energy dissipation behavior in the experiment rather well.
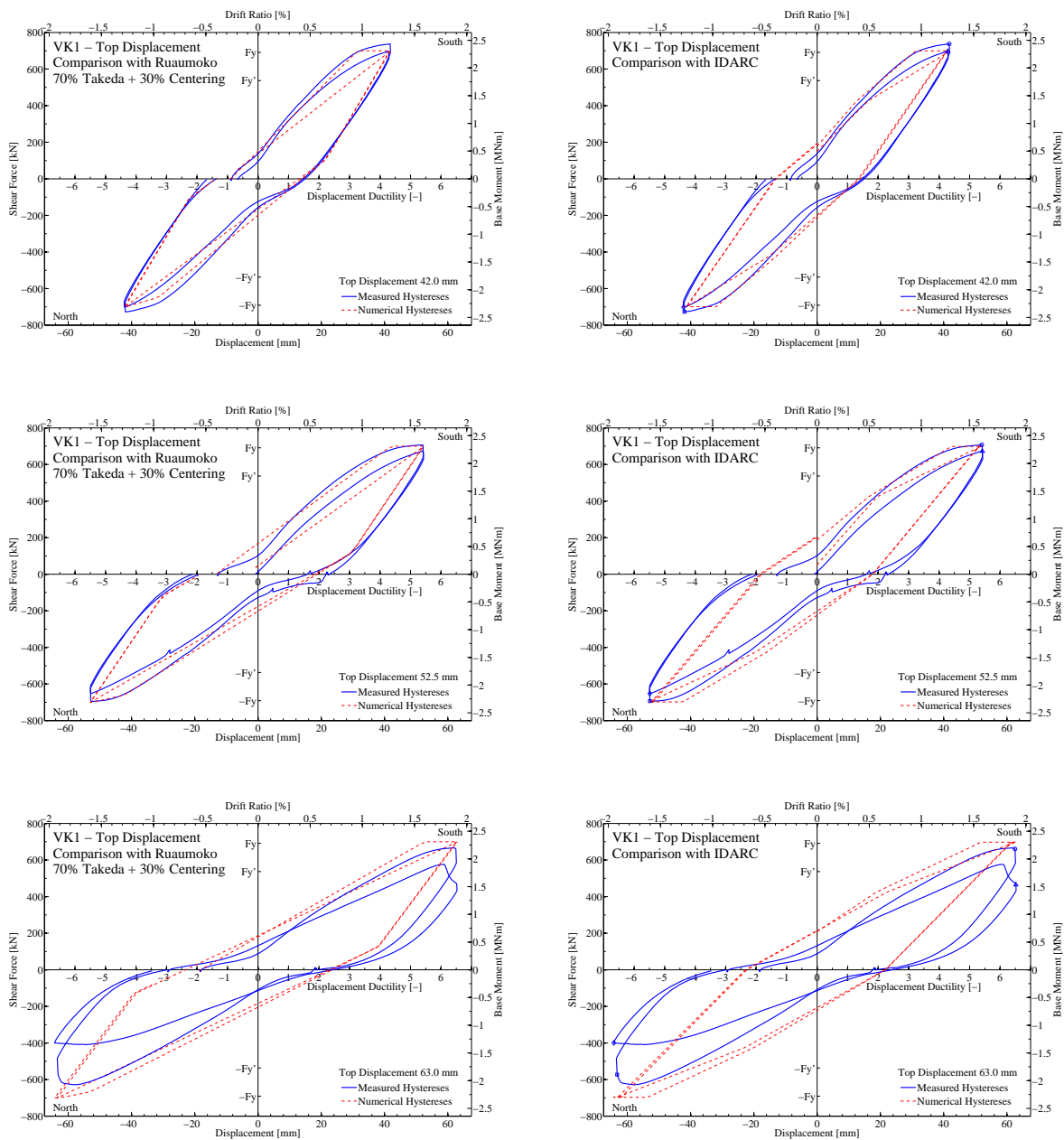
Fig. 4.68: Individual measured and numerical hysteresis loops for Test Unit VK1 without lap-splice
left: Numerical model using software code Ruaumoko [Car04],
right: Numerical model using software code IDARC [RVK06]

4.7 Influence of Strength Degradation

An alternative degradation model for VK2 was developed using the software code IDARC [RVK06]. The basis of the hysteretic rule is again the three parameter Ang model, as for the case of VK1. In addition, for VK2, cyclic strength degradation is introduced as a function of dissipated energy during previous cycles. The parameters defining the degradation relationship within IDARC were calibrated to approximate the measured response of VK2 during the experiment. The resulting numerical loops for the displacement history from the test are compared to the measured hystereses on the right side of Fig. 4.66. The corresponding comparison between dissipated energy histories from the test and the numerical model are shown on the right side of Fig. 4.67. These curves demonstrate that the energy dissipation characteristics of the numerical model are approximated very well for the displacement history used in the experiment.

A comparison between selected individual loops from the experiments and the different numerical models described above is shown in Fig. 4.68 and Fig. 4.69 in order to illustrate the level of accuracy reached by the calibration.
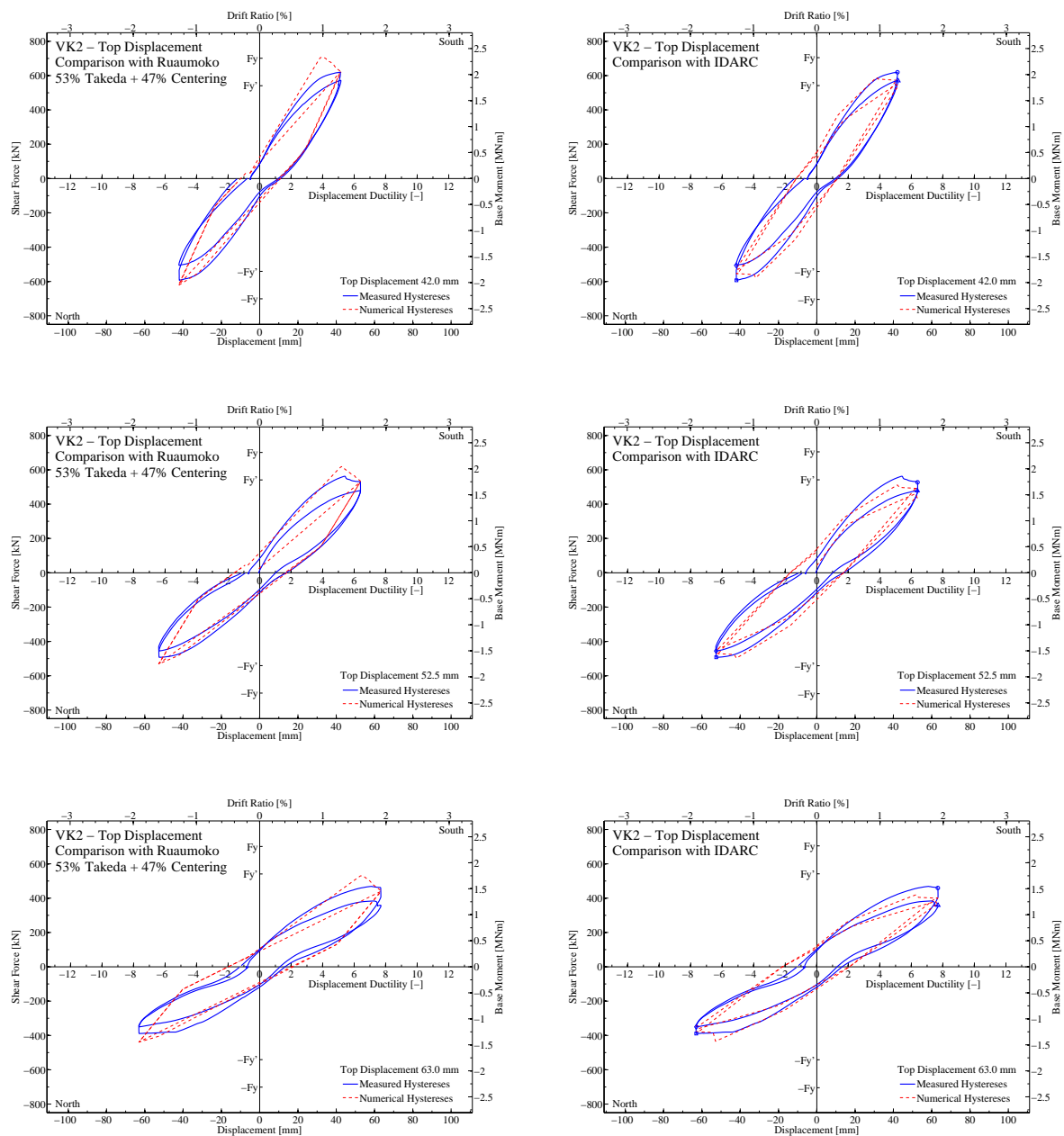

Fig. 4.69: Individual measured and numerical hysteresis loops for Test Unit VK2 with lap-splice
left: Ductility-dependent cyclic strength degradation model using software code Ruaumoko [Car04],
right: Dissipated energy dependent cyclic strength degradation model using software code IDARC [RVK06]

As the degradation in the Ruaumoko model for VK2 is purely deformation (i.e. ductility) dependent and the strength degradation in the IDARC model is a pure function of dissipated energy, these two approaches can be interpreted as boundary cases for the general Park and Ang damage model [PA85] which considers damage as the function of a weighted combination of these two parameters. It is conceptually inherent to such a calibration process that the two numerical models give a similar degrading hysteretic response as the one measured during the test of VK2 (see Fig. 4.66). However, as the two numerical representations are based on completely different types of parameters (deformations and dissipated energy), this good agreement will not be ensured for a general loading. The displacement history used in the experiment implies a unique relationship between peak displacements and dissipated energy, i.e. number and size of preceding cycles. For any other displacement history, the relationship between these two parameters will be different so that the way the strength loss develops will also deviate between the two models.

A better representation could probably be reached if the numerical rule would be formulated using a combination of the parameters for deformation and dissipated energy, as in the Park and Ang damage model. However, to establish such a relationship reliably, a series of experiments with varying load histories would be required. Furthermore, the software code would, of course, also need to allow an adequate representation of such a relationship by means of its implemented models. Several modeling alternatives have been tested during the calibration process and the two cases shown in Fig. 4.66 and Fig. 4.67 have turned out to give the best representation of the experimental results. Due to their boundary characteristics (with respect to the general Park and Ang damage model), they might be expected to give an upper and lower estimation of the strength degradation of VK2 for more general displacement histories.

The characteristic data of the model backbones for test units VK1 and VK2 are summarized in Tab. 4.14 as calibrated on the experimental measurements, but without consideration of degradation effects. For the ductility dependent degradation model of VK2 in Ruaumoko, the corresponding corner points, as defined in Fig. 4.70, are given in Tab. 4.15.

		VK1	VK2
Nominal yield displacement	Δ_y [mm]	9.77	8.22
Nominal force capacity	F_n [kN]	700	715
Initial stiffness	k_0 [MN/m]	71.6	87.0
Post-yield stiffness	$k_{post-yield}$ [MN/m]	0	0

Tab. 4.14: Characteristic data of model backbones for test units VK1 and VK2
as calibrated on experimental data

		Deflection	Force	
Onset of degradation	Δ_{deg} [mm] [a]	31.2	715	F_{deg} [kN]
	$\mu_{\Delta,deg}$ [-] [a]	3.8		
Residual capacity	Δ_{res} [mm] [a]	94.5	172	F_{res} [kN]
	$\mu_{\Delta,res}$ [-] [a]	11.5		
Total loss of strength	Δ_{ult} [mm] [a]	148	0	F_{ult} [kN]
	$\mu_{\Delta,ult}$ [-] [a]	18		

[a]   Definition of corner points according to Fig. 4.70.

Tab. 4.15: Characteristic data of deformation dependent degradation curve for test unit VK2
corresponding to experimentally calibrated backbone
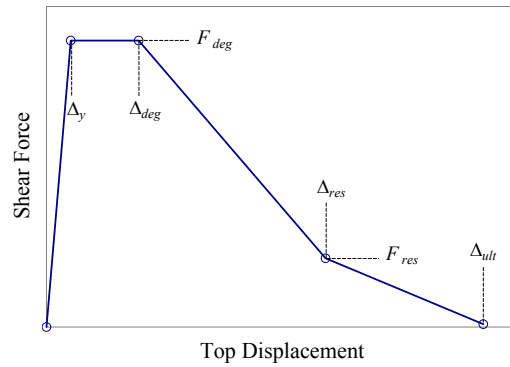
4.7 Influence of Strength Degradation

Fig. 4.70: Deformation dependent degradation backbone for Ruaumoko model of test unit VK2

Based on these hysteretic models for VK1 and VK2, the topic of a master thesis was developed aiming at studying the influence of cyclic strength degradation on the seismic displacement demand. In this master thesis, being co-tutored by the author, Kurmann [Kur09] used the previously developed hysteretic models for VK1 and VK2 to perform extensive dynamic analyses. Using the analysis results it was possible to compare the displacement demand of systems with cyclic strength degradation to that of systems without degradation. As the hysteretic models presented above are only valid for the particular test units on which they had been calibrated, Kurmann developed a second set of hysteretic models for VK1 and VK2 which was based on a numerical moment-curvature analysis and the plastic hinge concept [PCK07]. This approach allowed the variation of the pier heights within the study [Kur09] while keeping the same cross-section as that of the test units in the experiment. In this second calibration the backbones without consideration of strength degradation were purely based on the numerical analyses without influence of the experimental results. The corresponding characteristic data of the backbones, which then result equal for VK1 and VK2, are summarized in Tab. 4.16. The strength degradation characteristics for VK2 were also newly calibrated by Kurmann using the experimental data but adjusting the ductilities to the modified numerical backbone. The data for the new deformation dependent degradation curve in Ruaumoko are given in Tab. 4.17.

		VK1 & VK2
Nominal yield displacement	Δ_y [mm]	14.5
Nominal force capacity	F_n [kN]	715
Initial stiffness	k_0 [MN/m]	49.3
Post-yield stiffness	$k_{post\text{-}yield}$ [MN/m]	0

Tab. 4.16: Characteristic data of model backbones for test units VK1 and VK2
as computed by means of a numerical plastic hinge concept [Kur09]

		Deflection	Force	
Onset of degradation	Δ_{deg} [mm] [a]	25.8	715	F_{deg} [kN]
	$\mu_{\Delta,deg}$ [-] [a]	1.8		
Residual capacity	Δ_{res} [mm] [a]	72.6	250	F_{res} [kN]
	$\mu_{\Delta,res}$ [-] [a]	5.0		
Total loss of strength	Δ_{ult} [mm] [a]	141	0	F_{ult} [kN]
	$\mu_{\Delta,ult}$ [-] [a]	9.7		

[a]   Definition of corner points according to Fig. 4.70.

Tab. 4.17: Characteristic data of deformation dependent degradation curve for test unit VK2
as computed by means of a numerical plastic hinge concept [Kur09]

In Fig. 4.71, the two sets of model backbones for VK1 and VK2 (including strength degradation in the case of VK2) are compared to the corresponding measured backbone curves from the experiments. It can be seen that the general approximation of the measured response is fairly good. With respect to the degradation of VK2, the purely experimentally calibrated model represents rather a somewhat upper bound corresponding to the measured 1st cycle response, while the partly numerically determined model is closer to the backbone of the 2nd cycles, thus serving as a lower bound approximation.
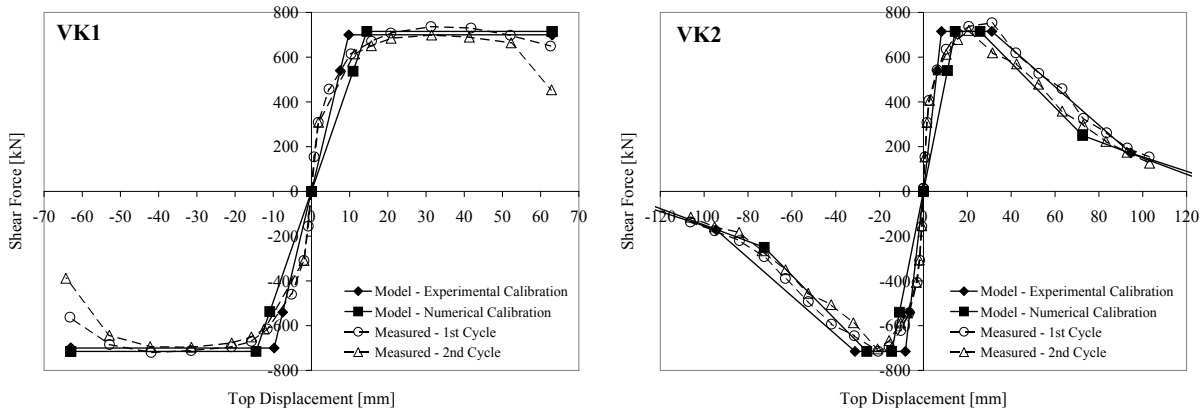
Fig. 4.71: Comparison between the two model backbones and the measured backbones
left: VK1 without strength degradation, right: VK2 with deformation dependent strength degradation

The two sets of model backbones for VK1 and VK2 are further compared to each other in Fig. 4.72. In particular, it is noteworthy that the initial stiffness of the two numerically determined backbones for VK1 and VK2 is considerably lower than the corresponding values from the calibration on the experimental data. Furthermore, the experimentally calibrated initial stiffness of VK2 is somewhat higher than that of VK1, which is related to twice the longitudinal reinforcement being effective within the inner part of the lap-splice of VK2. The various differing initial stiffnesses influence the dynamic response, and thus the displacement demand, especially in the elastic or low ductility range.
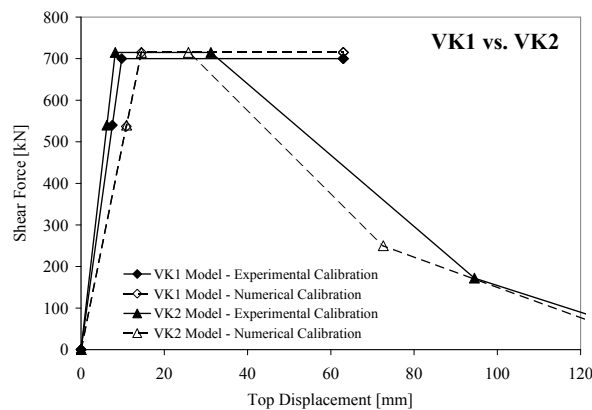
Fig. 4.72: Comparison between the model backbones of test units VK1 and VK2
(deformation dependent degradation for the case of VK2 as used in Ruaumoko)

One consequence is that the models based on the numerically determined backbone will always have the same dynamic response for VK1 and VK2, as long as the deformation demand remains below the limit ductility for onset of degradation and if deformation dependent strength degradation is modeled for VK2 (as in Ruaumoko). In the case of the experimentally determined backbones for VK1 and VK2, however, even before the onset of degradation the response of the two test units will not be the same, due to the differing initial stiffnesses. This latter type of modeling therefore results in a combination of two influences from the lap-splice in VK2, (a) the stiffer initial behavior and (b) the cyclic strength degradation at higher deformation demands. On one hand, these experimentally

calibrated models of VK1 and VK2 according to Tab. 4.14 and Tab. 4.15 represent the real behavior of the two test units in the most realistic manner, including the two-fold influence of the lap-splice in VK2. On the other hand, the numerically determined models, as defined in Tab. 4.16 and Tab. 4.17, allow an investigation of the pure influence of cyclic strength degradation on the displacement demand without the additional influence from elastic stiffnesses differing between VK1 and VK2.

Only the numerically determined models allow a direct variation of the pier height in order to study other geometric configurations. For this purpose, Kurmann [Kur09] used moment curvature analysis and a plastic hinge concept [PCK07] to estimate the force-displacement backbone of piers having the same cross-section but featuring varying heights. The parameters for the hysteretic behavior and the corner ductilities of the deformation dependent degradation curve in Ruaumoko [Car04] were kept the same as those of the numerical model for the original geometric configuration corresponding to the layout of the test units.

Generally, all analyses in Kurmann [Kur09] were conducted for full-scale piers. As the test units in the experimental campaign had a scale of 50%, an appropriate rescaling scheme for the geometry and force-displacement behavior was used to compute the corresponding full-scale characteristics. In Fig. 4.73 the hysteretic responses of full-scale bridge piers with an effective height of 6.6 m are compared for the case of numerically determined backbones as described above. For this purpose, inelastic time-history analysis (ITHA) on an individual single-degree-of-freedom (SDOF) pier with tributary mass at its top was conducted. On the left side, the response of a pier without lap-splice at its base is shown as computed with the two software codes Ruaumoko [Car04] and IDARC [RVK06] for an artificial spectrum-compatible ground motion with a design peak ground acceleration of $a_{gd} = 0.35$ g[31]. As might be expected, the resulting responses from the two software codes are quite similar. The minor differences are only related to the different hysteretic rules – the modified Takeda (in combination with an origin-centered rule) and the three parameter Park model – which were used in the two programs.
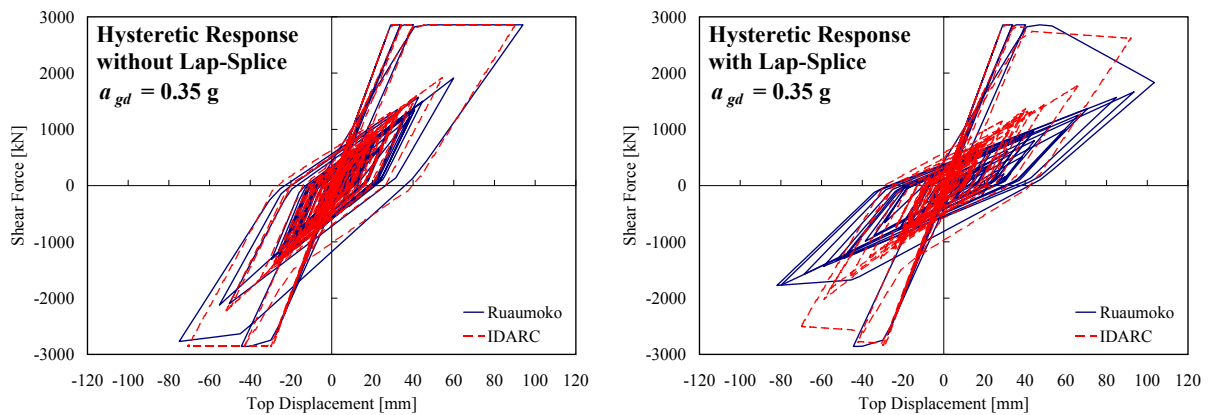
Fig. 4.73: Comparison of dynamic responses using Ruaumoko and IDARC for a ground motion with a_{gd} = 0.35g left: bridge pier without lap-splice, right: bridge pier with lap-splice

On the right side of Fig. 4.73, an equivalent comparison is made for the same pier, but this time with a lap-splice at its base (i.e. with cyclic strength degradation). Here it can be seen that, due to the different modeling of the strength degradation, the cyclic responses computed with the two programs deviate stronger. The deformation dependent degradation model in Ruaumoko results in a more pronounced loss of strength capacity than the IDARC model in which the degradation is formulated as a function of the dissipated energy. This effect, which could generally be found for other accelerograms as well, is related to the fact that the experimental displacement history, used for the calibration of the two degradation models, had a significantly different relation between peak

---

[31] The target spectrum for the accelerogram corresponds to the shape of the elastic spectra as defined in [SIA261]. According to [SIA261], the design peak ground acceleration of, here, a_{gd} = 0.35 g is modified to account for local soil conditions and importance of the structure. In the presented case these modifications result in an overall peak ground acceleration of a_g = 0.59 g.

displacement and dissipated energy than the resulting response history from the dynamic analyses. In some sense, as mentioned above, the two degradation models can be considered as upper and lower boundaries for the degradation effect, with the deformation dependent model in Ruaumoko typically resulting in a more pronounced loss of strength. However, it is noteworthy that despite considerable differences in loss of strength, shown on the right side of Fig. 4.73 (Ruaumoko 27% less residual strength than IDARC), the displacement demand differed only by 12%. It can therefore be assumed, that the effect of the differing models on the displacement demand is less pronounced than that on the loss of force capacity.

b) Results of Single-Degree-of-Freedom Analyses

The hysteretic models described in the preceding subsection were used by Kurmann [Kur09] for a comprehensive study on the influence of lap-splices on the seismic displacement demand of existing bridge piers. At first, he used single-degree-of-freedom (SDOF) models of individual piers to study the influence of lap-splices independent from other effects existing in an entire bridge structure. In the SDOF systems a tributary mass from the superstructure of 550 t was modeled which corresponds to the axial load ratio used in the experiments of VK1 and VK2 and can be considered to roughly represent a concrete superstructure with span widths in the range of 30 to 40 m.

The investigation on the SDOF behavior comprises, in total, eight different hysteretic models, resulting from the differences between (i) with vs. without lap-splice, (ii) experimentally calibrated vs. numerically determined backbone, and (iii) Ruaumoko vs. IDARC software code. Furthermore the elastic viscous damping ratio was modeled on one hand as $\xi_{el} = 2\%$ as well as $\xi_{el} = 5\%$ – in both cases as constant, i.e. initial stiffness or mass proportional damping. The analyses were conducted for three different levels of seismicity defined by design peak ground accelerations a_{gd} of 0.16 g, 0.35 g, and 0.50 g. Due to modification factors for soil type and importance of structure, these values were further increased by about 70%, resulting in overall peak ground accelerations a_g of 0.27 g, 0.59 g, and 0.84 g, respectively. In the following discussion, the excitations will be named by the design value a_{gd} of the peak ground acceleration although the effective values are higher. As the seismic zones in [SIA261] are typically characterized by a_{gd}, this discrepancy appears justified in order to enable a better comparison with the values prescribed by the code.

The dynamic analyses were conducted with four artificial accelerograms and four scaled recorded ground motions at each seismicity level mentioned above, except for $a_{gd} = 0.50$ g where only the artificial ground motions were used. The target spectra for the artificial accelerograms correspond to the elastic response spectra according to [SIA261] for soil class B ($S = 1.2$) and importance class III ($\gamma_f = 1.4$). The recorded real ground motions were scaled in order to approximate the target spectrum by minimizing the average quadratic error of the spectral accelerations over a period range of 0.5 s to 2.0 s. This range was expected to represent the relevant periods corresponding to the secant stiffnesses at peak displacement demand. Based on the analysis results for these ground motions, a second round of scaling was performed using an improved period range of 0.35 s to 1.0 s over which the deviations were minimized. Part of the analyses was repeated with these newly scaled recorded ground motions. It should be noted that, due to the large number of combinations resulting from the different modeling alternatives as well as seismicities and ground motions, not every possible permutation was analyzed. Details about the conducted analyses can be found in [Kur09].

The analysis results can be evaluated with respect to a variety of aspects. Before going into the details of the influence of lap-splices on the displacement demand, a brief discussion on the influence of the modeling alternatives will be given. In Fig. 4.74, the ratios between displacement demands from Ruaumoko analyses and those from the IDARC analyses are shown as a function of the drift ratio for a full-scale pier with an effective height of 6.6 m. Every point in the graphs corresponds to one pair of analyses conducted with the two software codes and the points are distinguished by peak ground acceleration and type of backbone determination.

As for the example cases of Fig. 4.73, the analyses without lap-splice, shown on the left side of Fig. 4.74, typically show little deviation between the two programs. This could be expected because the two hysteretic models used in the different software codes were calibrated to represent more or less the

same cyclic behavior. This rather good agreement is confirmed by the average displacement ratio of 1.03 and the corresponding rather low standard deviation of 6%.
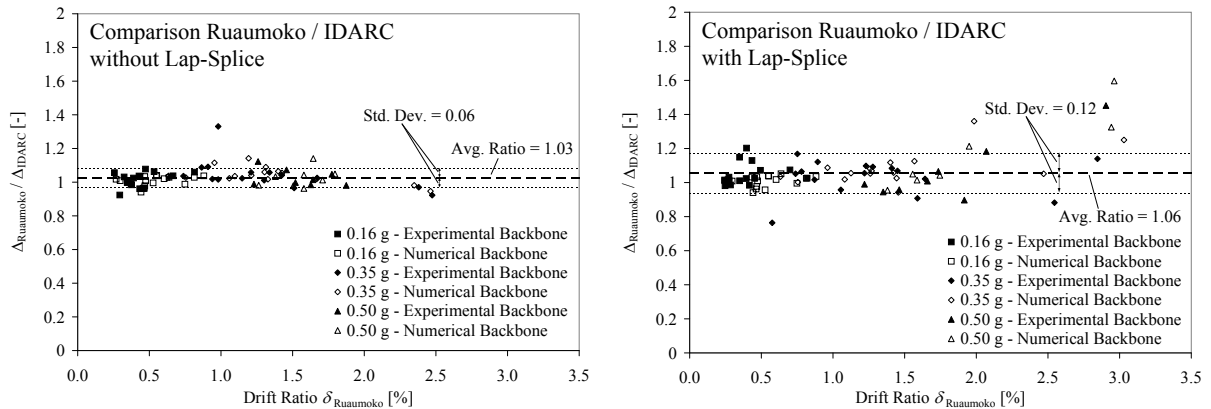

Fig. 4.74: Influence of software code on inelastic displacement demand (Data: [Kur09])
left: pier without lap-splice and strength degradation, right: pier with lap-splice and strength degradation[32]

As can be seen on the right side of Fig. 4.74, for the strength degrading case with lap-splice the deviations between the results of the two software codes are somewhat larger. While the average ratio of 1.06 can still be considered as fairly good, the scatter represented by the standard deviation of 12% shows some differences between the two programs. While the agreement is still good for lower drift ratios, especially above $\delta = 2\%$ somewhat larger differences can be encountered. For these larger drift ratios, the Ruaumoko model tends to result in higher displacement demands, which is related to the different modeling of strength degradation in the two programs as already discussed above in the context of Fig. 4.73. However, these stronger discrepancies appear to be limited to larger deformation demands corresponding to rather high seismicity levels where the deformation dependent strength degradation modeling of Ruaumoko results in significant loss of strength, while the energy dependent model of IDARC degrades less due to the limited number of cycles. For the Swiss seismicity of not more than $a_{gd} = 0.16$ g the differences between Ruaumoko and IDARC are significantly less pronounced thus making the results less dependent on the software code and the type of degradation modeling. If only the data for $a_{gd} = 0.16$ g are taken into account, an average ratio of 1.03 results between the Ruaumoko and the IDARC analyses with lap-splice. In this case, the standard deviation also reduces to 5%, underlining the better agreement between the two programs for the conditions of the highest seismic zone (3b) in Switzerland according to [SIA261].

Another issue that can be studied on the basis of the data from [Kur09] is the influence of the elastic viscous damping ratio on the displacement demand of inelastic SDOF systems with and without cyclic strength degradation. Several proposals to account for the influence of varying viscous damping ratios ξ on the average displacement demand of linear systems are presented in Section 4.4.2. These are defined in the form of a modification factor η according to equations (4.6) through (4.11). However, it is not necessarily obvious that the influence of constant (i.e. mass proportional) elastic viscous

---

[32] One extreme outlier point is not shown in the graph and it is also ignored for the statistical analysis. This particular point resulted from a Ruaumoko analysis with cyclic strength degradation. It occurred at a design peak ground acceleration of $a_{gd} = 0.50$ g and an elastic viscous damping ratio of $\xi_{el} = 2\%$ using the numerically determined backbone. For this configuration, a drift ratio of $\delta = 6.8\%$, corresponding to a displacement ductility of $\mu_\Delta = 15.4$, was computed. The residual force capacity at this deformation level resulted as 29 kN which is about 1% of the undegraded strength. These data can be interpreted as a sure failure for which the quantitative numerical values do not matter anymore. At the same time, neither the same case with $\xi_{el} = 5\%$, nor the corresponding analysis with IDARC, gave results which came even close to these data. Therefore, it is considered that including this extreme outlier point into the statistical evaluation would distort the results. Furthermore, it cannot be ruled out that the computed deformation demand is the consequence of numerical problems in the dynamic analysis, possibly as a result of a mutual interaction with the severe degradation.

damping ratios ξ_{el} on the displacement demand of inelastic systems is the same as in the case of linear elastic systems for which the corresponding modification factors η were developed originally.

In Fig. 4.75 the ratios between the displacement demands for $\xi_{el} = 2\%$ and $\xi_{el} = 5\%$ from the analyses by Kurmann [Kur09] are summarized. On the left side, the results from the analyses without lap-splice are shown. The average displacement ratio for this set of data is 1.20 with a standard deviation of 0.13. The equivalent data for the case with lap-splice are shown on the left side of Fig. 4.75. Here the average ratio amounts to 1.31 and the standard deviation of 0.26 is twice as high as that for continuous reinforcement without lap-splice, i.e. without cyclic strength degradation. The somewhat higher mean value for the case with lap-splice appears reasonable as a lower viscous damping here has some kind of progressive effect. At first, a reduction of viscous damping results in a higher displacement demand. As a consequence, the system experiences more strength degradation, which subsequently increases the deformations again.
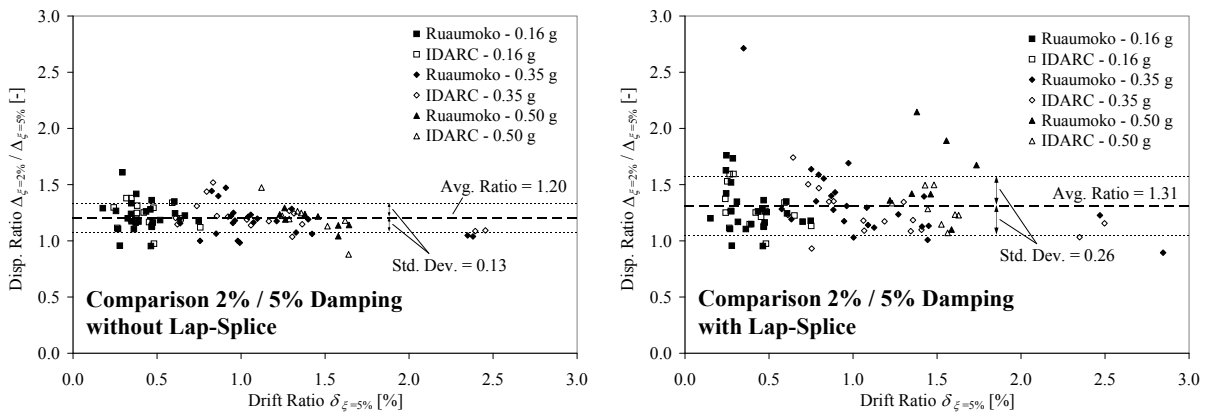

Fig. 4.75: Influence of elastic viscous damping ratio on inelastic displacement demand (Data: [Kur09])
left: Pier without lap-splice and strength degradation, right: Pier with lap-splice and strength degradation[32]

Generally, the two mean displacement ratios of 1.20 and 1.31 lie within the range of modification factors which are proposed for a change between $\xi = 5\%$ and $\xi = 2\%$ as given in Tab. 4.2 for linear systems. The computed mean ratio of 1.20 for the non-degrading systems compares favorably well with the prediction from equation (4.7), proposed in Eurocode 8 (2003) [EC8-1] and also adopted in the Swiss code [SIA261]. The higher displacement ratio of 1.31 for the degrading systems with lap-splice is represented well by equation (4.8) of the older version of Eurocode 8 from 1994 [EC8-1-1] which was also adopted by Tolis and Faccioli [TF99] for damping ratios $\xi \leq 5\%$. It may therefore be concluded that the proposals presented in Section 4.4.2 are generally also applicable to allow for the influence of constant elastic viscous damping on inelastic seismic response. In the given case, the non-degrading system was rather on the lower boundary of proposed values while the strength degrading system with lap-splice lay in the upper range of the values given in Tab. 4.2.

In a further evaluation of the data by Kurmann [Kur09] the influence of the lap-splice on the seismic displacement demand was studied. For this purpose, the same data from the SDOF analyses of full-scale piers with an effective height of 6.6 m as before were used to calculate the ratio between displacement demand with and without lap-splice. The resulting data points are shown in Fig. 4.76 as a function of drift ratio and distinguished by software code and peak ground acceleration. On the left side of Fig. 4.76 the displacement ratios for the experimentally calibrated force-displacement backbones are presented, while the right side shows the corresponding points for the numerically determined backbone.

It can be seen that a considerable difference exists between the displacement ratios for the experimentally calibrated backbone and the numerically determined backbone. This is particularly true at small deformation levels. This phenomenon is related to the fact that the initial stiffness of the numerical backbone is the same for the two cases with and without lap-splice, while for the experimental backbone the initial stiffness is also influenced by the lap-splice. In this latter case, the double amount of effective longitudinal reinforcement within part of the lap-splice increases the initial

stiffness of the pier. The stiffer elastic behavior of the member with experimental backbone and lap-splice leads to somewhat different behavior at low deformation levels, compared to the response of the corresponding pier without lap-splice. As might be expected and as is confirmed on the left side of Fig. 4.76, in many cases the initially stiffer pier with lap-splice results in lower displacement demands as long as the strength degradation does not come into play. This effect is not included in the models with numerically determined backbone. Therefore, on the right side of Fig. 4.76 the displacement demands of the piers with and without lap-splice are the same as long as no strength degradation occurs.
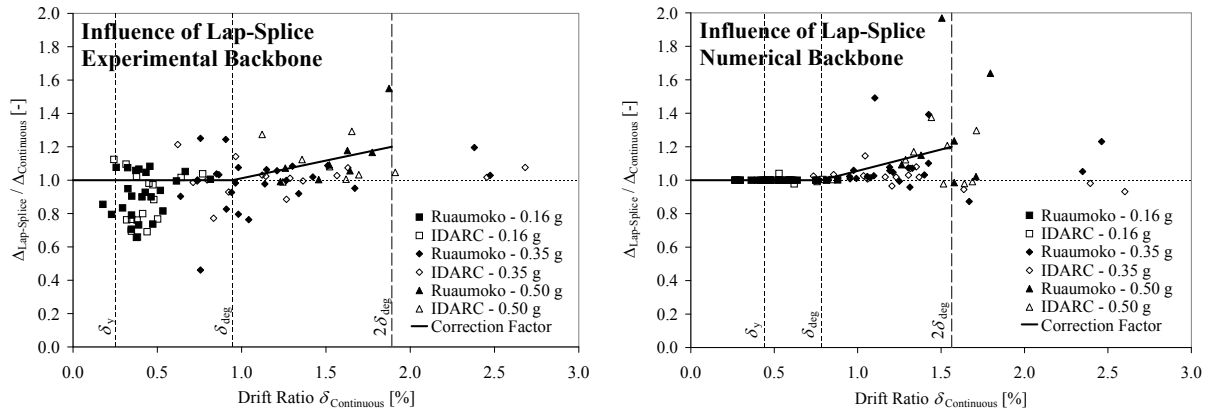

Fig. 4.76: Influence of lap-splice on inelastic displacement demand (Data: [Kur09])
left: Pier with experimentally calibrated backbone, right: Pier with numerically determined backbone[32]

As described in the context of the hysteresis calibration in Subsection a, the deformation dependent degradation model implemented in Ruaumoko uses a fixed ductility $\mu_{\Delta,deg}$ to define at which level the strength degradation starts (see Fig. 4.70, Tab. 4.15, and Tab. 4.17). As a consequence, for the Ruaumoko model with numerically determined backbone, no difference between the response of the piers with and without lap-splice can occur below this corner deformation (see right side of Fig. 4.76). In contrast, the strength degradation model of IDARC results in loss of strength as soon as energy is dissipated, so that the nominal yield displacement acts as an implicit deformation limit for the onset of strength degradation. This is the reason why even for the numerically determined backbone the IDARC results start to show small differences between systems with and without lap-splice already at smaller deformation levels (i.e. starting with the onset of inelastic displacement).

For a better interpretation of the data, three different deformation levels are marked in Fig. 4.76: (i) the nominal yield deformation, (ii) the drift ratio δ_{deg} corresponding to the onset of deformation dependent strength degradation as used in the Ruaumoko model, and (iii) twice the value of δ_{deg}. It can be seen that, in the majority of cases, even for $\delta > \delta_{deg}$ the displacement demands of piers with and without lap-splice remain at least in the same order of magnitude. This seems to be in general agreement with the findings reported in [FEMA440], where it is stated that cyclically strength-degrading systems often exhibit maximum displacements that are comparable to those of non-degrading systems. FEMA 440 further points out that the response of cyclically strength-degrading systems is in general dynamically stable, even for relatively weak systems and large ductilities. These conclusions are generally confirmed by Kurmann's analyses [Kur09].

From the data presented in Fig. 4.76 it can be seen that, as a tendency, after onset of strength degradation the systems with lap-splice experience a somewhat higher displacement demand. This effect appears to be a little more pronounced for the models with numerically determined backbone (right side of Fig. 4.76), where the cyclic strength degradation is considered in an isolated way, i.e. independent of other effects of the lap-splice. For the experimentally calibrated backbone (left side of Fig. 4.76), the increase of displacement demand due to strength degradation is superimposed by the higher initial stiffness which leads to some kind of diminishing effect.

Keeping the scatter of the data in mind, in Fig. 4.76 an attempt is made to roughly describe the trend of displacement ratios under the influence of cyclic strength degradation. The curve, named

"Correction Factor", remains constant at unity up to the deformation δ_{deg} at which the degradation starts in the deformation dependent Ruaumoko model. From this point on, the correction factor increases linearly up to a value of $\hat{\alpha}_{deg}$ at a drift ratio of $\delta = 2\delta_{deg}$. As the existing data do not allow any conclusions about the trends at higher deformation levels, it cannot be ruled out that the scatter beyond $\delta = 2\delta_{deg}$ increases significantly which might make it impossible to recognize any simple trends. The mentioned curve can be described on a general basis by the correction factor $\alpha(\delta)$ defined in equation (4.45).

$$\alpha(\delta) = \begin{cases} 1 \ , \ \textit{for } \delta \leq \delta_{deg} \\ 1 + \left(\hat{\alpha}_{deg} - 1\right) \cdot \left(\dfrac{\delta}{\delta_{deg}} - 1\right) \ , \ \textit{for } \delta_{deg} < \delta \leq 2\delta_{deg} \end{cases} \tag{4.45}$$

with $\alpha(\delta)$: Correction factor for the influence of cyclic strength degradation at drift ratio δ

δ_{deg}: Drift ratio at deformation dependent onset of cyclic strength degradation

$\hat{\alpha}_{deg}$: Correction factor for the influence of cyclic strength degradation at a drift ratio of $\delta = 2\delta_{deg}$

For the curve shown in Fig. 4.76 a tentative value of $\hat{\alpha}_{deg} = 1.2$ was chosen which gives a slightly conservative description for the majority of points, but is not able to capture some individual outliers at higher seismicities. Other – in particular somewhat higher – values for $\hat{\alpha}_{deg}$ may be chosen in order to reach higher levels of conservatism, although it may not be recommendable to rely on such a simple correction factor in very important and sensitive cases. In such situations, a more detailed inelastic dynamic analysis, in which the expected degradation characteristics are directly modeled, may be more justified – especially in the light of the limited data included in Fig. 4.76. For the mentioned value of $\hat{\alpha}_{deg} = 1.2$ equation (4.45) can be reduced to:

$$\alpha(\delta) = \begin{cases} 1 \ , \ \textit{for } \delta \leq \delta_{deg} \\ 0.8 + 0.2 \cdot \dfrac{\delta}{\delta_{deg}} \ , \ \textit{for } \delta_{deg} < \delta \leq 2\delta_{deg} \end{cases} \tag{4.46}$$

Generally, the expressions for the correction factor α in equations (4.45) and (4.46) can alternatively also be formulated as functions of other deformation measures, such as e.g. the pier top displacement Δ_{Top} or the displacement ductility μ_{Δ}. In this case, the drift ratios δ and δ_{deg} in equations (4.45) and (4.46) simply need to be replaced by the corresponding values of the alternative deformation measure[33]. In any case, the deformation level at onset of strength degradation, δ_{deg} in a drift ratio based formulation, needs to be determined in an appropriate way. This is a problem which is not related to the *deformation demand* on the pier, but rather to its *deformation capacity*.

For the pier layout studied here, which is based on the full-scale prototypes corresponding to the experimental test units VK1 and VK2, the drift ratios δ_{deg} at onset of strength degradation were calibrated as 0.95% and 0.78% for the experimental and the numerical backbone, respectively (compare Tab. 4.15, and Tab. 4.17). These two values can be roughly considered as upper and lower

---

[33] If equation (4.46) is formulated as a function of displacement ductility instead of drift ratio, it needs to be considered that, when applying the correction factor α to estimate the displacement demand of a degrading system, the uncorrected demand computation will be done using a non-degrading system. Therefore, the calculated ductilities will refer to the nominal yield displacement of this non-degrading system. However, the displacement Δ_{deg} at onset of degradation refers to the degrading system with lap-splice. For consistency reasons, the corresponding corner ductility needs to be computed as the ratio $\Delta_{deg,lap-splice}/\Delta_{y,continuous}$, i.e. the displacement $\Delta_{deg,lap-splice}$ of the system with lap-splice must be divided by the nominal yield displacement $\Delta_{y,continuous}$ of the non-degrading system with continuous reinforcement. This aspect only comes into play if the nominal yield displacement of the system with lap-splice differs from the nominal yield displacement of the corresponding system with continuous reinforcement.

boundaries for the analyzed configuration including a lap-splice length of $43 d_{bl}$ and a value of $\delta_{deg} \approx 0.8\%$ may serve as a conservative estimation in the given case. This value would certainly not be appropriate for other geometric pier lay-outs, even if the splice length was kept the same. Assuming that the onset of strength degradation is related to the local deformation level at the lap-splice, a pier with a higher aspect ratio than that of test unit VK2 ($L_v/l_w = 2.2$) would reach the same local deformation level at a higher drift ratio.

Assuming further that for a given cross-section the global top displacement of a cantilever pier at a certain local deformation level, i.e. for example a given base curvature, is roughly proportional to the square of the pier height (i.e. the shear span L_v)[34], the drift ratios corresponding to a defined local deformation level would be related linearly to the pier height. Furthermore, peak local strains for a given curvature are proportional to the section depth l_w. Based on these considerations and assumptions, a crude approximation for δ_{deg} at different aspect ratios than that of VK2 can be estimated by assuming that δ_{deg} should be more or less proportional to the aspect ratio L_v/l_w. Using the lower boundary of $\delta_{deg} \approx 0.8\%$ for an aspect ratio of $L_v/l_w = 2.2$, the value of δ_{deg} for varying aspect ratios can be roughly estimated by means of equation (4.47) for a splice length of $43\ d_{bl}$.

$$\delta_{deg}\left(L_v/l_w\right) \approx 0.8\% \cdot \frac{L_v/l_w}{2.2} \approx 0.35\% \cdot L_v/l_w \tag{4.47}$$

with $\quad L_v/l_w$: $\quad$ Aspect ratio of pier

Introducing equation (4.47) into equation (4.46), the correction factor α can be estimated directly as a function of the drift ratio δ and the aspect ratio L_v/l_w, corresponding to equation (4.48).

$$\alpha(\delta) \approx \begin{cases} 1 \ , \ for \ \delta \leq 0.35\% \cdot L_v/l_w \\ 0.8 + \dfrac{\delta}{1.75\% \cdot L_v/l_w} \ , \ for \ 0.35\% \cdot L_v/l_w < \delta \leq 0.7\% \cdot L_v/l_w \end{cases} \tag{4.48}$$

Generally, if an individual SDOF pier with lap-splice is analyzed without explicit consideration of potential cyclic strength degradation, the factor α as defined by equations (4.45), (4.46), and (4.48) can be used to roughly correct the computed deformation demand in the form of equation (4.49). This way, simplified analysis techniques which are not capable of directly capturing cyclic strength degradation can be used to compute the deformation demand of an equivalent non-degrading system assuming continuous reinforcement, while allowing for the lap-splice by means of the correction factor α. It needs to be stressed that this approach must be considered as a very crude estimation and all the approximate assumptions mentioned above should be kept in mind. In particular, it should be noted that the calibrated degradation models for the analyses are based only on a single experiment – that of test unit VK2. Nevertheless, due to the typically limited influence of strength degradation on the displacement demand (compare Fig. 4.76 and [FEMA440]), this simplified approach may serve as a tentative approximation in ordinary cases. For very important or particularly sensitive structures a more detailed dynamic analysis with direct modeling of cyclic strength degradation may be

---

[34] It is a common assumption that the nominal yield displacement is approximately proportional to the square of the pier height (see e.g. [PCK07]). In a plastic hinge approach the plastic displacements corresponding to a given plastic curvature are normally considered proportional to the pier height and the plastic hinge length. At least part of the plastic hinge length is often also assumed as proportional to the pier height, while other additional parts may be considered as independent of it (see e.g. equation (2.3)). Assuming that the total inelastic displacement corresponding to a certain base curvature is proportional to the square of the pier height would implicitly mean that the plastic hinge length is directly proportional to the pier height, which may not be fully correct but rather overestimates the influence of the pier height to some extent. Nevertheless, this crude assumption may serve for some approximate estimations concerning the influence of different geometric configurations.

recommendable. The same holds true if, for example, the splice length differs significantly from the value of 43 d_{bl} tested in the experiment. Furthermore, the correction factor α should not be applied for deformation levels higher than $2\delta_{deg}$, as these were not sufficiently covered by the underlying analyses.

$$\delta_{lap-splice} \approx \delta_{continuous,\text{mod}} = \alpha\left(\delta_{continuous}\right) \cdot \delta_{continuous} \tag{4.49}$$

with $\delta_{lap\text{-}splice}$:   Drift ratio demand of degrading pier with lap-splice

            $\delta_{continuous}$:   Drift ratio demand of corresponding non-degrading pier without lap-splice
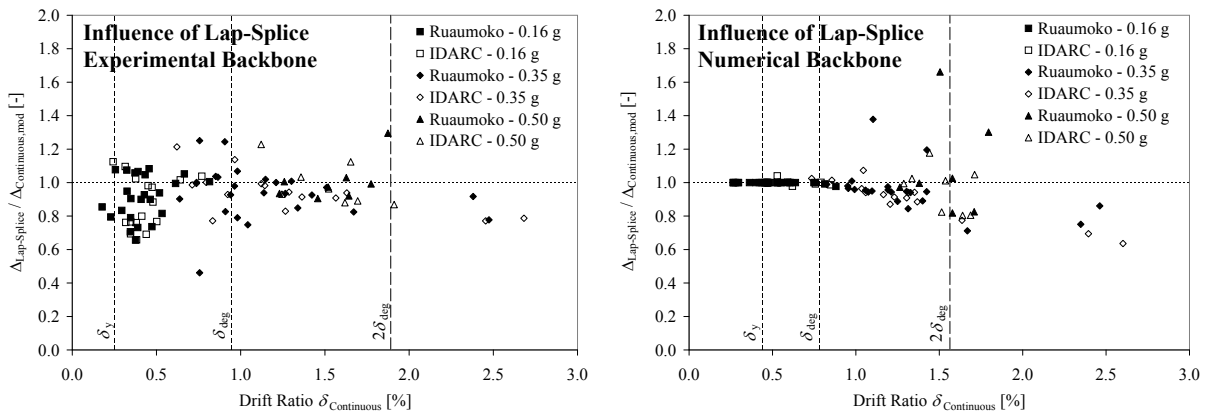
Fig. 4.77: Modified displacement ratios including modification factor for degradation influence (Data: [Kur09])
left: Pier with experimentally calibrated backbone right: Pier with numerically determined backbone[32]

In Fig. 4.77 the deformation demand of the degrading system with lap-splice is compared to the corresponding demand of the non-degrading systems modified by the correction factor α as defined by equation (4.49). It can be seen that, especially for the models with experimentally calibrated backbone, shown on the left side of Fig. 4.77, the approximation by equation (4.49) in the range of $\delta_{deg} \leq \delta \leq 2\delta_{deg}$ is reasonable and the scatter is not higher than that typically encountered in other branches of earthquake engineering. For the models with numerically determined backbone, shown on the right side of Fig. 4.77, the approximation within this deformation range is conservative in the majority of cases. Some few individual points exist which may not be considered as acceptable anymore, which reemphasizes that for important structures a more detailed analysis might be required.
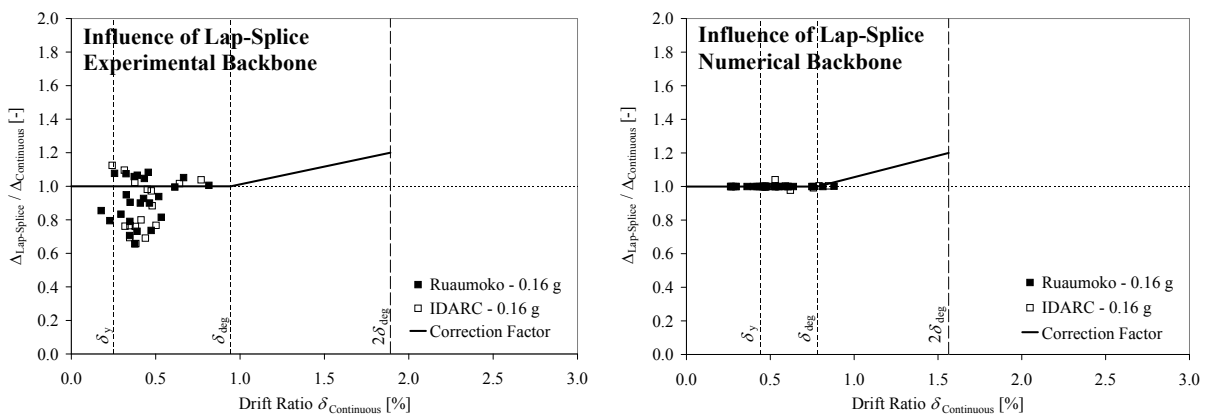
Fig. 4.78: Influence of lap-splice on inelastic displacement demand for $a_{gd} = 0.16$ g (Data: [Kur09])
left: Pier with experimentally calibrated backbone right: Pier with numerically determined backbone[32]

It is noteworthy that those points with significant unconservatism are all related to peak ground accelerations higher than those defined in [SIA261]. They may therefore be considered as not particularly important for the Swiss seismicity. To better illustrate the Swiss situation, based on the

analyses by Kurmann [Kur09], in Fig. 4.78 the same data as in Fig. 4.76 are shown again, but only including those points corresponding to a design peak ground acceleration of $a_{gd} = 0.16g$ as defined in [SIA261] for the highest Swiss seismic zone 3b [35]. It can be seen that the deformation levels experienced by the individual SDOF piers, as computed for this seismicity level, hardly reach into the range where significant strength degradation occurs. As a consequence, for none of the SDOF configurations analyzed by Kurmann a significant increase of displacement demand due to lap-splice degradation was found.

Generally, it cannot be ruled out that other configurations, not studied in detail by Kurmann [Kur09], might show more influence from cyclic-strength degradation, even for Swiss seismic conditions. However, concerning the aspect ratio, it may be assumed that the value of $L_v/l_w = 2.2$ used in the analyses is likely to represent rather the lower range of typical Swiss bridge piers. Kurmann conducted a parameter study for higher aspect ratios, using the numerically determined backbones for the same cross-section as before, but with varying pier heights. From these analyses, conducted with design peak ground accelerations of $a_{gd} = 0.16g$ and $a_{gd} = 0.35g$, he found that for both, piers with continuous longitudinal reinforcement as well as with lap-splices at the base, the drift ratio demand tends to increase when the aspect ratio rises stepwise from $L_v/l_w = 2.2$ to $L_v/l_w = 4.4$. However, this increase of drift ratio δ is less than proportional to the aspect ratio L_v/l_w. At the same time, the ductility demand of the piers tended to either remain essentially constant or decrease with increasing aspect ratio. It may therefore be concluded that the local deformation demands, in terms of strains, rather tend to reduce at higher aspect ratios. Therefore, it is unlikely that the seismic behavior of lap-splices, which depends on the local deformation demands, becomes more critical at higher aspect ratios.

Although further research concerning the seismic behavior of bridge piers with lap-splices is desirable, both experimentally and numerically, for the time being and as a tentative approach, it may be assumed that the above presented analyses represent rather critical conditions and that other realistic geometric configurations in Switzerland are unlikely to be significantly more critical. This means that, if the splice length is not significantly shorter than $43d_{bl}$, as used in the test of VK2, no extreme influence of the lap-splice on the displacement demand of individual single bridge piers should be expected. It is important to note that this assumption is limited to the Swiss situation, consisting of typical detailing and seismicity. If a certain analysis suggests that cyclic strength degradation is likely to occur, under the mentioned conditions it appears reasonable to estimate its influence by means of the tentative approach outlined above, according to equations (4.45) through (4.49). Further research should review this proposal and possibly either verify or recalibrate it. In particular, it should be noted that the presented findings would not be applicable to significantly shorter splice lengths, nor to seismicities which result in significantly higher deformation demands than those studied in the analyses presented above.

c) Results of Multi-Degree-of-Freedom Analyses

The results presented in the preceding subsection exclusively referred to the seismic behavior of individual single-degree-of-freedom bridge piers with tributary superstructure mass. These analyses allowed studying the consequences of cyclic strength degradation in an isolated manner without any influences from other effects. However, normally in bridge structures the bridge piers are coupled by the superstructure among each other and with the abutments. Therefore, the seismic behavior – also in the case of cyclic strength degradation – becomes somewhat more complex. It may be assumed that, on a general basis, the inherent redundancies existing in entire bridge structures rather mitigate the effects of cyclic strength degradation. If an individual pier starts loosing strength this will cause a redistribution of forces within the structure resulting in a partial unloading of the degrading pier. At the same time the adjoining members may provide some restraint to the degrading column and thus limit its displacement demand, which again limits the progression of strength degradation.

To check these theoretical considerations, Kurmann [Kur09] performed inelastic time history analyses on the four different bridge models shown in Fig. 4.79. Each of the bridges has a total length of 168 m

---

[35] Modification factors for soil type ($S = 1.2$) and importance of structure ($\gamma_f = 1.4$) are taken into account additionally, increasing the overall peak ground acceleration to $a_g = 0.27g$.

and consists of 5 spans. Using effective pier heights of 6.6 m and 13.2 m, three symmetric configurations and one asymmetric structure were assembled. For every configuration dynamic analyses were performed once modeling the piers without strength degradation, and once including cyclic strength degradation. In the first case, all piers of the bridge had continuous reinforcement, while in the second case all piers featured lap-splices at their bases. No mixed bridge configurations in which only some of the piers would have lap-splices were considered.

The piers had the same cross-sections as in the SDOF analyses discussed in the preceding subsection. For the piers with an effective height of 6.6 m, exactly the same hysteretic models were used as in the SDOF study. Both, the experimentally calibrated backbones for the force-displacement curves of the piers as well as the numerically determined backbones were studied separately for every bridge configuration. For the piers with an effective height of 13.2 m the hysteretic rules of the 6.6 m piers were modified in a simplified manner. For this purpose, the force capacity of the 6.6 m piers was reduced by 50% and all characteristic displacements defining the hysteretic model were multiplied by a factor of 4 corresponding to the square of the height ratio. The abutments of all bridges were modeled as flexible with an elasto-plastic hysteretic rule.
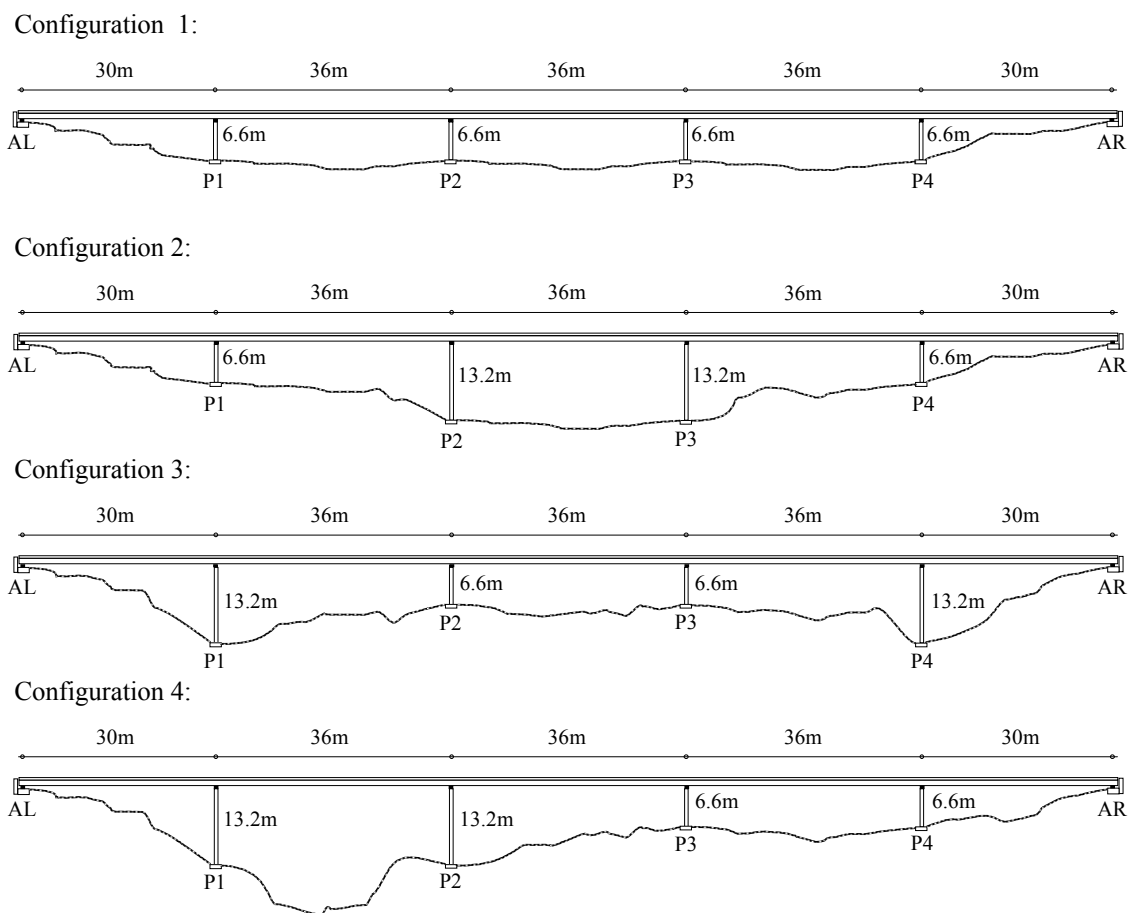
Fig. 4.79: Bridge configurations considered in MDOF analyses by Kurmann [Kur09]

All analyses were performed with the software code Ruaumoko [Car04] using the purely deformation dependent degradation model for the piers with lap-splices, while the IDARC model based on the degradation rule depending on dissipated energy was not used for the MDOF analyses. As discussed in Subsection *b*, the deformation dependent degradation model in Ruaumoko can be considered rather as an upper boundary for the degradation effects, so that the results are assumed to be conservative. Only the bridge response in the transverse direction was considered in the analyses. For every resulting bridge model the same three seismicity levels, defined by a_{gd} = 0.16 g, 0.35 g, and 0.50 g, and the same ground motion accelerograms as for the SDOF analyses of the preceding subsection were used.

4.7 Influence of Strength Degradation

The combination of all bridge configurations, modeling types, and ground motions resulted in a total of 448 dynamic MDOF analyses.

For each pier of every analysis the ratio between the displacement demand with lap-splice $\Delta_{lap-splice}$ and the displacement demand $\Delta_{continuous}$ of the same pier in a corresponding bridge without lap-splices was computed. The results are shown in Fig. 4.80 as a function of the ductility demand of the pier without lap-splice. Here the displacement ductility was chosen instead of the drift ratio as in the case of the SDOF results (e.g. in Fig. 4.76), because the data presented in Fig. 4.80 refer to two different pier heights. For these two cases a certain drift ratio does not represent the same local deformation state, while the displacement ductility is still a suitable measure, in particular with respect to the question when and how cyclic strength degradation occurs. It should be noted that the yield displacements of the experimentally calibrated backbone curves differ from the yield displacements of the numerically determined backbones. Therefore, the displacement ductilities on the left side of Fig. 4.80, showing the data for the experimental backbone, cannot be compared directly to the ductilities on the right side, where the data for the numerically determined backbones are shown.

Fig. 4.80: Influence of lap-splice on inelastic displacement demand of piers
as part of MDOF bridge structures (Data: [Kur09])
left: Piers with experimentally calibrated backbone, right: Piers with numerically determined backbone[32]

The results in Fig. 4.80 generally correspond to the data shown in Fig. 4.76. The former refer to piers as members of entire MDOF bridge structures, while the latter represent individual SDOF piers with tributary superstructure mass. From a comparison between the two figures it can be seen that the MDOF results contain less values with displacement ratios higher than 1.4. In particular, an extreme outlier point as observed in the SDOF analyses and as discussed in footnote 32 (but not shown in Fig. 4.76) does not occur in the MDOF results. At the same time, the scatter, especially at lower displacement demands, appears to be higher in the MDOF analyses. These two effects are the result of the coupling between the various piers of a bridge by the superstructure and the alternative load-path offered by the superstructure and the abutments. This coupling leads to a certain redistribution of displacement demands between the individual piers of a bridge, increasing the deformations of some piers, while reducing that of others. As a consequence, the displacement ratio $\Delta_{lap-splice}/\Delta_{continuous}$ of piers as part of an MDOF structure does not only depend on the deformations of the individual pier itself anymore, but is rather a function of the combined response of all piers within the bridge.

For the pier models with numerically determined backbones this can be seen clearly by comparing the data shown on the right sides of Fig. 4.76 and Fig. 4.80 for displacement demands below the onset of strength degradation. While all the SDOF ratios computed with the Ruaumoko model in Fig. 4.76 (right) are equal to unity, this is not the case for the equivalent MDOF data in Fig. 4.80 (right). For a pier being part of a MDOF system, the displacement demand can also increase even if this particular pier itself does not experience any strength degradation, but rather because other columns within the structure experience degradation. Due to a redistribution of forces the demand on the non-degrading members is then also increased.

In Fig. 4.80 the same proposal for a correction factor as defined by equations (4.45) through (4.49) is shown. For a better interpretation and comparison the data in Fig. 4.80 are distinguished into three categories. On one hand the filled square markers represent the piers that experience the most strength degradation within every bridge, which is here being called "Primary Degradation". Further, the points called "No Degradation" belong to piers not experiencing any strength degradation due to their limited displacement demand. In between these two categories a third type of points exists, named "Secondary Degradation". These piers do suffer a certain amount of strength degradation themselves, but they are not the ones within the bridge that degrade the most (because then they would fall into the category "Primary Degradation").

Looking at these three categories, it can be seen that for the MDOF piers with primary degradation in Fig. 4.80 the approximation by the correction factor is somewhat better than for the SDOF piers in Fig. 4.76. This is related to the existence of less extreme cases for the MDOF piers due to the effects discussed above. In contrast, for the piers with secondary or no degradation the approximation provided by the correction factor may be considered somewhat less satisfying if the value of the correction factor is determined individually for every pier as a function of its very own deformation level. This phenomenon can also be explained by the previous discussion concerning the coupling effect of the MDOF bridge structure and the redistribution of forces and displacement demands. In a system where degradation occurs (at least in one pier), the demand of the piers with secondary or no degradation is also increased by the pier with the more pronounced primary degradation.

To better illustrate this effect, in Fig. 4.81 the data of Fig. 4.80 are reduced to points coming from bridges where at least one pier experiences strength degradation. Here it can be seen that a considerable number of piers with secondary or no degradation shows higher displacement demands than predicted using the correction factor. This emphasizes that a correction factor depending only on the individual pier deformation cannot capture the demand increase caused by the coupling with other piers that experience a stronger loss of strength within the same bridge system.
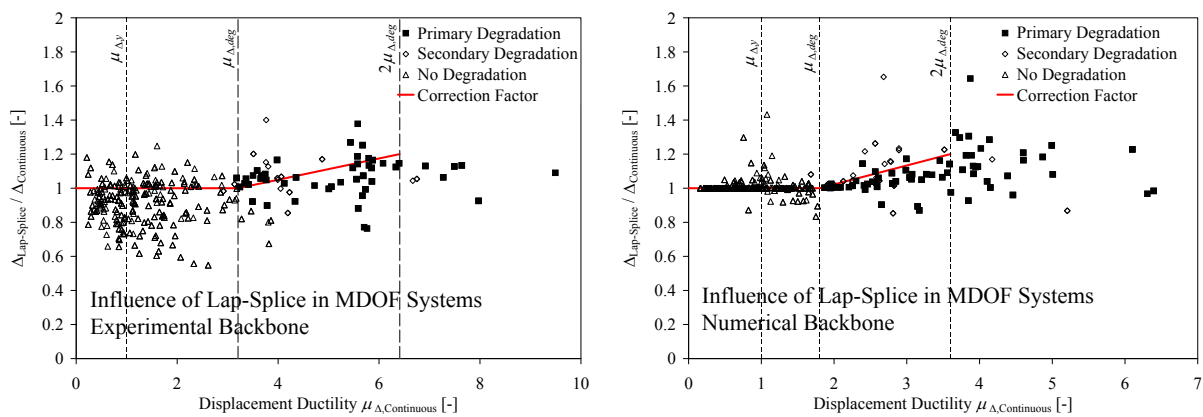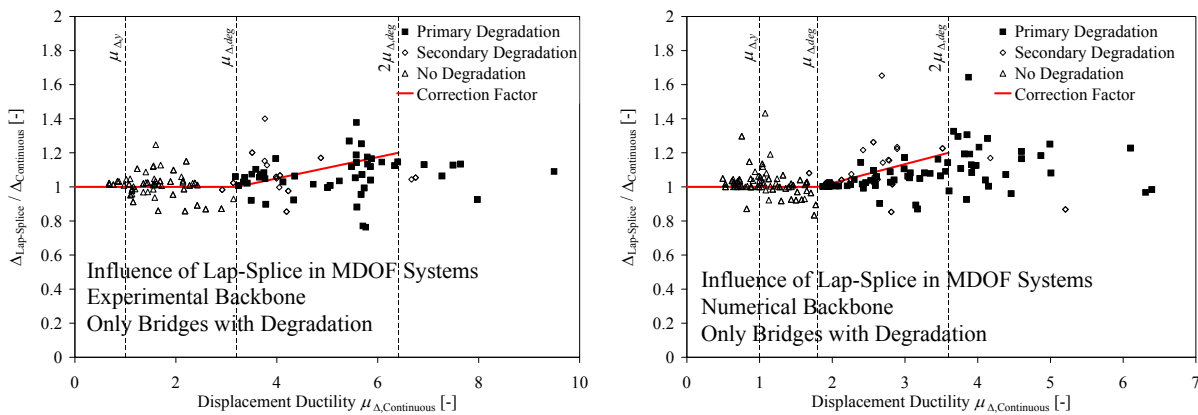

Fig. 4.81: Influence of lap-splice on inelastic displacement demand of piers
as part of MDOF bridge structures (Data: [Kur09])
here: Only data shown for bridges where at least one pier experiences strength degradation
left: Piers with experimentally calibrated backbone, right: Piers with numerically determined backbone[32]

Several approaches are imaginable how to overcome this problem. In any case, it appears reasonable that for the piers with secondary or no degradation the correction factor should not only be a function of their own degradation level, but should rather also depend on the deformation of the pier within the same bridge suffering most from the loss of strength (i.e. the pier with the primary degradation). A variety of possible combinations can be considered for this purpose. However, a simple and probably rather conservative solution consists of simply applying the correction factor determined for the pier with the most degradation (primary degradation) to all other piers (secondary or no degradation) of the same bridge as well.

In Fig. 4.82 the resulting modified displacement ratios are shown, being the quotient between the displacement $\Delta_{lap\text{-}splice}$ of the piers with lap-splice and the modified displacement $\Delta_{continuous,mod}$ of the

corresponding piers with continuous reinforcement. The latter displacement has been calculated as $\Delta_{continuous,mod} = \alpha \cdot \Delta_{continuous}$. In this relationship the correction factor was determined according to equation (4.46) for the deformation of the pier with the highest displacement ductility (and thus the most pronounced degradation) within the entire bridge structure. This means that for every bridge the highest correction factor occurring at its various piers is determined and this maximum factor is applied on all piers within the entire bridge.

Fig. 4.82: Modified displacement ratios applying the modification factor of the pier
with primary degradation on all piers of the same bridge (Data: [Kur09])
left: Piers with experimentally calibrated backbone, right: Piers with numerically determined backbone

This approach can also be used to estimate the displacement demand of a system with lap-splices in the piers using an analysis which was conducted without modeling of cyclic strength degradation. In this case, any point in Fig. 4.82 with a modified displacement ratio lower than unity represents a conservative approximation. It can be seen that for the large majority of the MDOF analyses conducted by Kurmann [Kur09] the suggested approach appears to give solutions on the safe side, without being overly conservative. The same data is reduced in Fig. 4.83 to results from bridges where at least one pier experiences strength degradation. Here it can be seen that the effect of cyclic strength degradation on the displacement demands is captured reasonably well with a certain conservative tendency. The resulting conservatism for the points with secondary or no degradation is not expected to cause significant problems in the majority of cases, as these piers – compared to the pier with the primary degradation – are unlikely to be the most critical ones within the bridge to be assessed.
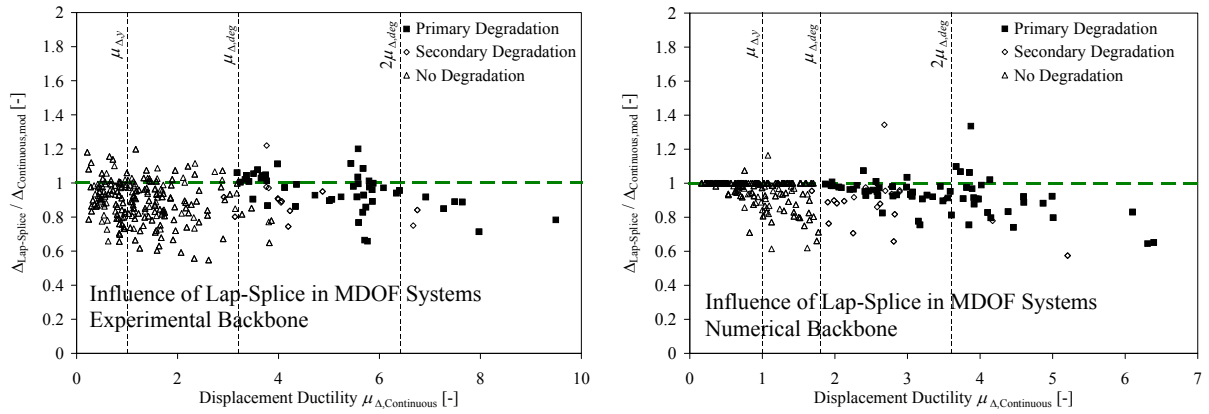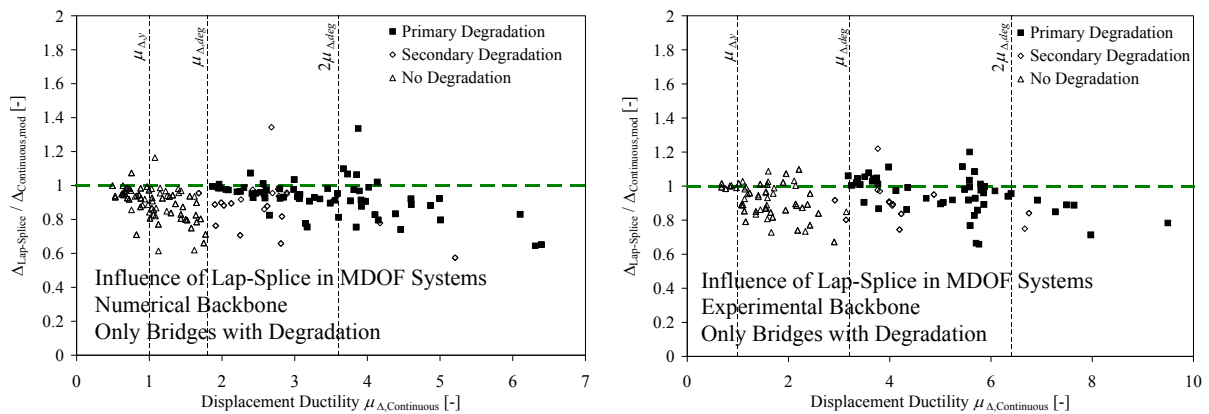

Fig. 4.83: Modified displacement ratios applying the modification factor of the pier
with primary degradation on all piers of the same bridge (Data: [Kur09])
here: Only data shown for bridges where at least one pier experiences strength degradation
left: Piers with experimentally calibrated backbone, right: Piers with numerically determined backbone

The very few unconservative results are still within a range of uncertainties as it may be encountered in other fields of earthquake engineering as well, e.g. in the context of estimating the seismic demand. In particular, it is noteworthy that the points in Fig. 4.83 representing an unconservatism of more than 10% are coming from analyses for a seismicity level of $a_{gd} = 0.50$ g. They are therefore not representative for the Swiss seismicity. Although this statement is limited to the data by Kurmann [Kur09] and cannot be generalized, it nevertheless gives a certain impression of the relevance for Swiss conditions. To visualize the relevance of cyclic strength degradation due to lap-splice failure for Swiss seismic conditions, in Fig. 4.84 the same data as in Fig. 4.80 are reduced to those points corresponding to analyses with a peak ground acceleration of $a_{gd} = 0.16$g, which represents the highest seismic zone 3b according to the Swiss code [SIA261]. It can be seen that the data by Kurmann [Kur09] suggest only a very limited influence from lap-splice degradation for Swiss conditions, which agrees with the corresponding finding from Fig. 4.78 for the SDOF analyses. This conclusion should only be considered valid as long as the splice length is not significantly shorter than the value of $43d_{bl}$ provided in the experimental test of VK2, as this was the basis on which the degrading hysteretic models for the analyses were calibrated.
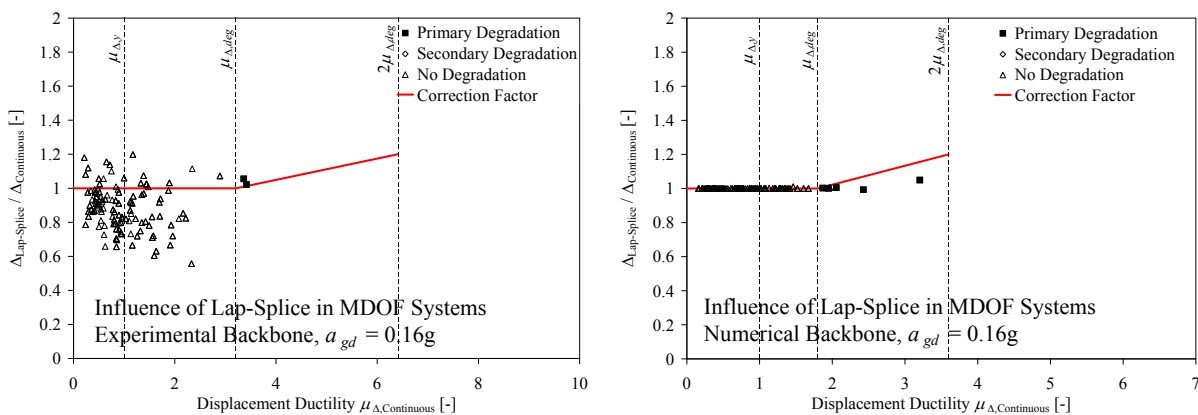
Fig. 4.84: Influence of lap-splice on inelastic displacement demand of piers as part of MDOF bridge structures
here: Only data shown from analyses with $a_{gd} = 0.16$g (Data: [Kur09])
left: Piers with experimentally calibrated backbone, right: Piers with numerically determined backbone[32]

d) Conclusions and Recommendations

Summarizing, it can be concluded that – based on the so far existing experimental and numerical data – cyclic strength degradation as a consequence of lap-splices in the plastic hinge regions of piers does not appear to have a dominating influence on the deformation demand for Swiss bridge piers. If the potential degradation is not directly modeled in the analysis, its effects can be taken into account approximately by the correction factor α, according to equations (4.45) through (4.49), suggested in the Subsection *b* for independent SDOF piers. In the case of a coupled MDOF bridge system, the displacement demand of each pier should be multiplied by the maximum correction factor determined for the most degrading pier. This correction should also be performed even for those piers that do not suffer from strength degradation themselves.

Further experimental as well as numerical research is desirable to verify that the proposed approach really is sufficiently conservative in the majority of cases. So far, the approach should not be used for displacement demands higher than two times the displacement at onset of degradation. It should, further, not be used for piers with shorter lap-splices than the ones underlying the presented analyses.

5 Experimental Test Campaign

5.1 Background

It has been shown in Section 2.1*b* that one of the most detrimental failure types that can occur to bridges results from damage to the substructure, i.e. primarily the piers. This failure type is so harmful because it can lead to a loss of support for the superstructure and subsequently result in a total collapse of the bridge. It has been observed after several earthquakes that particularly rather short and squat bridge piers have performed in an unsatisfactory manner, despite their massive cross-sections and a correspondingly considerable horizontal strength (see e.g. Fig. 2.10, Fig. 2.11). This is related to the fact that squat piers generally have lower flexural displacement capacities compared to more slender piers. Furthermore, they often feature an unfavorable relationship between flexural and shear capacity, which makes them prone to shear failure.

This potential risk is especially pronounced for piers with low transverse reinforcement ratios, as they are often found in older existing bridge piers (see e.g. Tab. 2.1). Such a shear failure can further reduce the pier's displacement capacity substantially, especially if it already occurs in the elastic range of the force-displacement relationship as in the case shown in Fig. 2.50. Consequently, the entire plastic part of the deformation capacity is lost and a brittle failure mode results. As an alternative, under cyclic-inelastic loading a shear failure can also occur in the inelastic range of the load-deformation relationship. In this case, the pier's displacement capacity is also reduced, but only part of the plastic deformation capacity is lost.

Aside from potential shear problems, lap-splices of the longitudinal reinforcement at the base of the piers represent another typical seismic deficiency in existing structures. Under cyclic-inelastic deformations these splices are likely to fail resulting in a severe degradation of flexural strength. The consequences of such a cyclic strength degradation on the displacement demand have been discussed in detail in Section 4.7.2. Generally, an interaction can also exist between lap-splice related strength degradation and the potential for an inelastic shear failure.

While both types of seismic deficiencies would be prevented in new structures designed for ductile behavior according to modern seismic codes, their occurrence cannot be ruled out in existing older bridges. Several international research projects have studied both the cyclic-inelastic shear strength of reinforced concrete columns (e.g. [AM92], [PVX94], [KP00], [SM04], [BRF04] , [EM05]) as well as the degradation behavior due to failing lap-splices in the plastic region ([CPS91], [Lyn+96], [MWC03]). However, aside from the significant uncertainties generally still remaining in the reliable description of both of these very complex phenomena, not all of the findings from the internationally performed experiments are directly applicable to existing Swiss bridge piers. This is on one hand related to the fact that internationally certain differences exist concerning important detailing properties. On the other hand, previous test campaigns did not include squat wall-type bridge piers which are considered to represent especially critical cases for Swiss bridges. Instead, the previous tests concentrated either on building columns or other types of bridge piers. Therefore, a need for additional tests has been identified, which should better represent the Swiss situation both in terms of pier type and detailing properties.

As a consequence, a first series of three large scale quasi-static cyclic tests on wall-type bridge piers has been performed in the laboratory of the Institute of Structural Engineering at ETH Zürich. The primary focus of the test campaign was on the potential for premature shear failure, on the influence of lap-splice failure under cyclic inelastic loading, and on potential interactions between these two types of damage. A further issue of investigation was the cyclic-inelastic deformation behavior of the pier models, both in terms of flexural as well as shear deformations. Since on one hand the seismic capacity is related to the global (top) displacement capacity, while on the other hand damage and failure is typically related to local deformations, special attention has been given to the relationships between global and local deformations in the elastic and the inelastic loading range.

In many previous tests it has been common to define failure as the point where a certain percentage of the transverse force capacity is lost compared to the peak strength. This appears to be a reasonable definition e.g. for structural walls whose primary purpose is the contribution of transverse stiffness and

strength. In contrast, a bridge column in first instance has to provide a vertical load bearing mechanism in order to carry the gravity loads from the superstructure. As long as other parts of the structure provide sufficient horizontal resistance (e.g. due to a second load path along the superstructure to the abutments), a certain loss of transverse strength at individual piers may be acceptable. A loss of axial load capacity, however, would inevitably cause a structural failure as the superstructure could not be supported by the piers anymore. Therefore, this loss of axial load capacity was considered in the test campaign as an additional object of investigation.

Numerical analyses have shown that under moderate seismic conditions the number of large inelastic cycles during an earthquake response may be rather limited. Instead, the structure is likely to perform a considerable number of rather smaller cycles after or between the larger inelastic cycles [BD06]. Some uncertainty exists about the hysteretic energy dissipation during such small cycles after the occurrence of large cycles. To investigate this aspect, some smaller cycles between the large cycles have been included into the load histories for the piers.

In total, the objectives of the test campaign can be summarized as follows:

(a)   Shear capacity under cyclic-inelastic loading
(b)   Behavior of lap-splices in plastic regions
(c)   Interaction between lap-splice failure and potential for shear failure
(d)   Loss of axial load bearing capacity
(e)   Flexural deformation behavior under cyclic-inelastic loading
(f)   Shear deformation behavior under cyclic-inelastic loading
(g)   Hysteretic behavior during small cycles after previous large inelastic cycles

In the following Section 5.2 the general layout of the test campaign is described. This comprises the design of the test units (Section 5.2.1), the test setup including the instrumentation (Section 5.2.2), a prediction of the anticipated behavior (Section 5.2.3), and the applied loading during the experiments (Section 5.2.4). In Section 5.3 the test results are summarized, consisting of a summary of the observations during the experiments (Section 5.3.1) and a comparison between the predicted and the experimental behavior (Section 5.3.2). Finally, in Section 5.4 the results from the experimental campaign are discussed and conclusions are drawn from the observed behavior.

5.2 Layout of Test Campaign

5.2.1 Design of Test Units

The layout of the three test units takes into account typical characteristics as they can be found in existing Swiss bridge piers. This refers to the shape of the piers, the properties of the materials, as well as to the amount and detailing of the reinforcement. In particular, the very low transverse reinforcement ratios, common in existing piers, have been reproduced in the layout of the models. In order to represent realistic conditions, the layout of the test units was chosen in general accordance with the characteristics of the sample bridge piers presented in Section 2.2.2*e* (see Tab. 2.1).

a) Geometry

The units were designed as models of rather squat wall-type cantilever bridge piers at a scale of 1:2. The geometry of all three test units was the same as shown in Fig. 5.1 and Fig. 5.2 (i.e. $L_v = 3.3$ m, $l_w = 1.5$ m, and $b_w = 0.35$ m), resulting in an aspect ratio of $L_v/l_w = 2.2$. The geometric data of the three Test Units VK1, VK2, and VK3 are summarized in Tab. 5.1.

		VK1	VK2	VK3
Effective height	L_v [m]		3.3	
Section depth	l_w [m]		1.5	
Section width	b_w [m]		0.35	
Clear concrete cover of transverse reinforcement	c_t [mm]		20	
Clear concrete cover of longitudinal reinforcement	c_l [mm]		26	
Aspect ratio	L_v/l_w [-]		2.2	

Tab. 5.1: Geometric data of Test Units VK1, VK2, and VK3

b) Reinforcement Layout

The layout of the transverse reinforcement was also kept equal in all three cases with hoops of a diameter $\varnothing = 6$ mm at a spacing of $s = 200$ mm, resulting in a very low transverse reinforcement ratio of $\rho_{sw} = 0.08\%$. No special measures were taken concerning the detailing of the hoops for ductile behavior. As a consequence, they were closed by simple 90° hooks of length 100 mm which could open after spalling of the cover concrete.

The longitudinal reinforcement of all three test units consisted of bars with a diameter of $\varnothing = 14$ mm distributed along the perimeter of the cross-section as shown in Fig. 5.2. Test units VK1 and VK2 featured a total of 28 bars resulting in a longitudinal reinforcement ratio of $\rho_{sl} = 0.82\%$, whereas Test Unit VK3 was provided with 42 bars of $\varnothing = 14$ mm corresponding to $\rho_{sl} = 1.23\%$. This increase of the longitudinal reinforcement ratio by 50% in VK3 (compared to VK1 and VK2) resulted in a higher moment capacity by roughly 20% which subsequently also increased the shear demand in the inelastic range by 20%.

While Test Units VK1 and VK3 featured continuous longitudinal reinforcement from the foundation to the pier top, Test Unit VK2 was designed with a lap-splice at the pier base. The length of this lap-splice was chosen in accordance with older Swiss design codes, which prescribed considerably longer splice lengths than those typically found e.g. in existing U.S. piers. In Tab. 5.2 an overview is given of the required minimum splice lengths according to past and present Swiss code generations. From these

data it can be seen that the minimum splice length for straight bars (i.e. without hooks) was never lower than 40Ø. If the code provisions had been followed for the detailing of existing bridges, it can therefore be assumed that no lap-splices with lengths shorter than $l_s = 40Ø$ should exist in Swiss bridge piers. As for the failure of lap-splices themselves this lower boundary value can be considered as the worst case of expected cases in Switzerland, a rounded splice length of $l_s = 600$ mm was chosen for the longitudinal reinforcement of Test Unit VK2 which corresponds to a value of 43Ø.
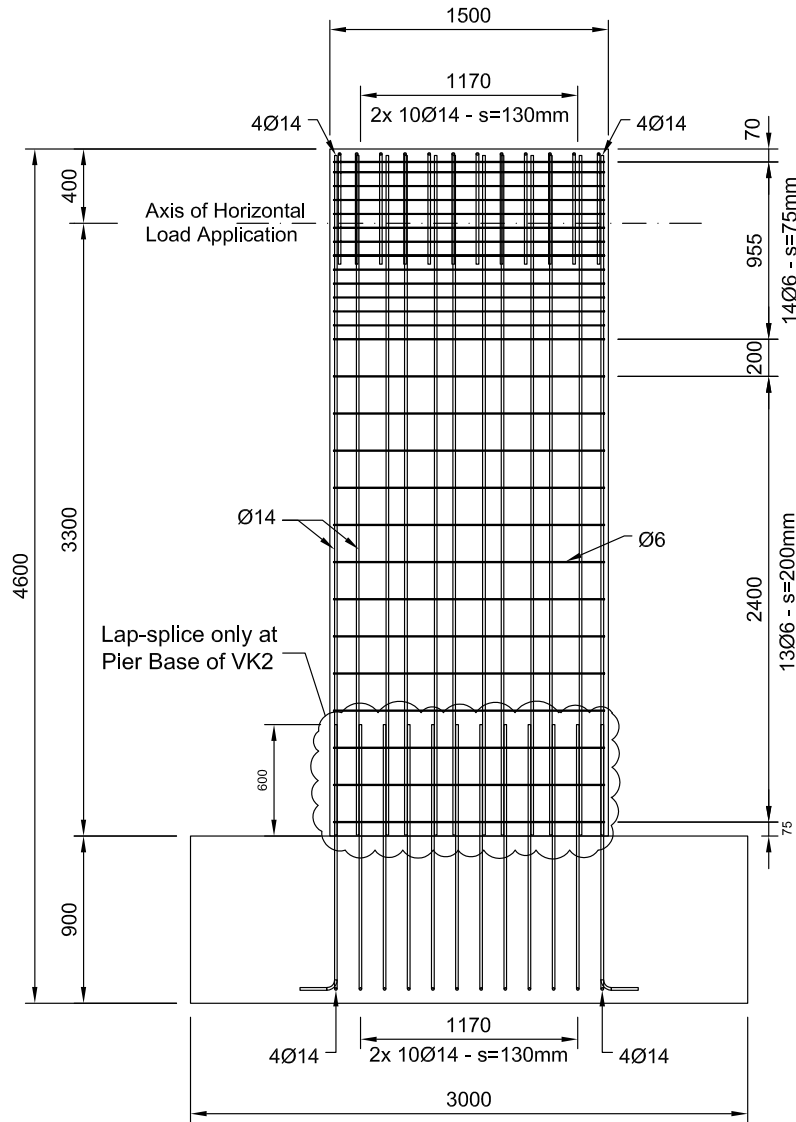

Fig. 5.1: Elevation with reinforcement layout of Test Unit VK2 featuring lap-splice at the pier base
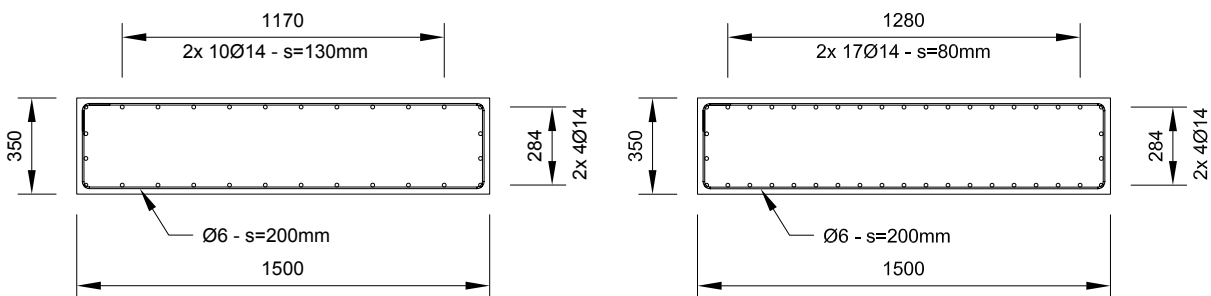(all dimensions in mm)

Fig. 5.2: Pier cross-section with reinforcement layout (all dimensions in mm)
left: Test Units VK1 and VK2, right: Test Unit VK3

Code Generation	Minimum Required Splice Lengths l_s according to Various Swiss Code Generations for Straight Bars without Hooks	
	General Conditions	In the Tension Zone (Longitudinal or Transverse Tension)
[SIA162-56]	only lap-splices with hooks or by welding	
[SIA162-68]	45Ø	65Ø
[SIA162-89]	40Ø	60Ø
[SIA262]	$f_{ck,cyl} \geq 30$MPa: 40Ø [(a)]	

[(a)] For concrete classes lower than C30/37, higher values than 40Ø must be provided for l_s (see [SIA262] for details). Generally (i.e. independent of the concrete class), the required splice length l_s according to [SIA262] can also be computed as a function of the reinforcement yield strength and the concrete bond strength. For higher concrete classes the computed splice length will then result somewhat lower than the value of 40 Ø given in the table.

Tab. 5.2: Minimum required splice lengths according to various Swiss code generations

A summary of the data for the reinforcement layout of the three test units is presented in Tab. 5.3. The detailed reinforcement layout of Test Unit VK2 including the lap-splice at the pier base is shown as an elevation in Fig. 5.1. The layout of Test Unit VK1 is equal to that of VK2, aside from the fact that VK1 does not feature a lap-splice at the pier base, but rather has continuous longitudinal reinforcement from the foundation up to the pier base. Test Unit VK3 also has continuous reinforcement without lap-splice. It differs from VK1 only by the higher longitudinal reinforcement ratio. The cross-sections of all three test units (outside the lap-splice in case of VK2) are depicted in Fig. 5.2.

		VK1	VK2	VK3
Longitudinal reinforcement layout	Ø [mm]	28 Ø14	28 Ø14	42 Ø14
Longitudinal reinforcement ratio	ρ_{sl} [%]	0.82	0.82	1.23
Transverse reinforcement layout	Ø - s [mm]	2 Ø6 - 200	2 Ø6 - 200	2 Ø6 - 200
Transverse reinforcement ratio	ρ_{sw} [%]	0.08	0.08	0.08
Lap-splice length longitudinal reinforcement	l_s [mm]	-	600	-

Tab. 5.3: Characteristic data for reinforcement layout of Test Units VK1, VK2, and VK3

c) Material Properties

In order to maintain similar conditions throughout the experimental campaign, it was attempted to keep essentially the same material properties for all test units. For this purpose, ready-mixed concrete of the same type has been used in all cases. The average compressive concrete strength[36] at the day of testing thus resulted as $f_{c,cyl}$ = 39 MPa, 35 MPa, and 34 MPa for Test Units VK1, VK2, and VK3, respectively.

To ensure the same material properties of the longitudinal reinforcement, the bars for all three test units have been taken from the same strand of the same production batch. The longitudinal reinforcement steel was of the type *topar-S 500C* and complied with the requirements for ductile steel type C according to [SIA262]. The steel showed a pronounced yield plateau at an average yield stress of $f_{s,l}$ = 520 MPa. Its ultimate tensile strength was measured as $f_{t,l}$ = 630 MPa at a strain of ε_{su} = 12.6%.

---

[36] Determined on cylinders of diameter d_{cyl} = 150 mm and height h_{cyl} = 300 mm.

The transverse reinforcement steel was also taken from the same strand of the same production batch for all three test units and it is equal to the steel used by Beyer for the diameter 6 mm bars in her tests on U-shaped RC walls. According to Beyer *et al.* [BDP08b], the steel did not show any yield plateau because of cold deformations after the production. As characteristic properties, Beyer *et al.* [BDP08b] give a yield stress[37] of $f_{s,w}$ = 518 MPa and an ultimate tensile strength of $f_{t,w}$ = 681 MPa at a strain of ε_{su} = 8.4%.

The complete data for the material properties of Test Units VK1, VK2, and VK3 are summarized in Tab. 5.4.

		VK1	**VK2**	**VK3**
Concrete compressive cylinder strength	$f_{c,cyl}$ [MPa]	35	39	34
Yield strength of longitudinal reinforcement	$f_{s,l}$ [MPa]		515	
Ultimate strength of longitudinal reinforcement	$f_{t,l}$ [MPa]		630	
Strain at peak stress of longitudinal reinforcement	ε_{su} [%]		12.6	
Yield strength of transverse reinforcement	$f_{s,w}$ [MPa]		518 [a]	
Ultimate strength of transverse reinforcement	$f_{t,w}$ [MPa]		681 [a]	
Strain at peak stress of transverse reinforcement	ε_{su} [%]		8.4 [a]	

[a] According to Beyer *et al.* [BDP08b].

Tab. 5.4: Material Properties of Test Units VK1, VK2, and VK3

d) Summary

As can be seen from the data presented in Tab. 5.1 through Tab. 5.4, aside from minor variations of the concrete strength, the three test units only differed with respect to their longitudinal reinforcement layout. All other aspects, i.e. the shape and dimensions of the piers, the layout of the transverse reinforcement and the material properties of the reinforcing steel, were kept the same in all three test units. Within the test series, unit VK1 featuring a continuous longitudinal reinforcement of ratio ρ_{sl} = 0.82% can be seen as a starting point from which the other two pier models have been developed by variation of a single property in each case. Test Unit VK2 was developed from VK1 by introducing a lap-splice at the pier base, while keeping the amount of longitudinal reinforcement equal to that of VK1. In contrast, in Test Unit VK3 the amount of longitudinal reinforcement was increased by 50%, compared to that of VK1, while the longitudinal bars were also continuous from the foundation up to the pier top without lap-splice.

As a consequence, by pairwise comparison between two of the test units each time the influence of the corresponding variation on the cyclic-inelastic behavior can be studied. Generally, the layout of Test Units VK1 and VK3 primarily aims at studying the flexural and shear behavior independent of the influence from lap-splices, while Test Unit VK2 allows the investigation of the additional influence related to a reinforcement splice. This refers to the development of a cyclic strength degradation due to failing lap-splices as well as to potential interactions between such strength degradation and the risk of shear failure.

---

[37] Yielding has been defined as the point where a plastic strain of 0.2% remains upon unloading.

5.2.2 Test Setup and Instrumentation

In Fig. 5.3 the experimental setup is shown which has been used for all three tests. The foundation block of the units was anchored to the strong floor by means of six prestressed rods. Two vertical actuators were located on a cross-beam on top of the test units in order to apply a constant axial load simulating the gravity loads from the superstructure. These two actuators were connected to prestressing tendons being anchored to the bottom of the strong floor. The horizontal forces and displacements at the top of each test unit were applied by means of a single actuator being located at a height of 3.3 m above the top surface of the foundation (i.e. the pier base). Load cells in each actuator were used to continuously measure the applied forces. Furthermore, the stroke of the horizontal actuator and the pressure in the vertical actuators were measured. In order to prevent sideways displacements (bending about the weak axis of the cross-section), two steel beams were used as side supports at the top of the piers[38]. This way it was warranted that only uniaxial displacements were applied.
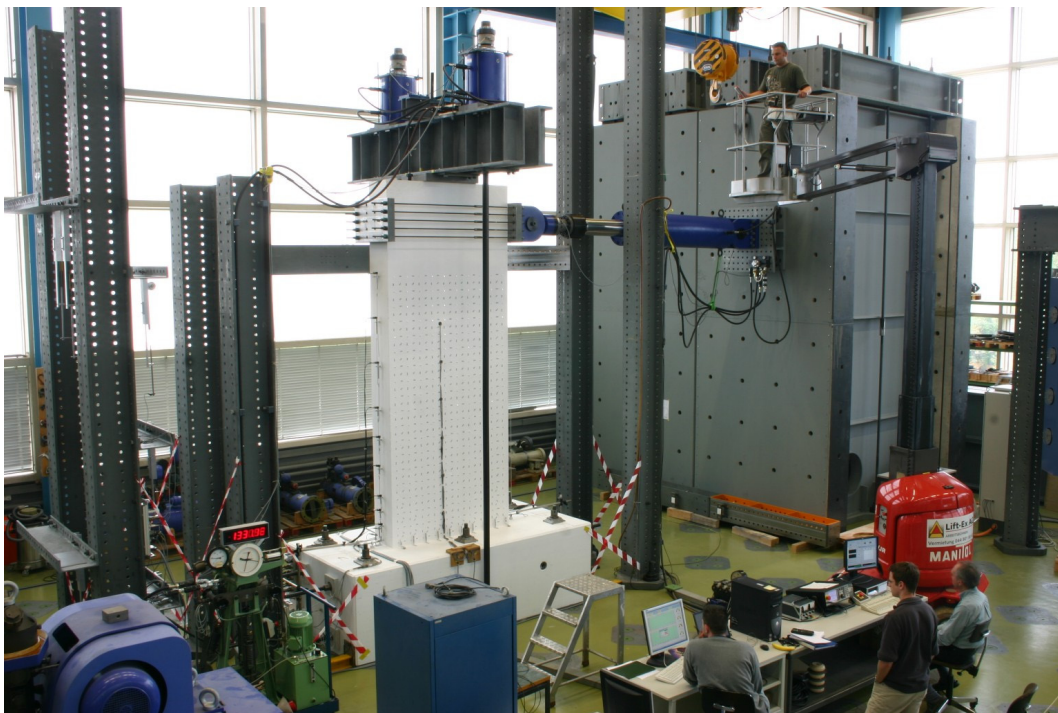
Fig. 5.3: Setup for quasi-static cyclic tests on wall-type bridge piers at ETH Zürich

In addition to the 5 hard-wired measurements controlling the actuators, the deformations of the piers were continuously measured by a total of additional 71 hard-wired instruments, comprising the following channels:

– 31 LVDTs (linear variable differential transformers)
– 4 String pot potentiometers
– 36 Strain gauges on the hoops

Ten LVDTs were located at each face of the pier measuring the edge deformations, thus allowing the computation of flexural and axial deformations. Further six LVDTs were used to measure the absolute horizontal displacements of the pier at several height levels and another two LVDTs measured the base sliding displacements at the construction joint between pier and foundation. Any potential horizontal sliding or uplifting of the foundation block was checked by means of three additional LVDTs. The four string pot potentiometers were located on the backside of the pier and measured the diagonal elongations in order to determine the shear deformations of the test units. At several height levels a total of six hoops were equipped with six strain gauges each – three on the front side and three

---

[38] In Fig. 5.3 only one of the beams providing the side support is in position. The second beam was added at the beginning of the test of VK1.

on the backside of the pier. This way the hoop strains could be measured at several points distributed over the pier.

In addition to the hard-wired measurements the detailed deformations of the test units were determined by Demec measurements (Whitmore gauge measurements) at selected load steps. For this purpose, 218 Demec points had been glued onto the surface of each test unit up to a height of 2.75 m above the pier base with a grid width of 150 mm by 150 mm. At each of the most relevant load steps a total of 604 Demec measurements were then performed manually between the individual Demec points allowing a full description of the deformation field over the grid area. Based on this deformation field, it is e.g. possible to determine with high precision the contributions from flexural and shear deformations to the total displacement or to compute the principal strains and their directions over the surface of the pier. For Test Unit VK1 such Demec measurements have been performed at peak displacement of 20 different load steps. For Test Unit VK2 the manual Demec measurements have been performed at 22 load steps and in the case of VK3 16 sets of Demec measurements have been conducted.

The various electronic measurements were complemented by manual measurements of crack widths at selected load steps. For this purpose, the most relevant flexure-shear cracks were chosen and on each crack the width was measured at 5 points distributed over the length of the crack. In the case of VK1 and VK2 each time a total of 15 cracks had been monitored this way, and the widths of 23 cracks were measured on Test Unit VK3.

5.2.3 Prediction of Behavior

In Section 5.1 it has been outlined that the principal objectives of the test campaign are the deformation behavior of the piers, the cyclic-inelastic shear strength, and the behavior of the lap-splices in the plastic hinge regions of the piers. Therefore, in the following subsections numerical predictions of the anticipated behavior with respect to these three aspects are presented. These predictions are based on existing theoretical models taken from the literature. These models were partly calibrated on international experiments using different material properties and differing detailing compared to the test units of this campaign being more representative of Swiss conditions. Therefore, aside from the general model uncertainties, additional accuracies due to the variation of properties cannot be ruled out. The test campaign will serve to check and possibly improve the adequacy of the existing models for wall-type bridge piers featuring typical characteristics of existing Swiss structures.

At first, in Subsection *a* the predominantly flexural load-deformation behavior of the piers is predicted. In Subsection *b* existing models for the prediction of the cyclic-inelastic shear strength are compared and in Subsection *c* the potential strength degradation due to failing lap-splices is discussed.

a) Load-Deformation Behavior

The prediction of the inelastic load-deformation behavior of the piers is based on a plastic hinge model equivalent to that used in Section 2.2.3 (see Fig. 2.48). For this purpose moment-curvature analyses are performed on the cross-sections depicted in Fig. 5.2 with the measured material properties given in Tab. 5.4. With these analyses the characteristic data presented in Tab. 5.5 can be computed corresponding to the definitions in [SIA2018], [PSC96], and [PCK07]. Aside from the moment at first yield M_y' and the nominal moment capacity M_n, the curvature at first yield ϕ_y' and the ultimate curvature ϕ_u result. In this case a compressive concrete strain of ε_{cu} = -0.005 has been used for the definition of ϕ_u, following the recommendations for assessment situations given in [PSC96][39]. Using equation (5.1) a nominal yield curvature ϕ_y can further be defined representing, together with the nominal moment M_n, the corner point of a bilinearized moment-curvature relationship at nominal yield (in analogy to that shown in Fig. 5.4 for the force-displacement curve).

		VK1	VK2	VK3
First yield moment	M_y' [kNm]	1772	1785	2124
Nominal moment capacity	M_n [kNm]	2280	2314	2808
First yield curvature	ϕ_y' [1/km]	2.47	2.44	2.54
Nominal yield curvature	ϕ_y [1/km]	3.18	3.16	3.36
Ultimate curvature for ε_{cu} = -0.005	ϕ_u [1/km]	17.2	18.6	14.5

Tab. 5.5: Characteristic data of numerical moment-curvature response prediction

For Test Unit VK2 the moment-curvature analysis has been performed at the base section just below the lap-splice, i.e. the same longitudinal reinforcement has been modeled as for VK1. Therefore, the

---

[39] A stricter value of ε_{cu} = -0.004 is recommended in [PSC96] for unconfined concrete in the case of the new design of structures. The same limit is prescribed in [SIA2018] for the assessment of existing building structures. This value may be considered as a rather conservative limit for the flexural deformation capacity of reinforced concrete members.

only difference between the two test units for this prediction is the slightly higher measured concrete strength in VK2 resulting in a close to equal moment-curvature behavior for the two piers.

$$\phi_y = \phi_y' \cdot \frac{M_n}{M_y'} \tag{5.1}$$

Using the plastic hinge length L_{pl} defined in equation (2.3) it is possible to compute a curved force-displacement relationship or to define a corresponding bilinear relationship as shown in Fig. 5.4. In both cases the underlying principles are generally related to the plastic hinge concept depicted in Fig. 2.48 and the corresponding mathematical relationships are given in [PCK07]. The resulting force-displacement curves for Test Units VK1 and VK3 are presented in Fig. 5.5. The nominal yield displacement Δ_y of the bilinearized force-displacement relationship is related to the first yield displacement Δ_y', the corresponding first yield force F_y', and the nominal force capacity F_n according to equation (5.2).

$$\Delta_y = \Delta_y' \cdot \frac{F_n}{F_y'} \tag{5.2}$$
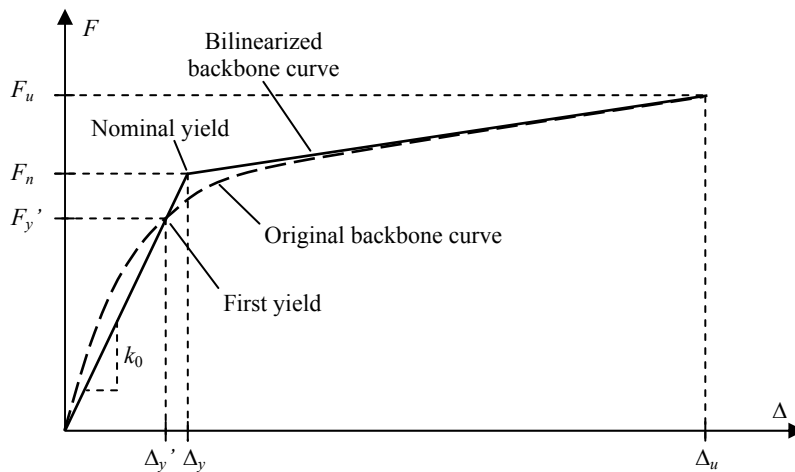
Fig. 5.4: Relationship between original curved and corresponding bilinearized load-deformation backbones
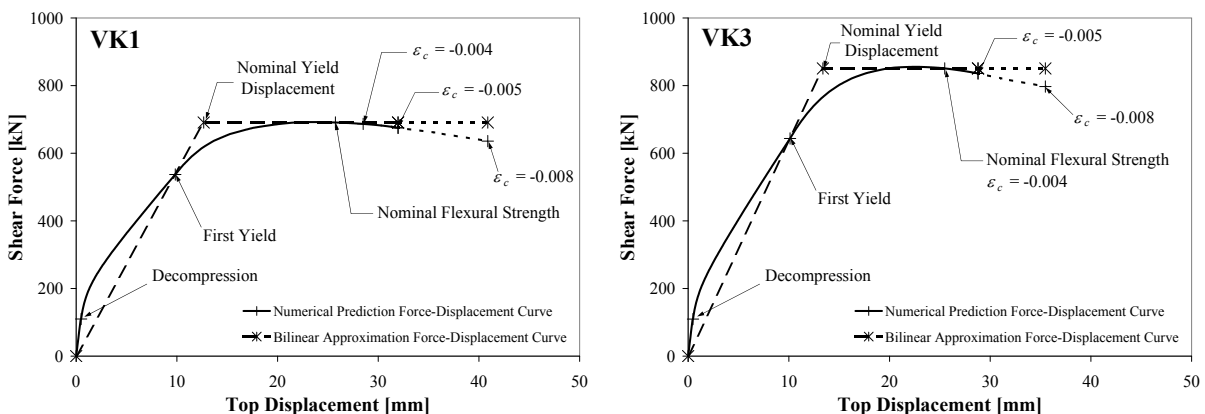
Fig. 5.5: Numerical prediction of force-displacement relationships based on plastic hinge approach
left: Test Unit VK1, right: Test Unit VK3

The failure criterion determining the flexural displacement capacity results from the strain limit for the concrete defined above as $\varepsilon_{cu} = -0.005$. For purely informative reasons, in Fig. 5.5 the dotted lines show how the curves would develop if a higher strain limit of $\varepsilon_{cu} = -0.008$ was used. At the same time,

it should be noted that the prediction of the ultimate displacement capacity also depends on the anticipated plastic hinge length L_{pl} as this relates the global top displacements to the local strains and curvatures at the pier base. The considerable uncertainties concerning the adequate value for L_{pl} and its subsequent consequences on the displacement capacity should be kept in mind.

It should further be noted that the predicted flexural response shows a decreasing force roughly after the point where the nominal capacity is achieved. This is partly related to the fact that the longitudinal reinforcement was modeled without strain hardening for the moment-curvature analyses. Due to the pronounced yield plateau of the reinforcing steel reaching up to a strain of about $\varepsilon_s = 0.025$, this choice appeared justified.

		VK1	VK2	VK3
First yield force	F_y' [kN]	537	541	644
Nominal force capacity	F_n [kN]	691	701	851
First yield displacement	Δ_y' [mm]	9.8	9.7	10.1
Nominal yield displacement	Δ_y [mm]	12.7	12.6	13.4
Ultimate displacement for $\varepsilon_{cu} = -0.005$	Δ_u [mm]	32.0	34.0	28.8

Tab. 5.6: Characteristic data of the numerical force-displacement response prediction based on the plastic hinge concept

In Tab. 5.6 the characteristic data of the predicted force-displacement relationships for the three test units are summarized. In the case of VK2, the influence of the lap-splice has been ignored for this simplified approximation, so that the corresponding load-deformation curve results almost equal to that of VK1 (in analogy to the near equality between the two moment-curvature relationships). This simplification ignores essentially three issues: (i) The stiffening effect in the elastic range due to the higher longitudinal reinforcement ratio within the lap-splice, (ii) the reduced plastic hinge length in the inelastic range also related to the larger amount of longitudinal reinforcement within the splice, and (iii) the potential strength degradation once the lap-splices start to fail under cyclic inelastic loading. The third issue will be further discussed in Subsection *c*, while the first two aspects will not be considered in this simplified prediction.

b) Shear Capacity

In the inelastic range, the shear demand within piers featuring a plastic mechanism only depends on the flexural strength of the member. This plastic mechanism – and thus the corresponding inelastic deformation capacity related to it – is only possible if the pier has sufficient shear strength so that the plastic hinges can develop. At the same time, it is known that the shear strength of reinforced concrete members tends to degrade under large cyclic-inelastic deformations. As a consequence, a shear failure cannot only occur in the elastic range where the force-displacement curve of the pier is still ascending. Instead, it can also develop in the inelastic range where the shear demand does not increase anymore because the shear capacity is decreasing with increasing deformations.

Generally, the (flexural) force-displacement relationship of the pier thus represents the deformation dependent shear demand curve, while a corresponding shear capacity curve can also be formulated as a function of the deformation – typically expressed as either curvature or displacement ductility. Using this type of visualization, a shear failure occurs at a potential intersection of the two curves, i.e. if the shear capacity curve falls below the force-displacement curve representing the shear demand. In Fig. 5.6 the predicted force-displacement relationships for Test Units VK1 and VK3 computed in the previous subsection (see Fig. 5.5) are compared to ductility dependent shear capacity curves resulting from various models proposed in the literature. As can be seen, although the qualitative trends

predicted by all deformation dependent shear capacity proposals appear to be similar, the quantitative scatter between the various models is large.
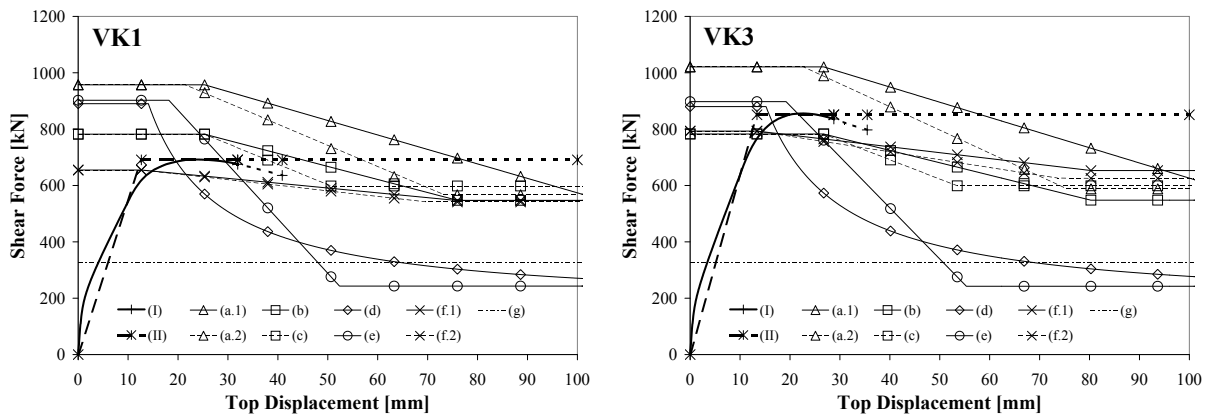
(I)	Curved prediction of force-displacement relationship according to Fig. 5.5
(II)	Bilinear approximation of force-displacement relationship according to Fig. 5.5; as dotted line without failure criterion
(a.1)	Cyclic-inelastic shear capacity of RC columns according to [KP00] as a function of displacement ductility
(a.2)	Cyclic-inelastic shear capacity of RC columns according to [KP00] as a function of curvature ductility
(b)	Cyclic-inelastic shear capacity of RC columns according to [SM04] as a function of displacement ductility
(c)	Cyclic-inelastic shear capacity of RC frame columns according to [FEMA356] as a function of displacement ductility
(d)	Cyclic-inelastic shear capacity of RC bridge columns according to [AM92] as a function of displacement ductility
(e)	Cyclic-inelastic shear capacity of RC bridge columns according to [Cal06] as a function of displacement ductility
(f.1)	Cyclic-inelastic shear capacity of RC members according to [BRF04], equation (8) as a function of displacement ductility; also adopted in [EC8-3]
(f.2)	Cyclic-inelastic shear capacity of RC members according to [BRF04], equation (7) as a function of displacement ductility
(g)	Static monotonic shear capacity of RC members according to [SIA262], equation (37) independent of ductility; using the minimum inclination of the compression struts being $\alpha = 25°$

Fig. 5.6: Comparison between predicted force-displacement relationship and
various models for the prediction of ductility dependent cyclic-inelastic shear capacity
left: Test Unit VK1, right: Test Unit VK3

For Test Unit VK1, only the models by Biskinis *et al.* [BRF04] suggest that a shear failure could occur in the essentially elastic range (although after first yield of the reinforcement). All other models predict that for the flexural strength of VK1 a shear failure could occur in the inelastic range if the flexural displacement capacity is large enough. In Subsection *a* it has been discussed that some uncertainty exists concerning the flexural displacement capacity which is e.g. related to the anticipated plastic hinge length L_{pl}. For the value of L_{pl} underlying the calculations in Subsection *a* and the strain limit of $\varepsilon_{cu} = -0.005$ for the concrete in compression, the flexural displacement capacity results as rather limited and only the shear strength models by Aschheim and Moehle [AM92] and that according to the Caltrans Seismic Design Criteria [Cal06] predict an inelastic shear failure before the flexural strain limit is reached. However, the dotted line in Fig. 5.6 prolonging the plastic part of the force-displacement relationship without limit suggests that, if higher than anticipated flexural deformation capacities should exist, all the other shear capacity models would also predict an inelastic shear failure for VK1 at some point.

Test Unit VK3 is subjected to a higher shear demand in the inelastic range due to the higher flexural capacity in the plastic hinge. As a consequence, for this case not only the models by Biskinis *et al.* [BRF04] predict a shear failure in the elastic range, but also the model by Sezen and Moehle [SM04] and the one according to [FEMA356] (being a modified version of the [SM04] model) suggest that a rather brittle shear failure already occurs in the ascending branch of the load-deformation curve (between the first yield and the nominal yield displacement). The model by Aschheim and Moehle [AM92] and the one according to the Caltrans Seismic Design Criteria [Cal06] predict an inelastic shear failure before the flexural strain limit is reached, as for the case of VK1. The model by Kowalsky and Priestley [KP00] suggests that for the flexural strength of VK3 an inelastic shear failure

could theoretically occur, but only if the flexural displacement capacity is higher than the value estimated using the plastic hinge model together with the chosen strain limit.

In this context it should be noted that in some of the models the shear strength is depending on the aspect ratio of the reinforced concrete member. Generally, this aspect ratio can be defined as the ratio L_v/l_w between the shear span and the *total section depth*, or as L_v/d using the *effective section depth* (d: distance from the compression edge to the center of the tension reinforcement). While the difference between these two definitions may be limited for columns or beams featuring two discrete reinforcement layers at the outer edges of the cross-section, a considerable influence on the computed shear strength can result for wall-type cross-sections where significant part of the longitudinal reinforcement is distributed over the section depth. In the above application of the various models the individual definition of the aspect ratio has been used wherever a clear statement about its definition was given in the literature. In those cases, where the aspect ratio is defined as L_v/d, for simplicity the effective section depth has been set to $d = 0.8\, l_w$ (as it would otherwise be load dependent). In the case of the model by Sezen and Moehle it is not explicitly stated in [SM04] which definition of the aspect ratio is supposed to be used. For the curves shown in Fig. 5.6 this model has been applied using L_v/d. If the aspect ratio for the model by Sezen and Moehle had been defined by L_v/l_w, a shear strength being higher by about 20% would have been predicted so that a less critical behavior with respect to potential shear failure would result.

Aside from the ductility dependent shear strength models included in Fig. 5.6, further models have been proposed in the literature for the estimation of the cyclic-inelastic shear strength without explicit consideration of the deformation level. These models do not allow any conclusions about the displacement at which an inelastic shear failure could occur, but may rather represent an estimation of the lower boundary of the shear strength even at large deformations. Such an approach is often adopted in seismic codes and regulations as e.g. [EC8-1], [EC8-2], [NZS3101], [ACI318], [FEMA273], [ATC32], or [ATC40]. In codes it is also common to define individual shear strength equations for reinforced concrete walls, columns, or beams. A further discussion of these models is beyond the scope of this text. However, it should be mentioned that for the test units of this experimental campaign the shear strengths based on the provisions of [NZS3101] and [ACI318] for the plastic zones of walls resulted similar to the residual shear strengths at high deformation levels according to the majority of the ductility dependent models shown in Fig. 5.6.

For comparison purposes, in the graphs of Fig. 5.6 the predicted shear strength according to [SIA262] has also been included. Although this model was originally not intended for cyclic-inelastic loading, at the current state it is implicitly referenced in [SIA2018] for the estimation of the shear strength in seismic assessment cases of existing building structures. If [SIA2018] is applied in an equivalent way on bridge piers, the shear strength model of [SIA262] would represent the current codified state for seismic applications. The underlying strut and tie model predicts the shear strength as directly proportional to the amount of transverse reinforcement. As a consequence, the very low transverse reinforcement ratio of $\rho_{sw} = 0.08\%$ results in a rather conservative shear strength estimation compared to the other models. However, for higher transverse reinforcement ratios this conservatism may not be warranted and the appropriateness of the [SIA262] shear strength model under cyclic-inelastic loading may be questionable.

Summarizing, it can be said that the various models for the prediction of the cyclic-inelastic shear strength suggest that the response of Test Units VK1 and VK3 may be considered potentially shear critical. The question whether a shear failure must actually be expected also depends on the flexural displacement capacity which the piers can develop. At the same time, the variability between the different models shows that a considerable uncertainty exists concerning the prediction of the shear strength. This uncertainty becomes even more significant if the models are to be used for the estimation of the reduced displacement capacity up to inelastic shear failure. The small angle between the intersecting curves for shear capacity and demand in Fig. 5.6 results in considerable variations of the estimated displacement capacity if only small differences of the predicted strength occur. Due to this problem, care should be taken with using this approach to determine the displacement capacity related to inelastic shear failure because the required reliability of the prediction may not be warranted. Alternative approaches have been proposed to directly estimate the displacement capacity of shear

critical reinforced concrete columns based on empirical equations (e.g. [EM05]). A discussion of the pros and cons of this conceptual approach is beyond the scope of this document.

The anticipated shear behavior of Test Unit VK2 will be discussed in the following Subsection *c* in combination with the influence of the potentially failing lap-splices and the subsequent flexural strength degradation.

c) Strength Degradation due to Lap-Splice Failure

In the case of Test Unit VK2 the response is not only a result of the general flexural deformation behavior outlined in Subsection *a* and the potential for cyclic-inelastic shear failure discussed in Subsection *b*, but is rather further influenced by the presence of the lap-splices of the longitudinal reinforcement at the pier base. It has already been mentioned in Subsection *a* that these lap-splices influence the flexural behavior both in the elastic and in the inelastic deformation range. Furthermore, the lap-splices can cause a strength degradation of the pier once they start failing under cyclic inelastic loading. This loss of flexural strength can subsequently also influence the potential for a shear failure as it reduces the shear demand in the inelastic range. Therefore, the cyclic strength degradation related to lap-splice failure is an important aspect for the realistic description of the seismic pier behavior.

Generally, the detailed load carrying mechanism within a lap-splice is rather complex, even under static monotonic loading. The force transfer between the spliced bars relies largely on the tension strength of the surrounding concrete and is therefore sensitive to the quality of the cover concrete. Priestley *et al.* [PSC96] have proposed a model which allows the estimation of the strength degradation resulting from lap-splice failure. According to this model, the lap-splices can sustain some limited cyclic-inelastic deformations if their length is sufficient to transfer the full force capacity of the bars under static monotonic loading. For the rather large splice length of $l_s = 43 \, d_{bl}$ adopted in Test Unit VK2 (see Section 5.2.1*b*) it can be assumed that this criterion is fulfilled so that the spliced bars can develop their full strength.

The model by Priestley *et al.* [PSC96] suggests that under increasing cyclic-inelastic deformations the concrete in the compression zone starts developing micro-cracks at strains of about $\varepsilon_c = -0.002$. This damage to the concrete strongly reduces its tension strength which is needed to sustain the bond stresses of the lap-splices in the following half-cycle of the loading when the former compression zone is put in tension. Due to this lack of tension strength, longitudinal bond cracks develop along the lap-splices causing their failure and initiating the strength degradation of the pier on the member level.
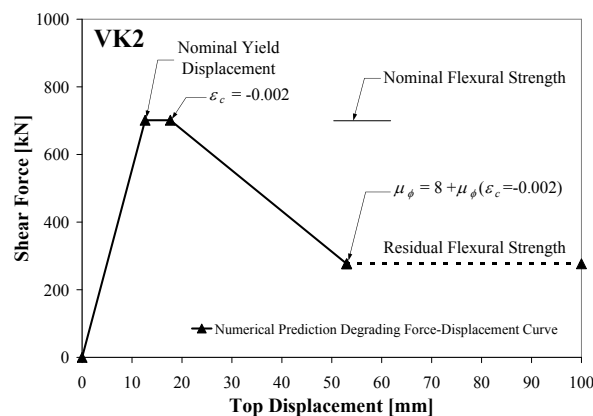
Fig. 5.7: Numerical prediction of degrading force-displacement relationship of Test Unit VK2 due to lap-splice failure based on the approach by Priestley et al. [PSC96]

As depicted in Fig. 5.7, the force-displacement backbone curve thus starts decreasing at a displacement corresponding to a concrete compression strain of $\varepsilon_c = -0.002$. According to Priestley *et al.* [PSC96], a residual flexural strength of the pier will remain even after the failure of all lap-splices as a result of eccentricity of the axial compression load. Based on experimental results,

Priestley *et al.* suggest that this residual strength is reached at a curvature ductility exceeding that of the onset of the degradation by a value of 8. Due to only limited experimental data, it is tentatively recommended in [PSC96] not to rely on higher deformation levels. Therefore, the force-displacement curve in Fig. 5.7 is drawn as a dotted line in this region.
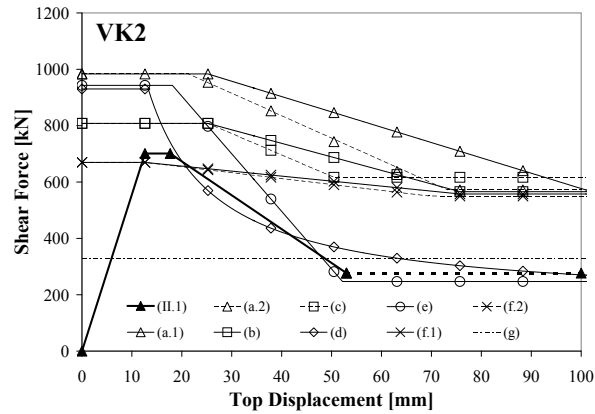
(II.1) Multilinear approximation of degrading force-displacement relationship according to Fig. 5.7
(a.1)   Cyclic-inelastic shear capacity of RC columns according to [KP00] as a function of displacement ductility
(a.2)   Cyclic-inelastic shear capacity of RC columns according to [KP00] as a function of curvature ductility
(b)   Cyclic-inelastic shear capacity of RC columns according to [SM04] as a function of displacement ductility
(c)   Cyclic-inelastic shear capacity of RC frame columns according to [FEMA356] as a function of displacement ductility
(d)   Cyclic-inelastic shear capacity of RC bridge columns according to [AM92] as a function of displacement ductility
(e)   Cyclic-inelastic shear capacity of RC bridge columns according to [Cal06] as a function of displacement ductility
(f.1)   Cyclic-inelastic shear capacity of RC members according to [BRF04], equation (8) as a function of displacement ductility; also adopted in [EC8-3]
(f.2)   Cyclic-inelastic shear capacity of RC members according to [BRF04], equation (7) as a function of displacement ductility
(g)   Static monotonic shear capacity of RC members according to [SIA262], equation (37) independent of ductility; using the minimum inclination of the compression struts being $\alpha = 25°$

Fig. 5.8: Comparison between predicted degrading force-displacement relationship of Test Unit VK2 and various models for the prediction of ductility dependent cyclic-inelastic shear capacity

Considering that the flexural strength also represents the shear demand in a plastic mechanism, it cannot be ruled out that the strength degradation related to lap-splice failure might also have an influence on the potential for shear failure. In Fig. 5.8 the estimation of the degrading force-displacement backbone of VK2 is compared to the various ductility dependent shear strength models discussed in Subsection *b*. This comparison suggests that – according to many of the models – the flexural strength might degrade faster than the shear strength. In this case it would be conceivable that the loss of flexural strength could prevent the pier from a shear failure. At the same time, it should be noted that the comparison presented in Fig. 5.8 implies that the shear carrying mechanism is not influenced by the degradation of the lap-splices. This assumption may not be fully warranted. Instead, it cannot be ruled out that the damage occurring in the lap-splice region may also influence the shear strength in a negative way. In this case, the shear capacity could also degrade faster and still decrease below the flexural strength thus resulting in an inelastic shear failure. Further (experimental) research is needed for a better understanding of these potential interrelations.

5.2.4 Loading

In each test, at first an axial compression force was applied in order to simulate the vertical gravity loads from the superstructure. For the piers of the sample bridges presented in Section 2.2.2 the axial load ratios based on the average expected concrete strengths have been estimated to fall in a range between 0.057 and 0.088 (see Tab. 2.1). Therefore, to represent realistic conditions a target axial load ratio in the order of 0.075 has been chosen. Based on a target concrete compression strength of $f_c \approx 35$ MPa, the required axial load at the base of the pier results as $N_{base} \cong 1370$ kN. As the weight of the pier wall together with that of the vertical actuators and the transverse cross-beam amounts to approximately 70 kN, the required vertical load to be applied by the vertical actuators on top of the piers results as $N_{top} = 1300$ kN. This load was applied to all three test units independent of the actual concrete strength in the individual cases. The resulting axial load ratios thus ranged between 0.067 and 0.077 as summarized in Tab. 5.7.

		VK1	VK2	VK3
Vertical load at pier top	N_{top} [kN]	1300		
Axial load at pier base	N_{base} [kN]	1370		
Axial load ratio at pier base	v_{base} [-]	0.067	0.075	0.077

Tab. 5.7: Vertical load applied to Test Units VK1, VK2, and VK3

This vertical load was kept constant throughout the entire test since it was supposed to represent the gravity load from the bridge superstructure. Cyclic horizontal displacements were then applied at the pier top with increasing amplitude. The conceptual load history used in all experiments is shown in Fig. 5.9. Generally, at each loading level two symmetric cycles with the same amplitude were conducted. In the initial elastic range these amplitudes were defined by the horizontal force level as fractions of the numerically determined *first yield load F_y'*. After the onset of yielding, the amplitudes of the cycles were defined as multiples of the nominal yield displacement at the top of the pier (i.e. the point of if the horizontal load application).
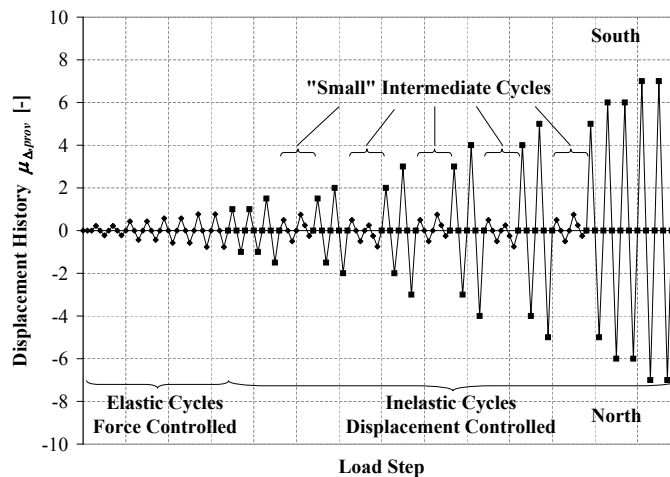
Fig. 5.9: General load history of quasi-static cyclic tests

The force F_y' at first yielding was taken from the numerical analyses presented in Section 5.2.3*a* and it is thus independent from the experimental measurements. It is defined as the point where either the first reinforcement bar starts yielding or where the concrete compressive strain reaches a value of $\varepsilon_c = -0.002$ (which ever occurs first [PCK07]). The computed values for F_y' are repeated in Tab. 5.8 for the three test units. Four different force amplitude levels were applied in the elastic range of the experiments (with two cycles each) being $0.25F_y$', $0.50F_y$', $0.75F_y$', and $1.00F_y$'.

For the definition of the displacement ductilities μ_Δ in the inelastic range the nominal yield displacements Δ_y from Tab. 5.6 could have been used which were computed numerically based on the plastic hinge approach. On the other hand, it is also possible to directly include the measured experimental deformation behavior into the definition of Δ_y. For this purpose, the first yield displacement Δ_y' is taken from the experiment as the displacement which is measured at a horizontal force equal to the computed first yield load F_y'. The values of Δ_y' measured during the two excursions (south and north) of the first cycle to F_y' are given in Tab. 5.8. The average between these two values is then used together with the numerically determined forces at first yield F_y' and nominal capacity F_n to compute the individual nominal yield displacements Δ_y of each test unit according to equation (5.2). The resulting values of Δ_y based on the experimental measurements are presented in Tab. 5.8.

			VK1	VK2	VK3
First yield load	F_y' [kN]	numerically computed	537	541	644
Nominal load capacity	F_n [kN]	numerically computed	691	701	851
Top displacement at first yield load	Δ_y' [mm]	measured at 1st cycle south	7.0	6.2	10.4
		measured at 1st cycle north	8.0	6.5	10.9
		1st cycle average	7.5	6.3	10.7
Nominal yield displacement	Δ_y [mm]	determined from 1st cycle average	9.6	8.2	14.1

Tab. 5.8: Characteristic force and displacement values of Test Units VK1, VK2, and VK3

As can be seen from these data, the resulting nominal yield displacements show some noticeable differences between the various test units. Basing the displacement ductilities μ_Δ for the determination of the target displacements in the inelastic range of the experiments on different nominal yield displacements Δ_y would result in different deformation amplitudes for the individual test units. In order to achieve a better comparability between the deformation patterns of the various piers it has been deemed preferable to define equal load steps for each test unit in the inelastic range. Therefore, a *provisional nominal yield displacement* of $\Delta_{y,prov} = 10.5$ mm has been chosen for the definition of the ductility steps in the inelastic range of the load history for all three experiments. This choice has the consequence that the multiples of $\Delta_{y,prov}$ do not correspond to real displacement ductility levels μ_Δ of the individual test units, but rather also only represent *provisional displacement ductilities* $\mu_{\Delta,prov}$ being used for the control of the experiments. The corresponding real displacement ductilities μ_Δ then must be computed separately and will not result in integer numbers (see Section 5.3.1*j*).

Based on the above defined provisional nominal yield displacement, the load history in the inelastic range started with two cycles each to (provisional) ductility levels of $\mu_{\Delta,prov} = 1.0$ and $\mu_{\Delta,prov} = 1.5$. From then on, the target displacements were increased by full ductility levels up to failure (i.e. $\mu_{\Delta,prov} = 2, 3, 4,$ etc.) performing two cycles at each amplitude. At the loading levels from $\mu_{\Delta,prov} = 1.5$ up to $\mu_{\Delta,prov} = 5$, two small cycles were inserted between the two large cycles to the full target ductility (see Fig. 5.9). These intermediate small cycles shall bring some insight into the energy dissipation behavior during small cycles after the occurrence of larger inelastic cycles (see objectives in Section 5.1). In the test of VK1 these smaller cycles were defined by force amplitudes. The first small cycle was symmetric using target forces of $\pm 0.50F_y'$, while the second small cycle was chosen to be asymmetric with force amplitudes of $+0.75F_y'$ and $-0.25F_y'$. For Test Units VK2 and VK3 the intermediate small cycles were defined by the top displacements measured during the corresponding cycles of VK1 since equivalent deformation states were deemed more comparable than equal force levels.

5.3 Test Results

5.3.1 Observations

In this section the behavior of the three test units will be discussed as observed during the experiments. At first, in Subsection *a* the development of the crack patterns in the various test units will be described. Afterwards, in Subsections *b* through *h* the observed behavior in the inelastic range and especially the development of damage as well as the individual failure mechanisms will be discussed. In Subsection *i* the test units are shown at the various states throughout the experiments together with the measured hysteresis loops up to these points. Finally, in Subsection *j* the achieved ductility capacities based on the nominal yield displacements of the individual test units are discussed.

a) Development of Cracks in Test Units VK1, VK2, and VK3 up to $\mu_{\Delta,prov}$ = 1.5

Despite the different reinforcement layouts of the test units, they showed noticeable similarities with respect to the development of their crack patterns. Up to a horizontal force level of $F_{hor} = 0.25 \, F_y$' all three piers remained uncracked. Only an almost invisible crack occurred at the base as a result of decompression and the absence of tension strength in the construction joint. First flexural cracks in the piers were observed at the next load step defined by a horizontal load of $F_{hor} = 0.5 \, F_y$'. These cracks grew and their number further increased during loading to $F_{hor} = 0.75 \, F_y$', but they remained purely flexural up to this point. At first yielding (i.e. $F_{hor} = F_y$') the flexural cracks had started to incline and thus first shear cracks developed in all three test units. At this stage the crack widths in the piers were not larger than 0.3 mm.

Between the load steps corresponding to $F_{hor} = F_y$' and $\mu_{\Delta,prov}$ = 1.5 the crack patterns further developed both in terms of number as well as length. At $\mu_{\Delta,prov}$ = 1.5 (top displacement Δ_{Top} = 15.75 mm, drift ratio δ = 0.48%) the complete pattern had developed in each of the test units consisting of flexural cracks turning into inclined shear cracks. The crack widths in the piers at this stage ranged mostly up to 0.6 mm. It is noteworthy that the largest widths occurred in the inclined part of the cracks (i.e. in the shear cracks), whereas in the flexural part at the edges the widths only reached values of about 0.4 mm. In Test Unit VK3, having the largest shear demand, one shear cracked had a width of 0.9 mm. It is further noteworthy that in Test Unit VK2 the base crack reached a width of 1.4 mm, while the other two test units had base crack widths of only about 0.7 mm. This is a result of the lap-splice in VK2 which caused a significant reduction of the plastic hinge length and subsequent strain concentrations in the immediate base region. Aside from these cracks with still rather limited widths, no signs of further damage was observed in any of the test units at $\mu_{\Delta,prov}$ = 1.5.

At higher displacement levels during the load history the crack pattern did not change anymore, neither in terms of development of new cracks nor in terms of length of the cracks. Instead, from $\mu_{\Delta,prov}$ = 2 on (top displacement $\Delta_{Top} \geq 21$ mm, drift ratio $\delta \geq 0.64\%$) only the widths of the pre-exiting cracks were growing and eventually different types of damage developed which are further described in Subsection *b*.

b) Development of Damage in Test Units VK1, VK2, and VK3 up to $\mu_{\Delta,prov}$ = 2

At $\mu_{\Delta,prov}$ = 2 (top displacement Δ_{Top} = 21 mm, drift ratio δ = 0.64%) still no real damage had occurred to any of the piers. However, Test Units VK2 and VK3 showed minor longitudinal cracks in the compression zones which indicated first signs of critical concrete compression strains at the edges (see Fig. 5.10). In contrast, the compression zone of Test Unit VK1 still appeared fully undamaged. The largest crack widths within the piers ranged between 1.0 mm and 1.5 mm. In addition to these cracks within the piers, Test Unit VK2 showed a rather wide open base crack with a width of 3 mm, whereas VK1 and VK3 had base crack widths of only 1 to 1.5 mm. The load deformation behavior at $\mu_{\Delta,prov}$ = 2 showed stable hysteretic response without strength degradation and with still rather limited energy dissipation.

c) Development of Damage in Test Units VK1, VK2, and VK3 up to $\mu_{\Delta,prov} = 3$

At the next load step of $\mu_{\Delta,prov} = 3$ (top displacement $\Delta_{Top} = 31.5$ mm, drift ratio $\delta = 0.95\%$) the first noticeable damage occurred to Test Units VK2 and VK3 (see Fig. 5.11), especially in the second cycle to this amplitude. While VK3 showed pronounced spalling of cover concrete in the compression zones combined with an onset of longitudinal bar buckling, VK2 experienced only minor concrete spalling. However, VK2 developed a large bond crack along one of the outer spliced bars at the pier edge. This bond crack having the same length as the entire lap-splice was a rather sure sign of complete failure of this splice, which is also reflected by the noticeable drop of flexural strength seen especially in the hysteresis of the second cycle (see Fig. 5.11). Based on the amount of strength degradation, it can be assumed that by the second cycle the outer four reinforcement bars in each tension zone of the cross-section were essentially ineffective due to bond failure of the lap-splices. Test Unit VK3 also showed some limited strength degradation in the second cycle. However, this loss of strength may rather be related to a certain deterioration of the shear carrying mechanism instead of a flexural degradation. In contrast, Test Unit VK1 remained essentially undamaged at $\mu_{\Delta,prov} = 3$ and showed stable hysteretic response without any strength degradation. The only sign of starting damage in VK1 were first very small longitudinal cracks in the edges of the compression zone indicating the onset of concrete deterioration in compression.

The deformation behavior of VK1 at $\mu_{\Delta,prov} = 3$ was predominantly flexural which was also reflected by the measured crack widths. While its flexural cracks reached values up to 2.5 mm (especially one crack in the lower part of the pier) and the width of the base crack also ranged between 1.5 mm and 2.5 mm, its shear cracks did not exceed values of 1.0 to 1.2 mm. For Test Unit VK2 the mainly flexural behavior was even more pronounced. Especially with the incipient failure of lap-splices the flexural deformations tended to concentrate in one crack just above the splice and in the base crack below it. The width of the former reached values of about 2 to 2.5 mm, while the base crack opened up even further reaching a width of 4 mm. The inclined shear cracks in VK2 did not exceed widths of 1 to 1.5 mm. In contrast, Test Unit VK3 showed a stronger influence of the shear carrying mechanism. While the shear cracks in VK3 reached widths of up to 1.8 mm, the flexural cracks did not exceed 1.5 mm. The width of the base crack was also in the range of 1.5 to 2 mm.

d) Development of Damage in Test Units VK1, VK2, and VK3 up to $\mu_{\Delta,prov} = 4$

At $\mu_{\Delta,prov} = 4$ (top displacement $\Delta_{Top} = 42$ mm, drift ratio $\delta = 1.27\%$) Test Unit VK1 also showed noticeable signs of damage. Significant spalling of cover concrete in the bottom regions of the compression zones was observed, accompanied by beginning buckling of the longitudinal reinforcement bars in compression (see Fig. 5.12). However, as the stable hysteretic response shows, this onset of damage did not have any significant influence on the functionality of the load carrying mechanisms. In contrast, Test Unit VK2 showed further strength degradation compared to the previous load steps. The combination of successive large concrete strains in compression and bond stresses from the lap-splices during the cyclic loading caused concrete spalling in the edge regions over the entire height of the splices. The amount of measured strength degradation suggests that by the second cycle to $\mu_{\Delta,prov} = 4$ the lap-splices of approximately the outer 6 reinforcement bars in each tension zone must have had failed causing the corresponding bars to become ineffective. At the same top displacement, Test Unit VK3 already showed severe damage to the compression zones, including substantial concrete spalling also in the core regions of the compression zones and pronounced buckling of the longitudinal reinforcement bars in compression. Furthermore, two diagonal shear cracks reaching down to the damaged compression zones started opening up and clearly indicated the onset of shear critical behavior. This developing shear mechanism also resulted in a significant strength degradation of VK3, especially in the second cycle to $\mu_{\Delta,prov} = 4$.

The still primarily flexural deformation behavior of Test Unit VK1 at this loading level was reflected by its crack pattern. The largest crack widths occurred in the flexural cracks, with particularly one crack in the bottom part of the pier opening up about 4 mm. The base crack of VK1 reached widths of about 2 to 3 mm, while the widths of the shear cracks did not exceed values of 1 to 1.5 mm. In the case of Test Unit VK2 at $\mu_{\Delta,prov} = 4$ the previously observed trend for a concentration of the predominant

flexural deformations in two cracks just above and below the failing lap-splices continued. The crack above the splices reached widths in the range of 3 to 5 mm, while the base crack opened up approximately 7 mm. The shear cracks in VK2 had widths of only about 1 to 1.5 mm, thus remaining at a similar level as in the previous loading level (i.e. $\mu_{\Delta,prov} = 3$). In contrast, the fully different behavior of VK3 can be seen from the fact that here the shear cracks dominated with widths in the range of 3 to 4 mm, while the largest flexural cracks within the pier only reached values of about 1.5 mm. The width of the base crack fell in the same range as the other flexural cracks, being about 1.5 mm.

e) Development of Damage in Test Units VK1, VK2, and VK3 up to $\mu_{\Delta,prov} = 5$

The emerging shear critical behavior of VK3 further aggravated in the first cycle to $\mu_{\Delta,prov} = 5$ (top displacement $\Delta_{Top} = 52.5$ mm, drift ratio $\delta = 1.59\%$) and finally lead to a complete shear failure in the second cycle which was accompanied by a coinciding complete loss of axial load capacity. As can be seen from the hystereses shown in Fig. 5.13, VK3 already lost substantial part of its horizontal force capacity during the first cycle. This strength degradation was closely related to noticeable sliding motions along the diagonal shear cracks which already indicated the type of failure mechanism that was evolving. These sliding motions resulted in plastic shear displacements, but also in corresponding axial deformations. Under the cyclic loading and the subsequent sliding along the two crosswise shear cracks the pier started to separate into four concrete wedges (see Fig. 5.13). During the first cycle of horizontal loading to $\mu_{\Delta,prov} = 5$, the axial force tended to push the upper wedge downwards thus driving the left and right wedges outwards. As a consequence, the sliding along the shear cracks resulted in a shortening but also in a widening of the pier.

One consequence of this behavior was that in the center region of VK3, where the two shear cracks crossed, a severely damage zone developed. The sliding motions of changing direction lead to a grinding of the concrete in the entire core region of the test unit and the axial shortening of the pier also resulted in substantial buckling of the longitudinal reinforcement bars in the same region. Severe damage was also observed in the outer parts of the plastic hinge region at the base of VK3. Significant part of the concrete compression zones was lost and the longitudinal reinforcement bars also buckled in this region. In the second cycle to $\mu_{\Delta,prov} = 5$, Test Unit VK3 could still survive the first excursion to the south at very low remaining transverse force capacity – and accompanied by continuous sliding along the diagonal shear crack. The friction force that could be transferred across this crack obviously was still just enough to keep the pier in equilibrium. However, shortly after entering into the subsequent north excursion and at a rather marginal top displacement, the sliding motions along the other shear crack accelerated and the combination of axial load and rather low horizontal force could not be equilibrated by friction across the diagonal crack any more. The combined shear and axial load failure at this point was a consequence. A real bridge pier in this condition could not have supported the superstructure anymore and a complete failure of the neighboring bridge spans would have been unavoidable.

Although the concrete spalling at the base of Test Unit VK1 had also progressed at $\mu_{\Delta,prov} = 5$, the general condition of the pier was still reasonably good. The damage to the compression zones had rather spread upwards in the cover concrete and not so much inwards into the core of the cross-section. This way, not too much compression zone and effective section depth were lost. As a result of the significant height over which the cover concrete had spalled, the outer longitudinal reinforcement bars could freely buckle. However, under subsequent tension these bars restraightened again and were still able to provide their full capacity. This fairly good behavior is also reflected by the still rather stable hysteresis loops of VK1 shown in Fig. 5.13. No real signs of significant strength degradation were visible during the two cycles of $\mu_{\Delta,prov} = 5$.

In the case of Test Unit VK2, the general behavior already observed in the preceding load steps kept on developing further at $\mu_{\Delta,prov} = 5$. With increasing top displacement more lap-splices at the base successively failed, causing a subsequent progression of cyclic strength degradation. In this context, it should be mentioned that the front side (shown in the upper row of Fig. 5.13) and the backside of the pier developed a noticeably different behavior. In the construction process, the piers were lying

horizontally during pouring of the concrete with the backside being at the bottom and the frontside being on the top. As a consequence, the reinforcement at the backside had better bond conditions than that on the frontside. This difference was further intensified by the differing curing conditions of the two sides of the pier. While the backside had been covered by the formwork during curing, the frontside had an open surface during the first 24 hours after pouring of the concrete (as a result of a deficient curing process). It must be assumed that these different curing conditions on the two sides of the pier resulted in differing tension strengths of the concrete at the pier surfaces. This influences the load carrying mechanism of the lap-splices because the bond stresses and the force transfer from one bar to another in a lap-splice rely on the tension strength of the surrounding concrete.

Together with the generally different bond conditions due to the different bar positions during pouring of concrete, a significant faster progression of lap-splice failure resulted on the front side of the pier compared to the backside. As a result, on the front side of VK2 the cover concrete had detached at $\mu_{\Delta,prov} = 5$ over the outer 50 cm of the section depth and over a height corresponding to the length of the lap-splices. Although in this region concrete is still visible in Fig. 5.13, it was possible to determine by knocking that behind the cover concrete a hollow gap had developed, resulting in a surface shell being separated from the core concrete. It must be assumed that in this region no forces could be transferred between the spliced bars anymore. However, on the backside of the pier where better bond conditions and a higher concrete tension strength at the surface prevailed, hardly any separation of the cover concrete could be detected. Instead, the majority of the lap-splices over the section depth still appeared essentially intact. Based on the measured loss of flexural strength, it can be assumed that by the 2nd cycle to $\mu_{\Delta,prov} = 5$ about 7 to 8 lap-splices had failed in each tension zone. Aside from the four bars at the outer edges of the cross-section, three more lap-splices were ineffective on the front side due to the separation of the cover concrete shell. It cannot be ruled out that, additionally, one lap-splice on the backside had become (partly) ineffective. Despite the substantial loss of capacity in the tension cord due to the failing lap-splices, it is noteworthy that the compression zones on both sides of the cross-section still remained rather undamaged, apart from the spalling of the cover concrete. As a consequence, at this loading level still no significant loss of effective section depth related to damage to the concrete compression zones was observed.

The varying behavior of the Test Units was also reflected by the measured crack widths at this deformation state. The last time the crack widths of VK3 were measured was at the first excursion (to the south) during the first cycle to $\mu_{\Delta,prov} = 5$. Here, the large diagonal crack had already opened up 5 mm, while all flexural cracks – including the base crack – did not have widths of more than 0.5 mm anymore. This concentration of damage and deformation to the diagonal crack already clearly indicated the emerging failure mechanism. In contrast, the deformation behavior of Test Unit VK1 was still flexure dominated. Especially one flexural crack in the lower region of the pier reached a width of about 5 to 6 mm, while other flexural cracks ranged between 1 and 2.5 mm and the base crack of VK1 opened up some 3 to 4 mm. At the same time, the widths of the shear cracks did not exceed 1.5 to 2 mm. In Test Unit VK2, the predominantly flexural deformations kept concentrating primarily in one large crack above the lap-splices and in another one at the base below the splices. As a consequence, the base crack reached a width of about 10 mm and the crack above the splice had a width of 5 to 7 mm. Due to the degradation of strength, the widths of the other flexural cracks did not exceed 0.25 mm anymore and the shear cracks remained at about 1 to 1.5 mm.

f) Development of Damage in Test Units VK1 and VK2 up to $\mu_{\Delta,prov} = 6$

At a loading level of $\mu_{\Delta,prov} = 6$ (top displacement $\Delta_{Top} = 63$ mm, drift ratio $\delta = 1.91\%$) only Test Units VK1 and VK2 remained. A rather significant change of behavior could be observed in the case of Test Unit VK1. In contrast to the previous load steps, VK1 now also developed considerable damage to the compression zones including substantial loss of material in the concrete core. This damage started in the first cycle to $\mu_{\Delta,prov} = 6$ and further progressed significantly during the second cycle shown in Fig. 5.14. The change of behavior is also well represented by the measured hysteretic response showing for the first time a noticeable strength degradation of VK1 – especially in the second cycle.

Generally, the response and the damage behavior of VK2 continued at $\mu_{\Delta,prov} = 6$ in a similar way as in the previous load steps. Although a significant difference between the damage progression of the lap-splices on the front side and the backside was still noticeable, now the cover concrete in the outer regions of the backside also started detaching. It can therefore be assumed that on the backside additional lap-splices over the section depth had also failed. However, in the center region of the section depth still more intact splices remained on the backside than on the front side where the majority of the splices can be assumed as ineffective by this time. Furthermore, at this loading level the concrete in the compression zones also started showing signs of noticeable damage. It can be assumed that in the edge regions only limited strength (if any) of the concrete in compression was left. Based on the geometric progression of the separation of cover concrete, approximately 10 lap-splices on each side of the section depth must have been ineffective by the second cycle of $\mu_{\Delta,prov} = 6$. On the other hand, the measured strength degradation cannot be fully explained only by these 10 ineffective reinforcement bars. Therefore it appears likely that the damaged concrete in the compression zones resulted in an effective reduction of the section depth causing an additional loss of flexural strength.

The crack widths measured at VK1 still suggested a predominantly flexural deformation behavior. Especially one flexural crack in the lower region reached a width of about 6 mm and the base crack had a width of about 4 mm. The shear cracks in VK1 had opened up somewhat further than in previous load steps, but still did not exceed widths of about 2.5 mm. The starting disintegration of the concrete in the lower region of Test Unit VK2 made it difficult to measure reliable crack widths at $\mu_{\Delta,prov} = 6$. Generally, the previously observed primary concentration of flexural deformations in one crack just above the lap-splices and another one just below it (i.e. at the pier base) was also observed at this loading stage. The width of the base crack was determined as approximately 10 to 12 mm, while that above the lap-splice had a width of about 5 to 7 mm. The widths of the shear cracks were measured in a range of 1 to 1.5 mm thus remaining essentially unchanged compared to the previous load step.

g) Development of Damage in Test Units VK1 and VK2 up to $\mu_{\Delta,prov} = 7$

During the attempt to go to the first excursion to the south of the first cycle to $\mu_{\Delta,prov} = 7$ (top displacement $\Delta_{Top} = 73.5$ mm, drift ratio $\delta = 2.23\%$), Test Unit VK1 showed significant strength degradation. The transverse force at first increased up to a value of 335 kN at a top displacement of 48 mm, but then started to decrease again with increasing deformations (see Fig. 5.15). At a displacement of $\Delta_{Top} = 59$ mm and with a remaining transverse force capacity of 280 kN, the pier failed suddenly opening up a diagonal shear crack. The failure was accompanied by a loud noise and some concrete debris spreading over a range of about 2 m around the test unit. The upper part of the pier immediately started sliding down the wide open diagonal crack causing a combined shear and axial load failure.

This failure type of VK1 thus was conceptually similar to that of VK3 observed at a lower top displacement. In both cases the shear failure was accompanied by an immediate loss of the axial load capacity which would result in a complete collapse of the neighboring spans in a real bridge. The primary difference between the two failure types is that in the case of VK3 the upcoming shear failure had developed noticeably over several cycles, whereas VK1 did not show any signs of severe shear distress until very shortly before the actual failure. While the diagonal shear cracks of VK3 continuously opened up and also experienced significant sliding motions well before the final failure, the deformation behavior and the crack pattern of VK1 was still predominantly of a flexural type almost until the end. The widths of the shear cracks in VK1 remained in a rather limited range throughout most part of the experiment. Only at the very end of the test these shear cracks opened up very suddenly initiating the complete failure of the pier.

Test Unit VK2 went on with the development of the same damage patterns already observed in the previous load steps. The proceeding failure of lap-splices coupled with a progressing damage to the concrete compression zones resulted in a further loss of lateral strength, as can be seen from the hysteresis loops depicted in Fig. 5.15. On the front side of the pier, featuring the poorer bond conditions (see discussion in Subsection *e*), essentially no lap-splices remained that could still transfer

significant forces. On the backside with the better bond conditions, only in the center third of the section depth some intact lap-splices remained that were capable of transferring tension forces between the longitudinal reinforcement bars. The remaining lateral strength in the second cycle to $\mu_{\Delta,prov} = 7$ (top displacement $\Delta_{Top} = 73.5$ mm, drift ratio $\delta = 2.23\%$) is close to the force capacity that would result from a direct diagonal compression strut (i.e. from the eccentricity of the axial load at the pier base) without contribution from any flexural reinforcement if the entire concrete section depth still contributed to the resistance. However, due to the damage to the concrete in the outer parts of the base region, some reduction of the effective section depth at this load step must be assumed. Therefore, the flexural resistance is likely to be the result of very limited contribution from the remaining reinforcement and a reduced eccentricity of the axial load.

No crack widths in either of the test units were measured anymore at this loading level.

h) Development of Damage in Test Unit VK2 up to $\mu_{\Delta,prov} = 10$

Subsequently, two cycles at $\mu_{\Delta,prov} = 8$, 9, and 10 each (top displacement $\Delta_{Top} = 64$, 94.5, and 105 mm, drift ratio $\delta = 2.55\%$, 2.86%, and 3.18%) were applied to Test Unit VK2. The final state following the second cycle of $\mu_{\Delta,prov} = 10$ is shown in Fig. 5.16 after the removal of the loose concrete debris in the base region of the pier. During the various load steps the last remaining lap-splices failed due to spalling of the cover concrete. In parallel, the concrete compression zones in the lower part of the test unit disintegrated completely. As a result, by the second cycle of $\mu_{\Delta,prov} = 10$ the lateral force capacity had reduced to 115 kN corresponding to about only 15% of the maximum strength attained during previous load steps. Due to the absence of any contribution from longitudinal reinforcement, the remaining flexural strength is the result of pure direct strut action with the axial load having an eccentricity of 8.5 cm at the base. This behavior can be interpreted as almost some form of a hinge developing at the base of the pier.

The test of VK2 was stopped after the second cycle to $\mu_{\Delta,prov} = 10$. Despite the almost complete loss of horizontal force capacity, the pier was still able to carry the full axial load of 1370 kN. However, upon dismantling of the test unit after the end of the experiment it could be seen that the remaining core at the base only consisted of rather loose concrete debris. The damage to the base zone of the pier thus was substantial – even in the remaining part of the concrete. Therefore the ultimate condition at $\mu_{\Delta,prov} = 10$ should not be considered a stable state anymore, not even for the vertical load bearing mechanism. Under a real three dimensional dynamic excitation and without the lateral support at the top, the pier would have hardly been able to safely carry the vertical loading in this condition anymore.

i) Overview of Test Units at Various Loading Stages throughout the Experiments

In the following Fig. 5.10 through Fig. 5.16 all three test units are shown at different deformation states throughout the load history. Starting at $\mu_{\Delta,prov} = 2$, shown in Fig. 5.10, an overview of the piers is presented in the upper row of each figure. This way the condition of the individual test units at the same top displacement can be compared. In the middle row of each figure the corresponding measured hystereses up to the given peak displacement are shown indicating the influence of any damage on the load-deformation behavior of the piers. In the bottom row of each figure close-ups are presented showing the details of the damage developing throughout the load history. It should be noted that any displacement ductilities given in the pictures always refer to the provisional value of the nominal yield displacement of $\Delta_{y,prov} = 10.5$ mm, i.e. the given ductilities are also only the provisional values $\mu_{\Delta,prov}$ (see Section 5.2.4).

Fig. 5.10: Damage state and hystereses at a top displacement of $\Delta_{top} = 21$ mm
left: Test Unit VK1, center: Test Unit VK2, right: Test Unit VK3

Fig. 5.11: Damage state and hystereses at a top displacement of Δ*top* = 31.5 mm
left: Test Unit VK1, center: Test Unit VK2, right: Test Unit VK3

Fig. 5.12: Damage state and hystereses at a top displacement of Δ_top = 42 mm
left: Test Unit VK1, center: Test Unit VK2, right: Test Unit VK3

*Fig. 5.13: Damage state and hystereses at a top displacement of Δ$_{top}$ = 52.5 mm
left: Test Unit VK1, center: Test Unit VK2, right: Test Unit VK3*

Fig. 5.14: Damage state and hystereses at a top displacement of Δ_{top} = 63 mm
left: Test Unit VK1, center: Test Unit VK2

5.3 Test Results

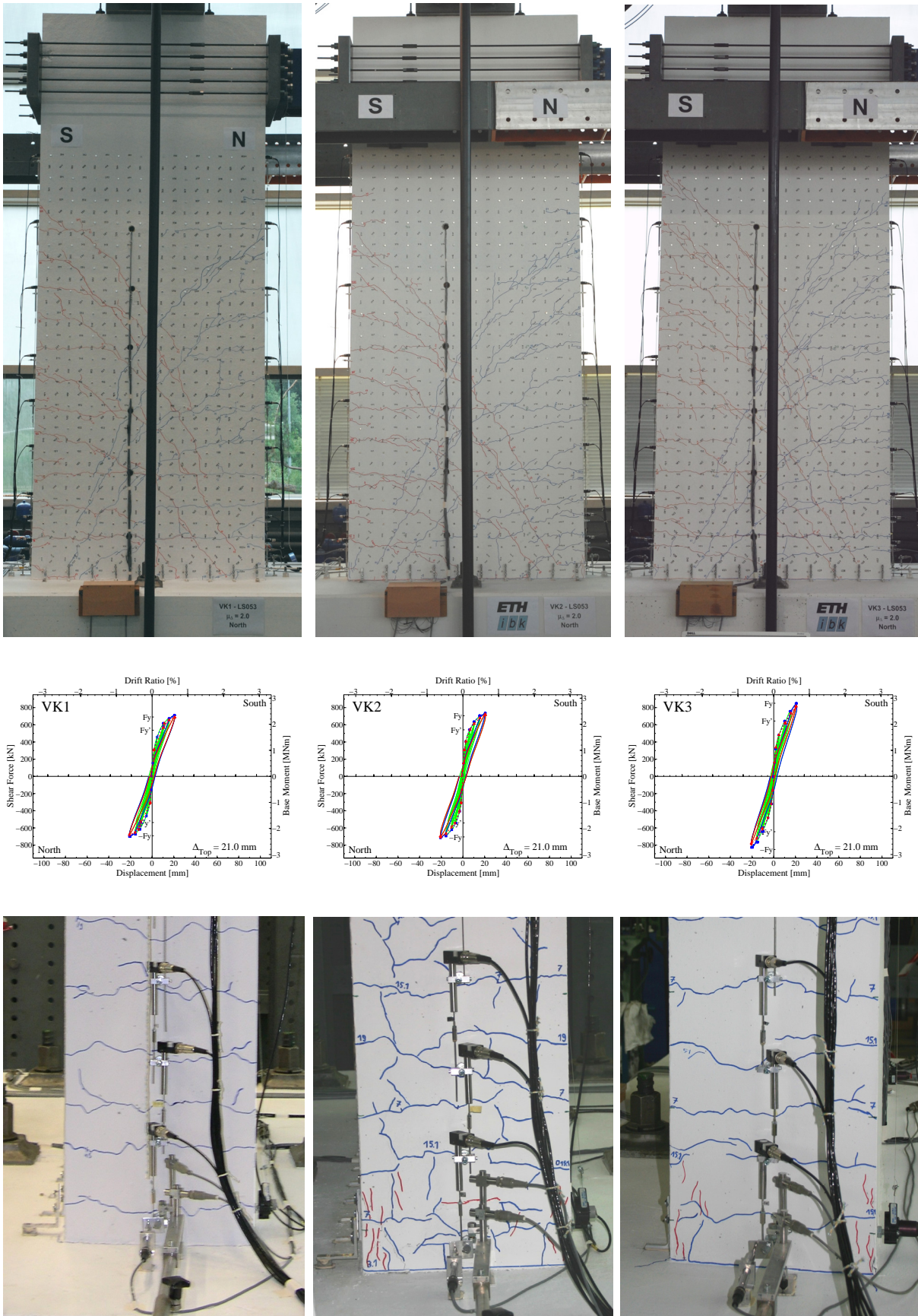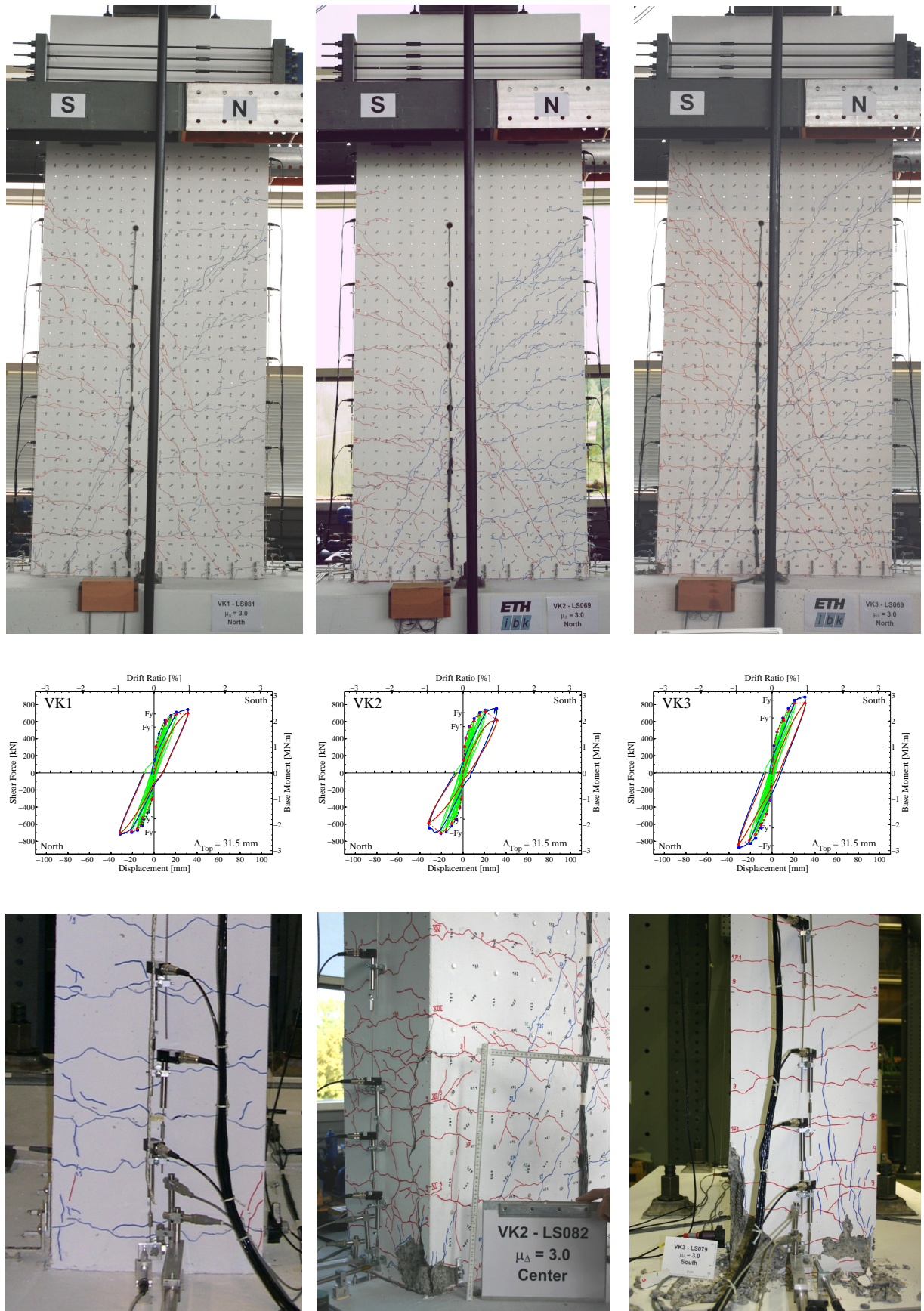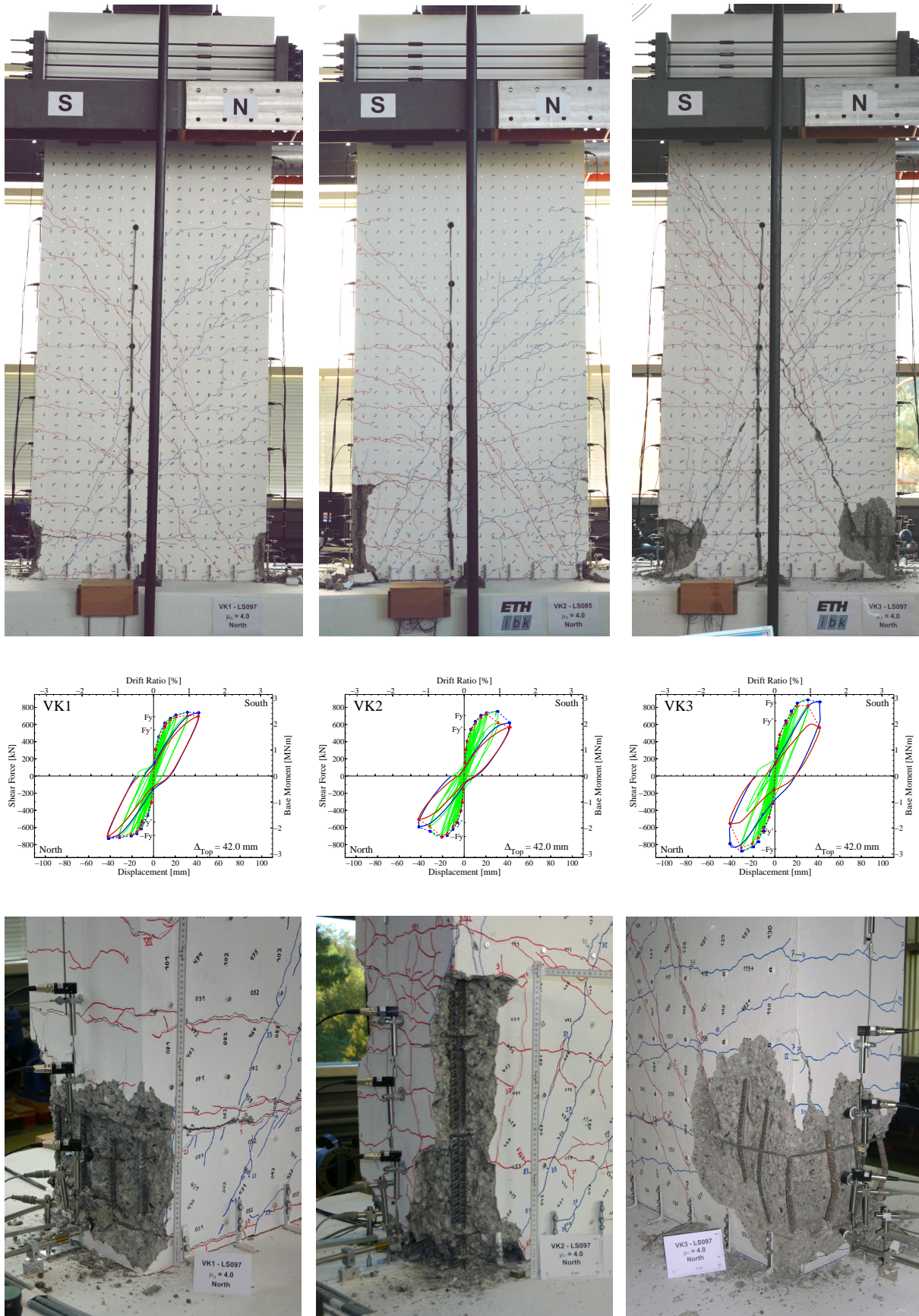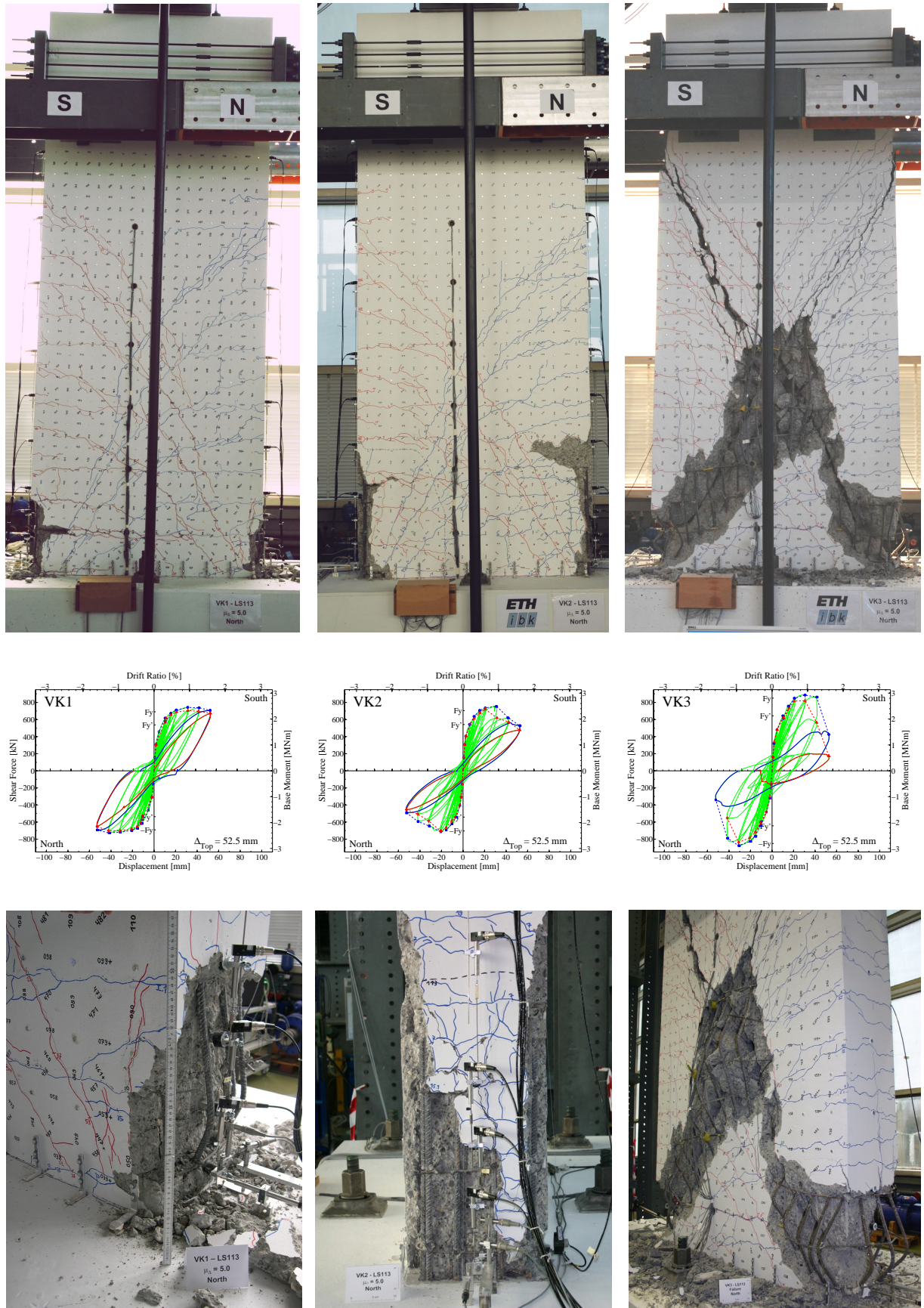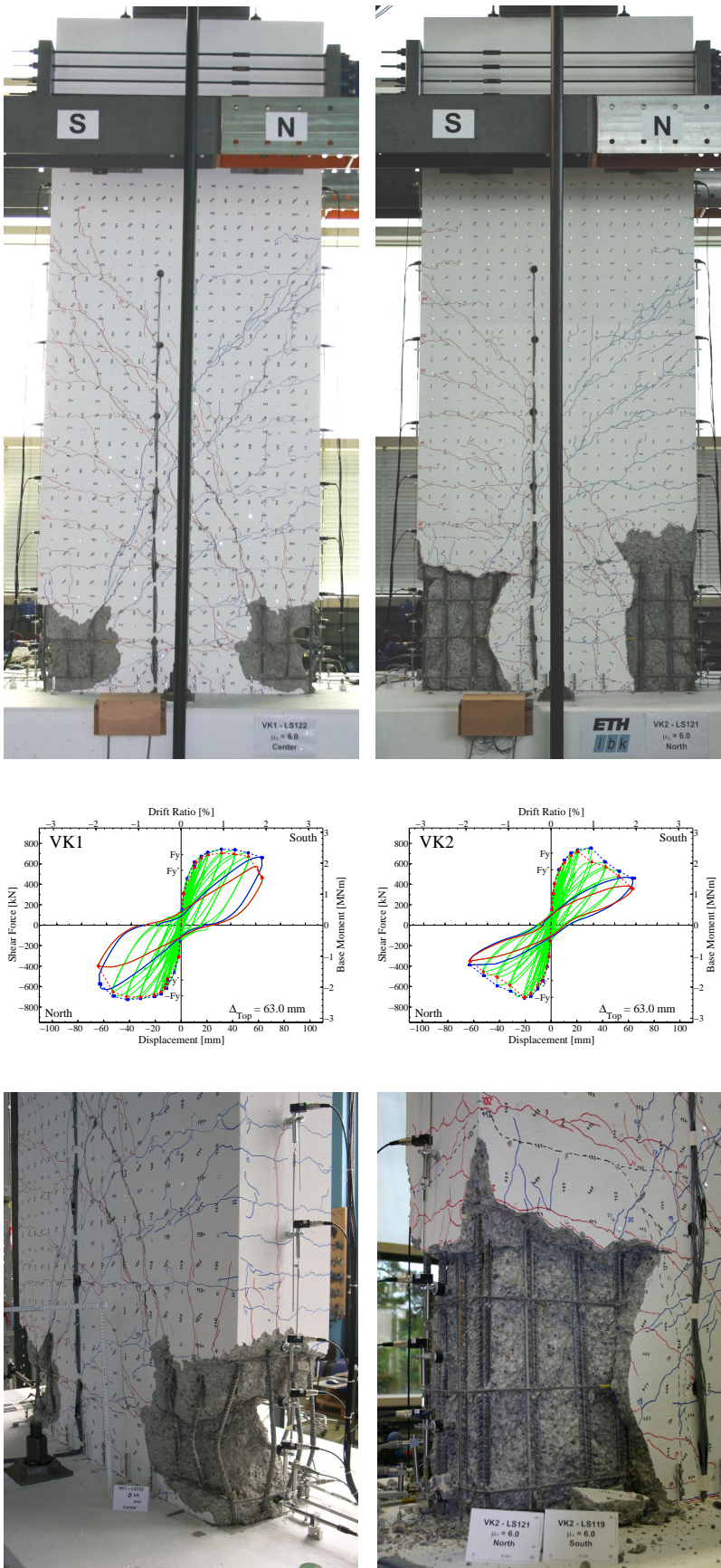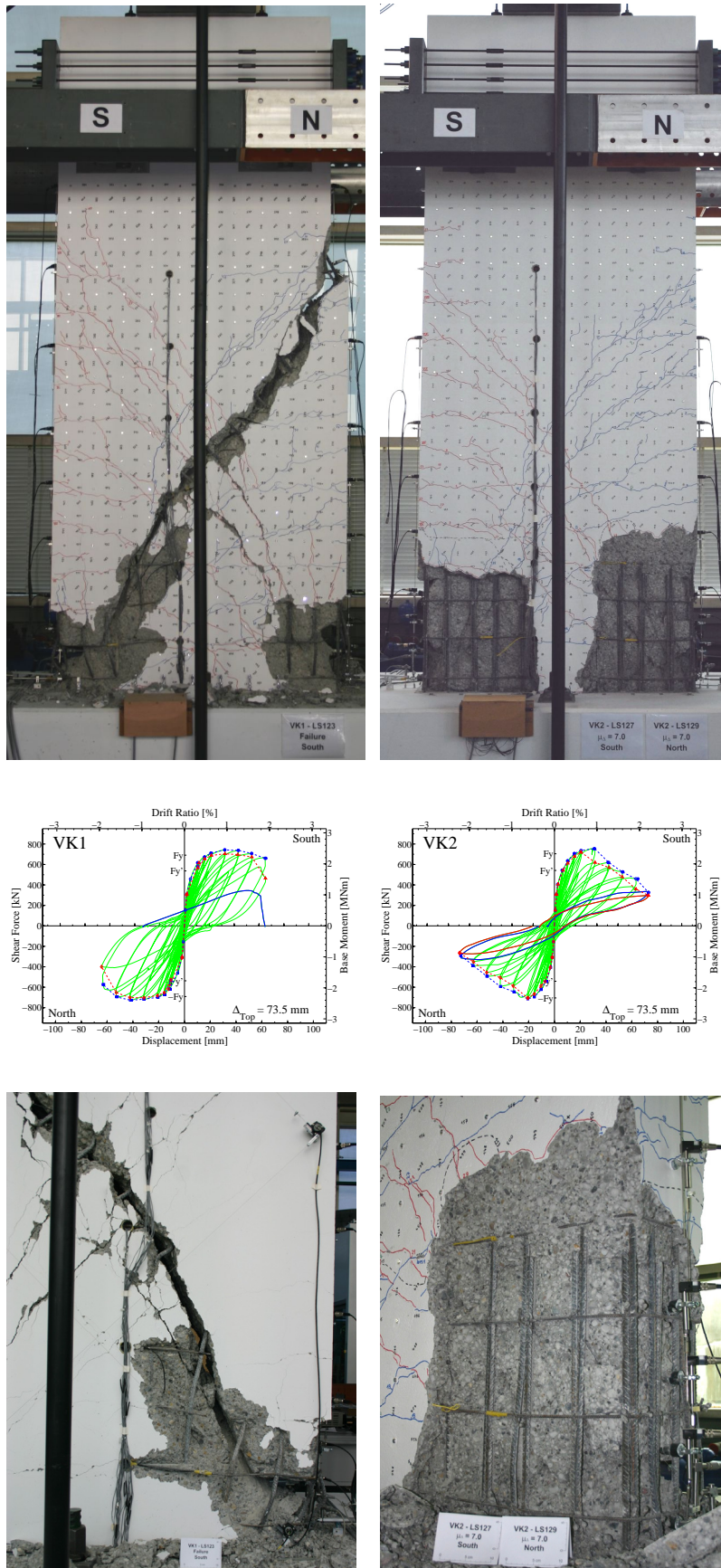Fig. 5.15: Damage state and hystereses at a top displacement of Δ_{top} = 73.5 mm
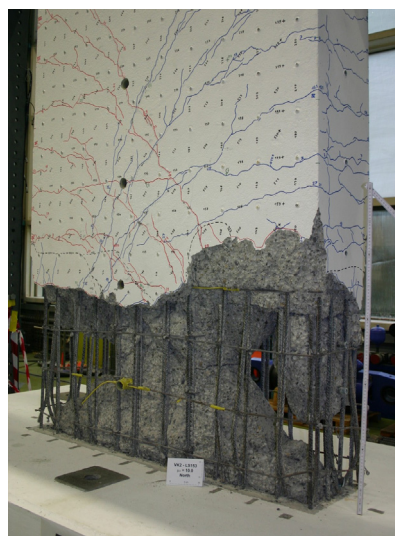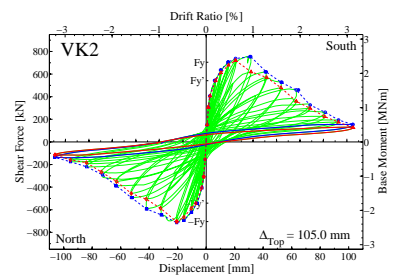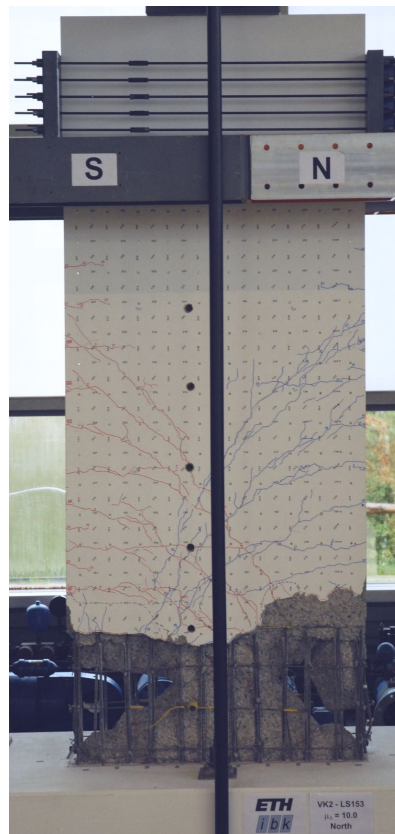left: Test Unit VK1, center: Test Unit VK2

Fig. 5.16: Damage state and hystereses at a top displacement of Δ_{top} = 105 mm
center: Test Unit VK2

j) Ductility Capacities of Test Units

In Section 5.2.4 it has been outlined that for the definition of the load steps in the inelastic range of the experiments a common *provisional nominal yield displacement* of $\Delta_{y,prov} = 10.5$ mm was used to define the corresponding *provisional displacement ductilities* $\mu_{\Delta,prov}$. As the real nominal displacements $\Delta_{y,VK1}$, $\Delta_{y,VK2}$, and $\Delta_{y,VK3}$ individually determined for the three test units differed from $\Delta_{y,prov}$ (see Tab. 5.8), the real displacement ductilities also differed from the provisional values $\mu_{\Delta,prov}$ used for the control of the experiments. An overview of the actual displacement ductilities $\mu_{\Delta,VK1}$, $\mu_{\Delta,VK2}$, and $\mu_{\Delta,VK3}$ corresponding to the various load steps is presented in Tab. 5.9. Based on these data it can be seen that Test Unit VK1 achieved a maximum displacement ductility at combined shear and axial load failure of $\mu_{\Delta,VK1} = 6.5$. The displacement ductility capacity of Test Unit VK3 at the same failure mode amounted to $\mu_{\Delta,VK3} = 3.7$. The test of VK2 was stopped at a displacement ductility of $\mu_{\Delta,VK2} = 12.8$ with hardly any horizontal force capacity left but still being able to carry the applied axial load.

	Nominal Yield Displacement			
	Provisional	Test Unit VK1	Test Unit VK2	Test Unit VK3
	$\Delta_{y,prov}$ [mm]	$\Delta_{y,VK1}$ [mm]	$\Delta_{y,VK2}$ [mm]	$\Delta_{y,VK3}$ [mm]
	10.5	9.6	8.2	14.1
Top Displacement	Displacement Ductility			
	Provisional	Test Unit VK1	Test Unit VK2	Test Unit VK3
Δ_{top} [mm]	$\mu_{\Delta,prov}$ [-]	$\mu_{\Delta,VK1}$ [-]	$\mu_{\Delta,VK2}$ [-]	$\mu_{\Delta,VK3}$ [-]
10.5	1	1.1	1.3	0.74
15.75	1.5	1.6	1.9	1.1
21	2	2.2	2.6	1.5
31.5	3	3.3	3.8	2.2
42	4	4.4	5.1	3.0
52.5	5	5.4	6.4	**3.7** [a]
63	6	**6.5** [a]	7.7	---
73.5	7	---	8.9	---
84	8	---	10.2	---
94.5	9	---	11.5	---
105	10	---	**12.8** [b]	---

[a] Combined shear and axial load failure of pier.
[b] End of experiment.

Tab. 5.9: Overview of ductility levels for Test Units VK1, VK2, and VK3 during the experiments

It should be noted that the achieved deformation capacities also depend on the definition of the failure criteria. For structural walls (in building structures) it is e.g. not uncommon to define failure as the point where the horizontal force capacity has dropped to (less than) 80% of the peak strength. In the case of Test Unit VK1 this criterion was achieved during the second excursion (to the north) of the first cycle to $\mu_{\Delta,prov} = 6$ (top displacement $\Delta_{Top} = 63$ mm, drift ratio $\delta = 1.91\%$) corresponding to a real displacement ductility of $\mu_{\Delta,VK1} = 6.5$. The final shear and axial load failure occurred at the same deformation level, but after the completion of two full cycles. In contrast, Test Unit VK3 reached the 80% strength limit in the second cycle to $\mu_{\Delta,prov} = 4$ (top displacement $\Delta_{Top} = 42$ mm, drift ratio

$\delta = 1.27\%$) corresponding to a real displacement ductility of $\mu_{\Delta, VK3} = 3.0$. The final shear and axial load failure thus occurred at one deformation step later than the 80% strength criterion. For Test Unit VK2 this definition of the acceptable degradation of the horizontal strength would result in a significant limitation of the deformation capacity. Here, the force capacity had already reduced to less than 80% of the peak strength during the second excursion (to the north) of the second cycle to $\mu_{\Delta, prov} = 3$ (top displacement $\Delta_{Top} = 31.5$ mm, drift ratio $\delta = 0.95\%$). Following this criterion, failure of Test Unit VK2 would thus be defined at a real displacement ductility of $\mu_{\Delta, VK2} = 3.8$.

In this context it should be mentioned that the achieved ductility capacities also depend on the particular way how the nominal yield displacements are defined. As discussed e.g. in [DWB99] and [PMT03], significant differences can exist between various definitions of the nominal yield displacement and subsequently between the corresponding definitions of displacement ductilities. Therefore, when comparing ductility capacities it is always important that they refer to equivalent definitions of the yield displacement (and the failure criteria).

5.3.2   Comparison between Prediction and Experimental Behavior

In this section the behavior observed and measured during the experiments is compared to the corresponding predictions presented in Section 5.2.3. At first, in Subsection *a* the load-deformation behavior is discussed. In Subsection *b* the predictions for the cyclic-inelastic shear strength are compared to the observed behavior, and Subsection *c* is dedicated to the cyclic-strength degradation due to lap-splice failure.

a) Load-Deformation Behavior

In Fig. 5.17 through Fig. 5.19 the deformation behavior of the three test units is depicted. In each case, on the left side the experimentally measured force-displacement backbone curves of the four half cycles are compared to the numerically predicted backbones from Section 5.2.3*a* (without consideration of strength degradation in the prediction for VK2). The numerically determined curves are drawn as solid lines up to a strain limit of $\varepsilon_{cu} = -0.005$ for the concrete in compression. For purely informative purposes they are further elongated as dotted lines up to a concrete strain of $\varepsilon_c = -0.008$. On the right side of the figures, the relative contribution of the various deformation components to the top displacement is shown in cumulative form. The following four contributions to the total top displacement are distinguished:

  (i)   Sliding motions at the pier base (i.e. in the construction joint between pier and foundation)
  (ii)   Shear deformations
  (iii)   Flexural deformations from opening of the base crack only
  (iv)   Flexural deformations above the base crack

All deformation components have been determined using the grid of Demec measurements (see Section 5.2.2) as they are more reliable, more accurate, and also have a higher geometric resolution than the hard-wired LVDT and string pot measurements. The high quality of the Demec measurements is also confirmed by the fact that the sum of the individual deformation components fits almost perfectly to the measured top displacement, as can be seen by the cumulative relative displacements reaching essentially 100% in Fig. 5.17 through Fig. 5.19. It should be noted that the flexural deformation from opening of the base crack (iii) consists of two sub-contributions. The first one is the strain penetration of the longitudinal reinforcement into the foundation block (i.e. pull-out of the bars from the foundation) and the second sub-contribution comes from reinforcement strains in the pier above the base. Both parts together result in the discrete base crack. Based on the existing measurement data, it is not possible to reliably determine the amount of individual contribution from these two parts to the base crack.

From the comparison between the numerically predicted and the experimentally measured backbone curves (left side of Fig. 5.17 through Fig. 5.19) it can be seen that the general shape of the load-deformation curves can be captured by the rather simple numerical plastic hinge model. In the elastic

5.3 Test Results

region the numerical predictions for Test Units VK1 and VK2 tend to underestimate the experimental stiffness to some extent. This is also confirmed by the comparison of the elastic stiffnesses k_0 presented in Tab. 5.10 which result from a bilinearized approximation of the backbone curves following the principles shown in Fig. 5.4.

Fig. 5.17: Deformation behavior of Test Unit VK1
left: Comparison between numerically predicted and experimentally measured backbone
right: Experimentally measured relative contribution of deformation components

Fig. 5.18: Deformation behavior of Test Unit VK2
left: Comparison between numerically predicted (without degradation) and experimentally measured backbone
right: Experimentally measured relative contribution of deformation components
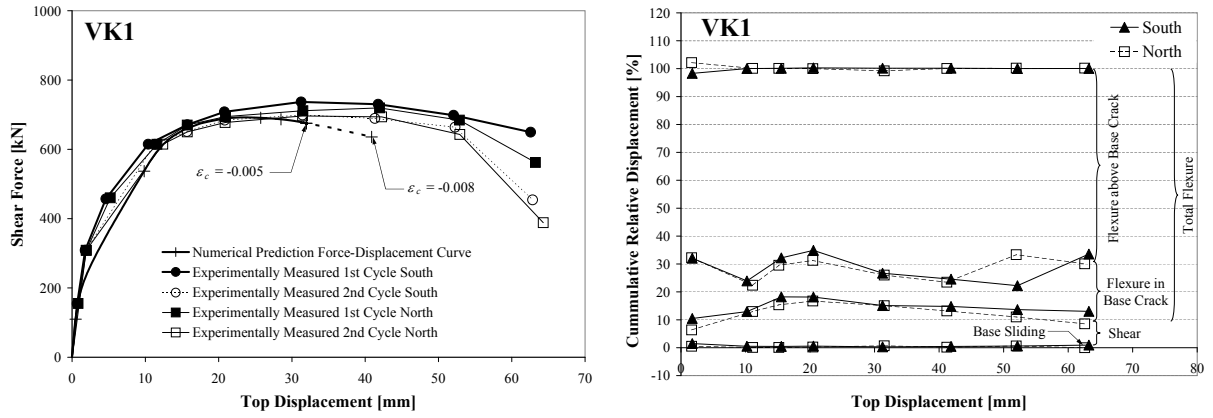

Fig. 5.19: Deformation behavior of Test Unit VK3
left: Comparison between numerically predicted and experimentally measured backbone
right: Experimentally measured relative contribution of deformation components
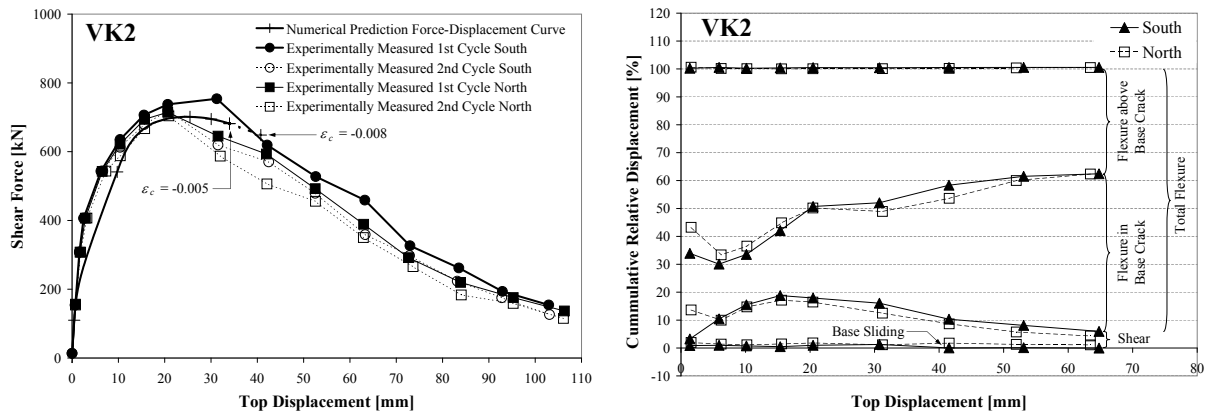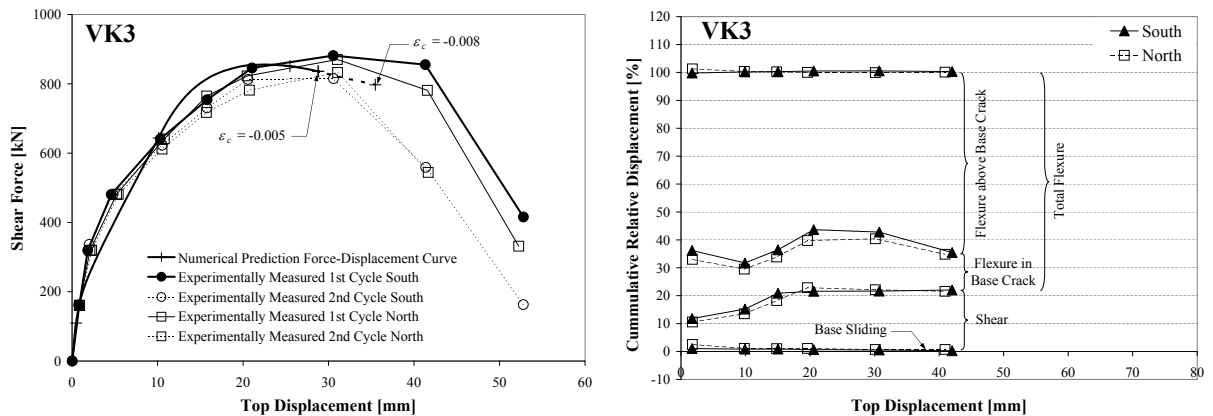
While the rather simple numerical model predicts first yield displacements Δ_y' being almost equal for all three test units, the experimentally determined values for Δ_y' differ significantly among the various test units (and from the numerical predictions). As a consequence, the elastic stiffnesses k_0 based on the numerical model are essentially proportional to the flexural strength of the cross-sections. However, the corresponding stiffnesses k_0 determined from the experimental results does not follow this trend. Instead, here Test Unit VK3 even has the lowest elastic stiffness of all test units despite its highest flexural strength. The difference between the measured stiffnesses of VK1 and VK2 (see Tab. 5.10) is largely related to the lap-splice at the base of VK2. The effectively double amount of longitudinal reinforcement along the splice length results in a stiffening of the tension chord at the base of the pier where the curvatures are most relevant for the flexural deformations. As this effect was not considered in the plastic hinge model, the numerically predicted values of k_0 for VK2 cannot reflect this difference compared to VK1.

			VK1	VK2	VK3
First yield load	F_y' [kN]	numerically computed	537	541	644
Top displacement at first yield load	Δ_y' [mm]	numerically computed	9.8	9.7	10.1
Elastic transverse stiffness	k_0 [MN/m]	numerically computed	55	56	64
Top displacement at first yield load	Δ_y' [mm]	experimentally determined 1st cycle average	7.5	6.3	10.7
Elastic transverse stiffness	k_0 [MN/m]	experimentally determined 1st cycle average	72	85	60

Tab. 5.10: Comparison between numerically computed and experimentally determined elastic stiffnesses k_0

Concerning the deformation behavior in the inelastic range, it can be seen from the comparisons in Fig. 5.17 and Fig. 5.19 (left) that the chosen plastic hinge model appears to result in conservative estimations of the flexural displacement capacity for Test Units VK1 and VK3. In both cases the numerical model together with the strain limit of ε_{cu} = -0.005 for the concrete in compression would have limited the allowable top displacement to levels being noticeably lower than those achieved in the experiments. In particular, it should be noted that the failure types observed in the tests of VK1 and VK3 were due to shear problems. Considering the flexural behavior alone, the piers might have sustained even larger deformations.

This underprediction of the observed flexural displacement capacity may to some extent be related to the rather conservative strain limit of ε_{cu} = -0.005 which does not go very far beyond the strains which are usually expected to cause concrete spalling [PSC96]. In fact, comparing the predicted displacement capacities presented in Tab. 5.6 to the corresponding damage observations discussed in Section 5.3.1, it can be seen that at these deformation levels the onset of concrete spalling was observed in the experiments. Therefore, the chosen strain limit of ε_{cu} = -0.005 could rather be interpreted as a damage control limit state instead of a real ultimate or survival limit state. However, it should be noted that, generally, the cyclic-inelastic behavior can become more critical if reinforcement buckling after spalling of the cover concrete results in subsequent fracture of the longitudinal bars. This phenomenon was not observed in neither of the three test units. Despite the occurrence of bar buckling, the flexural reinforcement did not fracture upon restraightening in subsequent tension. This behavior, which has influenced the flexural response of the piers after concrete spalling in a positive way, cannot be generalized.

Aside from any strain limits defined at the local level, the prediction of the top displacement at flexural failure also depends on the chosen value for the plastic hinge length L_{pl}. Its relevance for the

given problem is related to the fact that the plastic hinge length essentially couples the local deformations (i.e. the strains and curvatures) to the global deformations of the member (i.e. the top displacement). A higher value of L_{pl} thus results in a larger prediction for the top displacement capacity if the same local strain limits are adopted. A considerable number of different equations have been proposed in the literature for the estimation of L_{pl} (see e.g. [Hin02]) reflecting the existing uncertainty in its determination. The appropriate choice of the plastic hinge length based on an empirical equation should also consider the individual boundary conditions underlying the specific experiments used for the calibration of such equations. This can e.g. refer to the properties of the reinforcement steel or to the member geometry (see also discussion in Section 2.2.3).

The fact that the measured shear force kept increasing at displacement levels where the numerically predicted force-displacement curve already started decreasing can also be related to uncertainties in the estimation of the plastic hinge length, possibly combined with the neglect of strain hardening in the numerical model of the reinforcement. In this context it is also noteworthy that the maximum strength achieved by Test Unit VK2 was about 2.3% higher than that of VK1 (in both cases at a top displacement of $\Delta_{Top} = 31.5$ mm) despite the same amount and type of longitudinal reinforcement in the base section. The difference was even more pronounced at the preceding load step to a top displacement of $\Delta_{Top} = 21$ mm where the shear force of VK2 exceeded that of VK1 by 4.2%. These differences are likely to be related to the lap-splice in the base region of VK2 which results in a significant reduction of the effective plastic hinge length. As a consequence, for the same top displacement VK2 required higher base curvatures – and thus also larger reinforcement strains – than Test Unit VK1. It is therefore likely that VK2 entered into the strain hardening range of the reinforcement, while VK1 may have remained in the yield plateau.

From the relative contribution of the various deformation components to the total displacements of the piers, shown on the right side of Fig. 5.17 through Fig. 5.19, it can be seen that the deformation behavior of all three test units was primarily flexural throughout the entire loading range covered by the Demec measurements. The influence of sliding motions in the base crack of the pier was essentially negligible in all cases and hardly exceeded the range of the measuring tolerance. The highest contribution from shear deformations was observed for Test Unit VK3 reaching up to 22% of the top displacement, while the peak relative contribution of shear deformations in VK1 and VK2 only amounted to 18%. This is generally inline with the higher shear demand in the case to VK3 due to its higher flexural strength. The remaining approximately 80-90% of the total displacements were contributed by flexural deformations in all test units and at all loading levels.

It is noteworthy that the absolute shear displacements kept increasing in the inelastic range although the shear force did not increase further during this loading phase[40]. In the case of Test Unit VK3 the relative contribution of the shear deformations to the total displacement remained almost constant in a range of 20-22% throughout the inelastic part of the load history (see right side of Fig. 5.19). Although in Test Unit VK1 the relative contribution of shear deformations decreased slightly at larger displacements, it still remained rather stable in a range of 10-15% (see right side of Fig. 5.17). A similar behavior has already been observed by Dazio *et al.* [DBB09] and Beyer *et al.* [BDP08a] in previous static-cyclic tests on structural RC walls. The observation that the relative contribution from shear deformations remains rather constant in the inelastic range shows that the shear carrying mechanism tends to soften in a similar way as the flexural mechanism under increasing inelastic deformations.

At the same time, the behavior of Test Unit VK2 shows that the absolute shear force also has a strong influence on the shear deformations in the inelastic range. In parallel with the degradation of the flexural strength – representing the shear demand – the relative contribution of shear deformations also decreases in VK2 (see right side of Fig. 5.18). At a later stage, even the absolute shear deformations decrease. In a less pronounced way the same phenomenon can also be discovered in the last cycle to $\Delta_{Top} = 63$ mm of Test Unit VK1. During the first excursion to the south (1st cycle at $\Delta_{Top} = 63$ mm) the shear force dropped only by 7% compared to the corresponding excursion of the previous loading

---

[40] The behavior of Test Unit VK2 at large deformations represents an exception. Due to the severe strength degradation related to the lap-splice failure, the absolute shear displacements in VK2 started decreasing again for top displacements exceeding 52.5 mm.

level (1st cycle at $\Delta_{Top} = 52.5$ mm). In parallel the relative contribution of the shear deformations decreased from 13.1% to 12.1% of the total displacements. On the other hand, during the subsequent north excursion (1st cycle at $\Delta_{Top} = 63$ mm) the shear force dropped by 18% compared to the corresponding north excursion of the 1st cycle at $\Delta_{Top} = 52.5$ mm. Here, the relative contribution of the shear deformations decreased from 10.4% to 8.6%. In both cases – the north and the south excursion – the decrease of relative shear deformations was almost proportional to the reduction of the shear force.

From this behavior it can be concluded that the observation of rather constant relative contributions from the shear deformations to the total top displacement in the inelastic range appears to be limited to cases where the shear force remains rather constant without significant strength degradation. In degrading systems the shear demand enters into the description of the behavior as an additional parameter.

Concerning the flexural behavior, it can be seen on the right sides of Fig. 5.17 and Fig. 5.19 that for Test Units VK1 and VK3 the relative contribution from opening of the base crack also remained rather stable within a range of 10-20% during the inelastic loading phase. The flexural behavior of VK2 differed noticeably from that of the other two test units (see right side of Fig. 5.18). The relative contribution from the base crack already increased from approximately 20% to 35% during the inelastic loading before the failure of the lap-splices and grew further during the strength degradation up to almost 60% at a top displacement of $\Delta_{Top} = 63$ mm. This behavior complies with the general observations outlined in Section 5.3.1. As long as the lap-splices are intact, the increased reinforcement along their length results in a strong reduction of the effective plastic hinge length. Consequently, the inelastic deformations tend to concentrate in the base crack while only very small flexural crack widths develop over the height of the lap-splices. During and after the failure of the splices, large part of the flexural deformations concentrate in one crack just above them and in the base crack below the lap-splices (see Section 5.3.1).

b) Shear Capacity

In Fig. 5.20 the ductility dependent shear capacity models presented in Section 5.2.3b are compared to the measured force-displacement backbones of Test Units VK1 and VK3. This comparison is conceptually similar to that shown in Fig. 5.6 for the numerical prediction of the backbones for VK1 and VK3. In order to be consistent with the experimentally measured demand curve (i.e. the force-displacement backbone), in Fig. 5.20 the shear capacity curves have also been computed based on experimentally determined displacement ductilities, i.e. they were calculated using the measured average nominal yield displacements Δ_y given in Tab. 5.8 and correspond to the real displacement ductilities $\mu_{\Delta,VK1}$ and $\mu_{\Delta,VK3}$ given in Tab. 5.9. In Fig. 5.20 the shear capacity model by Kowalsky and Priestley [KP00] was only included in its displacement ductility dependent version, whereas the formulation as a function of curvature ductility was not considered because curvature ductilities cannot be determined uniquely from the experimental data.

This comparison in Fig. 5.20 shows that, using the measured force-displacement curve, the majority of the shear strength models would have predicted an earlier occurrence of shear failure than observed in both experiments. For the case of Test Unit VK1, the displacement ductility dependent version of the shear capacity model by Kowalsky and Priestley [KP00] almost contacts the demand curve exactly at the point of failure. For Test Unit VK3 the same model overpredicts the shear strength at the point of failure by some 100 kN. In this context it should be mentioned that in the numerical prediction presented in Fig. 5.6 the curvature ductility dependent version of this model gave a somewhat lower shear strength for this configuration which would come closer to the observed behavior during the experiment.

At the same time, the curves in Fig. 5.20 show how difficult it is conceptually to achieve a reliable prediction of the reduced displacement capacity at inelastic shear failure. The fact that most of the shear capacity models suggest a rather low gradient of the decreasing strength with ductility would result in a close to tangential intersection with the inelastic part of the force-displacement curve at the point of failure. This creates a large sensitivity to uncertainties in the prediction of the shear strength. Only marginal variations of the shear capacity can already result in large differences of the

displacement at failure. Further uncertainties result from the fact that no strict and unique definition for the determination of the nominal yield displacement exists which is the basis of the displacement ductility entering into the shear capacity models as a parameter.
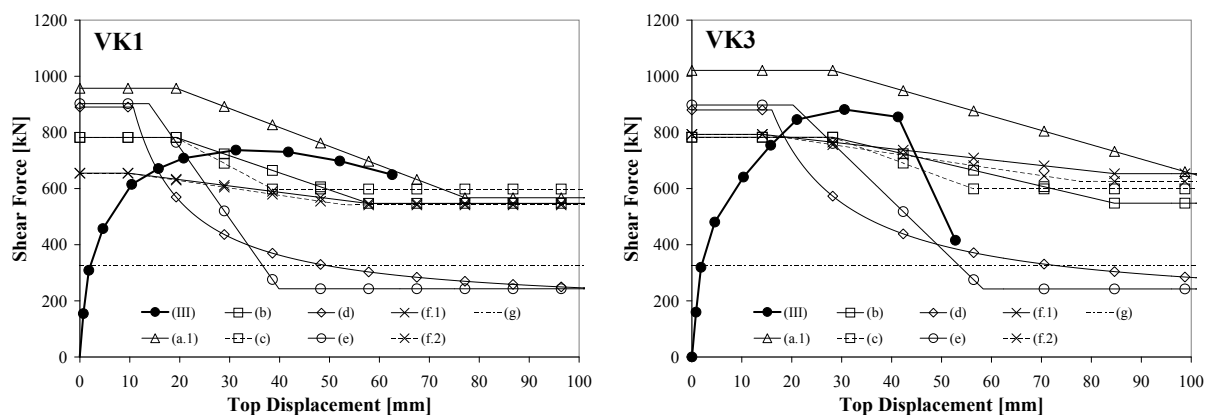
(III)   Measured force-displacement backbone for south excursion of the 1st cycles (see Fig. 5.17 and Fig. 5.19)

(a.1)   Cyclic-inelastic shear capacity of RC columns according to [KP00] as a function of displacement ductility

(b)   Cyclic-inelastic shear capacity of RC columns according to [SM04] as a function of displacement ductility

(c)   Cyclic-inelastic shear capacity of RC frame columns according to [FEMA356] as a function of displacement ductility

(d)   Cyclic-inelastic shear capacity of RC bridge columns according to [AM92] as a function of displacement ductility

(e)   Cyclic-inelastic shear capacity of RC bridge columns according to [Cal06] as a function of displacement ductility

(f.1)   Cyclic-inelastic shear capacity of RC members according to [BRF04], equation (8) as a function of displacement ductility; also adopted in [EC8-3]

(f.2)   Cyclic-inelastic shear capacity of RC members according to [BRF04], equation (7) as a function of displacement ductility

(g)   Static monotonic shear capacity of RC members according to [SIA262], equation (37) independent of ductility; using the minimum inclination of the compression struts being $\alpha = 25°$

Fig. 5.20: Comparison between ductility dependent cyclic-inelastic shear capacity models and experimentally measured force-displacement relationships for Test Units VK1 (left) and VK3 (right)

c) Strength Degradation due to Lap-Splice Failure

In Fig. 5.21 the prediction of the degrading load-displacement backbone due to lap-splice failure (presented in Fig. 5.7) is compared to the measured response of Test Unit VK2 (see Fig. 5.18). It should be noted that the prediction is purely numerically based and does not contain any input from the experimental results. In particular, this means that both the strain limit for the onset of degradation as well as the curvature ductility at which the predicted residual strength is reached (thus defining the gradient of the degradation) were determined based on the numerical plastic hinge approach as outlined in Section 5.2.3c. Determining these characteristic local deformations for the degradation model from the experimental measurements would result in a modified prediction. However, the determination of the local strains and the curvature ductilities from the experimental data is not necessarily unique, so that the application of the model would still contain some uncertainties concerning its parameters. Therefore, only the purely numerical version of the prediction is included in Fig. 5.21 representing exactly the model as originally proposed in [PSC96].

It can be seen that the prediction qualitatively fits the experimental behavior in a reasonable way. However, quantitatively a noticeable difference between the model prediction and the measured response of Test Unit VK2 exists. This refers primarily to the displacement defining the onset of degradation as well as to the gradient of the degrading backbone. From this comparison it is not possible to determine whether the differences result from the definition of the theoretical deformation limits in the degradation model or from inaccuracies in determining them by means of the numerical plastic hinge approach. A different value for the plastic hinge length would e.g. also have influenced the predicted force-displacement backbone.
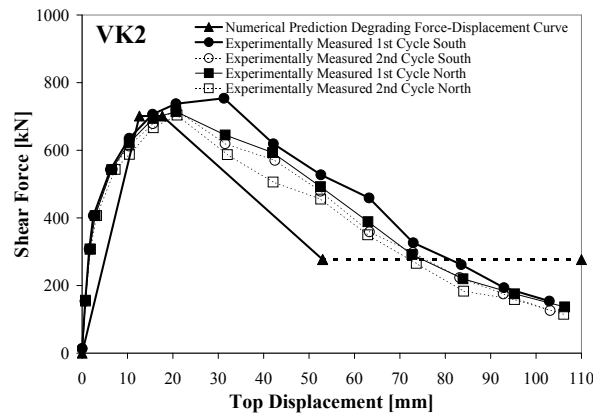
Fig. 5.21: Comparison between numerically predicted and experimentally measured force-displacement relationships for Test Units VK2 including cyclic strength degradation due to lap-splice failure

At the same time, it is important to note that the 1st excursion to the south of the 1st cycle consistently resulted in higher flexural strengths than the following three excursions of the two cycles at each deformation level during the degradation. This behavior is conceptually consistent with the reasoning for the cyclic-inelastic lap-splice failure according to [PSC96]. As outlined in Section 5.2.3c, it is assumed that at first the concrete surrounding a lap-splice is damaged due to excessive compression strains. The actual failure of the splice then occurs in the subsequent excursion to the other direction when the lap-splice is loaded by tension forces that cannot be transferred by the previously damaged concrete anymore. Following this notion, a degradation of flexural strength due to lap-splice failure should not occur during the first excursion to a new (i.e. larger) deformation level, but rather develops in the following excursions to the same top displacement. This behavior is confirmed reasonably well by the four experimental backbone curves of Test Unit VK2 shown in Fig. 5.21. In almost all cases, the flexural strength during the first excursion to a new displacement level was close to that of the last excursion during the preceding deformation level, so that no real degradation was observed at this transition. The loss of strength always occurred during the following excursions to the same deformation level, which complies with the conceptual background of the numerical degradation model by Priestley *et al.* [PSC96].

Another conclusion that can be drawn from the comparison between numerically predicted and measured force-displacement response of Test Unit VK2 is that the experimental behavior does not confirm the assumed convergence towards a (stable) residual flexural strength at large displacements. Although some flexural strength resulting from eccentricity of the axial load exists even after any contribution from the flexural reinforcement has ceased, this resistance keeps degrading with increasing deformations. The reduction of the maximum possible eccentricity due to loss of concrete in the compression zones results in the continuous development towards an effective concrete hinge in the center of the pier base. Therefore the assumption of a backbone further approaching zero flexural strength after failure of all lap-splices – as underlying the calibrated models depicted in Fig. 4.70 and Fig. 4.72 – appears more appropriate for the description of this degradation type at large displacements. On the other hand, it is questionable whether this deformation range should still be used for the seismic resistance as the pier is not expected to perform reliably with this extent of damage.

At lower deformation levels, the model from [PSC96] resulted in a rather conservative prediction of the degrading behavior itself. This means that it predicted an earlier and faster loss of strength with increasing top displacement than observed in the experiment. However, it should be kept in mind that this underprediction of the flexural resistance also causes an underestimation of the shear demand in the inelastic range. Therefore, the numerical prediction should not be considered as conservative in every aspect. Instead, it might be worthwhile considering if a second model prediction aiming at representing an upper bound estimation of the flexural strength would be necessary for the assessment concerning the potential for shear critical behavior.

5.3 Test Results

This distinction does not only apply to the prediction model, but also to the measured experimental response. For the flexural response itself, the lower backbone curve measured during the second excursion (to the north) of the second cycles (see Fig. 5.21) may be more relevant because the higher curves during earlier excursions do not represent stable flexural behavior during several inelastic cycles. It should be noted that this lower boundary of the experimental response is approximated better by the numerical prediction for VK2 than the higher curves during previous excursions. On the other hand, for the assessment of the shear strength the upper backbone curve measured during the first excursion (to the south) of the first cycles governs as it represents the highest shear demand.

Therefore, in Fig. 5.22 this upper boundary for the experimentally measured force-displacement backbone of Test Unit VK2 is compared to the various ductility dependent shear strength models already discussed in Sections 5.2.3*c* and 5.3.2*b*. As in the case of VK1 and VK3 presented in Fig. 5.20, the curvature ductility dependent formulation of the model by Kowalsky and Priestley [KP00] is not included in the comparison for VK2 and the displacement ductilities for all other shear strength models in Fig. 5.22 are related to the experimentally determined nominal yield displacement of VK2 according to Tab. 5.8, i.e. they correspond to the real displacement ductilities $\mu_{\Delta,VK2}$ summarized in Tab. 5.9.
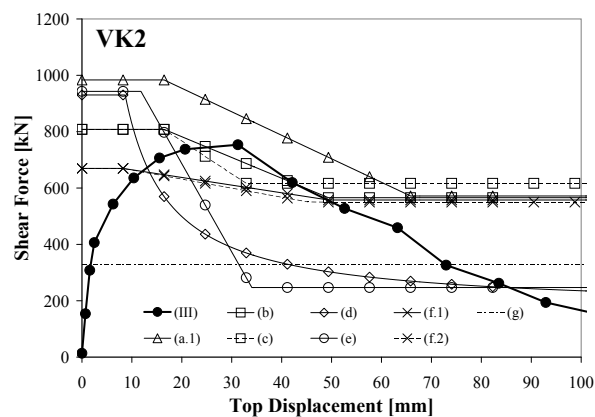
(III)   Measured force-displacement backbone for south excursion of the 1st cycles (see Fig. 5.18)
(a.1)   Cyclic-inelastic shear capacity of RC columns according to [KP00] as a function of displacement ductility
(b)   Cyclic-inelastic shear capacity of RC columns according to [SM04] as a function of displacement ductility
(c)   Cyclic-inelastic shear capacity of RC frame columns according to [FEMA356] as a function of displacement ductility
(d)   Cyclic-inelastic shear capacity of RC bridge columns according to [AM92] as a function of displacement ductility
(e)   Cyclic-inelastic shear capacity of RC bridge columns according to [Cal06] as a function of displacement ductility
(f.1)   Cyclic-inelastic shear capacity of RC members according to [BRF04], equation (8) as a function of displacement ductility; also adopted in [EC8-3]
(f.2)   Cyclic-inelastic shear capacity of RC members according to [BRF04], equation (7) as a function of displacement ductility
(g)   Static monotonic shear capacity of RC members according to [SIA262], equation (37) independent of ductility; using the minimum inclination of the compression struts being $\alpha = 25°$

Fig. 5.22: Comparison between ductility dependent cyclic-inelastic shear capacity models and experimentally measured force-displacement relationship for Test Unit VK2

The curves presented in Fig. 5.22 show that – in contrast to the observed experimental response of VK2 without shear failure – the majority of the shear strength models would have predicted a shear failure at rather small displacements when compared to the measured force-displacement backbone. This assessment result differs noticeably from that based on the comparison with the numerically predicted degrading backbone curve shown in Fig. 5.8. In the purely numerical prediction only the shear strength model according to [SIA262] and the two models by Biskinis *et al.* [BRF04] suggested a clear shear failure occurring in the elastic range. The model by Aschheim and Moehle [AM92] predicted a degradation of the shear strength being almost tangential to the degradation of the flexural strength with a slight intersection in the degrading branch of the numerical force-displacement curve and the Caltrans model [Cal06] suggested a shear failure close to the point where the predicted

residual moment capacity is achieved. The shear capacity curves according to the other models did not intersect with the numerical force-displacement backbone in Fig. 5.8.

The different conclusions resulting from Fig. 5.8 and Fig. 5.22 are related on one hand to the noticeable difference between the numerical prediction of the degrading force-displacement curve and the upper boundary experimental backbone measured during the 1st excursion of the 1st cycles (see Fig. 5.21). On the other hand, the difference between the numerically predicted and the experimentally determined nominal yield displacement also influences the displacement ductilities entering into the various shear strength models. The smaller experimental nominal yield displacement results in a higher gradient of the shear strength degradation in Fig. 5.22. The combination of these two effects gives a more shear critical impression for Test Unit VK2 in Fig. 5.22.

The only shear capacity model that does not predict a shear failure when compared to the measured force-displacement response for VK2 (see Fig. 5.22) is the one by Kowalsky and Priestley [KP00] (in its displacement ductility dependent formulation). At onset of the flexural degradation it gives a shear strength being about 100 kN higher than the corresponding demand. From then on the gradient of the decreasing shear strength is rather similar to that of the degrading flexural response so that the absolute margin between shear demand and capacity roughly remains constant. Nevertheless, even based on this model the safety of Test Unit VK2 against inelastic shear failure was not very large. For example, a slightly lower gradient of the flexural strength during degradation could have brought the curves representing shear demand and capacity closer together. For a new structure following capacity design principles and considering potential flexural over-strength the provided safety margin against shear failure in Test Unit VK2 would hardly be considered acceptable.

5.4 Discussion of the Experimental Results

The three test units of the experimental campaign generally performed in a similar way as described by the various predictive models presented in Section 5.2.3. It could be seen that Test Units VK1 and VK3 were indeed shear critical and that a shear failure can occur in the inelastic deformation range although the shear demand does not increase anymore in this loading phase. This means that the shear capacity degrades with increasing inelastic deformations as suggested by the ductility dependent shear strength models included in Fig. 5.6. From the test on VK2 it can also be concluded that the flexural strength degradation related to failure of lap-splices in the plastic hinge region develops in a conceptually similar way as predicted by the model by Priestley *et al.* [PSC96]. It was further observed that an interaction between lap-splice failure and potentially shear critical behavior can occur. The fact that Test Unit VK2 did not fail in shear although VK1 having the same properties aside from the absence of the lap-splice experienced a shear failure shows that the theoretical situation depicted in Fig. 5.8 can occur in real practical cases as well. If the shear demand – being related to the flexural strength – degrades faster with inelastic deformations than the shear capacity, a shear failure can be prevented by the failing lap-splices.

As a consequence, the various prediction models discussed in Section 5.2.3 are confirmed qualitatively by the results from the test campaign. On the other hand, concerning the quantitative accuracy of the predictions it has been shown in Section 5.3.2 that considerable uncertainties still exist. These uncertainties can be found on all levels of the predictions, i.e. the inelastic flexural load-deformation behavior (e.g. yield displacement, plastic hinge length), the inelastic shear strength, and the flexural strength degradation due to lap-splice failure. As the estimation of the displacement at potential inelastic shear failure is very sensitive to the uncertainties in the prediction of the deformation dependent shear strength, it is hardly possible at the current state to a reliably estimate the displacement capacity related to this failure mechanism.

If such a ductility dependent shear strength model featuring uncertainties is applied on an also uncertain prediction of the degrading flexural response of a pier with lap-splice, the result concerning occurrence of and displacement at a potential shear failure may become even less reliable. Although it has been found in the case of Test Unit VK2 that the flexural degradation prevented a shear failure, this observation should not simply be generalized. It cannot be ruled out that other configurations might yield a significantly different behavior. For example, a test on a model of a squat bridge pier with rectangular hollow cross-section and lap-splices at the base by Pinto *et al.* [PMT03] did not show any flexural strength degradation because the splices did not experience bond failure. Instead, the longitudinal reinforcement fractured at the base as a result of preceding bar buckling and pronounced concentration of inelastic strains below the lap-splice.

In another study, Lynn *et al.* [Lyn+96] tested RC frame columns subjected to double-bending featuring short lap-splices ($l_s = 20\, d_{bl}$) only at the column bases. In these static-cyclic tests they observed flexural strength degradation due to lap-splice failure. However, in contrast to the behavior of Test Unit VK2, the columns by Lynn *et al.* [Lyn+96] nevertheless experienced shear failures during the inelastically degrading response phase and subsequently also lost their axial load bearing capacity. It appears likely that, to some extent, this differing behavior was related to the double-bending and especially to the fact that the upper plastic hinge – due to the absence of lap-splices – did not experience any flexural strength degradation. Consequently, the shear demand in these double-bending columns did not degrade as strongly as it would have degraded in a single-bending cantilever column. This phenomenon may also have relevance for bridge piers being subjected to limited double-bending due to higher mode torsional superstructure response or torsional restraint from the superstructure (see Section 3.4.1 and 3.4.3).

In this context it should also be kept in mind that the splice length in Test Unit VK2 was chosen to rather represent a lower boundary of what would be considered as representative for older Swiss bridge piers. Longer lap-splices or hooks at the ends of the spliced bars have also been common in older bridges designed according to previous code generations. Such detailing alternatives have not been considered in the test campaign. It cannot be ruled out that they would influence the inelastic flexural behavior at the pier base in a sense that strength degradation occurs at a later stage or with a lower gradient. This different behavior could also influence the interaction with the ductility

dependent shear capacity, possibly causing a shear failure despite the flexural degradation. The mentioned experimental results by other researchers and the above theoretical considerations indicate that it should not be relied on a generalization assuming that a lap-splice failure in the plastic hinge region automatically prevents an inelastic shear failure.

At the same time, the observations during the test of VK2 also show how sensitive the force transfer within a lap-splice reacts to the bond conditions and to the local tension strength of the surrounding cover concrete (see Section 5.3.1*e*). It is known that the position and the direction of the reinforcement bars during pouring of concrete have a significant influence on the bond conditions. This effect as well as the sensitivity of the concrete tension strength at the surface to the curing conditions were clearly noticeable from the different development of lap-splice failure between the two sides of VK2. At the backside of the pier, where the better conditions were present, the lap-splice failure progressed significantly slower than on the front side which was on top during pouring of concrete. This sensitivity can introduce additional uncertainties to the degrading behavior. For bridge piers having been cast in-situ it can be expected that the bond conditions for the vertical reinforcement bars and the tension strength of the surrounding cover concrete should be rather good. In this case, the flexural degradation could be expected to develop somewhat slower than in the test of VK2, where only one side featured comparably good conditions for the lap-splices.

Concerning the rather positive flexural behavior of Test Units VK1 and VK3 up to the occurrence of the final shear failure, the buckling behavior of the longitudinal reinforcement after concrete spalling plays an important role. Buckling of the longitudinal reinforcement in the plastic hinge region is commonly considered critical because it has been observed in various previous tests that the bars can fracture under subsequent tension forces in the following half-cycle (see e.g. [DWB99]). Therefore, in the ductile design of new structures it is intended to prevent the buckling of the longitudinal reinforcement by means of closely spaced hoops in the critical regions. The transverse reinforcement in Test Units VK1 and VK3 – representing the properties of older existing piers not designed for ductile behavior – was not detailed to provide significant restraint against buckling of the longitudinal reinforcement. Especially the large hoop spacing of $s = 200$ mm (equivalent to 400 mm on the full-scale prototype level) allowed an almost free buckling of the bars.

However, despite the resulting ineffectiveness of the buckled bars in compression they did not fracture upon restraightening under tension in subsequent half-cycles. As a consequence, neither in VK1 nor in VK3 any longitudinal bar fracture was observed during the entire load histories. The large hoop spacing, which on one hand facilitated an early occurrence of buckling, on the other hand resulted in rather low curvatures in the buckled bars as the deformations were distributed over a considerable length. In those cases where bar fracture had been observed subsequent to buckling in previous tests, the failure was related to the large inelastic strains developing in the strongly curved buckling shape. Due to the absence of these excessive strains during buckling, the bars of Test Units VK1 and VK3 could always restraighten again and still sustain sufficient inelastic deformations in tension. Therefore, the large hoop spacing did not only cause an early onset of bar buckling, but also aided in limiting its negative effects on the inelastic flexural response of the piers.

Although the development towards the shear failure differed to some extent between Test Units VK1 and VK3, the final step of the two failure mechanisms showed noteworthy parallels. In both cases the ultimate failure occurred at a point where the extent of damage to the compression zones of the two piers was very similar (see Fig. 5.13 right and Fig. 5.15 left). The diagonal failure cracks of both piers ended in these heavily damaged compression zones and the combined shear and axial load failures were the result of a sliding motion along these cracks. The failure thus consisted of the upper parts of the piers being pushed down diagonally into the region where previously the concrete compression zones had been located. The damage to the compression zone thus triggered the shear failure as the lost concrete in this region could not provide any resistance against the observed diagonal motion anymore.

The load carrying mechanism underlying this behavior can be interpreted as follows. During earlier load steps the less damaged concrete compression zone represented the support for the diagonal compression strut carrying the shear force down to the pier base. Due to the squatness of the test units, part of this strut is coming directly from the point where the horizontal load is applied at the top, while another part is related to a strut-and-tie mechanism including the hoops as ties. As both mechanisms

involve a diagonal strut coming down to the concrete compression zone at the base, the bearing capacity of the support for the strut at this point is crucial for the shear resistance of the pier. Once the concrete in this region is damaged too much, this support for the strut is missing and the mechanism that had provided the shear strength so far cannot function anymore.

As an alternative mechanism, the hoops now would have to transfer large part of the shear force over the diagonal crack into the lower part of the pier. From there, a new compression strut could develop which would be supported further inside the base section where the concrete still has sufficient strength to bear the diagonal compression force. However, the very low amount of transverse reinforcement provided in the test units was by far insufficient to transfer the shear force over the diagonal crack, so that this alternative load carrying mechanism could not develop and the failure resulted in the form described above.

Generally, it is common to distinguish between two types of shear failure. On one hand, a shear failure can occur in diagonal tension due to insufficient transverse reinforcement, or on the other hand it can be the result of an insufficient strength of the diagonal compression struts, e.g. due to a very thin web. The observed failure mode of Test Units VK1 and VK3 does not really fit into either of the two categories. The diagonal tension mechanism – consisting of a combination of the hoops and the concrete tension strength – was generally capable of carrying the entire shear force as confirmed by the response during the preceding phases of the inelastic loading. The same holds true for the diagonal compression struts having substantial strength due to the large web thickness.

The observed shear failure in both test units may rather be considered as a secondary consequence of the substantial damage coming from the large flexural rotations at the base. The local destruction of the support for the diagonal compression strut was not related to a lack of strength, but was rather a result of excessive flexural strains. The subsequent failure mechanism could have probably been prevented by a (substantially) higher diagonal tension strength (i.e. more hoops). But the fact that this higher amount of transverse reinforcement became necessary was also related to the previous flexural damage at the base as the provided diagonal tension strength was sufficient for the previously existing load carrying mechanism. It was therefore not a degradation of the diagonal tension strength that caused the final shear failure, but rather a change of the shear bearing mechanism for which the existing diagonal tension strength was not sufficient. The need for this change of mechanism was triggered by the flexural damage that had developed up to this point. As a consequence, the shear failure observed in the case of VK1 and VK3 can also be interpreted to have been triggered by the flexural damage to the compression zones at the base.

6 Conclusions

6.1 Summary

The purpose of this document and of the underlying research project is to provide a basis for the displacement based seismic assessment of existing bridges. Such a task has become necessary in Switzerland because the seismic risk has been underestimated in the past. As a consequence, the related seismic safety of the existing bridge stock appears uncertain and requires checking. For this purpose, the Swiss Federal Roads Authority (ASTRA) has established a program to assess all bridges on the national highway system. The research results presented in this document shall serve as a basis for an efficient and realistic seismic analysis of existing bridges. Special emphasis has been put on appropriate analysis approaches for moderate seismic conditions – as e.g. being representative for Switzerland. Demand levels corresponding to higher seismicity conditions have been considered additionally in order to provide approaches that are more generally applicable. These investigations also served to determine the limits of possibly simpler analysis methods which may be sufficient under moderate seismic conditions, but which might not be appropriate for stronger earthquake loading anymore.

In Section 2, an overview has been given of the various aspects influencing the seismic safety of existing bridges in general, as well as the specific Swiss situation. For this purpose, a variety of typical damage patterns were presented which have occurred in past earthquakes. The different types of damage are discussed with respect to their reasons, their influence on the overall safety of the structure and their relevance under moderate seismic conditions. Based on these discussions, it could be concluded that especially the unseating of the superstructure and the failure of the piers represent failure modes that can cause the partial or total collapse of bridge structures.

To take into account the specific situation in Switzerland, at first, the seismic code provisions throughout the last 60 years have been compared to the requirements of the current code generation. An overview of typical characteristics of existing Swiss bridges has been given on one hand concerning general data of the bridge stock and on the other hand more detailed in the form of specific properties of three sample bridges. The code comparisons have shown that the prescribed seismic demand levels have risen drastically during the last decades. In addition, it was found that many existing bridges feature certain detailing deficiencies that would not be allowed in a ductile new design following modern seismic codes.

Applying the principles of the currently existing Swiss recommendations for the seismic assessment of existing building structures, it was shown that a critical behavior of some existing bridge piers during an earthquake would be predicted based on these rather simple analysis methods. It was found that especially short squat piers bear an increased seismic risk. This is related to the fact that such piers generally feature a lower flexural displacement capacity, while furthermore also being prone to rather brittle shear failure. Concerning the criteria for the acceptability of damage to bridges in the context of an assessment, it has been discussed that the potential consequences can go well beyond the direct damage to the structure itself or to people using it at the moment of an earthquake. The indirect consequences to the national economy can result as significantly larger than the direct detriment if important routes of the transportation infrastructure are interrupted for a longer time period.

The results of any seismic analysis can only be as good as the underlying mechanical model of the structure. Therefore, considerable attention has been given to the conceptual modeling of bridges, specifically for seismic loading. A reasonable compromise should be found between, on one hand, a possibly simple and well understandable model and, on the other hand, a model which is sufficiently complex to capture all relevant aspects of the seismic response. This includes e.g. the consideration of potential inelastic behavior or the appropriate representation of multi-modal response. It has been shown that, aside from the flexural stiffness of the superstructure, its torsional and rotational behavior can also influence the demand on the piers in several ways. The actual form of this influence and the extent of its relevance depend on the individual properties of the superstructure and its support by bearings and the substructure. Especially the torsional stiffness and the rotational inertia of the superstructure are characteristic parameters for these phenomena.

6.1 Summary

Based on a parametric study, the influence of the rotational superstructure inertia on the multi-modal response of a single cantilever pier has been investigated. An approach has been proposed to allow for these effects in an approximate manner in simplified analyses not explicitly taking into account the rotational inertia of the superstructure. Furthermore, the influence of the superstructure torsional stiffness on the transverse bridge response has been discussed using an example bridge configuration. It could be shown that this aspect can change the plastic mechanism developing in the structure. At the same time, it was found that in bridges with bearing supported superstructures the limited moment capacity that can be transferred by the bearings limits the rotational restraint of the pier tops by the superstructure.

Another aspect that can be very important for a realistic model of a bridge is the soil-structure interaction at the pier foundations and at the abutments. As long as the soil-foundation systems remain linear elastic, they only introduce additional flexibility to the system. However, it has been shown that uplifting of a spread pier foundation or inelastic deformations in the soil can cause a nonlinear moment-rotation behavior of the soil-foundation system, which may be considered as some form of plastic hinge developing underneath the footing. Depending on the relationship between the flexural strength of the pier and the effective moment capacity of the spread foundation, the soil structure interaction at pier foundations can even change the plastic mechanism of the pier. Based on an inelastic Winkler spring representation, a practically applicable concept has been proposed which can capture the most relevant effects of the soil-structure interaction at spread foundations. The estimation of the required elastic stiffness and the yield stress of the Winkler springs is discussed in detail and recommendations are given how to determine these parameters based on settlement calculations and on the bearing strength of the soil. It has been shown that the resulting nonlinear moment-rotation relationship can be further simplified as an inelastic spring, making its introduction into a mechanical model of the entire bridge structure very efficient. The consequences of the inelastic soil flexibility at the pier foundations on the global bridge response and on the local pier demands have been discussed based on numerical results from bridge analyses.

Concerning the soil-structure interaction at the abutments, it has been outlined that the flexibility of the embankments and their large masses cause them to be vibrational systems of their own interacting with the superstructure via the abutments. Experience from real instrumented bridges as well as theoretical considerations show that the soil-structure interaction at the abutments can strongly influence the behavior of the entire bridge structure. For rather short bridges under transverse excitation this phenomenon can be the primary aspect almost completely controlling the seismic response of the system. For longer bridges, the influence of the soil-structure interaction at the abutments tends to diminish with distance. However, in the end regions of the bridge, and also for the outer piers, this aspect may still have a dominating relevance. A simplified engineering model for the transverse behavior of the abutment-embankment system has been proposed which combines a truncated shear wedge model of the embankment with established modulus reduction curves to allow for the inelasticity of the soil. This concept can be used to develop a simple inelastic spring based on the geometry of the embankment and limited data about the embankment soil properties. It has been shown how the hysteretic properties of such an inelastic spring can be determined based on the modulus reduction curves. In addition, a simplified approach has been proposed to estimate the tributary mass of the embankment. Both the inelastic spring and the tributary mass can be introduced into the dynamic bridge model in a very efficient manner making the concept applicable in engineering practice. A comparison with the seismic response of an instrumented bridge has shown reasonably good agreement between the recorded abutment behavior and the prediction based on the proposed engineering model. To allow for the remaining inevitable uncertainties, it is recommended to perform a sensitivity analysis varying the most relevant parameters of the abutment-embankment model within a range of reasonable assumptions.

In the context of an appropriate definition of the seismic input loading, the current state of research on multi-support excitation has been summarized and discussed. Several reasons exist for the spatial variation of the ground motions resulting in a loss of synchronism and loss of coherence between the individual bridge foundations. Among others, these effects are related to a time-shift of the seismic waves, to reflections along their path, and to differing local soil conditions at the various footings. The response of a bridge structure to multi-support excitation can be divided into a dynamic and a pseudo-static part. From the presented discussions it can be concluded that in the majority of cases it is not

necessary to explicitly apply varying ground motions to the foundations, but that rather the simplified approach included in [EC8-2] is sufficient and provides conservative demand estimations. According to this method, the dynamic part of the response is determined by applying a synchronous excitation to all footings as this is considered the worst case for this response component. The pseudo-static part is then estimated by statically applying differential displacements at the bridge supports. An estimation of the combined response results from superposition of the two contributions. Aside from the consequences on the deformation demand of the bridge members, the multi-support excitation also influences the potential for superstructure unseating. This problem can be handled reliably by geometric criteria for required minimum seat lengths at the superstructure supports as those given in [ASTRA05a].

Aside from the hysteretic behavior of the bridge members, typically other sources of energy dissipation exist in a structure. It is common to cover these effects in an approximate manner by means of a certain amount of modal viscous damping added to the bridge model. This elastic viscous damping can e.g. comprise effects from foundation damping, nonstructural damping, or small-cycle hysteretic energy dissipation not covered by the numerical load-deformation rules. The required elastic viscous damping ratio and the appropriate damping model (constant or tangent stiffness proportional damping matrix) depend on the types of energy dissipation that are supposed to be covered. This also depends on the chosen structural model and on the damping effects already included in it. A discussion concerning this topic has been presented in the text which can provide some guidance for the required choices in the case of individual bridge structures.

For the seismic analysis of a bridge, inelastic time history analysis (ITHA) has the potential for the most complete description of the response. It can conceptually capture the dynamic properties and the inelastic behavior of the structure as well as the excitation by ground motions in a detailed manner. The quality of the results thus primarily depends on the accuracy with which the dynamic model and the input loading can be described. Despite these advantages, ITHA is likely to be used for seismic bridge assessment only in extraordinary cases. Its complexity makes the practical application of ITHA and the interpretation of the corresponding analysis results not only rather demanding but also potentially prone to errors. As an alternative, for ordinary applications a variety of simplified analysis techniques have been developed in the past representing different levels of approximation. These simplified methods can be distinguished between force based and displacement based approaches. In the more traditional force based techniques internal force actions are calculated which are compared to the strengths of the members. This approach has conceptual problems with describing the response in the inelastic range of the structure. This is a major drawback of force based analyses because the inelastic deformation range is of great relevance for the seismic response of RC structures. Displacement based analysis methods are better capable of describing the response at these demand levels making them the preferred approach in modern seismic engineering.

Several displacement based analysis approaches have been reviewed with respect to their capability of estimating the seismic displacement demand of bridges under transverse loading. Concerning the quality of a demand prediction by a certain analysis method it can be distinguished between the global demand estimation and the prediction of the relative displacement shape. The global demand can for example be represented by the displacement of a reference point on the superstructure, which is typically chosen as the point of largest deformation. It can be interpreted as an indicator whether an analysis method is capable of accurately estimating the magnitude of the overall deformation demand on the bridge structure. The accuracy of the local demand prediction at the individual pier tops furthermore depends on the quality with which the deformation shape is predicted by the method. The capability of reliably capturing these two issues thus determines whether an analysis approach is appropriate for the prediction of the seismic deformation demand of bridges.

The global demand of a MDOF system is influenced by the degree of inelastic response in a similar way as the seismic demand of inelastic single-degree-of-freedom (SDOF) systems. This analogy has proven to be very useful for the development of simplified displacement based analysis procedures. Therefore, the estimation of the displacement demand of inelastic SDOF systems has been discussed in detail. Current codes typically define the seismic input loading in the form of response spectra, which determine the demand of linear elastic SDOF systems. Hence, it is especially useful if the demand of an inelastic SDOF system can be estimated approximately from the response of a

corresponding elastic system. Two conceptual approaches exist for this purpose, one using displacement modification factors and the other being based on an equivalent visco-elastic linearization. Several proposals from the literature have been discussed and evaluated for each of the conceptual approaches. Noticeable differences with respect to the resulting inelastic demand predictions have been found. Partly, these differences may be considered as general uncertainties inherent to the problem. However, based on comparisons with the results from inelastic time history analyses (ITHA) on MDOF systems, some procedures could be identified as possibly more suitable than others. Based on these more appropriate methods, reasonably good predictions of the global mean ITHA results could be achieved using the simplified methods for the demand estimation of inelastic SDOF systems.

Several simplified analysis methods for MDOF systems have been evaluated with respect to their ability to estimate the deformation shapes determined by ITHA. The considered approaches included rather simple linear procedures, such as the response spectrum analysis or the lateral force method, as well as more advanced nonlinear static concepts, as e.g. conventional or multi-modal pushover analysis. It was found that the quality of the predicted displacement shapes depends on the properties of the individual bridges and on the demand level which is related to the assumed seismicity. In particular, the relevance of higher modes and the question how uniformly inelastic actions develop throughout the structure at increasing demand levels appeared to strongly influence the quality of the simplified predictions. Both aspects depend on the irregularity of the bridge as very irregular structures tend to excite higher modes stronger, while also causing more uneven distributions of ductility demands at different piers. The influence of non-uniform distributions of inelasticity on the displacement shape also depends on the seismicity level as this effect tends to become more pronounced at higher ductility demands.

Except the multi-modal pushover analysis, the mentioned analysis concepts for MDOF structures are also included in some European and Swiss codes and guidelines, such as [EC8-2], [EC8-3], and [SIA2018]. In all of these documents the global displacement demand is estimated based on the so-called *equal displacement approximation*, which assumes that the peak displacement demand of an inelastic SDOF system is approximately equal to that of a linear elastic system having the same initial stiffness. As a consequence the various analysis procedures only differ in their prediction of the displacement shape. However, as the validity of the *equal displacement approximation* is limited to certain conditions (especially concerning the fundamental elastic period), it was found that the procedures according to the mentioned provisions could predict rather erroneous global displacement demands if those conditions were not fulfilled.

It has been found that this deficiency could be mitigated largely if the principles for the demand estimation of inelastic SDOF systems, mentioned above, are included into the MDOF analysis procedures. Although these concepts also make use of the displacement demand of elastic systems, they apply certain modifications which improve the demand prediction for inelastic systems compared to the *equal displacement approximation*. Due to the approximate analogy between the inelastic behavior of a SDOF system and the global response of inelastic MDOF systems, the same modifications can be applied on these latter cases. Corresponding modified analysis procedures for inelastic MDOF bridge systems have been proposed. Based on comparisons with mean ITHA results, it could be shown that the demand predictions by these modified analysis methods are greatly improved. This is especially true in cases falling outside the validity range of the *equal displacement approximation*.

In total, the proposed modifications concerning the estimation of the global deformation demand have been considered for four different displacement based analysis procedures. These methods differ with respect to the required effort in their application and with respect to the achievable accuracy under various conditions. The modified approaches have been tested on 9 different sample bridges at three different levels of seismicity. The corresponding analysis results were then compared to the mean demand predictions from ITHA. Based on this evaluation, recommendations have been given concerning the appropriate range of application for each of the modified analysis procedures. In particular, it has been proposed to generally apply the various approaches successively with increasing sophistication. This way, it can be decided after every step whether the next, more sophisticated, procedure is still required or if the so far computed results can already be considered as sufficiently

reliable. Furthermore, the availability of several sets of results serves for mutual checking and can thus help detecting errors in the analyses.

Generally, it was found that under moderate seismicity conditions – as being representative for the Swiss situation – the linear analysis methods (i.e. response spectrum analysis and lateral force methods) may already give a rather reasonable demand estimation in many cases. This is especially true if the proposed modification to allow for the influence of inelasticity on the global deformation demand is taken into account. In some cases, where adjoining piers experience significantly differing ductility demands (typically short piers between taller piers), additional inelastic analyses might be recommendable. However, the results from the elastic analyses may already be useful to identify these cases. At higher seismicity levels, which cause larger ductility demands, the application of inelastic pushover analysis procedures is generally recommendable. These should include the proposed modifications for an improved estimation of the global deformation demand. However, even in such cases the simpler elastic analyses should also be performed as they can serve for checking the more complex inelastic results, which might be somewhat more prone to errors.

All of the presented analysis methods presume that the hysteretic response of the structure before failure is stable during several cycles of loading. In the new design of a structure, such a behavior can be achieved by means of certain detailing requirements which ensure that no degradation occurs during inelastic cycles. However, in existing structures corresponding detailing criteria are typically not fulfilled. A widespread seismic deficiency of existing structures is represented by lap-splices of the longitudinal reinforcement in the potential plastic hinge regions of reinforced concrete piers. Such lap-splices are likely to fail under severe cyclic loading, causing a degradation of the flexural strength with every cycle.

In an inelastic time history analysis this behavior can theoretically be directly included, provided an appropriate hysteretic model for the description of the cyclic strength degradation is available. However, considering it in one of the simplified analysis procedures discussed above is not directly possible. Therefore, it has been investigated how the cyclic strength degradation influences the seismic displacement demand of a structure in comparison to a corresponding system without degradation. For this purpose, hysteretic models of cyclically degrading piers were calibrated on experimental results which represent the characteristics of lap-splices being typical for existing Swiss bridges built throughout the last fifty years. Based on the findings of this study, an empirical relationship has been developed which approximately describes the increase of the displacement demand due to cyclic strength degradation, compared to the demand of a non-degrading system. With this relationship it is possible to modify the results from a simplified analysis on a non-degrading system in order to take into account the effects from cyclic strength degradation in an approximate manner.

Following the presented recommendations for the modeling of bridge structures and applying the proposed displacement based analysis methods, as outlined above, it can be expected that a reasonable estimation of the seismic response will be achieved. However, due to the approximations by the engineering models and the simplifications within the analysis approaches, some inaccuracies cannot be ruled out completely and any seismic analysis will always bear a considerable amount of uncertainty. This relates to all steps within an assessment procedure, from the definition of the seismic input loading, over the dynamic model of the structure, up to the analysis procedure. More complex approaches at each stage might mitigate this problem to some extent, but it will not be resolved completely. Therefore, it is recommended to keep the assessment procedure within a reasonable range of complexity in order to maintain its feasibility. The inevitable uncertainties should be taken into account by means of a variation of the most relevant modeling assumptions within a reasonable range. The sensitivity to these assumptions should be investigated and appropriate conclusions for a sufficiently conservative demand estimation should be drawn from the variation. Possibly more reliable results can be achieved performing certain sensitivity analyses on a reasonably complex model than conducting only a single analysis on a very sophisticated model.

For the assessment of the seismic safety of a bridge, the realistic description of the cyclic-inelastic behavior of its piers is a crucial issue. Therefore, an experimental campaign consisting of 3 large-scale quasi-static cyclic tests on wall-type bridge piers has been conducted. The test units were designed to represent typical Swiss RC piers built before the establishment of modern seismic design codes. They featured very low amounts of transverse reinforcement without any special detailing measures for

enhanced ductility, as common in existing older Swiss bridge piers. Together with the rather low aspect ratio of $L_v/l_w = 2.2$, the test units thus were expected to be potentially shear critical. One of the test units, VK2, furthermore featured a lap-splice of the flexural reinforcement at the pier base, while the longitudinal reinforcement of the other two units, VK1 and VK3, was continuous from the foundation to the top. Lap-splices at the pier base can cause problems for the seismic behavior as they are likely to fail under large cyclic-inelastic deformations being concentrated in the base region. The test units were instrumented by 76 hard-wired measurements each. Additionally, electronic Demec measurements were performed manually at the surface of the test units in order to determine the complete deformation field of the piers at selected load steps. They were complemented by manual measurements of the crack widths at various points distributed over the surface of each pier.

The two test units with continuous flexural reinforcement (i.e. without lap-splice at the base), VK1 and VK3, showed rather stable flexural response up to deformation levels being higher than the predicted displacement capacity according to [SIA2018]. Both piers experienced a shear failure in the inelastic range which was accompanied by an immediate loss of axial load capacity. In the case of real bridge piers, this failure mode would cause a complete collapse of at least the two adjacent bridge spans. The shear strength model according to [SIA262], which is referenced in [SIA2018], would have predicted a shear failure to occur already in the elastic deformation range of the test units. For reinforced concrete members with very low transverse reinforcement ratios, the shear strength model of [SIA262] was found to be rather conservative. Several other shear strength models that had been developed especially for the estimation of the ductility-dependent cyclic-inelastic shear strength of RC members showed considerable scatter with respect to the displacement at which a potential shear failure would occur. This visualizes the still existing large uncertainty concerning the prediction of this important failure mode. The way in which the observed failure mechanisms developed in both test units with continuous reinforcement suggests that the flexural damage in the plastic hinge zone triggered the final shear and axial load failure. In each case, the failure occurred when the damage to the flexural concrete compression zone at the pier base had progressed so far that the diagonal compression strut carrying the shear force did not find a support anymore. As a consequence, a diagonal shear crack opened up along which the upper part of the pier started sliding downwards.

Test unit VK2 featuring a lap-splice at the base did not experience a shear failure although – aside from the splice – it was designed equal to VK1 having continuous reinforcement. The splices of VK2 started failing before the deformation level at which test unit VK1 had failed in shear. The failure of the lap-splices caused the flexural strength to degrade, so that the reduced shear demand in the inelastic range did not exceed the also degrading ductility-dependent shear capacity anymore. Instead, with increasing displacement demands successively all splices failed and at higher deformation levels additionally the concrete compression zones were increasingly lost due to excessive strains. As a consequence, the base region of VK2 developed towards a concrete hinge almost completely losing its flexural strength. Only a very small remaining eccentricity of the axial load still provided a rather low moment resistance at large deformation levels. Despite the severe damage to the base region, test unit VK2 was still able to carry the applied axial load up to the end of the experiment. However, the condition of the pier at this state cannot be considered as stable anymore and should not be utilized for the seismic displacement capacity.

6.2 **Outlook**

The presented research results show that modern displacement based analysis approaches can serve for a reasonably realistic assessment of the seismic behavior of bridges. This also shows that the intensive international research efforts which have been undertaken throughout the past decades have helped considerably in better understanding the complex phenomena influencing the seismic response of structures. However, it has also been outlined that significant uncertainties still exist with respect to many issues. While a good qualitative understanding of the relevant effects has already been achieved, a reliable quantification in detail is often still a difficult task. Therefore, a large number of issues still remain to be resolved by future research. Probably one of the most important tasks will be the reduction of the large uncertainties still being immanent to many current concepts. Although it would be unrealistic to strive for full accuracy by future models, at least considerable improvement may be possible in many respects. Some topics for further research that are related to the seismic assessment of bridges will be summarized below.

1. *Soil-structure interaction at abutments*

   As outlined in Sections 3.5.2 and 6.1, the soil-structure interaction at abutments can have a strong influence on the seismic response of bridges. For rather short structures, it can even be the dominating aspect almost completely controlling the behavior. Due to its large relevance, it appears necessary to pay sufficient attention to this detail in the modeling process for the bridge. The proposed engineering model is based on theoretical considerations concerning the dynamic behavior of soil embankments. It has also been shown to agree reasonably well with the measured behavior of an instrumented real bridge. However, further research on this topic is still required. This refers both to experimental as well as theoretical investigations. In this context it is recognized that realistic experimental tests on abutment-embankment systems are very difficult to conduct. This is especially true if the large-scale behavior under cyclic – or possibly even dynamic – loading is to be determined. Although some tests on the longitudinal abutment behavior have already been conducted, e.g. in California, further experimental investigations also on the transverse behavior are needed. To some extent, large-scale experiments might be complemented by small-scale centrifuge testing. This form of experimental investigation may be more appropriate for performing entire test series in which the influence of several varying parameters could be studied. Independent of the scale of an experiment, due attention should be given to an appropriate test setup. An appropriate representation of realistic boundary conditions appears crucial for the quality of the test results. In particular, this refers to a sufficiently accurate representation of the embankment and its soil conditions, as they would be expected in a real case.

   Detailed numerical analyses of the soil-structure interaction at abutments have already been performed in the past and with increasing computing power more sophisticated analyses are becoming available over time. Such analyses are the subject of current research by several international researchers. However, aside from the numerical solution strategies, such analyses also require reliable mechanical models which are able to realistically describe the complex soil behavior – possibly even under large cyclic and dynamic deformations. Although even complex numerical analyses cannot replace experimental testing, they are needed to extrapolate the experimental findings to a broader range of cases. In order to make these research results available for practical applications, it is recommended to use such rather complex analyses for the validation and calibration of simpler engineering models as e.g. those presented in this document.

2. *Soil-structure interaction at spread foundations*

   Similar problems as outlined above for the abutments also exist for the soil-structure interaction at spread foundations. To some extent, the behavior of a spread foundation might be somewhat better predictable as it is often influenced significantly by uplifting of the footing. This phenomenon is essentially related to equilibrium conditions which can be described with limited effort. As long as the soil remains elastic, the soil-foundation behavior can therefore be analyzed with standard engineering tools. The problem becomes somewhat more complex if the bearing

capacity of the soil starts to be exceeded locally, resulting in a yielding-type behavior. Capturing this type of response realistically is already rather complex under static-monotonic loading. It becomes even more difficult under dynamic-cyclic loading. Especially, estimating the resulting hysteretic response of the soil-foundation system is not straightforward anymore.

The simplified engineering model presented in this work may serve as a practical approximation. It is expected to give a reasonable estimation of the limited moment capacity of the soil-foundation system, which is important for a realistic representation of the expected plastic mechanism. However, the model in its current form should not be considered as capable of realistically estimating the hysteretic behavior in the inelastic range of the soil. For the development of improved response prediction models in this range, additional experimental data would be very helpful. The current experimental data basis is very limited. As for the abutments, generally large-scale tests appear preferable, but small-scale centrifuge tests may be a good means to complement them, especially as small-scale tests allow the conduction of entire test series which may not be possible at large scale. In either case, a realistic representation of the soil and boundary conditions would be essential in the test campaigns. If the focus of the experiments is also on the inelastic range of soil behavior, it is important that the chosen soil boxes are sufficiently large so that the relevant failure mechanisms can freely develop without disturbance from the boundary walls.

Advanced numerical analyses can serve to complement the experimental test campaigns. They may also allow the investigation of a larger variety of configurations and assumed soil conditions. Both the experimental as well as the numerical results should be used to further calibrate and verify simpler engineering models as the one presented in this work. These can then be used for practical assessment applications with an improved accuracy and reliability.

3. *Methods for the demand estimation of inelastic SDOF systems*

The displacement demand estimation of inelastic SDOF systems has been discussed in some detail. In these cases, the seismic input loading was defined in the form of elastic response spectra. As a consequence, the inelastic demand had to be related to that of an elastic system which could either be achieved applying a displacement modification factor or by means of an equivalent linearization. Both approaches bear a considerable uncertainty. Several alternatives are conceivable in order to partly reduce these uncertainties.

Generally, it would be possible to define inelastic displacement spectra which would allow the direct determination of the displacement demand based on some characteristic properties of the inelastic SDOF system. At the current state, the elastic response spectra represent mean curves and the displacement modification factors (or the corresponding equivalent linearization principles) also represent average values deduced from a larger set of underlying ground motions. This separate double averaging introduces unnecessary statistical uncertainties, which could be avoided by the direct use of mean inelastic displacement spectra. In this latter case, averaging would only have to be performed once, which is statistically preferable.

But even if elastic response spectra are to be used for the definition of the seismic input loading, the process of relating inelastic demand to the peak response of an elastic system could still be improved. The equivalent linearization concept by Iwan and Guyader ([IG79b], [Iwa80], [Guy04]) suggests that optimum equivalent linear systems can be determined if both the effective period and the equivalent viscous damping are taken as independent parameters in the calibration of empirical relationships. The intended advantage of this approach is not only to optimize the mean value of the demand predictions but also to reduce its uncertainty. However, even if such an optimum equivalent linear system can be determined properly, for the application in combination with a smooth elastic response spectrum an additional relationship is required which accounts for the influence of varying viscous damping ratios. This empirical relationship re-introduces considerable uncertainties to the demand predictions ruining large part of the effort related to the optimum linear system.

However, the general approach might still be promising if the two partial models – i.e. the development of an optimum linear system and the relationship to allow for different viscous

damping ratios – are directly combined together in the calibration process. As discussed above in the context of inelastic displacement spectra, this way two separate calibration procedures – each leading to individual average relationships – would be replaced by a single optimization process. From the statistical point of view this would yield improved results. It has been discussed in Section 4.5.3 that the results of such a combined optimization approach can also be interpreted as a form of effective displacement modification factor. The difference to the so-far existing types of displacement modification factors would be that the period, for which the elastic spectral displacement is determined, would not be fixed to the initial period of the inelastic system anymore. Instead, some effective period, which has been determined from the optimization process as a better representation of the inelastic system, would be used to read the elastic displacement from the response spectrum. The subsequent steps in the application would then be the same as for the traditional displacement modification factors. This means that the previously determined elastic displacement is multiplied by an empirical modification factor in order to estimate the inelastic demand.

It is expected that such a new approach could provide better demand estimations and it should especially reduce the scatter of the predictions compared to the so far existing methods. The only drawback of this concept would be that the effective period – as for the equivalent linearization methods in general – depends on the displacement demand so that an iterative solution is required in practical assessment applications. However, this extra effort should be limited and the improved quality of the results may outweigh this inconvenience.

Independent of the actual approach (conventional displacement modification factors, equivalent linearization, inelastic displacement spectra, or the modified concept outlined above), it appears recommendable to perform the required calibrations, underlying each of the methods, using realistic hysteresis rules. Traditionally, many empirical approaches had been developed for elasto-plastic, or maybe bilinear, hysteretic behavior of the inelastic SDOF system. The use of these hysteresis rules was less motivated by their appropriateness for real structures, but rather by the simplicity of their numerical implementation. Although some authors assume that, based on limited comparisons, the type of hysteretic rule should not influence the displacement demand very strongly, this assumption should not be generalized. Possibly, the encountered response similarities could have also been the result of several counteracting effects which, by chance, may have partly canceled each other out in these particular cases (e.g. lower energy dissipation versus better recentering behavior).

The most comprehensive consideration of different hysteretic rules has probably been included in the two equivalent linearization approaches by Priestley *et al.* [PCK07] and by Guyader [Guy04]. As can be seen on the right side of Fig. 4.21, the proposal by Priestley *et al.* [PCK07] e.g. suggests some difference between the "thin Takeda" and the "fat Takeda" models. Generally, the different hysteretic rules considered by Priestley *et al.* [PCK07] cover a wide range of behavior types occurring in real structures. Although Guyader [Guy04] has also included a variety of hysteresis models in his analyses, it is a bit of a drawback that his stiffness degrading model, which would conceptually be most suitable for the response of reinforced concrete structures, implies rather fat loops. These may be appropriate for well designed beams and frame structures. However, for RC piers – especially those of existing structures featuring some detailing deficiencies – these fat loops are likely to overpredict the hysteretic energy dissipation. For such applications, the "thin Takeda" rule according to Priestley *et al.* [PCK07] may be considered more appropriate. (Note that the response predictions based on Guyader's stiffness degrading model in Sections 4.5 and 4.6.3 were generally lower than those based on the "thin Takeda" model by Priestley *et al.*) It can thus be concluded that any empirical relationship used for the demand estimation of inelastic SDOF systems should possibly be calibrated using hysteretic rules which are appropriate for the anticipated type of structure. Taking into account this aspect in future developments is expected to improve the quality of the demand predictions.

Although it has been shown that the simplified MDOF analysis procedures presented in Section 4.6.3 can be expected to yield reasonable demand estimations in ordinary cases, it cannot be ruled out that more complex and extraordinary structures might require more sophisticated

analysis techniques. In such cases, inelastic time history analysis should be the preferred approach. As has been discussed in Section 4.2, for this analysis type the seismic input loading cannot be defined in the form of response spectra anymore, but rather ground motions accelerograms are needed. Although [EC8-2], Sections 3.2.3 and 4.2.4 give some criteria for the required number of ground motions and their selection, the actual choice and the scaling (or generation) of appropriate accelerograms for a particular application still remains a difficult task. If this problem arises more frequently, it might be worthwhile considering the establishment of several sets of ground motions corresponding to the various seismic zones of Switzerland and the different soil classes. These ground motion sets would have to generally comply with the currently existing response spectra and would complement them concerning the definition of the seismic loading under the various conditions. The availability of such ground motion sets would facilitate the application of ITHA significantly. However, this would not mean that ITHA should then be considered a standard analysis tool. Due to its complexity and its sensitivity to errors it should be limited to exceptional cases and should only be applied by experienced engineers with sufficient knowledge of the method.

4. *Influence of cyclic strength degradation due to lap-splice failure*

In Section 4.7.2, an empirical approach has been proposed for a simplified and approximate consideration of cyclic-strength degradation related to lap-splice failure. It should be kept in mind that the degrading hysteretic model used to calibrate this empirical method has been based on only one experiment performed on a single bridge pier model (plus a corresponding test of a non-degrading pier without lap-splice as a reference for comparison). It would be desirable to check, and possibly adjust, the developed relationship using additional degrading hysteresis models based on further experiments. Although internationally further experiments on RC columns with lap-splices exist, these cannot be considered as representative for existing Swiss bridge piers. Especially in the U.S., lap-splices in older structures had been designed significantly shorter than in Switzerland. Differences also exist with respect to typical bar diameters (larger diameters in the U.S. than in Switzerland). As a consequence, lap-splices in existing Swiss piers might be expected to perform somewhat better than those e.g. in the U.S. Mixing the results related to such different structural conditions in the development of a simplified approach would not be reasonable.

Currently, additional experiments on wall-type bridge piers featuring typical Swiss detailing characteristics are being performed at ETH Zürich in the framework of a follow-up research project. It is expected that the results from these tests will bring some additional insight into the failure of lap-splices. They should also allow verification or re-calibration of the presented empirical relationship for the effects of cyclic strength degradation.

5. *Cyclic-inelastic behavior of RC bridge piers*

The experimental campaign presented in Section 5 has shown that the displacement capacity of the two test units with continuous flexural reinforcement (VK1, VK3) was limited by a shear failure in the inelastic range. Several ductility-dependent shear strength models had predicted a potentially shear critical behavior of these piers. At the same time, a considerable scatter was found between the various models, especially with respect to the predicted displacement at shear failure. In order to reduce the uncertainties concerning the estimation of the deformation capacity at shear failure, additional experiments should be performed. In these further tests the most relevant parameters influencing the shear capacity should be varied. All test units in the first campaign presented in Section 5 had the same aspect ratio of $L_v/l_w = 2.2$. The behavior of further test units with differing aspect ratios should be studied as this parameter is expected to have a significant influence on the relationship between flexural and shear capacity. The transverse reinforcement ratio of $\rho_{sw} = 0.08\%$ used for the test campaign of Section 5 can be considered as the lower boundary of reasonable values in existing Swiss bridge piers. The influence of higher transverse reinforcement ratios should be studied experimentally. In particular, it would be interesting to investigate whether a rather limited increase of ρ_{sw} would already change the behavior or if the transverse reinforcement ratio needs to be increased strongly in order to achieve a noticeable change of the shear failure mechanism.

In the test with the lap-splice of the flexural reinforcement at the pier base (VK2) an interaction between the flexural strength degradation due to splice failure and the potential for shear failure was observed. In this particular case, the shear failure was prevented by the presence of the lap-splices in the plastic hinge region. The development of the cyclic strength degradation and its observed interaction with the shear behavior should be investigated by additional experiments. Relevant parameters such as the longitudinal reinforcement ratio, the aspect ratio, and the length of the lap-splices should be varied in order to study the consequences for the cyclic-inelastic behavior of piers with lap-splices.

Furthermore, it would be interesting to investigate the influence of the load history both on the lap-splice behavior and on the cyclic-inelastic shear capacity. Any damage to the piers can be expected to be the combined consequence of peak deformations and repeated cyclic loading. A better understanding of the relative contribution of each of these two effects would help applying damage models and failure criteria on more general load histories occurring during real earthquake response.

Currently, a second test campaign is underway in the course of a follow-up research project at ETH Zürich. In the course of this test series some of the above suggested parameter variations are already performed in order to further study the cyclic-inelastic shear behavior and the strength degradation due to lap-splice failure. The layout of the test units and the setup of the new experiments are generally comparable to the first test campaign outlined in Section 5. The results from both test series together will serve for the development of models describing the cyclic inelastic deformation behavior as well as for the definition of appropriate failure criteria for reinforced concrete piers featuring the specific characteristics of existing Swiss structures.

Aside from the identification of additional research requirements, some recommendations can also be given in order to improve the currently existing Swiss assessment provisions. It has been shown that the behavior of the piers may be considered as one of the key factors for the seismic safety of a bridge. According to the current version of the assessment guideline by ASTRA for Swiss bridges [ASTRA05a], in the first assessment stage a brief screening procedure is implemented in order to identify those bridges which will be subjected to further analyses. All other bridges are considered to possess a sufficient seismic safety and they are therefore excluded from the further assessment. A variety of criteria concerning several characteristics of a bridge are included in this initial screening stage, which serve for the decision about the further procedure. However, only one of these criteria refers to the bridge piers. This criterion defines that the bridge should be subjected to further analyses if "extreme differences between the transverse stiffnesses of adjoining piers" exist within the structure.

The results presented in Section 4.6.3 generally confirm that such extremely differing stiffnesses (typically related to varying pier heights) can result in rather adverse consequences for the displacement demand of shorter and stiffer piers. However, it cannot be ruled out that other cases might exist where critical behavior of the bridge substructure can occur. Due to the potentially catastrophic consequences of a column failure, a somewhat more cautious approach with respect to the piers might be justified. It should be noted that e.g. a brittle shear failure could limit the displacement capacity of a pier to a level being even lower than the (nominal) yield displacement. Deformation demands higher than this cannot only be expected in the case of extreme differences between pier stiffnesses.

In particular, it might be worthwhile considering other structural properties, as e.g. the effective heights or the aspect ratios of the piers, in such a screening procedure. These two properties influence both the flexural displacement capacity as well as the sensitivity to premature shear failure. Further characteristics having a significant influence on these two issues, as e.g. the amount and detailing of the (particularly transverse) reinforcement, are unlikely to be known at this brief screening stage. Therefore, they cannot reasonably be included here as decision criteria. However, the aforementioned geometric properties of the piers can be determined very quickly and easily. They should already be available for the screening. Another aspect which certainly also influences the risk of a pier failure is the level of seismic loading. As a consequence, in a lower seismic zone less strict criteria might be appropriate than in one of the higher seismic zones. As this information is also readily available during the screening process, it could easily be taken into account for the decision.

Based on these considerations, it is recommended that an additional criterion should be included in the initial screening stage of [ASTRA05a] in order to identify potentially critical bridge piers. The combination of pier height, aspect ratio and seismic zone might serve for a simple criterion which takes into account certain aspects of deformation demand and capacity. It should be avoided that a bridge featuring potentially critical piers could be excluded from the further assessment process only because an appropriate criterion for its detection is missing.

If a bridge does not fulfill the safety criteria even after a seismic analysis in the second assessment stage, [ASTRA05a] recommends performing a cost-benefit analysis essentially following the provisions of [SIA2018]. In order to account for the relevance of bridges as parts of the infrastructure, [ASTRA05a] suggests generally using the higher minimum compliance factor of structural importance class III which must be exceeded in order to allow a cost-benefit analysis (see [SIA2018] for details). However, aside from this increased minimum compliance factor, no further modifications have been conducted, compared to the regulations for building structures in [SIA2018].

It has been outlined in Section 2.2.4 that, in the case of bridges, the indirect damage to the national economy can easily exceed the direct structural losses if relevant parts of the infrastructure are interrupted by seismic damage. Hence, for bridges it might not be sufficient to only consider the direct losses (structural and personal) in a cost-benefit analysis. Instead, it may become necessary to give some consideration to the potential consequences on the infrastructure network that may result from a severe damage to the bridge. If important traffic routes could be interrupted, additional indirect economic damage might have to be included in the cost-benefit analysis. It may be recommendable to mention this aspect in [ASTRA05a] as it is not covered by the general provisions for building structures given in [SIA2018].

Annex A1   Equations for Spread Foundations on Inelastic Winkler Springs

In the following the equations describing the relationship between rotation θ_f and moment M_{fb} is deduced for a spread foundation on bilinear Winkler springs and under constant vertical load N_{fb}. The actions, deformations and the foundation geometry are defined as shown in Fig. A1.1. The resulting actions M_{fb}, N_{fb} and V_{fb} act at the base level of the foundation and they need to be in equilibrium with the soil stresses acting from below. The monotonic stress-settlement relationship of the soil in compression is assumed as bilinear without post-yield stiffness. In tension, the soil stresses are assumed to be zero, allowing a gap to develop between the uplifting foundation and the soil. The corresponding relationship is shown in Fig. A1.2.
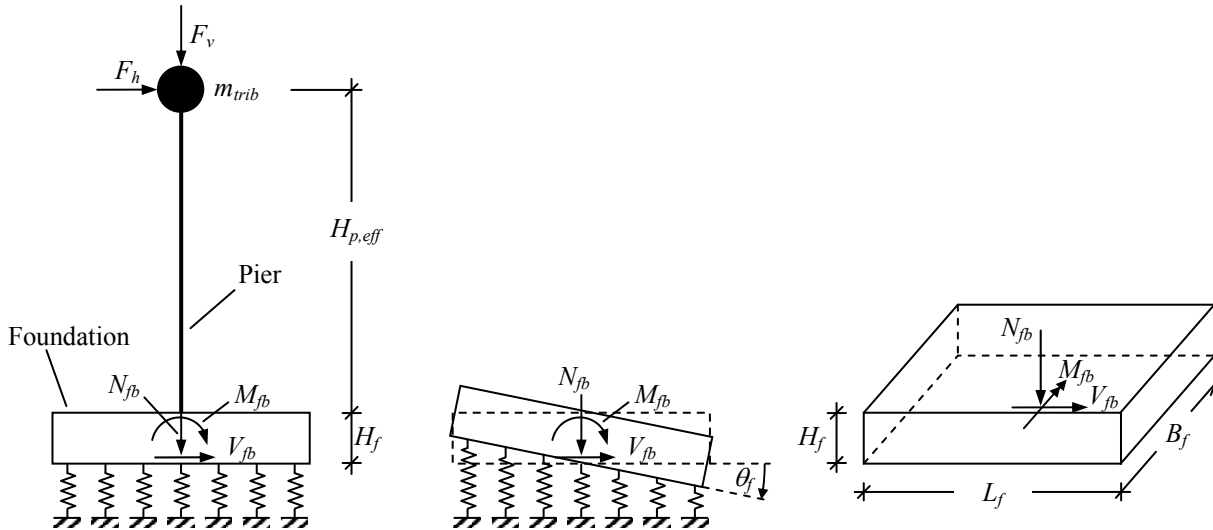
Fig. A1.1: Definition of actions, deformations and geometry of a spread foundation on Winkler springs
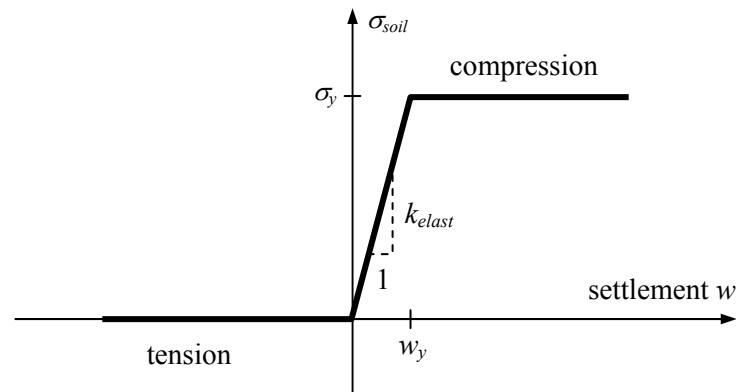
Fig. A1.2: Inelastic monotonic stress-settlement relationship for Winkler springs including uplifting in tension

Depending on the dimensions of the footing, the soil parameters and the loading, the foundation can be in one of four general stress states:

- Stress State 1:   Elastic soil response without gap (see Fig. A1.3)
- Stress State 2a: Elastic soil response with gap (see Fig. A1.4)
- Stress State 2b: Inelastic soil response without gap (see Fig. A1.5)
- Stress State 3:   Inelastic soil response with gap (see Fig. A1.6)

Generally, if the vertical load N_{fb} is kept constant, Stress States 1 through 3 occur in this order for increasing rotation θ_f. As will be shown below, the states 2a and 2b can only occur as mutual alternatives for a given soil-foundation system and a constant vertical load N_{fb}. The moment-rotation relationships $M_{fb}(\theta_f, N_{fb})$ for each of the stress states mentioned before are deduced in the following subsections.

a) Stress State 1: Elastic Soil Response without Gap

The distribution of settlements and soil stresses along the length of the foundation are shown in Fig. A1.3 for the case that the soil is still elastic and no uplifting occurs. The corresponding relationship between rotation θ_f and moment M_{fb} for this stress state is given in equation (A1.1). In this case, the M_{fb}-θ_f-relationship is independent of the vertical load N_{fb}. With increasing rotation θ_f, Stress State 1 will either be limited by uplifting at position 1 (Limit 1a) or by yielding of the soil at position 2 (Limit 1b). The corresponding limit rotations $\theta_{f,1a}$ and $\theta_{f,1b}$ can be computed according to equations (A1.2) and (A1.3), respectively.

Distribution of Settlements: Distribution of Soil Stresses:
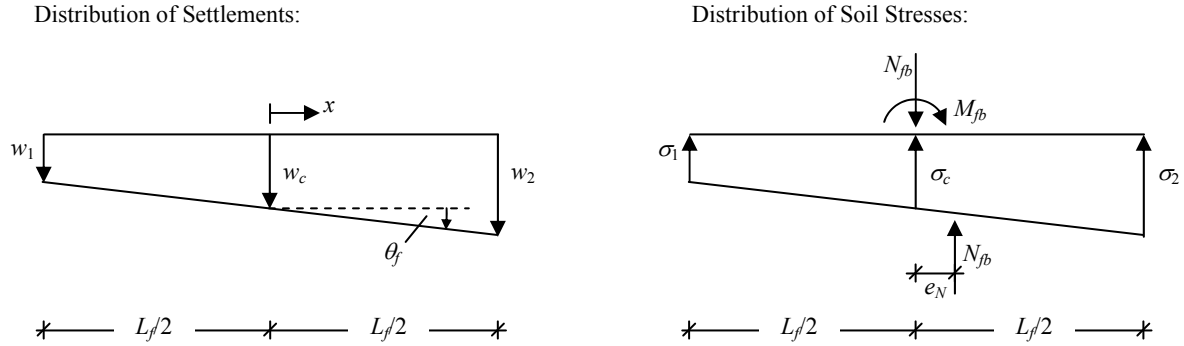
Fig. A1.3: Distribution of settlements and soil stresses for elastic soil response without gap

$$w(x) = w_c + x \cdot \tan\theta_f \qquad \Rightarrow \qquad \sigma(x) = k_{elast} \cdot w(x) = k_{elast} \cdot \left(w_c + x \cdot \tan\theta_f\right)$$

$$N_{fb} = B_f \cdot \int_{x=-\frac{L}{2}}^{\frac{L}{2}} \sigma(x)\,dx \qquad \Rightarrow \qquad N_{fb} = k_{elast}B_fL_f \cdot w_c \qquad \Leftrightarrow \qquad w_c = \frac{N_{fb}}{k_{elast}B_fL_f}$$

$$M_{fb} = B_f \cdot \int_{x=-\frac{L}{2}}^{\frac{L}{2}} x \cdot \sigma(x)\,dx \qquad \Rightarrow \qquad \boxed{M_{fb} = \frac{1}{12}k_{elast}B_fL_f^3 \cdot \tan\theta_f} \qquad (A1.1)$$

Limit 1a: Uplifting at position 1 $\qquad \Leftrightarrow \qquad w_1 \leq 0$

$$w_1 = w_c - \frac{L_f}{2} \cdot \tan\theta_f \leq 0 \qquad\qquad \Leftrightarrow \qquad \tan\theta_f \geq 2\frac{w_c}{L_f}$$

$$\Leftrightarrow \qquad \boxed{\tan\theta_f \geq \frac{2N_{fb}}{k_{elast}B_fL_f^2} = \tan\theta_{f,1a}} \qquad\qquad (A1.2)$$

$$\Leftrightarrow \qquad M_{fb,1a} = \frac{1}{6}N_{fb}L_f$$

<u>Limit 1b:</u>   Soil yielding at position 2 $\Leftrightarrow$ $w_2 \geq w_y$

$$w_2 = w_c + \frac{L_f}{2} \cdot \tan\theta_f \geq w_y = \frac{\sigma_y}{k_{elast}} = \frac{N_u}{k_{elast}B_f L_f} \qquad \Leftrightarrow \qquad \tan\theta_f \geq \frac{2}{L_f}\cdot\left(\frac{N_u}{k_{elast}B_f L_f} - w_c\right)$$

$$\Leftrightarrow \qquad \boxed{\tan\theta_f \geq \frac{2(N_u - N_{fb})}{k_{elast}B_f L_f^2} = \tan\theta_{f,1b}} \qquad\qquad\qquad (A1.3)$$

$$\Leftrightarrow \qquad M_{fb,1b} = \frac{1}{6}(N_u - N_{fb})L_f$$

with $N_u = \sigma_y L_f B_f$

Once one of the limit rotations, $\theta_{f,1a}$ or $\theta_{f,1b}$, has been reached the state of the foundation changes and enters into one of the two corresponding Stress States 2a or 2b that will be treated below. The question which state will follow depends on which one of the limit rotations is reached first. Thus, the foundation will uplift without yielding (Stress State 2a) if $\theta_{f,1a} < \theta_{f,1b}$ or it will yield without uplifting if $\theta_{f,1a} > \theta_{f,1b}$. By comparison of the expressions for $\theta_{f,1a}$ and $\theta_{f,1b}$, given in equations (A1.2) and (A1.3), it can be found that uplifting will occur if $N_{fb} < N_u/2$, while yielding will follow if $N_{fb} > N_u/2$, with N_u being the ultimate bearing capacity of the soil-foundation system under a pure vertical load. It can thus be concluded that the ratio N_{fb}/N_u controls whether Stress State 2a or the alternative Stress State 2b will occur for the given configuration of foundation, soil and vertical load.

$$\tan\theta_{1a} = \frac{2N_{fb}}{k_{elast}B_f L_f^2} < \tan\theta_{1b} = \frac{2(N_u - N_{fb})}{k_{elast}B_f L_f^2} \qquad \Leftrightarrow \qquad \boxed{N_{fb} < \frac{1}{2}N_u} \qquad (A1.4)$$

with $N_u = \sigma_y L_f B_f$

If $N_{fb} < N_u/2$, then Limit 1a governs and the foundation will lift up. If, in turn, $N_{fb} > N_u/2$, then Limit 1b governs and the soil will first enter into the inelastic range without uplifting. For the special case of $N_{fb} = N_u/2$, the foundation will uplift and the soil will yield at the same time, i.e. the system will omit the Stress States 2a/b and will directly jump from State 1 to State 3.

b) Stress State 2a: Elastic Soil Response with Gap

For the elastic stress state with uplifting of the foundation, the distribution of settlements and soil stresses along the length of the foundation are shown in Fig. A1.4. The corresponding relationship between rotation θ_f and moment M_{fb} for this stress state is given in equation (A1.5). It is valid between the two limiting rotations $\theta_{f,1a}$ and $\theta_{f,2a}$, but only if $N_{fb} < N_u/2$, as Stress State 2a does not occur otherwise. The upper limit rotation $\theta_{f,2a}$ for this stress state is defined by the yielding of the soil at position 2 and can be computed according to equation (A1.6). When this limit is exceeded, the system will enter into Stress State 3. If the vertical load N_{fb} is kept constant, it is not possible that Stress State 2b (inelastic soil without gap) will occur at some later stage. As a consequence, the occurrence of Stress State 2a excludes that of State 2b.

Distribution of Settlements: Distribution of Soil Stresses:
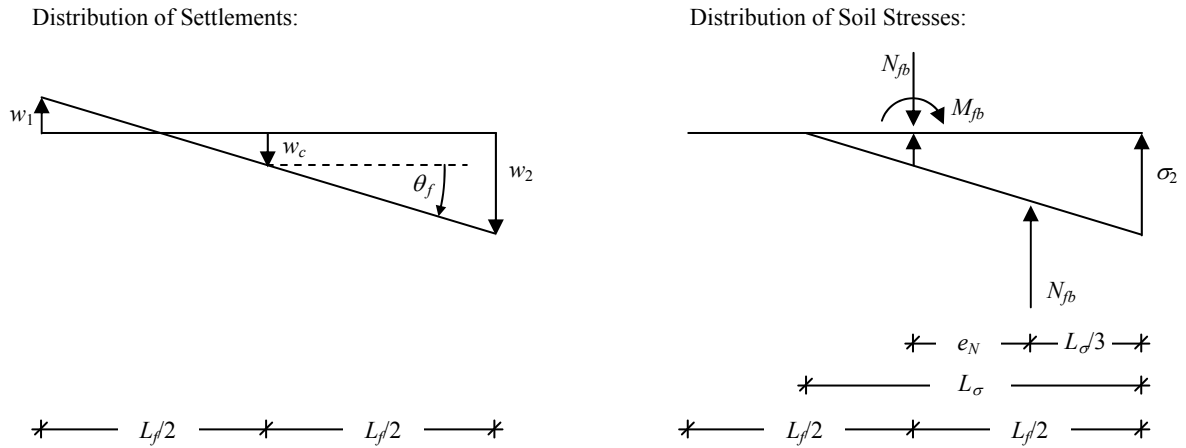
Fig. A1.4: Distribution of settlements and soil stresses for elastic soil response with gap

$$e_N = \frac{L_f}{2} - \frac{L_\sigma}{3} \qquad ; \qquad L_\sigma = 3\left(\frac{1}{2}L_f - e_N\right)$$

$$\sigma_2 = \frac{2N_{fb}}{B_f L_\sigma} \quad \Rightarrow \quad w_2 = \frac{\sigma_2}{k_{elast}} = \frac{2N_{fb}}{k_{elast}B_f L_\sigma}$$

$$\Rightarrow \quad \tan\theta_f = \frac{w_2}{L_\sigma} = \frac{2N_{fb}}{k_{elast}B_f L_\sigma^2} = \frac{2N_{fb}}{9k_{elast}B_f\left(\frac{1}{2}L_f - e_N\right)^2} \quad \Rightarrow \quad e_N = \frac{1}{2}L_f - \frac{1}{3}\sqrt{\frac{2N_{fb}}{k_{elast}B_f \cdot \tan\theta_f}}$$

$$\Rightarrow \quad \boxed{M_{fb} = N_{fb} \cdot e_N = N_{fb}\cdot\left[\frac{1}{2}L_f - \frac{1}{3}\sqrt{\frac{2N_{fb}}{k_{elast}B_f \cdot \tan\theta_f}}\right]} \quad \text{for } \theta_{f,1a} \le \theta_f \le \theta_{f,2a} \qquad (A1.5)$$

$$\Rightarrow \quad L_\sigma = \sqrt{\frac{2N_{fb}}{k_{elast}B_f \cdot \tan\theta_f}} \qquad ; \qquad w_2 = \sqrt{\frac{2N_{fb}\cdot\tan\theta_f}{k_{elast}B_f}}$$

Limit 2a: Soil yielding at position 2 $\Leftrightarrow$ $w_2 \geq w_y$

$$\Leftrightarrow \quad w_2 = \sqrt{\frac{2N_{fb} \cdot \tan\theta_f}{k_{elast}B_f}} \geq w_y = \frac{\sigma_y}{k_{elast}} = \frac{N_u}{k_{elast}B_f L_f}$$

$$\Leftrightarrow \quad \boxed{\tan\theta_f \geq \frac{N_u^2}{2k_{elast}B_f L_f^2 \cdot N_{fb}} = \tan\theta_{f,2a}} \tag{A1.6}$$

$$\Leftrightarrow \quad M_{fb,2a} = N_{fb}L_f \cdot \left[\frac{1}{2} - \frac{2}{3}\cdot\frac{N_{fb}}{N_u}\right]$$

with $N_u = \sigma_y L_f B_f$

c) Stress State 2b: Inelastic Soil Response without Gap

The distribution of settlements and soil stresses in the inelastic stress state without uplifting of the foundation are shown in Fig. A1.5. The corresponding relationship between rotation θ_f and moment M_{fb} for this stress state is given in equation (A1.7). It is valid between the two limiting rotations $\theta_{f,1b}$ and $\theta_{f,2b}$, but only if $N_{fb} > N_u/2$, as Stress State 2b does not occur otherwise. The upper limit rotation $\theta_{f,2b}$ for this stress state is defined by the uplifting of the foundation at position 1 and can be computed according to equation (A1.8). When this limit is exceeded, the system will enter into Stress State 3. If the vertical load N_{fb} is kept constant, it is not possible that Stress State 2a (Elastic soil with gap) will occur at some later stage. As a consequence, the occurrence of Stress State 2b excludes that of State 2a.
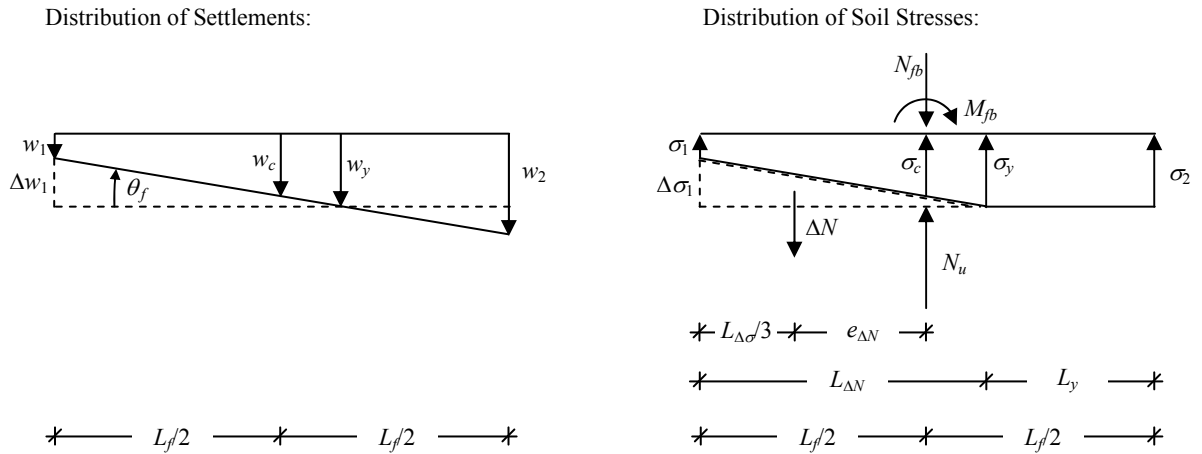
Distribution of Settlements:

Distribution of Soil Stresses:

Fig. A1.5: Distribution of settlements and soil stresses for inelastic soil response without gap

$$N_u = \sigma_y L_f B_f \qquad ; \qquad N_{fb} = N_u - \Delta N \qquad \Rightarrow \qquad \Delta N = N_u - N_{fb}$$

$$e_{\Delta N} = \frac{L_f}{2} - \frac{L_{\Delta N}}{3} \qquad \Rightarrow \qquad L_{\Delta N} = 3\left(\frac{L_f}{2} - e_{\Delta N}\right)$$

$$\Delta\sigma_1 = \frac{2\Delta N}{B_f L_{\Delta N}} = \frac{2\Delta N}{3B_f\left(\dfrac{L_f}{2} - e_{\Delta N}\right)} \qquad \Rightarrow \qquad \Delta w_1 = \frac{\Delta\sigma_1}{k_{elast}} = \frac{2\Delta N}{3k_{elast}B_f\left(\dfrac{L_f}{2} - e_{\Delta N}\right)}$$

$$\tan\theta_f = \frac{\Delta w_1}{L_{\Delta N}} = \frac{2\Delta N}{9k_{elast}B_f\left(\dfrac{L_f}{2} - e_{\Delta N}\right)^2} \qquad \Rightarrow \qquad e_{\Delta N} = \frac{L_f}{2} - \frac{1}{3}\sqrt{\frac{2\Delta N}{k_{elast}B_f \cdot \tan\theta_f}}$$

$$\Rightarrow \qquad \boxed{M_{fb} = \Delta N \cdot e_{\Delta N} = \left(N_u - N_{fb}\right)\cdot\left(\frac{L_f}{2} - \frac{1}{3}\sqrt{\frac{2\left(N_u - N_{fb}\right)}{k_{elast}B_f \cdot \tan\theta_f}}\right)} \qquad \text{for } \theta_{f,1b} \le \theta_f \le \theta_{f,2b} \qquad \text{(A1.7)}$$

$$\Rightarrow \qquad \Delta w_1 = \sqrt{\frac{2\Delta N \cdot \tan\theta_f}{k_{elast}B_f}} \qquad \Rightarrow \qquad w_1 = w_y - \Delta w_1 = \frac{N_u}{k_{elast}B_f L_f} - \sqrt{\frac{2\left(N_u - N_{fb}\right)\cdot \tan\theta_f}{k_{elast}B_f}}$$

<u>Limit 2b:</u> Uplifting at position 1 $\qquad \Leftrightarrow \qquad w_1 \leq 0$

$$\Leftrightarrow \qquad w_1 = \frac{N_u}{k_{elast} B_f L_f} - \sqrt{\frac{2\left(N_u - N_{fb}\right) \cdot \tan\theta_f}{k_{elast} B_f}} \leq 0$$

$$\Leftrightarrow \qquad \boxed{\tan\theta_f \geq \frac{N_u^2}{2k_{elast} B_f L_f^2 \cdot \left(N_u - N_{fb}\right)} = \tan\theta_{f,2b}} \qquad\qquad (A1.8)$$

$$\Leftrightarrow \qquad \boxed{M_{fb,2b} = \left(N_u - N_{fb}\right) L_f \cdot \left(\frac{1}{2} - \frac{2}{3} \cdot \frac{N_u - N_{fb}}{N_u}\right)}$$

d) Stress State 3: Inelastic Soil Response with Gap

The distribution of settlements and soil stresses in the inelastic stress state with uplifting of the foundation is shown in Fig. A1.6. The corresponding relationship between rotation θ_f and moment M_{fb} for this stress state is given in equation (A1.9). It is valid for rotations θ_f larger than $\theta_{f,2a}$ if $N_{fb} < N_u/2$ or larger than $\theta_{f,2b}$ if $N_{fb} > N_u/2$, respectively. Theoretically, no upper rotation limit exists in stress state 3 aside from the limiting value $\theta_f \rightarrow \pi/2$ (i.e. 90°). In this case $\tan \theta_f \rightarrow \infty$ and the moment M_{fb} approaches its supremum according to equation (A1.10). Stress State 3 cannot be followed by another stress state for increasing rotation θ_f if the vertical load N_{fb} is kept constant.

Distribution of Settlements: Distribution of Soil Stresses:
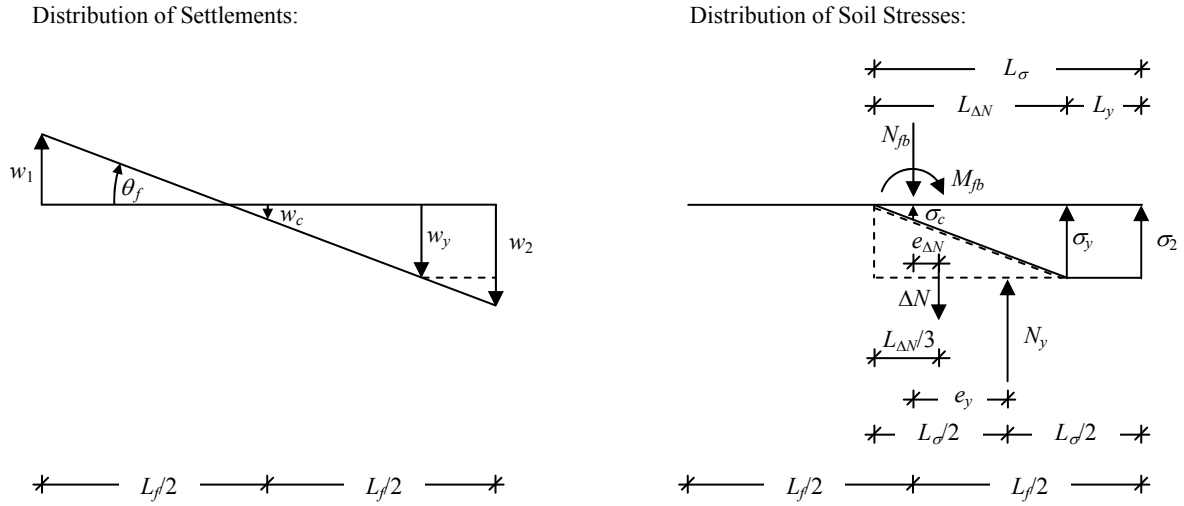

Fig. A1.6: Distribution of settlements and soil stresses for inelastic soil response with gap

$$N_u = \sigma_y L_f B_f \quad ; \quad N_y = N_u \frac{L_\sigma}{L_f} \quad ; \quad \Delta N = \frac{1}{2}\sigma_y B_f L_{\Delta N} = N_u \frac{L_{\Delta N}}{2L_f} \qquad \Rightarrow \qquad N_{fb} = N_y - \Delta N$$

$$\tan \theta_f = \frac{w_y}{L_{\Delta N}} = \frac{\sigma_y}{k_{elast}L_{\Delta N}} = \frac{N_u}{k_{elast}B_f L_f L_{\Delta N}} \qquad \Rightarrow \qquad L_{\Delta N} = \frac{N_u}{k_{elasr}B_f L_f \cdot \tan \theta_f}$$

$$\Delta N = \frac{N_u^2}{2k_{elast}B_f L_f^2 \cdot \tan \theta_f} \qquad \Rightarrow \qquad N_y = N_{fb} + \Delta N = N_{fb} + \frac{N_u^2}{2k_{elast}B_f L_f^2 \cdot \tan \theta_f}$$

$$L_\sigma = \frac{N_y}{N_u}L_f = \frac{N_{fb}}{N_u}L_f + \frac{N_u}{2k_{elast}B_f L_f \cdot \tan \theta_f} \quad \Rightarrow \quad e_y = \frac{L_f}{2} - \frac{L_\sigma}{2} = \frac{1}{2}L_f\left(1 - \frac{N_{fb}}{N_u}\right) - \frac{N_u}{4k_{elast}B_f L_f \cdot \tan \theta_f}$$

$$L_\sigma = \frac{L_f}{2} + \left(\frac{L_{\Delta N}}{3} - e_{\Delta N}\right) \qquad \Rightarrow \qquad e_{\Delta N} = \frac{L_f}{2} + \frac{L_{\Delta N}}{3} - L_\sigma = L_f\left(\frac{1}{2} - \frac{N_{fb}}{N_u}\right) - \frac{N_u}{6k_{elast}B_f L_f \cdot \tan \theta_f}$$

$$M_{fb} = N_y \cdot e_y - \Delta N \cdot e_{\Delta N} \qquad \Rightarrow \qquad \boxed{M_{fb} = \frac{1}{2}N_{fb}L_f\left(1 - \frac{N_{fb}}{N_u}\right) - \frac{N_u^3}{24L_f\left(k_{elast}B_f L_f \cdot \tan \theta_f\right)^2}} \qquad \text{(A1.9)}$$

Limit 3:   Infinite top displacement $\Leftrightarrow$ $\theta_f \to \dfrac{\pi}{2}$ $\Rightarrow$ $\tan\theta_f \to \infty$

$\Rightarrow$ $\boxed{M_{fb,3} = M_{fb,u} = \lim\limits_{\theta_f \to \frac{\pi}{2}} M_{fb} = \dfrac{1}{2} N_{fb} L_f \left(1 - \dfrac{N_{fb}}{N_u}\right)}$ (A1.10)

$\Rightarrow$ $\max e_N = \dfrac{L_f}{2}\left(1 - \dfrac{N_{fb}}{N_u}\right)$

e) Summary of Relationships

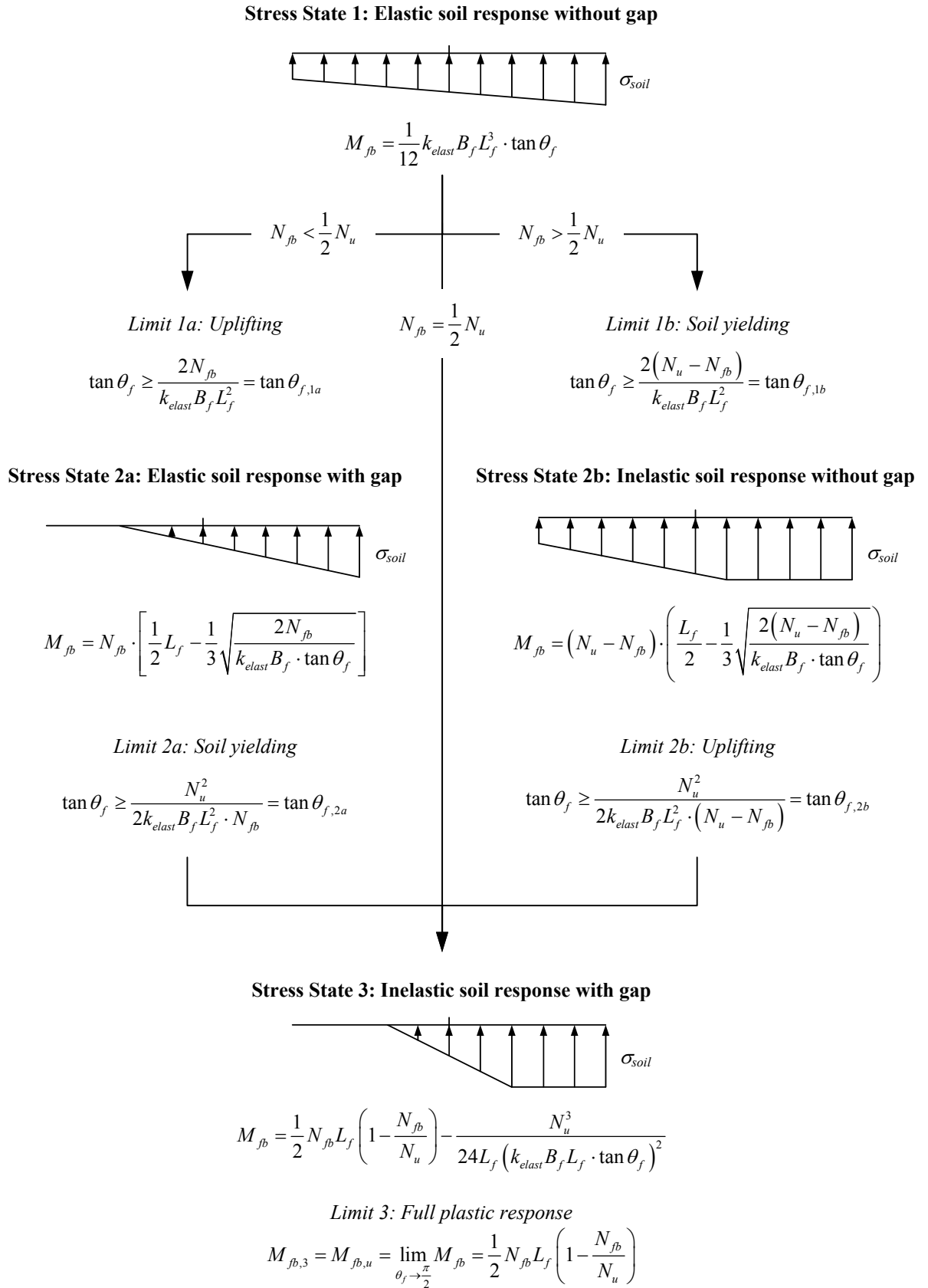The sequence of stress states and corresponding relationships can be summarized as follows:

Stress State 1: Elastic soil response without gap

$$M_{fb} = \frac{1}{12} k_{elast} B_f L_f^3 \cdot \tan\theta_f$$

$$N_{fb} < \frac{1}{2} N_u \qquad\qquad N_{fb} > \frac{1}{2} N_u$$

$$N_{fb} = \frac{1}{2} N_u$$

Limit 1a: Uplifting

$$\tan\theta_f \geq \frac{2N_{fb}}{k_{elast} B_f L_f^2} = \tan\theta_{f,1a}$$

Limit 1b: Soil yielding

$$\tan\theta_f \geq \frac{2\left(N_u - N_{fb}\right)}{k_{elast} B_f L_f^2} = \tan\theta_{f,1b}$$

Stress State 2a: Elastic soil response with gap

$$M_{fb} = N_{fb} \cdot \left[\frac{1}{2} L_f - \frac{1}{3} \sqrt{\frac{2N_{fb}}{k_{elast} B_f \cdot \tan\theta_f}} \right]$$

Stress State 2b: Inelastic soil response without gap

$$M_{fb} = \left(N_u - N_{fb}\right) \cdot \left(\frac{L_f}{2} - \frac{1}{3} \sqrt{\frac{2\left(N_u - N_{fb}\right)}{k_{elast} B_f \cdot \tan\theta_f}} \right)$$

Limit 2a: Soil yielding

$$\tan\theta_f \geq \frac{N_u^2}{2k_{elast} B_f L_f^2 \cdot N_{fb}} = \tan\theta_{f,2a}$$

Limit 2b: Uplifting

$$\tan\theta_f \geq \frac{N_u^2}{2k_{elast} B_f L_f^2 \cdot \left(N_u - N_{fb}\right)} = \tan\theta_{f,2b}$$

Stress State 3: Inelastic soil response with gap

$$M_{fb} = \frac{1}{2} N_{fb} L_f \left(1 - \frac{N_{fb}}{N_u}\right) - \frac{N_u^3}{24 L_f \left(k_{elast} B_f L_f \cdot \tan\theta_f\right)^2}$$

Limit 3: Full plastic response

$$M_{fb,3} = M_{fb,u} = \lim_{\theta_f \to \frac{\pi}{2}} M_{fb} = \frac{1}{2} N_{fb} L_f \left(1 - \frac{N_{fb}}{N_u}\right)$$

Fig. A1.7: Overview of M_{fb}-θ_f-relationship at different stress states

Annex A2   Theoretical Background of Simplified Analysis Methods

In this Annex the theoretical background of some existing simplified analysis procedures shall be presented. These simplified procedures allow the approximate estimation of the MDOF seismic displacement demand without a full dynamic (time history) analysis. For linear elastic behavior the response spectrum analysis and the lateral force method qualify for this purpose. In case of inelastic behavior the so-called pushover analysis can be used for the given task. It should be noted that nowadays not only one unique type of pushover analysis exists, but rather a considerable number of advanced pushover procedures have been developed. While the conventional pushover analysis was based on a constant acceleration shape vector approximating some kind of first mode response, the later developments attempted to also capture higher mode effects or the change of the mode shapes due to inelasticity and subsequent stiffness changes. In this annex, however, the discussion will be limited to the conventional pushover analysis without further modifications.

The purpose of the following sections is to provide the theoretical background of the various methods. Moreover, it is intended to show which simplifications are introduced at what points of the procedures. It will be seen how the individual concepts are related to each other. In particular, it will be shown that they are all based on common principles related to modal analysis and response analysis. In this context it is also interesting to investigate how they converge or not converge to each other under certain conditions (e.g. behavior of pushover analysis when applied on linear elastic system).

A2.1 Linear Elastic Methods

A2.1.1 Response Spectrum Analysis

The response spectrum analysis (RSA) makes use of the fact that, based on modal analysis, the dynamic response of linear elastic systems (having an appropriate damping matrix) can be split up into individual eigenmodes. The behavior of each eigenmode is equal to that of a corresponding SDOF system having the same natural period and modal damping. As a consequence, the seismic response of each mode can also be determined in a very simple manner as for a SDOF system using an elastic response spectrum. Up to this point, the response spectrum analysis does not represent any simplification, but rather captures the full dynamic system of the system accurately.

The only problem in the RSA is that the peak responses of the individual modes do not occur at the same time instants, but the information about the moment of occurrence is not available from the response spectrum. As a consequence, some uncertainties are involved in the superposition of the individual modal response. Normally, statistics based superposition methods as the so-called SRSS and CQC rules are used ([Cho01], [EC8-1]). As the general concept of the response spectrum analysis is well documented in the common literature on structural dynamics (e.g. [Cho01]), it will not be presented here in detail. The following discussion will rather give a brief summary of the most important equations required for the description of the response of a single mode. These relationships will be needed later on as they represent large part of the conceptual basis of the other simplified procedures. The superposition of various modes will not be discussed in this section.

The eigenvalue problem related to the modal response of the MDOF system is given by equation (A2.1). For a known eigenvector $\vec{\phi}_i$ the corresponding natural circular frequency ω_i and natural period T_i can be determined based on equation (A2.2). The participation factor Γ_i and the effective modal mass $m_{i,eff}^*$ follow according to equation (A2.3) and (A2.4), respectively. Note that it can be shown that the sum of the effective modal mass $m_{i,eff}^*$ corresponding to all n modes is equal to the total mass m_{tot} of the entire system, as given by equation (A2.5).

$$K\vec{\phi}_i = \omega_i^2 \cdot M\vec{\phi}_i \tag{A2.1}$$

with K: Stiffness matrix of MDOF system

            M: Mass matrix of MDOF system

            ω_i^2:   Eigenvalue of the i-th mode (equal to the square of the circular frequency ω_i)

            $\vec{\phi}_i$:   Eigenvector of the i-th mode

$$\omega_i^2 = \frac{\vec{\phi}_i^T K \vec{\phi}_i}{\vec{\phi}_i^T M \vec{\phi}_i} \qquad \Rightarrow \qquad T_i = 2\pi \sqrt{\frac{\vec{\phi}_i^T M \vec{\phi}_i}{\vec{\phi}_i^T K \vec{\phi}_i}} \tag{A2.2}$$

$$\Gamma_i = \frac{\vec{1}^T M \vec{\phi}_i}{\vec{\phi}_i^T M \vec{\phi}_i} = \frac{\vec{1}^T K \vec{\phi}_i}{\vec{\phi}_i^T K \vec{\phi}_i} \tag{A2.3}$$

$$m_{i,eff}^* = \frac{\left(\vec{1}^T M \vec{\phi}\right)^2}{\vec{\phi}_i^T M \vec{\phi}_i} = \Gamma_i \cdot \vec{1}^T M \vec{\phi} \tag{A2.4}$$

$$\sum_{i=1}^n m_{i,eff}^* = \sum_{i=1}^n m_i = \vec{1}^T M \vec{1} = m_{tot} \tag{A2.5}$$

The seismic peak displacement vector $\vec{\Delta}_i$ of the system in the i-th mode can then be determined based on the elastic spectral displacement $S_{d,el}$ at the natural period T_i and for the modal damping ratio ξ_i as given by equation (A2.6). The peak demand can alternatively be represented by equivalent forces $\vec{F}_i$ determined by the pseudo-acceleration $S_{a,el}(T_i, \xi_i)$ according to equation (A2.7). If these forces are applied on the system in a linear static analysis, they create exactly the same deformation and internal force response as the dynamic peak demand of i-th mode. Using the fact that $\vec{\phi}_i$ fulfills the eigenvalue problem of equation (A2.1), together with the relationship between the spectral displacement $S_{d,el}$ and pseudo-acceleration $S_{a,el}$, further representations of $\vec{\Delta}_i$ and $\vec{F}_i$ can be formulated as given in equations (A2.8) and (A2.9). The total base shear $V_{b,i}$, being the sum of all supported forces at peak demand, can be computed according to equation (A2.10).

$$\boxed{\vec{\Delta}_i = \vec{\phi}_i \cdot \Gamma_i \cdot S_{d,el}\left(T_i, \xi_i\right)} \tag{A2.6}$$

$$\boxed{\vec{F}_i = M\vec{\phi}_i \cdot \Gamma_i \cdot S_{a,el}\left(T_i, \xi_i\right)} \tag{A2.7}$$

$$\vec{F}_i = K\vec{\phi}_{ii} \cdot \Gamma_i \cdot \frac{1}{\omega_i^2} S_{a,el}\left(T_i, \xi_i\right) = K\vec{\phi}_{ii} \cdot \Gamma_i \cdot S_{d,el}\left(T_i, \xi_i\right) \tag{A2.8}$$

$$\vec{\Delta}_i = K^{-1}\vec{F}_i = K^{-1}M\vec{\phi}_i \cdot \Gamma_i \cdot S_{a,el}\left(T_i, \xi_i\right) \tag{A2.9}$$

$$V_{b,i} = \vec{1}^T \vec{F}_i = m_{i,eff}^* \cdot S_{a,el}\left(T_i, \xi_i\right) \tag{A2.10}$$

It is noteworthy that the vector $\vec{\phi}_i$ defines both, the shape of the displacements and the shape of the accelerations for the determination of the equivalent forces. This is the case because it is an eigenvector fulfilling the eigenvalue problem of equation (A2.1).

A2.1.2 Rayleigh Quotient

If a response spectrum analysis is performed, the natural frequencies of the MDOF system automatically result from the solution of the eigenvalue problem. However, in simplified procedures not including a modal analysis an alternative way to estimate the natural frequency of the system is required. In many cases it will be sufficient to determine the fundamental period of the first mode as this often tends to dominate the response. A common approximate method for the estimation of the first mode period is the *Rayleigh Quotient*, being essentially based on the relationship of equation (A2.2). For its application not the exact eigenvector $\vec{\phi}_1$ is used (as this is unknown), but rather an estimated shape vector is taken which is intended to approximate the real eigenvector.

While the exact vector $\vec{\phi}_1$, fulfilling the eigenvalue problem of equation (A2.1), defines both, the displacement shape as well as the acceleration shape for the lateral forces, an approximate vector cannot represent both. Therefore, in this case, it must be distinguished between an acceleration shape vector and a (different) displacement shape vector. For the computation of the *Rayleigh Quotient* initially an approximate acceleration shape vector $\tilde{\vec{\phi}}_{RQ,a}$ is assumed. Based on this vector a corresponding vector $\tilde{\vec{F}}_{RQ}$ of inertia forced can be computed according to equation (A2.11). Applying this force vector on the MDOF system in a linear static analysis, a corresponding displacement shape vector $\tilde{\vec{\phi}}_{RQ,u}$ according to equation (A2.12) can be computed. This displacement shape vector represents an improvement approximation of the eigenvector. Entering $\tilde{\vec{\phi}}_{RQ,u}$ into equation (A2.2), an estimation of the natural circular frequency $\tilde{\omega}_{RQ}$ and period $\tilde{T}_{RQ}$ can be computed as given by equation (A2.13).

$$\tilde{\vec{F}}_{RQ} = M \cdot \tilde{\vec{\phi}}_{RQ,a} \tag{A2.11}$$

$$\tilde{\vec{\phi}}_{RQ,u} = K^{-1} \tilde{\vec{F}}_{RQ} \tag{A2.12}$$

$$\tilde{\omega}_{RQ}^2 = \frac{\tilde{\vec{\phi}}_{RQ,u}^T K \tilde{\vec{\phi}}_{RQ,u}}{\tilde{\vec{\phi}}_{RQ,u}^T M \tilde{\vec{\phi}}_{RQ,u}} \qquad \Leftrightarrow \qquad \boxed{\tilde{\omega}_{RQ}^2 = \left(\frac{2\pi}{\tilde{T}_{RQ}}\right)^2 = \frac{\tilde{\vec{\phi}}_{RQ,u}^T \tilde{\vec{F}}_{RQ}}{\tilde{\vec{\phi}}_{RQ,u}^T M \tilde{\vec{\phi}}_{RQ,u}}} \tag{A2.13}$$

Generally, it is possible to iteratively improve the approximation for the eigenvector, and thus the estimation of the natural period. For this purpose, in the *m*-th iteration step the acceleration shape vector $\tilde{\vec{\phi}}_{RQ,a}^{(m)}$ is set equal to the displacement shape vector $\tilde{\vec{\phi}}_{RQ,u}^{(m-1)}$ of the previous, (*m*-1)-th, iteration step, as given by equation (A2.14). The improved force and displacement vectors, as well as the improved natural frequency of the *m*-th step then result from equations (A2.15) through (A2.17).

$$\tilde{\vec{\phi}}_{RQ,a}^{(m)} = \tilde{\vec{\phi}}_{RQ,u}^{(m-1)} \tag{A2.14}$$

$$\tilde{\vec{F}}_{RQ}^{(m)} = M \cdot \tilde{\vec{\phi}}_{RQ,a}^{(m)} \tag{A2.15}$$

$$\tilde{\vec{\phi}}_{RQ,u}^{(m)} = K^{-1} \tilde{\vec{F}}_{RQ}^{(m)} \tag{A2.16}$$

$$\left(\tilde{\omega}_{RQ}^{(m)}\right)^2 = \frac{\left(\tilde{\vec{\phi}}_{RQ,u}^{(m)}\right)^T K \tilde{\vec{\phi}}_{RQ,u}^{(m)}}{\left(\tilde{\vec{\phi}}_{RQ,u}^{(m)}\right)^T M \tilde{\vec{\phi}}_{RQ,u}^{(m)}} \quad \Leftrightarrow \quad \left(\tilde{\omega}_{RQ}^{(m)}\right)^2 = \left(\frac{2\pi}{\tilde{T}_{RQ}^{(m)}}\right)^2 = \frac{\left(\tilde{\vec{\phi}}_{RQ,u}^{(m)}\right)^T \tilde{\vec{F}}_{RQ}^{(m)}}{\left(\tilde{\vec{\phi}}_{RQ,u}^{(m)}\right)^T M \tilde{\vec{\phi}}_{RQ,u}^{(m)}} \tag{A2.17}$$

A2.1.3 Lateral Force Method

The lateral force method is an approach for the approximate estimation of the seismic demand of linear elastic MDOF systems. Its theoretical background can be deduced from the response spectrum analysis, introducing similar assumptions as for the computation of the Rayleigh quotient discussed in Section A2.1.2. The lateral force method results from the response spectrum analysis by introduction of the following three simplifying modifications:

(1) Only the response of the first mode is considered, assuming that this governs the overall response.

(2) The shape vector of the first mode is not computed exactly (as the eigenvector), but it is rather assumed as for the calculation of the Rayleigh quotient.

(3) To (partially) compensate for the deficiencies introduced by the first two simplifications, the activated mass in the first mode is artificially increased to the total mass of the system.

The reasoning for the third modification is related to the fact that, as shown in Section A2.1.1, the total base shear of the first mode in RSA is related to the corresponding effective modal mass of this mode. The remaining part of the total mass, not included in this effective modal mass, is excited in higher modes. As higher modes are ignored in the lateral force method, this deficit is intended to be compensated by assuming the entire system mass as activated in the first mode. On one hand, this influences the distribution of the forces related to the higher mode effective modal masses, as the first mode shape differs from that of the higher modes. On the other hand, in this approach the forces related to the higher mode effective modal masses are linearly additive, while in the response spectrum analysis a SRSS or CQC modal superposition would normally result in less than linear superposition.

The total base shear resulting from the lateral force method will therefore normally be higher than the superimposition of individual modal base shears in the response spectrum analysis. This can be interpreted as assuming a coincidental occurrence of all modal peak responses at the same time instant. While this assumption is obviously conservative concerning the sum of the masses, the results from the lateral force method nevertheless need not be a fully conservative approximation of the RSA response because the distribution of the forces in higher modes is not captured correctly. Especially on a local basis, certain demand underpredictions by the lateral force method therefore cannot be ruled out completely.

As the assumed shape factor will normally not be an eigenvector and thus does not fulfill the eigenvalue problem of equation (A2.1), it must be decided whether it is supposed to define the acceleration shape of the system or the corresponding displacement shape. For the lateral force method an acceleration shape vector $\tilde{\vec{\phi}}_{LFM,a}$ is assumed, in analogy to the Rayleigh quotient of Section A2.1.1. A corresponding participation factor $\tilde{\Gamma}_{LFM,a}$ and effective modal mass $\tilde{m}^{*}_{eff,a}$ can then be computed according to equations (A2.18) and (A2.19).

$$\tilde{\Gamma}_{LFM,a} = \frac{\vec{1}^{T} M \tilde{\vec{\phi}}_{LFM,a}}{\tilde{\vec{\phi}}^{T}_{LFM,a} M \tilde{\vec{\phi}}_{LFM,a}} = \frac{\vec{1}^{T} K \tilde{\vec{\phi}}_{LFM,a}}{\tilde{\vec{\phi}}^{T}_{LFM,a} K \tilde{\vec{\phi}}_{LFM,a}} \tag{A2.18}$$

$$\tilde{m}^{*}_{eff,a} = \tilde{\Gamma}_{LFM,a} \cdot \vec{1}^{T} M \tilde{\vec{\phi}}_{LFM,a} \tag{A2.19}$$

Following the above defined modification (2), the total base shear $\tilde{V}_{b}$ of the system must be based on an activated mass equal to the total mass m_{tot} of the system as given by equation (A2.20).

$$\tilde{V}_{b} = m_{tot} \cdot S_{a,el}\left(\tilde{T}, \xi\right) \tag{A2.20}$$

with $m_{tot} = \sum_{i=1}^{n} m_{i} = \vec{1}^{T} M \vec{1}$, i.e. sum of all masses

To achieve this increased total base shear, the individual forces, defined for RSA in equation (A2.7), must be multiplied by the ratio $m_{tot}/\tilde{m}^*_{eff,a}$. The resulting modified forces for the lateral force method then result according to equation (A2.21). Using the relationship between effective modal mass and participation factor, given in equation (A2.19), the expression for the lateral forces $\tilde{\tilde{F}}_{LFM}$ can be rewritten in the more common form shown in equation (A2.22).

$$\tilde{\tilde{F}}_{LFM} = \frac{m_{tot}}{\tilde{m}^*_{eff,a}} M \tilde{\tilde{\phi}}_{LFM,a} \cdot \tilde{\Gamma}_{LFM,a} \cdot S_{a,el}\left(\tilde{T},\xi\right) \tag{A2.21}$$

$$\boxed{\tilde{\tilde{F}}_{LFM} = M \tilde{\tilde{\phi}}_{LFM,a} \cdot \frac{m_{tot}}{\vec{1}^T M \tilde{\tilde{\phi}}_{LFM,a}} \cdot S_{a,el}\left(\tilde{T},\xi\right)} \tag{A2.22}$$

Applying the force vector $\tilde{\tilde{F}}_{LFM}$ on the system, the corresponding peak displacements $\tilde{\tilde{\Delta}}_{LFM}$ can subsequently be computed by means of a linear static analysis and result as given by equation (A2.23).

$$\boxed{\tilde{\tilde{\Delta}}_{LFM} = K^{-1}\tilde{\tilde{F}}_{LFM} = K^{-1}M\tilde{\tilde{\phi}}_{LFM,a} \cdot \frac{m_{tot}}{\vec{1}^T M \tilde{\tilde{\phi}}_{LFM,a}} \cdot S_{a,el}\left(\tilde{T},\xi\right)} \tag{A2.23}$$

Note that because $\tilde{\tilde{\phi}}_{LFM,a}$ does not fulfill the eigenvalue problem of equation (A2.1), the displacement vector <u>cannot</u> be computed directly in analogy to equation (A2.6), allowing for the increased base shear by multiplication with $m_{tot}/\tilde{m}^*_{eff,a}$. This is represented by inequation (A2.24).

$$\tilde{\tilde{\Delta}}_{LFM} \neq \frac{m_{tot}}{\tilde{m}^*_{eff}} \cdot \tilde{\tilde{\phi}}_{LFM,a} \cdot \tilde{\Gamma}_{LFM,a} \cdot S_{d,el}\left(\tilde{T},\xi\right) \tag{A2.24}$$

To formulate a relationship for the displacement vector that is similar to equation (A2.6), it is necessary to define an improved shape vector $\tilde{\tilde{\phi}}_{LFM,u}$ for the displacements as given by equation (A2.25). Based on $\tilde{\tilde{\phi}}_{LFM,u}$, the displacement vector resulting from the lateral force method can then be formulated as shown in equation (A2.26).

$$\tilde{\tilde{\phi}}_{LFM,u} = \tilde{\omega}^2 \cdot K^{-1}M\tilde{\tilde{\phi}}_{LFM,a} \tag{A2.25}$$

$$\tilde{\tilde{\Delta}}_{LFM} = \frac{m_{tot}}{\tilde{m}^*_{eff}} \cdot \tilde{\tilde{\phi}}_{LFM,u} \cdot \tilde{\Gamma}_{LFM,a} \cdot S_{d,el}\left(\tilde{T},\xi\right) \Rightarrow \quad \tilde{\tilde{\Delta}}_{LFM} = \tilde{\tilde{\phi}}_{LFM,u} \cdot \frac{m_{tot}}{\vec{1}^T M \tilde{\tilde{\phi}}_{LFM,a}} \cdot S_{d,el}\left(\tilde{T},\xi\right) \tag{A2.26}$$

For the practical application of the lateral force method an estimation of the first mode period $\tilde{T}$ is required in order to determine the elastic spectral pseudo-acceleration $S_{a,el}\left(\tilde{T},\xi\right)$ or displacement $S_{d,el}\left(\tilde{T},\xi\right)$. At the same time, as outlined above, an assumption for the acceleration shape vector $\tilde{\tilde{\phi}}_{LFM,a}$ is required. This assumption is not necessarily unique and in certain cases it might even be useful to consider more than one shape vector in order to allow for uncertainties concerning the influence of higher modes. For both purposes, the estimation of the natural period and for the estimation of an acceleration shape vector, it may be useful to combine the lateral force method with the concept of the Rayleigh quotient outlined in Section A2.1.1. Possible assumptions and combinations will be discussed below. It will be seen that the combination of lateral force method and Rayleigh quotient can also result in rather efficient solutions as certain synergies exist between the two concepts.

a) Load Distribution A:

If the Rayleigh quotient is used to estimate the fundamental period $\tilde{T}_{RQ}$ of the system, it is possible to use the same acceleration shape vector as for the computation of the Rayleigh quotient. As given by equation (A2.27), this means that the acceleration shape vector $\tilde{\vec{\phi}}_{LFM,a}$ for the lateral force method is set equal to the acceleration shape vector $\tilde{\vec{\phi}}_{RQ,a}$ used as input for the Rayleigh quotient. From equations (A2.28) and (A2.29) it can be seen that the corresponding participation factor $\tilde{\Gamma}_{LFM,a}$ and effective modal mass $\tilde{m}^*_{eff,a}$ then can be expressed by the already computed force vector $\tilde{\vec{F}}_{RQ}$ from the Rayleigh quotient.

$$\tilde{\vec{\phi}}_{LFM,a} = \tilde{\vec{\phi}}_{RQ,a} \tag{A2.27}$$

$$\tilde{\Gamma}_{LFM,a} = \frac{\vec{1}^T M \tilde{\vec{\phi}}_{RQ,a}}{\tilde{\vec{\phi}}^T_{RQ,a} M \tilde{\vec{\phi}}_{RQ,a}} = \frac{\vec{1}^T \tilde{\vec{F}}_{RQ}}{\tilde{\vec{\phi}}^T_{RQ,a} \tilde{\vec{F}}_{RQ}} \tag{A2.28}$$

$$\tilde{m}^*_{eff,a} = \tilde{\Gamma}_{LFM,a} \cdot \vec{1}^T M \tilde{\vec{\phi}}_{RQ,a} = \tilde{\Gamma}_{LFM,a} \cdot \vec{1}^T \tilde{\vec{F}}_{RQ} \tag{A2.29}$$

In a similar way, the force vector $\tilde{\vec{F}}_{LFM}$ for the lateral force method can also be expressed easily based on the force vector $\tilde{\vec{F}}_{RQ}$ from the Rayleigh quotient.

$$\tilde{\vec{F}}_{LFM} = \frac{m_{tot}}{\tilde{m}^*_{eff,a}} \cdot \tilde{\vec{F}}_{RQ} \cdot \tilde{\Gamma}_{RQ,a} \cdot S_{a,el}\left(\tilde{T}_{RQ}, \xi\right) \tag{A2.30}$$

$$\boxed{\tilde{\vec{F}}_{LFM} = \tilde{\vec{F}}_{RQ} \cdot \frac{m_{tot}}{\vec{1}^T \tilde{\vec{F}}_{RQ}} \cdot S_{a,el}\left(\tilde{T}_{RQ}, \xi\right)} \tag{A2.31}$$

The particular convenience of the approach comes into play when computing the corresponding system response, i.e. the displacement vector $\tilde{\vec{\Delta}}_{LFM}$ of the lateral force method according to equation (A2.32). Here, the linear static analysis performed for the determination of the Rayleigh quotient can be used. As shown by the rewritten form of $\tilde{\vec{\Delta}}_{LFM}$ in equation (A2.33), it is possible to use the displacement shape vector $\tilde{\vec{\phi}}_{RQ,u}$ from the Rayleigh quotient for the direct computation of $\tilde{\vec{\Delta}}_{LFM}$ without any further static analysis. Alternative expressions for $\tilde{\vec{\Delta}}_{LFM}$ are given in equations (A2.34) and (A2.35). The fact that no additional static analysis is required makes the approach not only convenient, but also very efficient in its application.

$$\tilde{\vec{\Delta}}_{LFM} = K^{-1} \tilde{\vec{F}}_{LFM} = K^{-1} \tilde{\vec{F}}_{RQ} \cdot \frac{m_{tot}}{\vec{1}^T \tilde{\vec{F}}_{RQ}} \cdot S_{a,el}\left(\tilde{T}_{RQ}, \xi\right) \tag{A2.32}$$

$$\boxed{\tilde{\vec{\Delta}}_{LFM} = \tilde{\vec{\phi}}_{RQ,u} \cdot \frac{m_{tot}}{\vec{1}^T \tilde{\vec{F}}_{RQ}} \cdot S_{a,el}\left(\tilde{T}_{RQ}, \xi\right)} \quad \Leftrightarrow \quad \tilde{\vec{\Delta}}_{LFM} = \tilde{\vec{\phi}}_{RQ,u} \cdot \tilde{\omega}^2_{RQ} \cdot \frac{m_{tot}}{\vec{1}^T \tilde{\vec{F}}_{RQ}} \cdot S_{d,el}\left(\tilde{T}_{RQ}, \xi\right) \tag{A2.33}$$

$$\tilde{\vec{\phi}}_{LFM,u} = \tilde{\omega}^2_{RQ} \cdot \tilde{\vec{\phi}}_{RQ,u} \tag{A2.34}$$

$$\tilde{\vec{\Delta}}_{LFM} = \tilde{\vec{\phi}}_{LFM,u} \cdot \frac{m_{tot}}{\vec{1}^T \tilde{\vec{F}}_{RQ}} \cdot S_{d,el}\left(\tilde{T}_{RQ}, \xi\right) \tag{A2.35}$$

b) Load Distribution B:

As an alternative to load distribution A, it can also be chosen to use the displacement shape vector $\tilde{\tilde{\phi}}_{RQ,u}$ from the Rayleigh quotient to compute the force distribution in the lateral force method. This means that the acceleration shape vector $\tilde{\tilde{\phi}}_{LFM,a}$ for the lateral force method is set equal to $\tilde{\tilde{\phi}}_{RQ,u}$, as given by equation (A2.36). This assumption can be expected to result in a somewhat better approximation of the first mode shape, as $\tilde{\tilde{\phi}}_{RQ,u}$ essentially represents the next step of the iterative procedure described in Section A2.1.2 for the improved estimation of the first mode properties. Whether it is really desirable to achieve a force distribution similar to that of the first mode shape needs to be decided separately.

$$\tilde{\tilde{\phi}}_{LFM,a} = \tilde{\tilde{\phi}}_{RQ,u} \tag{A2.36}$$

As no static analysis for a force distribution based on $\tilde{\tilde{\phi}}_{RQ,u}$ has been performed during the computation of the Rayleigh quotient, it is not possible to benefit from any synergies if load distribution B is chosen. As a consequence, the general procedure outlined by equations (A2.18) through (A2.26) must be followed. This includes an additional linear static analysis corresponding to equation (A2.23).

c) Load Distribution C:

Independent of the assumptions for the Rayleigh quotient, a special case results if a uniform acceleration shape is used for the lateral force method as defined by equation (A2.37). In this case, the participation factor according to equation (A2.38) results as unity and the effective modal mass according to equation (A2.39) becomes equal to the total system mass. It is noteworthy that in this case the ratio $m_{tot}/\tilde{m}^*_{eff,a}$, which is used to increase the lateral forces in equation (A2.21), also becomes unity. This means that the uniform acceleration shape of equation (A2.37) already activates the entire system mass and a further increase in the lateral force method is not necessary.

$$\tilde{\vec{\phi}}_{LFM,a} = \vec{1} \tag{A2.37}$$

$$\tilde{\Gamma}_{LFM,a} = 1 \tag{A2.38}$$

$$\tilde{m}^*_{eff,a} = \vec{1}^T M \vec{1} = m_{tot} \tag{A2.39}$$

As a consequence, the force vector is simplified according to equation (A2.40) and the total base shear results as given by the simple expression of equation (A2.41). The corresponding displacement demand can then be computed based on a linear static analysis, as given by equation (A2.42) or the alternative representation of equations (A2.43) and (A2.44).

$$\boxed{\tilde{\vec{F}}_{LFM} = M\vec{1} \cdot S_{a,el}\left(\tilde{T},\xi\right)} \tag{A2.40}$$

$$\boxed{V_b = \tilde{m}^*_{eff,a} \cdot S_{a,el}\left(\tilde{T},\xi\right) = m_{tot} \cdot S_{a,el}\left(\tilde{T},\xi\right)} \tag{A2.41}$$

$$\boxed{\tilde{\vec{\Delta}}_{LFM} = K^{-1}\tilde{\vec{F}}_{LFM} = K^{-1}M\vec{1}^T \cdot S_{a,el}\left(\tilde{T},\xi\right)} \tag{A2.42}$$

$$\tilde{\vec{\phi}}_{LFM,u} = \tilde{\omega}^2 \cdot K^{-1}M\vec{1} \tag{A2.43}$$

$$\tilde{\vec{\Delta}}_{LFM} = \tilde{\vec{\phi}}_{LFM,u} \cdot S_{d,el}\left(\tilde{T},\xi\right) \tag{A2.44}$$

A special case exists if the Rayleigh quotient has also been computed based on the same uniform acceleration shape vector, i.e. if equation (A2.45) applies. In this case, *load distribution C* also represents *load distribution A*. Based on the force vector from the Rayleigh quotient, then the very simple expression given in equation (A2.46) for the force distribution results. Using further the displacement shape vector from the Rayleigh quotient, the displacement demand according to the lateral force method can readily be determined by the very simple equation (A2.47). An alternative representation for the displacement demand can be formulated as given by equations (A2.48) and (A2.49).

$$\tilde{\vec{\phi}}_{RQ,a} = \tilde{\vec{\phi}}_{LFM,a} = \vec{1} \tag{A2.45}$$

$$\tilde{\vec{F}}_{LFM} = \tilde{\vec{F}}_{RQ} \cdot S_{a,el}\left(\tilde{T},\xi\right) \tag{A2.46}$$

$$\tilde{\vec{\Delta}}_{LFM} = \tilde{\vec{\phi}}_{RQ,u} \cdot S_{a,el}\left(\tilde{T},\xi\right) \tag{A2.47}$$

$$\tilde{\vec{\phi}}_{LFM,u} = \tilde{\omega}^2 \cdot \tilde{\vec{\phi}}_{RQ,u} \tag{A2.48}$$

$$\tilde{\vec{\Delta}}_{LFM} = \tilde{\vec{\phi}}_{LFM,u} \cdot S_{d,el}\left(\tilde{T},\xi\right) \tag{A2.49}$$

A2.2 Nonlinear Static Methods

A2.2.1 Pushover Analysis

The so-called pushover analysis is a nonlinear static analysis concept for the seismic demand estimation of inelastic MDOF structures. The conventional pushover analysis is based on the assumption that the inelastic MDOF system can be transformed into an equivalent inelastic SDOF system. For this SDOF system the peak displacement demand can be estimated, e.g. using principles as those outlined in Section 4.5. Subsequently, the response of the inelastic SDOF system is retransformed to the MDOF system by inversion of the previous transformation relationships, thus resulting in an estimation of the inelastic MDOF displacement demand. As a consequence, the conventional pushover analysis consists of two key principles:

(i)   A concept for the transformation process between the inelastic MDOF system and the corresponding equivalent SDOF system.

(ii) An approach to estimate the seismic demand of an inelastic SDOF system.

These two issues are rather independent of each other, so that different approaches for the two components can theoretically be combined freely, resulting in a variety of potential interpretations. As the concepts for the second part, i.e. the demand estimation of the inelastic SDOF system, have already been presented in Section 4.5, the following discussion will only focus on the transformation between MDOF and equivalent SDOF system.

The equivalent SDOF representation in conventional pushover analysis, as described for example in [Fre98], [KS98], [Faj00], and [FGD97], is based on two principal assumptions:

(1)   The seismic response of the MDOF system is governed by some kind of a predominant inelastic first mode.

(2)   The vibration in this assumed mode can be approximated by a constant acceleration shape vector.

During recent decades a considerable number of conceptual variations have been developed which drop at least one of these two assumptions, in order to either allow for higher mode effects or adapt the assumed mode shape in order to take inelastic stiffness variations into account. At the same time, these improved procedures also become more complex concerning theoretical background and applicability. To some extent, they therefore lose some of their simplistic convenience. In this section, only the concepts of the conventional pushover analysis, considering both of the mentioned assumptions, will be discussed. It should be noted that the procedures presented in [Fre98], [KS98], [Faj00], and [FGD97] share the same principles. Although the individual relationships for the determination of the equivalent SDOF system might differ between some of these literature sources, if applied consistently during the transformation and the subsequent retransformation to the original MDOF system again, all four approaches represent the same concept and give the same results.

In this section, a concept corresponding to the equivalent SDOF representation in the *capacity spectrum method* by Freeman [Fre98] will be presented. The method will be presented in a general form for inelastic systems. To visualize its theoretical roots in elastic modal and response spectrum analysis, the various assumptions and relationships will also be given in separate boxes for the assumption of linear elastic system behavior. This way, it can be seen how the method converges for the special case of a linear elastic MDOF system. At the same time, the given relationships also apply in the elastic range up to nominal yield of a system with a bilinearized inelastic behavior.

a) Transformation of the MDOF System into an Equivalent SDOF System

Approximation 1:

A (constant) acceleration shape vector $\tilde{\vec{\phi}}_{PO,a}$ is assumed for the representation of the inelastic MDOF response, in accordance with assumptions (1) and (2) mentioned above. This approximation is similar to those made for linear elastic systems when computing of the Rayleigh quotient or in the lateral force method (see Sections A2.1.2 and A2.1.3).

A corresponding participation factor and effective modal mass can be determined according to equations (A2.50) and (A2.51).

$$\tilde{\Gamma}_{PO,a} = \frac{\vec{1}^T M \tilde{\vec{\phi}}_{PO,a}}{\tilde{\vec{\phi}}_{PO,a}^T M \tilde{\vec{\phi}}_{PO,a}} \tag{A2.50}$$

$$\tilde{m}_{eff,a}^* = \tilde{\Gamma}_{PO,a} \cdot \vec{1}^T M \tilde{\vec{\phi}}_{PO,a} \tag{A2.51}$$

Based on the assumption that $\tilde{\vec{\phi}}_{PO,a}$ represents the relative acceleration shape at every time instant during the seismic response, the distribution of the inertia forces, $\tilde{\vec{F}}_{PO,MDOF}$, can be formulated in the general form of equation (A2.52) as a function of the parameter β. During the seismic response, β is time-dependent, i.e. $\beta = \beta(t)$. The corresponding base shear of the MDOF system results as given by equation (A2.53).

$$\tilde{\vec{F}}_{PO,MDOF}(\beta) = \beta \cdot M \tilde{\vec{\phi}}_{PO,a} \tag{A2.52}$$

$$V_{b,PO} = \vec{1}^T \vec{F}_{PO,MDOF} = \beta \cdot \vec{1}^T M \tilde{\vec{\phi}}_{PO,a} \tag{A2.53}$$

Performing an inelastic static analysis applying the forces $\tilde{\vec{F}}_{PO,MDOF}$ of equation (A2.52) for increasing values of the parameter β, the corresponding displacement vector $\tilde{\vec{\Delta}}_{PO,MDOF}$ according to equation (A2.54) can be computed. As a result, a parameterized relationship between the force vector and the displacement vector results. It is common to define one characteristic point within the MDOF structure as a *reference point*, whose displacements are supposed to represent the deformations of the entire MDOF system. While for buildings typically the point at the top of the structure (i.e. the roof) is chosen, [EC8-2] suggests for bridges the use of the superstructure center of mass as reference point. A reasonable assumption might also be the point of anticipated maximum deformation (e.g. estimated from a preceding linear response spectrum or lateral force method analysis). If the reference point has the *k*-th degree of freedom of the system, its displacement $\tilde{\Delta}_{PO,MDOF,ref}$ as a function of the parameter β is given by equation (A2.55).

$$\tilde{\vec{\Delta}}_{PO,MDOF}(\beta) = \tilde{\vec{\Delta}}_{PO,MDOF}\left(\tilde{\vec{F}}_{PO,MDOF}(\beta)\right) \tag{A2.54}$$

$$\tilde{\Delta}_{PO,MDOF,ref}(\beta) = \tilde{\Delta}_{PO,MDOF,k}\left(\tilde{\vec{F}}_{PO,MDOF}(\beta)\right) \tag{A2.55}$$

Based on these relationships, a pushover curve of the MDOF system can be defined. This pushover curve represents the displacement $\tilde{\Delta}_{PO,MDOF,ref}$ of the reference point as a function of the total base shear $V_{b,PO}$ of the system. Although this relationship can normally only be determined in a parameterized form, a graphical representation, as shown on the left side of Fig. A2.1, is nevertheless possible.

For linear elastic behavior, the displacement vector can be computed based on a linear static analysis according to equation (A2.56).

$$\tilde{\tilde{\Delta}}_{PO,MDOF}\left(\beta\right) = K^{-1}\tilde{\tilde{F}}_{PO,MDOF}\left(\beta\right) = \beta \cdot K^{-1}M\tilde{\tilde{\phi}}_{PO,a} \tag{A2.56}$$

In this case, it is also possible to define a corresponding displacement shape vector $\tilde{\tilde{\phi}}_{PO,u}$, according to equation (A2.57), so that the displacement vector can be formulated as given by equation (A2.58).

$$\tilde{\tilde{\phi}}_{PO,u} = K^{-1}M\tilde{\tilde{\phi}}_{PO,a} \tag{A2.57}$$

$$\tilde{\tilde{\Delta}}_{PO,MDOF}\left(\beta\right) = \beta \cdot \tilde{\tilde{\phi}}_{PO,u} \tag{A2.58}$$

Approximation 2:

If the acceleration shape vector $\tilde{\tilde{\phi}}_{PO,a}$ were an eigenvector of a linear elastic system, then the dynamic response of the MDOF in the corresponding eigenmode can be related to the response of an *equivalent SDOF system* having the same period as this mode and being excited by the same ground motions, as given by equation (A2.59). If $\tilde{\tilde{\phi}}_{PO,a}$ is not an eigenvector, the displacement shape will normally deviate from the acceleration shape vector. Moreover, for an inelastic system, strictly speaking, no individual modal response with corresponding mode shapes exists, so that equation (A2.59) cannot be considered as fully accurate. Nevertheless, as an approximation, it is assumed that also for inelastic MDOF systems with a reasonable choice for $\tilde{\tilde{\phi}}_{PO,a}$ a relationship similar to that of equation (A2.59) exists, which relates the response of the MDOF system to that of a fictional *equivalent SDOF system*.

$$\tilde{\tilde{\Delta}}_{PO,MDOF}\left(t\right) = \tilde{\tilde{\phi}}_{PO,a}\tilde{\Gamma}_{PO,a}\Delta_{SDOF}\left(t\right) \tag{A2.59}$$

Multiplying equation (A2.59) from the left side with any (arbitrary) vector $\vec{v}^{T}$ it is possible to solve the equation for the displacement u_{SDOF} of the equivalent SDOF system. Expressing the variability of the response by the (time-dependent) parameter β, the corresponding relationship for Δ_{SDOF} is given by equation (A2.60).

$$\Delta_{SDOF}\left(\beta\right) = \frac{\vec{v}^{T}\tilde{\tilde{\Delta}}_{PO,MDOF}\left(\beta\right)}{\vec{v}^{T}\tilde{\tilde{\phi}}_{PO,a}\tilde{\Gamma}_{PO,a}} \tag{A2.60}$$

While for a real constant (relative) shape of the displacement vector $\tilde{\tilde{\Delta}}_{MDOF}$ any choice of $\vec{v}^{T}$ yields the same result for Δ_{SDOF}, this is not true for an inelastic system where the shape of the displacement vector changes with increasing load level. In pushover analysis it is common to choose $\vec{v}^{T}$ in a way, so that it isolates the *k*-th degree of freedom, representing the previously defined *reference point*. If $\vec{v}^{T}$ is chosen correspondingly, as given by equation (A2.61), then the displacement Δ_{SDOF} of the equivalent SDOF system can be computed from the displacement of the reference point $\tilde{\Delta}_{PO,MDOF,ref}$, as given by equation (A2.62).

$$\vec{v}^{T} = \begin{bmatrix} 0 & \dots & 0 & 1 & 0 & \dots & 0 \end{bmatrix} \tag{A2.61}$$

$$\underset{\text{\textemdash}\ k\text{-th degree of freedom}}{\uparrow}$$

$$\Delta_{SDOF}\left(\beta\right) = \frac{\tilde{\Delta}_{PO,MDOF,k}\left(\beta\right)}{\tilde{\phi}_{PO,a,k}\tilde{\Gamma}_{PO,a}} \qquad \Leftrightarrow \qquad \boxed{\Delta_{SDOF}\left(\beta\right) = \frac{\tilde{\Delta}_{PO,MDOF,ref}\left(\beta\right)}{\tilde{\phi}_{PO,a,ref}\tilde{\Gamma}_{PO,a}}} \tag{A2.62}$$

with $\quad \tilde{\Delta}_{PO,MDOF,k}$ and $\tilde{\phi}_{PO,a,k}$ being the *k*-th elements of $\tilde{\tilde{\Delta}}_{PO,MDOF}$ and $\tilde{\tilde{\phi}}_{PO,a}$, respectively

For linear elastic behavior, equation (A2.56) can be introduced into the general equation (A2.60), resulting in equation (A2.63). Using the previously defined displacement shape vector $\tilde{\tilde{\phi}}_{PO,u}$, this relationship can be rewritten in the form of equation (A2.64).

$$\Delta_{SDOF}(\beta) = \frac{\beta}{\tilde{\Gamma}_{PO,a}} \cdot \frac{\vec{v}^T K^{-1} M \tilde{\tilde{\phi}}_{PO,a}}{\vec{v}^T \tilde{\phi}_{PO,a}} \tag{A2.63}$$

$$\Delta_{SDOF}(\beta) = \frac{\beta}{\tilde{\Gamma}_a} \cdot \frac{\vec{v}^T \tilde{\tilde{\phi}}_u}{\vec{v}^T \tilde{\tilde{\phi}}_a} \tag{A2.64}$$

For linear elastic behavior, any choice of $\vec{v}^T$ will yield the same result for Δ_{SDOF}. A particularly convenient solution for Δ_{SDOF} results if $\vec{v}^T$ is chosen according to equation (A2.65). In this case, the displacement of the equivalent SDOF system results as given by equation (A2.66).

$$\vec{v}^T = \tilde{\tilde{\phi}}_{PO,u}^T M \tag{A2.65}$$

$$\Delta_{SDOF}(\beta) = \frac{\beta}{\tilde{\Gamma}_{PO,a}} \cdot \frac{\tilde{\tilde{\phi}}_{PO,u}^T M \tilde{\tilde{\phi}}_{PO,u}}{\tilde{\tilde{\phi}}_{PO,u}^T M \tilde{\tilde{\phi}}_{PO,a}} \quad \Rightarrow \quad \Delta_{SDOF}(\beta) = \frac{\beta}{\tilde{\Gamma}_{PO,a}} \cdot \frac{\tilde{\tilde{\phi}}_{PO,u}^T M \tilde{\tilde{\phi}}_{PO,u}}{\tilde{\tilde{\phi}}_{PO,u}^T K \tilde{\tilde{\phi}}_{PO,u}} \tag{A2.66}$$

Note that, if the Rayleigh quotient is computed using the same acceleration shape vector $\tilde{\tilde{\phi}}_{RQ,a} = \tilde{\tilde{\phi}}_{PO,a}$ as that used in the pushover analysis, the corresponding displacement shape vector $\tilde{\tilde{\phi}}_{RQ,u}$ of the Rayleigh quotient also results equal to the displacement shape vector $\tilde{\tilde{\phi}}_{PO,u}$ of the pushover analysis, as given by equation (A2.67).

$$\tilde{\tilde{\phi}}_{RQ,u} = K^{-1} M \tilde{\tilde{\phi}}_{RQ,a} = \tilde{\tilde{\phi}}_{PO,u} \tag{A2.67}$$

As a consequence, the estimation of the natural circular frequency $\tilde{\omega}_{MDOF,RQ}$ based on the Rayleigh quotient results as given by equation (A2.68).

$$\tilde{\omega}_{MDOF,RQ}^2 = \frac{\tilde{\tilde{\phi}}_{PO,u}^T K \tilde{\tilde{\phi}}_{PO,u}}{\tilde{\tilde{\phi}}_{PO,u}^T M \tilde{\tilde{\phi}}_{PO,u}} \tag{A2.68}$$

By comparison with equation (A2.66) the very simple expression for the SDOF displacement as a function of the parameter b results as given by equation (A2.69).

$$\Delta_{SDOF}(\beta) = \frac{\beta}{\tilde{\Gamma}_{PO,a} \cdot \tilde{\omega}_{MDOF,RQ}^2} \tag{A2.69}$$

Definition:

It is defined that the force response F_{SDOF} of the equivalent SDOF system, for a given parameter β, shall be equal to the total base shear of the MDOF system and consequently results as given by equation (A2.70).

$$\boxed{F_{SDOF}\left(\beta\right) = \tilde{V}_{b,PO}\left(\beta\right) = \beta \cdot \vec{1}^T M \tilde{\bar{\phi}}_{PO,a}} \tag{A2.70}$$

Based on the thus defined force of the equivalent SDOF system and the corresponding displacement according to equation (A2.62), the transformed pushover curve for the SDOF system can be drawn, as depicted on the right side of Fig. A2.1. It is often useful to bilinearize the curved force-displacement relationship in order to define a nominal yield point, characterized by the nominal force capacity $F_{SDOF,n}$ and the nominal yield displacement $\Delta_{SDOF,y}$. The corresponding initial stiffness $k_{SDOF,0}$ results as the ratio of the previous two quantities. It should be noted that the bilinearization of a curved force-displacement relationship – especially if coming from a MDOF pushover analysis – may be neither straightforward nor unique in a given case. Aside from a simple engineering judgment assumption, several more theoretically based approaches are conceivable for this task. For example, Eurocode 8, part 1 [EC8-1], Annex B recommends choosing the bilinear approximation so as to provide the same deformation energy as in the original curve. This means that the area below the two curves on the right side of Fig. A2.1 shall be equal.
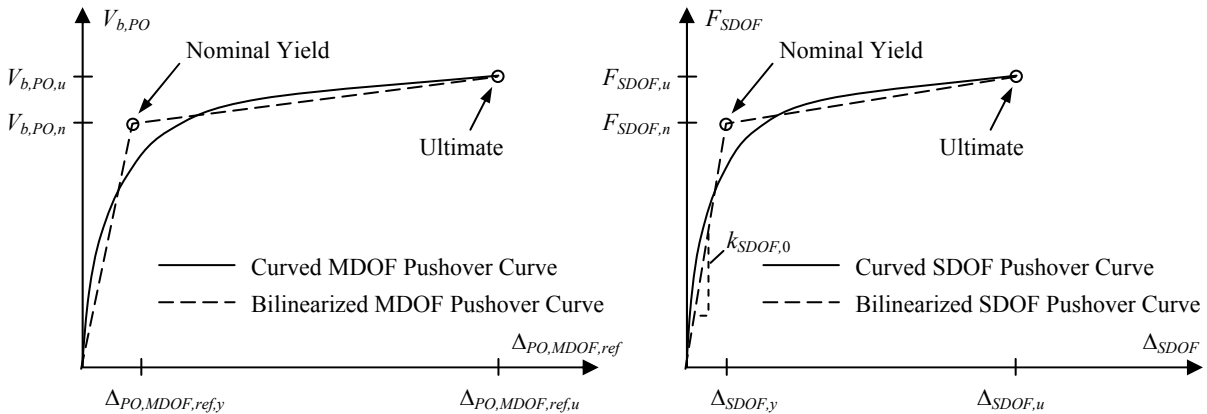
Fig. A2.1: Inelastic pushover curve and corresponding bilinearization
left: Total base shear vs. reference point displacement for MDOF system, right: Equivalent SDOF system

For linear elastic behavior, the force F_{SDOF} of the equivalent SDOF system, given by equation (A2.70), can be expressed defined by equation (A2.71).

$$F_{SDOF}\left(\beta\right) = \beta \cdot \vec{1}^T K \tilde{\bar{\phi}}_{PO,u} \tag{A2.71}$$

Based on the SDOF displacement according to equation (A2.69), subsequently follows the stiffness k_{SDOF} of the equivalent SDOF as given by equation (A2.72).

$$k_{SDOF} = \frac{F_{SDOF}}{\Delta_{SDOF}} = \vec{1}^T K \tilde{\bar{\phi}}_{PO,u} \cdot \tilde{\Gamma}_{PO,a} \cdot \tilde{\omega}_{MDOF,RQ}^2 \quad \Leftrightarrow \quad k_{SDOF} = \vec{1}^T M \tilde{\bar{\phi}}_{PO,a} \cdot \tilde{\Gamma}_{PO,a} \cdot \tilde{\omega}_{MDOF,RQ}^2 \tag{A2.72}$$

This relationship can be conveniently expressed by the very simple equation (A2.73).

$$k_{SDOF} = \tilde{m}_{eff,a}^* \cdot \tilde{\omega}_{MDOF,RQ}^2 \tag{A2.73}$$

Postulation:

To ensure that the equivalent SDOF system is representative of the MDOF structure in the demand estimation process, e.g. using a response spectrum, it is required that both systems shall have the same initial circular frequency ω_0. Estimating the elastic circular frequency of the MDOF system based on the Rayleigh quotient according to equation (A2.68), the requirement defined by equation (A2.74) results.

$$\omega_{SDOF,0}^2 = \frac{k_{SDOF,0}}{m_{SDOF}} = \tilde{\omega}_{MDOF,RQ,0}^2 \tag{A2.74}$$

Solving for the mass m_{SDOF} of the equivalent SDOF system and introducing the elastic SDOF stiffness $k_{SDOF,0}$ corresponding to equation (A2.73), The relationship given in equation (A2.75) follows. Hence, it can be seen that the SDOF mass m_{SDOF} must be set equal to the effective modal mass $\tilde{m}_{eff,a}^*$ of the MDOF system corresponding to the acceleration shape vector $\tilde{\tilde{\phi}}_{PO,a}$, in order to achieve equal natural frequencies between the MDOF and the equivalent SDOF system.

$$\boxed{m_{SDOF} = \frac{k_{SDOF,0}}{\omega_{SDOF,0}^2} = \frac{k_{SDOF,0}}{\tilde{\omega}_{MDOF,RQ,0}^2} = \tilde{m}_{eff,a}^*} \tag{A2.75}$$

Summary transformation from MDOF system to equivalent SDOF system:

Based on the previous deductions, all relationships are provided that are required for the transformation of the inelastic MDOF response to that of an equivalent SDOF system. Any general nonlinear force-displacement relationship between the displacement $\tilde{\Delta}_{PO,MDOF,ref}$ of the reference point and the total base shear $\tilde{V}_{b,PO}$ can be transformed into a corresponding SDOF pushover curve by means of equations (A2.62) and (A2.70). To achieve equal elastic periods between the two systems, the mass m_{SDOF} of the equivalent SDOF system must be chosen equal to the effective modal mass $\tilde{m}_{eff,a}^*$ of the MDOF system, as defined by equation (A2.75).

b) Estimation of Seismic Displacement Demand for Equivalent SDOF System

Any method capable of estimating the seismic displacement demand Δ_{inel} of an inelastic SDOF system can be applied, using the nonlinear force-displacement relationship (i.e. the pushover curve) of the equivalent SDOF system. If a bilinearization of the behavior is performed, the initial period $\tilde{T}_{SDOF,0}$ and the nominal yield strength $F_{SDOF,n}$ can be estimated. Using an elastic response spectrum, then the elastic spectral displacement $S_{d,el}$ and pseudo-acceleration $S_{a,el}$ can be determined, which allows the subsequent calculation of the strength ratio R_y. Based on the principles outlined in Section 4.5, then it is possible to compute a displacement modification factor C_R and use it for the estimation of the inelastic peak displacement $\Delta_{SDOF} = \Delta_{inel}$, as given by equation (A2.76).

$$\Delta_{SDOF} = \Delta_{inel} \qquad \text{, e.g. with:} \qquad \Delta_{inel} = C_R \cdot S_{d,el}\left(\tilde{\omega}_{SDOF,0}, \xi\right) \tag{A2.76}$$

For linear elastic system behavior, the displacement demand of the equivalent SDOF system can be estimated directly from the elastic displacement spectrum, as shown by equation (A2.77), and the force demand results as given by equation (A2.78).

$$\Delta_{SDOF} = S_{d,el}\left(\tilde{\omega}_{SDOF}, \xi\right) \tag{A2.77}$$

$$F_{SDOF} = m_{SDOF} \cdot S_{a,el}\left(\tilde{\omega}_{SDOF}, \xi\right) = \tilde{m}_{eff,a}^* \cdot S_{a,el}\left(\tilde{\omega}_{SDOF}, \xi\right) \tag{A2.78}$$

c) Retransformation of the Seismic Displacement Demand from the Equivalent SDOF System back to the Original MDOF System

The retransformation to the MDOF system is performed by means of the response parameter β. For this purpose the value of β is determined which corresponds to the estimated SDOF displacement Δ_{SDOF} on the inelastic pushover curve, shown on the right side of Fig. A2.1. The force vector $\tilde{\tilde{F}}_{PO,MDOF}$ can now be computed from this β value based on equation (A2.52). Any further MDOF system action or deformation then results from an inelastic static analysis of the structure under applied forces $\tilde{\tilde{F}}_{PO,MDOF}$. This analysis does not need to be performed anymore as it has already been conducted during the transformation into the equivalent SDOF system discussed in Subsection a. In particular, the displacement demand vector of the MDOF system is given by equation (A2.54) for the determined parameter β. With this, an estimation of the entire seismic peak response of the MDOF system is readily available.

For linear elastic system behavior, equation (A2.69) represents an explicit linear relationship between Δ_{SDOF} and the parameter β. Further considering equation (A2.77), it is possible to directly compute the corresponding β value as shown by equation (A2.79).

$$\beta = \tilde{\Gamma}_{PO,a} \cdot \tilde{\omega}_{MDOF,RQ}^2 \cdot S_{d,el}\left(\tilde{\omega}_{MDOF,RQ},\xi\right) \quad \Leftrightarrow \quad \beta = \tilde{\Gamma}_{PO,a} \cdot S_{a,el}\left(\tilde{\omega}_{MDOF,RQ},\xi\right) \qquad \text{(A2.79)}$$

The displacement vector $\tilde{\tilde{\Delta}}_{PO,MDOF}$ of the MDOF system can then be determined using equations (A2.56) through (A2.58). Various possible representations for $\tilde{\tilde{\Delta}}_{PO,MDOF}$ result as given by equations (A2.80) through (A2.83).

$$\tilde{\tilde{\Delta}}_{PO,MDOF} = \tilde{\tilde{\phi}}_{PO,u} \cdot \tilde{\Gamma}_{PO,a} \cdot \tilde{\omega}_{MDOF,RQ}^2 \cdot S_{d,el}\left(\tilde{\omega}_{MDOF,RQ},\xi\right) \qquad \text{(A2.80)}$$

$$\tilde{\tilde{\Delta}}_{PO,MDOF} = \tilde{\tilde{\phi}}_{PO,u} \cdot \tilde{\Gamma}_{PO,a} \cdot S_{a,el}\left(\tilde{\omega}_{MDOF,RQ},\xi\right) \qquad \text{(A2.81)}$$

$$\tilde{\tilde{\Delta}}_{PO,MDOF} = K^{-1}M\tilde{\tilde{\phi}}_{PO,a} \cdot \tilde{\Gamma}_{PO,a} \cdot \tilde{\omega}_{MDOF,RQ}^2 \cdot S_{d,el}\left(\tilde{\omega}_{MDOF,RQ},\xi\right) \qquad \text{(A2.82)}$$

$$\boxed{\tilde{\tilde{\Delta}}_{PO,MDOF} = K^{-1}M\tilde{\tilde{\phi}}_{PO,a} \cdot \tilde{\Gamma}_{PO,a} \cdot S_{a,el}\left(\tilde{\omega}_{MDOF,RQ},\xi\right)} \qquad \text{(A2.83)}$$

The corresponding MDOF force vector $\tilde{\tilde{F}}_{PO,MDOF}$ can be computed by introducing the parameter β from equation (A2.79) into the definition of $\tilde{\tilde{F}}_{PO,MDOF}$ according to equation (A2.52), resulting in the solution given in equation (A2.84).

$$\boxed{\tilde{\tilde{F}}_{PO,MDOF} = M\tilde{\tilde{\phi}}_{PO,a} \cdot \tilde{\Gamma}_{PO,a} \cdot S_{a,el}\left(\tilde{\omega}_{MDOF,RQ},\xi\right)} \qquad \text{(A2.84)}$$

Correspondingly, the total base shear of the MDOF system, being equal to the force demand of the equivalent SDOF system, results as given by equation (A2.85).

$$\tilde{V}_{b,MDOF}\left(\beta\right) = \tilde{m}_{eff,a}^* \cdot S_{a,el}\left(\tilde{\omega}_{MDOF,RQ},\xi\right) \qquad \text{(A2.85)}$$

A2.3 Comparison of Methods

For the interpretation and evaluation of the simplified procedures presented in the Sections A2.1 and A2.2 of this Annex it is interesting to investigate how they develop under certain limiting conditions. In particular, it is interesting to study whether they converge to one another under equal conditions. This refers, for example, to the question how the results from the pushover analysis relate to those from the response spectrum analysis and lateral force method if applied on a linear elastic structure.

If the system behavior is linear elastic and the assumed acceleration shape vector $\tilde{\tilde{\phi}}_{PO,a}$ used in the pushover analysis is the eigenvector of the first mode, fulfilling equation (A2.1), then it can be seen that the natural circular frequency computed by the pushover analysis based on (A2.86) becomes equal to the first mode circular frequency as following from the response spectrum analysis according to (A2.2). Furthermore, by comparison of equation (A2.83) with equation (A2.9) it can be seen that the deformation demand computed by the pushover analysis equals exactly the first mode deformations from the response spectrum analysis. Comparing equation (A2.84) with (A2.9) and equation (A2.85) with (A2.10), it follows that under these conditions the same holds true for the lateral inertia forces and for the corresponding total base shear. It can therefore be concluded that for a linear elastic system and an assumed acceleration shape vector equal to the first mode shape, the pushover analysis converges towards the first mode results from the response spectrum analysis. It is important to note that the higher modes, which would be superimposed using the SRSS or CQC rule in the response spectrum analysis, are <u>not</u> included in the conventional pushover analysis as presented in Section A2.2.1.

If the system behavior is linear elastic, but the chosen acceleration shape vector $\tilde{\tilde{\phi}}_{PO,a}$ is not an eigenvector according to equation (A2.1), then the circular frequency determined using equation (A2.87) from the pushover analysis results equal to the one from the Rayleigh quotient according to equation (A2.13) if the same acceleration shape vector is used. However, comparing equations (A2.84) from the pushover analysis to equation (A2.21) from the lateral force method, it can be seen that the lateral forces corresponding to the former do not result equal to those from the latter. The difference is related to the increasing factor $m_{tot}/\tilde{m}^*_{eff,a}$ introduced in the lateral force method, but not considered in the pushover analysis. An equivalent difference subsequently results between the deformation demand (compare equations (A2.83) and (A2.23)) and the total base shear (compare equations (A2.85) (A2.20)) computed by the two different methods.

By this comparison, which might also have relevance for inelastic systems with rather low ductility demands, it can be concluded that the conventional pushover analysis only captures the first mode response. The lateral force method, that does not (explicitly) capture higher modes either, uses the entire system mass for the determination of the forces, which implicitly corresponds to an increase by a factor of $m_{tot}/\tilde{m}^*_{eff,a}$ compared to the first mode actions and deformations. Such an additional safety measure is not included in the pushover analysis. This suggests that the results from the conventional pushover analysis applied on linear elastic (or near linear) systems might not be considered sufficiently conservative, especially if higher modes have a significant influence on the response. As shown by *load distribution C* for the lateral force method in Section A2.1.3, the increasing factor $m_{tot}/\tilde{m}^*_{eff,a}$ becomes unity if a uniform acceleration shape vector of the type $\tilde{\tilde{\phi}}_{LFM,a} = \vec{1}$ is chosen. This means that the entire system mass is implicitly activated for the lateral forces and no additional increase is required. It is conceptually possible to choose the same acceleration shape in the pushover analysis, which would at least mitigate the problem with respect to the sum of the forces applied on the system. However, it requires further considerations on an individual basis whether this uniform shape is appropriate for a given bridge structure in a specific case.

Annex A3   Results from Proposed MDOF Analysis Procedures

In this annex the results from the MDOF analyses presented in Section 4.6.3 are reproduced in a way which facilitates the interpretation of the various curves. For this purpose, the graphs already shown in Section 4.6.3 are separated by peak ground acceleration. This means that a separate figure is used for each of the three PGA levels considered for the analyses. The presented data, on one hand, consist of the MDOF deformation demands computed with a target displacement of the reference point based on the mean ITHA results, as discussed in Section 4.6.3*a*. On the other hand, the MDOF displacement demands resulting from the analysis methods proposed in Section 4.6.3*c* are also shown. In these latter cases, the same three ways of estimating the inelastic target displacement are considered as already presented in Section 4.6.3*c*. These are the use of a displacement modification factor according to [CC04] and the application of equivalent linearization principles based on [PCK07] and [Guy04]. Both equivalent linearization approaches were used in combination with the $\eta(\xi)$ relationship according to [EC8-1-1] (1994).

In total, for each bridge configuration and PGA level, a total of four sets of MDOF demand predictions result. In the figures shown below each group of four sets is presented together in order to enable easy comparison between the various solutions. Each set of curves consists of the results from the four simplified analysis procedures proposed in Section 4.6.3*c*, plus the mean ITHA demand estimations. All results are organized in Fig. A3.1 through Fig. A3.9 by PGA level and bridge configuration.

Fig. A3.1a: MDOF analysis results for bridge configuration 1 at a_gd = 0.16g
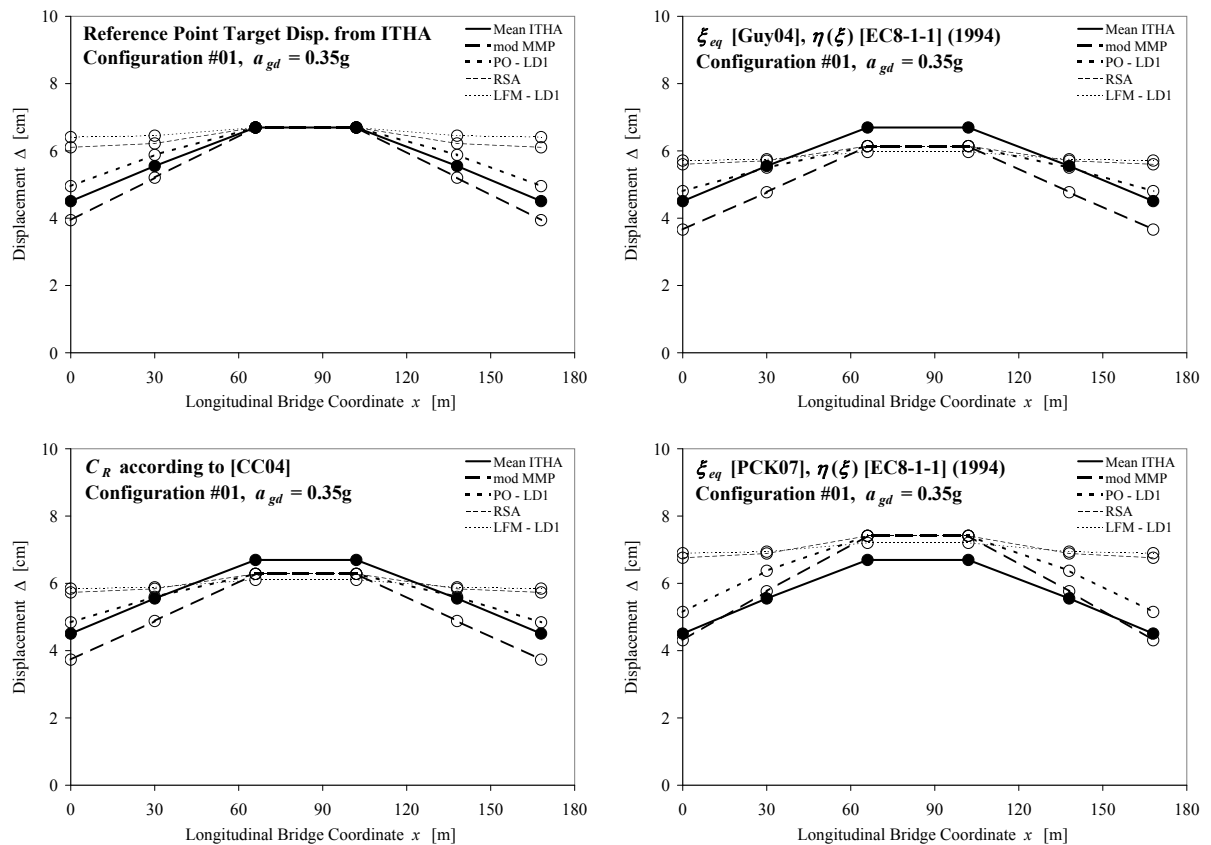
Fig. A3.1b: MDOF analysis results for bridge configuration 1 at a_gd = 0.35g
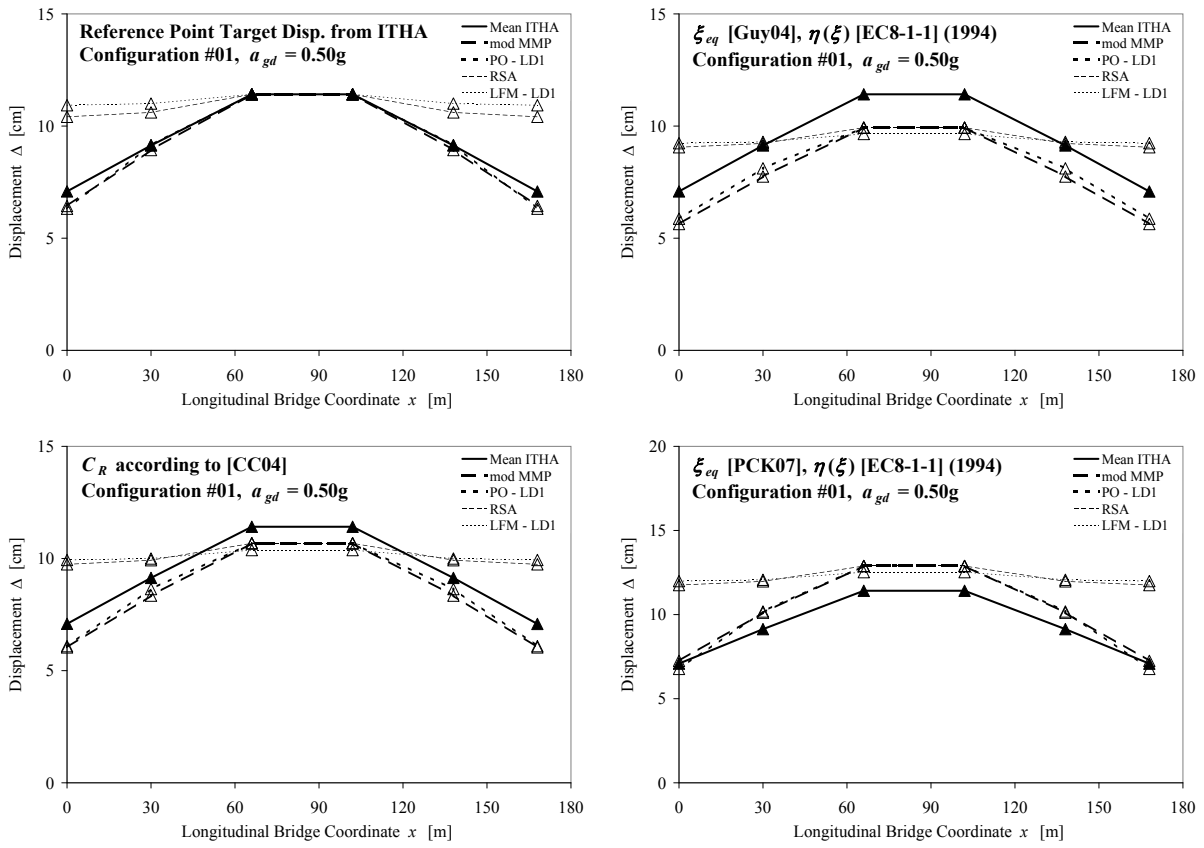
Fig. A3.1c: MDOF analysis results for bridge configuration 1 at a_{gd} = 0.50g
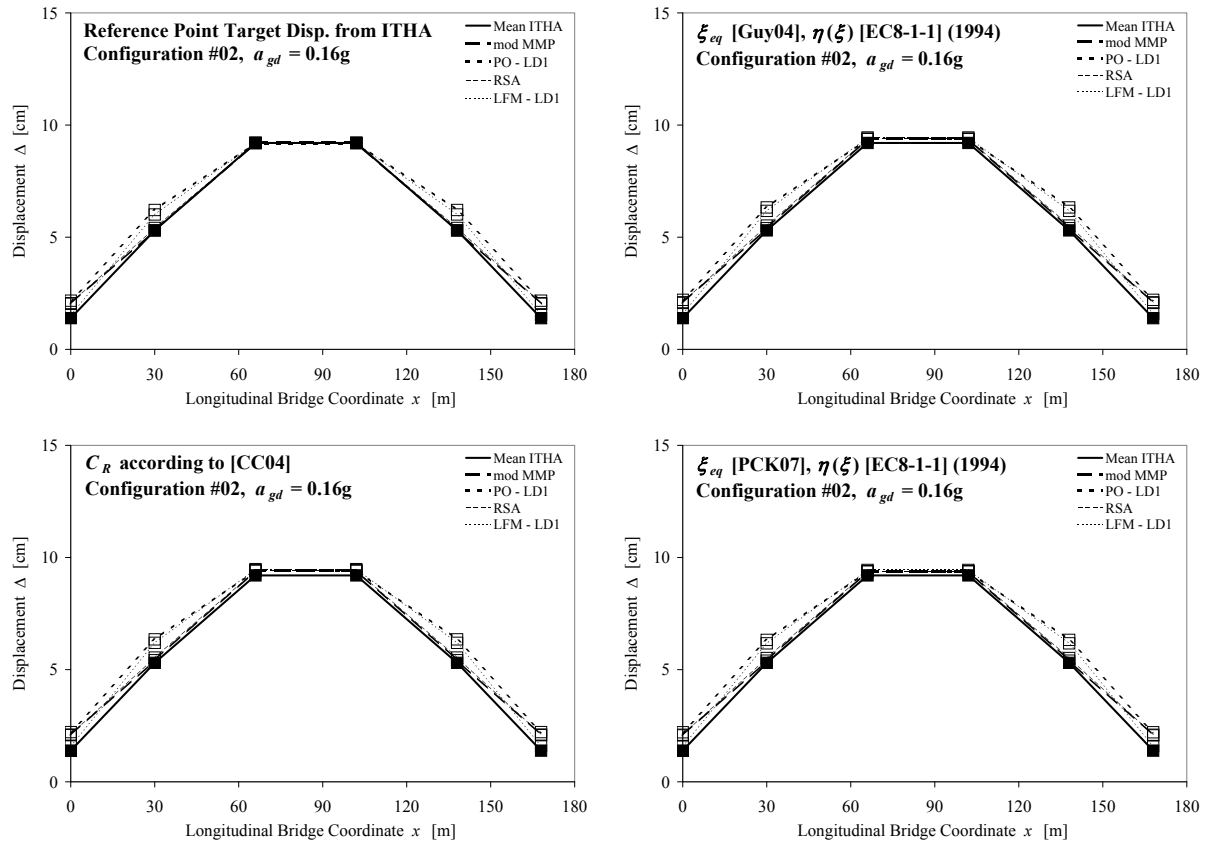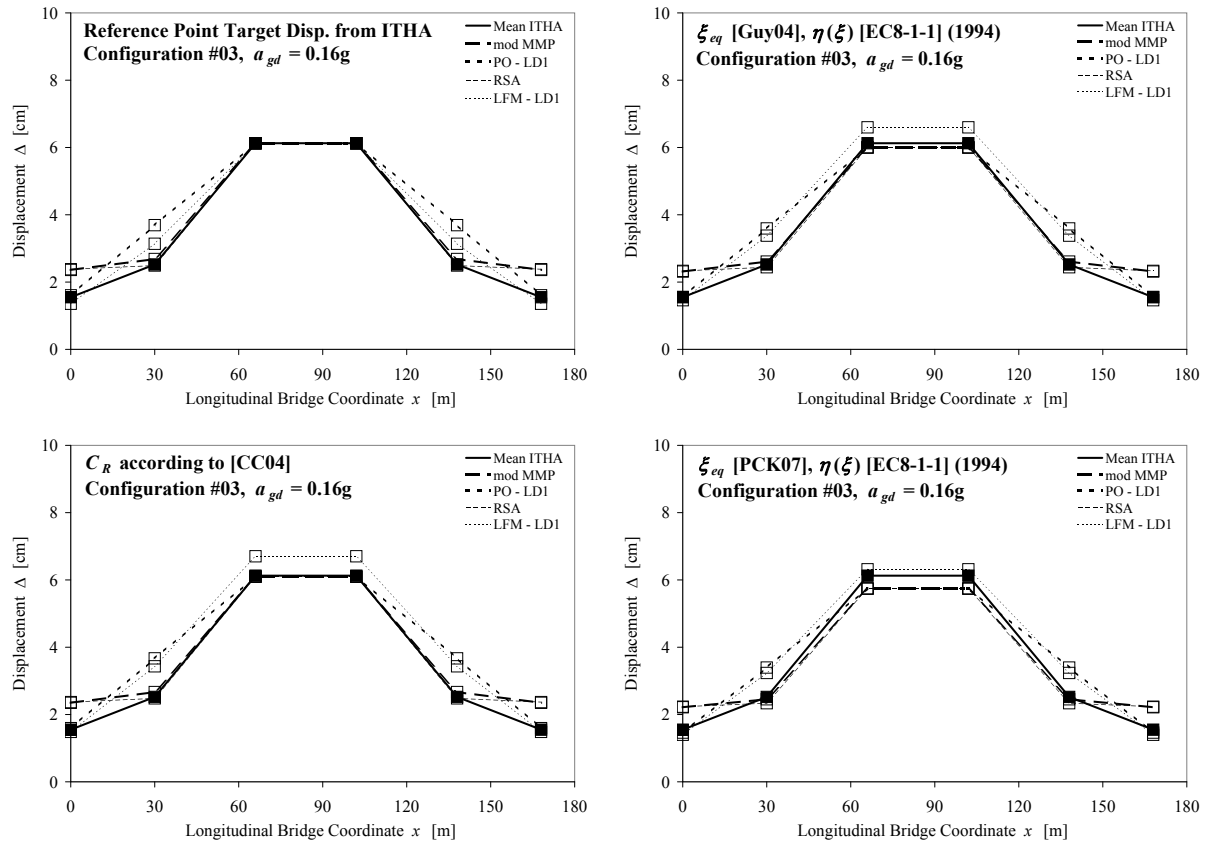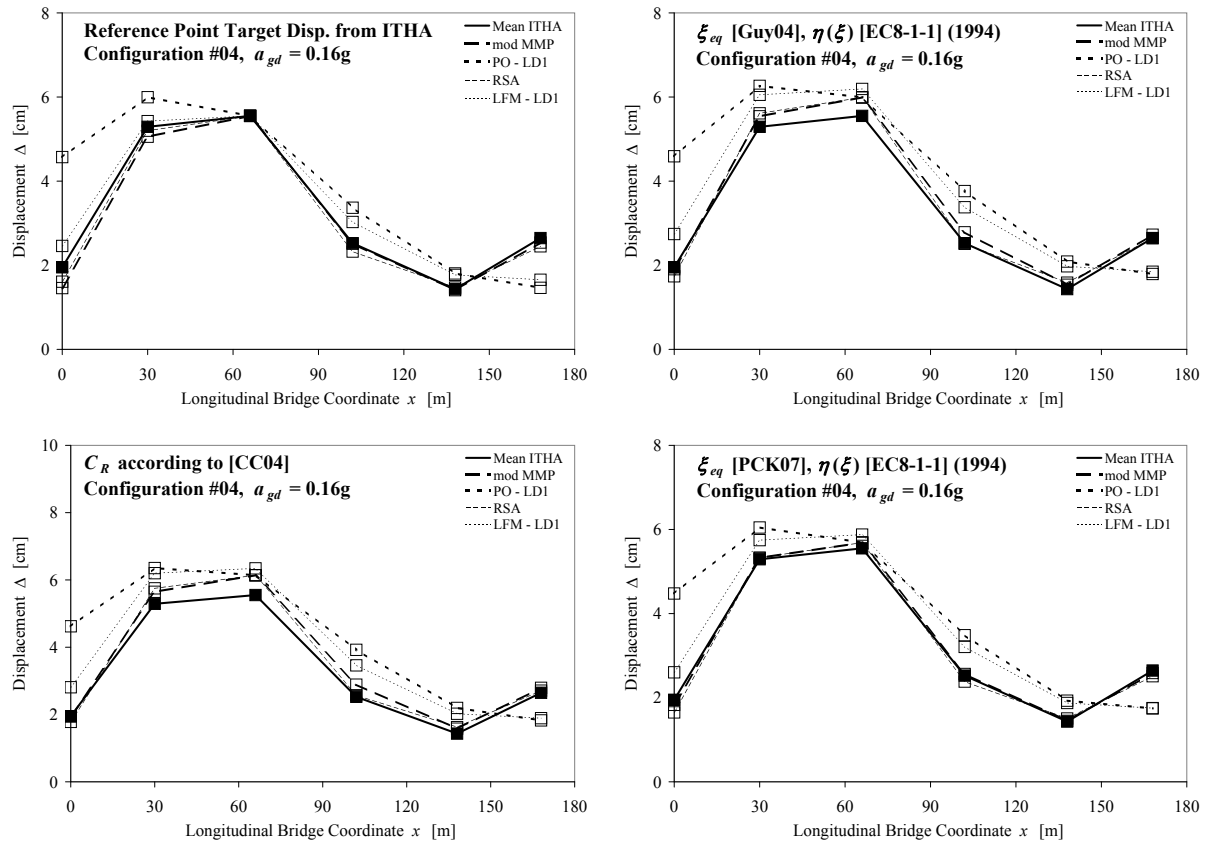
Fig. A3.2a: MDOF analysis results for bridge configuration 2 at a_gd = 0.16g
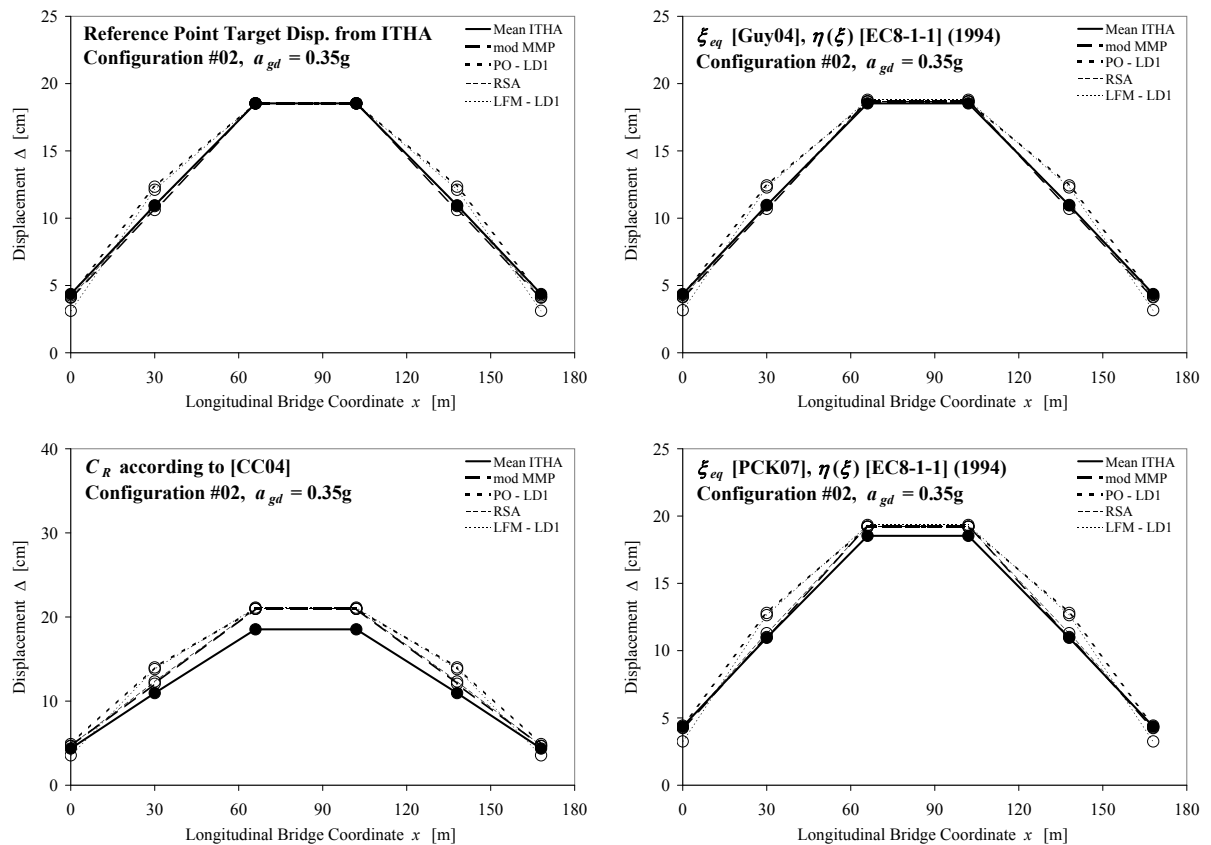
Fig. A3.2b: MDOF analysis results for bridge configuration 2 at a_gd = 0.35g
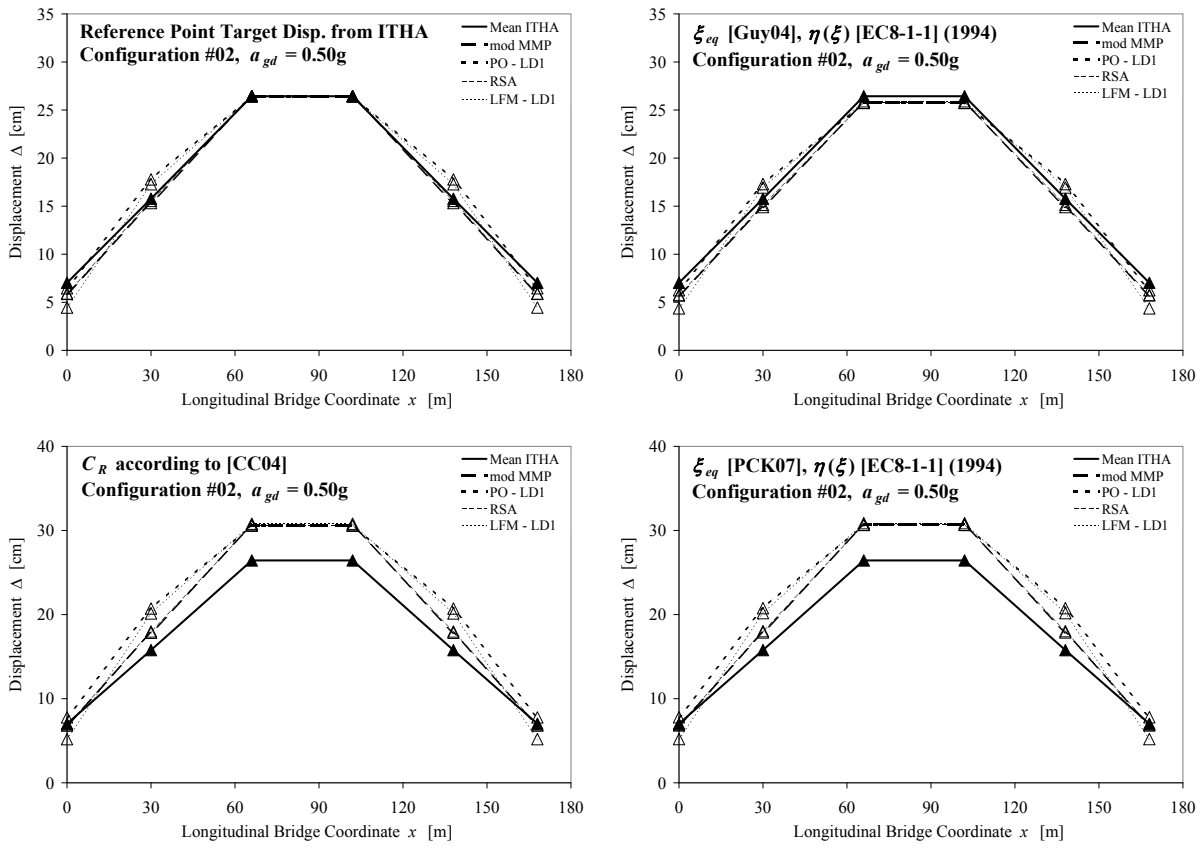
Fig. A3.2c: MDOF analysis results for bridge configuration 2 at a_{gd} = 0.50g

Fig. A3.3a: MDOF analysis results for bridge configuration 3 at a_gd = 0.16g
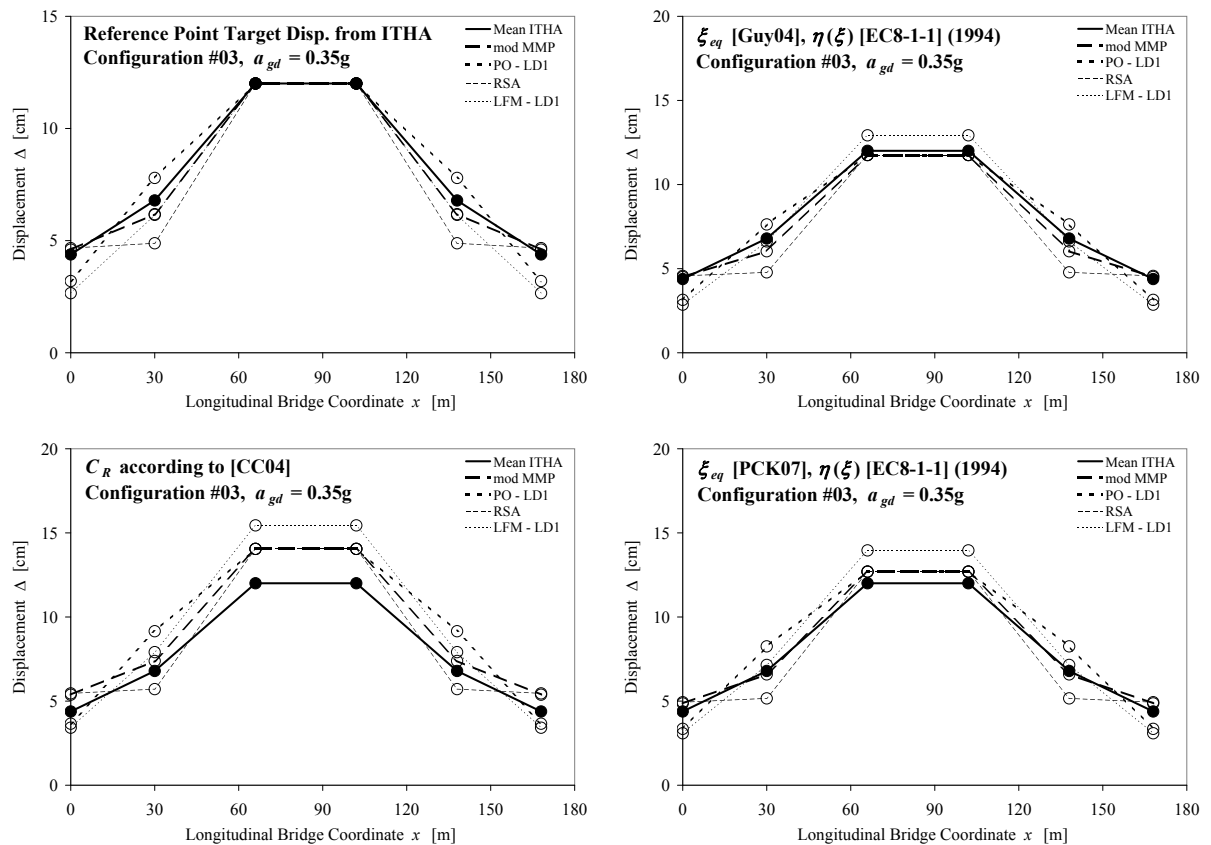
Fig. A3.3b: MDOF analysis results for bridge configuration 3 at a_gd = 0.35g
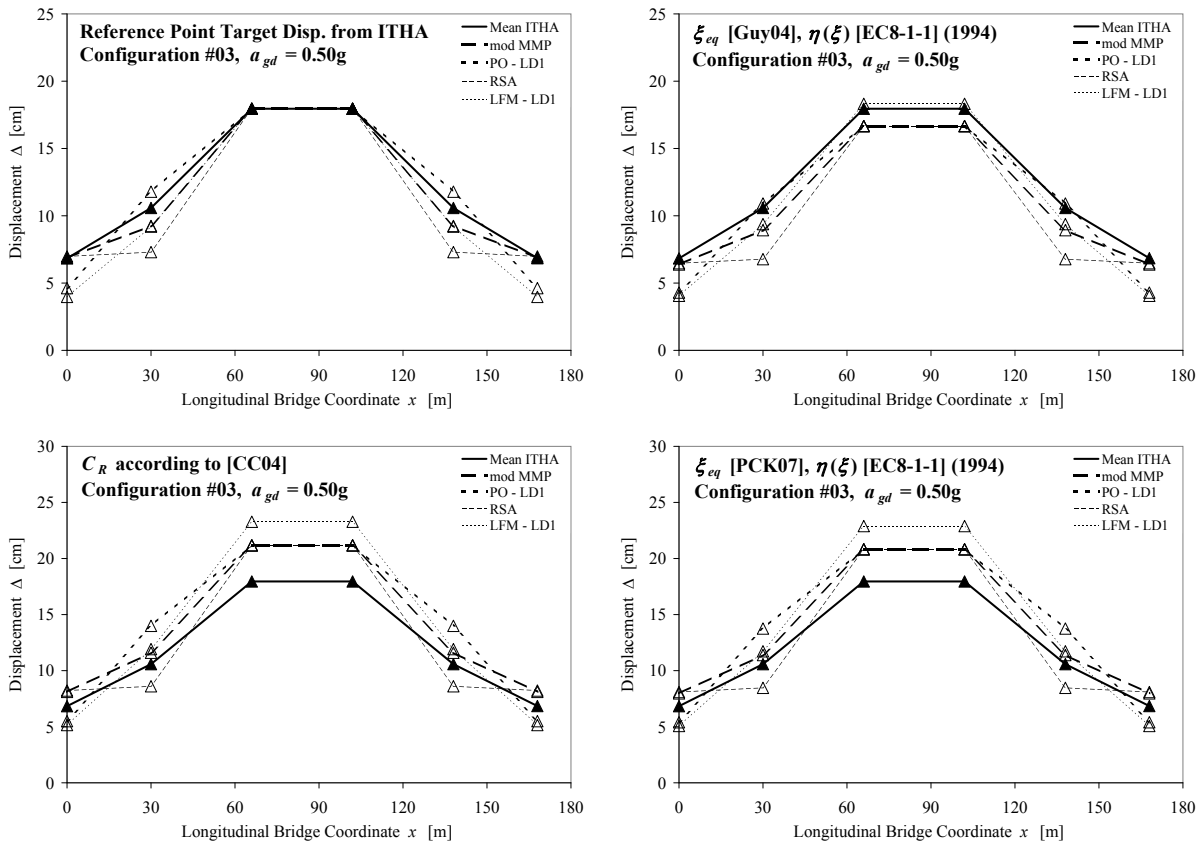
Fig. A3.3c: MDOF analysis results for bridge configuration 3 at a_{gd} = 0.50g

Fig. A3.4a: MDOF analysis results for bridge configuration 4 at a_{gd} = 0.16g
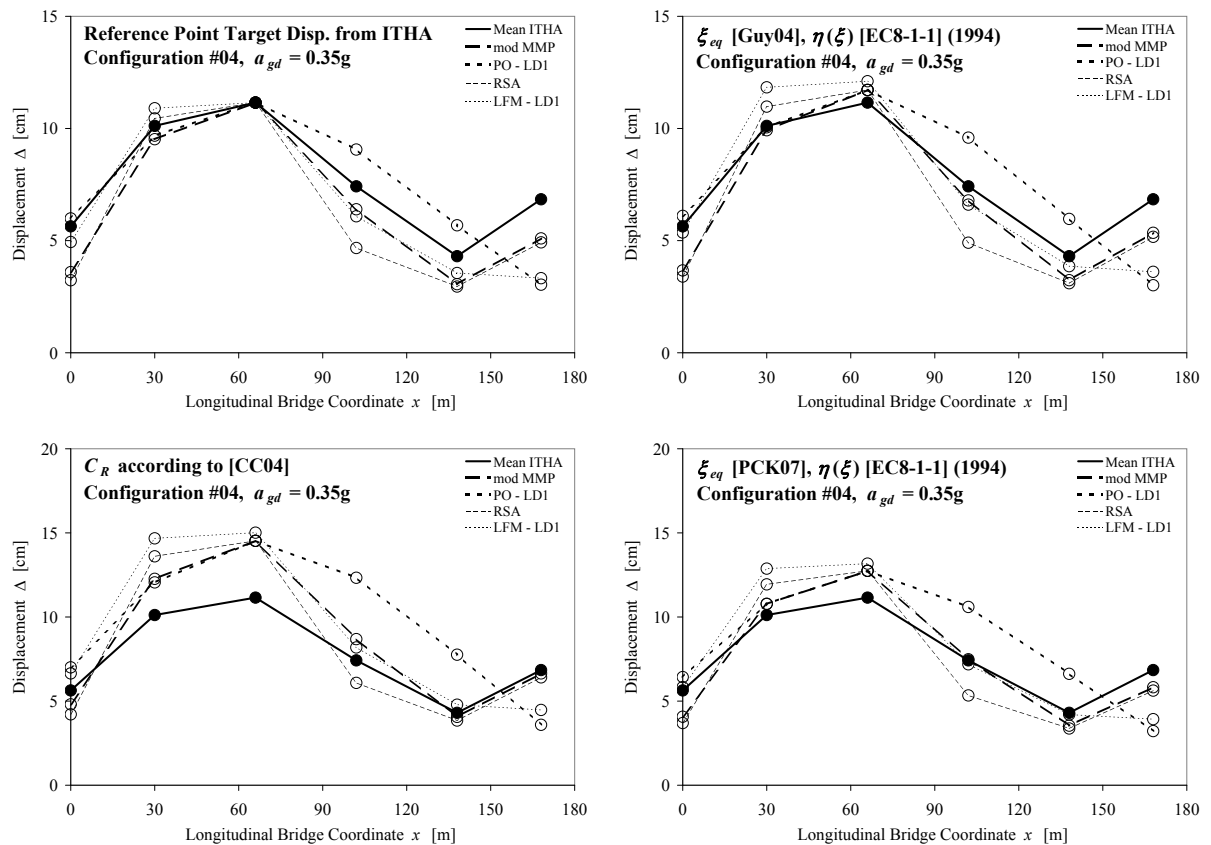
Fig. A3.4b: MDOF analysis results for bridge configuration 4 at a_{gd} = 0.35g
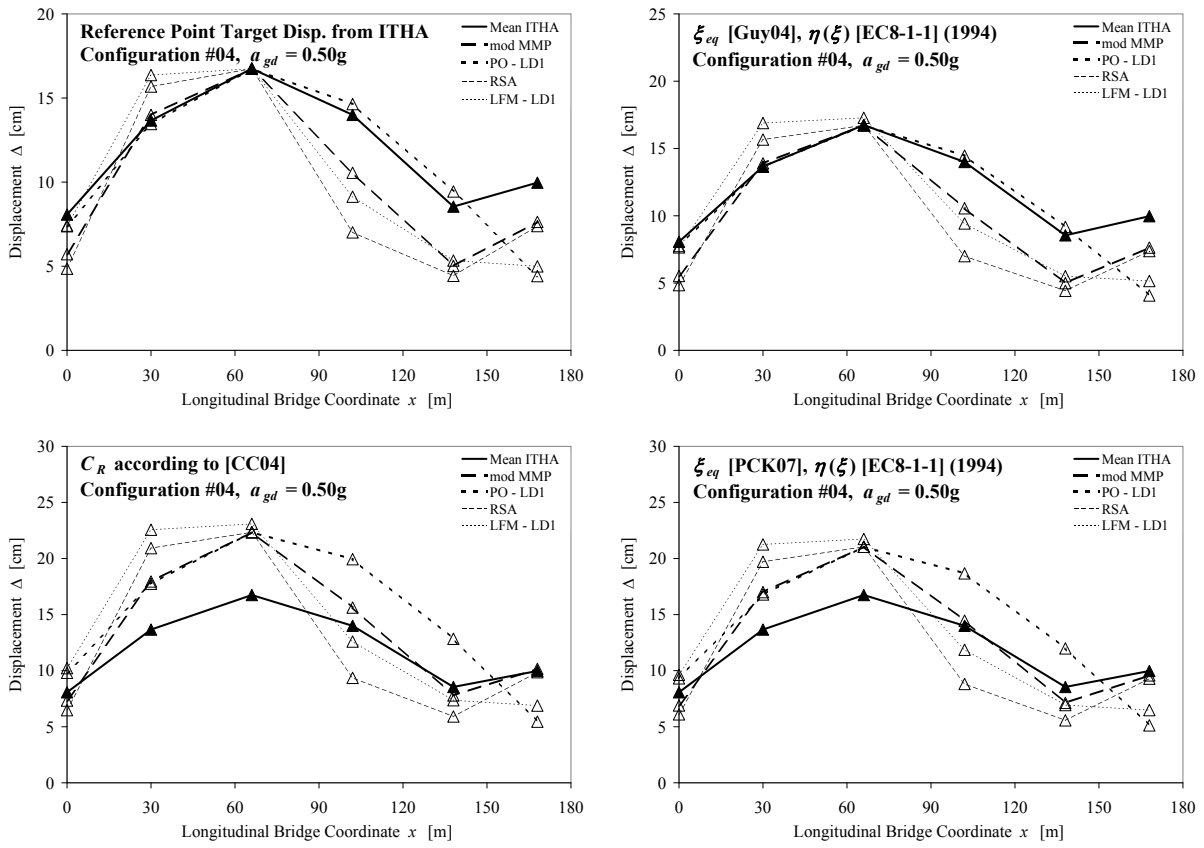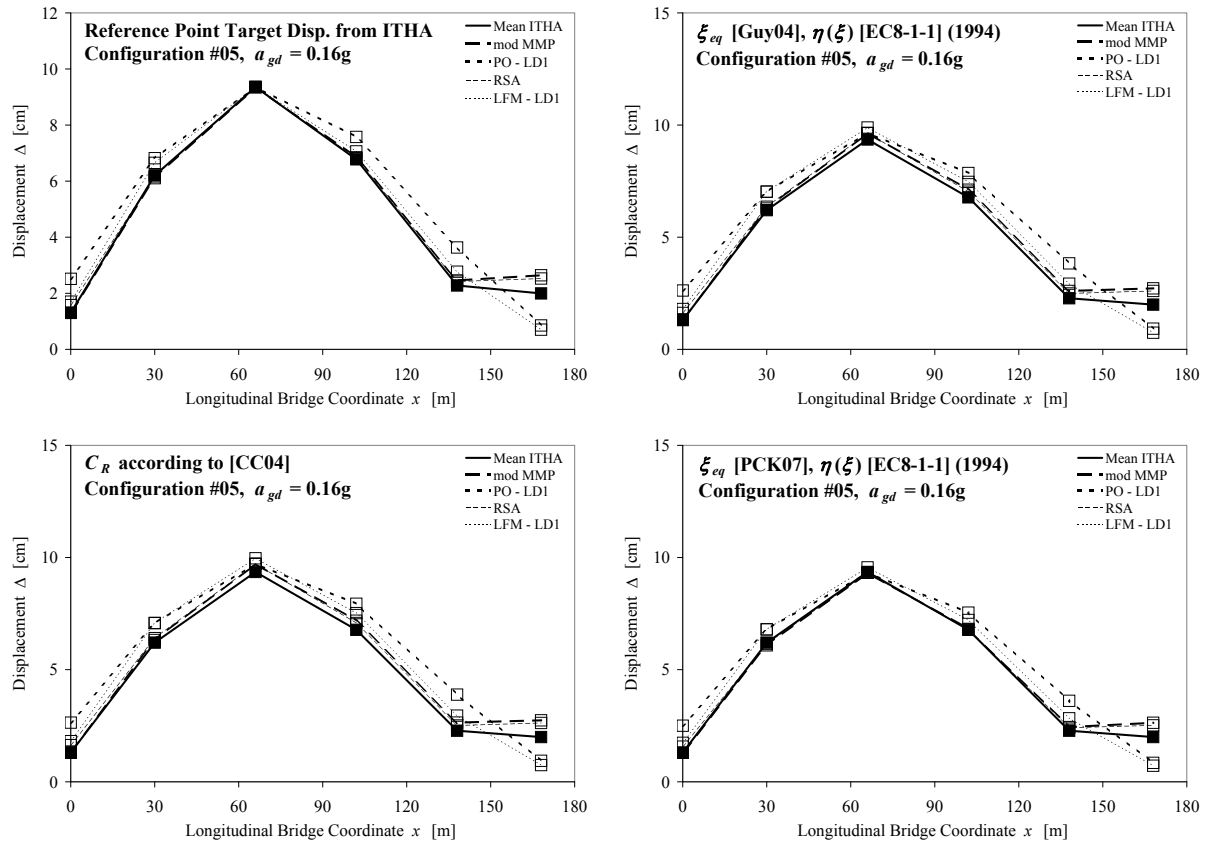
Fig. A3.4c: MDOF analysis results for bridge configuration 4 at a_{gd} = 0.50g

Fig. A3.5a: MDOF analysis results for bridge configuration 5 at a_{gd} = 0.16g
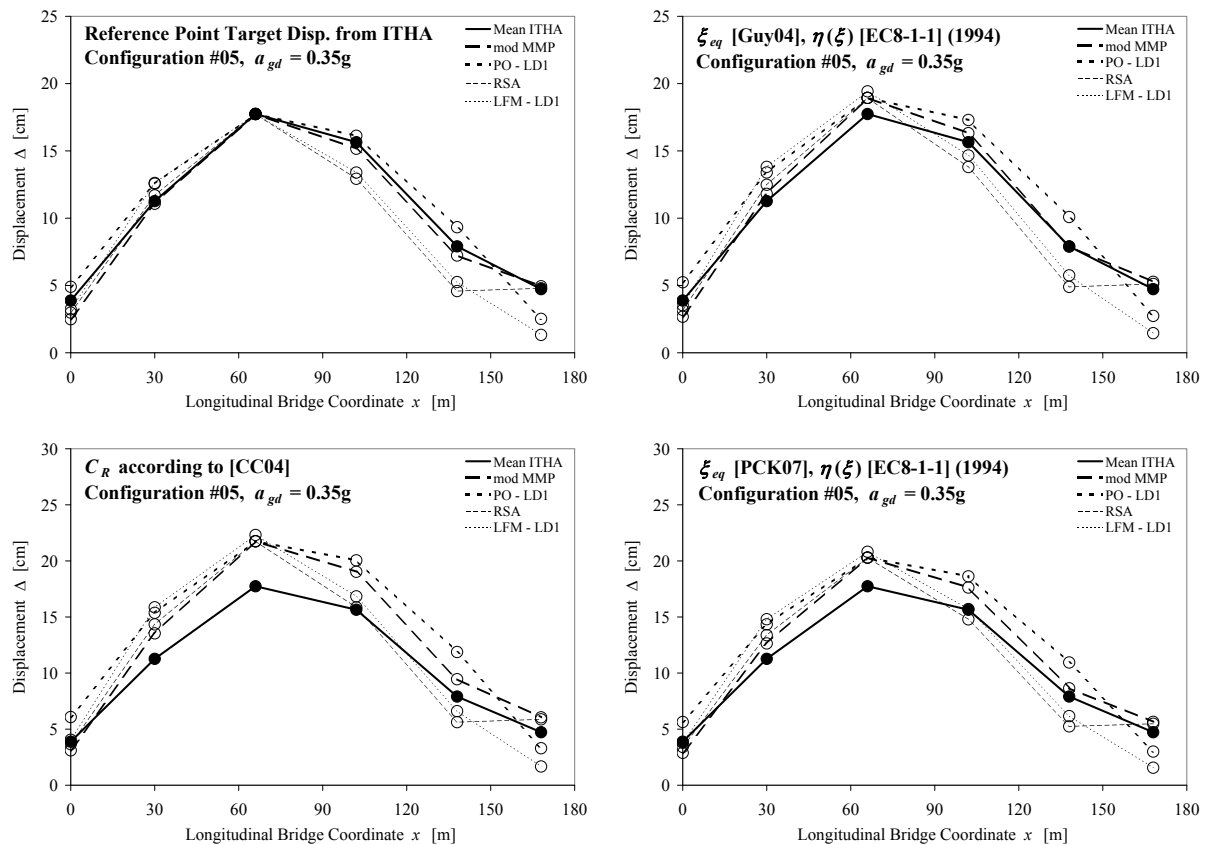
Fig. A3.5b: MDOF analysis results for bridge configuration 5 at a_{gd} = 0.35g
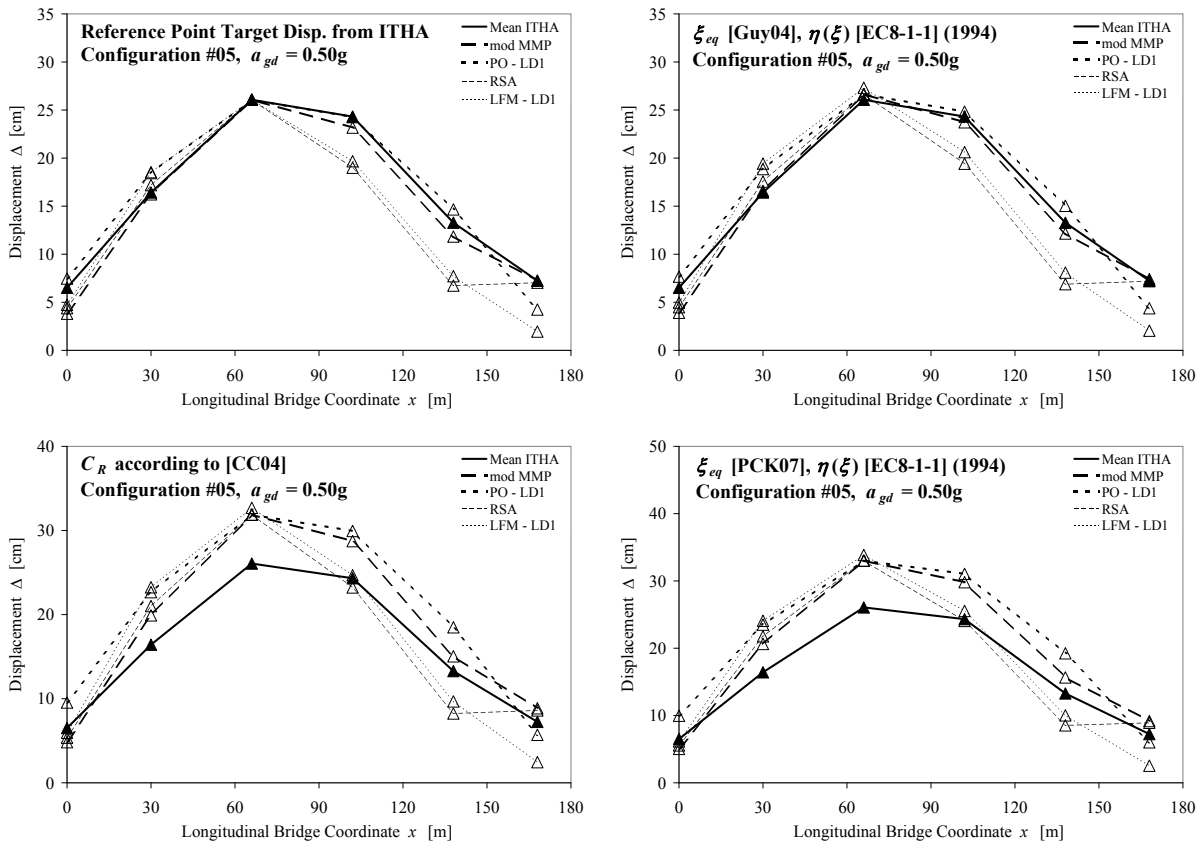
Fig. A3.5c: MDOF analysis results for bridge configuration 5 at a_{gd} = 0.50g

Fig. A3.6a: MDOF analysis results for bridge configuration 6 at a_{gd} = 0.16g
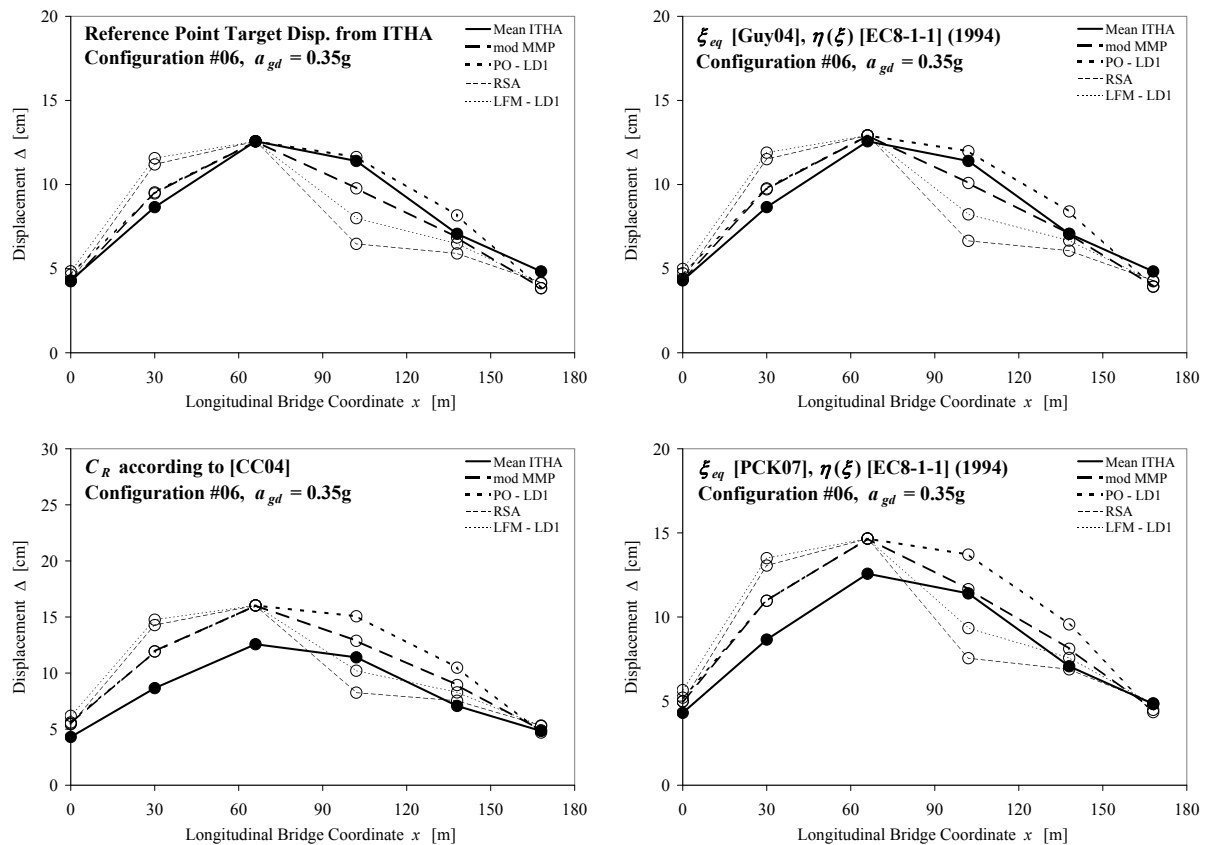
Fig. A3.6b: MDOF analysis results for bridge configuration 6 at a_{gd} = 0.35g
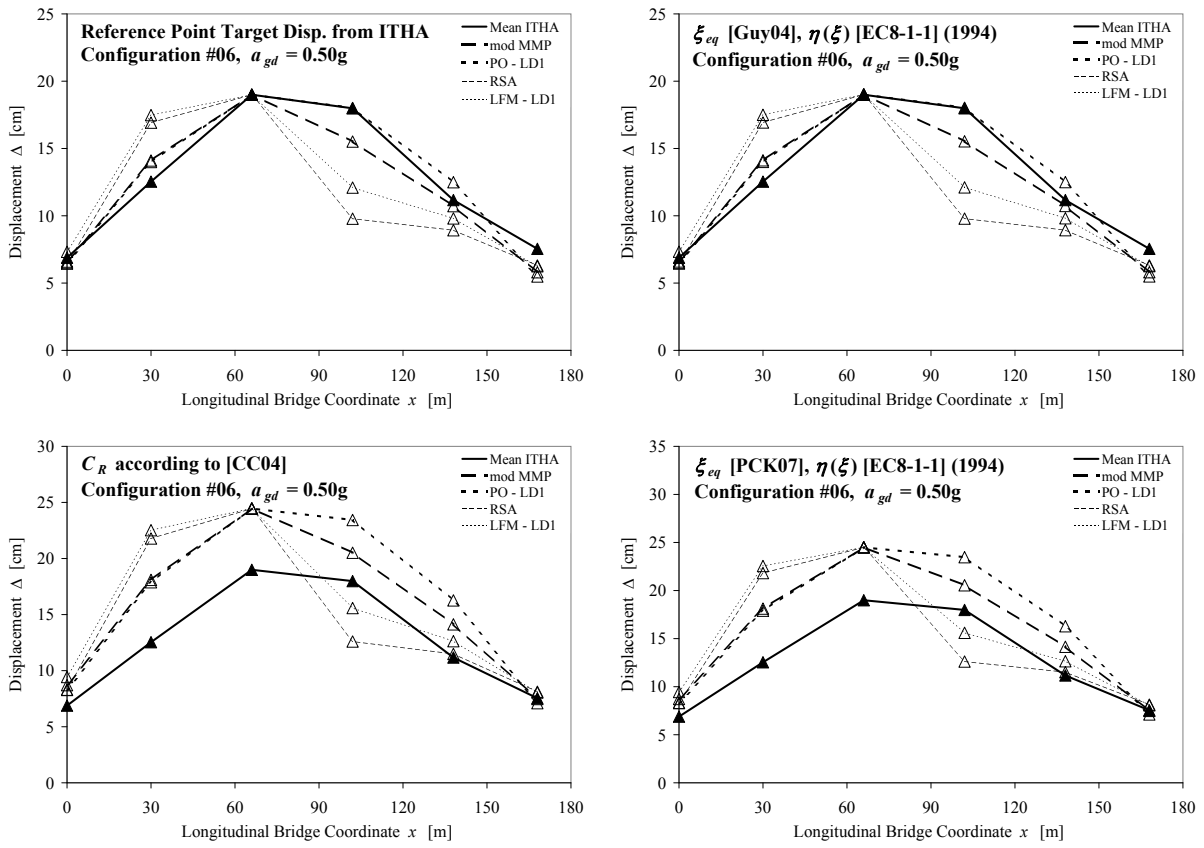
Fig. A3.6c: MDOF analysis results for bridge configuration 6 at a_{gd} = 0.50g
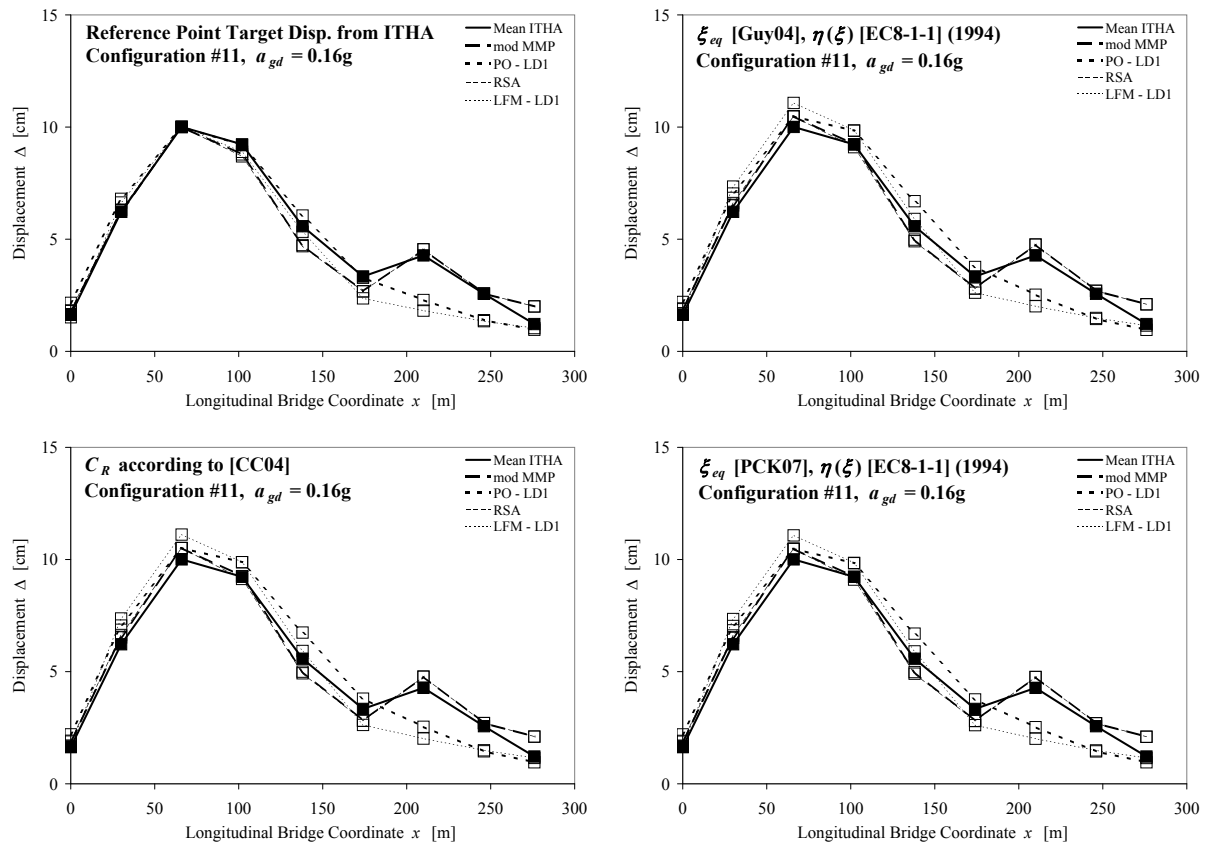
Fig. A3.7a: MDOF analysis results for bridge configuration 11 at a_{gd} = 0.16g
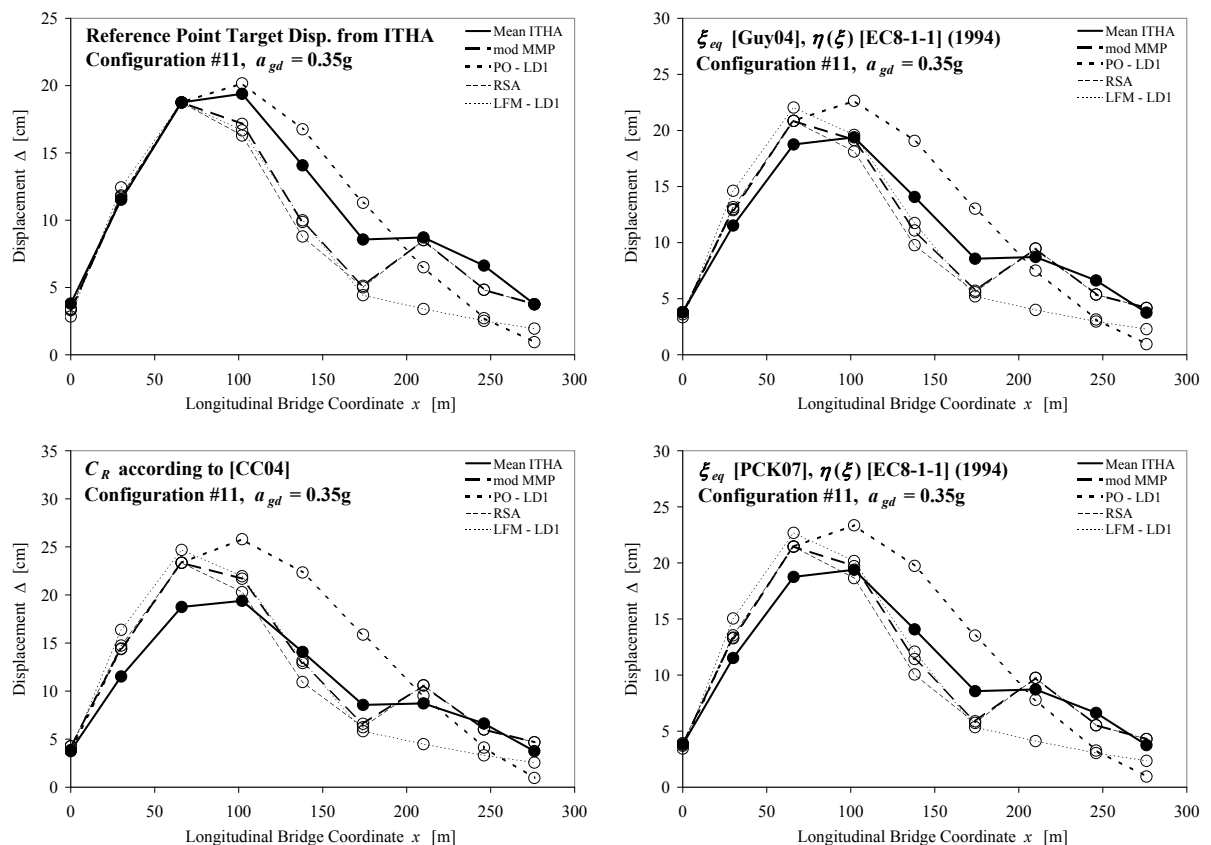
Fig. A3.7b: MDOF analysis results for bridge configuration 11 at a_{gd} = 0.35g
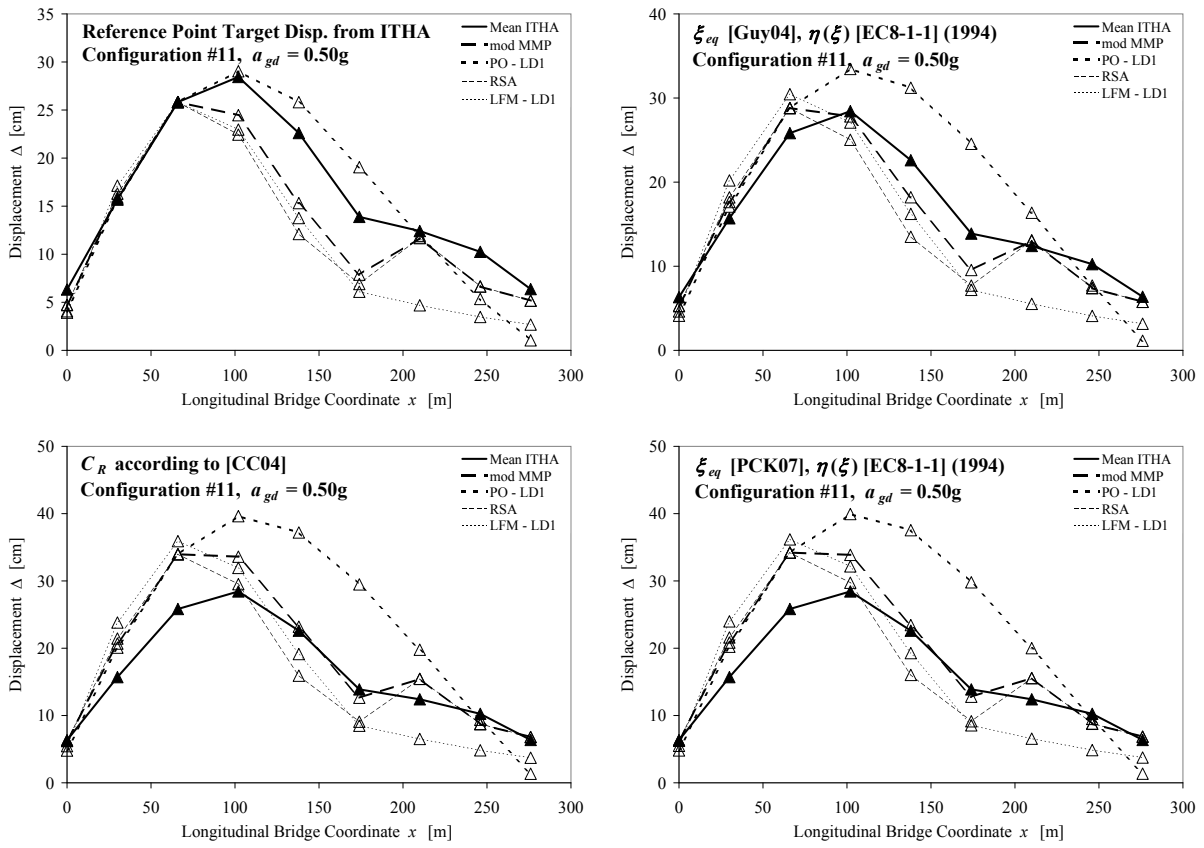
Fig. A3.7c: MDOF analysis results for bridge configuration 11 at a_{gd} = 0.50g
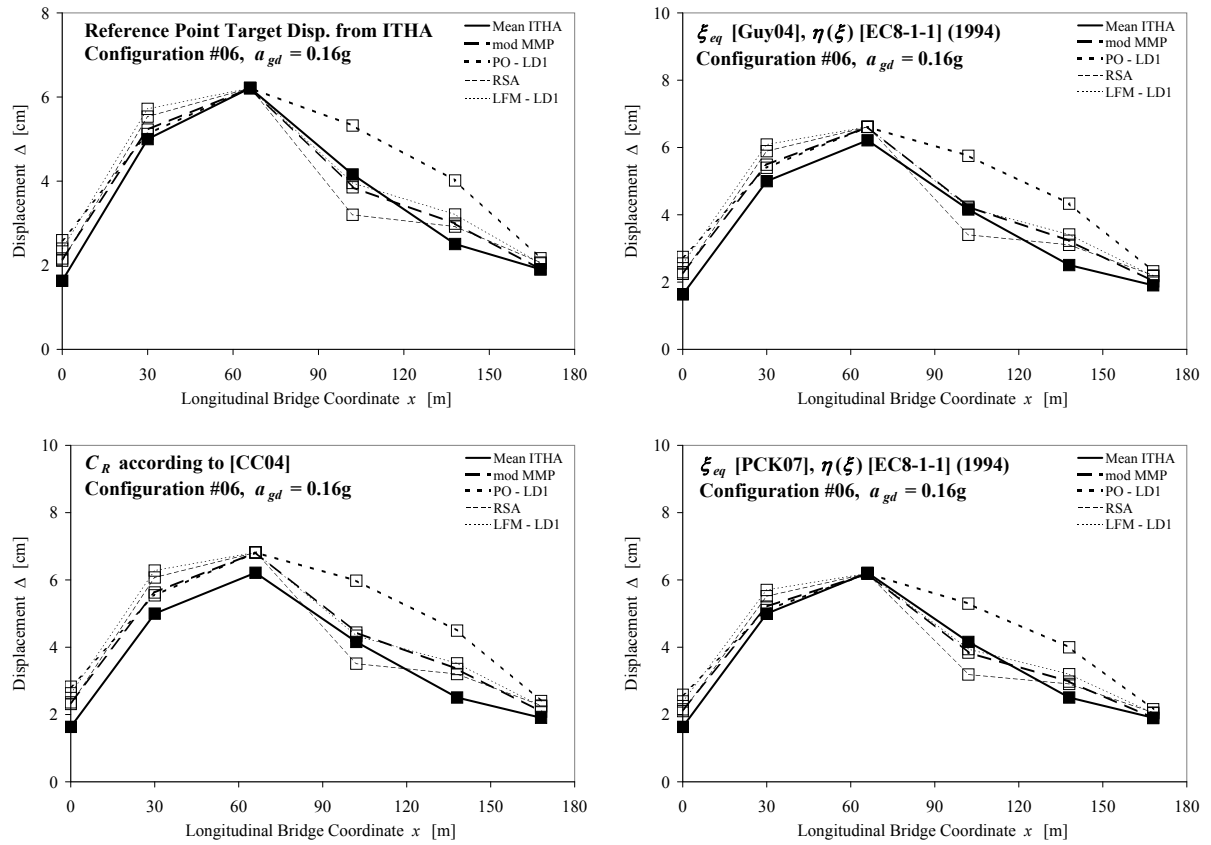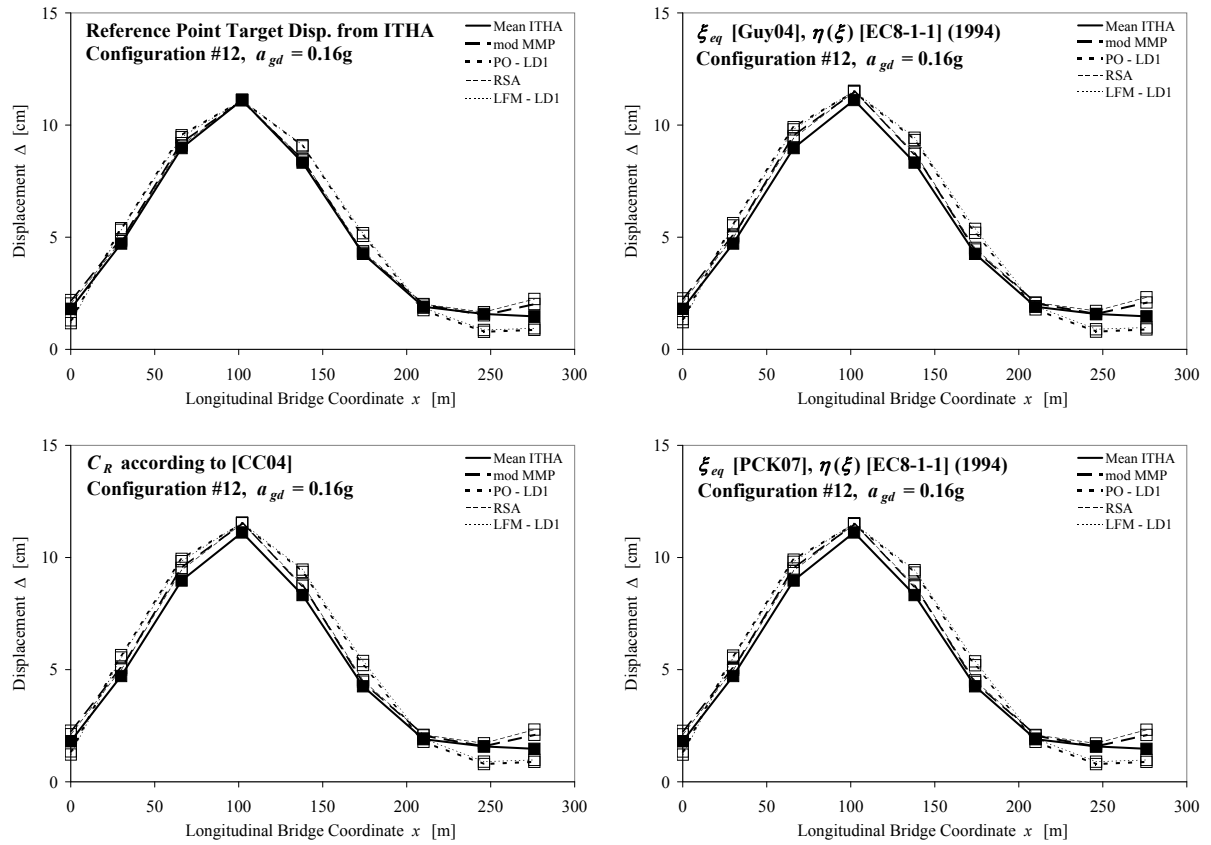
Fig. A3.8a: MDOF analysis results for bridge configuration 12 at a_{gd} = 0.16g
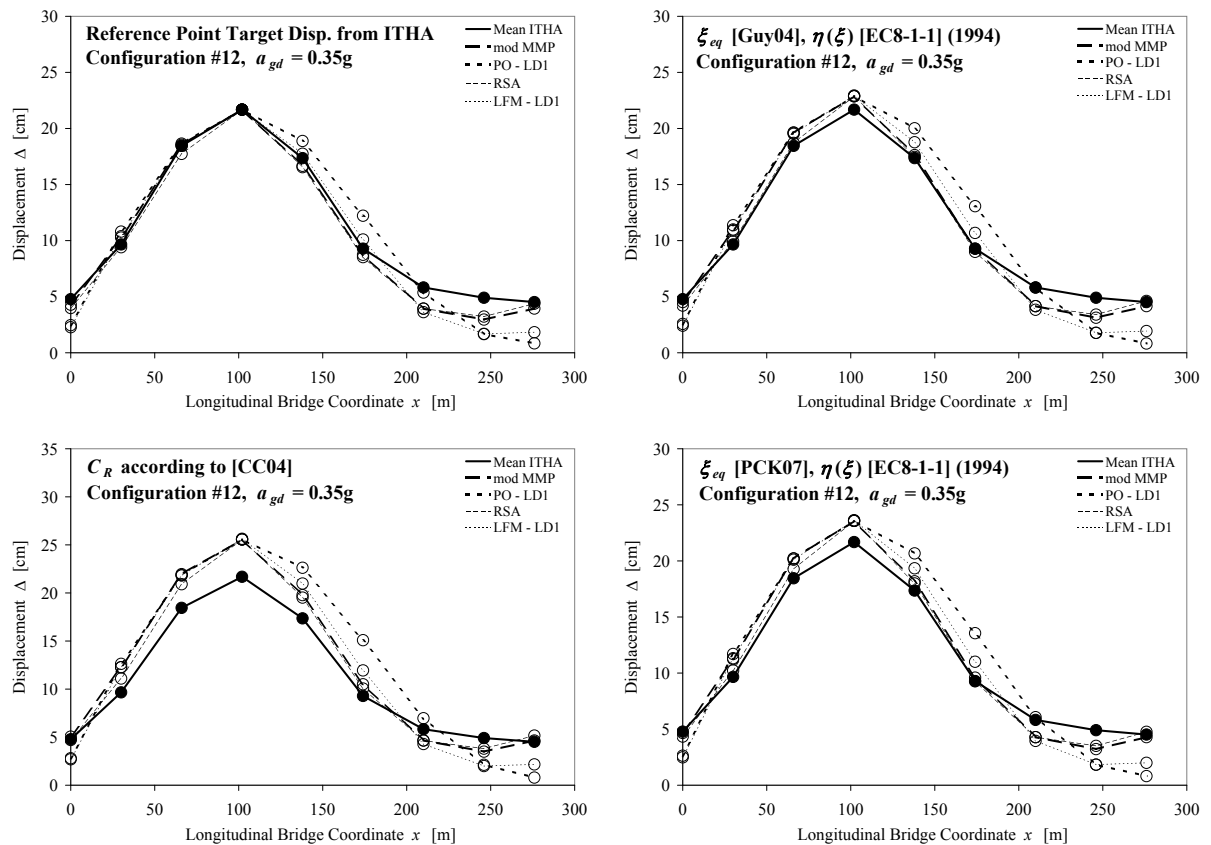
Fig. A3.8b: MDOF analysis results for bridge configuration 12 at a_{gd} = 0.35g
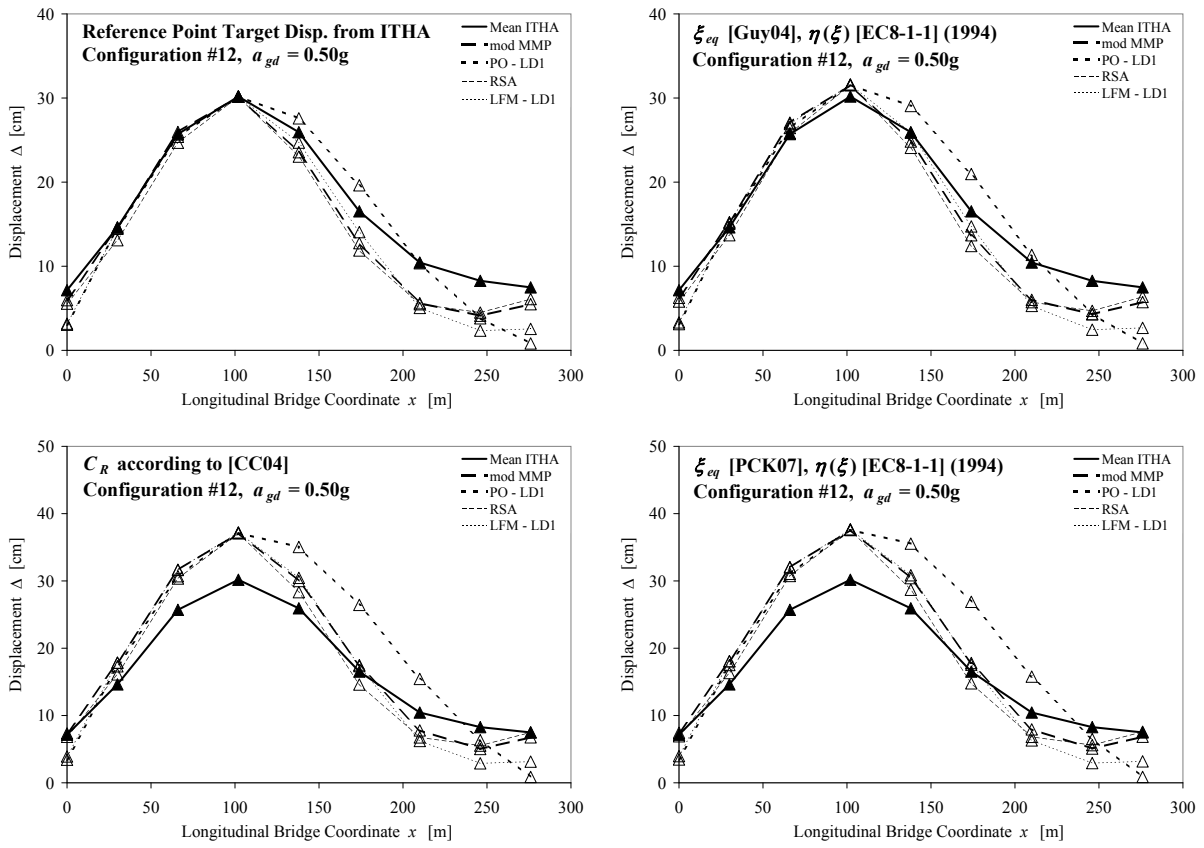
Fig. A3.8c: MDOF analysis results for bridge configuration 12 at a_{gd} = 0.50g

Fig. A3.9a: MDOF analysis results for bridge configuration 13 at $a_{gd} = 0.16g$
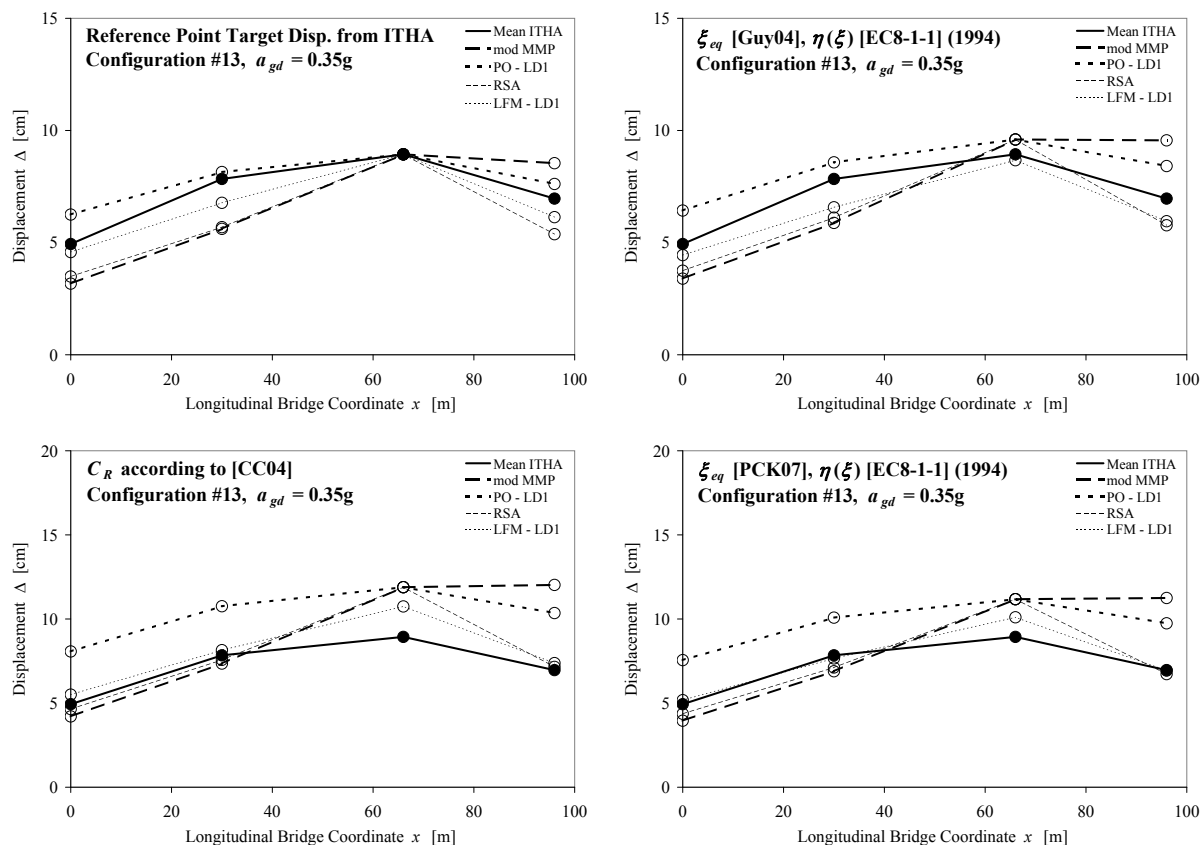
Fig. A3.9b: MDOF analysis results for bridge configuration 13 at $a_{gd} = 0.35g$

399
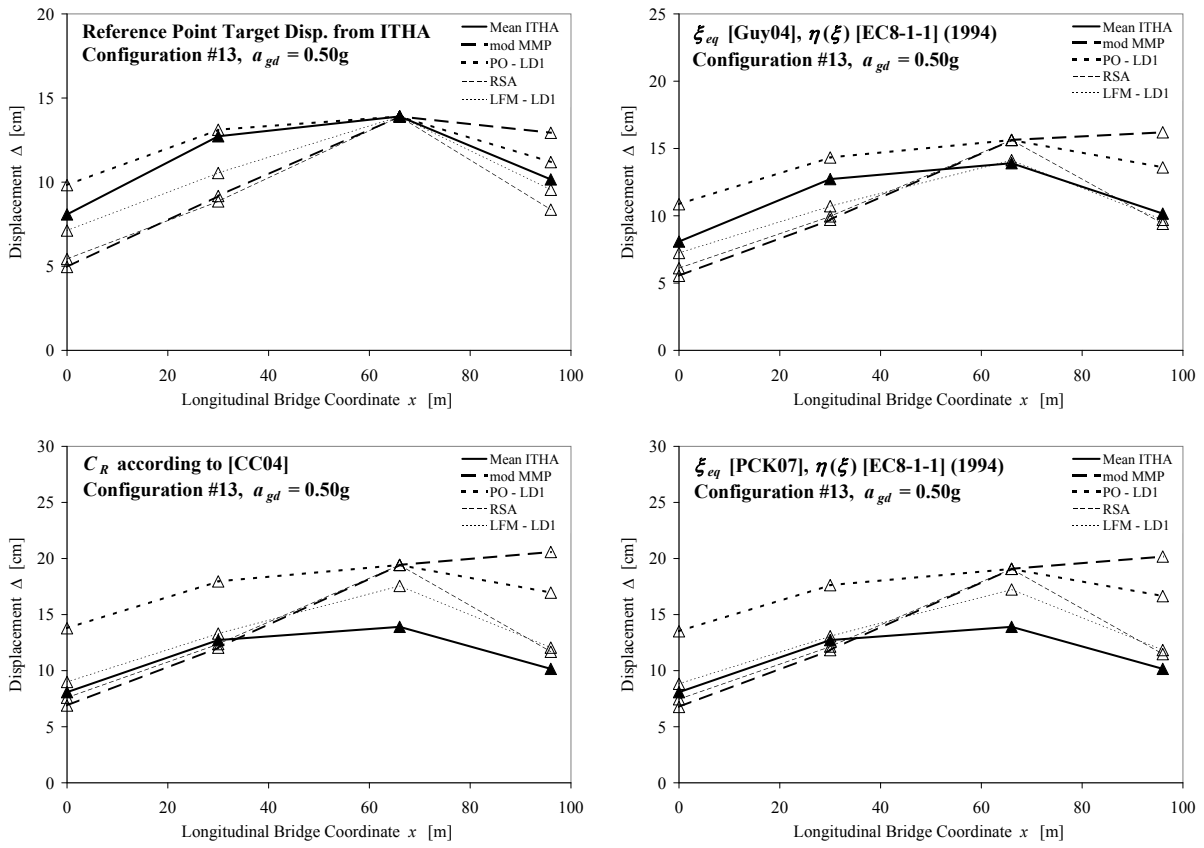
Fig. A3.9c: MDOF analysis results for bridge configuration 13 at $a_{gd} = 0.50g$
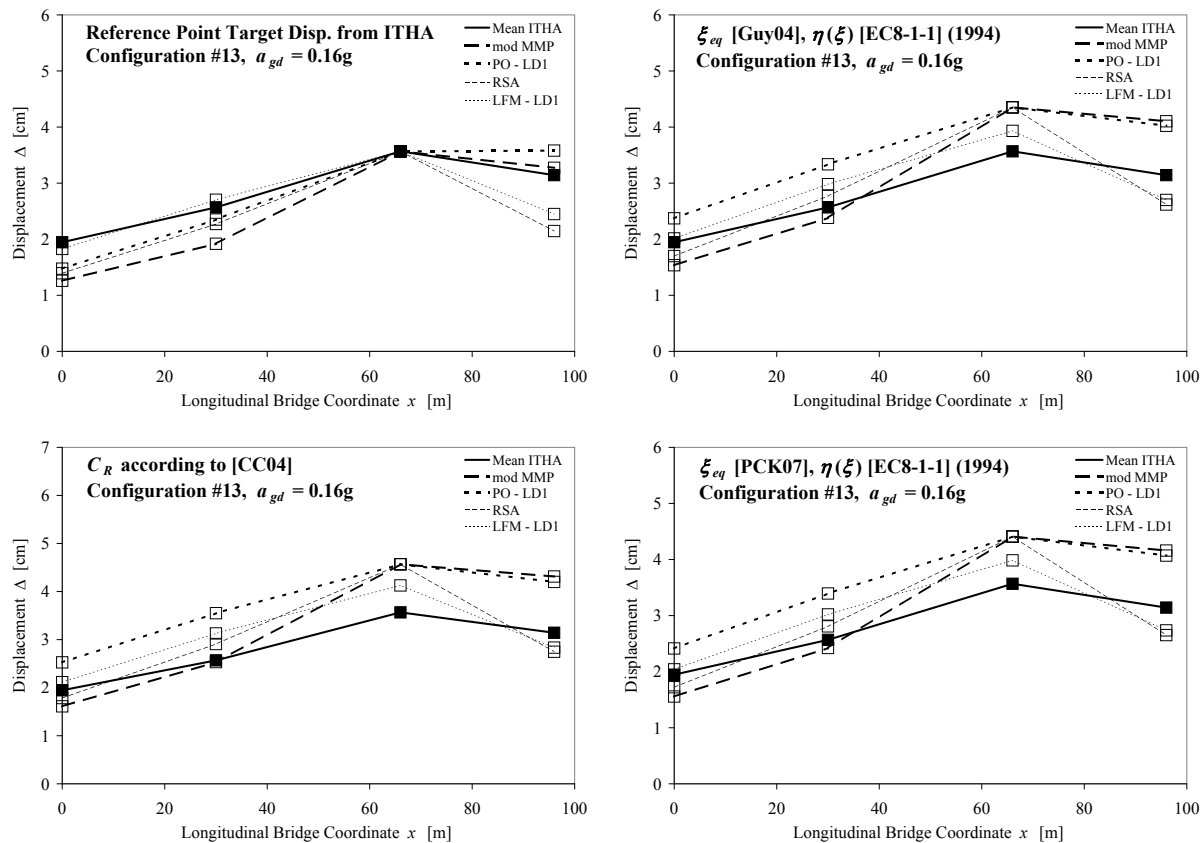
Notation

Latin lower-case symbols

a_g	peak ground acceleration
a_{gd}	dimensioning value of ground acceleration
b_w	width of concrete cross-section
c	damping coefficient
c_{cr}	critical damping coefficient
d	effective depth of cross-section (from compression edge to center of tension reinforcement)
d_{bl}	diameter of longitudinal reinforcement bar
e	void ratio of soil
f	cyclic frequency of vibration
f_c	compression strength of concrete
f_s	yield strength of reinforcement
f_{sk}	characteristic value of the yield strength of reinforcement
f_{sw}	yield strength of transverse reinforcement
f_{sm}	average value of the yield strength of reinforcement
f_t	ultimate tension strength of reinforcement
f_{tk}	characteristic value of the ultimate tension strength of reinforcement
f_{tm}	average value of the ultimate tension strength of reinforcement
g	acceleration of gravity ($g = 9.81$ m/s$^2 \approx 10$/m/s^2)
k_0	initial elastic stiffness of a bilinear force-displacement relationship; for a general nonlinear force-displacement relationship, k_0 is the secant stiffness between the origin and the point of first yield ($k_0 = F_y'/\Delta_y' = F_n/\Delta_y$)
$k_{post\text{-}yield}$	post-yield stiffness of a bilinear force-displacement relationship
k_{sec}	secant stiffness of an inelastic system between the origin and a point on the load-deformation curve corresponding to a certain deformed state
$m^*_{eff,i}$	effective modal mass of the i-th mode
l_s	lap-splice length
l_w	total section depth of wall cross-section
r	post-yield stiffness ratio $r = k_{post\text{-}yield}/k_0$
q	behavior factor for force based design according to [SIA261], [SIA262]
s	bar spacing
v_s	shear wave velocity of soil
x	depth of flexural compression zone

Notation

Latin upper-case symbols

A_c	gross area of concrete cross-section
A_{cv}	effective shear area of concrete cross-section ($A_{cv} = b_w d$)
A_{sw}	cross-sectional area of the stirrups
C_k	construction factor according to [SIA160-89]
C_R	displacement modification factor as a function of a force reduction factor R_y
C_μ	displacement modification factor as a function of the displacement ductility μ_Δ
F_n	nominal force capacity (corresponding to the nominal yield displacement Δ_y in a bilinear force-displacement relationship)
F_y'	force at first yield (corresponding to the first yield displacement Δ_y')
F_u	force capacity at ultimate displacement Δ_u
G_{max}	maximum soil shear modulus at small shear strains
G_{sec}	secant soil shear modulus at certain shear strain
I_p	plasticity index of cohesive soil
L_{pl}	plastic hinge length
L_{sp}	strain penetration length
L_v	length of shear span ($L_v = M/V$), distance between the point of maximum moment and the point of zero moment in a flexural member
M_E	uniaxial confined stiffness of soil
M_n	nominal moment capacity
M_y'	moment at first yield (corresponding to the first yield curvature ϕ_y')
R_y	force reduction factor for inelastic systems; also named: strength ratio
S	soil class factor
$S_{a,el}$	elastic spectral pseudo-acceleration (corresponds to S_e in [SIA261] and to S_{ad} in [SIA2018])
$S_{a,d}$	design spectral pseudo-acceleration (corresponds to S_d in [SIA261])
$S_{d,el}$	elastic spectral displacement (corresponds to S_{ud} in [SIA2018])
T	fundamental period
T_0	fundamental period of an inelastic system based on its initial elastic stiffness k_0
T_{eff}	effective fundamental period of an inelastic system based on its secant stiffness k_{sec}
V_R	shear capacity of RC members corresponding to failure in diagonal tension
$V_{R,max}$	shear capacity of RC members corresponding to failure of concrete struts in compression
V_{Rd}	design shear capacity

Greek lower-case symbols

α	inclination of compression field in RC member under combined shear and flexural action
α_{eff}	compliance factor according to [SIA2018]
γ_c	partial safety factor for concrete
γ_D	partial safety factor for displacement capacity
γ_f	importance factor of structure according to [SIA261]
γ_s	partial safety factor for reinforcing steel and prestressing steel
δ	drift ratio
δ_{deg}	drift ratio at onset of cyclic strength degradation in a deformation dependent degradation model
ε_{cu}	ultimate strain of concrete in compression
η	modification factor to account for the influence of viscous damping ratio ξ on the displacement demand
μ_Δ	displacement ductility
μ_ϕ	curvature ductility
ν	axial load ratio
ξ	viscous damping ratio
ξ_{el}	elastic viscous damping ratio
ξ_{eq}	equivalent viscous damping ratio
$\xi_{eq,hyst}$	equivalent viscous damping ratio related to hysteretic energy dissipation alone
ρ_{sl}	geometric ratio of longitudinal reinforcement
ρ_{sw}	geometric ratio of transverse reinforcement
ϕ_u	ultimate curvature
$\phi_y{}'$	first yield curvature (i.e. at first yield of longitudinal reinforcement)
ϕ_y	nominal yield curvature
ω	circular frequency of vibration [rad/s] (also angular frequency of vibration)
ω_0	fundamental circular frequency of an inelastic system based on its initial elastic stiffness k_0
ω_{eff}	effective fundamental circular frequency of an inelastic system based on its secant stiffness k_{sec}

Greek upper-case symbols

Δ_{Top}	top displacement of pier
$\Delta_y{}'$	first yield displacement
Δ_y	nominal yield displacement
Δ_u	ultimate displacement capacity
Δ_{ud}	design ultimate displacement capacity

Glossary

backbone	load deformation curve connecting the peak values of hysteretic response
CQC	complete-quadratic-combination modal superposition rule
deformation capacity	deformation at which a defined limit is exceeded at which the safety of the member is not guaranteed anymore
DDBD	direct displacement based design
ductility	ratio between a certain deformation and the corresponding nominal yield deformation
first yield	point where the yield strain is reached for the first time in a reinforcement bar or a defined concrete strain in compression is reached
ITHA	inelastic (dynamic) time history analysis
LFM	lateral force method
MDOF	multi-degree-of-freedom
MMP	multi-modal pushover analysis
nominal yield	yield point in a bilinear idealization of a nonlinear load-deformation relationship
PO	pushover analysis
RC	reinforced concrete
RSA	response spectrum analysis
SDOF	single-degree-of-freedom
shear span	distance between the point of maximum moment and the point of zero moment in a flexural member
SRSS	square-root-of-summed-squares modal superposition rule
SSI	soil-structure interaction
SSP	substitute structure method

References

[ACI318]   ACI 318M-05: Building Code Requirements for Structural Concrete. *American Concrete Institute*, Committee 318, Farmington Hills, Michigan, 2005.

[AE03]   Allotey, N., El Naggar, M.H.: Analytical Moment-Rotation Curves for Rigid Foundations Based on a Winkler Model. *Soil Dynamics and Earthquake Engineering*, Vol. 23, No. 5, pp. 367-381, 2003.

[Alv04]   Alvarez Botero, J.C.: *Displacement-Based Design of Continuous Concrete Bridges under Transverse Seismic Excitation*. Master thesis, Rose School, Pavia, 2004.

[AM92]   Aschheim, M., Moehle, J.P.: Shear Strength and Deformability of RC Bridge Columns Subjected to Inelastic Cyclic Displacements. *UCB/EERC-92/04*. Earthquake Engineering Research Center, UC Berkeley, 1992.

[ASTRA03]   ASTRA: *Einführung der neuern Normen (Swisscodes), Übergangsfristen, Regelungen* [Introduction of the New Codes (Swisscodes), Transition Periods, Regulations]. Circular 64-10.1/SI, Bundesamt für Strassen (ASTRA), Bern, January 24th, 2003.

[ASTRA05a]   ASTRA: *Beurteilung der Erdbebensicherheit bestehender Brücken* [Assessment of the Seismic Safety of existing Bridges]. Documentation by Wenk, Th. for Bundesamt für Strassen (ASTRA), Bern 2005.

[ASTRA05b]   ASTRA: *Überwachung und Unterhalt der Kunstbauten der Nationalstrassen* [Monitoring and Maintenance of the Artificial Structures on National Roads]. Bundesamt für Strassen (ASTRA), Bern 2005.

[ASTRA08]   ASTRA: *Nationalstrassen in Bundesbesitz* [National Roads in Federal Property]. http://www.astra.admin.ch/org/00135/00153/00155/index.html?lang=de, Press Release by Bundesamt für Strassen (ASTRA), Bern 2008.

[ATC32]   ATC-32: Improved Sesimic Design Criteria for California Bridges: Provisional Recommendations. *Applied Technology Council*, Redwood City, California, 1996.

[ATC40]   ATC-40: Sesimic Evaluation and Retrofit of Concrete Buildings. *Applied Technology Council*, Redwood City, California, 1996.

[Bac90a]   Bachmann, H.: Absturzsicherung von Balkenbrücken für Erdbebeneinwirkung [Protection against Unseating of Girder Bridges under Earthquake Loading]. *Bautechnik*, Vol. 67, No. 7, pp. 233-235, 1990.

[Bac90b]   Bachmann, H.: Sind Brückenlager für Erdbebenkräfte auszubilden? [Is it necessary to design bridge bearings for seismic forces?]. *Bauingenieur*, Vol. 65, No. 11, p. 499-504, 1990.

[Bac+95]   Bachmann, H. et al: *Vibration Problems in Structures*. Birkhäuser Verlag, Basel 1995.

[Bac02]   Bachmann, H.: *Erdbebensicherung von Bauwerken* [Securing Building Structures for Earthquake]. Birkhäuser Verlag, Basel, 2002.

[BD06]   Bimschas, M., Dazio, A.: Bridge Assessment in Regions of Moderate Seismicity – A Case Study. *Proceedings of the First European Conference on Earthquake Engineering and Seismology*, Paper No. 1256, Geneva, September 3-8, 2006.

[BDP08a]   Beyer, K., Dazio, A., Priestley, M.J.N.: Seismic Design of Torsionally Eccentric Buildings with U-Shaped RC Walls. Rose School, *Report 2008/03*, IUSS Press, Pavia, 2008.

[BDP08b]   Beyer, K., Dazio, A., Priestley, M.J.N.: Quasi-Static Cyclic Tests of Two U-Shaped Reinforced Concrete Walls. *Journal of Earthquake Engineering.*, Vol. 12, No. 7, pp. 1023-1053, 2008.

References

[BE99]   Bommer, J.J., Elnashai, A.S.: Displacement Spectra for Seismic Design, *Journal of Earthquake Engineering.*, Vol. 3, No. 1, pp. 1-32, 1999.

[Ber87]   Bernal, D.: Amplification Factors for Inelastic Dynamic P-Δ Effects in Earthquake Analysis. *Earthquake Engineering and Structural Dynamics*, Vol. 15, No. 5, pp. 635-651, 1987.

[Ber09]   Berweger, A.: *Evaluation von Näherungsverfahren zur Seismischen Analyse von MDOF Brückensystemen* [Evaluation of Approximate Methods for the Seismic Analysis of MDOF Bridge Systems]. Master Thesis, ETH Zürich, 2009.

[Bim06]   Bimschas, M.: Seismic Safety of Existing Bridges in Regions of Moderate Seismicity. *Proceedings of the 6th International PhD Symposium in Civil Engineering*, Zurich, August 23-26, 2006.

[Bla04]   Blandon Uribe, C.A.: *Equivalent Viscous Damping Equations for Direct Displacement Based Design*. Master thesis, Rose School, Pavia, 2004.

[BM03]   Brühwiler, E., Menn, C.: *Stahlbetonbrücken* [Reinforced Concrete Bridges]. 3. Auflage, Springer Verlag, Wien, 2003.

[Boa98]   Boarnet, G.B.: Business Losses, Transportation Damage, and the Northridge Earthquake. *Journal of Transportation and Statistics*, Special Issue on the Northridge Earthquake, Vol. 1, No. 2, pp.49-63, 1998.

[BP05]   Blandon, C.A., Priestley, M.J.N.: Equivalent Viscous Damping Equations for Direct Displacement Based Design. *Journal of Earthquake Engineering*, Vol. 9, Special Issue 2, pp. 257-278, 2005.

[BRF04]   Biskinis, D.E., Roupakias, G.K., Fardis, M.N.: Degradation of Shear Strength of Reinforced Concrete Members with Inelastic Cyclic Displacements. *ACI Structural Journal*, Vol. 101, No. 6, pp. 773-783, 2004.

[Cal06]   Caltrans: Seismic Design Criteria. Version 1.4. *California Department of Transportation*, Sacramento, California, 2006.

[Car04]   Carr, A. J.: *RUAUMOKO – Volume 2: User Manual for the 2-Dimensional Version*, Ruaumoko2D, Department of Civil Engineering, University of Canterbury, Christchurch, New Zealand, 2004.

[CC04]   Chopra, A.K., Chintanapakdee, C.: Inelastic Deformation Ratios for Design and Evaluation of Structures: Single-Degree-of-Freedom Bilinear Systems. *Journal of Structural Engineering*, ASCE, Vol. 130, No. 9, pp. 1309-1319, 2004.

[Cha00]   Chang, S.E.: Transportation Performance, Disaster Vulnerability, and Long-Term Effects of Earthquakes. *EuroConference on Global Change and Catastrophe Risk Management*, Earthquake Risks in Europe, Laxenburg, Austria, July 6-9, 2000.

[CES09a]   CESMD: Information for Strong-Motion Station El Centro – Hwy8/Meloland Overpass, CGS-CSMIP Station No. 01336. *Center for Engineering Strong Motion Data* (CESMD), a cooperative effort by U.S. Geological Survey (USGS) and California Geological Survey (CGS), www.strongmotioncenter.org, 2009.

[CES09b]   CESMD: Information for Strong-Motion Station Rio Dell – Hwy101/Painter St. Overpass, CGS-CSMIP Station No. 89324. *Center for Engineering Strong Motion Data* (CESMD), a cooperative effort by U.S. Geological Survey (USGS) and California Geological Survey (CGS), www.strongmotioncenter.org, 2009.

[CG02]   Chopra, A.K., Goel, R.K.: A Modal Pushover Analysis Procedure for Estimating Seismic Demands for Buildings. *Earthquake Engineering and Structural Dynamics*, Vol. 31, No. 3, pp. 561-582, 2002.

References

[CGC04]   Chopra, A.K., Goel, R.K., Chintanapakdee, C.: Evaluation of a Modified MPA Procedure Assuming Higher Modes as Elastic to Estimate Seismic Demands. *Earthquake Spectra*, Vol. 20, No. 3, pp. 757-778, 2004.

[Cho01]   Chopra, A.K.: *Dynamics of Structures*. Second Edition, Prentice-Hall, Upper Saddle River, New Jersey 2001.

[CPS91]   Chai, Y.H., Priestley, M.J.N., Seible, F.: Seismic Retrofit of Circular Bridge Columns for Enhanced Flexural Performance. *ACI Structural Journal*, Vol. 88, No. 5, pp. 572-584, 1991.

[Daz00]   Dazio, A.: Entwurf und Bemessung von Tragwandgebäuden unter Erdbebeneinwirkung [Layout and Design of Buildings with Structural Walls under Earthquake Actions]. *PhD Dissertation No. 13739*, ETH Zürich, 2000.

[Daz05]   Dazio, A.: Tragfähigkeit von Betonbauten [Capacity of Concrete Structures]. SIA-Documentation D 0211, Überprüfung bestehender Gebäude bezüglich Erdbeben, Einführung in das Merkblatt SIA 2018 [Assessment of Existing Buildings for Earthquakes, Introduction into Guideline SIA 2018], *Schweizerischer Ingenieur- und Architekten-Verein*, Zürich 2005.

[DBB09]   Dazio, A., Beyer, K., Bachmann, H.: Quasi-Static Cyclic Tests and Plastic Hinge Analysis of RC Structural Walls. *Engineering Structures*, Vol. 31, No. 7, pp. 1556-1571, 2009.

[DKN07]   Dwairi, H.M., Kowalsky, M.J., Nau, J.M.: Equivalent Damping in Support of Direct Displacement-Based Design. *Journal of Earthquake Engineering.*, Vol. 11, No. 4, pp. 512-530, 2007.

[DWB99]   Dazio, A., Wenk, T., Bachmann, H.: Versuche an Stahlbetontragwänden unter zyklisch-statischer Einwirkung [Tests on RC walls under cyclic-static action]. *IBK Report Nr. 239*, Institute of Structural Engineering, ETH Zürich, 1999.

[EC0]   Eurocode 0: Eurocode – Basis of structural design. EN 1990, *Comité Européen de Normalisation (CEN)*, Bruxelles, April 2002.

[EC1-1-1] Eurocode 1-1-1: Actions on structures – Part 1-1: General actions – Densities, self-weight, imposed loads for buildings, EN 1991-1-1, *Comité Européen de Normalisation (CEN)*, Bruxelles, April 2002.

[EC2-1-1] Eurocode 2-1-1: Design of concrete structures — Part 1-1: General rules and rules for buildings, EN 1992-1-1, *Comité Européen de Normalisation (CEN)*, Bruxelles, December 2004.

[EC8-1-1] Eurocode 8-1-1: Design provisions for earthquake resistance of structures – Part 1-1: General rules - Seismic actions and general requirements for structures, ENV 1998-1-1, *Comité Européen de Normalisation (CEN)*, Bruxelles, 1994.

[EC8-1]   Eurocode 8-1: Design of structures for earthquake resistance – Part 1: General rules, seismic actions and rules for buildings, EN 1998-1, *Comité Européen de Normalisation (CEN)*, Bruxelles, December 2004.

[EC8-2]   Eurocode 8-2: Design of structures for earthquake resistance – Part 2: Bridges. EN 1998-2, *Comité Européen de Normalisation (CEN)*, Bruxelles, November 2005.

[EC8-3]   Eurocode 8-3: Design of structures for earthquake resistance – Part 3: Assessment and retrofitting of buildings. EN 1998-3, *Comité Européen de Normalisation (CEN)*, Bruxelles, June 2005.

[EGN06]   Empelmann, M., Girmscheid, M., Nowak, D.: Realistic Modelling of the Deformation Behaviour of Box Girder Bridges under Seismic Actions. *Proceedings of the First European Conference on Earthquake Engineering and Seismology*, Paper No. 1446 Geneva, September 3-8, 2006.

References

[EK88]   Eibl, J., Keintzel, E.: Seismic Shear Forces in RC Cantilever Shear Walls. *Proceedings of the 9th World Conference on Earthquake Engineering*, Volumne VI, Paper No. VI-9-1-1, Tokyo-Kyoto, Japan, 1988.

[EM05]   Elwood, K.J., Moehle, J.P.: Drift Capacity of Reinforced Concrete Columns with Light Transverse Reinforcement. *Earthquake Spectra*, Vol. 21, No. 1, pp. 71-89, 2005.

[Faj00]   Fajfar, P.: A Nonlinear Analysis Method for Performance-Based Seismic Design. *Earthquake Spectra*, Vol. 16, No. 3, pp. 573-592, 2000.

[FD94]   Fenwick, R., Davidson, B.: The Influence of Different Hysteretic Forms on Seismic P-Delta Effects. In: Park, R. (editor), *Seismic Design and Retrofitting of Reinforced Concrete Bridges*, Proceedings of the Second International Workshop held in Queenstown, New Zealand, 9-12 August 1994.

[FEMA273]   FEMA 273: NEHRP Guidelines for the Seismic Rehabilitation of Buildings. Prepared by Applied Technology Council (ATC-33 Project) for *Federal Emergency Management Agency*, Washington, D.C., 1997.

[FEMA356]   FEMA 356: Prestandard and Commentary for the Seismic Rehabilitation of Buildings. Prepared by American Society of Civil Engineers (ASCE) for *Federal Emergency Management Agency*, Washington, D.C., 1997.

[FEMA440]   FEMA 440: Improvement of Nonlinear Static Seismic Analysis Procedures. Prepared by Applied Technology Council (ATC-55 Project) for *Federal Emergency Management Agency*, Washington, D.C., 2005.

[FGD97]   Fajfar, P., Gašperšič, P., Drobnič, D.: A Simplified Nonlinear Method for Seismic Damage Analysis of Structures. In: Fajfar, P., Krawinkler, H. (eds.), Seismic Design Methodologies for the Next Generation of Codes, *Proceedings of the International Workshop on Seismic Design Methodologies for the Next Generation of Codes*, Bled, Slovenia, June 24th-27th, 1997.

[fib07]   Fédération Internationale du Béton: Seismic Bridge Design and Retrofit – Structural Solutions. *fib bulletin 39*, Lausanne, Switzerland, 2007.

[Fre98]   Freeman, S.A.: The Capacity Spectrum Method as a Tool for Seismic Design, *Proceedings of the 11th European Conference on Earthquake Engineering*, Paris, September 6-11th, 1998.

[Gaz06]   Gazetas, G.: Seismic Design of Foundatios and Soil-Structure Interaction. *Proceedings of the First European Conference on Earthquake Engineering and Seismology*, Keynote Adress K7, Geneva, September 3-8, 2006.

[GBP05]   Grant, D.N., Blandon, C.A., Priestley, M.J.N.: Modelling Inelastic Response in Direct Displacement-Based Design. Rose School, *Report 2005/03*, IUSS Press, Pavia, 2005.

[GC97]   Goel, R.K., Chopra, A.K.: Evaluation of Bridge Abutment Capacity and Stiffness during Earthquakes. *Earthquake Spectra*, Vol. 13, No.1, pp. 1-23, 1997.

[Goe96]   Goel, R.K.: Bridge Abutment Stiffness during Earthquakes. *Proceedings of the 11th World Conference on Earthquake Engineering*, Paper No. 1315, Acapulco, Mexico, 1996.

[GI06]   Guyader, A.C., Iwan, W.D.: Determining Equivalent Linear Parameters for Use in a Capacity Spectrum Method of Analysis. *Journal of Structural Engineering*, ASCE, Vol. 132, No. 1, pp. 59-67, 2006.

[GRD98]   Gordon, P., Richardson, H.W., Davis, B.: Transport-Related Impacts of the Northridge Earthquake. *Journal of Transportation and Statistics*, Special Issue on the Northridge Earthquake, Vol. 1, No. 2, pp.21-36, 1998.

[GS74]   Gülkan, P., Sozen M.: Inelastic Responses of Reinforced Concrete Structures to Earthquake Motions. *ACI Journal*, Vol. 71, No. 6, pp. 604-610, 1974.

References

[Guy04]   Guyader, A.C.: A Statistical Approach to Equivalent Linearization with Application to Performance-Based Engineering. *Report No. EERL 2004-04*, Earthquake Engineering Research Laboratory, California Institute of Technology, Pasadena, California, 2004.

[GV76]   Gasparini, D.A., Vanmarcke, E.H.: *SIMQKE – A Program for Artificial Motion Generation*. User's Manual and Documentation, Department of Civil Engineering, Massachusetts Institute of Technology, Boston, 1976.

[HHS96]   Harichandran, R.S., Hawwari, A., Sweidan, B.N.: Response of Long-Span Bridges to Spatially Varying Ground Motion. *Journal of Structural Engineering*, ASCE, Vol. 122, No. 5, pp. 476-484, 1996.

[Hin02]   Hines, E.M.: *Seismic Performance of Hollow Rectangular Reinforced Concrete Bridge Piers with Confined Corner Elements*. PhD thesis, University of California, San Diego, 2002.

[IA01]   Inel, M., Aschheim, M.A.: Nonlinear Embankment Contribution to the Seismic Response of Short Bridges. *Proceedings of the KEERC-MAE Joint Seminar on Risk Mitigation for Regions of Moderate Seismicity*, University of Illinois at Urbana-Champaign, August 5-8, 2001.

[IA04]   Inel, M., Aschheim, M.A.: Seismic Design of Columns of Short Bridges Accounting for Embankment Flexibility. *Journal of Structural Engineering*, ASCE, Vol. 130, No. 10, pp. 1515-1528, 2004.

[IG79a]   Iwan, W.D., Gates, N.C.: Estimating Earthquake Response of Simple Hysteretic Structures. *Journal of the Engineering Mechanics Division*, ASCE, Vol. 105, No. EM3, pp. 391-405, 1979.

[IG79b]   Iwan, W.D., Gates, N.C.: The Effective Period and Damping of a Class of Hysteretic Structures. *Earthquake Engineering and Structural Dynamics*, Vol. 7, No. 3, pp. 199-211, 1979.

[Ine02]   Inel, M.: *Displacement-based strategies for the performance-based seismic design of short bridges considering embankment flexibility*. PhD thesis, University of Illinois at Urbana-Champaign, 2002.

[Iwa80]   Iwan, W.D.: Estimating Inelastic Response Spectra from Elastic Spectra. *Earthquake Engineering and Structural Dynamics*, Vol. 8, No. 4, pp. 375-388, 1980.

[JCSS01]   JCSS: Probabilistic Model Code, Part 1 – Basis of Design, 12th Draft, *The Joint Committee on Structural Safety*, 2001.

[KBD08]   Kuhn, M., Bimschas, M., Dazio, A.: Influence of Soil Flexibility on the behavior of Existing Bridges in Regions of Moderate Seismicity. *Proceedings of the 14th World Conference on Earthquake Engineering*, Paper No. 05-02-0129, Beijing, China, October 12-17, 2008.

[KK08]   Kemfert, C., Kooths, S.: Die wirtschaftlichen Folgen von Bahnstreiks [The Economic Consequences of Railway Strikes]. DIW Wochenbericht Nr. 03/2008, *Deutsches Institut für Wirtschaftsforschung*, http://www.diw.de/documents/publikationen/ 73/78044/08-3-1.pdf, Berlin 2008.

[KN92]   Krawinkler, H., Nassar, A.A.: Seismic Design Based on Ductility and Cumulative Damage Demands and Capacities. In: Fajfar, P., Krawinkler, H. (eds.), *Nonlinear seismic analysis and design of reinforced concrete buildings*, Elsevier Applied Science, New York, 1992.

[KP00]   Kowalsky, M.J., Priestley, M.J.N.: Improved Analytical Model for Shear Strength of Circular Reinforced Concrete Columns in Seismic Regions, *ACI Structural Journal*, Vol. 97, No. 3, pp. 388-396, 2000.

References

[KPK09]   Katsaras, C.P., Panagiotakos, T.B., Kolias, B.: Effect of Torsional stiffness of prestressed concrete box girders and uplift of abutment bearings on seismic performance of bridges. *Bulletin of Earthquake Engineering*, Vol. 7, No. 2, pp. 363-375, 2009.

[KS98]   Krawinkler, H., Seneviratna, G.D.P.K.: Pros and Cons of a Pushover Analysis of Seismic Performance Evaluation. Engineering Structures, Vol. 20, Nos. 4-6, pp. 452-464, 1998.

[Kuh07]   Kuhn, M.: *Seismische Analyse bestehender Schweizer Brücken mittels numerischer Methoden* [Seismic Analysis of Existing Swiss Bridges by Means of Numerical Methods], Diploma thesis, ETH Zürich, Switzerland, 2007.

[Kur09]   Kurmann, D.: *Seismic Analysis of Existing Bridges with Detailing Deficiencies*. Master Thesis, ROSE School Pavia, conducted at ETH Zürich, Switzerland, 2009.

[KUBA05]   ASTRA: *KUBA-DB – Kunstbauten Datenbank* [Database of Artificial Structures]. CADRZ for Bundesamt für Strassen (ASTRA), Bern 2005.

[Lan+07]   Lang, H.-J., Huder, J., Amann, P., Puzrin, A.M.: *Bodenmechanik und Grundbau* [Soil Mechanics and Foundation Engineering]. 8. ergänzte Auflage, Springer Verlag, Berlin 2007.

[Lup+05]   Lupoi, A., Franchin, P., Pinto, P.E., Monti, G.: Seismic design of bridges accounting for spatial variability of ground motion. *Earthquake Engineering and Structural Dynamics*, Vol. 34, No. 4, pp. 327-348, 2005.

[Lyn+96]   Lynn, A.C., Moehle, J.P., Mahin, S.A., Holmes, W.T.: Seismic Evaluation of Existing Reinforced Concrete Building Columns. *Earthquake Spectra*, Vol. 12, No. 4, pp. 715-739, 1996.

[MA03]   Miranda, E., Akkar, S.D.: Dynamic Instability of Simple Structural Systems. *Journal of Structural Engineering*, ASCE, Vol. 129, No. 12, pp. 1722-1726, 2003.

[Mac94]   MacRae, G.A.: P-Δ Effects on Single-Degree-of-Freedom Structures in Earthquakes. *Earthquake Spectra*, Vol. 10, No. 3, pp. 539-568, 1994.

[Mar85]   Maragakis, E.: A Model for the Rigid Body Motions of Skew Bridges. *Report No. EERL 85-02*, Earthquake Engineering Research Laboratory, California Institute of Technology, Pasadena, California, 1985.

[MB94]   Miranda, E., Bertero, V.V.: Evaluation of Strength Reduction Factors for Earthquake-Resistant Design. *Earthquake Spectra*, Vol. 10, No. 2, pp. 357-379, 1994.

[Mir93]   Miranda, E.: Site-Dependent Strength-Reduction Factors. *Journal of Structural Engineering*, ASCE, Vol. 119, No. 12, pp. 3503-3519, 1993.

[Mir00]   Miranda, E.: Inelastic Displacement Ratios for Structures on Firm Sites. *Journal of Structural Engineering*, ASCE, Vol. 126, No. 10, pp. 1150-1159, 2000.

[Mir01]   Miranda, E.: Estimation of Inelastic Deformation Demands of SDOF Systems. *Journal of Structural Engineering*, ASCE, Vol. 127, No. 9, pp. 1005-1012, 2001.

[MJ87]   Maragakis, E.A., Jennings, P.C.: Analytical Models for the Rigid Body Motions of Skew Bridges. *Earthquake Engineering and Structural Dynamics*, Vol. 15, No. 8, pp. 923-944, 1987.

[MNP96]   Monti, G., Nuti, C., Pinto, P.E.: Nonlinear response of bridges under multisupport excitation. *Journal of Structural Engineering*, ASCE, Vol. 122, No. 10, pp. 1147-1159, 1996.

[MP98]   Monti, G., Pinto, P.E.: Effects of multi-support excitation on isolated bridges. In: Proceedings of the U.S.-Italy Workshop on Seismic Protective Systems for Bridges, edited by I.M. Friedland, M.C. Constantinou, *Technical Report MCEER-98-0015*, pp.225-247, 1998.

References

[MPP88]   Mander, J.B., Priestley, M.J.N., Park, R.: Theoretical Stress-Strain Model for Confined Concrete. *Journal of Structural Engineering*, ASCE, Vol. 114, No. 8, pp. 1804-1826, 1988.

[MPT93]   MacRae, G.A., Priestley, M.J.N., Tao, J.: P-Δ Design in Seismic Regions. *Report No. SSRP - 93/05*, Department of Applied Mechanics and Engineering Sciences, University of California, San Diego, 1993.

[MR94]   McCallen, D.B., Romstad, K.M.: Dynamic Analyses of a Skewed Short-Span, Box-Girder Overpass. *Earthquake Spectra*, Vol. 10, No.4, pp. 729-755, 1994.

[MR02]   Miranda, E., Ruiz-García, J.: Evaluation of Approximate Methods to Estiamte Maximum inelastic Displacement Demands. *Earthquake Engineering and Structural Dynamics*, Vol. 31, No. 3, pp. 539-560, 2002.

[MWC03]   Melek, M., Wallace, J.W., Conte, J.P.: Experimental Assessment of Columns with Short Lap Splices Subjected to Cyclic Loads. *PEER report 2003/04*, Pacific Earthquake Engineering Research Center, 2003.

[Neg+00]   Negro, P., Paolucci, R., Pedretti, S., Faccioli, E.: Large Scale Soil-Structure Interaction Experiments on Sand under Cyclic Loading. *Proceedings of the 12th World Conference on Earthquake Engineering*, Paper No. 1191, Auckland, New Zealand, 2000.

[NH82]   Newmark, N.M., Hall, W.J.: *Earthquake Spectra and Design*. Earthquake Engineering Research Institute (EERI), Berkeley, California, 1982.

[NK91]   Nassar, A.A., Krawinkler, H.: Seismic Demands for SDOF and MDOF Systems. *Report No. 95*, The John A. Blume Earthquake Engineering Center, Stanford University, California, 1991.

[NZS3101]   NZS 3101: Concrete Structures Standard, Part 1 – The Design of Concrete Structures. *Standards Council*, Wellington, New Zealand, 2006.

[PA85]   Park, Y.J., Ang, A.H.S.: Mechanistic Seismic Damage Model for Reinforced Concrete. *Journal of Structural Engineering*, ASCE, Vol. 111, No. 4, pp. 722-739, 1985.

[PBM90]   Paulay, T., Bachmann, H., Moser, K.: *Erdbebenbemessung von Stahlbetonbauten* [Seismic Design of Reinforced Concrete Buildings]. Birkhäuser Verlag, Basel, 1990.

[PCK07]   Priestley, M.J.N., Calvi, G.M. and Kowalsky, M.J.: *Displacement-Based Seismic Design of Structures*. IUSS Press, Pavia, Italy 2007.

[PE00]   Petak, W., Elahi S.: The Northridge Earthquake USA and its Economic and Social Impacts. *Proceedings of the EuroConference on Global Change and Catastrophe Risk Management*, Earthquake Risks in Europe, Laxenburg, Austria, July 6-9, 2000.

[PE05]   Price, T.E., Eberhard, M.O.: Factors Contributing to Bridge-Embankment Interaction. *Journal of Structural Engineering*, ASCE, Vol. 131, No. 9, pp. 1345-1354, 2005.

[Pet+08]   Petrini, L., Maggi, C., Priestley, M.J.N., Calvi, G.M.: Experimental Verification of Viscous Damping Modeling for Inelastic Time History Analyzes. *Journal of Earthquake Engineering*, Vol. 12, Supplement 1, pp. 125-145, 2008.

[PG05]   Priestley, M.J.N., Grant, D.N.: Viscous Damping in Seismic Design and Analysis. *Journal of Earthquake Engineering*, Vol. 9, Special Issue 2, pp. 229-255, 2005.

[PMT03]   Pinto, A.V., Molina, J., Tsionis, G.: Cyclic Tests on Large-Scale Models of Existing Bridge Piers with Rectangular Hollow Cross-Section. *Earthquake Engineering and Structural Dynamics*, Vol. 32, No. 13, pp. 1995-2012, 2003.

[Pop73]   Popovics, S.: A Numerical Approach to the Complete Stress-Strain Curve of Concrete. *Cement and Concrete Research*, Vol. 3, pp. 583-599, 1973.

References

[PP92]   Paulay, T., Priestley, M.J.N.: *Seismic Design of Reinforced Concrete and Masonry Buildings*. John Wiley & Sons, New York 1992.

[PP07]   Pettinga, J.D., Priestley, M.J.N.: Accounting for P-Delta Effects in Structures when using Direct Displacement-Based Design. Rose School, *Report 2007/02*, IUSS Press, Pavia, 2007.

[Pri03]   Priestley, M.J.N.: *Myths and Fallacies in Earthquake Engineering, Revisited*. The Ninth Mallet Milne Lecture. IUSS Press, Pavia, Italy 2003.

[PRK87]   Park, Y.J., Reinhorn, A.M., Kunnath, S.K.: IDARC − Inelastic Damage Analysis of Reinforced Concrete Frame − Shear-Wall Structures, *Technical Report NCEER-87-0008*, National Center for Earthquake Engineering Research, 1987

[PSC96]   Priestley, M.J.N., Seible, F., Calvi, G.M.: *Seismic Design and Retrofit of Bridges*. John Wiley & Sons, New York 1996.

[PVX94]   Priestley, M.J.N., Verma, R., Xiao, Y.: Seismic Shear Strength of Reinforced Concrete Columns, *Journal of Structural Engineering*, ASCE, Vol. 120, No. 8, pp. 2312-2327, 1994.

[RM03]   Ruiz-García, J., Miranda, E.: Inelastic Displacement Ratios for Evaluation of Existing Structures. *Earthquake Engineering and Structural Dynamics*, Vol. 32, No. 8, pp. 1237-1258, 2003.

[RRC02]   Rodriguez, M.E., Restrepo, J.I., Carr, A.J.: Earthquake-Induced Floor Horizontal Accelerations in Buildings. . *Earthquake Engineering and Structural Dynamics*, Vol. 31, No. 3, pp. 693-718, 2002.

[RVK06]   Reinhorn, A.M., Valles-Mattox, R., Kunnath, S.: IDARC 2D Version 6.1, User's Guide. *http://civil.eng.buffalo.edu/idarc2d50*, Department of Civil, Structural, and Environmental Engineering, University at Buffalo, New York, February 2006.

[SB89]   Somaini, D., Bachmann, H.: Erdbebenverhalten von Balkenbrücken mit fester Lagerung in Längsrichtung [Earthquake response of girder bridges with fixed bearings in longitudinal direction]. *IBK Report Nr. 171*, Institute of Structural Engineering, ETH Zürich, 1989.

[SE05]   Seligson, H.A., Eguchi, R.T.: The True Cost Of Earthquake Disasters: An Updated Tabulation Of Losses For The 1994 Northridge Earthquake, *Proceedings of the International Symposium on Earthquake Engineering*, Awaji, Japan, January 13 − 16, 2005.

[SGS88]   Sun, J.I., Golesorkhi, R., Seed, H.B.: Dynamic Moduli and Damping Ratios for Cohesive Soils. *Report No. UCB/EERC-88/15*, Earthquake Engineering Research Center, University of Californiy, Berkeley, 1988.

[SI70]   Seed, H.B., Idriss, I.M.: Soil Moduli and Damping Factors for Dynamic Response Analyses. *Report No. EERC 70-10*, Earthquake Engineering Research Center, University of Californiy, Berkeley, 1970.

[SIA160-56]   SIA 160: Normen für die Belastungsannahmen, die Inbetriebnahme und die Überwachung der Bauten [Codes for Assumptions of Actions, the Operation, and the Monitoring of Structures]. *Schweizerischer Ingenieur- und Architekten-Verein*, Zürich 1956.

[SIA160-70]   SIA 160: Norm für die Belastungsannahmen, die Inbetriebnahme und die Überwachung der Bauten [Code for Assumptions of Actions, the Operation, and the Monitoring of Structures]. *Schweizerischer Ingenieur- und Architekten-Verein*, Zürich 1970.

[SIA160-89]   SIA 160: Einwirkungen auf Tragwerke [Actions on Structures]. *Schweizerischer Ingenieur- und Architekten-Verein*, Zürich 1989.

References

[SIA161-56]   SIA 161: Normen für die Berechnung und die Ausführung von Stahlbauten [Codes for the Calculation and Construction of Steel Structures]. *Schweizerischer Ingenieur- und Architekten-Verein*, Zürich 1956.

[SIA162-56]   SIA 162: Normen für die Berechnung und Ausführung der Beton- und Eisenbetonbauten [Codes for the Calculation and Construction of Concrete and Reinforced Concrete Structures]. *Schweizerischer Ingenieur- und Architekten-Verein*, Zürich 1956.

[SIA162-68]   SIA 162: Norm für die Berechnung, Konstruktion und Ausführung von Bauwerken aus Beton, Stahlbeton und Spannbeton [Codes for the Calculation, Detailing, and Construction of Plain Concrete, Reinforced Concrete, and Prestressed Concrete Structures]. *Schweizerischer Ingenieur- und Architekten-Verein*, Zürich 1968.

[SIA162-89]   SIA 162: Betonbauten [Concrete Structures]. *Schweizerischer Ingenieur- und Architekten-Verein*, Zürich 1989, Teilrevision 1993.

[SIA260]   SIA 260: Grundlagen der Projektierung von Tragwerken [Basis of Structural Design]. *Schweizerischer Ingenieur- und Architekten-Verein*, Zürich 2003.

[SIA261]   SIA 261: Einwirkungen auf Tragwerke [Actions on Structures] . *Schweizerischer Ingenieur- und Architekten-Verein*, Zürich 2003.

[SIA262]   SIA 262: Betonbau [Concrete Structures]. *Schweizerischer Ingenieur- und Architekten-Verein*, Zürich 2003.

[SIA263]   SIA 262: Stahlbau [Steel Structures]. *Schweizerischer Ingenieur- und Architekten-Verein*, Zürich 2003.

[SIA462]   SIA 462: Beurteilung der Tragsicherheit bestehender Bauwerke [Assessment of the Safety of Existing Structures]. *Schweizerischer Ingenieur- und Architekten-Verein*, Zürich 1994.

[SIA2018]   SIA 2018: Überprüfung bestehender Gebäude bezüglich Erdbeben [Assessment of existing buildings concerning earthquakes]. *Schweizerischer Ingenieur- und Architekten-Verein*, Zürich, 2004.

[SK97]   Studer, J.A., Koller, M.G.: *Bodendynamik*. Springer Verlag, Berlin, 1997.

[SKP03a]   Sextos, A.G., Kappos, A.J., Pitilakis K.D.: Inelastic dynamic analysis of RC bridges accounting for spatial variability of ground motion, site effects and soil-structure interaction phenomena. Part 1: Methodology and analytical tools. *Earthquake Engineering and Structural Dynamics*, Vol. 32, No. 4, pp. 607-627, 2003.

[SKP03b]   Sextos, A.G., Kappos, A.J., Pitilakis K.D.: Inelastic dynamic analysis of RC bridges accounting for spatial variability of ground motion, site effects and soil-structure interaction phenomena. Part 2: Parametric study. *Earthquake Engineering and Structural Dynamics*, Vol. 32, No. 4, pp. 629-652, 2003.

[SM04]   Sezen, H., Moehle, J.P.: Shear Strength Model for Lightly Reinforced Concrete Columns. *Journal of Structural Engineering*, ASCE, Vol. 130, No. 11, pp. 1692-1703, 2004.

[Som85]   Somaini, D.R.*:* Erdbebenverhalten schwimmend gelagerter Balkenbrücken bei Berücksichtigung der Boden-Struktur-Interaktion und der horizontal wandernden Wellen [Seismic Behavior of Floating Girder Bridges Considering the Soil-Structure-Interaction and the Horizontally Travelling Waves]. *PhD Dissertation No. 7793*, ETH Zürich, 1985.

[SS76]   Shibata, A., Sozen, M.: Substitute Structure Method for Seismic Design in R/C. *Journal of the Structural Division*, ASCE, Vol. 102, No. 1, 1976.

[SS06]   SeismoSoft: SeismoStruct - A Computer Program for Static and Dynamic Nonlinear Analysis of Framed Structures, Version 4.0.3 (Build 30), *www.seismosoft.com*, 2008.

References

[SSD00]   Shinozuka, M., Saxena, V., Deodatis, G.: Effect of spatial variation of ground motion on highway structures. *Technical Report MCEER-00-0013*, Multidisciplinary Center for Earthquake Engineering Research (MCEER), University at Buffalo, New York, 2000.

[SWI84]   Seed, H.B., Wong, R.T., Idriss, I.M., Tokimatsu, K.: Moduli and Damping Factors for Dynamic Analyses of Cohesionless Soils. *Report No. UCB/EERC-84/14*, Earthquake Engineering Research Center, University of Californiy, Berkeley, 1984.

[TDL98]   Tremblay R., Duval C., Léger P.: Effects of Viscous Damping Models, Hysteretic Models and Ground Motion Characteristics on Seismic P-Delta Strength Amplification Factors. In: Usami, T., Itoh, Y. (editors), *Stability and Ductility of Steel Structures*, Elsevier, pp. 103-118, 1998.

[TF99]   Tolis, S.V., Faccioli, E.: Displacement Design Spectra, *Journal of Earthquake Engineering*, Vol. 3, No. 1, pp. 107-125, 1999.

[Val+96]   Valles, R.E., Reinhorn, A.M., Kunnath, S.K., Li, C., Madan, A.: IDARC 2D Version 4.0 – A Program for the Inelastic Damage Analysis of Buildings. *Technical Report NCEER-96-0010*, National Center for Earthquake Engineering Research, State University of New York at Buffalo, 1996.

[VFF94]   Vidic, T., Fajfar, P., Fischinger, M.: Consistent Inelastic Design Spectra: Strength and Displacement. *Earthquake Engineering and Structural Dynamics*, Vol. 23, No. 5, pp. 507-521, 1994.

[Wat06]   Watanabe, Y.: Impact of the Kobe Earthquake on transportation and port logistics. Advanced Topics for Marine Technology and Logistics, SOI Asia Course, *www.soi.wide.ad.jp/class/20060026*, Tokyo University of Marine Science and Technology, 2006.

[WK04]   Watanabe, G., Kawashima, K.: Effectiveness of Cable-Restrainer for Mitigating Rotation of a Skewed Bridge Subjected to Strong Ground Shaking. *Proceedings of the 13th World Conference on Earthquake Engineering*, Paper No. 789, Vancouver, Canada, 2004.

[WBL87]   Werner, S.D., Beck, J.L., Levine, M.B.: Seismic Response Evaluation of Meloland Road Overpass Using 1979 Imperial Valley Earthquake Records. *Earthquake Engineering and Structural Dynamics*, Vol. 15, No. 2, pp. 249-274, 1987.

[Wer+94]   Werner, S.D., Crouse, C.B., Katafygiotis, L.S., Beck, J.L.: Use of Strong Motion Records for Model Evaluation and Seismic Analysis of a Bridge Structure. *Proceedings of the 5th U.S. National Conference on Earthquake Engineering*, Vol. 1, pp. 511-520, Chicago, Illinois, July 10-14, 1994.

[WS86]   Wolf, J.P., Somaini, D.R.: Approximate Dynamic Model of Embedded Foundation in Time Domain. *Earthquake Engineering and Structural Dynamics*, Vol. 14, No. 5, pp. 683-703, 1986.

[WT90a]   Wilson, J.C., Tan, B.S.: Bridge Abutments: Formulation of Simple Model for Earthquake Response Analysis. *Journal of Engineering Mechanics*, ASCE, Vol. 116, No. 8, pp. 1828-1837, 1990.

[WT90b]   Wilson, J.C., Tan, B.S.: Bridge Abutments: Assessing Their Influence on Earthquake Response of Meloland Road Overpass. *Journal of Engineering Mechanics*, ASCE, Vol. 116, No. 8, pp. 1838-1856, 1990.

[Yaz09]   Yazgan, U.: The Use of Post-Earthquake Residual Displacements as a Performance Indicator in Seismic Assessment. *PhD Dissertation No. 18645*, ETH Zürich, 2009.

[YK03]   Yashinsky, M., Karshenas, M.J.: *Fundamentals of Seismic Protection for Bridges*. MNO-9, Earthquake Engineering Research Institute (EERI), Oakland, California 2003.

References

[ZM02]   Zhang, J., Makris, N.: Kinematic Response Functions and Dynamic Stiffnesses of Bridge Embankments. *Earthquake Engineering and Structural Dynamics*, Vol. 31, No. 11, pp. 1933-1966, 2002.